The Influences of Lateral Ground-Tilting on Channel Morphology and Alluvial Architecture

by

Jeffrey Peakall

Submitted in accordance with the requirements
for the degree of Doctor of Philosophy

Department of Earth Sciences and School of Geography
University of Leeds

September 1995

The candidate confirms that the work submitted is his own and that appropriate credit has been given where reference has been made to the work of others.

CONTAINS
PULLOUTS

ABSTRACT

This thesis characterises and quantifies the influence of lateral ground-tilting on rivers in terms of: i) channel planform changes and migration style, ii) temporal and spatial patterns of channel movement, and, iii) the preserved alluvial architecture formed by aggrading fluvial systems. A dual field and physical modelling approach is used to examine the impact of tilting on river channels at a range of temporal and spatial scales. Fieldwork was undertaken on the Carson River, Nevada, USA which has been proposed as an example of avulsive downdip channel movement towards an active basin-bounding fault (Leeder, 1993). Froude scale models of both meandering and braided rivers were established in a stream table which could simulate aggradation and be tilted laterally.

Quantification of the Holocene history of the Carson River, combined with independent dating of movements on the basin-bounding fault, allows the alluvial-tectonic relationships to be analysed. In addition to local tectonics, factors which may also affect channel movement such as climate change, regional periods of channel incision and intrinsic channel avulsion are investigated. The Carson River is shown to possess a more complex spatial relationship with fault movement and lateral tilting than that envisaged by Leeder (1993). Phases of channel onlap towards the locus of subsidence after fault events are separated by channel offlap during periods of tectonic quiescence. In addition, lag times between faulting and channel movement appear to be short.

The preserved alluvial architecture modelled in flume experiments on aggrading braided streams is subdivided into a number of key depositional niches and their geometries quantified. A number of cross-stream and vertical variations in niche geometries can be attributed to the timing, magnitude and frequency of imposed lateral tilting, and confirm Leeder and Alexander's (1987) conceptual model of progressive downdip channel movement in response to lateral tilting. No unambiguous relationship between channel bend parameters and imposed lateral ground-tilting could be defined in the meandering river experiments because the rate and type of bend development masks the impact of tilting. However, the rate of channel movement towards the downtilted margin appears to increase after tilting and be directly related to tilt magnitude.

A new model of progressive downdip channel migration in response to lateral tilting is presented which resolves the incompatibility of previous models. In addition, a criterion based on the rate of tilting is proposed in order to distinguish between channels that respond to tectonic tilting either by avulsion or by gradual downdip migration.

ACKNOWLEDGEMENTS

My thanks to Joanne Wilkin for braving the large Grizzly Bear in Montana and to Jon Freeman, Neil Woodhouse, Drs Tim Salter, Jim Best, Phil Ashworth, Richard Collier and Professor Mike Leeder for help during the Nevada fieldwork. Ann Wintle and Michèle Clarke are thanked for the luminescence dating and subsequent discussion. My thanks to all who allowed me to borrow equipment, namely John Bridge for the vibracore rig and associated training, Dr J. Trexler for the auger, and Alan Ramelli and Jim Yount for the loan of and help with the GPS equipment. Alan Ramelli and Jim Yount were also kind enough to allow me access to the Genoa Fault trenching data. Arnold Settelmeyer and his family are thanked for their help in locating early aerial photographs and the archaeological report. The author is grateful to all the landowners and the local Gun Club for land access, notably Arnold Settelmeyer, and Brian Wallace the Chairman of the Washoe Tribe. Finally, my thanks to the following who also aided the Carson River fieldwork; Hal Turner at the Dept. of Transportation, Douglas County Soil Conservation Service, John Bell, Bob Watters, Bureau of Land Management, USGS Water Resources-Carson City, Nevada State Parks, Jack Moore at the Douglas County Assessor's office, and the State Department of Water Resources for the 1938 air photographs.

The sed lab and George offices are thanked for camaraderie under fire, cups of tea and a healthy degree of cynicism. Notables include Mike Stewart, John Livesey, Stuart M^{c}Lelland, Pete Talling, Joanne Wilkin, Clare Stephens, Julie Roden, James Maunder, Karen Braithwaite, Alma López-Avilés, Neil Woodhouse and Tracy Harris. My flatmates over the past four years are thanked for yet more cups of tea: the ubiquitous Mike Stewart, Tracy Harris and Pete Talling, plus Sandra Collier, Barbara Kidd, Jon Rathjen, Mike Burgin, Kate Le Breton, Lotta Hagström and Angela Purcell. My thanks to Andrea Day for smiling, laughing and generally cheering me up.

My parents and family are thanked enormously for their friendship, support during the writing of this thesis, and for funding my early university years. Alison Manson, Lois Wright, Alistair French and David Appleyard kindly produced a number of the illustrations and are thanked for both their help and cheerfulness. Sean Bennett, Mike Kirkby and Mike Bowman (BP) provided much helpful advice and discussion. Professor Mike Leeder is thanked for his boundless enthusiasm and uncanny ability to always make the world look brighter. However, my greatest thanks must go to the long suffering and extremely patient, Drs. Phil Ashworth and Jim Best. This research has greatly benefited from their skill, wisdom, perseverance, and wit.

Finally, my thanks to BP Exploration who sponsored this project and whose share price appears to have mirrored the progress of this thesis; some deep lows, wild fluctuations and at the time of submission close to an all time high.

CONTENTS

Chapter 5. Experimental Study on the Effects of Lateral Tilting on Meandering and Braided Rivers 113

LIST OF FIGURES

Chapter 1. Introduction and Background to Study

Chapter 2. The Influence of Lateral Tilt On Rivers

Chapter 3. Theoretical Background to Physical Modelling

Chapter 4. Experimental Apparatus and Procedure

Chapter 5. Experimental Study on the Effects of Lateral Tilting on Meandering and Braided Rivers

Chapter 6. Meander Morphometry and Palaeohydrological Analysis

Chapter 7. The Impact of Half-Graben Neotectonics on Axial River Development: The Carson River, Nevada

Appendix B. Explanation of the Meander Morphometry Analysis Program (M-MAP)

Appendix C. Additional Ground Surveys of Carson River Channel Belt Meander Bends

LIST OF TABLES

LIST OF SYMBOLS

Symbol	Description
A	Channel cross-sectional area (m^2)
A_b	Channel bankfull cross-sectional area (m^2)
A_g	Glacierized area (m^2)
B	Baseflow of a hydrograph (m^3 s^{-1})
C	Roughness function / constant of integration, from logarithmic 'law of the wall'
C_d	Drag coefficient for a V-notch weir
C_{D0}	Drag coefficient for a solitary particle in relative motion with an infinite fluid
C_H	Central height of a meander bend (m)
d	Flow depth (m)
d_*	Reference value of d in the Bagnold (1980) equation (m)
d_b	Channel bankfull mean depth (= A_b/w_b) (m)
d_c	Critical flow depth (m)
d_m	Mean depth of channel (m)
d_{max}	Maximum depth of channel (between banktop and thalweg) (m)
D	Grain-size diameter (m)
D_{50}	The 50th percentile of the grain-size diameter (m)
D_*	Reference value of D in the Bagnold (1980) equation (m)
e	The base of natural logarithms
EXP	The exponential function, calculates e^X
f	Frictional resistance (N)
F	Force (N); Frequency of a length
Fr	Froude number
g	Gravitational constant (m s^{-2})
h_f	Frictional head loss (m)
H	Arc height (m)
H_E	Energy flux per unit weight flux (m)
i_b	Transport rate of bedload by immersed weight per unit width (kg m^{-1} s^{-1})
$(i_b)_*$	Reference value of i_b in the Bagnold (1980) equation (kg m^{-1} s^{-1})
k	Constant (units vary)
k_s	Surface roughness (m)
L	Length (dimension); denotes a length scale when used with subscripts
L_a	Arc length (m)
L_{arc}	Arc wavelength (m)
L_c	Chord length, between inflection points (m)

L_m	Meander wavelength (m)
L_{max}	Maximum meander wavelength (m)
ln	Natural logarithm
m	Power in gamma function for hydrograph
M	Mass (dimension); Percentage of silt-clay in the channel perimeter; earthquake magnitude
M_b	Meander belt width (m)
M_B	Bodywave magnitude
M_L	Local magnitude
M_s	Surface wave magnitude
M_w	Moment magnitude
n	Manning's resistance coefficient 'n'
nA	Niche percentage area occurrence (%)
nL	Niche length (m)
nL_m	Mean niche length (m)
nL_{max}	Maximum niche length (m)
p	Probability
q	Fluid discharge per unit width (m^3 m^{-1} s^{-1})
Q	Fluid discharge (m^3 s^{-1})
Q_b	Bankfull discharge (m^3 s^{-1})
Q_m	Mean / Average discharge (m^3 s^{-1})
Q_{max}	Maximum discharge for hydrograph (m^3 s^{-1})
Q_{mm}	Mean discharge of the month of maximum discharge (m^3 s^{-1})
Q_o	Initial discharge for hydrograph (m^3 s^{-1})
Q_s	Calculated solution for hydrograph discharge (m^3 s^{-1})
Q_y	Mean discharge of the maximum year of discharge (m^3 s^{-1})
$Q_{1.5}$	Discharge of the 1.5 year recurrence interval (m^3 s^{-1})
r	Pearson's product-moment correlation coefficient
r^2	Coefficient of determination
r_c	Radius of curvature (m)
R	Hydraulic radius (m)
Re	Flow Reynolds number
Re_*	Grain Reynolds number
s	Distance between series datapoints (m)
S_b	Channel bed slope
S_g	Effective gravity gradient
$S_N\%$	Percentage scatter about the mean
SC_{bd}	Silt-clay content of bed material (%)

SC_{bk}	Silt-clay content of bank material (%)
SE	Standard error of the estimate in regression analysis (log units or % as stated)
St	Strouhal number
t	Time (s)
t_{pk}	Time at which peak discharge is reached in hydrograph (s)
t_1	Initial value of time in gamma function for hydrograph (s)
T	Time (dimension); Temperature (°C)
U_*	Shear velocity (m s^{-1})
V	Downstream velocity (m s^{-1})
V_F	Terminal fall velocity (m s^{-1})
w	Channel width (m)
w_b	Bankfull width (m)
w_u	Unit width (m)
Y	Bend amplitude (m); Cross-stream distance (m)
Z_d	Drainage density (km / km^2)
We	Weber number
α	Angle of V-notch weir (degrees)
β	Surface energy correction factor
γ_s	Immersed specific weight of solids (kg m^{-1} s^{-2})
δ_{sub}	Thickness of the viscous sub-layer (m)
θ	Curvature of meander bend or meander segment (degrees or radians)
θ_t	Dimensionless time
λ	Scale factor; Darcy-Weisbach friction factor
λ_w	Wavelength (m)
μ	Dynamic / absolute / molecular viscosity (kg m^{-1} s^{-1})
ν	Kinematic viscosity (m s^{-1})
Π	Dimensionless group
ρ	Density of fluid (kg m^{-3})
ρ_s	Density of sediment (kg m^{-3})
σ	Surface tension (N m^{-1})
σ_n	Standard deviation
τ_c^*	Dimensionless critical shear stress
τ_c	Critical bed shear stress (N m^{-2})
ϕ	Pipe diameter (m)
ω	Stream power per unit bed area (kg m^{-1} s^{-1})
ω_o	Nominal threshold value of ω for initial bed movement (kg m^{-1} s^{-1})
$_{m,p}$	Subscripts denote model and prototype respectively

LIST OF ACRONYMS

AMS	Accelerator mass spectrometry
ASCII	American standard code for information interchange
CCTV	Closed circuit television
CNSB	Central Nevada seismic belt
CSV	Comma separated values
DOS	Disk operating system
dpi	Dots per inch
ECSB	Eastern California seismic belt
ED	Equivalent dose
EDM	Electronic distance meter
FSM	Froude scale model
GBNWSS	Great Basin and northern west sagebrush steppe
GPS	Global positioning system
IRSL	Infra-red stimulated luminescence
M-MAP	Meander morphometry analysis program
MRE	Most recent event
NIH	National Institutes of Health
NSNFFZ	Northern Sierra Nevada frontal fault system
OLS	Ordinary least squares
OSL	Optically stimulated luminescence
PDF	Probability density function
PE	Penultimate event
PVC	Polyvinyl chloride
TL	Thermoluminescence
VCR	Video cassette recorder
WLSZ	Walker lane shear zone

Nevada offers extremes of weather and climate...
it is the direst of the fifty states.
(Houghton *et al.*, 1975).

If one tells the truth, one is sure, sooner or later,
to be found out.
(Oscar Wilde, 1894).

Chapter 1. Introduction and Background to Study

1.1 Introduction

Over the last fifteen years there has been an increasing realisation of the importance of local tectonics in influencing the development of river channels. Examples of channel response to zones of uplift and subsidence have been documented for both rivers and canals in terms of changes in channel pattern, hydraulic geometry and long profile (e.g. Leary *et al.*, 1981; Russ, 1982; Burnett and Schumm, 1983; Ouchi, 1985; Schumm, 1986; Gregory and Schumm, 1987; Wells and Dorr, 1987a; Jorgensen, 1990). Experimental studies have also examined the response of rivers to uplift and subsidence (Ouchi, 1985; Jin and Schumm, 1987). In contrast to the studies on tectonically-influenced axial changes in river morphology, there have been relatively few field studies on the magnitude and effects of *lateral* tilt on modern rivers and their deposits (e.g. Nanson, 1980; Alexander and Leeder, 1987; Leeder and Alexander, 1987; Reid, 1992; Alexander *et al.*, 1994), and no experimental studies. However, a large number of field studies infer lateral tilting from the asymmetric position of a channel with respect to its valley (e.g. Plumley, 1948; Coleman, 1969; Price and Whetstone, 1977; Schumm *et al.*, 1982; Veldkamp, 1992; Cox, 1994). Lateral tilting has also been suggested as a possible causative mechanism for large scale lateral planation by rivers (Osborn and du Toit, 1991).

1.2 Causative mechanisms for ground-tilting and possible channel responses

A number of tectonic settings have been identified in which lateral tilting of river channels can occur. These include extensional half-grabens, pull-apart basins in transcurrent conditions, and foreland basins and growth folds in compressional regimes (Alexander and Leeder, 1987). There is also evidence that lateral tilting may be caused in 'stable' tectonic areas, by the transmission of stresses from plate boundaries (see Section 2.3). In addition, non-tectonic mechanisms such as large-scale differential compaction or variations in isostatic recovery may produce lateral ground-tilting.

For the simple case of a tectonically active half-graben, two end members of a continuum of possible channel responses to lateral ground-tilting may be envisaged (Fig. 1.1). In the first end member, a channel may avulse downtilt and form a new channel

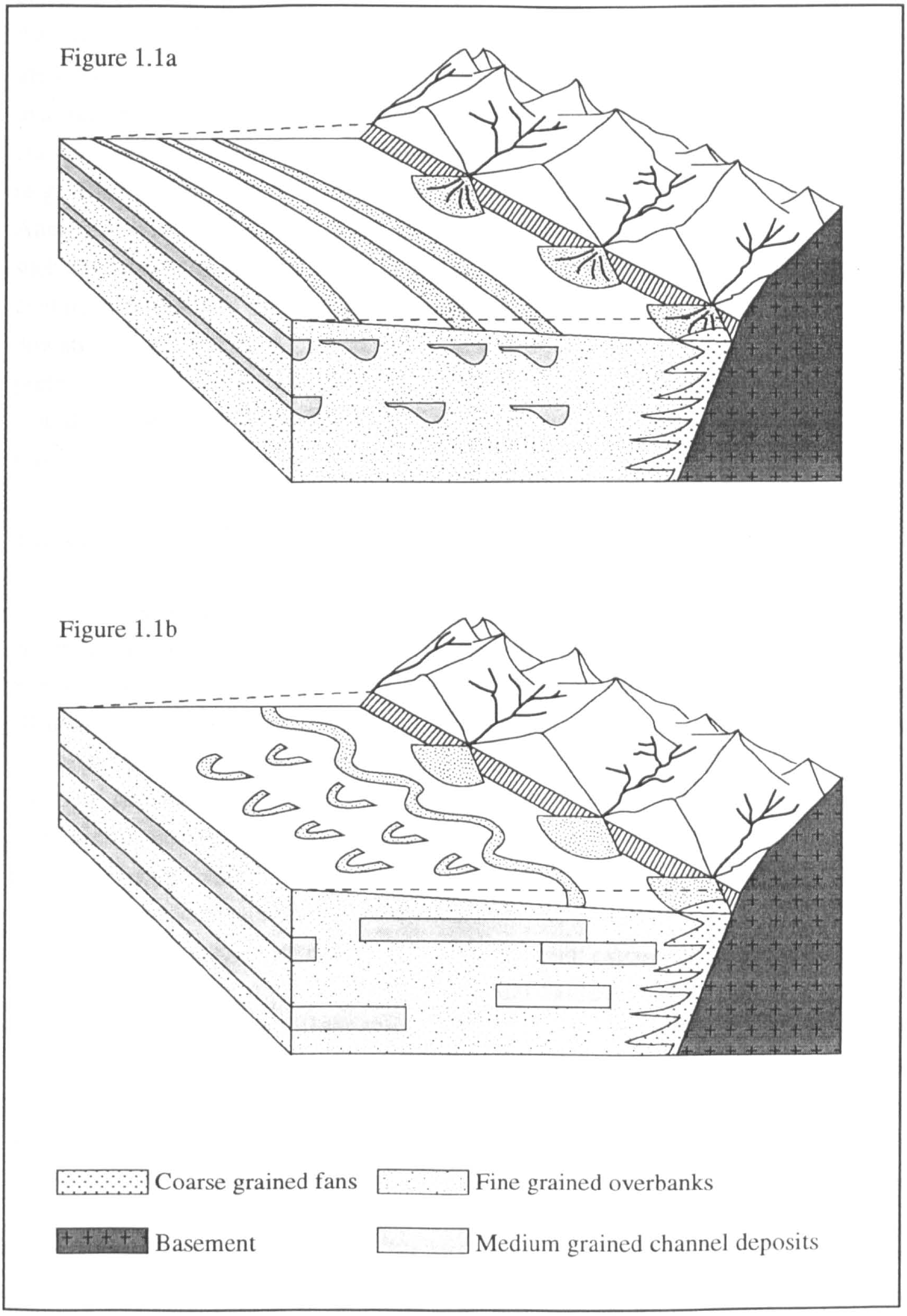

Figure 1.1. Two idealised end members of a continuum of fluvial responses to lateral tectonic tilting: a) Avulsion, leaving a series of abandoned channels uptilt, and depositing ribbon sandstones, b) Continuous down-dip movement with successive cut-off of updip meander loops, and the formation of sheet sandstones in the subsurface.

closer to the basin bounding fault (Fig. 1.1a). Successive channel avulsions may bring the channel close to the active fault. This sudden channel switching would be preserved in the subsurface as a series of ribbon sandstones or coarse grained deposits. The channel avulsions may be an instantaneous response to a single seismic event, due to bank failure and breaching, localised uplift across the channel, or deposition of mass flow deposits. (e.g. Ulrich, 1941; Wadia, 1975; Walters, 1975; Youd and Wieczorek, 1982). Alternatively, channel avulsion may be triggered after tilting by an autocyclic process such as channel crevassing or migration into a former channel belt. At the other end of the continuum a river may undergo slow downtilt migration due to preferential erosion on the downtilted side (Fig. 1.1b). In the example shown, meander loops are assumed to be preferentially abandoned on the uptilt side of the channel. Gradual downdip migration would be characterised by a series of sheet sandstones or coarse-grained deposits, in the rock record (Fig. 1.1b).

1.3 The significance of lateral ground-tilting of river channels

Studies of uplift, subsidence and axial tilting of channels have demonstrated that deformation is associated with increased channel instability (Schumm, 1986; Gregory and Schumm, 1987). Rates of uplift and tilting can also be quite large in comparison to channel gradients, with localised aseismic uplift rates in the range of 1-10 mm yr^{-1} and maximum magma associated uplift rates of 60-200 mm yr^{-1} (Castle *et al.*, 1984; Leeder, 1991). In addition, fault events can have vertical throws in the order of several metres. The imposition of similar tilt magnitudes in a lateral direction would also be expected to increase channel instability and therefore to have important implications in terms of river engineering, flooding and channel navigation.

Many hydrocarbon reservoirs are located in extensional rifts which have undergone widespread tilting. Laterally tilted axial river deposits within these rifts may form a series of subtle traps (Gabrielsen *et al.*, 1995), but their economic importance will depend on the style of channel response to ground-tilting, in conjunction with the overall subsidence rate. If the subsidence rate was high and the channel response to ground-tilting was primarily through avulsion, then small poorly-connected reservoirs will be formed. In contrast, if progressive down-dip movement predominates, coupled with low subsidence rates, a spatially extensive, well connected reservoir will be produced.

Lateral tilting was incorporated into early computer based process-models of alluvial stratigraphy (Fig. 1.2; Bridge 1979; Bridge and Leeder, 1979) and has subsequently been included in more advanced two-dimensional (Bridge and Mackey, 1993a; Mackey, 1993) and three-dimensional process-models (Mackey and Bridge, 1995). These models work by simulating periodic lateral tilting, channel avulsion,

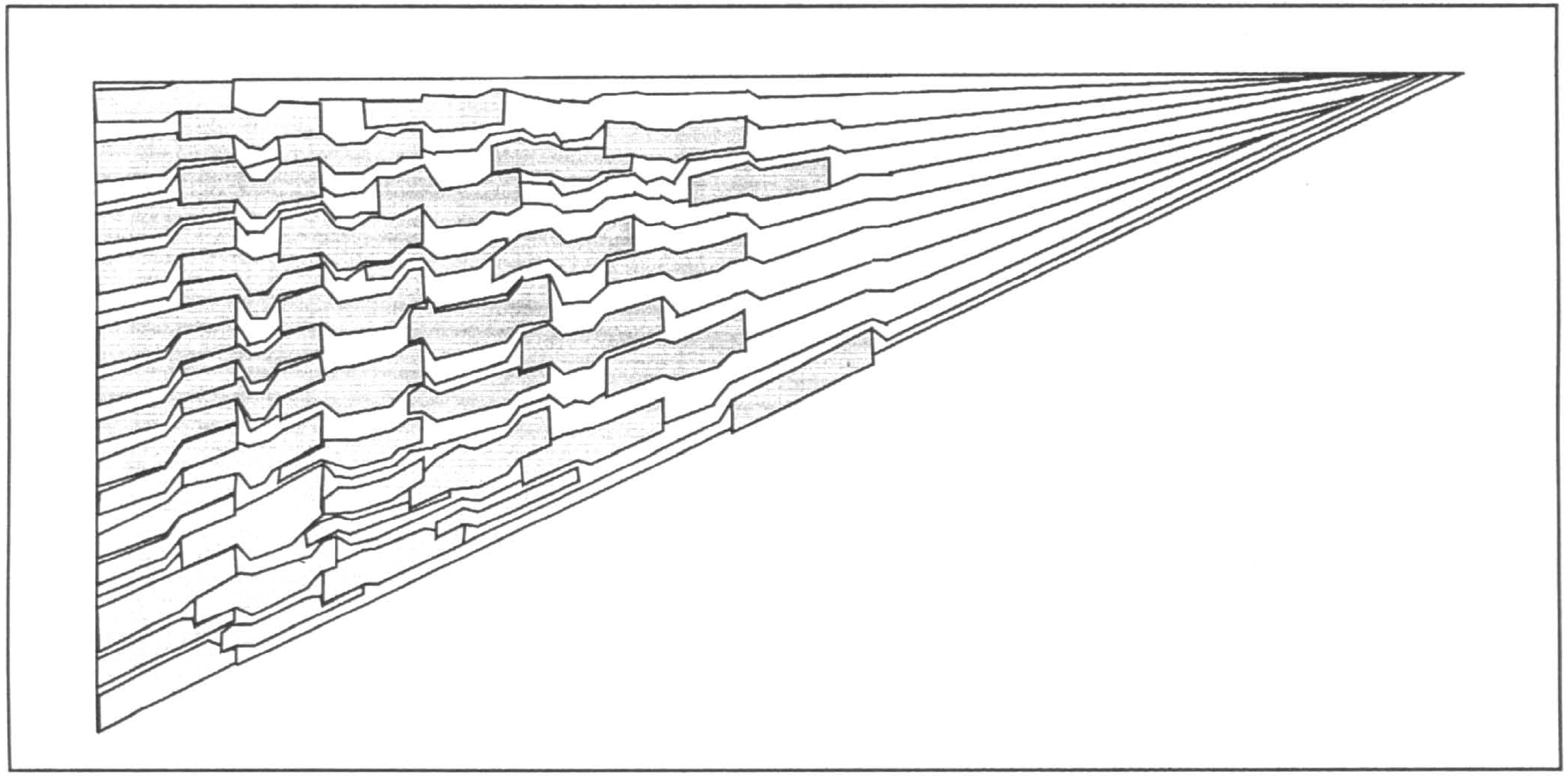

Figure 1.2. An example of output from a laterally tilted two-dimensional alluvial architecture model. A view of a half-graben in cross-section, bounded by a fault on the left hand side. Each block represents a channel belt and each cross-stream line represents a floodplain surface at a point in time. Note the increase in channel density and interconnectedness towards the downtilted margin. Adapted from Bridge and Leeder (1979).

deposition of overbank sediments, and compaction, to build up an alluvial stratigraphy. The simulation of laterally tilted alluvial stratigraphy by process-modelling has proved useful in understanding and modelling hydrocarbon reservoirs (Melvin, 1993) and in interpreting ancient alluvial deposits (e.g. Marzo *et al.*, 1988; Mack and Seager, 1990; Mack and James, 1993). However, one of the main limitations of these process-models is that channel response to lateral tilting is only by avulsion and not by progressive downdip migration. This deficiency reflects the limited understanding of the two processes of channel migration and lack of a criterion for differentiating between them. A second limitation is the paucity of quantitative data with which to test and constrain computer models of alluvial stratigraphy.

Further work is needed on alluvial-tectonic relationships, particularly where there is a lateral as well as axial tilt component. In addition, the useful and commonly used process-based alluvial architecture models require more independent testing. A combined field and flume modelling approach is flexible and detailed enough to examine such issues.

1.4 Aims of the research

The aim of this thesis is to characterise and quantify the effects of lateral ground-tilting on rivers, in terms of: i) channel planform changes and migration style, ii) temporal and spatial patterns of channel movement, and, iii) the preserved alluvial architecture formed by aggrading fluvial systems. This aim can be subdivided into four main objectives:

1) To examine the spatial and temporal relationships of alluvial-tectonic interaction in a proposed example of avulsive downdip channel movement towards an active basin-bounding fault.

2) To quantify the impact of variations in the magnitude, timing and frequency of imposed lateral tilt increments, on the alluvial architecture of braided rivers.

3) To examine the effects of lateral tilting on meandering river planforms and to synthesize apparently conflicting models of channel response to lateral tilting (Nanson 1980; Alexander and Leeder, 1987) and,

4) To investigate the controlling mechanism(s) for avulsive versus gradual downdip response to lateral ground-tilting.

1.5 Thesis structure

A brief outline of the thesis structure is presented, followed by a more detailed synopsis of each chapter. Chapter 2 reviews and synthesizes previous work on the influence of lateral tilting on rivers. The theoretical background to, and methodology of the physical modelling experiments on rivers is detailed in Chapters 3 and 4. Chapter 5 presents the results of the meandering and braided river experiments, while Chapter 6 reviews and introduces new approaches to the study of meander morphometry. The new approaches to bend parameter measurement discussed in Chapter 6 are utilised in Chapter 7, which is a detailed field study of the influence of lateral tilting on an axial river, and of the interaction between tectonics and channel movement. Chapter 8 summarises the main conclusions derived from the combined field and flume modelling work. A more detailed synopsis of each chapter is presented below.

- **Chapter 2** reviews and describes the impact of lateral tectonic tilt on river systems. Tectonic settings that induce ground-tilting are reviewed and examples presented of both avulsive and gradual down-dip channel response to lateral tilting. A criterion is proposed for distinguishing between the two styles of channel response, and a new model described for progressive lateral down-dip movement. An important consequence of lateral tilting is the asymmetric position of a channel with respect to the valley axis. Other possible causes of river asymmetry are described and the application of channel asymmetry to the interpretation of buried tectonic structures reviewed. The relationship between proposed examples of large-scale lateral river migration and studies of Holocene river response to lateral tilting is described. Finally, criteria for the identification of tilt-affected deposits in the rock record are reviewed.
- **Chapter 3** discusses the classification of physical models and reviews the development of physical modelling theory over the past century. Similarity theory and dimensional analysis which form the mathematical basis for 'scale' modelling are treated systematically and developed from first principles. The key parameters of fluid flow (flow Reynolds number, Froude number and Weber number) are derived using dimensional analysis and each of these terms is then defined and the implications for modelling considered. Three increasing levels of similarity, geometric, kinematic and dynamic are introduced and used as a framework for discussing the physics of flow in a model and the interaction of the flow with sedimentary particles. Finally the modelling of overbank sediments and time are considered.
- **Chapter 4** describes the equipment and methodology used for lateral tilt experiments on meandering and braided channel patterns. All the experiments were conducted in a uniquely designed stream table. Details are presented of the stream table and associated equipment, data collection methods, and evolution of the experimental

methodology as data collection techniques were refined. A single grain-size mix was used for all the experiments and the rationale for using the chosen sediment distribution is explained.

☐ **Chapter 5** describes two sets of flume experiments which test criteria for the recognition of lateral ground-tilting, identified from the study of Leeder and Alexander (1987). This chapter documents a number of advances in the modelling of coarse-grained meandering rivers and examines the imposition of lateral tilting on the channel planform. A second set of experiments on aggrading braided rivers allowed the preserved alluvial architecture to be classified in terms of sedimentary niches and the geometry of these niches to be measured. Variations in the size, frequency of occurrence and the spatial distribution of these niches are examined and the influence of lateral tilting considered in terms of the timing, magnitude and frequency of occurrence of tilt events.

☐ **Chapter 6.** The study of meander morphometry has led to the definition of a series of empirically derived relationships between bend parameters which are the basis for the majority of palaeohydrological analyses of single thread channels. This chapter reviews the different approaches to measuring the meander planform and examines the definitions of each of the planform variables. Two new techniques for measuring and analysing morphometric data from meandering rivers are presented and discussed. Finally, the existing equations for the prediction of palaeodischarge are reviewed and more precise relationships defined using an enlarged database. These new equations, bend definitions and measurement techniques are used for palaeohydrological analysis of the Carson River in chapter 7.

☐ **Chapter 7**. The Carson River, in north-western Nevada, USA, has been proposed as an example of avulsive downdip channel movement towards an active basin bounding normal fault (Leeder, 1993). This chapter investigates the avulsive history of the palaeochannels of the Carson River using radiocarbon and luminescence dating, palaeohydrology and surveying at a range of scales. In addition, independent dating of the basin bounding fault allows the Holocene alluvial-tectonic interactions to be studied. Floodplain gradients were measured perpendicular to the range front and the spatial distribution of lateral gradients analysed. Avulsion periods, lag times between faulting and channel avulsion, and patterns of channel onlap and offlap have been generated, and could be used to constrain and improve half-graben process-models. The Holocene history of the Carson River is more complex than that envisaged by Leeder (1993), with interaction between tectonics, climate change and intrinsic channel processes.

☐ **Chapter 8** summarises the major conclusions derived from this preceding research and recommends future avenues of research.

Chapter 2. The Influence of Lateral Tilt on Rivers

2.1 Synopsis

This chapter reviews and describes the impact of lateral tectonic tilt on river systems. Tectonic settings that induce ground-tilting are reviewed and examples presented of both avulsive and gradual down-dip channel response to lateral tilting. A criterion is proposed for distinguishing between the two styles of channel response, and a new model described for progressive lateral down-dip movement. An important consequence of lateral tilting is the asymmetric position of a channel with respect to the valley axis. Other possible causes of river asymmetry are described and the application of channel asymmetry to the interpretation of buried tectonic structures reviewed. The relationship between proposed examples of large-scale lateral river migration and studies of Holocene river response to lateral tilting is described. Finally, criteria for the identification of tilt-affected deposits in the rock record are reviewed.

2.2 Tectonic settings inducing ground-tilting

Alexander and Leeder (1987) noted that significant gradients, perpendicular to axial drainage, could form in extensional, transcurrent and compressional regimes. The dominant basin style in extensional regimes is the half-graben interspersed with grabens (Fig. 2.1a). Rotation of the basin bounding faults from high to low-angles, leads to incremental lateral tilting of axial facies on the hanging wall (Fig. 1.1; Jackson and McKenzie, 1983). Long half-grabens, such as those of the Basin and Range, are normally bounded by a series of fault segments with maximum lengths approximately equal to the thickness of the seismogenic zone (Jackson and White, 1989; Crone and Haller, 1991; dePolo *et al.*, 1991; Zhang *et al.*, 1991). Individual segments produce scoop shaped basins that may be linked by a single axial river system. Bends in strike-slip zones produce pull-a-part basins which show intrabasinal tilt dominantly perpendicular to the direction of the main fault (Alexander and Leeder, 1987) (Fig. 2.1b). In foreland basins (Fig. 2.1c) the locus of subsidence migrates due to thrusting, and along strike changes in thrusting intensity produce variations in sedimentation analogous to those along extensional fault segments. Compressional growth folds may also progressively tilt the ground surface on their flanks, as has been hypothesised for the late Carboniferous Barren Red Measures of the southern North Sea (Leeder, 1993).

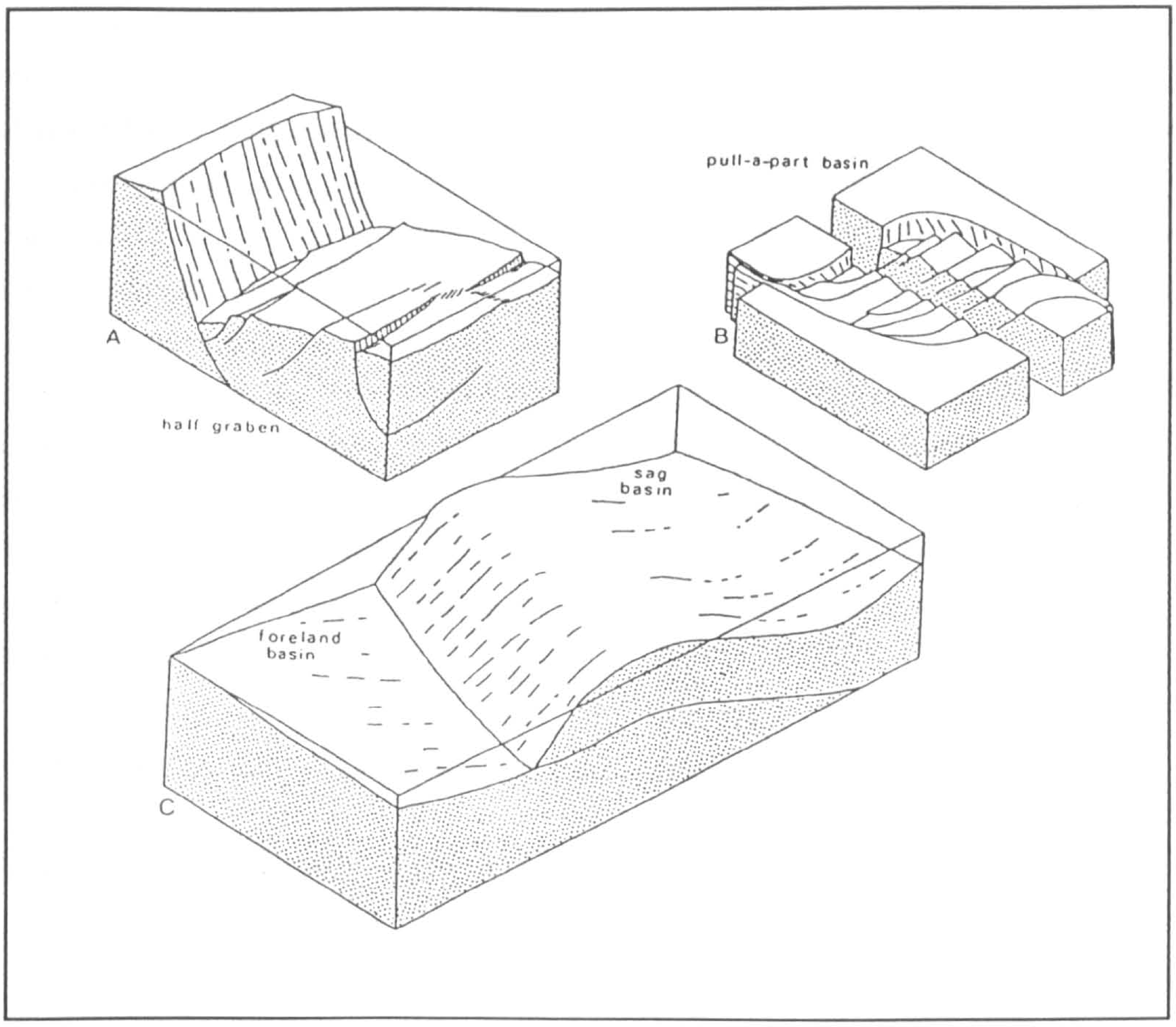

Figure 2.1. Tectonic settings inducing significant ground-tilting perpendicular to axial drainage. A) Half-graben deformed by antithetic and synthetic faulting. B) Pull-apart basin. C) Foreland basin and sag basin associated with a moving thrust sheet. From Alexander and Leeder (1987).

2.3 Ground-tilting in 'stable' continental settings

There is evidence that significant lateral movement of rivers can occur even in so called 'stable' continental regions, both on a local and a regional scale, although the driving mechanisms remain unclear. On a local scale, geodetic surveys of uplift and subsidence rates on certain topographic features in the North American mid-continent show rates that would have quickly generated far more topographic relief than is observed (Meade, 1975; Officer and Drake, 1981). A number of workers have therefore proposed that oscillatory motion of these basement blocks would explain the observed paradox (Brown and Oliver, 1976; Adams, 1980) with Adams (1980) estimating a periodicity of approximately 3000 years from an analysis of downvalley changes in tilting on major rivers. Localised lateral migration of several rivers has been interpreted in terms of these block movements (Schumm *et al.*, 1982; Mississippi, Section 2.5.3).

There also appears to be a regional trend of west and south-west migration of rivers in the mid-continent of the United States, with the exception of the Mississippi (Adams, 1980; Schumm *et al.*, 1982; Cox, 1994). Adams (1980) postulated that this was due to postglacial rebound of the Great Lakes region. However, an analysis of river terraces in the Mississippi Embayment demonstrates that south-westerly movement was not always synchronous (Cox, 1994). These variations in river migration are interpreted in terms of movement on a series of inferred high-angle, northwest trending faults, in response to the regional stress field which is compressional in an ENE-WSW direction (Zoback and Zoback, 1989; Zoback, 1992a,b). The studies of Adams (1980) and Cox (1994) raise the possibility that there is oscillatory block motion in an ESE-WSW direction which would account for river migration being locally out of phase, in combination with overriding regional tilting from tectonically transmitted stresses from the plate margins and / or from glacial rebound.

2.4 Holocene and Modern examples of avulsion due to ground-tilting

2.4.1 Long Valley Caldera

The only example in the literature of a clear relationship between tectonically induced lateral tilt and river avulsion, is the Long Valley Caldera Dome, eastern California (Reid, 1992). Periodic inflation and subsidence of the dome has caused recent switching between two parallel meander belts. A series of older meander belts are also interpreted to have formed by periodic avulsion related to ground-tilting. After being relatively stable from 1905 the dome started rising again in 1979 and has risen over 0.4 m by 1984 (Castle *et al.*, 1984; Savage *et al.*, 1987; Fig. 2.2). Reid (1992) divides the Owens River, which crosses the eastern flank of the active dome, into four sections based on the overall morphology of the present channel belts (Fig. 2.2). Section I is dominantly a single channel but sections II, III and IV have two channel belts parallel to one another separated by a 200-300 m wide relict planar surface. Geodetic surveys indicate that the channel in section II avulsed downtilt at some point between 1856-1878, and was probably triggered by the 1872 Big Pine earthquake (M=7.7-7.8; Reid, 1992). The morphology of the currently active channel in section II also supports the suggestion of recent avulsion as it has very few abandoned oxbows and the parallel inner channel is occupied by an underfit stream that has not significantly modified the pre-existing meander wavelengths.

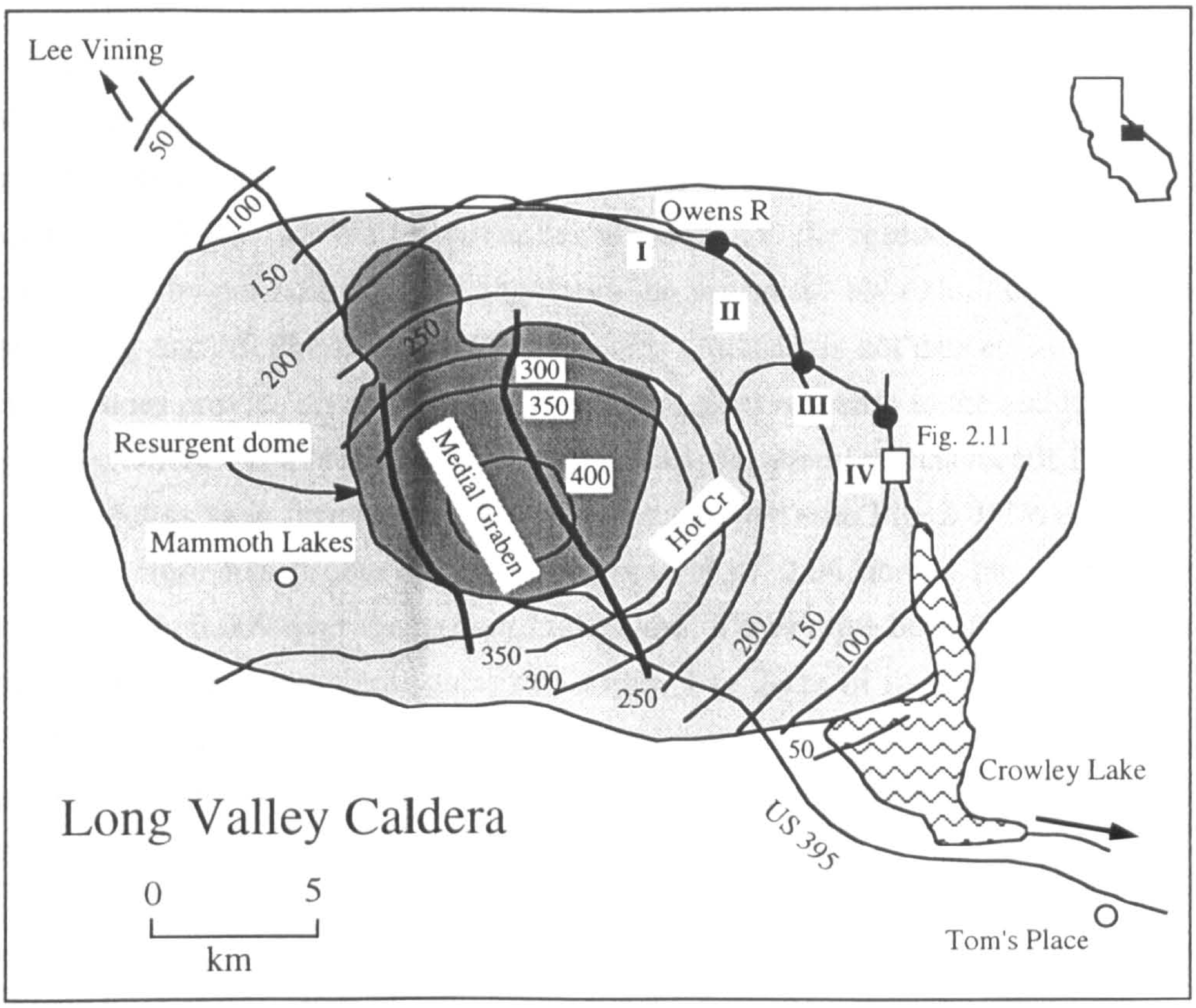

Figure 2.2. Generalised map of the Long Valley Caldera, eastern California, showing the course of the Owens River which is subdivided into four sections (I-IV). The location of the aerial photograph (Fig. 2.11) is marked. After Reid (1992).

At the start of reach II the downstream gradient drops to a fairly constant 0.0025 until entering Crowley Lake (see Fig. 2.2). The interfluve between the two channel belts in sections II-IV has a maximum lateral gradient of 0.0026 in section II, which declines to 0.0014 in section IV (Reid, 1992). Therefore, cross-stream gradients are 50%-105% of the downstream gradients. Since the avulsion, the new meander belt has slowly migrated further down the flank of the dome (see Section 2.5). There have probably been five avulsions since the Pleistocene (Reid, 1992), although preservation of the older belts is insufficient to rule out categorically any progressive down-dip migration. The average recurrence interval of a large surface rupture earthquake in the Owens Valley has been estimated at not more than 3000 years (Pinter, 1995) which suggests that instantaneous tectonic tilting was not the trigger for all of the avulsions.

2.4.2 Walker River

The Walker Basin, Nevada is a half-graben with a prominent fault-derived range front and a history of Holocene faulting on its western side (Dohrenwend, 1982; Demsey, 1987). A hydrologically closed lake towards the southern end of the basin has undergone a rapid drop in lake levels since 1882, at an average rate of 0.4 m per year (Blair and McPherson, 1994). The Walker River has responded to the receding shoreline and falling water levels, by periodically avulsing down the progressively exhumed half-graben dip-slope (Blair and McPherson, 1994). While this situation is not caused by active ground-tilting, it does provide an opportunity to examine river response to the sudden influence of a lateral gradient. As a result of the lake-level fall, the shoreline has receded by 15 km and 12 small deltas have formed and later been abandoned (see Fig. 2.3). Previous tilting of the valley floor has produced a lateral gradient of 0.04 across the whole basin and approximately 0.009 over the exposed lake floor. There have been three periods of rapid westerly downtilt movement (onlap) to within 1 to 2 km of the fault, separated by two easterly avulsions (offlap). Since the lake level has dropped the Walker River has incised into cohesive muds which probably limits gradual downslope movement and instead favours avulsion (Blair and McPherson, 1994).

2.4.3 Kosi River

The Kosi River in northern India has migrated a total of 113 km westward in 228 years through 12 avulsions (Wells and Dorr, 1987a). The Kosi fan is also an area of high seismicity with 74 major earthquakes in the last 200-250 years (Wadia, 1975). Some workers have proposed that the Kosi River is migrating due to tectonic tilting (e.g., Williams, 1982). However, the link between sudden tilting (seismic events) and avulsion has not been established (Wells and Dorr, 1987a). The avulsions and associated unidirectional movement can instead be explained by autocyclic processes operating on this low-angle fan (Wells and Dorr, 1987a; see Section 2.7). Lateral tilt magnitudes for the mid-Kosi fan have been measured at 0.0001-0.00024 (Wells and Dorr, 1987b), these being one to two orders of magnitude lower than gradients reported for proposed examples of lateral planation (Section 2.6) and an order of magnitude less than the avulsion dominated Long Valley Caldera (Reid, 1992).

2.4.4 Discussion

Frequent channel avulsion (<100 years) can be related to a range of processes, including rapid lake level fall (Blair and McPherson, 1994) and fan deposition (Wells and

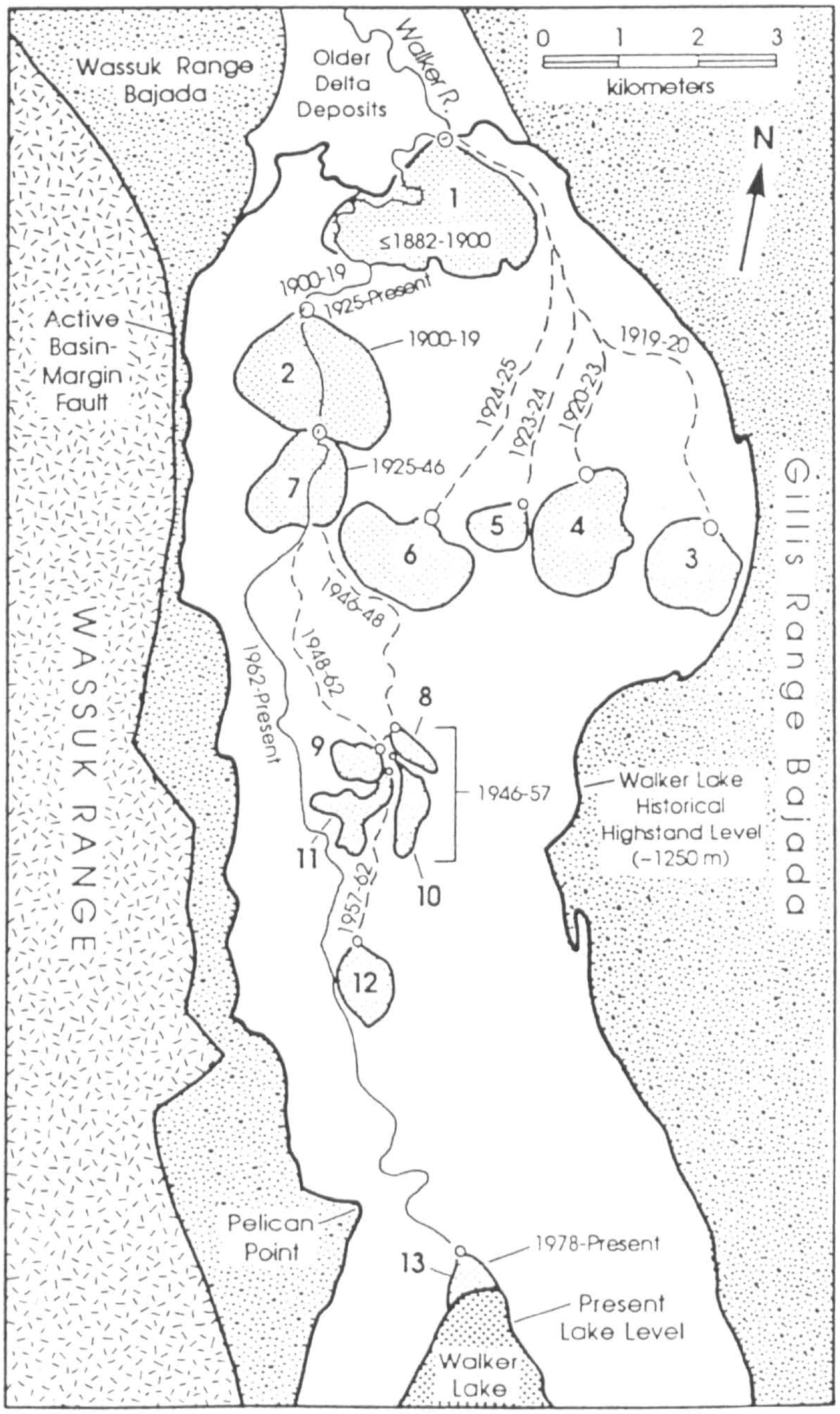

Figure 2.3. History of delta-lobe switching and associated channel movement in the Walker Lake Basin, during the years 1882-1994. From Blair and McPherson (1994).

Dorr, 1987a). Anomalously high rates of tectonic movement may also have similar rates, although evidence is limited[1] (Reid, 1992). Other processes such as delta aggradation associated with rapid sea-level rise (Frazier, 1969; Törnqvist, 1994), have average avulsion intervals of approximately 1000 years. An average avulsion interval of 1000 years has also been used for alluvial architecture modelling (Bridge and Leeder, 1979). Historical records will therefore not be long enough in many tectonic settings to adequately relate avulsion to tectonism. Consequently, dating techniques should be used to recognise the influence of lateral tilting on examples with larger avulsion intervals than the previously cited studies. Chapter 7 is an example of such a study.

2.5 Holocene and Modern examples of progressive channel migration due to ground-tilting

2.5.1 Madison and South Fork rivers

Leeder and Alexander (1987) suggested that the imposition of a lateral tilt has caused a gradual down-dip translation of the Madison and South Fork meander belts in south-west Montana, with the concurrent abandonment of up-dip meander bends as oxbow lakes. Evidence of lateral ground-tilting is provided by the 1959 Hebgen Lake earthquake (M_s=7.3) which caused extensive faulting along the eastern edge of Hebgen Lake and along the Madison Range Fault (Fig. 2.4; Myers and Hamilton, 1964). The floodplains of the Madison and South Fork rivers were tilted by approximately 0.00022 to the north-northwest, and 0.00019 to the north, respectively (Alexander *et al.*, 1994; see Fig. 2.4). This tilting was oblique to the downstream axes of the South Fork River and the lower reaches of the Madison River, thereby increasing the lateral gradients. The lateral tilt hypothesis of Leeder and Alexander (1987) has recently been tested, revealing a more complex history of channel development (Alexander *et al.*, 1994).

The increasing age of abandoned loops on the south-western side of the active South Fork channel belt, indicates gradual channel movement towards the north-east. The South Fork River also shows a marked reduction in bend size through the Holocene, and progressive channel belt width reduction by a process of periodic incision (see Fig. 2.5a). However, Alexander *et al.*, (1994) note that alluvial fan growth may have also influenced the migration of the South Fork River. In contrast, no significant reduction in meander bend width has occurred on the Madison River, a point which is seemingly anomalous in the light of the well constrained Holocene palaeohydrological history of rivers in the temperate zone (Starkel *et al.*, 1991). The river appears to have undergone rapid lateral

---

[1] Although, there have been an estimated 5 avulsions during the Holocene, these may have been related to relatively short lived periods of inflation and subsidence of the Long Valley Caldera Dome.

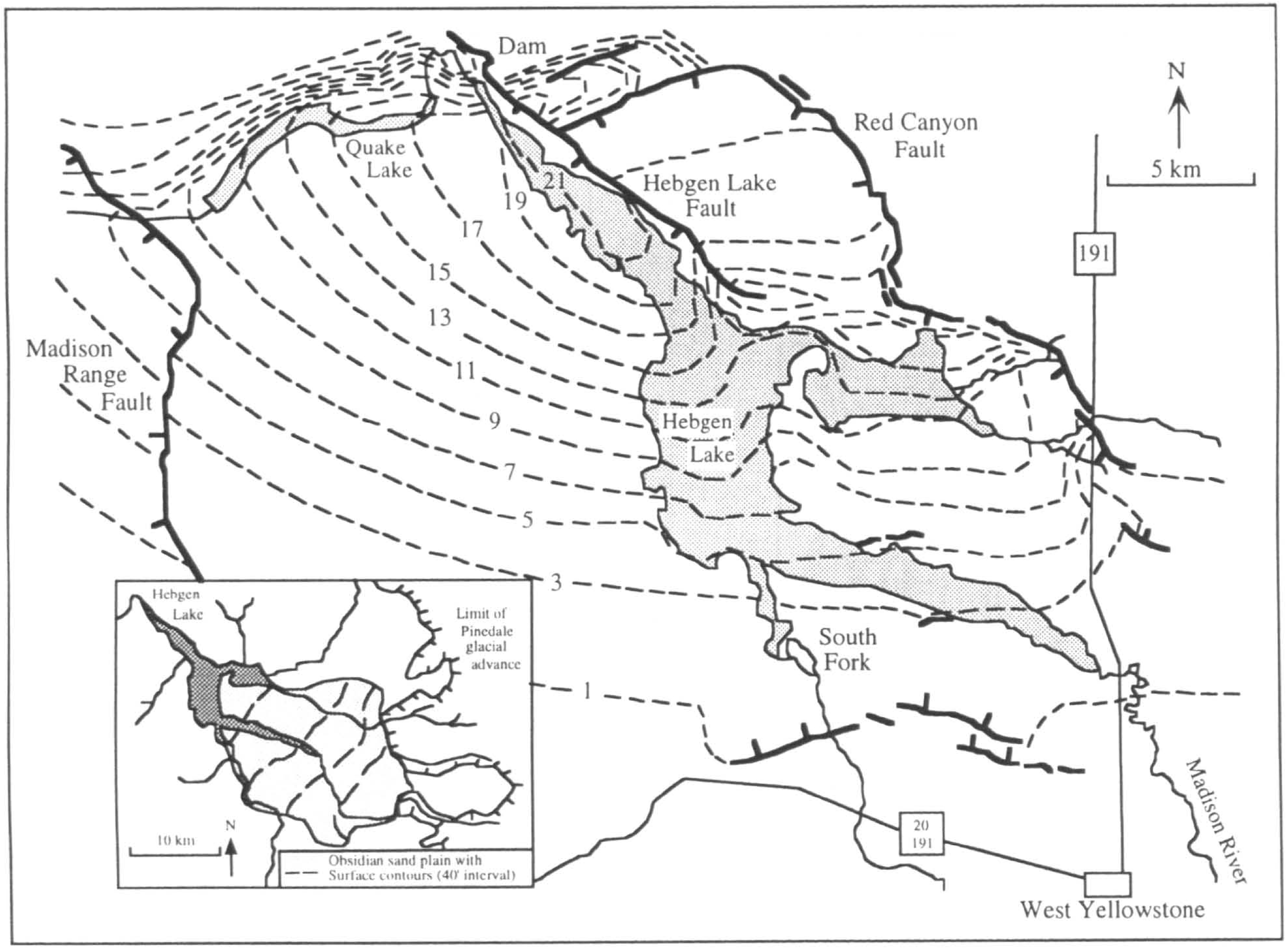

Figure 2.4. The Hebgen Lake drainage basin, SW Montana, with associated ground deformation from the 1959 earthquake. Adapted from Alexander *et al.*, (1994).

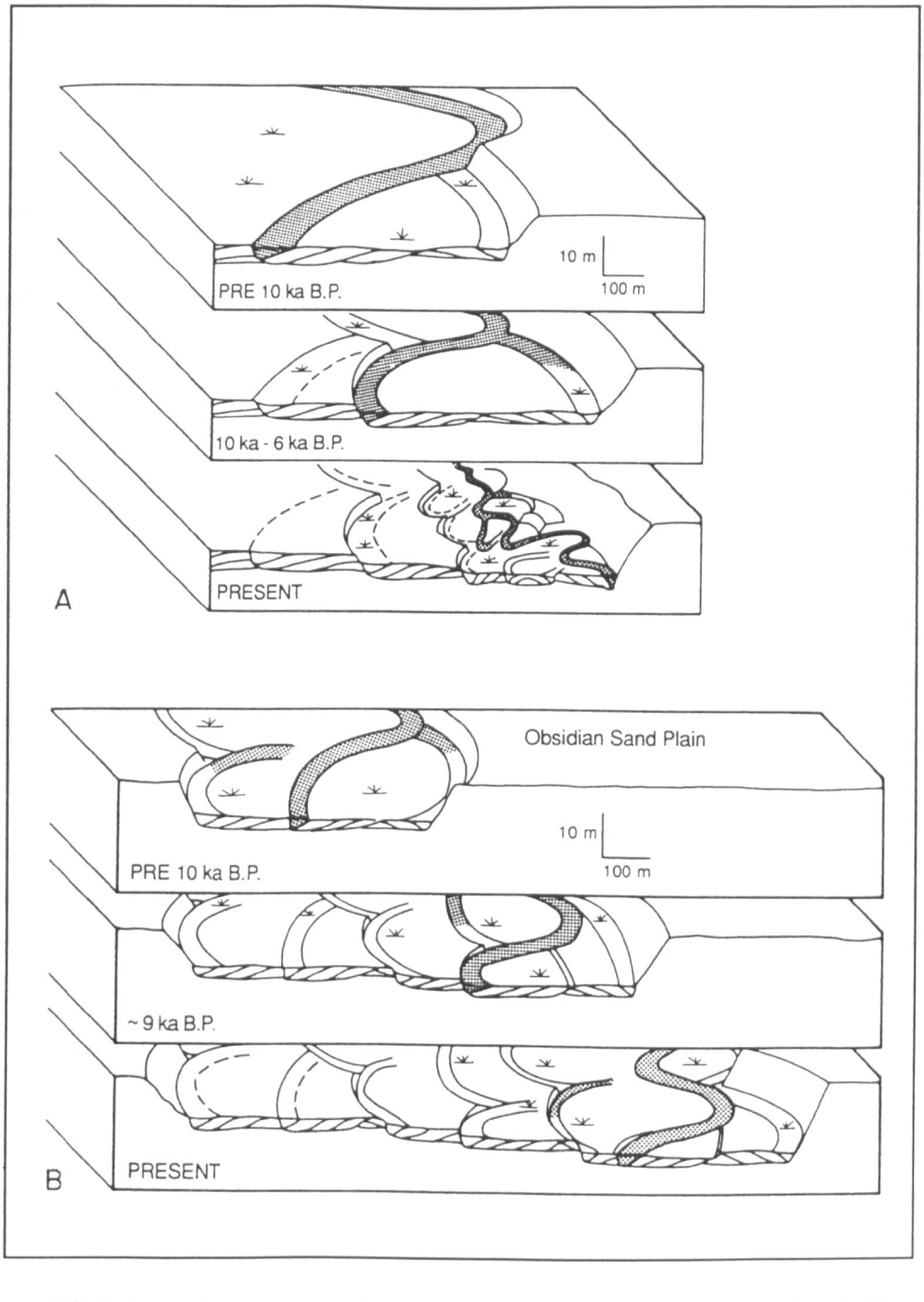

Figure 2.5. Schematic evolution of asymmetrical meander belts in the South Fork and Madison Rivers, Montana. A) The South Fork River: the right hand side (downtilt) of the channel belt has not moved significantly during the Holocene. However, the meander bends have undergone successive wavelength and amplitude reduction, which coupled with periods of incision has formed an asymmetric channel belt. B) The Madison River: a rapid phase of lateral movement occurred in the early Holocene and the river has subsequently occupied an asymmetric position with respect to its valley. In contrast to the south Fork River, meander bend size has not changed appreciably and a series of meander loops have been abandoned on the uptilt terraces. From Alexander *et al*., (1994).

movement accompanied by episodic incision during the early Holocene across a glacially sourced obsidian sand plain (Fig. 2.5b). Small terrace remnants preserved on the eastern side of the valley with minimum abandonment ages of 6.33 and 4.64 ka, indicate that no further eastern movement has taken place since that time. The Madison River has subsequently undergone further incision, producing a bluff over 20 m high. The active channel belts of both the Madison and South Fork rivers appear to have been in their present positions for approximately 3000 years.

Alexander *et al.*, (1994) interpret the preference of the South Fork River for the eastern side of its meander belt and the early Holocene rapid lateral movement of the Madison River, in terms of tectonically induced ground-tilting. However, the Madison and South Fork Rivers have also been influenced by a combination of incision (in this case partially caused by lake level fluctuations), climate change and possible fan growth, which increase the complexity of channel development. In both rivers, incision appears to have aided asymmetry by making lateral uptilt movement more difficult.

2.5.2 Beatton River

In contrast to the Montana example, Nanson (1980) presented a model for the Beatton River, Canada, where the river remains on the uptilt (w) side of the floodplain, despite an inferred isostatically imposed lateral gradient (Fig. 2.6). A quantitative analysis of the river position at 42, 0.5 km intervals downstream indicated that 44% of the floodplain width was to the west and 56% to the east. Nanson (1980) argued that the easterly facing meander bends migrated faster and consequently became tighter, eventually leading to chute cutoff on the downtilt side (see Fig. 2.6b). However, the Beatton River is restricted from migrating laterally over a significant distance due to its narrow floodplain (Fig. 2.6a) and therefore may not be directly comparable to examples of unconfined streams (Schumm *et al.*, 1982; Schumm, 1986; Cox, 1994). Mathews (1978) used buried fluvial gravel surfaces to estimate that the last glacial isostatic depression and uplift cycle (the past 27,000 years) imposed a net lateral tectonic tilt of at least 0.00004. The overall lateral tilting since the Wisconsin glaciation is estimated at approximately 0.0003-0.0004. However, no cross-sections were measured to calculate the present lateral tilt of the floodplain and to confirm the validity of Mathews' (1978) estimate for past tilting. The lack of cross-sections is particularly important since there is evidence that isostatic tilting of the region may have stopped approximately 8,000 years ago, and that the majority of the tilting took place in the first 500 years after the last glaciation (Mathews *et al.*, 1970; Andrews and Retherford, 1978).

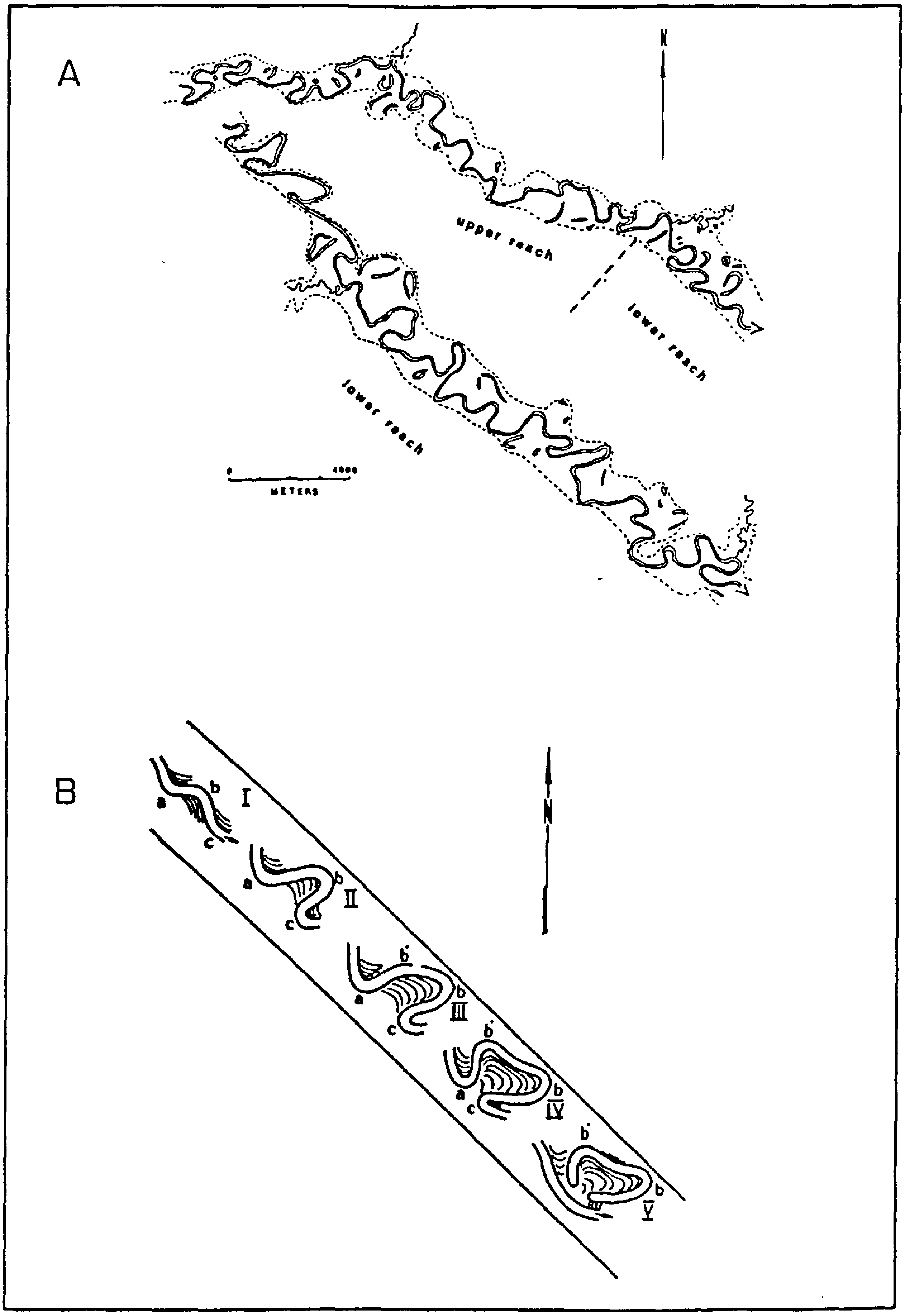

Figure 2.6. Model of meander bend development and cutoff on the Beatton River, Canada. A) Location map of Beatton River reaches studied by Nanson (1980). Dashed lines mark the edge of the floodplain and therefore lateral movement of the channel belt is restricted. The estimated direction of tectonic tilting is towards the east. B) Five-stage model of meander bend development and cutoff. An initially symmetrical channel (I) undergoes rapid bend expansion on the downtilt side due to increased erosive potential (II, III). Further bend expansion leads to chute cutoff and meander abandonment on the down-dip side (IV and V). From Nanson (1980).

2.5.3 Mississippi River

The Mississippi River shows evidence for both regional and local tectonic tilting in the vicinity of New Madrid, Missouri. A series of large earthquakes (M_B=7.1-7.4) occurred in 1811-1812 (Nuttli, 1973) and the area has the highest intraplate seismic moment release in the world (Johnston, 1989).

Regional tilting

Recent analysis of drainage-basin symmetry suggests that late Pleistocene tilting in the New Madrid Seismic Zone was towards the south-east (Cox, 1988a, b). Geomorphological mapping also indicates that the Mississippi has successively moved towards the south-eastern side of the valley since the early Wisconsin glaciation approximately 70,000 years ago, whilst the channel pattern changed from braided to meandering (Saucier, 1974). However, the style of river response to the hypothesised ground-tilting is difficult to identify since the older surfaces are covered in braidplains and therefore do not have asymmetric distributions of loop cutoffs. The river must have undergone some periodic avulsions, since it has cut through the bedrock high of Crowley's Ridge at a number of points (see Fig. 2.7). Since the last avulsion the river has had a meandering pattern but has been restricted to a relatively narrow floodplain adjacent to a sharp bluff, cut in Pleistocene and Pliocene sediments. The considerable time frame of movement and the erosion into the eastern bluff, suggests that the majority of the river movement has been in the form of progressive down-dip migration.

Localised tilting

The 1811-1812 New Madrid earthquakes were not associated with regional ground-tilting but with local movement on the Lake County Uplift (Russ, 1982). This uplift is strongly asymmetric and uneven with two pronounced bulges on the eastern edge and a gently sloping surface dipping towards the west (see Figs. 2.8 and 2.9). The majority of the uplift is estimated to have taken place within the last 6000 years, with a northward movement in activity from Ridgely Ridge to Tiptonville Dome, which has formed dominantly in the last 2000 years (Russ, 1982). With the exception of Tiptonville Dome, the steepest lateral slope is almost due west and has a gradient of approximately 0.00028. The Mississippi River displays aspects of both the Nanson (1980) and Leeder and Alexander (1987) models. Adjacent to Lake County Uplift the Mississippi River is generally situated in the centre or western edge of the floodplain, in contrast to the reaches to the north and south (see Fig. 2.7). Russ, (1982, p.106) notes that "it is conceivable

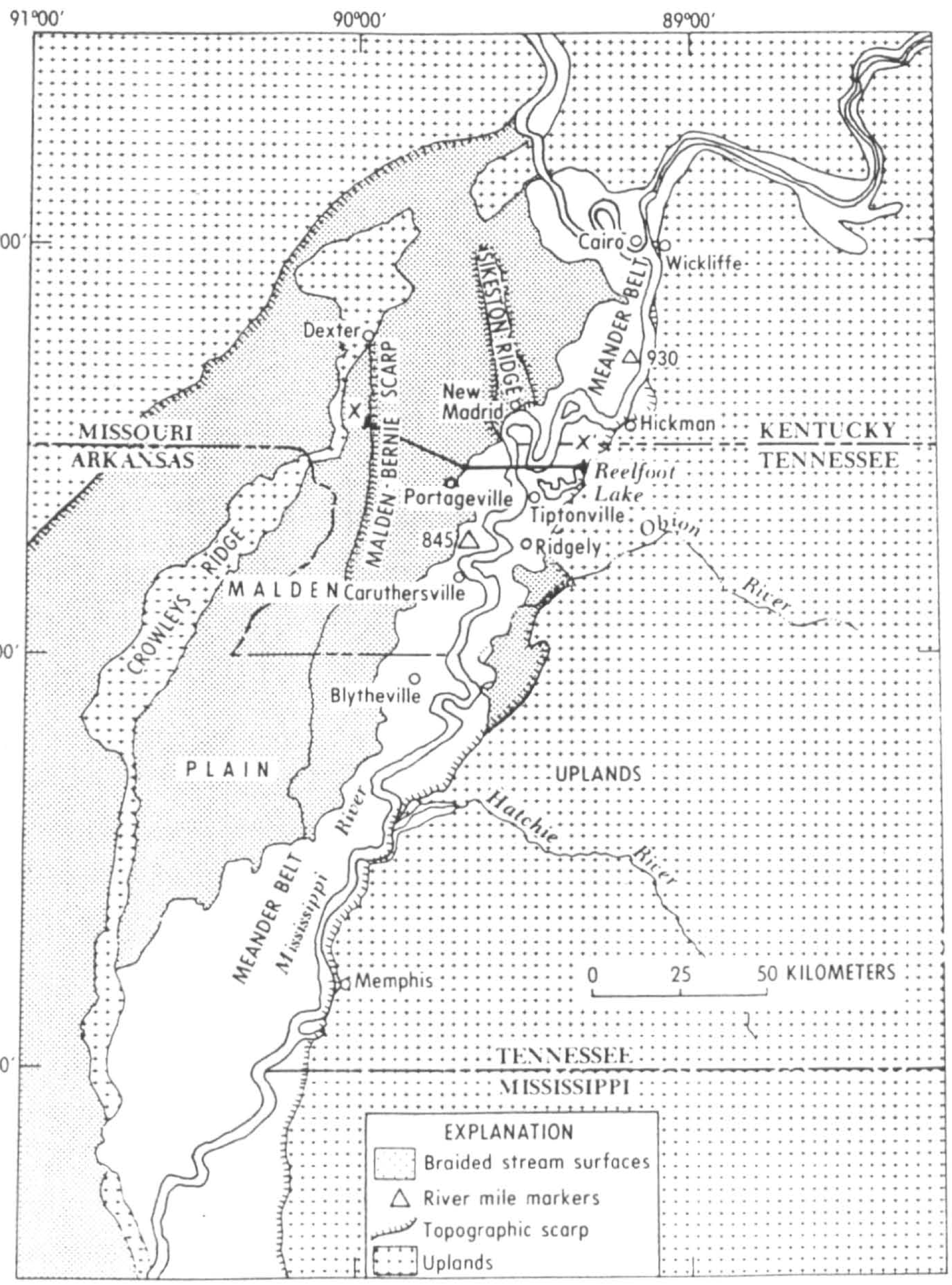

Figure 2.7. Generalised map of the Upper Mississippi Embayment. Note how the Mississippi River is adjacent to the eastern bank both north and south of the New Madrid area. From Russ (1982).

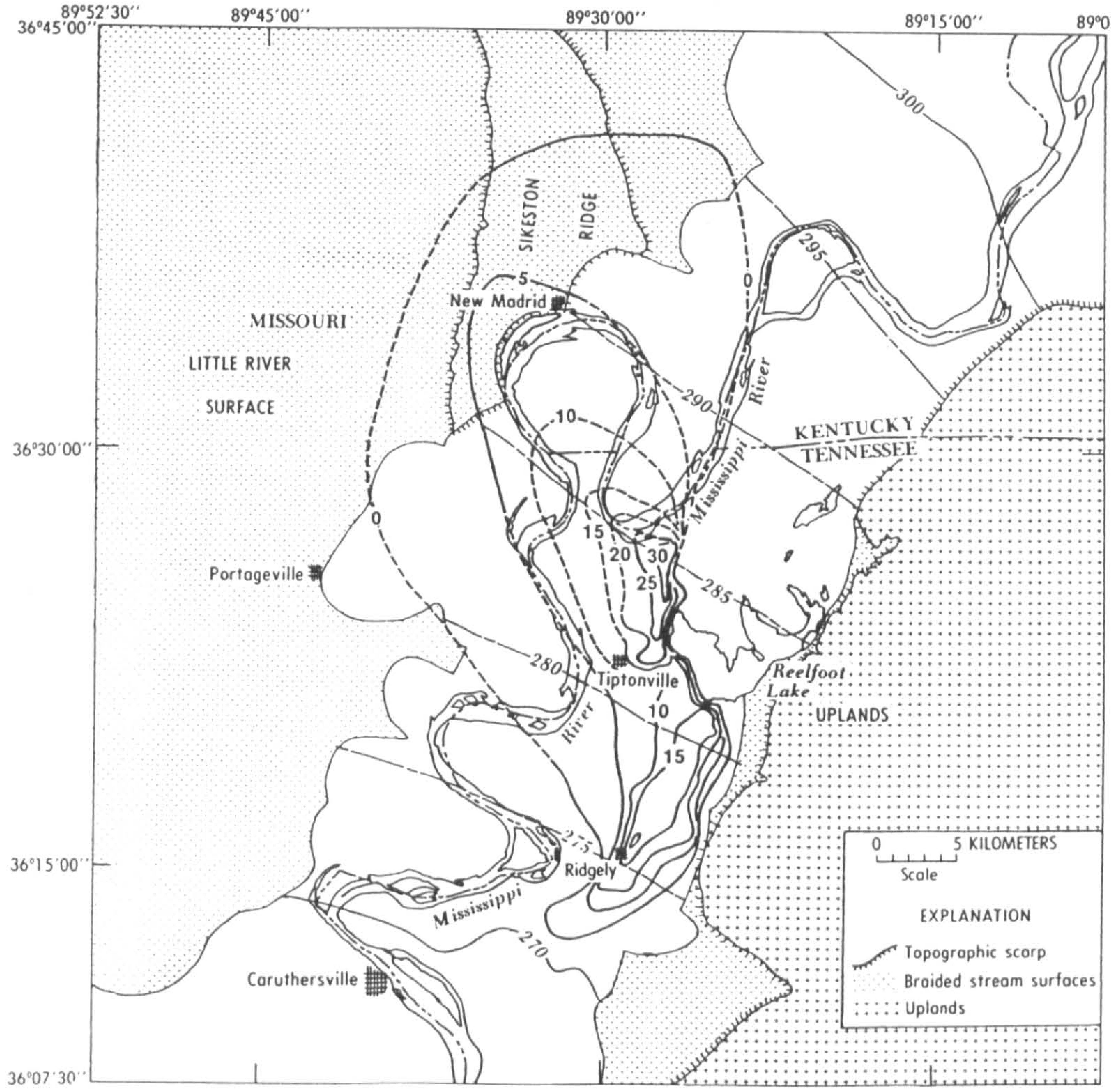

Figure 2.8. Uplift contours on the Lake County Uplift, upper Mississippi Embayment. All contours are in feet. The thick lines represent uplift, and the thin lines represent pre-uplift idealised meander belt contours. In both cases, solid and dashed lines represent direct and indirect measurement, respectively. From Russ (1982).

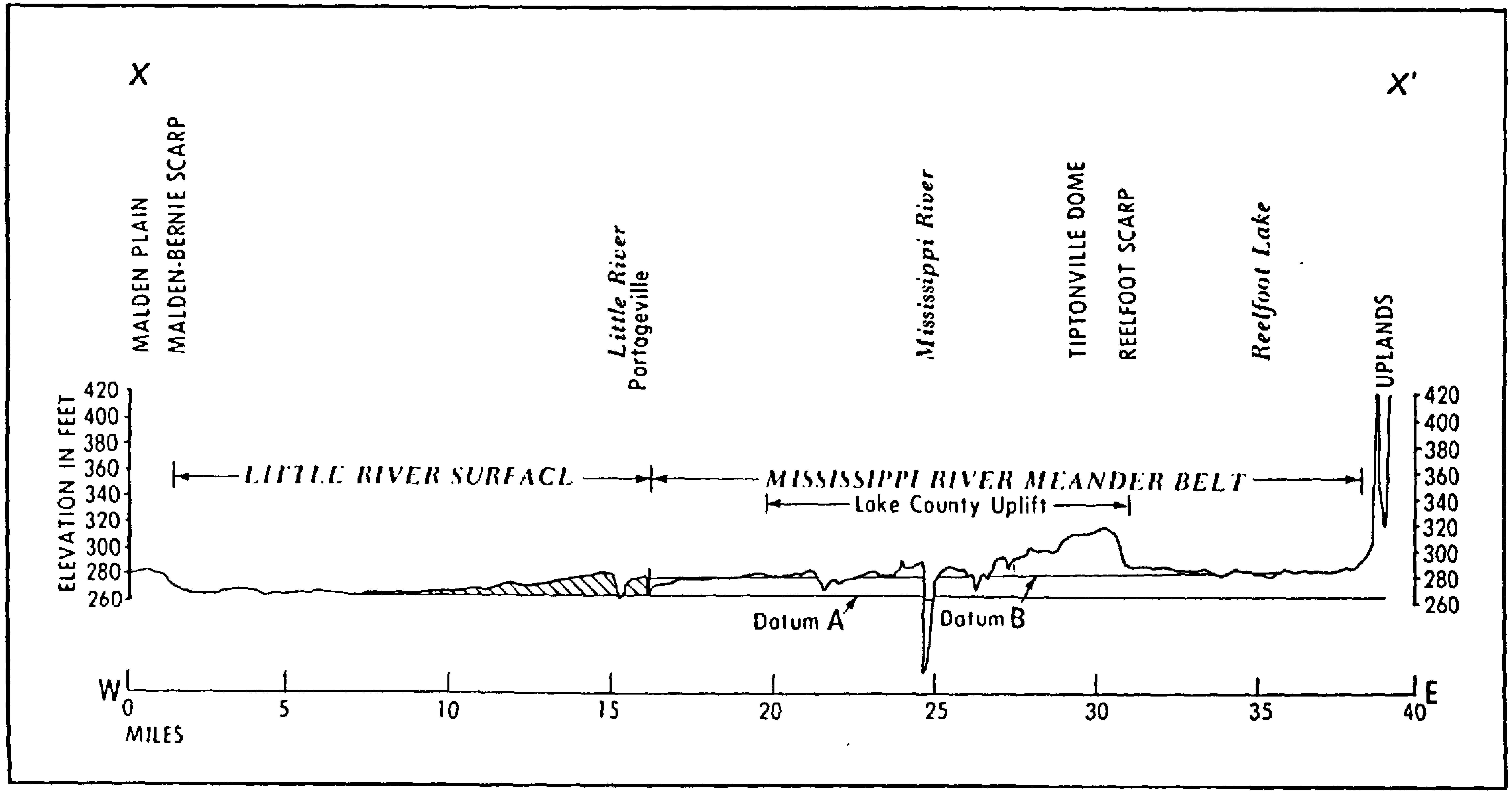

Figure 2.9. Topographic cross-section of the Lake County Uplift and inner Mississippi Valley. Datum A represents the original level of the Little River Surface (see Fig. 2.8), while Datum B is the height of the aggraded Mississippi floodplain prior to uplift. The dashed area of the section is the Portageville bulge which is the product of recent overbank and crevasse splay deposition, and not of uplift. Vertical exaggeration 211:1. From Russ (1982).

that the river has been deflected to the west as a result of tectonic uplift". This statement can be substantiated by a range of geomorphological evidence which Russ (1982) notes, but does not consider in the context of lateral tilting. Three abandoned meander loops are preserved on the uptilt side of Tiptonville Dome and Ridgely Ridge (Fig. 2.10), and may represent uptilt loop cutoff associated with progressive downtilt channel migration, as envisaged by Leeder and Alexander (1987). Geomorphological mapping of the course of the Mississippi River over a period of 150 years also suggests that the downtilt bends have migrated towards the west (Russ, 1982).

In contrast, the large bend that the town of New Madrid overlooks, has a geometry and recent movement history that indicates that it will eventually undergo neck cutoff on the eastern side, in the manner of the Beatton meander loops (Nanson, 1980). The history of bend cutoff on the New Madrid stretch of the Mississippi provides evidence for the suggestion of Schumm *et al.*, (1982) that the Beatton River meander loops (Nanson, 1980) might be anomalous, due to the restricted floodplain width. While the Mississippi was free to migrate laterally, bend cutoff appears to have been on the updip side, and only the presence of a lateral restriction has modified the process of meander bend abandonment. No avulsion has taken place, probably due to the lack of an outlet to the south of Portageville (Fig. 2.8). Instead, overbank and crevasse splay deposits have smoothed out the edge of the uplift and created the Portageville bulge (Fig. 2.9).

2.5.4 Owens River

The Owens River in eastern California also shows evidence for progressive lateral migration. Details of the history and avulsive behaviour of the Owens river and its interaction with the resurgent dome of the Long Valley Caldera have been presented in Section 2.4.1. Of the four morphological reaches identified by Reid (1992), the southerly segments III and IV show signs of significant gradual down-dip movement (Fig. 2.2). Both sections are estimated to have formed about 1000 years ago, by comparison of the density of oxbows with the approximately 120 year old reach II (Reid, 1992). Measurement of the channel position with respect to the centre of the channel belt, in a manner analogous to Nanson (1980), provides evidence for gradual down tilt migration (Reid, 1992). The Owens River in sections III and IV occupies an average position 55.8 and 59.9% of the way across its channel belt in the downtilt direction. An analysis of the bank material also indicates progressive movement in section IV as 24% of the downtilt bank is eroding ancient floodplain material in contrast to 6.4% of the uptilt bank. In places, the channel has reoccupied abandoned meander loops on the down-dip side, resulting in a thalweg that passes through successive bends, that are convex in the

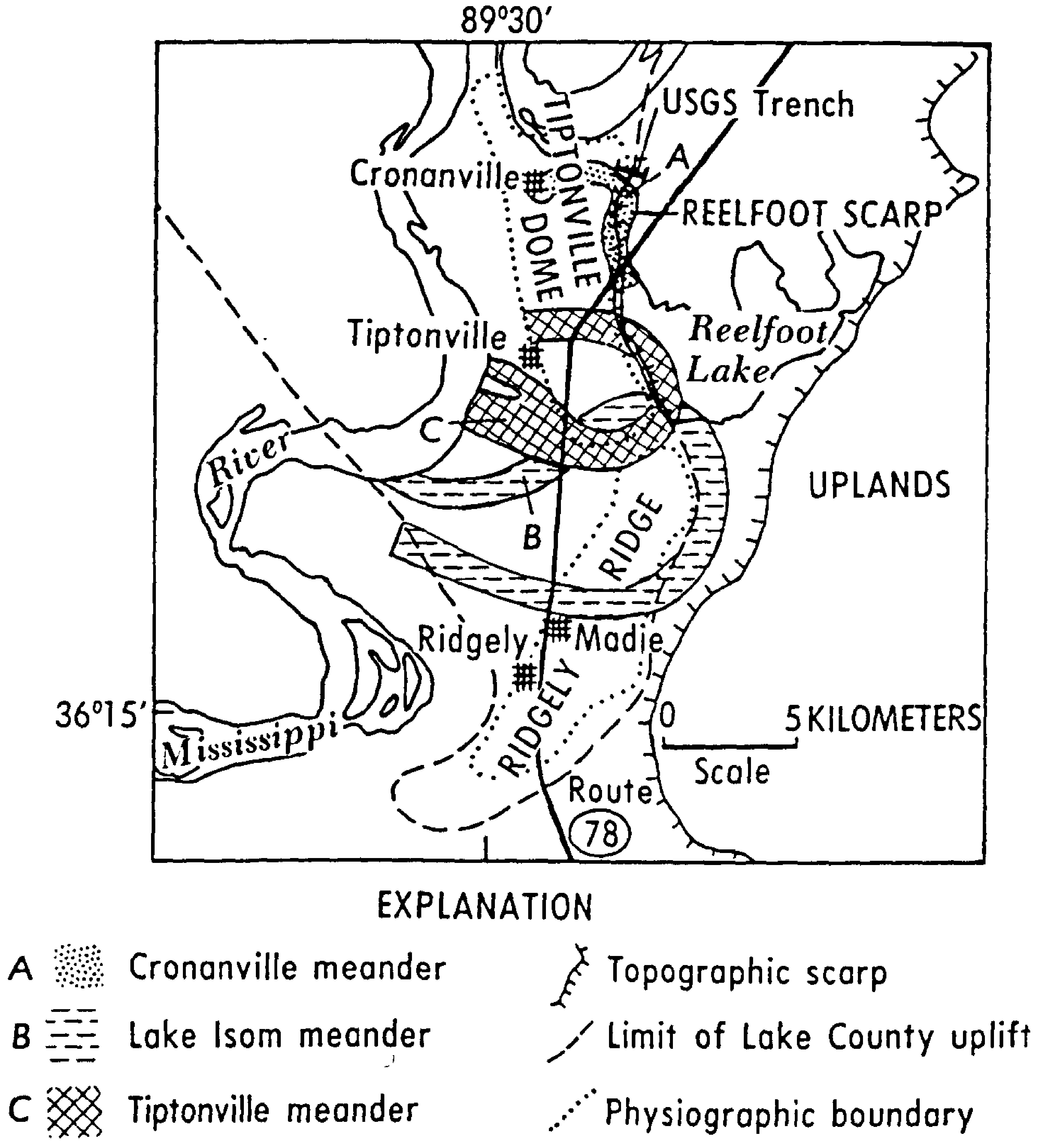

Figure 2.10. Map of abandoned meander loops on the south-eastern edge of the Lake County Uplift. From Russ (1982).

downtilt direction (see Fig. 2.11). Point-bars have formed on the downtilt cusps between the reoccupied convex bends, as the river has adjusted towards a more symmetrical planform. Additionally, an analysis of photos between 1972 and 1990 show that outerbank terraces have formed on some highly sinuous bends on the uptilt bank (Reid, 1992). Outerbank terraces, often referred to as concave benches (Page and Nanson, 1982) or counterpoint bars (Lewin, 1983a), have previously been observed in bends that have become stalled in the downstream direction (Carey, 1969; Woodyer, 1975; Hickin, 1978; Nanson and Page, 1983). However, the defining characteristic produced by stalling is the production of very tightly curved bends immediately downstream of lower sinuosity bends. It is these rapid downstream variations in sinuosity that are reproduced by reoccupation of successive convex down-dip bends.

2.5.5 Synthesis

The observations of Leeder and Alexander (1987), Nanson (1980) and Reid (1992) can be synthesized into a single unifying model of progressive down-dip channel migration, in response to lateral tilting (Fig. 2.12). A river with a well developed channel-belt may initially respond to lateral ground-tilting by migrating downtilt, through increased erosion of down-dip meander bends (Fig. 2.12a). As the channel migrates, it may reoccupy adjacent convex downtilt meander bends, forming a series of contiguous convex downdip bends, separated by sharp cusps (Fig. 2.12b). These bends are modified by point-bar formation on the cusps on the downtilt side, and concave bench formation on the uptilt side (Fig. 2.12c). Both processes combine to increase the symmetry of the channel planform. Once the channel reaches the edge of its former channel-belt, the river will begin to preferentially abandon meander loops on the uptilt side, so long as the downtilt side is free to move down slope (Fig. 2.12d). Reid (1992) has suggested that concave benches may still form during this stage. When the channel reaches the downtilt floodplain boundary, the rate of migration will slow and individual meanders will begin to erode cusps into the boundary. These cusps restrict the migration rate of the bend apex, and therefore downstream meander translation leads to chute cutoff and abandonment of down-dip meander bends (Fig. 2.12e). Meander bends will be largely reworked if gradual erosion continues on the downtilt side, leaving relatively homogeneous deposits in the rock record. Migration and reworking of coarse grained rivers by this process, may account for the homogeneous gravel deposits observed in many of the proposed examples of large-scale lateral planation (Section 2.6).

The two apparently conflicting models of Nanson (1980) and Leeder and Alexander (1987) are seen as two separate stages within this overall model, and have both been described from the Mississippi River in the vicinity of New Madrid. This newly

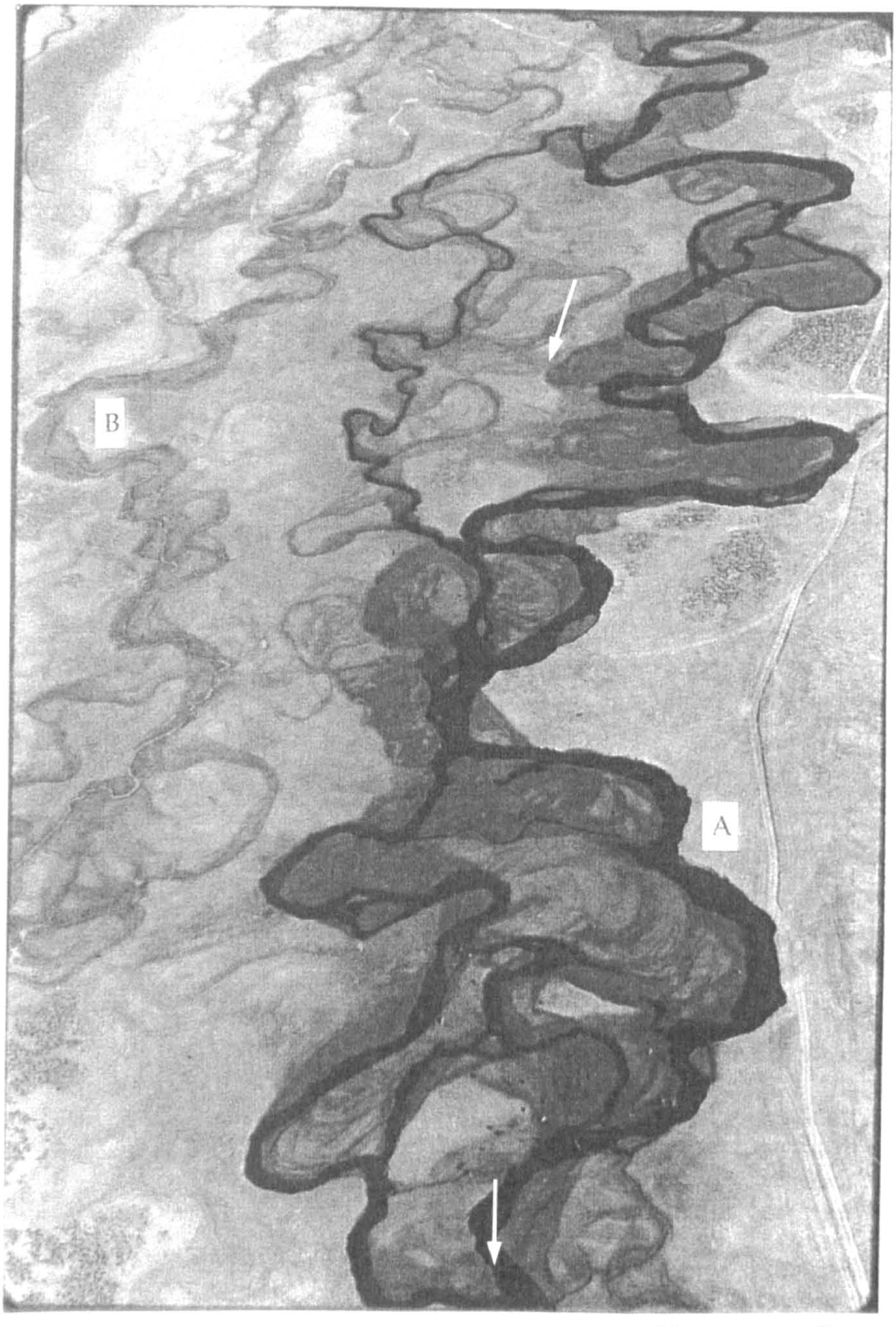

Figure 2.11. Upvalley view of the Owens River meander belts, eastern California, in section IV (see Figure 2.2 for location). Three outwardly convex bends form the channel of the modern river (A) in the lower right and may mark the down-dip migration of the river and the reoccupation of previously abandoned oxbows. Sharp cusps are present between the convex downtilt bends. From Reid (1992).

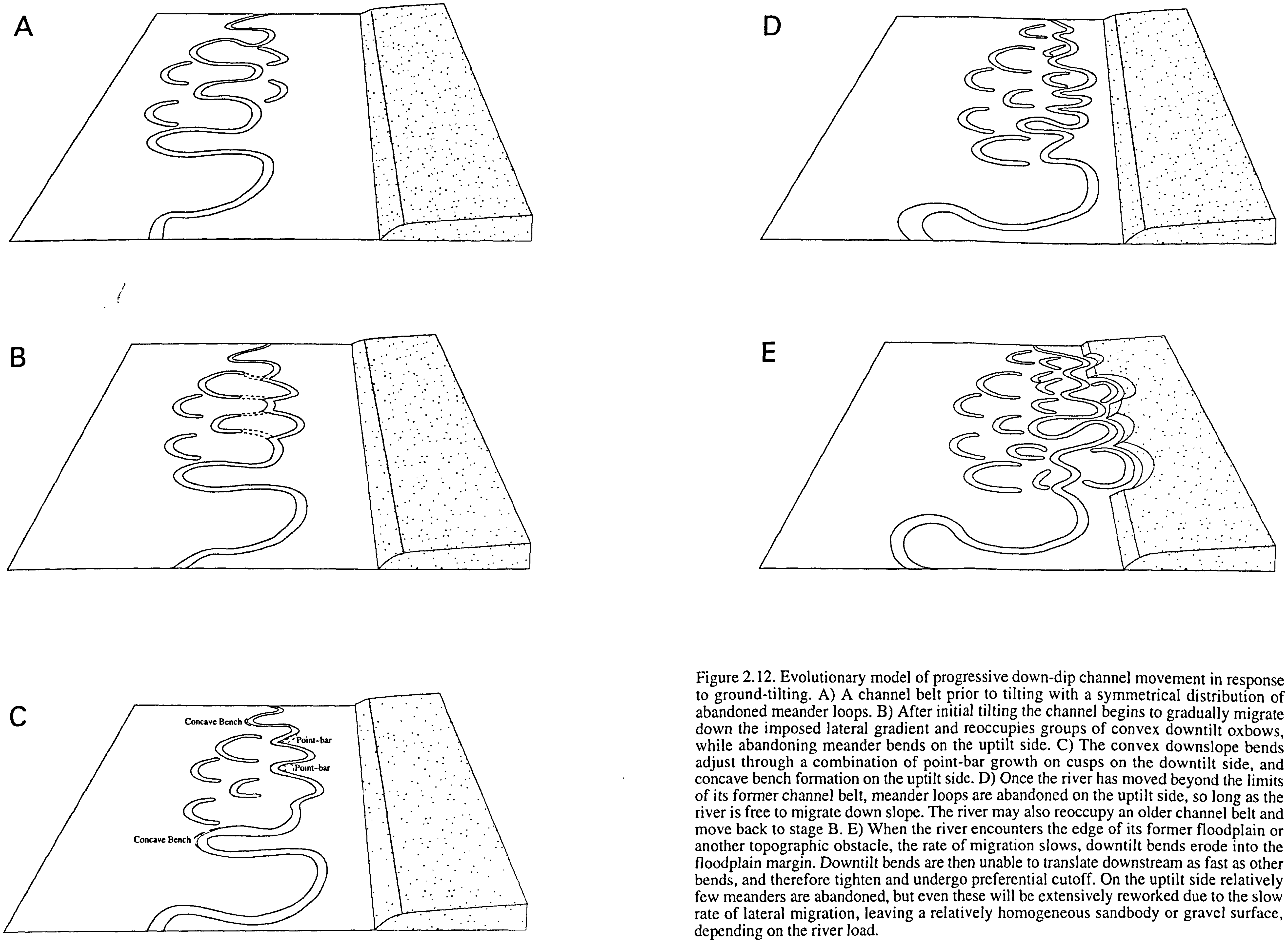

Figure 2.12. Evolutionary model of progressive down-dip channel movement in response to ground-tilting. A) A channel belt prior to tilting with a symmetrical distribution of abandoned meander loops. B) After initial tilting the channel begins to gradually migrate down the imposed lateral gradient and reoccupies groups of convex downtilt oxbows, while abandoning meander bends on the uptilt side. C) The convex downslope bends adjust through a combination of point-bar growth on cusps on the downtilt side, and concave bench formation on the uptilt side. D) Once the river has moved beyond the limits of its former channel belt, meander loops are abandoned on the uptilt side, so long as the river is free to migrate down slope. The river may also reoccupy an older channel belt and move back to stage B. E) When the river encounters the edge of its former floodplain or another topographic obstacle, the rate of migration slows, downtilt bends erode into the floodplain margin. Downtilt bends are then unable to translate downstream as fast as other bends, and therefore tighten and undergo preferential cutoff. On the uptilt side relatively few meanders are abandoned, but even these will be extensively reworked due to the slow rate of lateral migration, leaving a relatively homogeneous sandbody or gravel surface, depending on the river load.

proposed model may provide a means of estimating the relative timing of renewed tectonic ground-tilting from an analysis of the channel planform.

2.6 Large scale lateral planation by rivers

A number of workers have advocated the importance of lateral fluvial erosion in creating wide plains (Gilbert, 1877; Davis, 1899; Blackwelder; 1931; Johnson, 1931; Mackin, 1937; Cotton, 1939; Crickmay 1974, 1975; Osborn and du Toit, 1991). In contrast, most textbooks have suggested that lateral planation can only occur over a very limited areal extent (Thornbury, 1969; Small, 1972; Ollier, 1981; Hart, 1986). Osborn and du Toit (1991) propose examples of lateral planation across three orders of magnitude, from the 100 km^2 of the Red Deer River in Alberta, Canada, through the 1600 km^2 upland deposits of southern Maryland, to the 350,000 km^2 area of the Northern Great Plains of North America (see Table 2.1). The Northern Great Plains are marked by a series of outliers which are capped by fluvial gravels and have a range of elevations between 120-830 m above the level of present day rivers. These deposits are postulated to have formed by alternating periods of lateral movement and incision, but the surfaces have not been dated and therefore the hypothesis cannot be verified. Evidence for lateral movement is stronger in the case of southern Maryland, since palaeocurrent directions agree with the inferred movement history (Schlee, 1957). The grain-size of the deposited gravel also decreases towards the modern course of the Potomac River (Schlee, 1957). At the smallest scale, Osborn and du Toit (1991) note gently inclined slopes updip from modern rivers.

The development of large plains suggests that the rate of downcutting is generally slow and uniform. Rates of incision, range from 0.037-0.133 m ka^{-1}, and lateral gradients from 0.0010 to 0.0160 (Table 2.1). Osborn and du Toit (1991, p.259) conclude their review by stating that, "enough evidence has accumulated to indicate that lateral planation of rivers was responsible for creating at least some of the low-relief plains east of the North American Cordillera, as well as elsewhere".

A causative mechanism for lateral planation remains problematic. However, the larger examples formed over periods of 1 to 10 million years (see Table 2.1) and therefore incision is presumably related to either tectonics or eustasy. Third-order sea level cycles have durations of approximately 1 to 10 Ma (Vail *et al.*, 1977; Haq *et al.*, 1987) but the drop in base-level of approximately 100 metres is unlikely to propagate hundreds of kilometres into the centre of a large continent such as North America, since extension of the fluvial system across the continental shelf, and accompanying channel planform change can accommodate much of the vertical drop (Schumm, 1993; Wescott, 1993).

Table 2.1. Proposed examples of large-scale unidirectional lateral planation†

Area	River	Lateral migration km	Incision m	Time period Ma	Lateral Slope	Migration rate m ka^{-1}	Incision rate m ka^{-1}	Study
Alberta, Canada	Ancestral Bow	100	350	ND	0.0035	ND	ND	Glen and Osborn, 1986
Alberta, Canada	Red Deer	5	ND	ND	ND	ND	ND	Osborn and du Toit, 1991
NE. Montana, USA	Ancestral Missouri	80	365	10	0.0046	8.0	0.037	Colton *et al.*, 1986
NE. Montana, USA	Ancestral Yellowstone	56	400	7	0.0071	8.0	0.057	Colton *et al.*, 1986
S. Dakota, USA	Rapid Creek	8	125	ND	0.0156	ND	ND	Plumley, 1948
W. Nebraska, USA	Pumpkin Creek	6	ND	2.0	ND	3.0	ND	Diffendal and Corner, 1983
Wyoming, USA	Bighorn	10	160	1.2	0.0160	8.3	0.133	Palmquist, 1983
S. Maryland, USA	Potomac	90	90	ND	0.0010	ND	ND	Hack, 1955; Schlee, 1957

ND = No Data. † All examples are collated from the review of Osborn and du Toit, 1991.

Additionally, the sea level drops are not large enough to account for all of the observed incision (Table 2.1).

An alternative explanation may lie in epeirogeny, that is the uplift of plate interiors. A number of mechanisms have been suggested for this process, including thermal isostasy associated with upwelling mantle plumes, penetrative magmatism, phase changes in the upper mantle, and mechanical models such as glacial isostasy and flexure. Average rates of uplift are in the range of 10-200 m Ma^{-1} (Summerfield, 1991), which agrees well with observed rates of incision for proposed examples of lateral planation (Table 2.1). Glacial-isostatically induced tilt magnitudes and rates can be quite significant, particularly in areas which appear to have short relaxation times, such as western Canada and Greenland (Lasca, 1967; Mathews *et al.*, 1970; Ten Brink, 1974). Magnitudes reported for southern British Columbia range from 0.00095 - 0.0019 (Mathews *et al.*, 1970) to 0.00285 (Fulton, 1969). While glacial-isostasy may control the lateral tilt and asymmetric position of some modern rivers (Adams, 1980; Nanson, 1980), glacial-interglacial cycles have also been linked with Milankovitch control (e.g., Hays *et al.*, 1976; Imbrie *et al.*, 1984) and have a typical periodicity in the order of 80,000 years. This time frame is too short to account for the proposed large-scale examples of lateral planation, although there may be a net tectonic tilt between glacial periods as demonstrated in western Canada (Mathews, 1978). Another suggestion for modern river asymmetry is that regional tilting may be associated with tectonically transmitted stresses from the plate margins (Cox, 1994). Tilt block movement has been interpreted in terms of oscillatory motion with periodicities as small as 3000 years (Adams, 1980), however, the possibility remains that a net tectonic tilt may be applied as noted for glacial cycles. In contrast, Summerfield (1991) argues that the sheer size of the regions affected by epeirogeny (up to 1000 km across), coupled with the high rates of uplift, suggests that the cause must be deeper than the crust and probably involves the entire thickness of the lithosphere and possibly part of the asthenosphere.

2.7 Alternative explanations for river asymmetry

In addition to tectonic ground-tilting a number of alternative explanations have been proposed to explain river asymmetry and were grouped by Cox (1994) into internal fluvial processes and external forces. Internal fluvial processes: A number of studies indicate that a preferred direction of movement can occur on low-angle alluvial fans purely through autocyclic mechanisms (Rossi, 1976; Kesel, 1985; Wells and Dorr, 1987a; Singh *et al.*, 1993). The dominant mechanism appears to be the aggradation of former channel courses and associated levees, which later act as barriers to channel movement, therefore promoting channel migration in a single direction (Wells and Dorr, 1987a). The theoretical three-dimensional alluvial architecture model of Mackey and Bridge (1995) produces these autocyclic preferential migration processes and associates them with progressive up-valley movement of avulsion points. A similar mechanism of asymmetry due to movement away from the gravel lag deposits within the channel was also suggested by Hack (1955).

External forces: One of the traditional explanations for river asymmetry is the Coriolis force created by the spin of the Earth which deflects objects to the west or east in the northern and southern hemispheres, respectively. The majority of rivers outlined in Table 2.1 were deflected to the west and are all in the northern hemisphere. However, the influence of the Coriolis force in river bends is debatable (Dinga, 1969), since the force is relatively small in comparison with centrifugal forces (see Dingman, 1984). An alternative proposal is river migration along a shallowly dipping resistant substrate, through a combination of incision and lateral movement. This has previously been referred to as monoclinal shifting (e.g. Gilbert, 1877; Cox, 1994). Fan growth from either basin edge is another cause of river asymmetry and can counteract the ground-tilt if the stream power of a river is too low to remove the fan deposits (Saucier and Smith, 1986; Leeder and Gawthorpe, 1987; Gordon and Heller, 1993; Travis and Nunn, 1994). In particular, basinward migration of rift-border faults can form large prograding fans by cannabilization of former deposits, forcing an axial river towards the hanging-wall dip slope (Leeder and Jackson, 1993; Dart *et al.*, 1995). Where large alluvial fans are absent, an asymmetric tributary distribution may still cause lateral movement of the river, due to the restriction of sediment supply on one side of the river (Dinga, 1969). Other suggestions for river asymmetry include the influence of prevailing winds (Fairchild, 1932; D.Smith in Osborn and du Toit, 1991) and bank aspect induced, freeze-thaw cycle asymmetry (Lawler, 1986), both of which were postulated to cause preferential bank erosion on one side of the channel.

2.8 Channel-belt asymmetry as a tool for tectonic interpretation

A number of authors have used the asymmetric position of rivers with respect to their valleys to infer the tectonic history or structure of an area (Mike, 1975; Price and Whetstone, 1977; Reid, 1992; Cox, 1988a, 1994). Cox (1988a, 1994) introduced a statistical method for quantifying the direction and magnitude of river asymmetry (see Fig. 2.13). Topographic profiles are taken perpendicular to the valley axis and the asymmetry magnitude (T) calculated from the ratio of the distance from the meanderbelt midline to basin midline (Da), to the drainage divide to basin midline length (Dd). The direction and magnitude (T) can then be considered as a single vector quantity and plotted on maps or on polar plots. Allocyclic control is indicated by a marked asymmetry, in contrast to autocyclic processes which should show a random distribution of asymmetry. Ideally, only dendritic drainage networks should be used as a full range of channel directions are required in order to identify the strongest direction of asymmetry.

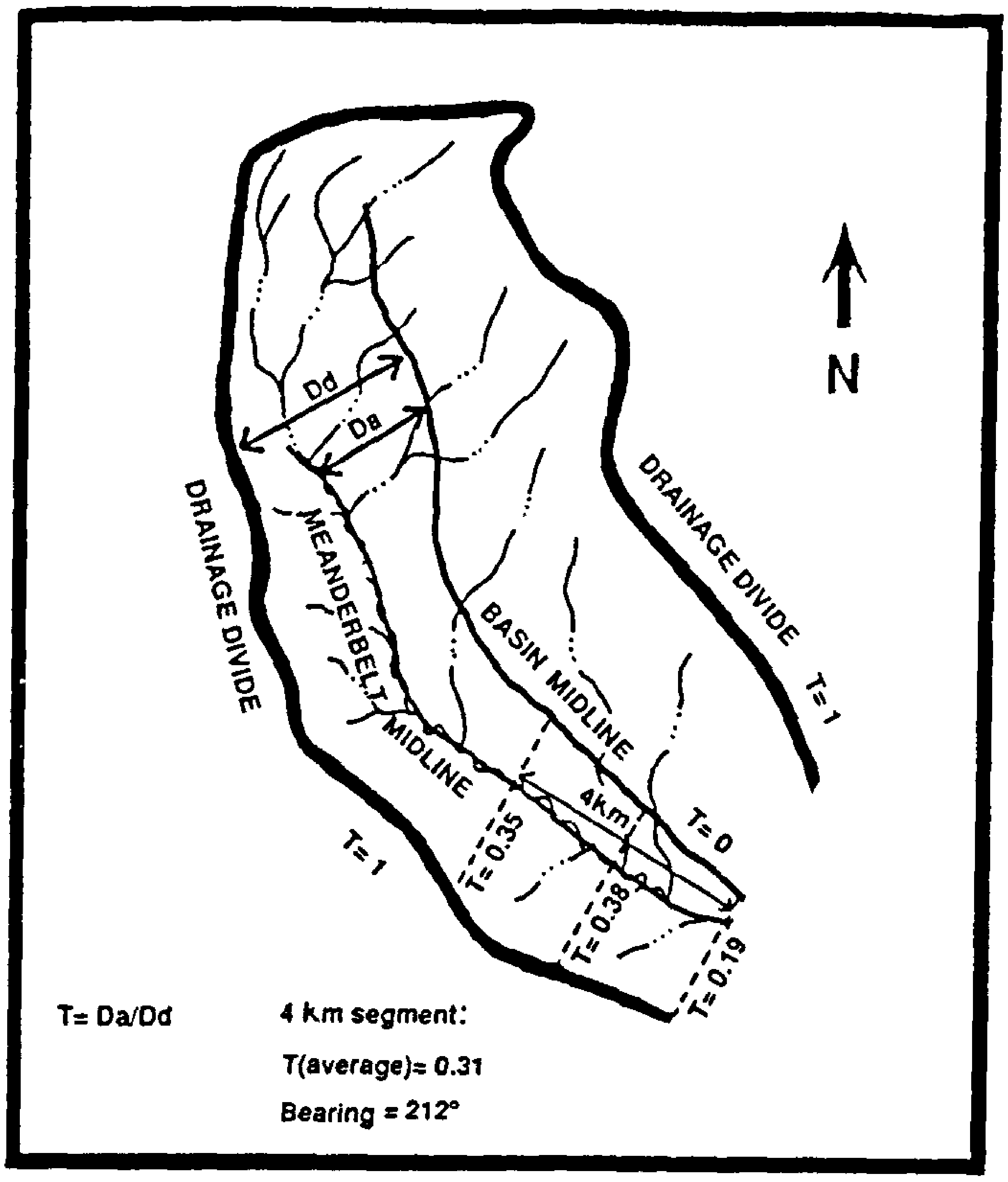

Figure 2.13. Outline of statistical method for calculating the direction and magnitude of river asymmetry. The asymmetry magnitude (T) is the ratio Da/Dd, where Da=the distance from the active meander-belt midline to the basin midline, and Dd=the distance from the drainage divide to the basin midline. Direction of asymmetry is measured perpendicular to the meanderbelt midline. From Cox (1994).

The statistical technique outlined above cannot differentiate between ground tilting and other possible causes of river asymmetry, and therefore some independent information is required to support a hypothesis of ground-tilting. In the Mississippi embayment studied by Cox (1994), geological strata dipped predominantly in the opposite direction to the observed river asymmetry, indicating that the asymmetry was not derived from gradual movement down a bedding-plane (monoclinal shifting) but probably from ground-tilting. Independent support for ground-tilting was provided by geological and geomorphological evidence for tilting of preserved Pleistocene sediments (Cox, 1988a).

2.9 Studies of tectonic tilting in the rock record

2.9.1 Introduction

A large number of studies have used theoretical alluvial architecture models to interpret ancient fluvial systems (e.g. Allen and Williams, 1982; Behrensmeyer and Tauxe, 1982; Bridge and Diemer, 1983; Blakey and Gubitosa, 1984; Bridge and Gordon, 1985; Gordon and Bridge, 1987; Kraus and Middelton, 1987; Schuster and Steidtman, 1987; Marzo *et al.*, 1988; Mack and Seager, 1990; Mack and James, 1993). However, very few of these studies show any evidence of the influence of lateral tilting (see Table 2.2). An exception is the work of Marzo *et al.*, (1988) in the central southern Pyrennean foreland basin which demonstrated a progressive movement of axial drainage. Sheet sandstone development is attributed to thrust-induced gradient rejuvenation which controls channel avulsion, fan progradation and basin aggradation. Three-dimensional reconstruction of meander belts in part of the Loranca basin, central Spain, also shows a progressive deflection in palaeochannel deposits in an aggrading system (Díaz-Molina *et al.*, 1995). This axial deflection has similarly been attributed to growth of a ramping anticline with a consequent increase in localised tectonic tilt.

2.9.2 Rio Grande rift

A more detailed example of the effects of lateral tilting in the ancient rock record is given by Mack and Seager (1990) and Mack and James (1993), who describe the Rio Grande rift. The Camp Rice and Palomas Formations represent axial fluvial facies that were deposited in the southern Rio Grande rift during the Pliocene-Pleistocene (Fig. 2.14). Subsequent incision, probably related to capture of the upper Rio Grande by the lower Rio Grande, has exposed up to 100 m of sediment (Mack and Seager, 1990). The initiation of downcutting is unknown, but a minimum age for incision to within 35 m of the present day floodplain has been estimated from cross-cutting basalt flows at approximately 0.55 Ma (Seager *et al.*, 1984). Excellent three-dimensional exposure, combined with a tectonic setting that has not significantly changed since the time of deposition, has allowed the alluvial-tectonic relationships to be observed and mapped. Schematic cross-sections illustrate the differences in distribution of the axial fluvial facies between half-grabens and grabens (Fig. 2.15). Both the Palomas and Mesilla half-grabens have axial-fluvial facies that are located within a few kilometres of the basin-bounding fault (Fig. 2.15a, c), as predicted by alluvial architecture models that incorporate lateral tilting (Bridge and Leeder, 1979; Blair and Bilodeau, 1988;

Table 2.2. Outlines for studies of ancient fluvial strata interpreted using theoretical alluvial architectural models

Study	Sedimentary Description	Sedimentary Interpretation	Basin Interpretation	Evidence for Lateral Tilt
Allen & Williams (1982)	Isolated upward-fining sandstones in a mudstone dominated succession containing calcretes	River influenced transitional tidal flats. Stable between upbuilding phases of mudflat	None	None
Behrensmeyer & Tauxe (1982)	(1) Widespread sheet sands and silts (2) Shoe-string sands and large volumes of silt and clay	(1) Uplift affecting the source area, giving valley cut-and-fill deposits (2) Autocyclic driven avulsion of one or more parallel fluvial systems	Foreland basin. Rivers draining the mountain front, perpendicular to the basin axis	Lateral tilt eliminated as a possible mechanism in both cases
Bridge & Diemer (1983)	Multistorey sandstones showing evidence of lateral accretion and separated by fine grained units	Periodic avulsion with aggradation. Alluvial plain deposits	None	Local floodplain tilting may account for variations in the relative sandstone proportion
Blakey & Gubitosa (1984)	(1) Mixture of very broad thin sheets, sheets and ribbon sandstones (2) Tripartite facies distribution into sheet-ribbon-sheet	(1) Both braided and meandering rivers coupled with changing subsidence rates (2) Diapiric salt activity - braided and meandering streams - changing subsidence rates	Basin was located on the western edge of the North American continent during Late Triassic	(1) None (2) Local tectonic tilt is associated with the movement of salt, but the succession is interpreted in terms of vertical subsidence rates
Bridge & Gordon (1985)	Multistorey sandstones showing evidence of lateral accretion, with interbedded mudstones	Periodic avulsion with aggradation	The sediments form part of the Catskill wedge which has been interpreted as a foreland basin fill	None

Table 2.2. (Continued). Outlines for studies of ancient fluvial strata interpreted using theoretical alluvial architectural models

Study	Sedimentary Description	Sedimentary Interpretation	Basin Interpretation	Evidence for Lateral Tilt
Gordon & Bridge (1987)	Multistorey sandstones showing evidence of lateral accretion, with interbedded mudstones	Periodic avulsion with aggradation	Lowland alluvial plain (part of the Catskill wedge - see outline of Bridge and Gordon, 1985)	"The effects of preferred tectonic tilting of the floodplain are not possible to assess" (p.244)
Kraus & Middleton (1987)	(1) Multistorey sandbodies with a few single-storey sandbodies (2) Ribbon sandstones surrounded by fine grained sediments	(1) Meandering channels-comparatively slow subsidence (2) Meandering channels showing faster subsidence	Both sequences were deposited in Laramide intermontane basins	None
Schuster & Steidtman (1987)	Dominantly ribbon sandstones in fine grained sediments. A few multistorey sandstones.	Low sinuosity channels. Rapid subsidence due to thrust emplacement and regional flexure	Foreland basin	None
Marzo *et al.*, (1988)	Multistorey sheet sandstones showing lenticular-bedded bodies and lateral-accreted bodies, interbedded with mudstones	Braided (lenticular) and meandering (lateral) deposits with increasing avulsion down-stream	Foreland basin. Thrust stacking in the hinterland and surficial thrust displacement to the foreland	Lateral control by alluvial fan progradation and uplift of the thrust sheet due to thrusting
Mack and Seager (1990) Mack and James (1993)	(1) Half-graben - composed almost entirely by multistorey sandbodies (2) Graben - multistorey sandbodies with 40% mudstone	Low sinuosity, sandy bedload streams. Avulse close to the locus of maximum deposition in the half-graben case	Symmetrical and asymmetrical rift basins	Lateral tilting accounts for the difference between the asymmetric and symmetrical basin facies. Confirms the theoretical models

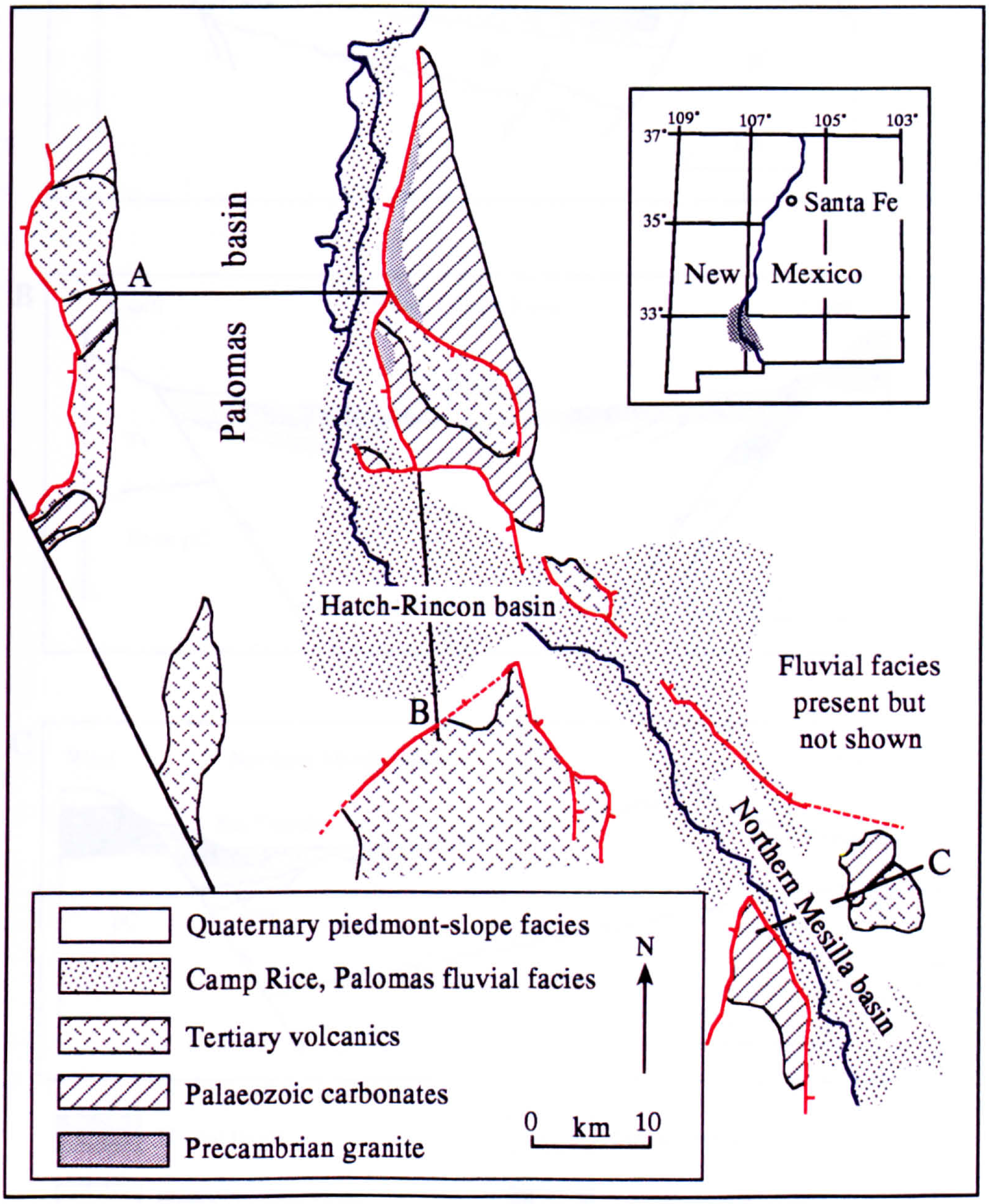

Figure 2.14. Outline geological map of the southern Rio Grande rift, showing the position of the axial river deposits and the locations of schematic cross-sections (Fig. 2.15). River flow is from north to south. Adapted from Mack and Seager (1990).

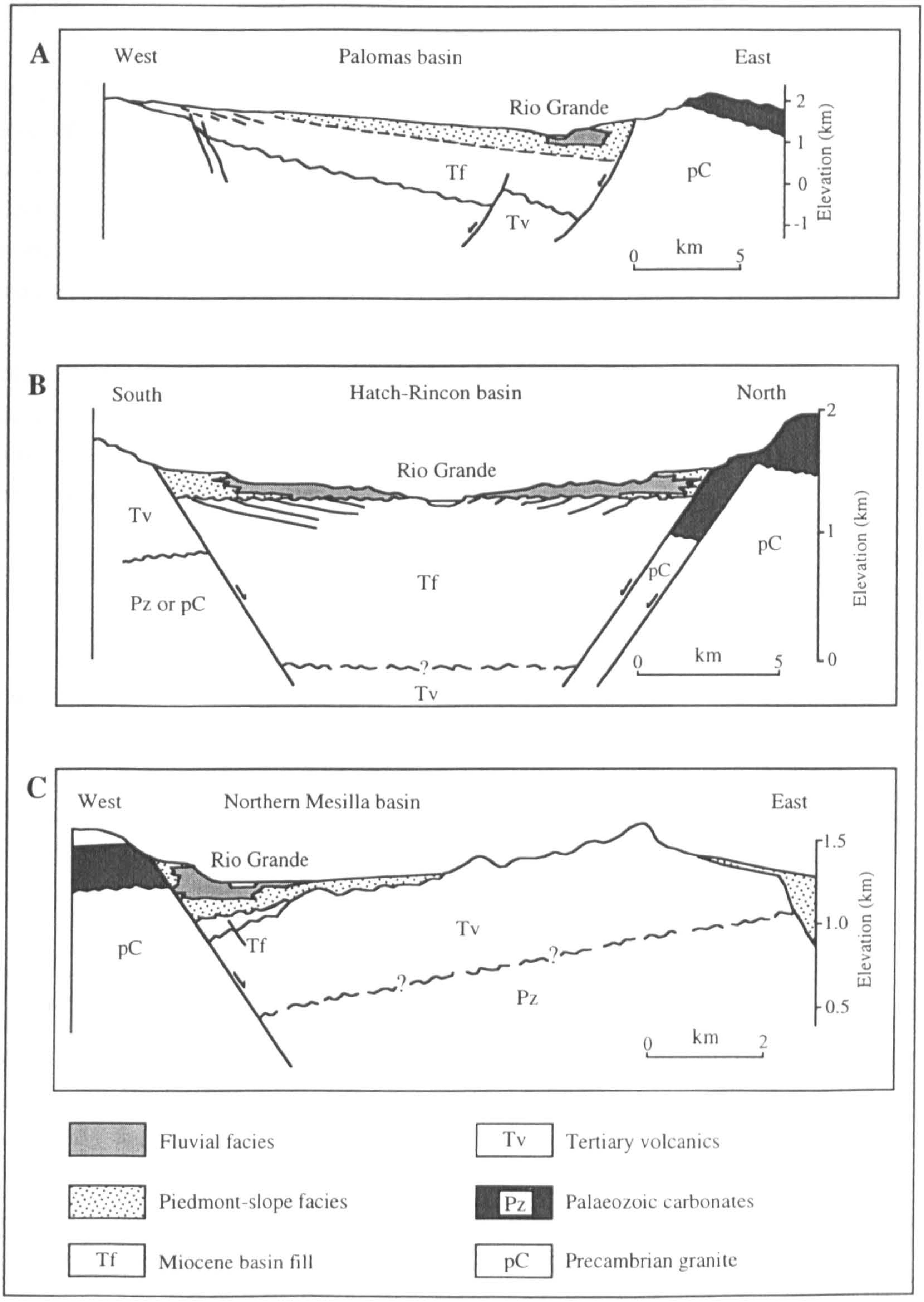

Figure 2.15. Schematic cross-sections of the southern Rio Grande rift. A) Palomas basin, B) Hatch-Rincon basin and C) Northern Mesilla basin. The position of sections is marked on Figure 2.14. Elevations are in metres above sea level. Adapted from Mack and Seager (1990).

Heller *et al.*, 1988). This is in contrast to the Hatch-Rincon graben which has a symmetrical distribution of river sediments (Fig. 2.15b).

The axial-fluvial deposits of the Palomas and Mesilla basins are dominantly composed of multistorey sandbodies, interpreted as the deposits of low-sinuosity, sandy bedload streams which have undergone frequent avulsion (Mack and Seager, 1990). Erosive channel contacts within the multistorey sheets, and the presence of ribbon sandstones, suggest that avulsion was probably the major mode of channel movement within the asymmetric basins of the Rio Grande rift. A number of sheet sandstone channels have also been identified and are attributed to the process of lateral migration. However, there does not appear to be any evidence to suggest progressive down-dip migration of channels. The fluvial deposits of the Hatch-Rincon graben are composed of large laterally extensive multistorey sandbodies that are separated by a much higher percentage of overbank deposits (40% instead of <1%) than the half-graben basins, and incorporate well-developed palaeosols (Mack and James, 1993).

2.9.3 Criteria for the recognition of progressive down-dip movement in the ancient

Three possible criteria for recognising examples of gradual down-dip channel movement in the rock record can be identified from the study of Leeder and Alexander (1987):

1) an increase in the lateral extent of sandbodies (of single or multithread channel origin) relative to predicted values from general estimates of channel belt width (e.g., Collinson, 1978; Fielding and Crane, 1987; Bridge and Mackey, 1993b),

2) an increase in the width of channel belt sandbodies (of single or multithread channel origin) with increasing proximity to the basin-bounding or formerly active fault. The underlying control being increased tilting and / or growth folding towards the basin bounding fault (see Fig. 2.16); and,

3) a bias in the preservation of point-bar deposits due to the progressive cutoff and preservation of bends in the updip direction. Lateral accretion surfaces within the point-bar deposits dip preferentially upslope when viewed in cross-section (see Fig. 2.16).

For criteria 1 and 2, ancient gravel bed rivers would show a contrast between coarse-grained facies encased within sand or mud dominated deposits.

Few studies have used any of these proposed criteria to identify gradual down dip migration in the rock record. An exception is the study of Woolfe, (1992) who noted a

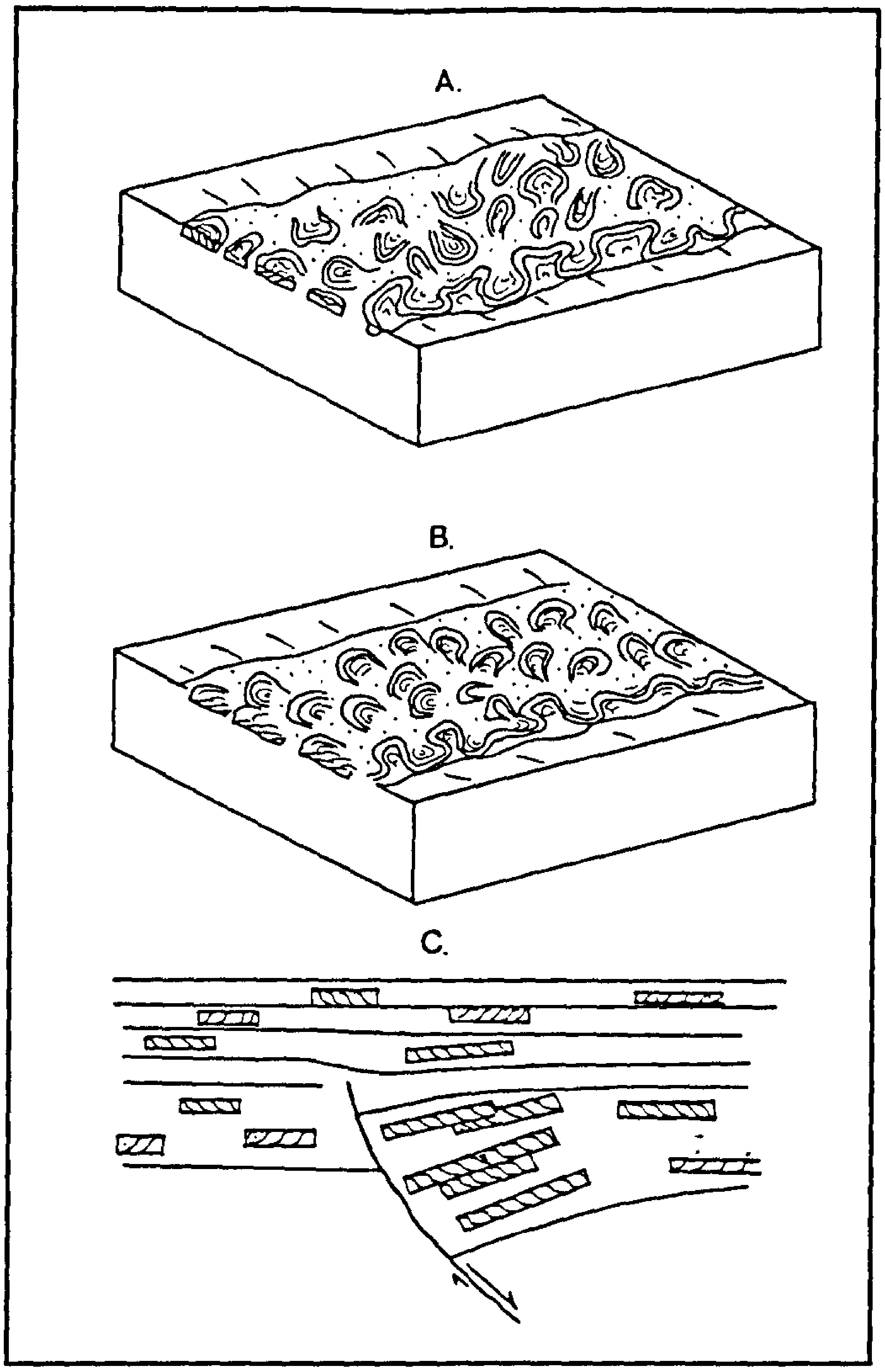

Figure 2.16. Suggested planform and cross-sectional development of an axial river undergoing progressive down-dip movement. A) Avulsion of the channel down-dip, leaving a random distribution of meander loops. B) Plan view of progressive lateral down-dip movement, with preferentially preserved meander loops on the uptilt side. C) Cross-sectional view of sandbody distribution in a half-graben controlled by a growth fold. Gradual down-dip movement elongates sandbody width and forms lateral accretion surfaces that dip preferentially upslope. From Leeder and Alexander (1987).

preservation bias of point-bars in the Weller Coal Measures of Allan Hills, Antarctica. Diverse palaeocurrents within single sheets and variation in palaeocurrent directions between sandstone sheets were interpreted in terms of preferential preservation of left and right handed point-bars. These preservation biases suggest that the rivers migrated down a lateral gradient and that the direction of the lateral gradient reversed through time. The sandbodies have been interpreted as the products of non-avulsive meandering rivers draining extensive peat swamps (Woolfe *et al.*, 1991). Two possible causative mechanisms can be implied for the formation of lateral gradients in the Weller Coal

Measures of Allan Hills. Firstly, differential compaction of the underlying peat may have caused lateral ground tilting. However, any original differences in peat depth and therefore subsequent compaction could have been caused by variations in subsidence rates (e.g., Fielding, 1987), possibly related to basin floor tilting. A second mechanism is by direct tectonic tilting. A possible tectonic component is indicated by braided river deposits which were sourced from highlands to the east and periodically prograded over the meandering deposits (Woolfe *et al.*, 1991; Woolfe, 1992). This progradation suggests that some episodic faulting may have been occurring on at least one basin margin.

The first criterion is difficult to test or use for the identification of progressive down-dip migration because of the intrinsically high variation between mean bankfull depth and channel-belt width (Bridge and Mackey, 1993b). For example, the combined dataset of Bridge and Mackey (1993b) has a standard error of 0.324 log units and therefore the 95% confidence limits span a range of approximately 1.3 log units. Additionally, bankfull depth may be obscured by the tendency for channel belts to erode into one another close to the fault, thereby creating multistorey sandstones (e.g., Mack and James, 1993). In these cases, relationships between channel width and channel-belt width have to be used (e.g., Zeller, 1969; Williams, 1986; Bridge and Mackey, 1993b). Even where channel-belt size variations greater than about 1.5 orders of magnitude exist in the rock record, outstanding exposure is required in order to accurately clarify them. Similarly, excellent exposure is required to test or use the second criterion of an increase of channel-belt width with increasing proximity to the fault. A second limitation is that classic half-graben models require high aggradation rates in order for channel-belts close to the fault to have a high preservation potential. However, as previously discussed, high rates of aggradation tend to favour avulsion (e.g., Törnqvist, 1994).

2.10 Discussion

The response of rivers to tectonic tilting can be categorised into two types: avulsive movement and gradual down-dip migration (Alexander and Leeder, 1987; Leeder and Alexander, 1987). However, a criterion is required to delineate between these two types of channel adjustment. Table 2.3 summarises the magnitudes and rates of tectonic tilting for those examples discussed, and includes the lateral planation examples. Induced lateral tilt gradients vary over two orders of magnitude but appear to have no clear relationship with planform response. There is also no significant correlation between the style of movement and the ratio of lateral:downstream gradients, although in the majority of cases the lateral tilt is comparable or larger than the downstream slope. In contrast, the rate of tilting appears to correlate with the style of movement, with avulsive examples having rates $\geq 7.5 \times 10^{-3}$ radians ka^{-1}, while average gradual migration rates are 2 to 3

Table 2.3. Examples of laterally tilted rivers: tilt magnitudes, tilt rates and channel responses

Study Area	Source	Lateral Slope	Downstream Slope	Lateral / Downstream (%)	Tilt Rate (radians / 1000 years)[¥]	Channel Response
Walker Basin (Nevada)	Blair and McPherson (1994)	0.009	0.0017	512	2.9 x 10^{-2} [§]	Avulsion
Long Valley Caldera (Owens River)	Reid (1992)	0.0008-0.0026	0.0025	32-104	7.5 x 10^{-3} [◊]	Avulsion
Madison River (Montana)	Leeder and Alexander (1987)	0.01-0.015	0.0034[α] 0.001[β]	294-441[α] 1000-1500[β]	5.0 x 10^{-4} - 7.5 x 10^{-4} [Δ]	Migration
Beatton River	Nanson (1980)	0.0003-0.0004 (estimated)	0.0003	100-133	1.4 x 10^{-5} - 1.9 x 10^{-5} [‡]	Migration
Lake County Uplift (Mississippi River)	Russ (1982)	0.00028	0.00019 - 0.00033[#]	85-147	4.7 x 10^{-5} [†]	Migration
Lateral Planation Studies	Table 2.1	0.0010-0.0160	No Data	No Data	1.3 x 10^{-5} - 4.6 x 10^{-7}	Migration

[¥] Note: radians are a ratio of arc length to radius. Therefore, for small angles radians and gradients are interchangeable as the arc length can be approximated as a straight line

[§] No tectonic tilting took place in this example as the base-level (lake surface) fell by 0.4 m / year, exposing a previously tilted surface. The calculated tilt magnitude is for tilting associated with movement of 0.4 m / year on the basin-bounding fault across this 14 km wide half-graben, and assumes that the basin behaves as a rigid tilt block

[◊] Average slopes associated with tectonic uplift between 1979-1983 (Castle *et al.*, 1984) and probably too high for a longer term (1000 year) average

[α] Downstream slope and lateral:downstream slope of the modern river. [β] Downstream slope and lateral:downstream slope, prior to the building of a dam (Jackson, 1964)

[Δ] Based on tilting starting at the time of initial terrace formation which has been dated as 20 ± 3 ka (Adams and Locke, 1990; Adams *et al.*, 1992) and is taken here as 20 ka

[‡] Based on estimate of movement since the last glacial maximum which is assumed to be approximately 21 ka (Williams *et al.*, 1993)

[#] Taken from the levee slopes within and immediately upstream of the uplift (Russ, 1982)

[†] Rate of tilting based on the estimated 6,000 year active period of the Lake County Uplift (Russ, 1982)

orders of magnitude smaller (Table 2.3). However, caution should be adopted when using this criterion to infer past tilting rates from the nature and distribution of palaeochannels, since it is based on a relatively small number of studies, many of which are based on assumptions (see Table 2.3). In the case of the Madison River, which has the largest tilt rate for an example of gradual migration, the accompanying periods of incision may have restricted avulsive movement (Alexander *et al.*, 1994). However, there does appear to be some evidence that tilt rate is significant in its affect upon channel response.

The discussion of lateral tilting in this chapter could be more widely applied in studies on the interaction between rivers and active tectonics (e.g. Gregory and Schumm, 1987; Jorgensen, 1990). In particular, studies have concentrated on either recognising down valley or cross-valley changes, but have not identified examples where the two processes operate simultaneously. Jorgensen (1990) studied the effects of active tectonics on a number of rivers in the United States and interpreted the results in terms of downstream changes. However, some of Jorgensen's data also suggest the presence of lateral tilting, notably in the case of the Humboldt River in Nevada which turns through 70° within the studied reach (Fig. 2.17). Analysis of the long profile of the Humboldt River and its terraces, in combination with the mapped faults and relevelling lines, suggest that there is a zone of subsidence approximately perpendicular to reaches 2 and 3 (Fig. 2.17). There is clear evidence of river response to subsidence, with the area downstream of the maximum subsidence having a reduced sinuosity due to backtilting (reach 2), and the area upstream having an increased sinuosity and undergoing rapid aggradation (reach 4). However, the average position of the river with respect to its channel belt within and upstream of the zone of subsidence is dominantly on the southern side of the valley, suggesting the presence of ground-tilting (e.g., Nanson, 1980; Reid, 1992). Reach 4 is also characterised by slow lateral migration, growth of very tight meander bends and abandonment of bends. The interaction of lateral and downstream tilting as proposed for reach 4, leads to large numbers of very tight bends being cutoff on the up-dip and down-dip sides when the channel is unconstrained and constrained, respectively. In contrast, lateral movement accompanied by backtilting would leave relatively few, low sinuosity bends on the uptilt side.

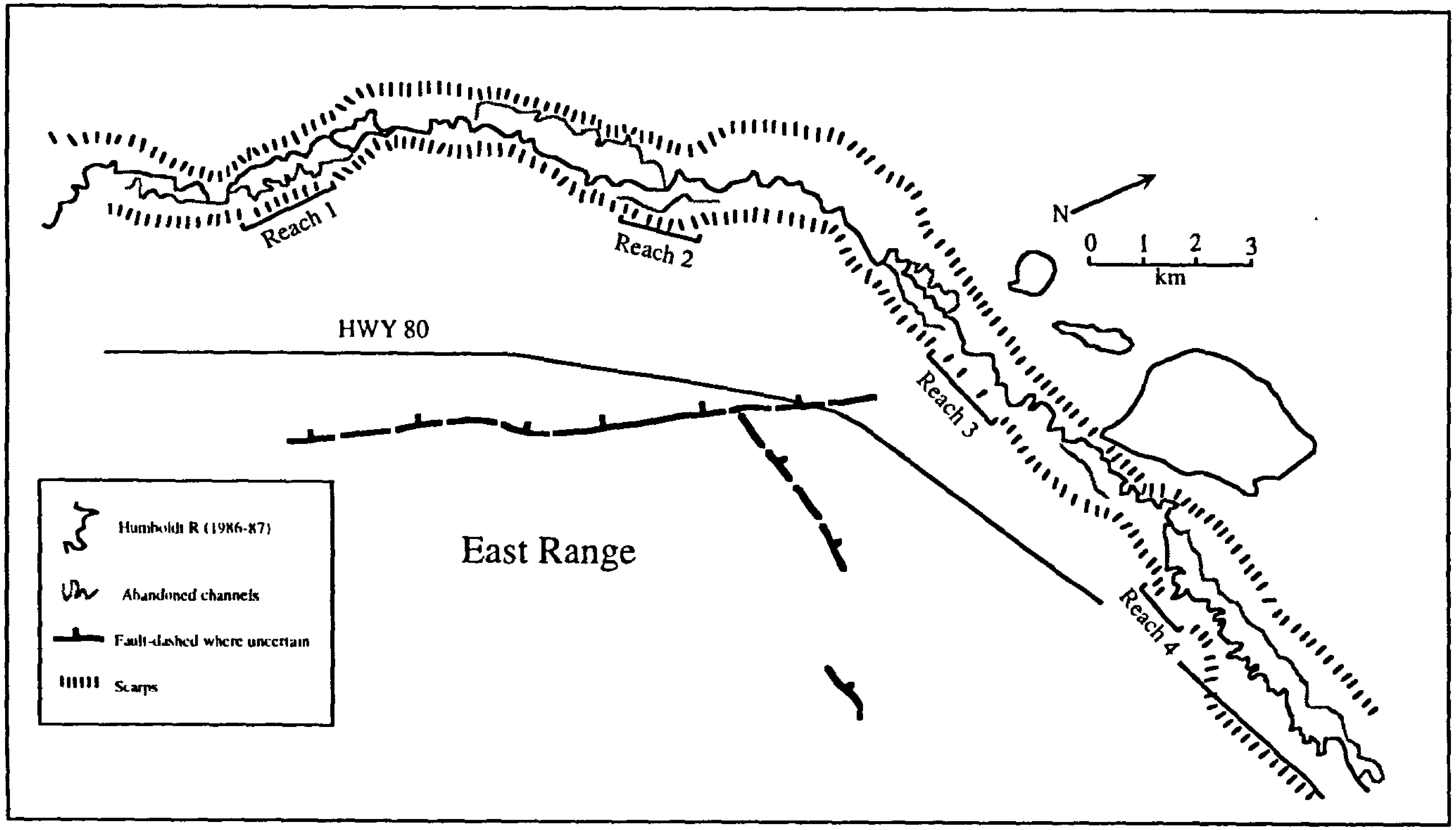

Figure 2.17. Map of the Humboldt River, in the vicinity of Rose Creek, Nevada. Adapted from Jorgensen (1990).

2.11 Summary

This chapter has discussed the influence of lateral tilt on rivers and has highlighted several new points:

☐ A new model of progressive downtilt migration has been presented that unifies the studies of Nanson (1980) and Leeder and Alexander (1987), which have previously been viewed as conflicting models. In addition, an initial channel response to tilting has been suggested, based on the work of Reid (1992) on the Long Valley Caldera, eastern California. Further supporting evidence for this conceptual model of gradual down-dip movement has been detailed from the Mississippi River, in the vicinity of the New Madrid Seismic Zone.

☐ A criterion based on the rate of tilting is proposed to distinguish between channels that respond to tectonic tilting by avulsion or by gradual down-dip migration. There appears to be a division between these two styles of channel response at a tilt rate of approximately 7.5×10^{-4} to 7.5×10^{-3} radians ka^{-1}, although caution should be adopted when using these values since they are based on a relatively small number of poorly constrained examples. However, this type of criterion would allow both avulsive and gradual migration to be incorporated into two and three-dimensional alluvial architecture models.

☐ Three possible criteria for recognising examples of gradual down-dip channel movement in the rock record have been identified from the study of Leeder and Alexander (1987). Two of these criteria are unlikely to be substantiated using the rock record. The third criterion of a preservation bias in point-bar deposits can be examined in the rock record (Woolfe, 1992).

☐ The channel planform has usually been interpreted in terms of either downstream or cross-stream tilting. However, in any case where the direction of tilt is oblique to the long profile of a river, a component of downstream and cross-stream tilting will exist. Planform interpretation should consider such possibilities.

☐ The areal extent, time-scale and magnitude of incision in proposed examples of large-scale lateral planation, suggests that the causative mechanism is some form of epeirogenic uplift.

Chapter 3. Theoretical Background to Physical Modelling

3.1 Synopsis

This chapter discusses the classification of physical models and reviews the development of physical modelling theory over the past century. Similarity theory and dimensional analysis, which form the mathematical basis for 'scale' modelling, are treated systematically and developed from first principles. The key parameters of fluid flow (flow Reynolds number, Froude number and grain Reynolds number) are derived using dimensional analysis and each of these terms is then defined and the implications for modelling considered. Three increasing levels of similarity, geometric, kinematic and dynamic are introduced and used as a framework for discussing the physics of flow in a model and the interaction of the flow with sedimentary particles. Finally, the modelling of overbank sedimentation and time are considered.

3.2 Model classification

At the simplest level, physical models of rivers have traditionally been divided on the grounds of specificity, that is how closely they replicate a prototype, and by the boundary conditions (Chorley, 1967; Schumm *et al.*, 1987). Generic or analogue models reproduce certain features of a natural system even though the driving forces, processes, materials and geometries may differ from the original (Chorley, 1967). At the other end of the specificity continuum, scale models attempt to simulate exactly, some or all of the key parameters of the system, either from a specific prototype or from general values. Scale models are based on similarity theory which produces a series of dimensionless parameters, which fully characterise the flow. In an idealised situation every variable could be perfectly scaled in the model. However, in the majority of experiments this is not possible since water is used as the fluid in both prototype and model. The density and viscosity of the fluid affect two of the major flow variables, namely the flow Reynolds number, which represents the ratio of inertial to viscous forces and the Froude number, which expresses the ratio of inertial to gravitational forces. If the fluid is identical in the model and prototype, only one of these variables can be correctly scaled. To overcome this problem, the scaling of the flow Reynolds number is relaxed, whilst maintaining a turbulent flow, whilst the Froude number is correctly scaled (see Section 3.4 for further details). This technique is known as Froude Scale Modelling (FSM), although often the complexity of the system results in the Froude number being only approximately scaled.

The vast majority of analogue, scale and Froude scale models used in the field of earth sciences have very open physical boundary conditions, that is both the banks and bed are fully erodible, with the edges of the experimental apparatus serving as the ultimate constraint. This is not the case in the engineering literature where two main types of modelling are used; fixed-bed studies, which have non-erodible boundaries and no sediment transport, and movable-bed experiments where the substrate is free to move within a constrained channel. The former are widely used to study the effect of man-made structures such as spillways and conduits on flow pattern while the latter are usually used to scale sediment transport rates and hydraulics in open-channel flows such as rivers and estuaries.

Physical models cannot be scaled down indefinitely since a point is reached where flow depths and velocities are too small to transport the substrate. For many movable-bed models, laboratory space and construction cost may also act as the ultimate constraint. In these cases, distorted models are applied with different horizontal and vertical length scales. To achieve precise modelling of sediment transport in a distorted model, supplementary slope is often added and changes are made to the velocity and discharge scales. It is not possible to fully predict the magnitudes of these adjustments and therefore a process of verification is used, whereby variables are altered until the model reproduces changes that were previously observed in the prototype.

As noted earlier, most Froude scale models do not achieve perfect similarity with the prototype and in some cases the similarity is limited. Recently, some authors (e.g., Church quoted in Ashmore 1991a; 1991b; Leddy, 1993) have suggested that since these models produce general rather than exact features, they should also be called generic models. This is because existing classifications, outlined above, revolve around the concept of specificity. The major difference however, between generic models and FSM models, is that the degree of replication of reality can be estimated and accounted for in a Froude scale model, and not in a generic model. This has three major advantages:

1) some parameters will be modelled correctly and their effects can then be interpreted,
2) other processes may not be correctly modelled but can still be estimated and subsequently interpreted, and
3) different models can be quantitatively compared.

Davies (1987) even argues that in the case of bedload transport in braided rivers, Froude scale models are likely to be more accurate than the limited data that can be obtained from a prototype river. This would certainly not be the case in many traditional generic studies.

However, in order to fully utilise the potential of Froude scale modelling, much more detail should be routinely published on the model flow hydraulics. Additionally, definitions for parameters should be clearly stated. For example, slope is one variable used in the calculation of shear velocity which is also used for computation of the grain Reynolds number. Three possible slopes (valley slope, bed slope or water surface slope) could be used, but are not generally specified. Additionally, a consensus is required on the definition of specific parameters. For example different authors use either the D_{50}, D_{90} or $D_{100}/1.8$ for the grain Reynolds number, which makes comparison difficult (see Table 3.1 and Section 3.6.1). Despite these problems, FSM is a valid and potentially strong technique for investigating river behaviour in a controlled environment. The rest of this chapter will elaborate on the details of the FSM technique / approach.

3.3 Historical background

Physical modelling has been an important technique in the study of rivers for well over a century. Early studies included those of Fargue who studied the Garonne River at Bordeaux in 1875 (Zwamborn, 1967), Reynolds (1887) who examined sediment movement qualitatively in a model of the River Mersey estuary and Vernon-Harcourt (1889) who studied the Seine estuary. At a much smaller scale, Thompson (1879) examined the flow of water around a bend. These initial studies scaled only a few parameters (the horizontal distance in the case of Fargue and horizontal and vertical distances and tidal period in the case of Reynolds). It was not until the development of Buckingham's (1915) Π theorem that the mathematical basis was in place to attempt scale modelling of all relevant parameters. In 1942, the American Society of Civil Engineers published a manual on hydraulic models (ASCE, 1942) followed in 1950 by 'Similitude in Engineering' (Murphy, 1950). Since 1950 there have been a large number of publications on physical modelling including the influential work of Yalin (1971) who greatly expanded the modelling theory, Franco (1978) who analysed movable-bed modelling techniques, and Schumm *et al.*, (1987) on landform development and fluvial processes.

Froude scale modelling has only recently been applied to the study of rivers within the earth sciences (e.g. Ashmore, 1982, 1985, 1988; Southard *et al.*, 1984; Davies and Lee, 1988; Hoey and Sutherland, 1989; Young and Davies, 1990; Hoey and Sutherland, 1991; Young and Davies, 1991; Leddy *et al.*, 1993; Ashworth *et al.*, 1994; Warburton and Davies, 1994a; Ashworth, 1995), and the vast majority of studies have been generic models (e.g. Tiffany and Nelson, 1939; Friedkin, 1945; Leopold and Wolman, 1957; Brush and Wolman, 1960; Ackers, 1964; Hickin, 1972; Schumm and Khan, 1972; Zimpfer, 1975; Begin, 1979; Parker *et al.*, 1982; Gardner, 1983; Ouchi, 1985; Jin and Schumm, 1987; Schumm *et al.*, 1987).

3.4 Similarity theory

If a set of parameters present in both the field prototype and model are at a constant ratio or scale, then the two systems are said to be similar. Perhaps the most intuitive example is that of shape, where the geometric properties remain the same irrespective of the magnitude of the length scale. The application of this simple principle through the development of similarity theory in the early part of the twentieth century greatly advanced the use of physical models.

For any given system, there are many possible types of similarity, but in the case of open-channel flow most can be adequately described by three; geometric, dynamic and kinematic.

- Geometric similarity [L] is where the ratio of the geometric lengths (width, length, depth and so on) and angles are equal.

- Kinematic similarity [LT] involves the comparability of motion of both fluid and sediment particles. This implies both spatial or geometric similarity as seen in the flow paths of particles and temporal similarity as qualified by velocities and accelerations.

- Dynamic similarity [MLT] refers to ratios of forces, both in terms of masses and the forces acting upon those masses.

Other types of similarity, such as thermal and chemical similarity do exist but are not relevant to this study.

3.4.1 Introduction to dimensional analysis

The three types of similarity outlined above may be expressed in dimensionless form through consideration of their fundamental dimensions. Geometric similarity deals only with lengths, so: $L_m / L_p = \lambda_L$ where λ_L is a scale factor for length and L_m and L_p are the lengths for the model and prototype respectively. Kinematic similarity is a ratio of velocities (V) and therefore has dimensions of both length (L) and time (T): $\lambda_V = V_m / V_p$ where $\lambda_T = T_m / T_p$ and $\lambda_L = L_m / L_p$. The same process can be used for dynamic similarity which, since it is a force, has dimensions of mass, length and time (MLT^{-2}), to give $\lambda_F = F_m / F_p$. In order to create a model observing these three types of similarity, it is necessary to determine the magnitude of each of the scales: the methods of dimensional analysis provide a mathematical framework for doing this.

There are three different methods of analysis, the indicial method, Buckingham's method and the matrix method. The matrix method (Langhaar, 1980; Barr, 1983) is the most powerful and is widely available on computer. All three methods are based on the fact that any physical quantity can be broken down into the three fundamental units of mass, length and time. A full mathematical treatment of dimensional analysis is not presented here as it is comprehensively reviewed in many texts (e.g., Langhaar, 1980; Chadwick and Morfett, 1986). However, two examples of open-channel flow are used to illustrate the power of this technique. The first and simplest example is for fixed-bed modelling since only the flow and boundary parameters need to be considered. The second example of movable-bed modelling (Section 3.4.3) is complicated by the addition of sedimentary particles.

3.4.2 Fixed bed modelling

In order to use dimensional analysis, the quantities that control a given system must first be selected and placed in terms of their fundamental units. For an open channel flow, with a fixed bed, these controlling variables are normally taken as: the properties of the fluid, dynamic viscosity (μ) and density (ρ); the boundary conditions of the channel, normally hydraulic radius (R) and surface roughness (k_s); the bed slope (S_b), downstream velocity (V) and the gravitational constant (g) (Yalin, 1971). Some authors use an additional frictional resistance term (f) (Chadwick and Morfett, 1986) which is important for laminar and transitional flows since frictional resistance is a product of viscosity, but can be ignored for fully turbulent flows where resistance is independent of viscosity (ASCE, 1963). Surface roughness (k_s) is normally calculated from Nikuradse's (1933) work on flow in pipes, and is defined as "the sand grain diameter for a sand-coated surface which has the same limiting value of λ" (i.e., rough turbulent), where λ is the Darcy-Weisbach friction factor (Fig. 3.1; French, 1985, p.115). The Darcy-Weisbach friction factor is in turn defined as,

$$\lambda = \frac{2h_f gD}{LV^2} \qquad \text{(Eq. 3.1)}$$

where h_f is the head loss due to friction.

Three governing variables must be chosen to obtain a solution from these seven variables μ,ρ,R,k_s,S_b,V and g, using dimensional analysis. These principal variables are generally taken as ρ, R and V since this has been found to generate two key flow parameters, the Froude and flow Reynolds numbers. The method generates n-3

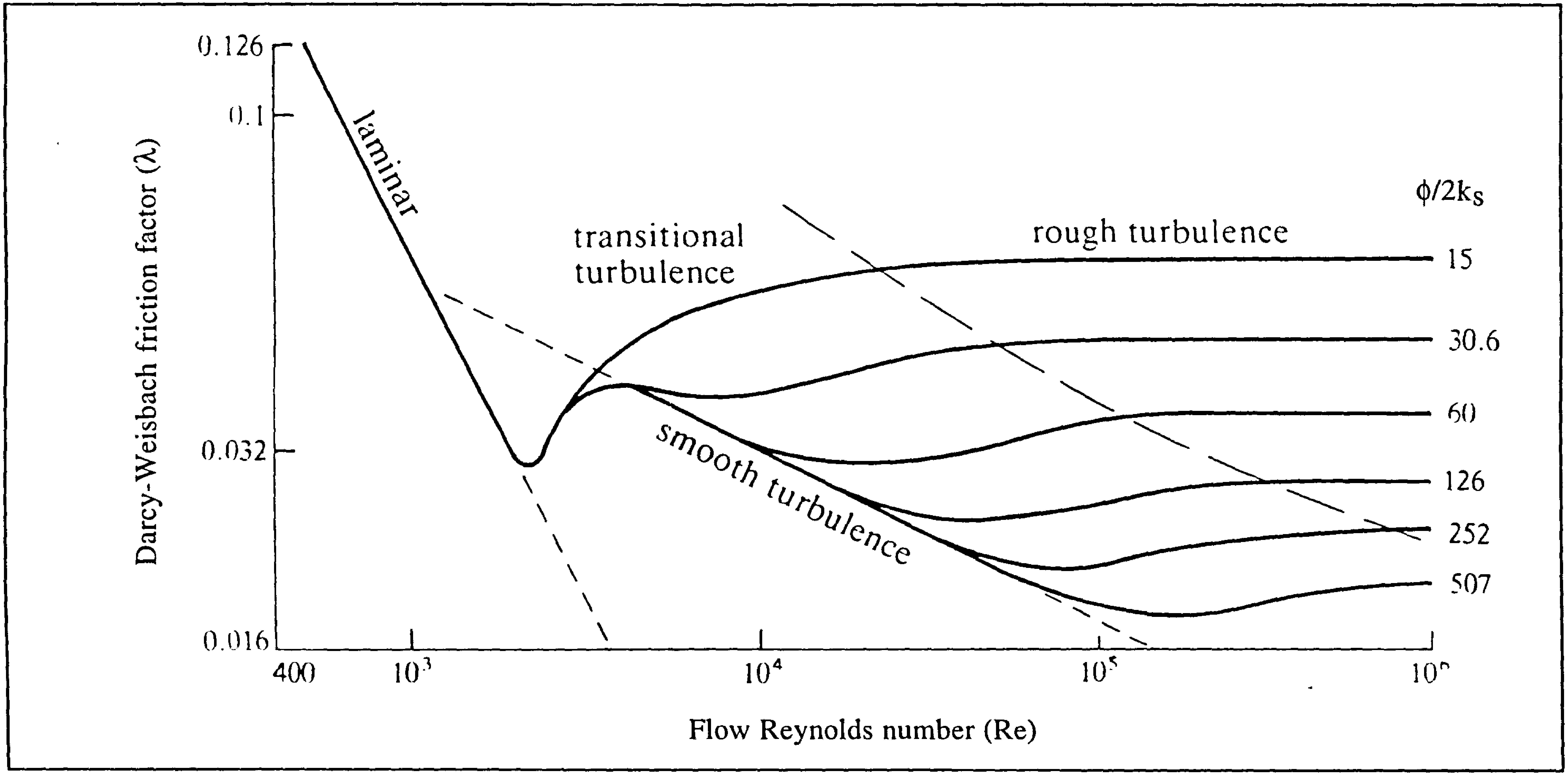

Figure 3.1. Graphical representation of relative roughness ($\phi/2k_s$), Darcy-Weisbach friction coefficient (λ) and flow Reynolds number for pipe flow. ϕ is the pipe diameter and k_s is the surface roughness. Note that λ approaches a constant relative roughness value in the rough turbulent flow field. Adapted from Chadwick and Morfett, (1986). Data from Nikuradse, (1933).

dimensionless terms where 'n' is the number of variables and 3 is the number of governing variables. These are referred to as 'Π' terms. In the example considered here, four terms are produced:

$$\Pi_1 = \frac{\rho R V}{\mu} = Re \qquad \text{(Eq. 3.2)}$$

$$\Pi_2 = \frac{V^2}{gR} = Fr \qquad \text{(Eq. 3.3)}$$

$$\Pi_3 = \frac{k_s}{R} \qquad \text{(Eq. 3.4)}$$

$$\Pi_4 = S_b \qquad \text{(Eq. 3.5)}$$

The Π_1 term is the flow Reynolds number describing the ratio of the inertial forces to the viscous forces and consequently the degree of turbulence of a fluid. The Π_2 term is the Froude number describing the ratio of inertial to gravitational forces in a fluid and classifies a flow as either subcritical (<1), critical (1) or supercritical (>1).

If the ratio between prototype and model could be kept identical for all four of these terms, the model would be a perfect representation of the prototype. This perfection is rarely obtainable in hydraulic modelling as may be illustrated by considering the Froude and Reynolds numbers. The difficulties involved in finding a reasonably priced fluid with the correct properties for each experiment has resulted in water being almost universally used in experimental studies. In addition, standard practise is to use room temperatures (15-20°C) in the model, although prototype temperatures can be considerably different, for instance in the case of proglacial streams. These temperature changes may involve significant changes in viscosity (see Fig. 3.2) and smaller changes to fluid density and surface tension. Several workers have altered the viscosity by using heated water (e.g., Boguchwal and Southard, 1990; Young and Davies, 1990; Warburton and Davies, 1994a). Boguchwal and Southard (1990) used temperatures up to 75°C and showed that this could improve the effective flow depth by a factor of 2.3 relative to 10°C water, as well as changing the velocity and discharge scales. Southard and Boguchwal (1990b) demonstrated that temperature variation could also account for changes in bed configuration and incorporated a factor to account for water temperature in a revised bedform stability diagram (see Fig. 3.3; Southard and Boguchwal, 1990a). For the purpose of the present discussion the simplest case, that of ρ_m (model) = ρ_p (prototype) and $\mu_m = \mu_p$, is considered as assumed by previous workers (Henderson, 1966; Yalin, 1971). The Reynolds number can then be rearranged to give:

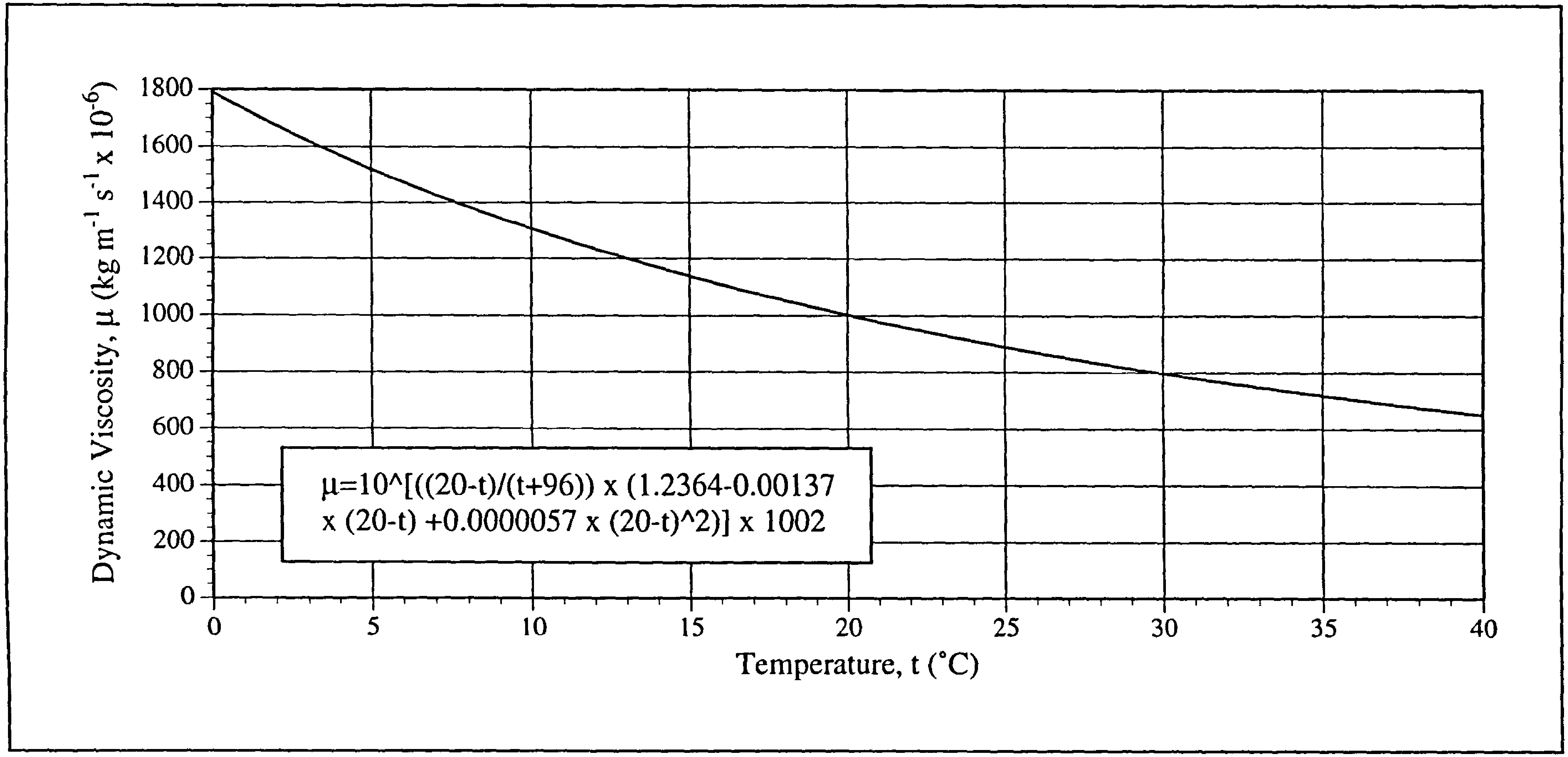

Figure 3.2. Variation of dynamic viscosity with temperature for water at about standard pressure. Data from Kestin *et al.*, (1978). Dynamic viscosity, μ in the equation has units of kg m^{-1} s^{-1}.

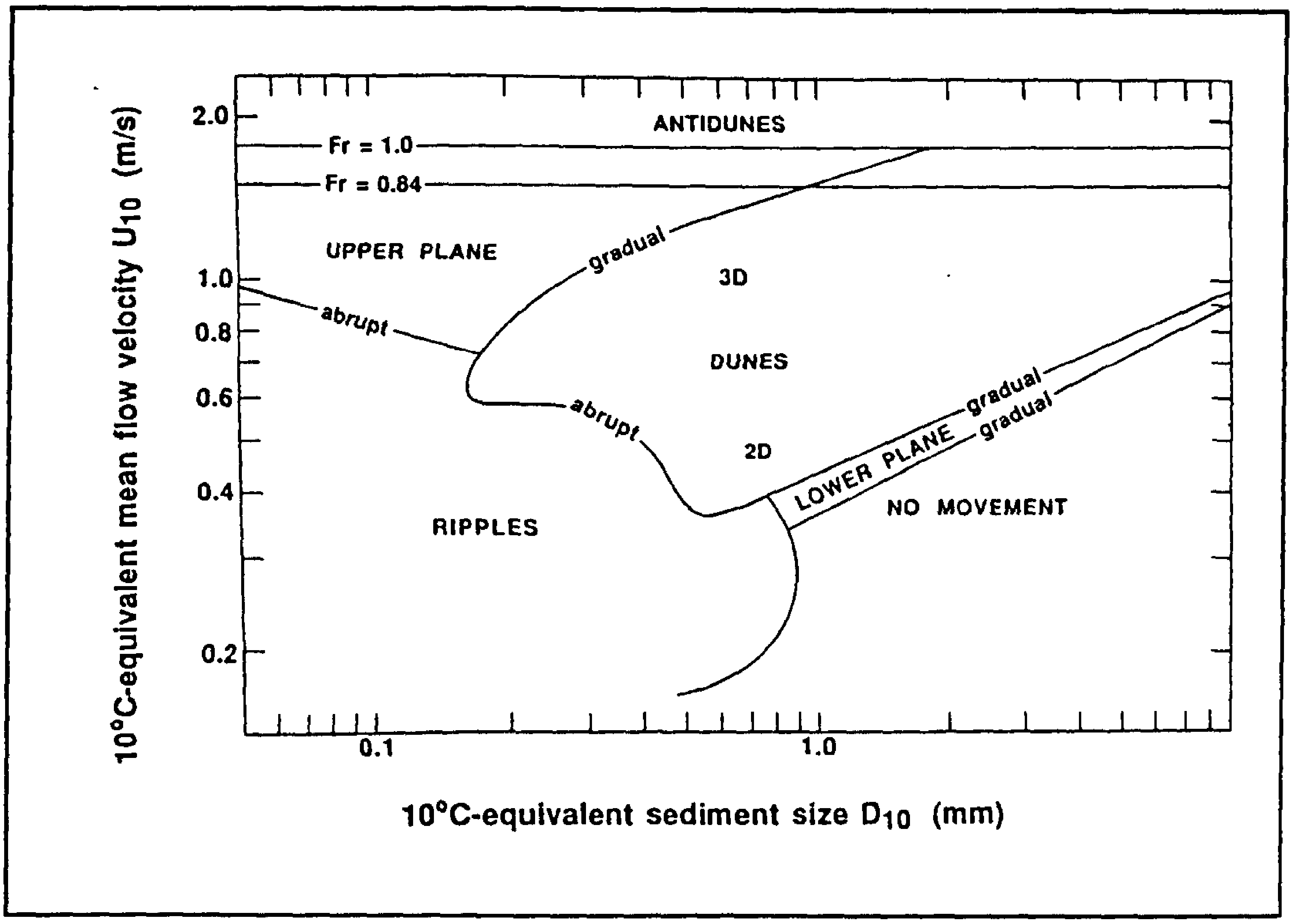

Figure 3.3. Schematic dimensionless velocity-size bedform stability diagram for 10°C equivalent flow depths of 0.25-0.40 m. From Southard and Boguchwal, (1990a).

$$V_pR_p = V_mR_m \quad \text{or} \quad \frac{V_m}{V_p}\,(=\lambda_v) = \frac{R_p}{R_m} \qquad \text{(Eq. 3.6)}$$

In the case of the Froude number, since the gravitational constant g remains constant for both model and prototype, then,

$$\frac{V_m^2}{V_p^2} = \frac{R_m}{R_p} \qquad \text{(Eq. 3.7)}$$

Therefore

$$\frac{V_m}{V_p}\,(=\lambda_v) = \left\{\frac{R_m}{R_p}\right\}^{0.5} \qquad \text{(Eq. 3.8)}$$

The only way that these two equations can be resolved is if R_m is equal to R_p. Therefore the flow Reynolds number is commonly relaxed, with the proviso that in the case of open channel flows, it remains within the fully turbulent flow field. There is disagreement as to exactly which value of the flow Reynolds number constitutes fully turbulent flow, with the engineering literature dominated by values of 4000 to 12500 and most of the geomorphological and sedimentological literature standardised on a value of 2000 (e.g., Leeder, 1982; Richards, 1982) or 2500 (Knighton, 1984). This issue is elaborated in the discussion below.

3.4.3 Movable bed modelling

If a movable bed is considered instead of a fixed bed, then the flow can be considered as a two-phase flow with both fluid and particles. The following set of parameters is used to describe these flows: μ, ρ, S_b, R, g and two parameters which describe the sediment, ρ_s (the sediment density) and D, (the characteristic grain-size of the sediment). There is no agreement as to what dominant grain-size should be selected with either the D_{50}, D_{90} or $D_{100}/1.8$ (Hoey and Sutherland, 1991) grain-size being used. Some studies even alternate between adopting the D_{50} (Ashmore, 1985, 1991a) and the D_{90} grain-size (Ashmore, 1982 and 1991b). Some of these variables can be replaced by other dependent parameters. For example, the shear velocity $U_* = \sqrt{gRS_b}$ can replace S_b and the immersed specific weight of grains in the fluid $\gamma_s = g(\rho_s - \rho)$ can replace g giving; $\mu, \rho, R, D, \rho_s, U_*, \gamma_s$. These variables also produce n-3 or 4 Π terms:

$$\Pi_1 = \frac{R}{D} \qquad \text{(Eq. 3.9)}$$

$$\Pi_2 = \frac{\rho_s}{\rho} \qquad \text{(Eq. 3.10)}$$

$$\Pi_3 = \frac{\rho U_* D}{\mu} = Re_* \qquad \text{(Eq. 3.11)}$$

$$\Pi_4 = \frac{\rho U_*^2}{\gamma_s D} = \tau_c{}^* \qquad \text{(Eq. 3.12)}$$

The Π_1 and Π_2 terms represent relative roughness of the sediment and relative density respectively.

The Π_3 term is the grain Reynolds number (Re_*) which is a measure of the roughness of the bed relative to the thickness of the viscous sub-layer. The viscous sub-layer is defined as "the thin layer in a flow, adjacent to the solid surface, in which the flow has negligible fluctuations of velocity" (Massey, 1983). Therefore, viscous forces are relatively important in relation to inertial forces. The thickness of the viscous sub-layer, δ_{sub}, is defined by Keulegan (1938) as,

$$\delta_{sub} = \frac{11.6\nu}{U_*} \qquad \text{(Eq. 3.13)}$$

where ν is the kinematic viscosity. If the grain-size diameter is smaller than the thickness of the viscous sub-layer, the bed is described as smooth whilst if a particle penetrates through the sub-layer it is termed hydrodynamically rough.

The Π_4 term expresses the Shields (1936) equation which is normally rearranged as:

$$\tau_c{}^* = \frac{\tau_c}{(\rho_s-\rho)gD} \qquad \text{(Eq. 3.14)}$$

where τ_c is the critical bed shear stress defined as the minimum force capable of initiating sediment movement for a particular grain-size, and $\tau_c{}^*$ is the dimensionless critical shear stress, defined as τ_c divided by the weight per unit area of the surface grain layer.

Together, $\tau_c{}^*$ and Re_* form the axes of the Shields entrainment diagram (Shields, 1936; see Fig. 3.4). The scatter of points on the Shields diagram may be used to define an entrainment threshold above which a flow is capable of eroding and transporting sediment. The Shields diagram also shows $\tau_c{}^*$ becoming constant and thus independent of Re_* at a value of approximately 0.056 and therefore,

$$\tau_c = 0.056\,(\rho_s-\rho)gD \qquad \text{(Eq.3.15)}$$

However, only unimodal, perfectly sorted grain-sizes were used by Shields and therefore the angle of repose of the grains, hiding effects and mutual particle interference are not accounted for. Fenton and Abbott (1977) allowed for the effects of relative exposure on the Shields curve and demonstrated that the critical bed shear stress, $\tau_c{}^*$, can vary from 0.3 for well-packed sediments to 0.01 for beds with easily moved, perched grains. They termed these 'under-loose' and 'over-loose' beds, respectively.

The Shields curve can be divided into smooth, transitional and rough boundaries. The upper limit of the smooth boundary can be taken as a grain Reynolds number of 5 or less (Schlichting, 1968; Ashworth *et al.*, 1994). However, there is no agreement on the lower limit of the rough boundary, that is the point at which the value of τ_c becomes constant. Rouse (1950) added a threshold line and placed the critical value at 400. Subsequent workers have redrawn the line, with plots asymptoting to 350 (Richards, 1982) and 1000 (Henderson, 1966; Novak and Cábelka, 1981). Earlier work by

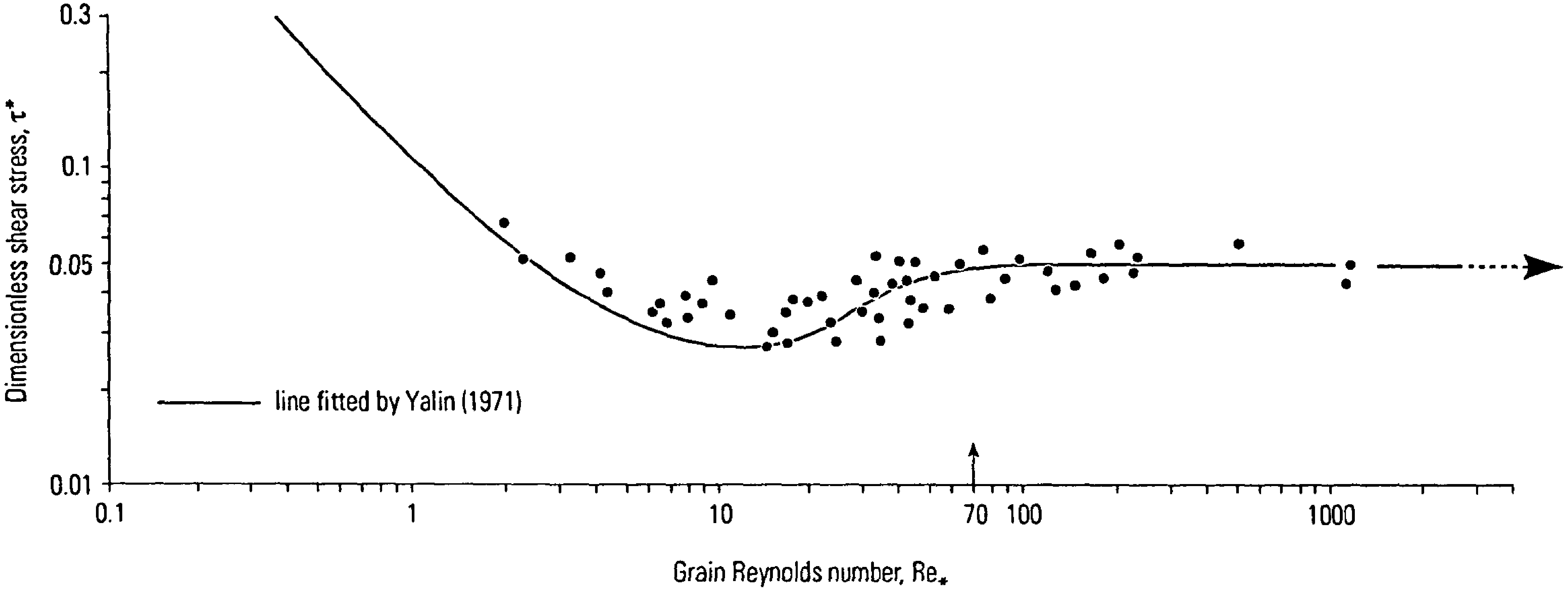

Figure 3.4. Shields entrainment graph as interpreted by Yalin (1971, Fig. 6.2, p.154). The curve flattens out at a value of 70 (see arrow), which marks the boundary between transitional and fully turbulent flow. After Ashworth *et al.*, (1994).

Nikuradse (1933) on pipe flow boundary conditions produced a very similar but much better constrained plot to Shields (see Fig. 3.5), with the fully rough category being defined as $Re_* > 70$ (Schlichting, 1968). Yalin's (1971) version of the Shields diagram (Fig. 3.4) takes note of this work (see Yalin, 1971, Fig. 3.3, p.58) and also shows a value of 70. Yalin (1971) argues that since a Re_* value of 70 corresponds to the critical stage of sediment transport, it should form the scaling limit for particle Reynolds in hydraulic models. The majority of recent FSM studies have followed this argument (e.g. Ashmore, 1982; Davies and Lee, 1988; Young and Davies, 1990; Ashmore, 1991a; Ashmore, 1991b; Hoey and Sutherland, 1991; Warburton and Davies, 1994a).

Parker (1979) divorced the concepts of boundary roughness and constant τ_c by arguing that the flow becomes hydraulically rough if $Re_* > 15$ but becomes constant at about 30. Ashworth *et al.*, (1994) also note that the scatter in the Shields diagram allows for either a 'dip' or a horizontal line to be plotted from $Re_* = 5$ and argue that "the minimum grain Reynolds number may be relaxed as long as a Re_* value of approximately 15 is exceeded" (Ashworth *et al.*, 1994, p.119). Jaeggi (1986) advocates that the minimum value of Re_* that can be used is 5 since ripple formation occurs in models with lower grain Reynolds numbers. However, Jaeggi (1986) notes that for $Re_* < 70$, the beginning of motion is not correctly reproduced and therefore distorts the grain-size distribution by increasing the size of the finest material, so that shear velocities calculated for the prototype sediment are scaled correctly. Novak and Cábelka (1981, p.130) place the 'dip' of the Shields curve even lower, at a value of 3.5.

The fully rough flow field in combination with the particle Reynolds number is used to define the optimum length scale, λ_L, for modelling. Adopting Yalin's (1971) Re_* value of 70, yields an optimum length scale of:

$$\lambda_L = \left(\frac{70}{Re_{*p}}\right)^{2/3} \qquad \text{(Eq. 3.16)}$$

where Re_{*p} is that of the prototype.

When modelling a two-phase flow, it must be remembered that the modeller must still account for the specific dimensionless properties of the fluid, that is the flow Reynolds and Froude numbers that were derived previously.

3.5 Geometric similarity

Geometric form is the simplest type of similarity to achieve. The maximum length scale can be calculated using equation 3.16. In the case of Froude scale modelling both the vertical and horizontal scales are kept the same although when modelling large rivers, or when constrained by laboratory space, it may be necessary to use a distorted model in

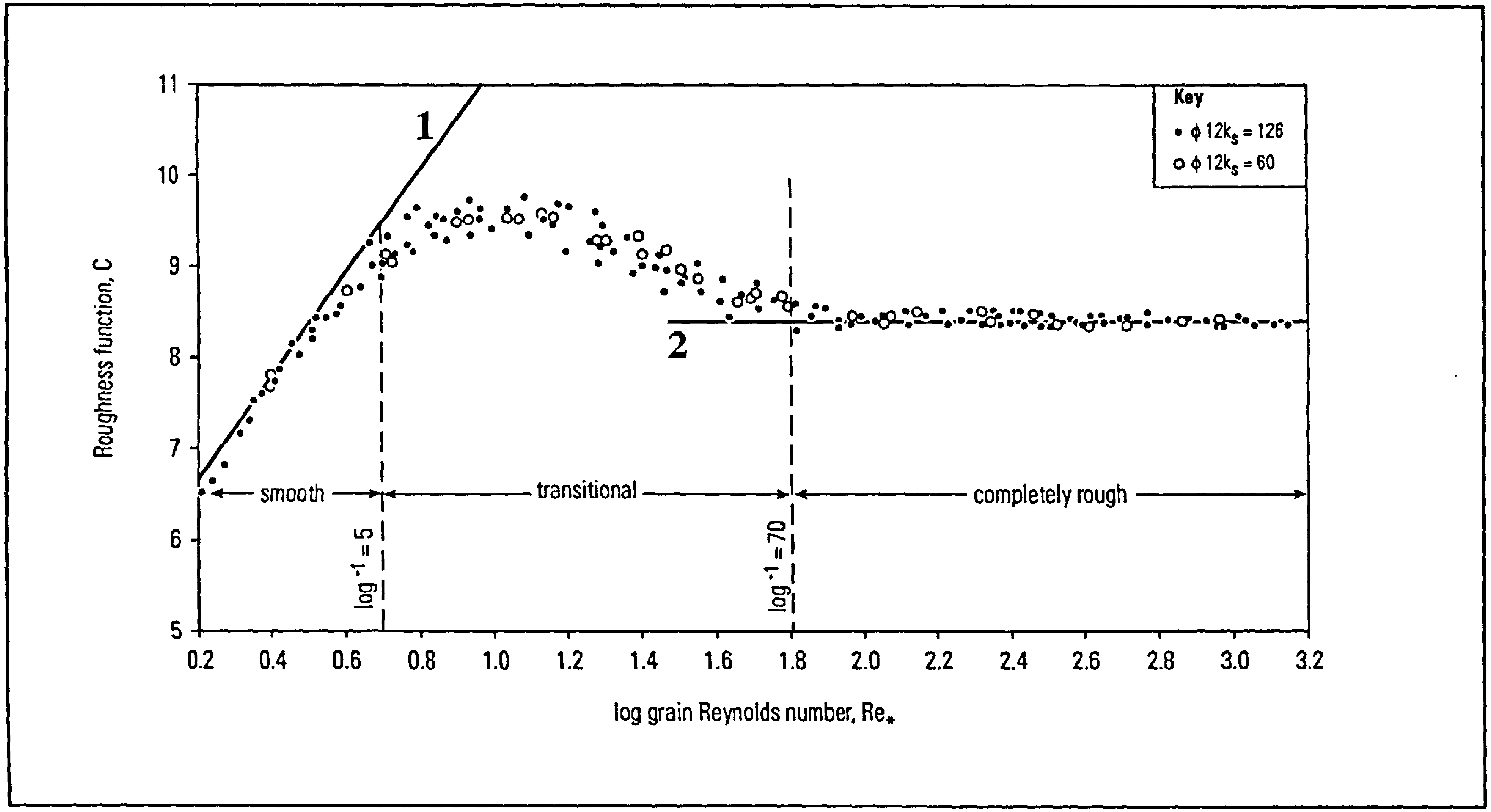

Figure 3.5. Roughness function, C, in terms of grain Reynolds number (Re_*), for pipe flow. The lower limit for the completely rough boundary layer corresponds to a grain Reynolds number of 70. C is from Prandtl's (1952) logarithmic 'law of the wall' which characterises the velocity profile of a flow (stated as: $V/U_* = 5.75\ U_* \log (d/k_s)+C$) and is frequently referred to as the constant of integration. Line (1) represents a hydraulically smooth boundary and line (2) a completely rough boundary. The two datasets represent different ratios of pipe diameter (ϕ) to surface roughness (k_s) which plot separately for Re against λ (see Fig. 3.1). Adapted from Schlichting, (1968).

which the horizontal and vertical scales are different. This fact was recognised by Reynolds (1887, 1889, 1890, 1891), whose models all had distorted scales. Typically, the horizontal scale is much larger than the vertical scale, e.g. 1:31800 to 1:33 (Reynolds, 1887).

The geometric similarity of Froude scale models has been applied to the geometry and spatial distribution of shales (Ashworth and Best, 1994; Ashworth *et al.*, 1994), as well as a host of planform features, including avulsion (Ashmore, 1991b; Leddy *et al.*, 1993), channel development and remnant bars (Ashmore, 1988, 1991a, 1993; Lisle *et al.*, 1991), and chutes and lobes (Southard *et al.*, 1984).

3.6 Kinematic similarity

Kinematic and dynamic similarity are difficult to consider separately since the motion and forces of the fluid, or of the grains, are interrelated. However, there are a number of cases where even if the model geometries are scaled perfectly, the fluid or particle motion will still be dissimilar since they involve non-linear functions. This is the case for particle settling and for fluid flow fields. In addition, surface tension forces do not scale but may have an effect on the fluid motion.

3.6.1 Surface tension and the Weber number

Surface tension is the tensile force per unit length (N m^{-1}) acting perpendicular to a line drawn on the surface of a fluid. Surface tension results from the difference between the internal molecular forces of a liquid and the forces between liquid molecules and an adjacent surface and varies as a function of temperature (Fig. 3.6). In rivers, the effects of surface tension are largely insignificant (Dingman, 1984, p.85), but if a model has too large a vertical scale, and consequently too small a flow depth, surface tension can be important. The addition of a surface tension term, σ, into dimensional analysis gives a Π term known as the Weber number (We):

$$We = \frac{\rho V^2 d}{\sigma} \qquad \text{(Eq. 3.17)}$$

which represents the ratio between the inertial forces and surface tension forces. The velocity and time scales for perfect scaling of surface tension effects are given by:

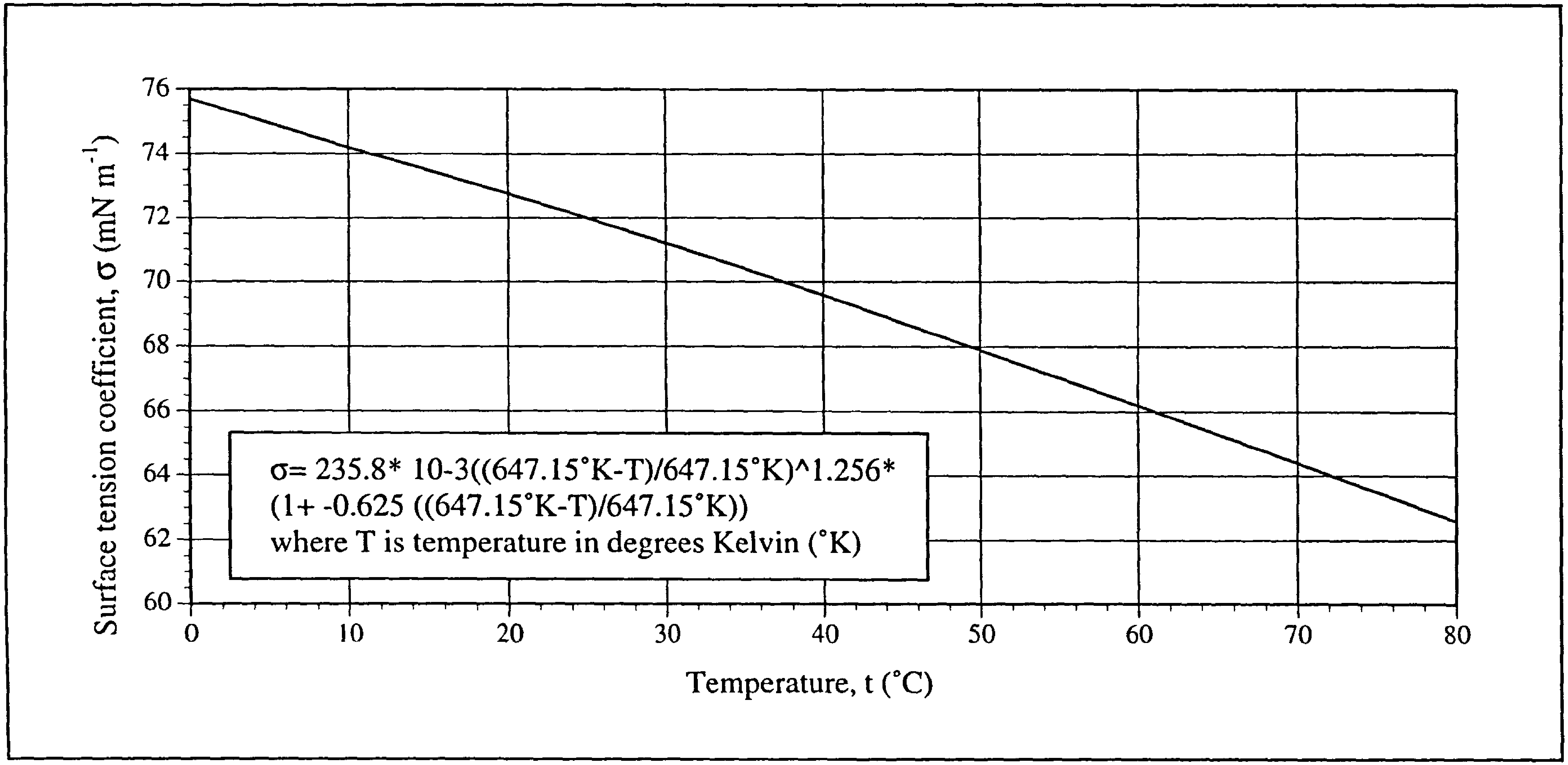

Figure 3.6. Variation of the surface tension coefficient with water temperature, for water against air at about standard pressure. Data from Vargaftik *et al.*, (1983).

$$\lambda_v = \left(\frac{\lambda_\sigma}{\lambda_d\,\lambda_\rho}\right)^{0.5} \qquad \text{(Eq. 3.18)}$$

$$\lambda_T = \left(\frac{\lambda_d^3\,\lambda_\rho}{\lambda_\sigma}\right)^{0.5} \qquad \text{(Eq. 3.19)}$$

(after ASCE, 1942)

In the case of a Froude scale model, where the fluid density, ρ, is kept the same in both model and prototype and where λ_v is controlled by correctly scaling the Froude number and relaxing the flow Reynolds number, it is not possible to correctly scale the Weber number. However, a similar argument can be made for the Weber number as that used for the relaxation of the Reynolds number, namely that so long as the surface tension effects are insignificant then exact scaling is unnecessary. However, there is no current consensus as to the critical value for surface tension (Peakall and Warburton, 1995).

Maxwell and Weggel (1969) provide a theoretical approach utilising the energy equation with an additional surface energy term. They show that the minimum energy flux per unit weight flux (H_E) may be given by:

$$H_E = d + \frac{q^2}{2gd^2} + \beta\frac{\sigma}{\rho g d} \qquad \text{(Eq. 3.20)}$$

where g is acceleration due to gravity, q is the fluid discharge per unit width and β is a surface energy correction factor given by the ratio of the surface velocity to the mean velocity. Maxwell and Weggel (1969) make the simplifying assumption that β is equal to unity rather than a lower value, and differentiating with respect to d gives a minimum energy flux per unit weight flux (H_E) for given q:

$$\frac{q^2}{g\,d^3} = 1 - \frac{\sigma}{\rho g d^2} \qquad \text{(Eq. 3.21)}$$

which can be restated in terms of the more familiar Froude and Weber numbers:

$$Fr^2 = 1 - \frac{1}{We} \qquad \text{(Eq. 3.22)}$$

To investigate the critical value of surface tension, the critical flow is assumed to be that for which the energy flux per unit weight flux is a minimum. From equation 3.22 this is realised when the Weber number is at a value of unity. As ρ, g and σ are all constants for a given temperature, the critical depth can be calculated as:

$$d_c = \left(\frac{\sigma}{\rho g}\right)^{0.5} \qquad \text{(Eq. 3.23)}$$

The critical depth is therefore the value for which the unit discharge (q) would be zero, implying ponding of the fluid. In a Froude scale model the minimum value of q corresponds to a unit discharge high enough to maintain fully turbulent flow. Adopting a value for the flow Reynolds number of 2000, treating velocity as a constant and assuming the flow depth equals the critical depth, a critical unit discharge can be approximated using the continuity equation for flow:

$$q_c = V d_c w_u \qquad \text{(Eq. 3.24)}$$

where w_u is unit width. By substituting q back into the energy equation the normal critical depth of open channel flow d_c can be calculated:

$$d_c = \left(\frac{q^2}{g}\right)^{1/3} \qquad \text{(Eq. 3.25)}$$

This value of d_c can then be substituted back into the Weber number to yield a minimum Weber number for the flow. As an example, for a flow Reynolds number of 2000 the critical flow depth is 7.41 mm and the critical Weber number is 7.4 for water at 20°C.

However, there are a number of assumptions in the approach of Maxwell and Weggel (1969) which can be questioned. If equation (3.24) is substituted into equation (3.21) it gives:

$$\frac{V^2}{gd} = 1 - \frac{\sigma}{\rho g d^2} \qquad \text{(Eq. 3.26)}$$

One variable (depth) is common to both sides of the equation. On the right hand side all parameters are constant except for depth, however altering depth on the right hand side will not change the left hand side from zero, so long as the velocity remains at zero. Substituting the Froude law relationship, (Eq. 3.3) into equation (3.26) so that the Weber number is expressed in its standard form, yields:

$$\frac{V^2}{gd} = 1 - \frac{\sigma}{\rho V^2 d} \qquad \text{(Eq. 3.27)}$$

There are now two expressions which are common to both sides and for the Weber number to be unity, both V and d must be greater than zero, and as a consequence the left-hand side can not equal zero. Even if velocity is taken to be vanishingly small, the form of the expression is changed.

However, the value of 7.4 from the above calculations, is similar to the value outlined by Novak and Cábelka, (1981, p.39) who stated that a flow velocity of >0.23 m s^{-1} and a depth of greater than 15 mm is required to avoid surface tension effects (therefore, We=11). In contrast, French (1985) states that "from a practical viewpoint, if model depths are greater than 50 mm, surface tension effects can usually be ignored". A large proportion of this disparity is based on the choice of critical flow Reynolds number for fully turbulent flow since French adopts a figure of 12500, which produces a critical depth of 25 mm and a critical Weber number of 85. This agrees well with the statement of Dake (1983) that surface tension is insignificant if We>100 and of Jain *et al.*, (1978) who observed no surface tension effect in models of intakes if We>120. These critical values can be compared using a plot of Weber numbers as a function of depth and flow velocity (Fig. 3.7). A more detailed discussion of critical Weber numbers is provided in Peakall and Warburton (1995).

If the Weber numbers fall below or within the suggested range of critical values (≈10-120), then a range of surface tension induced wave phenomena, including capillary waves, can affect models. These wave phenomena are considered in more detail in Section 3.6.2.

3.6.2 Flow regimes

Froude scale modelling is based on the premise that the flow Reynolds number can be relaxed so long as it remains fully turbulent (Section 3.4.2). In practice however, many studies have values that fall into the transition zone (taken as 500<Re<2000) (Ashmore, 1991a, b; Ashworth *et al.*, 1994; Warburton and Davies, 1994a). Many other studies do not quote values for flow Reynolds number, but may fall into this transitional category (see Table 3.1). Ashworth *et al.*, (1994) state that velocity and depth measurements for their flow Reynolds numbers were taken for the largest channels in the experiment. This would take many of the flow Reynolds numbers in the lower order channels, much further into the transitional zone, as presumably is the case in most of the previously cited studies. Flow also varies between sub-critical and super-critical in many experiments (Table 3.1), giving a wide combination of flow conditions, as found in field prototypes (e.g. Ashworth *et al.*, 1994).

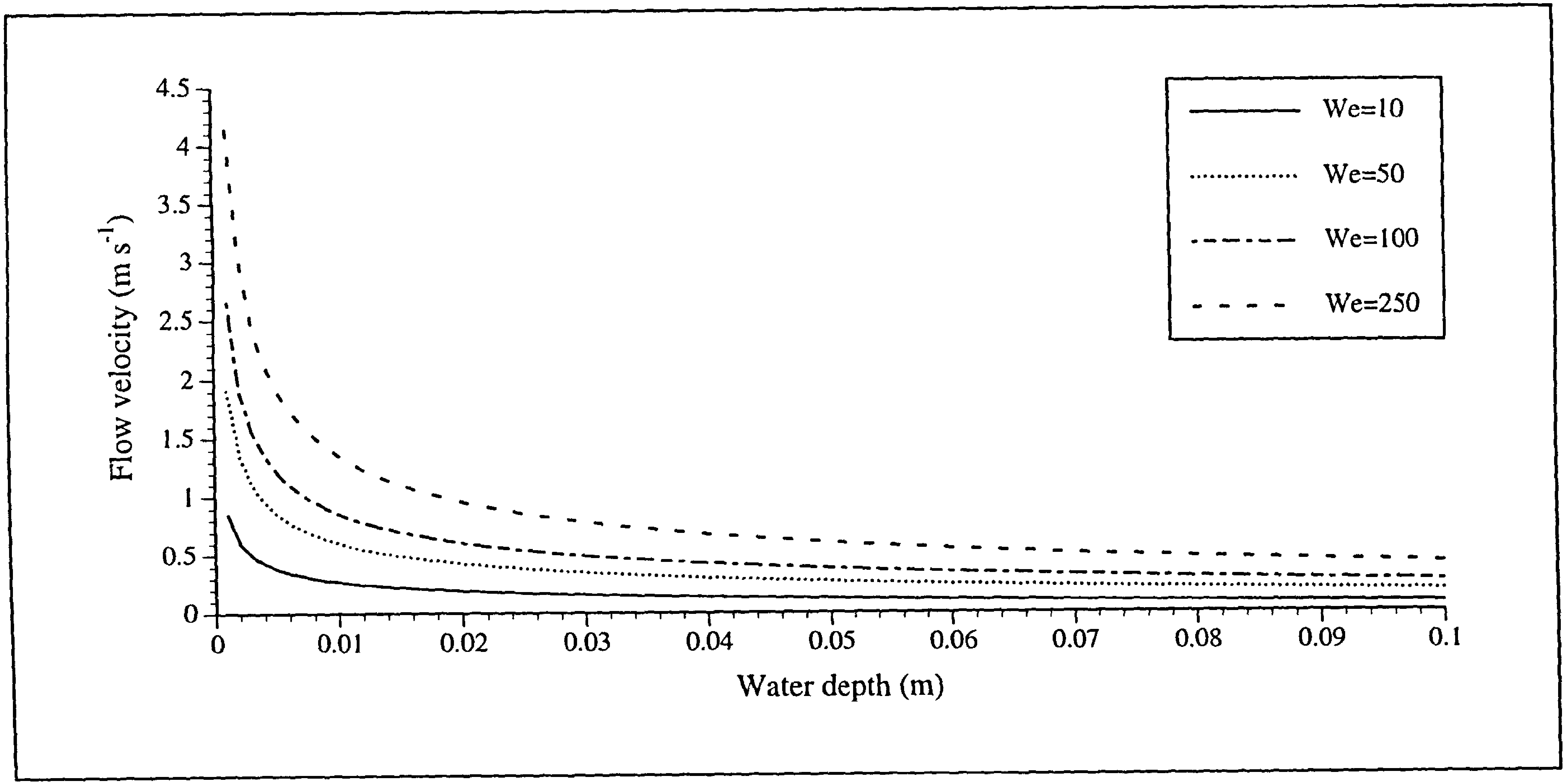

Figure 3.7. Plot of Weber number as a function of water depth and flow velocity. After Peakall and Warburton, (1995).

Table 3.1. Compilation of flow variables from the physical modelling literature

Paper (Author, Year)	Weber Yes/No	Temp. Yes/No	Velocity Yes/No	Depth Yes/No	Calculated We range	Fr	Re	Re*
Ashmore (1982)	No	No	No	No	None	Av >1	Av= 2200	Av= 62
Ashmore (1988)	No	No	No	No	None	0.56-0.93	No	36-103
Ashmore (1991a)	No	No	No	Yes	None	0.56-0.93	920-4760	36-103
Ashmore (1991b)	No	No	Yes	Yes	10.5-64.8$^{\Delta}$	Av>1	Av =1900	90-130
Ashworth *et al.*, (1994)	No	No	No	Yes	None	0.43-0.61	1885-2632	18.1-56.4
Davies & Lee (1988)	No	No	No	No	None	No	No	No
Hoey & Sutherland (1989)	No	No	Yes	Yes	3.75-17.6$^{\Delta}$	No	No	No
Hoey & Sutherland (1991)	No	No	I	I	5.40$^{I\ \Delta}$	0.44-1.54	No	32.1-140.6
Jin and Schumm (1987)	No	No	I	I	7.02$^{I\ \Delta}$	No	No	No
Schumm & Khan (1972)	No	No	Yes	Yes	29.6-160$^{\Delta}$	0.33-1.82	6366-21154$^{\Delta}$	No
Southard *et al.*, (1984)	No	No	No	Yes	None	No	No	No
Warburton & Davies (1994a, b)	Yes	Yes	Yes	Yes	1.27-16.0†	0.36-1.2†	2230-3400^{I}	42.3-105.5†
Wolman & Brush (1961)	No	Yes	Yes	Yes	1.63-206	0.56-1.09	6700-98300	9.0-100.8
Young & Davies (1990)	No	Yes	No	Yes	None	0.3-0.6	No	No

Notes: Av = Average value. $^{\Delta}$ For papers that do not quote water temperature, variables are calculated assuming a value of 15°C. † Range is calculated based on two standard deviations from the mean. ^{I} Initial condition only. For Re* calculations the D_{50} is used by Ashmore, (1988, 1991a); and Wolman and Brush, (1961); the D_{90} by Ashmore, (1982, 1991b); Ashworth *et al.*, (1994); and Warburton and Davies (1994a, b); and the $D_{100}/1.8$ by Hoey and Sutherland (1991).

Experimental studies have shown that there are a series of flow instabilities associated with the change from laminar to transitional through to fully turbulent flow (Stuart, 1965; Tani, 1969; Karcz and Kersey, 1980). In addition, shallow, steady, uniform flows on steep gradients (e.g. >2%) can break down into a pulsating motion and are associated with free-surface flow instabilities which first appear at Froude numbers of 0.5 (Karcz and Kersey, 1980). Experimental studies on shallow flows (<5 mm) by Karcz and Kersey (1980) showed that the following series of bedforms developed in well sorted sand under gradually increasing Re numbers: smooth bed; flow-aligned ridge and trough pattern; combined ridge and rhomboid pattern; and rhomboid configuration (see Fig. 3.8). Rhomboid patterns that occur in the transitional turbulent-supercritical regime and their associated oblique diagonal standing waves, may occur in many FSM models, since surface instability waves persist beyond a flow Reynolds number of 1000 (Karcz and Kersey, 1980, p.270).

Surface tension (Section 3.6.1) also affects the flow surface and is known to produce capillary waves, which are short-lived and of small wavelength (λ_w < 4 mm; Lighthill, 1978). A large number of flow instability parameters also include a surface tension force, but show a weak correlation with experimental evidence (Krantz and Goren, 1970; Lin, 1970; Krantz and Goren, 1971; Lin, 1971). Karcz and Kersey (1980) added commercially available surface tension reducing additives to some of their flows and noted that "in all cases the flow was stabilized, i.e., the transverse instability surges were either poorly developed or failed to appear" (p.287). However, they did note some disturbed patches of flow and suggested that the additives might suppress turbulence development rather than directly affect surface instabilities. The engineering community also makes extensive use of surface tension reducing additives, for example, in studies of weir geometries (e.g., Maxwell and Weggel, 1969; French, 1985).

3.6.3 Particle settling

The particle fall velocity in a stationary fluid can be considered using two different equations. Stokes' law only considers viscous resistance forces and is expressed as:

$$V_F = \frac{gD^2(\rho_s - \rho)}{18\mu} \qquad \text{(Eq. 3.28)}$$

where V_F is the fall velocity of a particle. For particles smaller than 0.1 mm in water this relationship holds very well, but Stokes' law does not account for boundary layer separation behind a falling particle and a consequent increase in the fluid drag. For larger

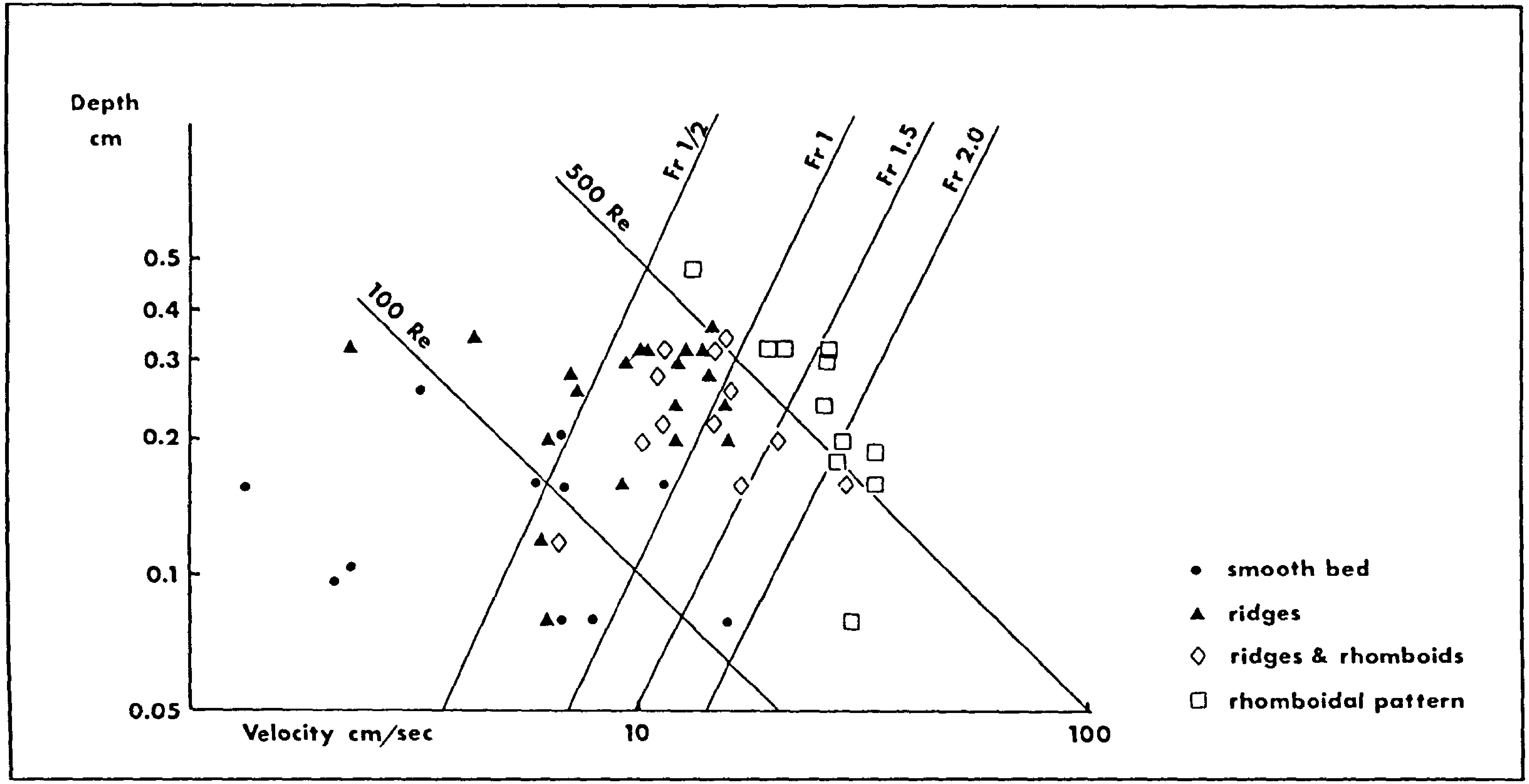

Figure 3.8. Bedforms associated with free surface instabilities as a function of flow depth and velocity, for well sorted sand-bed experiments. From Karcz and Kersey, (1980).

particles Newton derived an expression incorporating the effects of boundary layer separation, which is known as the impact law:

$$V_F = \left(\frac{4}{3} \frac{(\rho_s - \rho) g D}{C_{D0}\, \rho} \right)^{0.5} \qquad \text{(Eq. 3.29)}$$

where C_{D0} is the drag coefficient for a solitary particle falling through an infinite fluid.

The impact law is not a particularly good approximation of experimental results, even for particles above 1 mm (see Fig. 3.9).

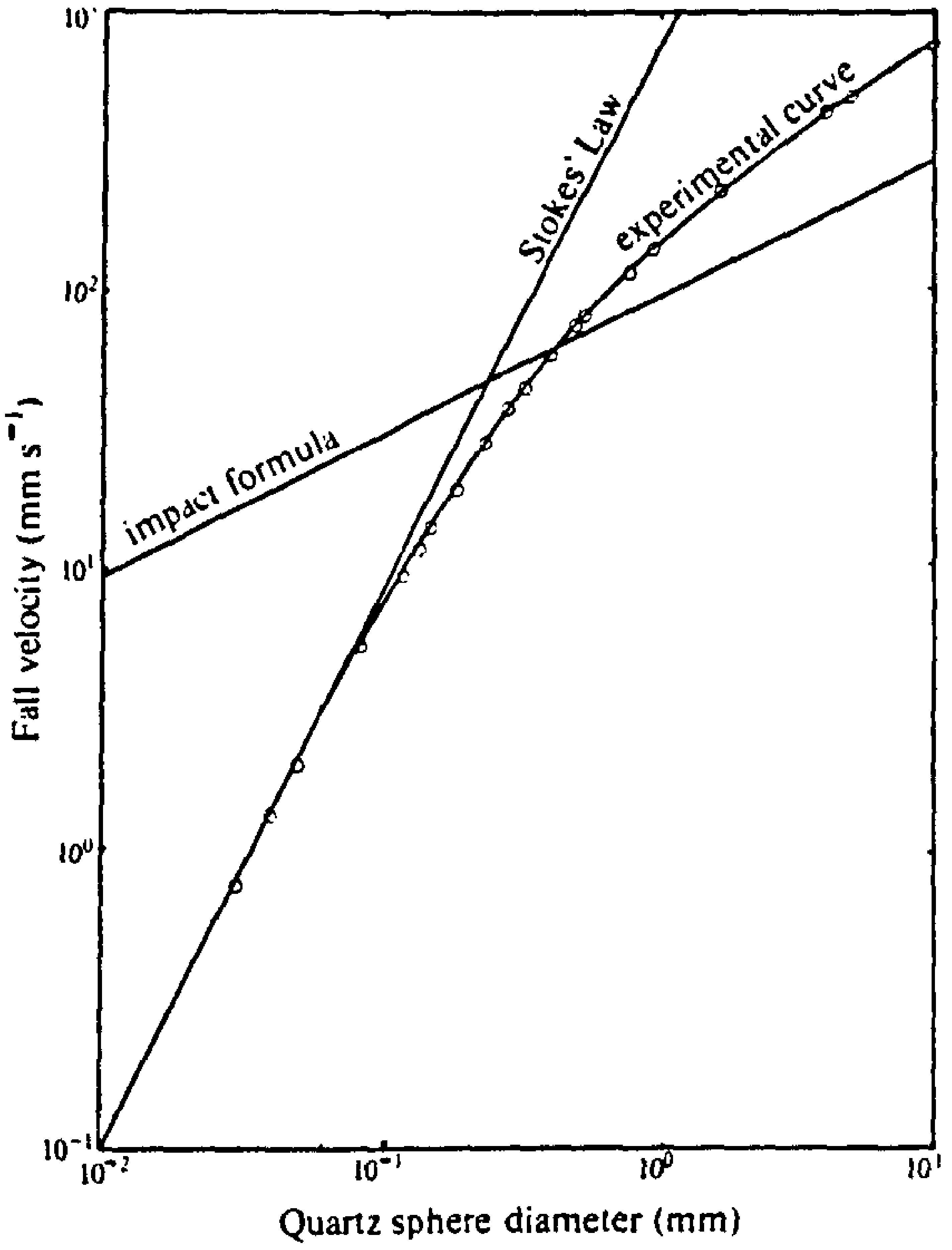

Figure 3.9. Graph of fall velocity as a function of grain diameter, for water at 20°C, plotted against the predictions of Stokes' law and the impact formula. From Leeder (1982) using data from Gibbs *et al.*, (1971).

The experimental curve does, however, break into two distinct linear segments, one characterised by Stokes' law and the other broadly delineated by the impact law. When both model and prototype grain-sizes fall in one or other of these two areas a linear scaling ratio can be applied. However, if the prototype grain-size is in the 'impact region' and the model is in the field of Stokes' law, then the function is non-linear and consequently cannot be perfectly scaled.

For Froude scale models, the scaling factor for velocity can be derived by rearranging the Froude equation (Eq. 3.3) such that:

$$\lambda_V = \left(\frac{V_m}{V_p}\right) = \left(\frac{g_m L_m}{g_p L_p}\right)^{0.5} = (\lambda_g \lambda_L)^{0.5} \qquad \text{(Eq. 3.30)}$$

where L is a length scale which in this case is the depth of the flow. Since λ_g is unity, then,

$$\lambda_V = (\lambda_L)^{0.5} \qquad \text{(Eq. 3.31)}$$

For particles settling through a flow, the fall velocity, V_F, should also have the same scale ratio, so that kinematic similarity is obtained. However, an examination of Stokes' law will show that this may not always be the case. If the fluid density, temperature (i.e., fluid viscosity) and sediment density are kept constant between prototype and model, then equation 3.28 reduces to:

$$V_F = kD^2 \qquad \text{(Eq. 3.32)}$$

where k is a constant. Re-writing equation 3.32 in terms of scale ratios, and noting that the grain-size is the length scale in this case, gives:

$$\lambda_{V_F} = (\lambda_L)^2 \qquad \text{(Eq. 3.33)}$$

Considering the impact law (Eq. 3.29) in the same manner, gives a scale ratio for fall velocity of:

$$\lambda_{V_F} = (\lambda_L)^{0.5} \qquad \text{(Eq. 3.34)}$$

The fall velocities of the particles relative to the downstream velocity are therefore much smaller in the model than the prototype, if the grain-size distribution can be characterised by Stokes' law in both prototype and model, or if the model grain-size is characterised by Stokes' law and the prototype by the impact law. Saltating particles consequently have larger hop lengths and heights than the geometric scale ratio would suggest, and some fine-grained material may remain in suspension rather than being deposited. This limitation could be overcome by altering the grain-size distribution in a fashion highlighted by Jaeggi (1986) for sediment entrainment (see Section 3.4.3). However, if both the model and prototype grain-size distributions are characterised by the impact law then the fall velocities scale with the downstream velocities. In practice, model sediment smaller than approximately 0.1 mm does not scale correctly, while larger grain-sizes do scale correctly.

3.7 Dynamic similarity

The above discussion concerning geometric and kinematic similarity has shown that in many cases it is not possible to create a perfect model in terms of dimensions and comparability of motion. However, in the following treatment of the forces acting on a grain and the associated sediment transport, perfect geometric and kinematic similarity are assumed.

Scale relations for dynamical similarity can be derived from equations 3.9 to 3.12. If the grain Reynolds number is expressed using kinematic viscosity, i.e.,

$$Re_* = \frac{U_* D}{\nu} \qquad \text{(Eq. 3.35)}$$

then the following scales can be derived:

$$\lambda_{U_*} \lambda_D = \lambda_\nu \qquad \text{(Eq. 3.36)}$$
$$\lambda_{U_*}{}^2 \lambda_{\gamma_s}{}^{-1} \lambda_D{}^{-1} = \lambda_\rho{}^{-1} \qquad \text{(Eq. 3.37)}$$
$$\lambda_d \lambda_D = 1 \qquad \text{(Eq. 3.38)}$$
$$\lambda_{\rho_s} = \lambda_\rho \qquad \text{(Eq. 3.39)}$$

(after Yalin, 1971)

The length scale for the immersed specific weight of the sediment, λ_{γ_s}, can be broken down into two separate length scales,

$$\lambda_{\gamma_s} = \lambda_g \lambda_{\rho_s} \qquad \text{(Eq. 3.40)}$$

where λ_g is the gravity length scale. Since the gravity scale between model and prototype is unity, and $\lambda_{\rho_s} = \lambda_\rho$ (Eq. 3.39) then Eq. 3.40 can be rewritten as,

$$\lambda_{\gamma_s} = \lambda_\rho \qquad \text{(Eq. 3.41)}$$

Substituting λ_ρ for λ_{γ_s} in equation 3.37 and rearranging gives:

$$\lambda_{U_*}{}^2 \lambda_\rho{}^{-1} \lambda_D{}^{-1} = \lambda_\rho{}^{-1} \qquad \text{(Eq. 3.42)}$$

and therefore

$$\lambda_{U_*}{}^2 = \lambda_D \tag{Eq. 3.43}$$

By substituting Eq. 3.43 into Eqs. 3.36 and 3.38, a complete set of scales can be derived:

$$\lambda_{U_*} = (\lambda_v)^{1/3} \tag{Eq. 3.44}$$
$$\lambda_d = (\lambda_v)^{2/3} \tag{Eq. 3.45}$$
$$\lambda_D = (\lambda_v)^{2/3} \tag{Eq. 3.46}$$
$$\lambda_{\rho_s} = \lambda_\rho \tag{Eq. 3.47}$$
$$\lambda_{\gamma_s} = \lambda_\rho \tag{Eq. 3.48}$$

It follows that since d, D and U_* have different length scales with respect to kinematic viscosity, then it is theoretically impossible to achieve dynamic similarity of sediment transport in a model if the same fluid and temperature as the prototype are used (Yalin, 1971). This only refers to models that have grain Reynolds numbers below the critical threshold for a fully turbulent boundary (Section 3.4.3), since above this threshold, equation 3.44 can be excluded from the analysis. Many Froude scale models have grain Reynolds numbers below 70 (if Yalin's threshold Re_* of 70 is assumed; see Table 3.1) and therefore cannot model sediment transport correctly. In addition, sediment fall velocities do not scale properly in a FSM experiment (Section 3.6.3). Yalin (1963, 1971) derives a scale ratio for sediment transport rate, λ_s, by dimensional analysis,

$$\lambda_s = (\lambda_L)^{1.5} \tag{Eq. 3.49}$$

for models for fully turbulent flow.

Froude scale studies rarely model suspended sediment, due to the limitations of using fine-scaled sediment (see Section 3.8.1) and those studies that have used fine-sediment (e.g., Leddy *et al.*, 1993; Ashworth *et al.*, 1994) have not measured sediment transport rates. However, several studies have compared the observed bedload sediment transport from FSM models with transport equations (Ashmore, 1988; Hoey and Sutherland, 1989; Young and Davies, 1990, 1991; Warburton and Davies, 1994a). Young and Davies (1990) compared the empirically-based equations of Bagnold (1980) and Schoklitsch (1962) with their flume data and found a very strong agreement (see Fig. 3.10). The Bagnold (1980) equation had the strongest correlation with an average under-prediction of 18% for steady flows and just 1% for unsteady flows. Hoey and Sutherland, (1989) concluded that the Bagnold (1980) equation was more accurate and consistent than the Ackers and White (1973) equation (see Fig. 3.11), whilst Ashmore

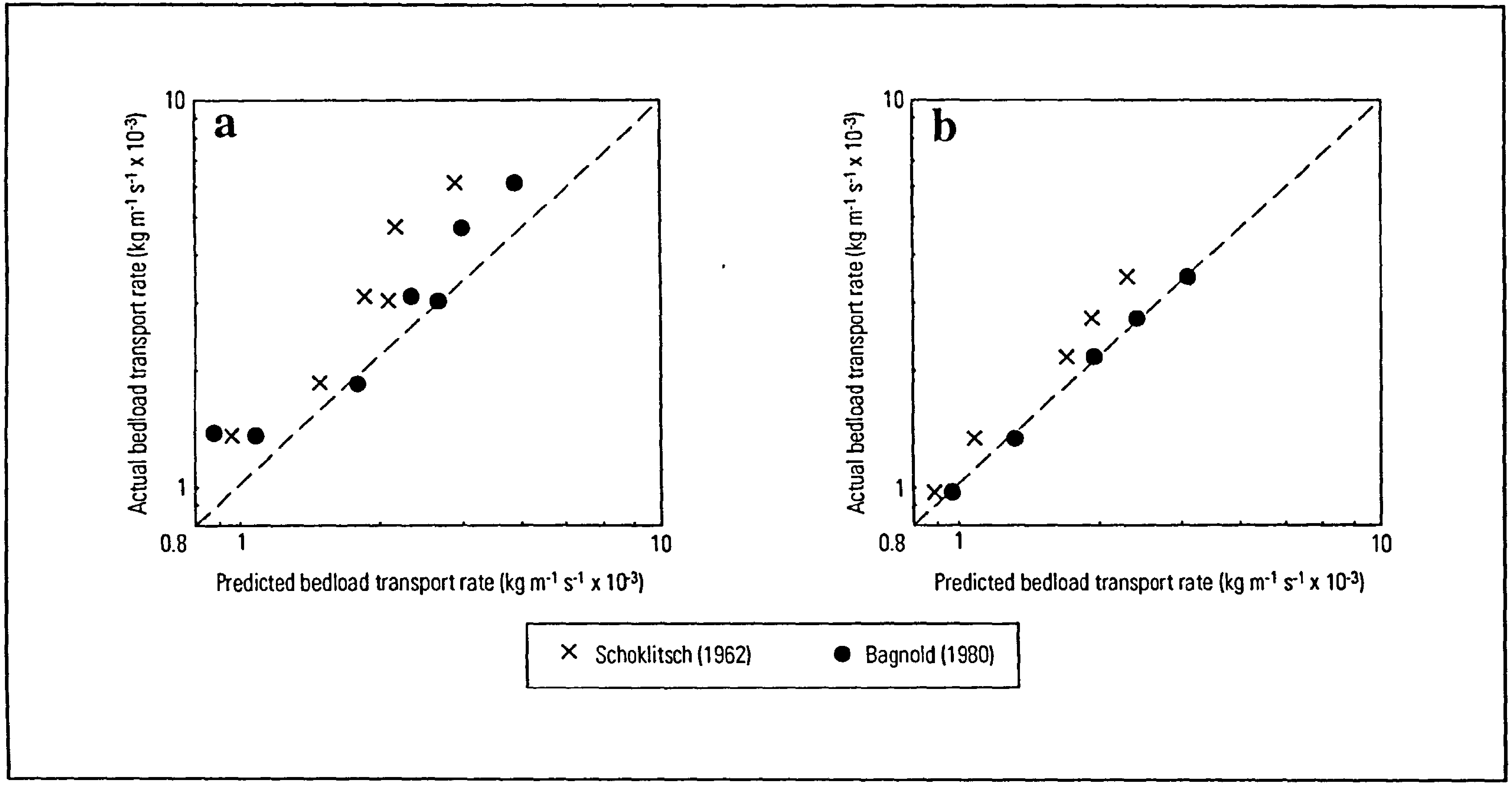

Figure 3.10. Bedload transport rate predictions from Young and Davies (1990) for (a) steady flows and (b) unsteady flows. Crosses are for the Schoklitsch (1962) equation and circles are for the Bagnold (1980) equation. Dotted line is for a perfect 1:1 relationship. After Young and Davies, (1990).

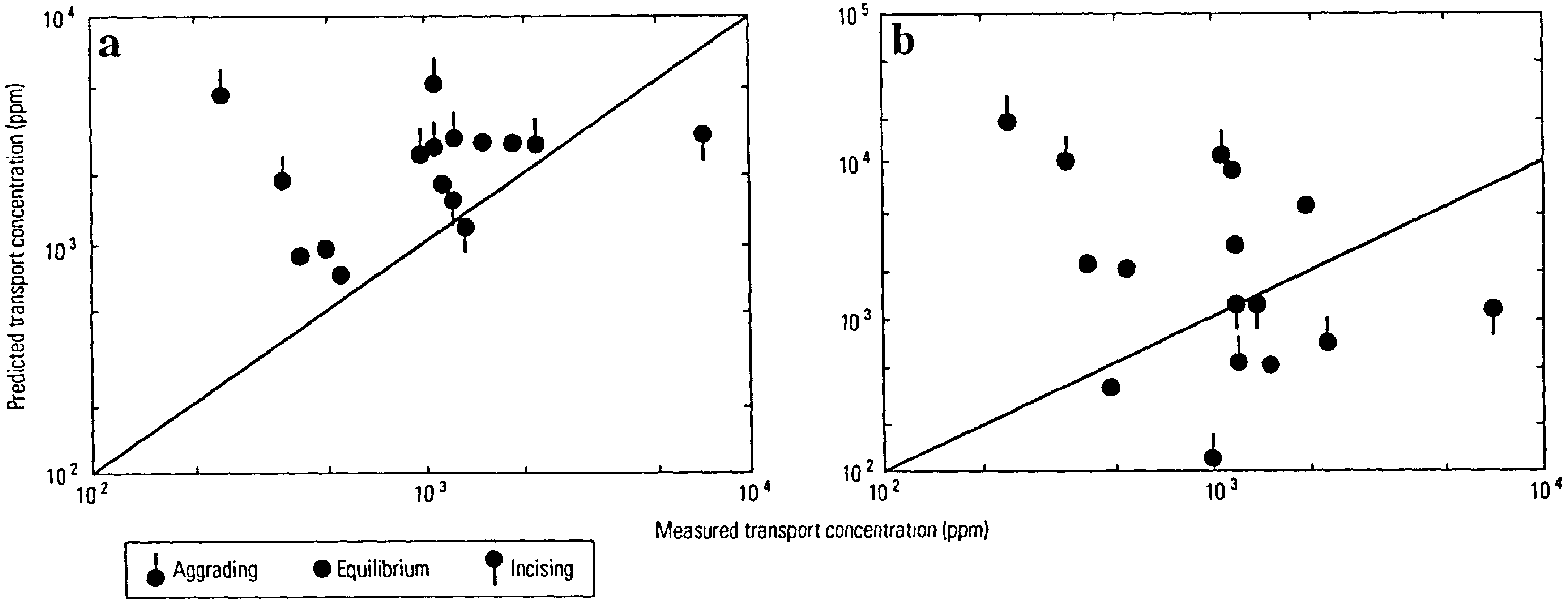

Figure 3.11. Bedload transport rate predictions for steady flows, from Hoey and Sutherland, (1989). Measured transport concentrations by dry weight against; (a) the Bagnold (1980) equation, and (b) the Ackers and White (1973) equation. After Hoey and Sutherland, (1989).

(1988) also demonstrated a good prediction using Bagnold's relationship. The formation of bedload pulses or waves in flumes has been studied by several authors (Ashmore, 1988; Kuhnle and Southard, 1988; Young and Davies, 1990; Hoey and Sutherland, 1991; Young and Davies, 1991; Warburton and Davies, 1994a) and the associated temporal variation in sediment transport rates (Fig. 3.12) may account for much of the scatter in correlations of bedload transport rate with discharge (e.g., Figs. 3.10 and 3.11).

Bagnold's (1980) equation can be expressed as,

$$i_b = (i_b)_* \left(\frac{\omega-\omega_o}{(\omega-\omega_o)_*}\right)^{1.5} \left(\frac{d}{d_*}\right)^{-0.66} \left(\frac{D}{D_*}\right)^{-0.5} \qquad \text{(Eq. 3.50)}$$

where i_b is the specific submerged mass transport rate, ω is the stream power per unit area, and ω_o is a nominal value of ω for initial bed movement. Variables marked with asterisks are reference values given by Bagnold (1980). The main problem in using equation 3.50 lies in choosing the threshold stream power value, ω_o. The simplest solution is to gradually increase the flow rate and note the conditions at which sediment movement starts (e.g., Young and Davies, 1990), although ω_o can be estimated using the flow depth and bulk subsurface grain-size (Hassan *et al.*, 1992). There can also be a problem measuring both ω and average d, due to thin films of water (<2 mm) held by surface tension on bar tops (Ashmore, 1988).

A dimensional analysis can be made for stream power in terms of length scales, noting that Bagnold (1980) expresses stream power as,

$$\omega = \rho q S_g \qquad \text{(Eq. 3.51)}$$

where q=unit discharge and S_g is the effective gravity gradient, normally taken as the water surface slope. Slope remains the same between prototype and model (Eq. 3.5) and if the density of the fluid is also identical then the only length scales are those for q. Since,

$$q = Vd \qquad \text{(Eq. 3.52)}$$

then by substituting the length scales for V and d, from Eqs. 3.30 and 3.31,

$$\lambda_\omega = (\lambda_L)^{0.5}\,\lambda_L = (\lambda_L)^{1.5} \qquad \text{(Eq. 3.53)}$$

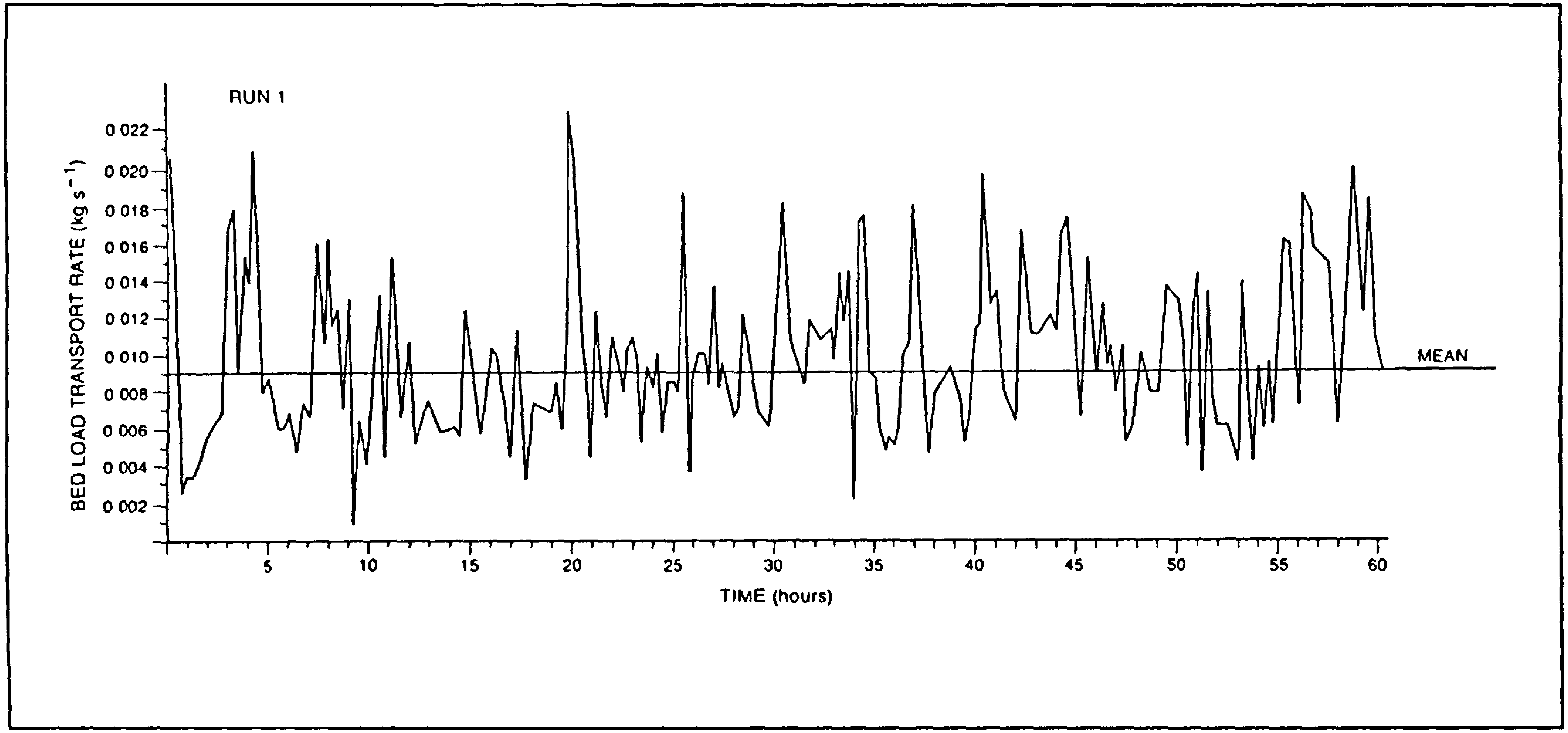

Figure 3.12. Temporal variability of bedload transport in a braided Froude scale model. From Ashmore, (1988).

It is therefore not surprising that the power function of the Bagnold equation (1980), which is a modified version of stream power, agrees well with model experiments.

In summary, many Froude scale model studies have grain Reynolds numbers below Yalin's threshold value of 70, and therefore have theoretical differences in the kinematic and dynamic properties of grains. However, in practice, sediment transport rates, at least in terms of bedload, seem to agree reasonably well with Yalin's (1971) scale ratio and Bagnold's (1980) transport equation.

3.8 Modelling of floodplain sediments

Floodplains are difficult to model because they either contain a significant amount of fine-grained material and are therefore cohesive, and/or they are covered in a layer of vegetation, which makes them more resistant to erosion. In addition, replication of microtopography such as swales and dips is difficult but is important for overbank deposition.

3.8.1 Use of fine grained sediment

Clay minerals are cohesive due to a combination of two forces, the weak Van der Waals' forces which all matter is subject to, and ionic bonds which form through the process of cation exchange between clay minerals. These intermolecular forces act in many cases as a fundamental limit on modelling, since cohesionless coarse sand and gravel can only be scaled down as far as silt sizes, without adding cohesion. Consequently, this limits both the overall scale of the model and can also lead to a truncation of the grain-size curve. It is even harder to model sediments that contain clay and therefore have cohesion, as these forces are scale independent. This leads to the cohesion forces being far too strong in the model relative to the erosional fluid forces.

The previous discussion makes a direct link between clay minerals and clay sizes which is frequently the case in nature. However, other materials can fall within the clay size range, including silica flour which has recently been used to extend the grain-size distribution down to 1 μm (Leddy *et al.*, 1993; Ashworth *et al.*, 1994). Some of this very fine material may travel solely in suspension or be repeatedly deposited and re-entrained. The use of such fine grained silica flour also leads to significant capillary forces which mimic prototype cohesion. This is a very desirable attribute in many models as several fluvial properties, such as sinuosity and hydraulic geometry, may vary with cohesion. For example, the weighted mean percent silt-clay (M) may be used as a surrogate for cohesion and shows a strong relationship with hydraulic geometry (Schumm, 1960a, b; 1968). Previous workers have added low concentrations of clay minerals to models in order to increase cohesion (e.g., Schumm and Khan, 1972) but this has often caused erosion to cease (see Section 5.5 for discussion).

Another approach to modelling fine-grained sediment, particularly where physical space restraints lead to scale limitations, is to distort the model (see Section 3.5) and in particular change the density of the grains. Use of lower density sediment allows larger particles to mimic the movement and transport dynamics of smaller particles, thereby avoiding cohesion. Another possible approach is to use clays and anti-flocculation agents (e.g., Calgon), but re-entrainment of deposited material may still remain a problem.

3.8.2 The water table

The water table is an important attribute of a floodplain and one which is rarely mentioned in the modelling literature. A flume with inner permeable and outer impermeable walls can be used to control the water table (Edgar, 1973; Zimpfer, 1975; Mosley, 1976). Whilst this approach works well with fine to medium sand, capillary forces in very fine-grained sediment tend to restrict the velocity of the 'groundflow'. In experiments which do not control the water table, the sediment may become completely saturated (e.g., Leddy *et al.*, 1993; Ashworth *et al.*, 1994). This can minimise erosion if pore pressures are high enough to force flowing water away from the bed. Equally, this saturated state can help capillary forces mimic cohesion (see Section 3.8.1). However, saturated fine-grained sediment can take several weeks to dry completely, and therefore may restrict sectioning of the sediment to examine the preserved alluvial architecture, if time is a constraint.

3.8.3 Vegetation

Vegetation plays an important role in strengthening the banks and floodplain, particularly in coarse-grained rivers where inter-particle cohesion is largely unimportant. There has been very little research on modelling floodplain vegetation, although Marsden (1981) attempted this by planting differing densities of toothpicks and tested wheat, rape, cress, lawn seed and budgie seed, before growing mustard in a generic braided model. The results demonstrated that there was an optimum planting density for maximum floodplain accretion, and Marsden (1981) recommended that the approach be extended to a larger model that could incorporate scale effects. Jin and Schumm (1987) used a two layer floodplain composed of a clay-rich layer above sand (see Fig. 5.9), which in some respects simulates vegetation, by providing protection to the floodplain surface and to the upper bank (*cf.* Zimmerman *et al.*, 1967; Smith, 1976). However, the two-layer floodplain model does not allow realistic depositional architectural elements, such as lateral accretion surfaces and backwater deposits to form. Additionally, Jin and Schumm (1987) did not run overbank flows and therefore the effectiveness of the floodplain for trapping sediment is unknown.

3.9 The modelling of time

One of the primary objectives of physical modelling is to change the observed time-scale, thus permitting study of a wider range of processes and landforms. Two different approaches to the modelling of time are possible, one based on dimensional analysis and the other on magnitude-frequency analysis.

3.9.1 Dimensional analysis of time-scales

An expression for dimensionless time (θ_t) can be derived by dimensional analysis of $\mu, \rho, R, k_s, S_b, V$ and g (as used in Section 3.4.2). Selecting R, ρ and V as basic quantities as before, gives:

$$\theta_t = \frac{tV}{R} \qquad \text{(Eq. 3.54)}$$

The hydraulic radius, R, is the characteristic length of the system (L), and Eq. 3.54 can be restated as,

$$St = \frac{tV}{L} \qquad \text{(Eq. 3.55)}$$

which is a form of the Strouhal number, St. The Strouhal number can be used to calculate the timescales for different types of motion within a model. The general model time-scale (λ_t) and the timescale for downstream or cross-stream velocity $(\lambda_t)_V$ can be calculated by considering equation 3.55 in terms of length scales and noting that $\lambda_V = (\lambda_L)^{0.5}$ (Eq. 3.31). The general and velocity time-scales are therefore given by:

$$(\lambda_t) \text{ or } (\lambda_t)_V = \frac{\lambda_L}{(\lambda_L)^{0.5}} = (\lambda_L)^{0.5} \qquad \text{(Eq. 3.56)}$$

These scales differ from the previously derived time-scale for sediment transport, λ_s, which had a scale ratio of $(\lambda_L)^{1.5}$ (Eq. 3.49). Similarly, the fall velocity of a particle as characterised by Stokes' Law (Section 3.6.3) was stated as $\lambda_{V_g}=(\lambda_L)^2$ (Eq. 3.33) and if substituted into the Strouhal criterion, gives a timescale of $(\lambda_t)v_g=(\lambda_L)^{-1}$. Yalin (1971) also notes a series of other time-scales:

$$(\lambda_t)_y = (\lambda_L)^2 \qquad \text{(Eq. 3.57)}$$

$$(\lambda_t)_x = (\lambda_L)^{0.5} \qquad \text{(Eq. 3.58)}$$

$$(\lambda_t)_m = (\lambda_L)^{-1} \qquad \text{(Eq. 3.59)}$$

where $(\lambda_t)_y$ is the vertical erosion / accretion; $(\lambda_t)_x$ is the downstream displacement of sediment from one place to another; and $(\lambda_t)_m$ is the grain motion during saltation in either the horizontal or vertical dimensions. Vertical bed surface change is therefore the fastest, then the sediment transport rate, followed by the displacement of sediment or fluid in the downstream direction, and finally the slowest processes are the individual motion of grains during saltation and the fall velocity, i.e.,

$$(\lambda_t)_y < \lambda_s < (\lambda_t)_x, (\lambda_t)v < (\lambda_t)_m, (\lambda_t)v_g \qquad \text{(Eq. 3.60)}$$

Ashmore (1988), in reviewing Yalin's (1971) work, stated that "the time-scale for sediment transport cannot be calculated for a model based on water flow parameters" (p.692). This statement is ambiguous since time-scales for sediment transport can be calculated (e.g., Eq. 3.49). However, Ashmore's basic premise would appear to be that no single all encompassing sediment transport time-scale exists. This can cause confusion when trying to interpret experimental results. For example, there has been debate as to whether short term fluctuations in bedload rates should be scaled in terms of total sediment transport rate, $(\lambda_L)^{1.5}$, or in terms of downstream displacement of grains, $(\lambda_L)^{0.5}$ (Ashmore, 1988; Young and Davies, 1991). This may have important ramifications for the modelling of alluvial architecture. For example, since vertical erosion and deposition are much faster than horizontal processes, there may be distortions in the size of scours and overbank splays. Initial work on shale dimensions (Ashworth and Best, 1994; Ashworth *et al.*, 1994) suggests that the influence of multiple timescales is limited, but specific experiments on these aspects are still required.

3.9.2 Hydrograph scaling

An alternative approach to modelling time within physical models is through use of the geomorphological concept of the magnitude-frequency of events on a given system. The discharge frequency for a river is approximately log-normal (curve B, Fig. 3.13) while the magnitude of bedload transport increases beyond an initial threshold (Q_t), as a power function of excess discharge (curve A). The product of the magnitude of sediment

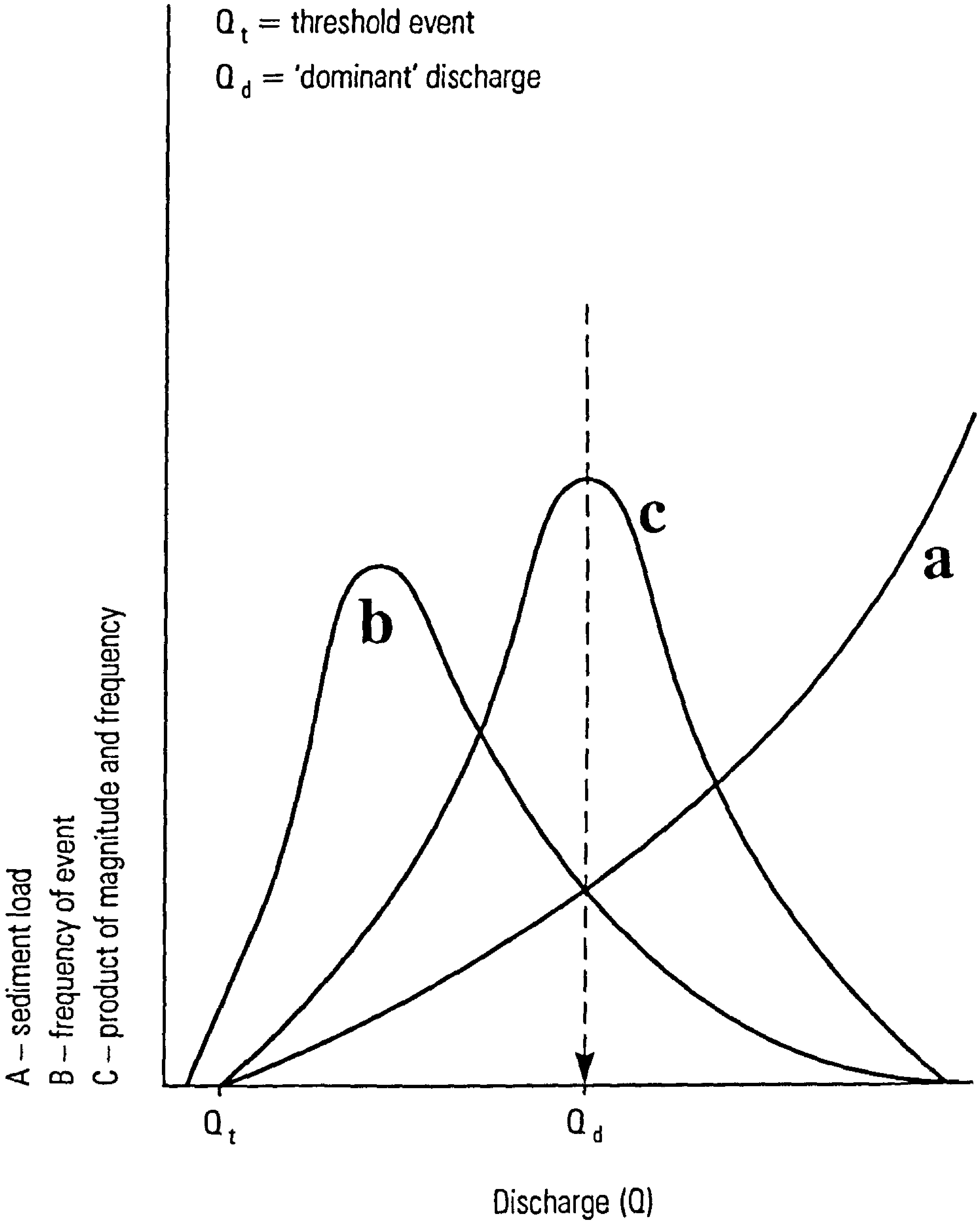

Figure 3.13. Magnitude-frequency plot of river discharges and sediment load. After Richards (1982) based on work by Wolman and Miller, (1960).

transport and flow frequency (curve C) shows that medium sized events account for the most work. The apex of the magnitude frequency curve (Q_d) is known as the 'dominant' or 'effective' discharge, and has been shown to correlate well with the bankfull discharge in many rivers (Wolman and Miller, 1960).

Most physical models use a constant discharge which is approximately at the bankfull level and therefore correlates with the 'dominant' discharge. Through the use of hydrographs it is theoretically possible to compress the timescale by imposing a small number of medium to high-magnitude flood events on a system (e.g., a 50 year flood, a 500 year flood etc). However, if a large number of high magnitude flood events are imposed, they may alter the nature of the system that is being modelled, since the hydraulic parameters may begin to reflect this artificial 'dominant' discharge, instead of the bankfull flow. A limited number of studies have used hydrographs but have not specifically examined the magnitude-frequency effects (e.g., Davies and Lee, 1988; Young and Davies, 1990, 1991; Leddy *et al.*, 1993; Ashworth *et al.*, 1994). The modelling of hydrographs has other advantages in addition to compressing the timescale. For instance, many important fluvial processes such as overbank sedimentation, avulsion and bend cutoffs, usually occur at high flows. Low stage alteration of the channel pattern and deposition of fine-sediment is also very important, especially in braided rivers. Therefore, these aspects can only be modelled by a range of discharges.

There are two aspects which must be considered when modelling hydrographs: scaling of the discharge and scaling time. The scale ratio for discharge can be found through a consideration of the continuity equation of flow (Eq. 3.24), and gives:

$$\lambda_Q = (\lambda_L)^{0.5} \lambda_L \lambda_L = (\lambda_L)^{2.5} \qquad \text{(Eq. 3.61)}$$

In contrast the time-scale for the fluid, $(\lambda_t)_V$, is $(\lambda_L)^{0.5}$ (Eq. 3.56). Model hydrographs are therefore flatter than their prototype equivalents (Leddy, 1993). Previous studies have used stepped hydrographs with step intervals averaging approximately 2-10 minutes (e.g., Ashworth *et al.*, 1994). The braided river experiments reported in this study used 0.5 minute discharge increments through the use of a precisely calibrated computer controlled valve (see Section 4.3.2).

3.10 Summary

Two broad classes of physical model can be defined: generic and scaled. Scale models can be further sub-divided into Froude scale models (FSM) and distorted, movable-bed models. There are three increasing levels of similarity which may be considered in physical modelling: geometric, kinematic and dynamic. For a Froude scale model, the scaling ratio for any given variable can be calculated using dimensional analysis. However, if certain properties remain constant, for example, gravity, surface tension, fluid viscosity and density, as is the case for most FSM experiments, then perfect similarity cannot be achieved. Some authors have therefore suggested that many FSM models should really be called generic (Ashmore, 1991a, b; Leddy, 1993; Ashworth, 1995). However, this confuses the situation further. The major difference between generic and FSM modelling is not how closely they replicate reality, but in whether the degree of closeness to reality can be estimated or not. FSM models allow the degree of replication to be either chosen in advance or estimated afterwards and allows comparison to be made between different models. Generic models have none of these advantages. Model variables should be clearly defined and routinely published and ideally, consensus should be reached on the definition of many parameters, in order to enable comparison between different FSM experiments.

Despite the difficulty in achieving kinematic and dynamic similarity in many FSM's, a number of complex processes may still be modelled closely, for example bedload transport, depositional architecture and planform river processes. The recent use of fine-grained cohesionless sediment and hydrographs within Froude scale models further increases the model's realism. However, there is a need for experimental work to address specific modelling problems. For example, simple experiments on the influence of surface tension and further work on scaling vegetation would allow these properties to be fully incorporated into models: Finally, a clearer understanding is required of the effects of a range of processes acting at different timescales within a model. This is particularly pertinent if further progress is to be made in extending FSM studies into the third dimension through examination of the alluvial architecture of aggrading systems.

Chapter 4. Experimental Apparatus and Procedure

4.1 Synopsis

This chapter describes the equipment and methodology used for lateral tilt experiments on meandering and braided channel patterns (Chapter 5). All the experiments were conducted in a wide stream table (Fig. 4.1) which has a unique design since the inlet feeder channel can be gradually raised during an experiment, allowing aggradation of the fluvial model. A steel mesh at the downstream end of the flume permits channels to migrate freely since water and sediment can exit the flume whilst deposition can take place on the floodplain in non-channelised areas. Details are presented of the stream table and associated equipment, data collection methods and evolution of the experimental methodology as data collection techniques were refined. A single grain-size mix was used for all the experiments and the rationale for using the chosen sediment distribution is explained.

4.2 The stream table

A stream table 5.5 m long, 3.65 m wide and 0.5 m deep was used for all the experimental work (Chapter 5, see Figs. 4.1 and 4.2). The stream table is constructed of 10 mm thick industrial sheet plastic supported by a steel girder framework. One side-wall of the flume consists of clear perspex to permit observation of sedimentary processes and preservation. The downstream end of the flume is made of galvanised steel mesh with 3 mm diameter holes. This allows the passage of both water and bedload from active channels, but keeps the floodplain sediment *in situ* as this is only reworked by limited throughflow. This unique exit design minimises drawdown effects and allows flume wide aggradation or degradation of the fluvial system. Interlocking steel blocks mounted on plinths at the four corners support the weight of the flume and can be altered to allow the flume to be tilted in any direction by up to 3%. A steel girder bridge mounted on two steel rails spans the width of the flume. A point gauge attached to the downstream end of the bridge allows precise point coordinates to be recorded since both the bridge and the supporting rails are graduated.

An inlet channel is attached to the centre of the upstream wall and rests on an extension to the steel girder framework. The inlet mechanism consists of an inner channel

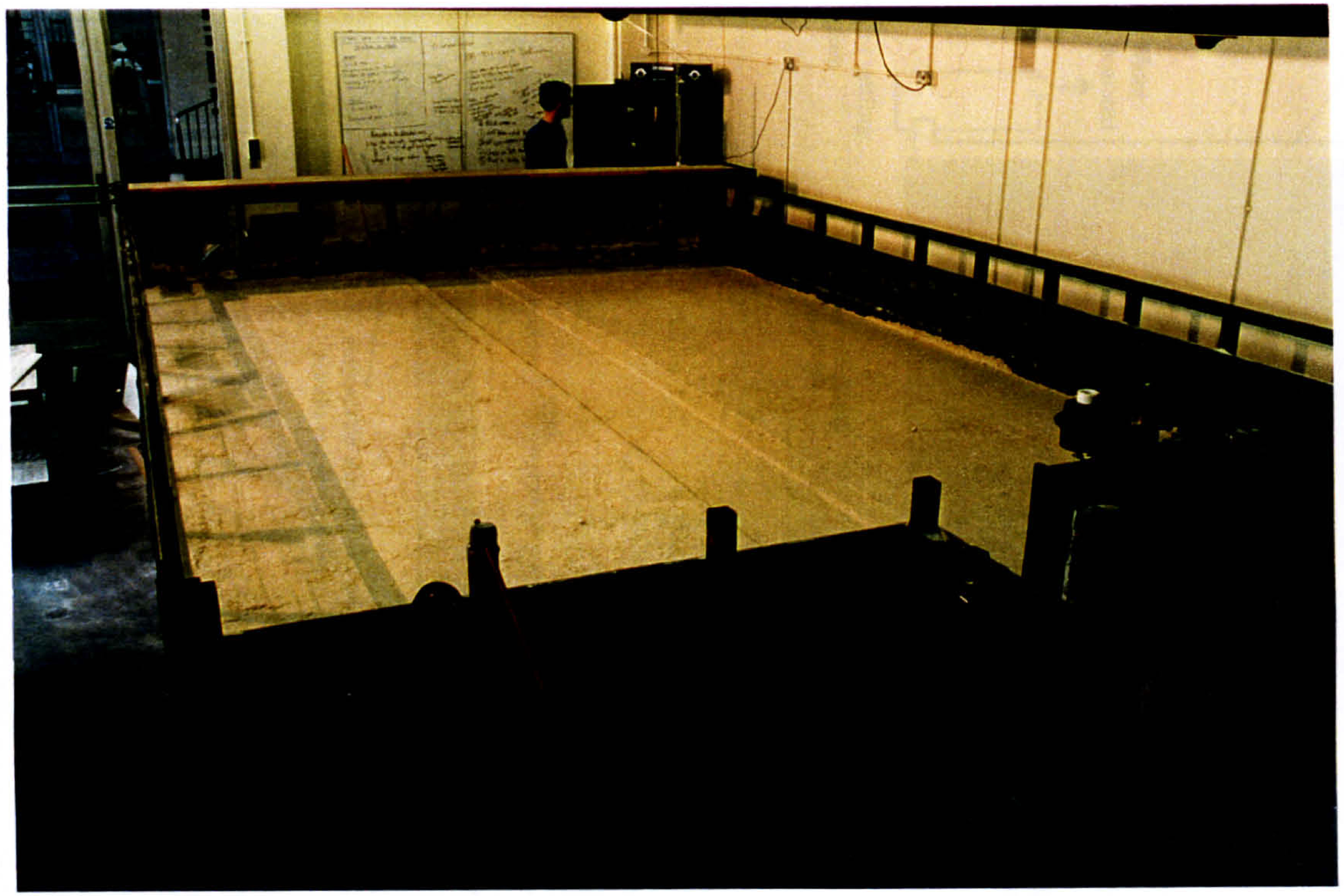

Figure 4.1. View of the stream table looking downstream prior to the start of a braided modelling experiment. The bed surface has been levelled and a 0.4 m wide channel cut in the centre. The inlet channel and part of the motor driven racking system are at the bottom right and the measurement bridge is at the downstream end of the stream table.

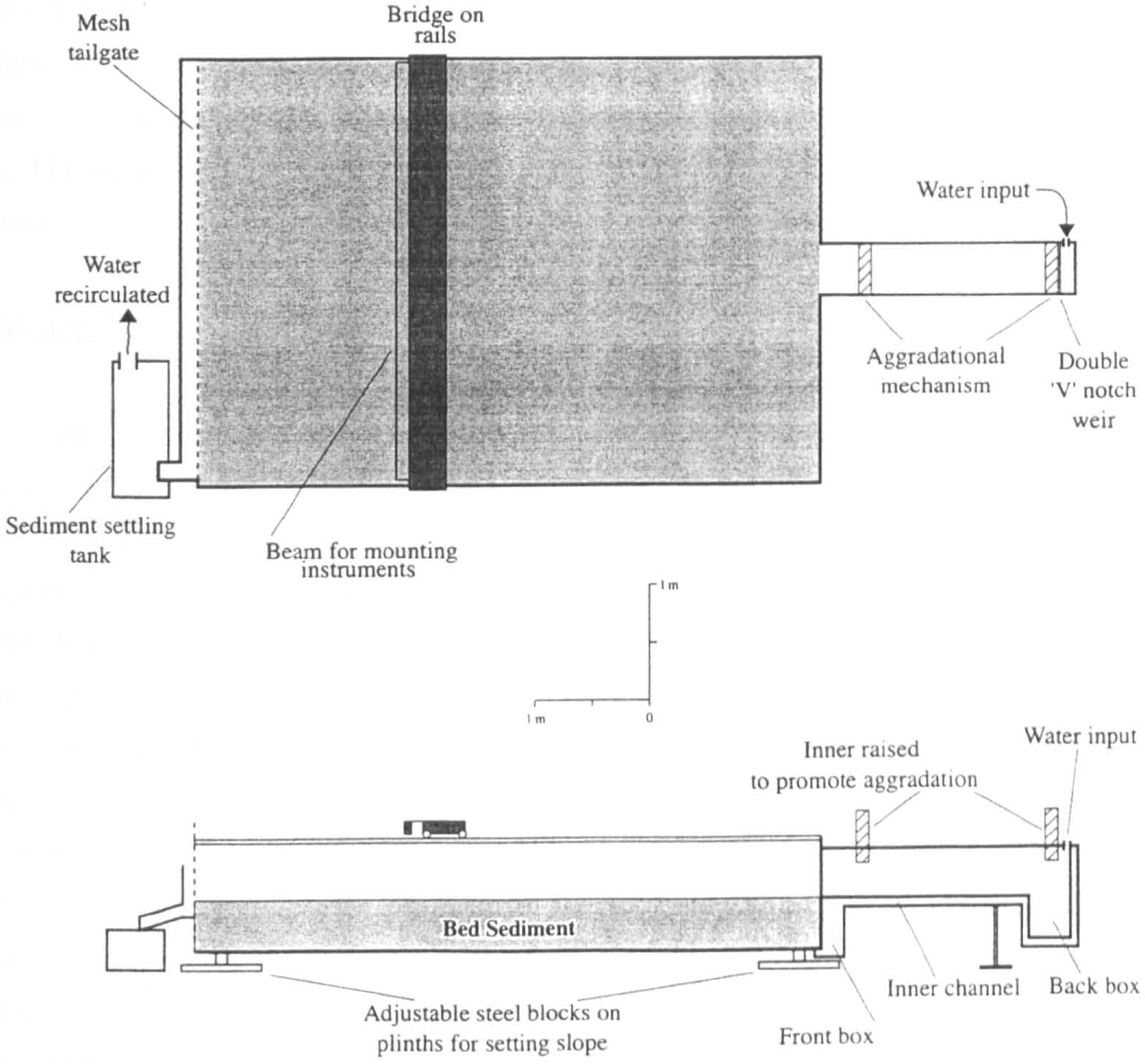

Figure 4.2. Planform and cross-section of the stream table. Water enters into the backbox, flows over a double V-notch weir and exits through a steel mesh into a settling tank. Coarse grained sediment is trapped in the settling tank and the water flows into a reservoir tank from where it is recirculated. The inner inlet channel can be raised to allow aggradation of the sediment. Adapted from Ashworth *et al.*, (1994).

(external dimensions of 2.4 m long, 0.4 m wide and 0.1 m deep) with a backbox, supported on a cradle by an outer frame (see Fig. 4.2). A double V-notch weir is situated between the backbox and the inner channel for the measurement of flow (Section 4.3.1). The inner channel moves vertically to allow runs to start with a different bed thickness and promote aggradation during an experiment. Vertical movement of the inner channel is controlled by a motor driven racking system connected to two screwthread rods attached to the outer cradle. Each rod has a 2 mm thread and the electric stepper motors move by quarter of a revolution per time increment, giving a minimum vertical movement of 0.5 mm. The time increment for the stepper motors can be adjusted to any multiple of 36 seconds.

4.3 Water delivery and control

The stream table uses a recirculating water supply system. Water for the flume is stored in a 6.8 m^3 tank located one floor below the stream table, is pumped through 15 m of 0.075 m diameter pipe and then passes through a flow control valve before entering the backbox of the inlet channel through flexible piping (Fig. 4.2). After passing over a double V-notch weir (see Section 4.3.1) water flows down the inlet channel and into the flume. An inclined gutter (0.11 m wide x 0.20 m deep) collects water and sediment from the downstream end of the flume and funnels them into a small settling tank which is divided into two compartments. Bulk sediment transport rates are recorded by placing a tray onto rails in the settling tank. Most of the coarse sediment is trapped in the tray and water exits over a step cut into one side. Some additional fine grained sediment settles out in the tank before the water flows back into the main reservoir tank. The majority of the remaining fine grained silica flour settles out in the main tank although some is recirculated.

A pump with constant discharge potential of 15.5 l s^{-1} and a hydraulic head of 33.3 m was used for experiments M7, M8 and M9 (Note: M refers to a meandering pattern). At low flow rates of 0.5 to 1.0 l s^{-1} the sensitivity of the flow control valve limited the precision of the discharge. Additionally, at low flow rates the dissipation of excess heat from the pump caused a gradual rise in water temperature during a run and therefore changes in water viscosity (see Fig. 4.3). Later experiments used a smaller 2100 W pump with a maximum flow rate of 5 l s^{-1} and a maximum hydraulic head of 8 m which reduced water temperature variation during runs to 1-2°C (see Fig. 4.4).

A manually controlled 0.075 m diameter full shut-off gate valve was initially used to control flow rate, through a slow process of flow rate measurement and valve adjustment. An electro-pneumatic valve was installed prior to experiment M8 and operated by a variable resistance manual control which improved both the speed and

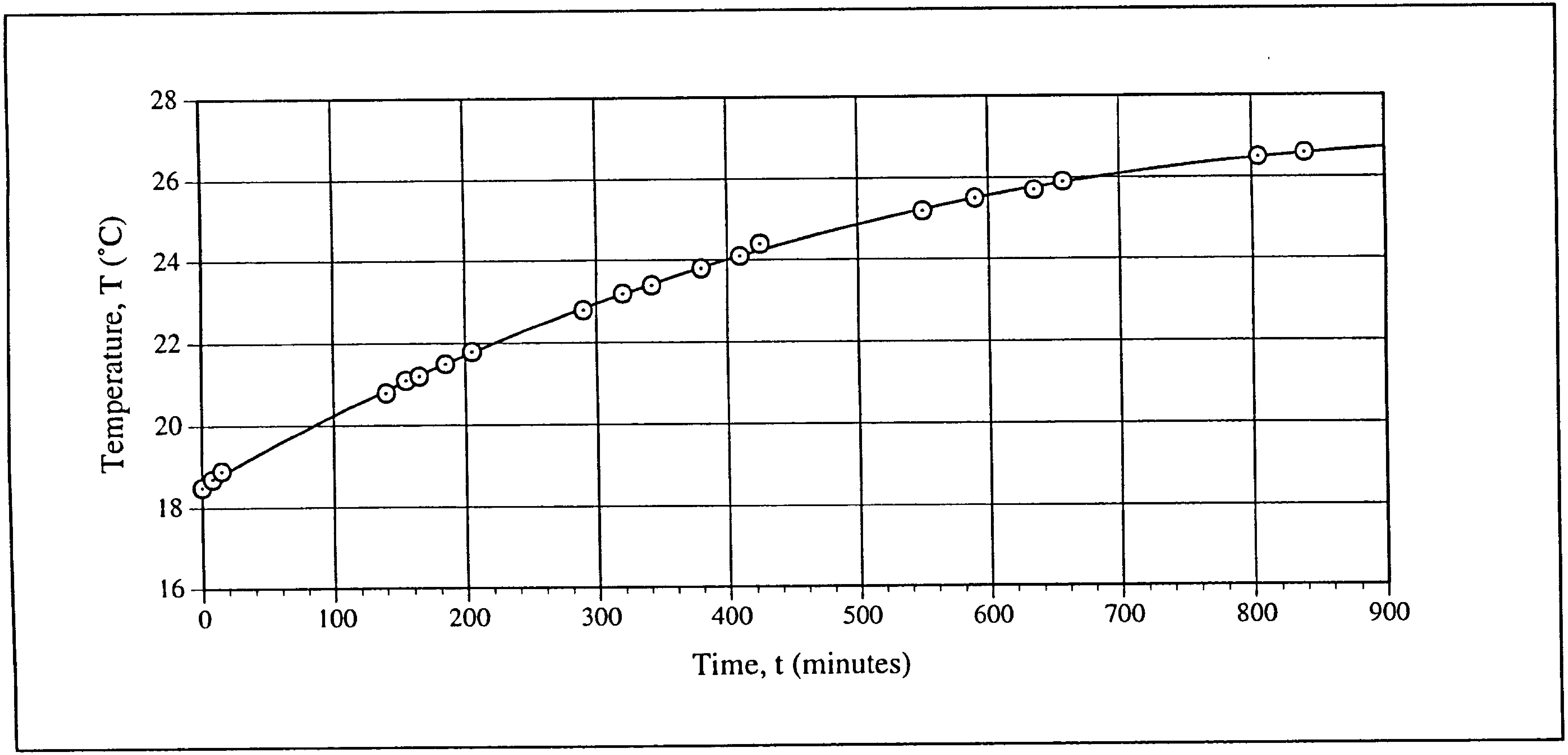

Figure 4.3. Temperature variation with time for a run using the initial pump (discharge potential 15.5 l s^{-1}, hydraulic head 33.3 m). The water temperature increased by approximately 8°C in 14 hours which has a dramatic effect on water viscosity (see Figure 3.2).

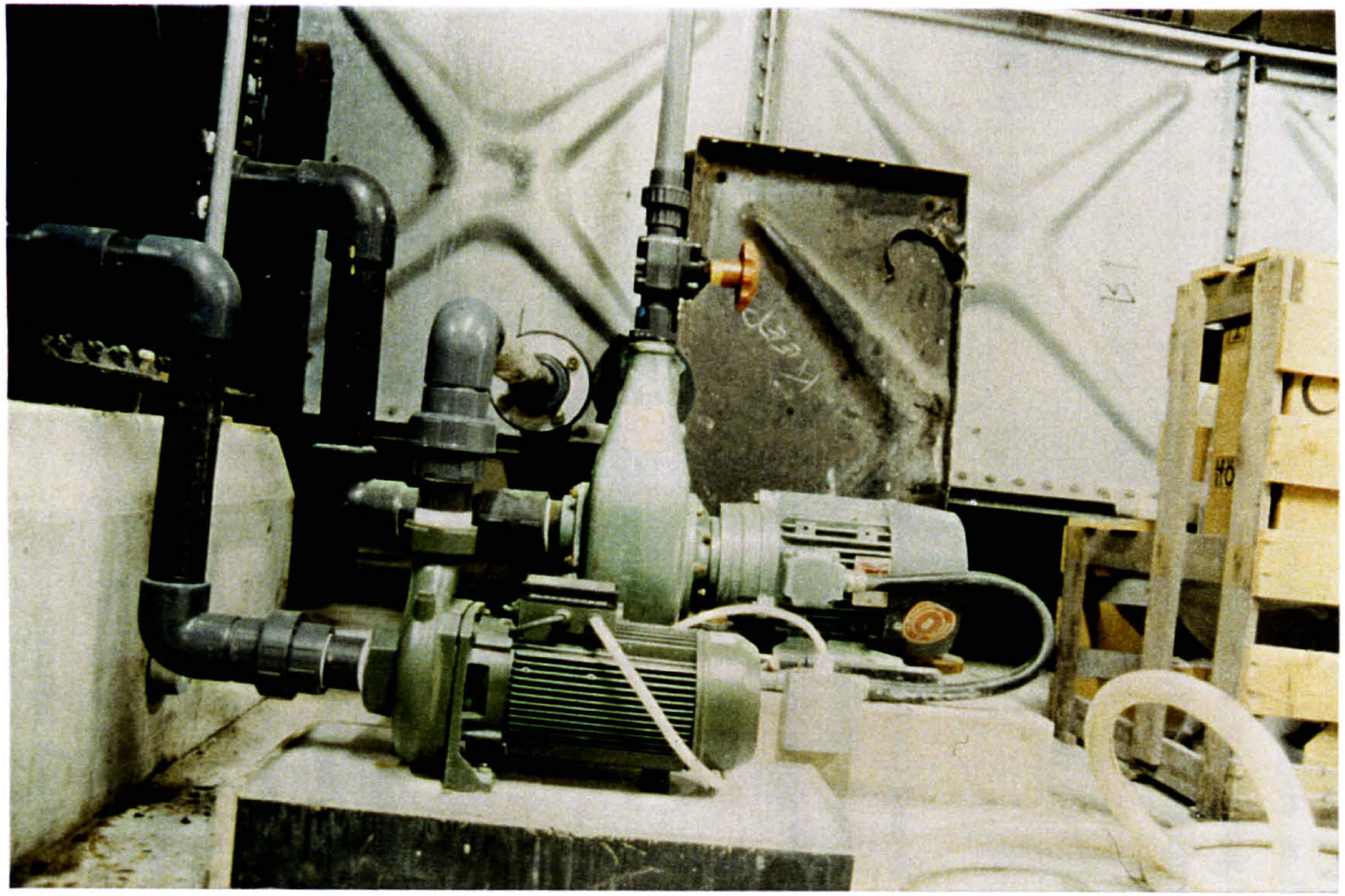

Figure 4.4. View of the two different pumps used in the flume experiments. The large pump at the rear was used for early experiments while the small pump (foreground) reduced problems of excess head and fixed discharge potential. Both pumps are connected to the reservoir tank at the far left. The small pump is 0.33 m long.

precision of discharge control. However, the excess discharge potential and hydraulic head of the original pump, combined with the extremely abrasive silica flour, led to significant wear on the valve stem and seat. A toughened tungsten cobalt chromium alloy stem and seat were therefore fitted to the electro-pneumatic valve prior to run M11. The addition of a digital to analogue converter board to an IBM compatible PC gave full computer control to the electro-pneumatic valve. At the same time, maximum valve sensitivity was achieved by installing a new smaller pump. The valve has an equal-percentage response and therefore has a greater sensitivity at the lower end of the discharge range (0-2 $\mathrm{l\,s^{-1}}$). The valve was calibrated by measuring the time taken for the flow to fill a fixed volume: the resulting calibration curve was characterised by fitting a third order polynomial curve (Fig. 4.5).

4.3.1 Double V-notch weir

A double V-notch weir is located on the downstream face of the backbox (see Fig. 4.2) and is used for measuring flow rates in the early experiments. Each weir is 0.09 m high, has a notch angle of 90° and a bevelled face at an angle of 45° in the downstream direction.

The discharge for a V-notch weir is given by,

$$Q = \frac{8}{15} C_d (2g)^{0.5} \tan(\alpha/2)\, d^{2.5} \qquad \text{(Eq. 4.1)}$$

where C_d is the drag coefficient, α is the angle of the weir and d is the depth upstream of the weir. To avoid drawdown effects, the depth should ideally be measured at a distance 4-5d upstream of the weir (BS 3680), although measurement limitations in these experiments restricted this to 0.5d. The drag coefficient (C_d) is not strictly a constant for a given weir as it is a function of flow Reynolds number, Weber number and the flow depth (Chadwick and Morfett, 1986). However, if the fluid forms a free 'jet' that falls clear of the weir plate, then C_d can be taken as a constant. For the double V-notch weir in the flume, the water nappe clings to the downstream face of the weir and causes unsteady, fluctuating flow due to the combined effects of surface tension and viscosity. This makes measurement of the flow rate difficult, but more importantly affects the fluid flow in the flume for a distance of several metres. An average drag coefficient of 0.71 has been calculated for each V-notch giving a combined drag coefficient of 1.42 for the weir (see Fig. 4.6).

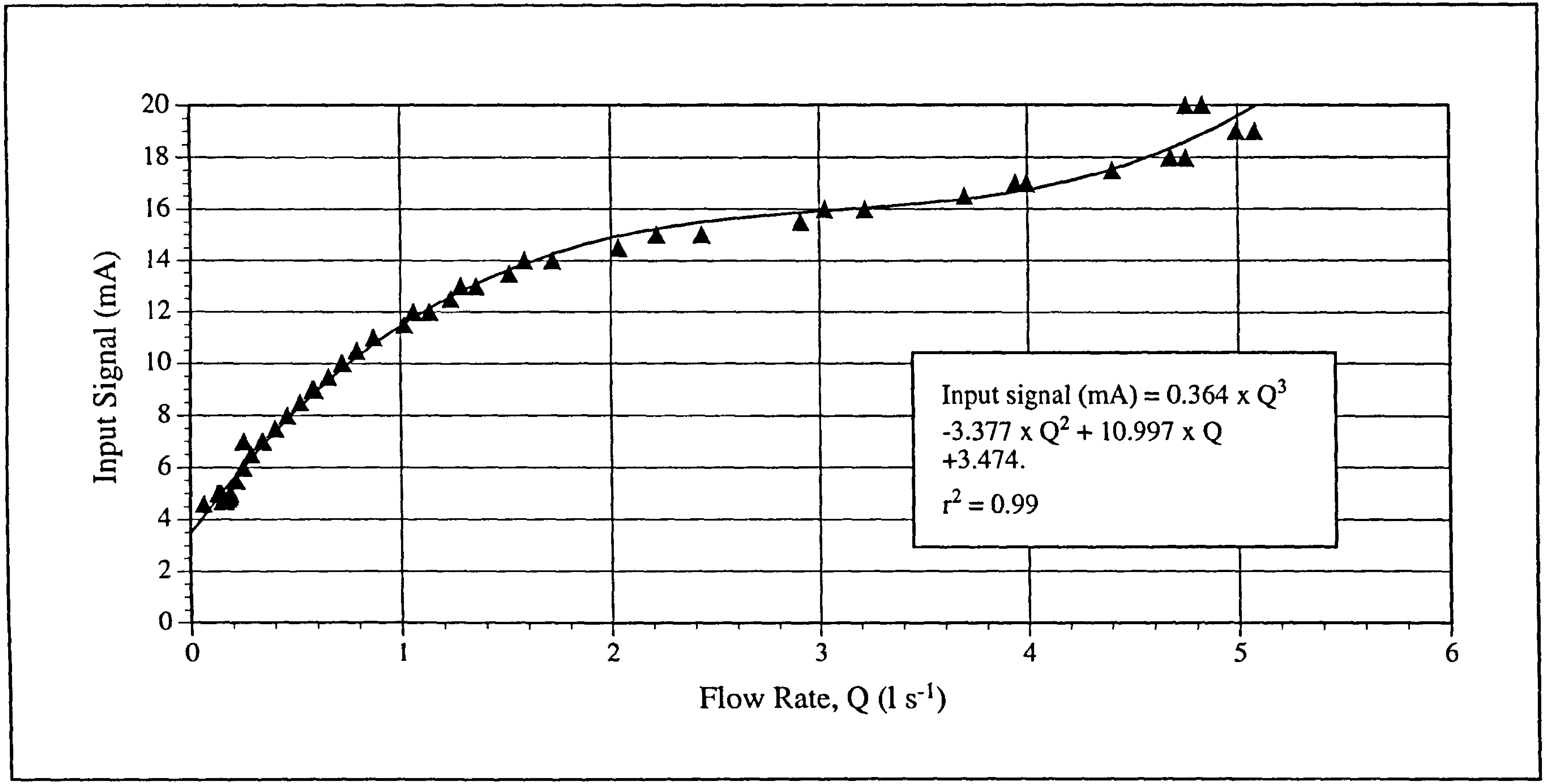

Figure 4.5. Calibration of the computer controlled electro-pneumatic valve. The valve is of an equal percentage type and therefore the flow increases as a power function of the input signal and only alters as the maximum pumping capacity of the pump is reached. Sensitivity is therefore greatest for small discharges. A third order polynomial curve is fitted to the data and the equation is shown in the bottom right.

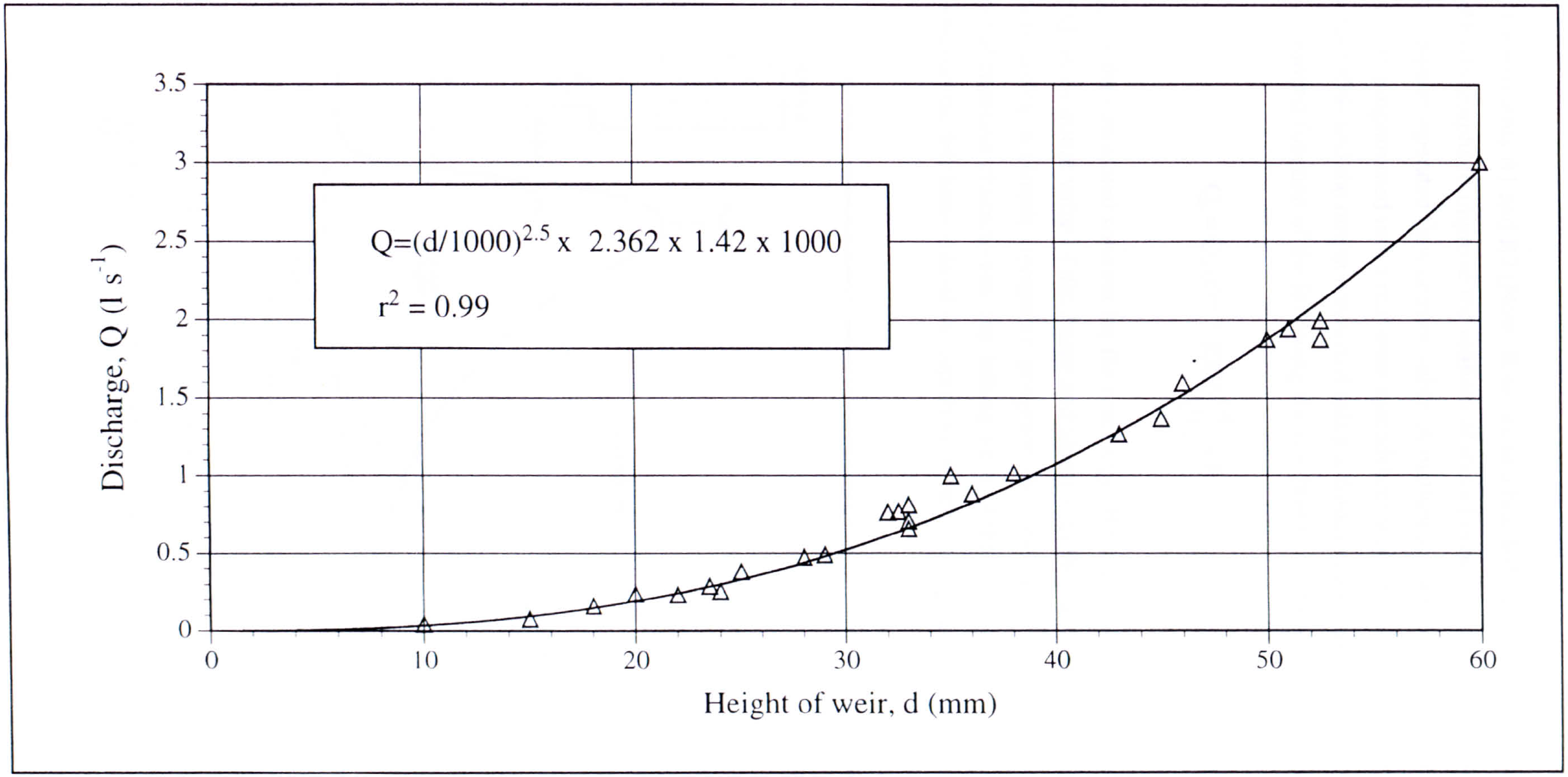

Figure 4.6. Calculation of the combined drag coefficient for the double V-notch weir. The standard equation for a 90° V-notch weir is shown and has been solved for the drag coefficient of 1.42 (see text).

4.3.2 Curve fitting to prototype hydrographs

Experiments B1 and B2 (Note: B refers to a braided pattern) incorporated the use of flood hydrographs to improve the realism of model conditions. Hydrographs were set using a computer operated flow control valve. A mathematical formula based on a gamma function was programmed into a real time spreadsheet with input/output driver capability (IoCalc for DOS) and the output converted using a digital to analogue board.

A gamma function of the following form is fitted to a chosen hydrograph:

$$Q_s = Q_o (t)^m * \mathrm{EXP}\left(\frac{-t}{t_1}\right) + B \tag{Eq. 4.2}$$

where Q_s is the calculated solution for the discharge, B is the hydrograph baseflow and t is time. Q_o is an initial value of discharge and along with the variables m and t_1 is solved iteratively using a simple computer program (see example in Appendix A). The exponential function characterises the falling limb of the hydrograph, while the power relationship on the left hand side of the equation models the rising limb (see Fig. 4.7).

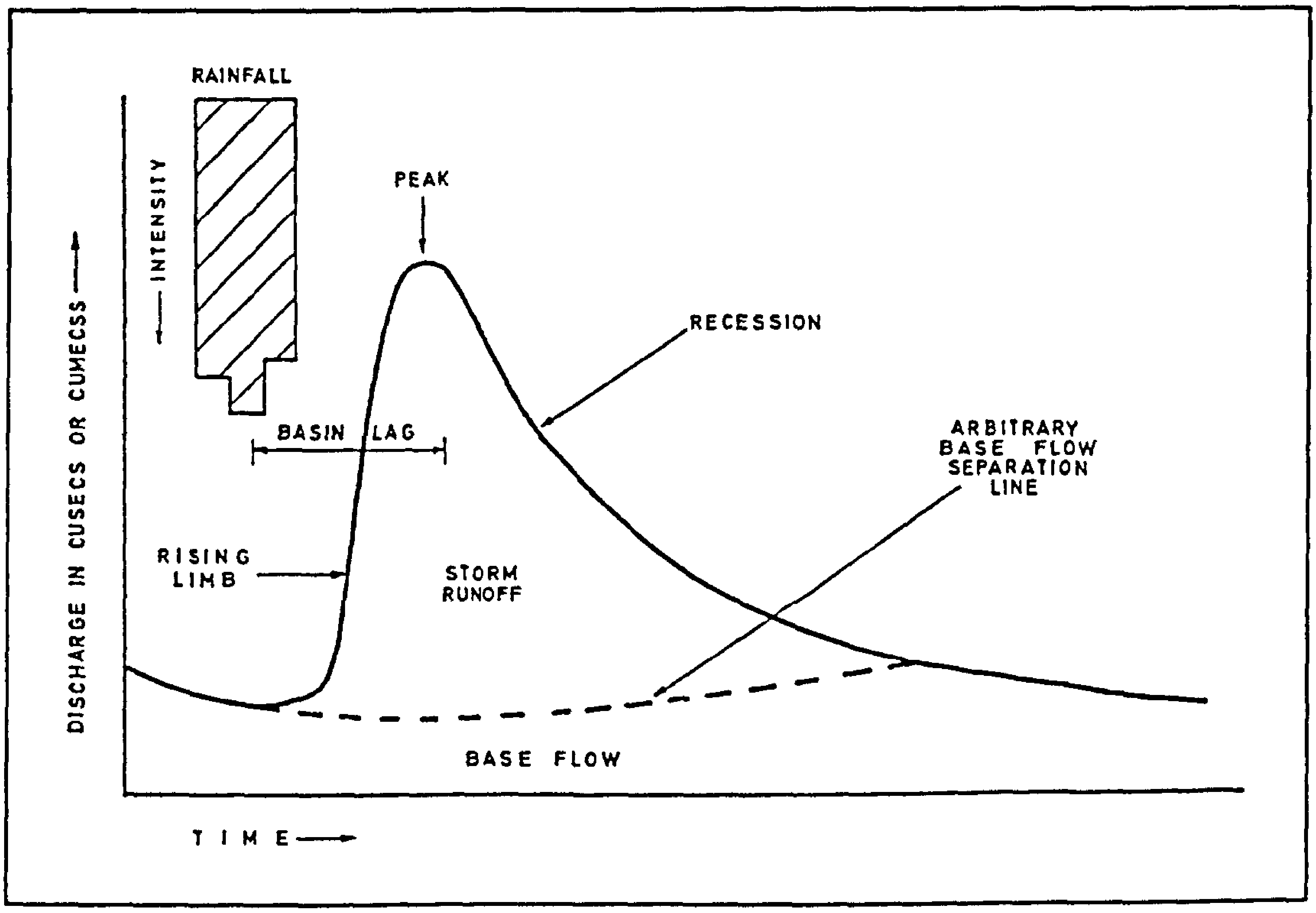

Figure 4.7. Major components of a flood hydrograph. The recession limb is also referred to as the falling limb. From Rodda (1969).

In order to simplify the solution to this equation, two further relationships are used. The peak discharge, Q_{max} is given by:

$$Q_{max} = Q_o (mt_l)^m e^{-m} \qquad \text{(Eq. 4.3)}$$

and occurs at time t_{pk}, given by:

$$t_{pk} = mt_l \qquad \text{(Eq. 4.4)}$$

Both t_{pk} and Q_{max} are taken from the chosen hydrograph. To fit a curve to a scaled hydrograph a range of 'm' values and the iterative incremental increase, are chosen (e.g., 1 to 20 at increments of 0.1). The smaller the incremental rise, the higher the degree of precision. For each increment, equation 4.4 can be solved for t_l since t_{pk} is known. Substituting the value of t_l into equation 4.3 along with a knowledge of Q_{max} allows the second expression to be solved for Q_o. The calculated values are then compared against the original values using two different expressions. The first is $E= \Sigma\ (Q_A-Q_s)^2$ = a minimum and the second is $F= \Sigma\ |Q_A-Q_s|$ = a minimum, where Q_A is the scaled prototype discharge. The latter expression has been used in this study since it provides a stronger correlation with the chosen hydrograph (see Fig. 4.8). The hydrograph flowrate was adjusted every 30 seconds using the computer controlled valve.

4.4 Video imaging

A Panasonic WV-CD130 colour CCTV camera with a Molynx 4.8 mm 1:1.8 wide angle lens was mounted directly above the centre of the flume and imaged an area of approximately 3.8 x 2.5 m. Signals from the video camera were fed into a Digital WV-108 mixing desk and then a Panasonic S-VHS AG6720A time-lapse video recorder which could be set to record between 0.31 and 50 fields per second (note: 2 fields are interlaced to form a single frame on a standard VCR). Lighting was provided by two 1250 W tungsten arc lights which were mounted centrally above each side of the flume, for runs M7 and M8. However, problems with hot spots of light intensity were noted which reduced the quality of video images (see Fig. 5.8a, b). For all later runs both arc lights were mounted to one side of the flume which provided an even decrease in light intensity parallel to the axis of the stream table (see Fig 5.8c, d). A second Panasonic colour WV-CL350 CCTV camera with a WV-LZ80/2 6-12 mm 1:1.4 vari-focal lens could be attached to the downstream edge of the bridge or mounted on a tripod to allow close up shots of the stream table. The images from both cameras could also be recorded simultaneously onto a single tape using the mixing desk. Average surface flow velocities

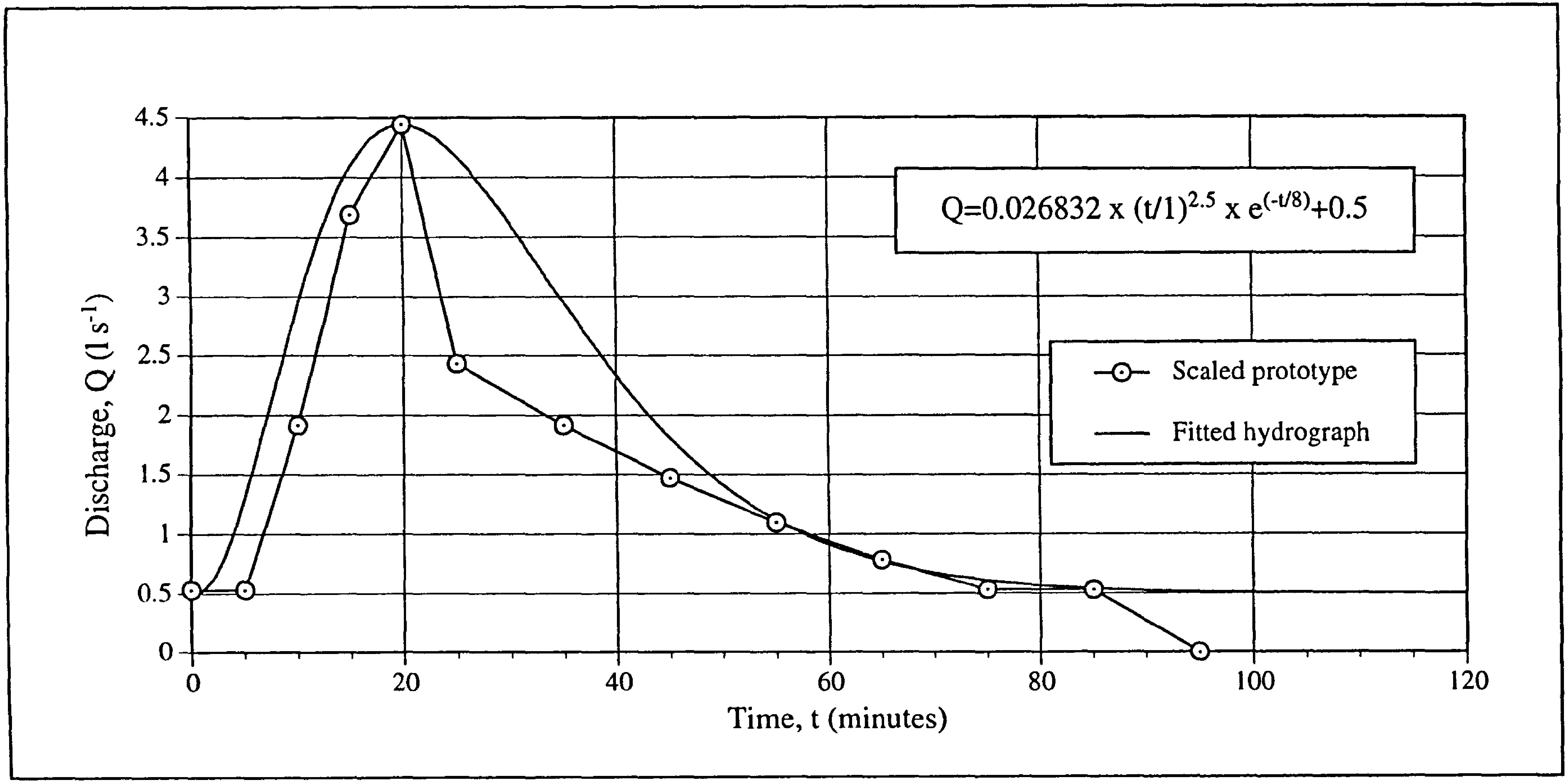

Figure 4.8. Curve fitting to a stepped hydrograph using a gamma function. The stepped hydrograph was used in the experiments of Ashworth *et al.*, (1992) and Ashworth and Best (1994) and has a similar form to the Sunwapta River, Canada and other upland braided rivers (Ashworth *et al.*, 1992). Flume runs B1 and B2 used the fitted hydrograph. The fitted hydrograph returns to a baseflow after 100 minutes and then the flow can be stopped or another hydrograph undertaken.

were calculated from the videos by measuring the travel distance between frames, of small coated paper or polystyrene floats and were converted to mean flow velocities by multiplying by 0.67.

4.5 Flume surface measurement

A point gauge fitted to the instrument bar of the bridge allows measurement of the flume surface. All point gauge measurements were taken onto a square paper base to prevent insertion into the sand bed. A survey of the stream table after run M7 allowed vertical errors to be estimated. The rails were surveyed at 0.5 m intervals downstream from 1-5 m (Note: 0 m is taken as the downstream end of the flume). For each downstream interval the instrument rail on the bridge (see Fig. 4.2) was measured at 0.6 m increments in order to estimate any bending of the bar in different locations. Distances were taken using tapes fixed to the flume wall and to the instrument rail of the bridge. All height measurements from the point gauge were then corrected for the deflection of the beam. The instrument measurement rail was found to be deflected downwards in the centre by up to 5.5 mm which is significant since total relief on a channel is rarely greater than 20 mm and frequently 10 mm or less. In addition, vertical height differences of 4.7-8.0 mm, corresponding to lateral tilts of 0.13% to 0.22%, were measured between the two bridge rails. The supporting plinths at each corner of the flume were adjusted by 6.5 mm on one side of the flume leaving a 3.3 mm height variation (0.09% lateral tilt) along the flume due to warping of both bridge supporting rails (Fig. 4.9), which is significant as run M11 had an imposed lateral tilt of only 0.21%.

After run M8 the stream table was re-surveyed and each base plate was adjusted so that the stream table base was level. The highest point on the rails was located and each stanchion was then raised to within ±0.25 mm of the same height and spot welded. The bridge measurement bar was also re-surveyed at this time and found to still have maximum deflections of 5.5 mm. All subsequent sand surface cross-sections measured with the point gauge were adjusted accordingly.

4.6 Sediment supply and measurement

Trials with a motor driven sediment feeder were unsuccessful due to the absorbtion of moisture by the silica flour which formed aggregates and clogged the feeder. For the experiments on meandering and braided patterns, sediment was therefore weighed and then continuously hand fed into the inlet channel over 10 and 5 minute intervals respectively. During the meandering experiments sediment input was adjusted if significant aggradation or degradation of the channel was taking place, in order to

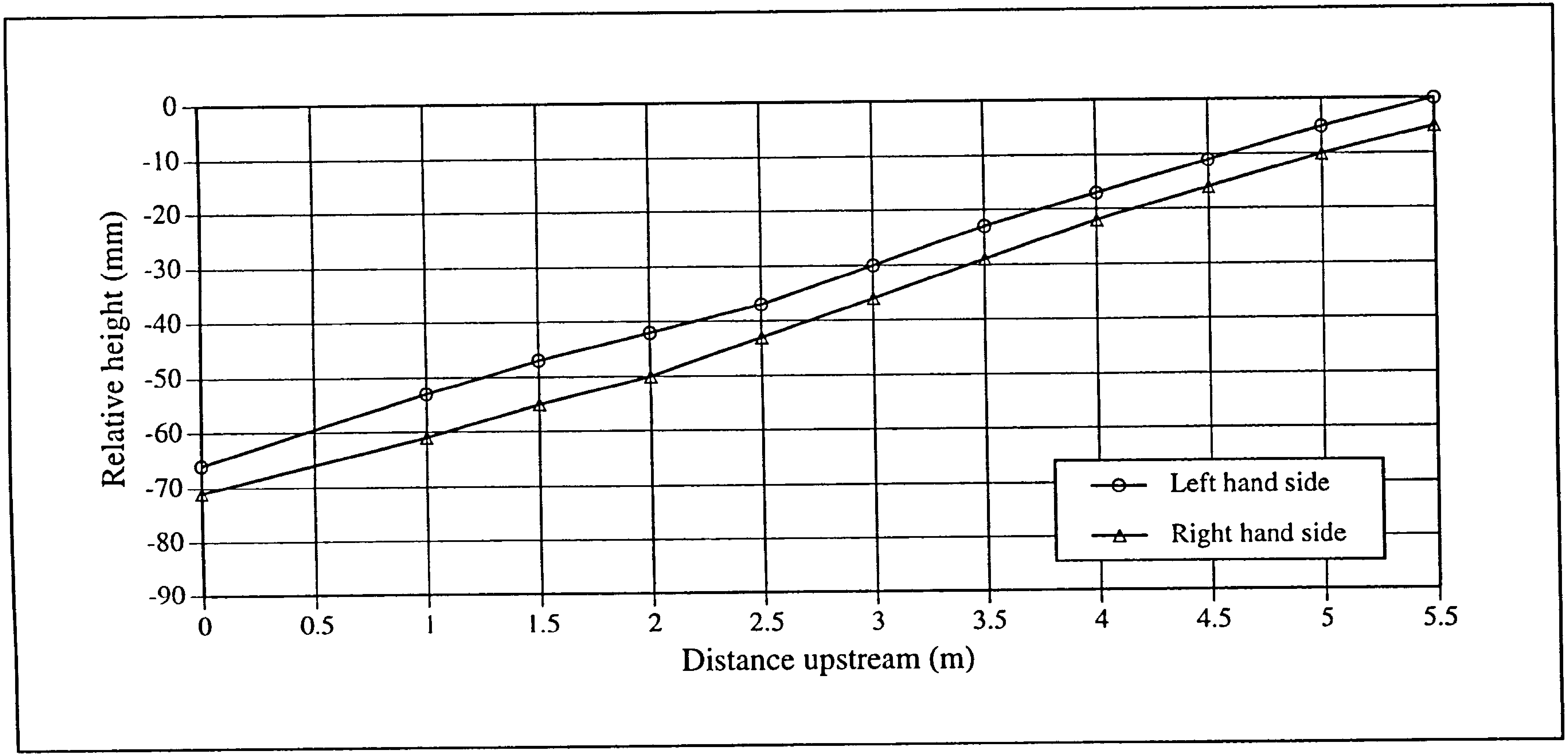

Figure 4.9. Longitudinal profiles of the bridge supporting rails, prior to run M9.

maintain a state of equilibrium. Small pins placed through the mesh at the height of the initial flow surface allowed quantitative aggradation / degradation data to be measured at the flume exit. Flow energy was dissipated as the water entered the flume from the inlet channel by small pebbles (D=10-30 mm) which avoided large-scale scouring. The level of the sand bed relative to these pebbles provided an estimate of aggradation / degradation at the upstream end of the flume. For the experiments on braided patterns, the sediment feed rate had a similar form to that estimated for the Sunwapta river, Canada and other steep coarse grained braided rivers, and is a smoothed form of the distribution used by Ashworth *et al.*, (1992) and Ashworth and Best, (1994) (Fig. 4.10). Sediment transport is initially high but declines rapidly on the falling limb of the hydrograph, simulating sediment exhaustion. During some hydrographs at the peak flow rate, small quantities of coloured sand were introduced into the sediment feed (0.1 to 0.2 kg min^{-1}), in order to act as time horizons in the preserved alluvial fill.

Local aggradation and degradation rates were measured by taking cross-sections at regular intervals using the point gauge (see Section 4.5). Stopping and restarting the runs at short intervals did not change the equilibrium of an experiment. The experiments on braided patterns also used 0.15 m long, 2 mm diameter marker pins which were graduated at 10 mm intervals and inserted into the bed sediment. Three lines of marker pins were arranged across the flume with an average spacing of 0.2 m between pins. These markers allowed some observations of local water depth and aggradation rate during an experiment and gave an indication of the spatial variation in aggradation / degradation rates. Water depths were also measured by inserting thin pieces of card into the flow and measuring the wetted distance. At several intervals during run B1 coloured sediment was sprinkled over the central portion of the flume (3 m long x 2.5 m wide) and then lightly rolled into the surface to act as a widespread time line. The coloured sediment used was epoxy-resin coated Chroma[1] sand which was pre-washed in a weak detergent solution to reduce its hydrophobic properties.

Bulk bedload sediment samples were taken at 1 hour intervals prior to run M11 and then at 0.5 hour intervals up to run B1. For the first 10 hours of run B1 while a channel pattern was forming, samples were taken at 20 minute intervals. At flow rates above 2.5 l s^{-1} the impact of the outflowing water on the collecting tray is sufficient to over-top the settling tank and consequently no bulk sediment rates were taken during the hydrographs.

---

[1] Trademark of Hepworth Minerals and Chemicals

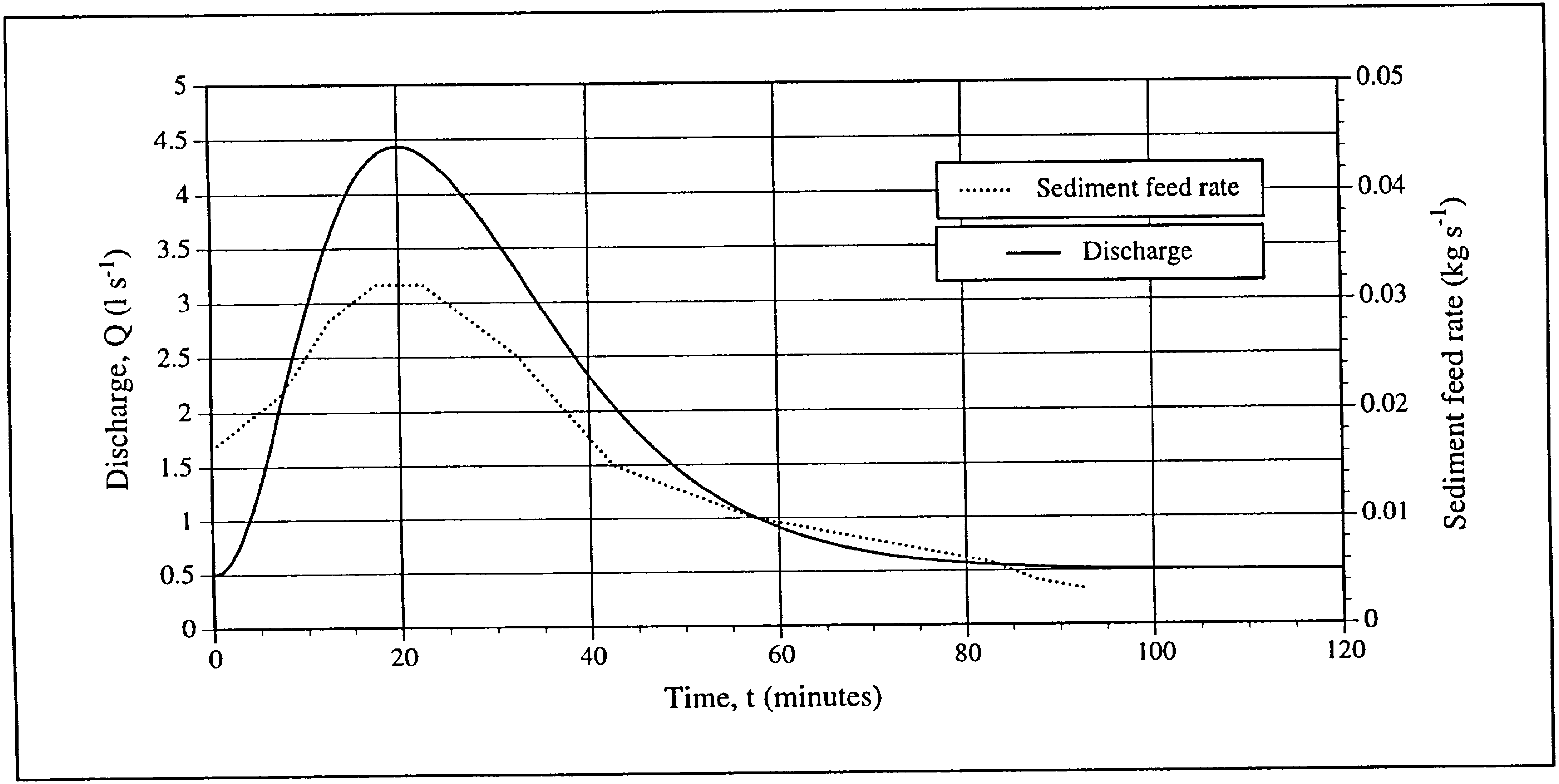

Figure 4.10. Sediment feed rate and hydrograph used in the braided modelling runs. The sediment feed rate has a similar form to that estimated for the Sunwapta river, Canada and other upland braided rivers, and is a smoothed form of the distribution used by Ashworth *et al.*, (1992) and Ashworth and Best, (1994).

4.7 Sediment characteristics

All of the experiments used a grain-size distribution based on a 1:20 scale reduction of sediment that makes up zones 2 and 3 of the Ivishak Formation, Prudhoe Bay oilfield, Alaska (Figs. 4.11 and 4.12). There were a number of advantages in choosing this distribution:

(1) experiments could be directly compared with previous work which used the same distribution (e.g., Ashworth *et al.*, 1992; Ashworth and Best, 1994)
(2) the grain-size curve has a fine grained tail which allows excellent discrimination of sedimentary niches (Ashworth and Best, 1994)
(3) the form of the grain-size curve is similar to some modern day gravel-bed braided rivers with a bimodal distribution (e.g., the Sunwapta River, Alberta - see Ashworth *et al.*, 1994, Figure 6.5, p. 125)
(4) the form of the distribution is representative of some other ancient deposits which have been attributed to a braided river origin (e.g., the Bunter Pebble Beds of central England, Steel and Thompson, 1983; Salter *et al.*, 1993), and,
(5) the use of a single grain-size with a variation in the bed (or valley) slope allows the meandering and braided patterns to be more closely compared.

Zones 2 and 3 of the Ivishak Formation (Fig. 4.12) form a significant reservoir unit of the Prudhoe Bay oilfield, Alaska, and have been interpreted as braided river deposits which coarsen upwards to the top of zone 3 (Lawton, 1985; Atkinson *et al.*, 1991; Salter *et al.*, 1993). Grain-size data were only collected for the upper 50 m of Zone 2, above the level delineated by the field wide 'hot' shale referred to as 21N, and from all 20 m of Zone 3 (see Fig. 4.12). Core photography (e.g., Fig. 4.13) of zones 2 and 3 from three wells (M7, R1 and WETW) on the western edge of the Prudhoe Bay field (Fig. 4.11) was projected onto a screen, overlain with a grid and point counted for all particles greater than 2 mm diameter (Ashworth and Best, 1992). A total of 13,030 values were measured from the three cores. Using the same slides the relative proportion of <2 mm grains was also estimated. 21 thin-sections were made from the core and point counted to evaluate the grain-size distribution of the <2 mm fraction. The maximum grain-size resolution for the thin-sections was 0.05 mm. Grain-size data for the gravel (>2 mm) and the sand (<2 mm) were grouped into half-phi classes and the percentage frequency of each class calculated. The gravel and sand groups were then multiplied by the core average frequency of occurrence (i.e., if 60:40 gravel to sand then the gravel and sand frequencies were multiplied by 0.6 and 0.4 respectively) (Ashworth and Best, 1992).

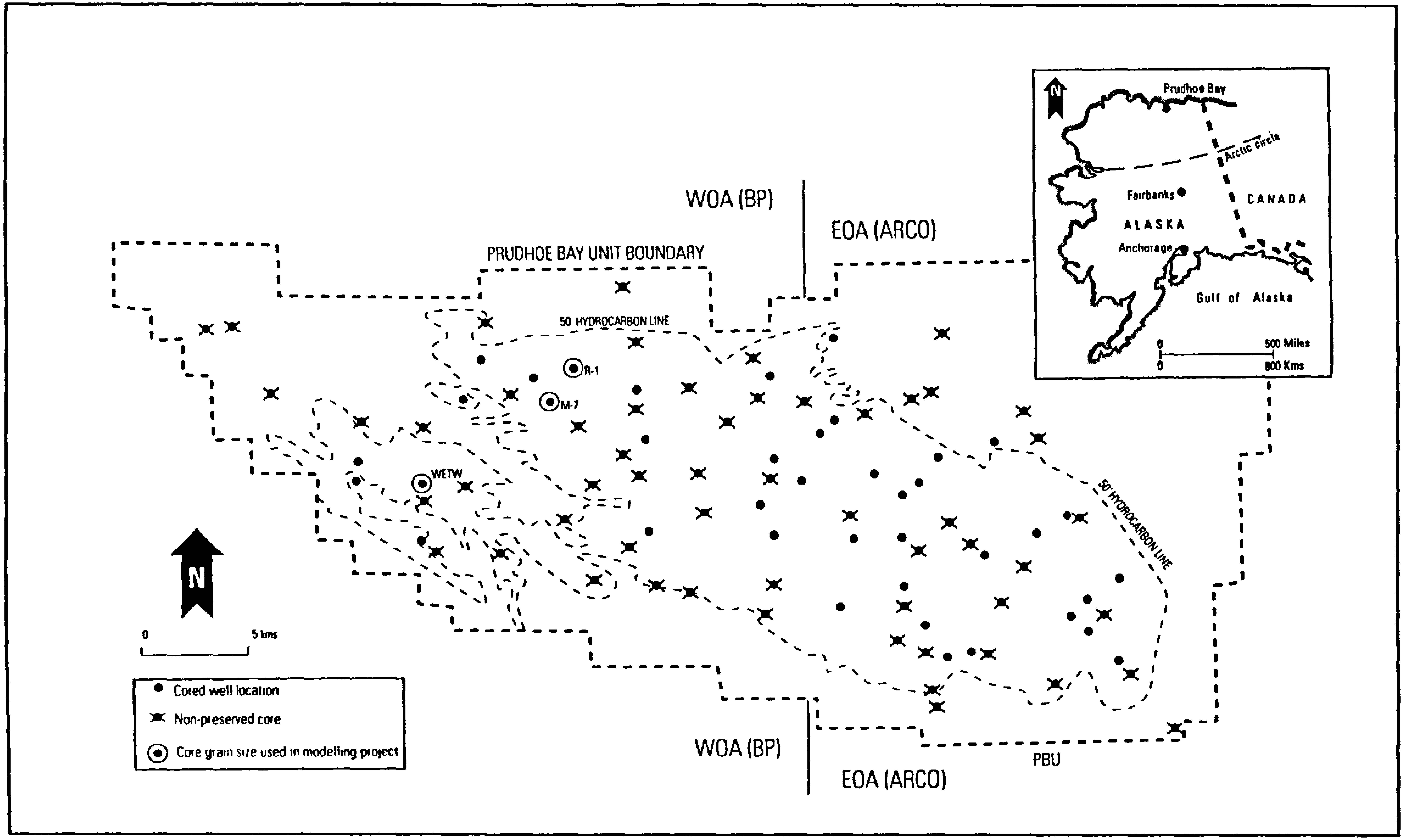

Figure 4.11. Location and areal extent of the Prudhoe Bay oilfield and position of wells used for the estimation of grain-size data. WOA and EOA represent the west operating area and east operating area respectively and PBU the Prudhoe Bay unit. Adapted from Ashworth and Best, (1992), map originally provided by BP Exploration, Alaska.

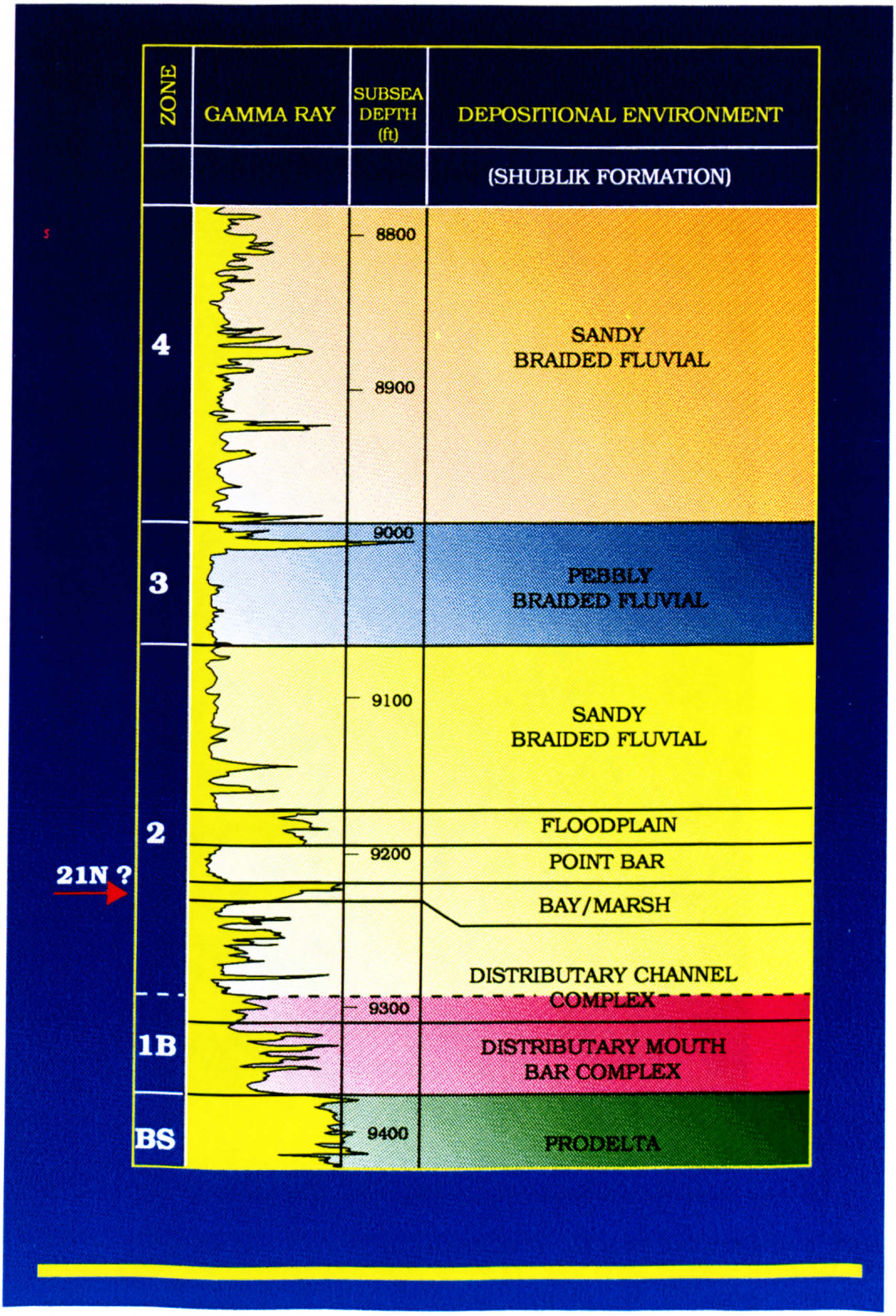

Figure 4.12. Stratigraphic section through the Ivishak Formation, Prudhoe Bay, Alaska. The lower limit of zone 2 to be analysed is marked by the the field wide 'hot' shale 21N as identified by the gamma ray peak. Adapted from Lawton, (1985).

Figure 4.13. Core sample from the Ivishak Formation. 109 point measurements of grain-size were taken on this section of core from the M7 well in the Prudhoe Bay field. The bimodal nature of the grain-size distribution can be clearly seen. Photograph courtesy of Ashworth and Best.

The average grain-size distribution of zones 2 and 3 of the Ivishak Formation had a mean of 2.7 mm and was distinctly bimodal (Fig. 4.14, Table 4.1; Ashworth and Best, 1992). To enable the flow to remain fully rough (i.e. $Re_* > 15$, see Section 3.4.3) in a 1:20 scale model the distribution was translated to a coarser mean grain-size of 7.5 mm and then divided by a factor of 20 (see Figs. 4.14 & 4.15; Ashworth *et al.*, 1992). In order to clearly discriminate fine grained deposition and preservation the fine-tail of the scaled adjusted Ivishak distribution was boosted which consequently made the distribution unimodal (Fig. 4.15). Due to the limited number of commercially available sediment types an exact match to the upper part of the 1:20 adjusted Ivishak grain-size distribution was not possible (see Fig. 4.15, Table 4.1; Ashworth *et al.*, 1992). However, given the downstream and fieldwide variations in grain-size within zones 2 and 3 of the Ivishak Formation, these grain-size changes are probably insignificant. The flume grain-size was machine mixed in two separate five tonne batches (A and B) from an amalgamation of seven individual grain-size distributions. This produced a sediment with a mean grain-size of 0.21 mm (Fig. 4.15). There appear to be small differences between sediment batch A and batch B, possibly due to variations within the commercially supplied sediment.

Sediment batch A was used for experiments M7 and M8 and sediment batch B was used for runs M9, M11, B1 and B2. The finest grained material was preferentially removed through time by erosion and settled out in the main water tank, prior to the water being recirculated. The magnitude of this preferential removal was estimated for sediment B after the completion of run M11, by comparing sieve analyses of the original and the depleted (recycled) sediment. Figure 4.16 illustrates that the sediment had become significantly depleted in the finer grades (< 0.150 mm). Whilst the main sediment mix could not be corrected for fine grained depletion and remixed between runs, the sediment fed in during a run was either fresh sediment (meandering runs) or had been corrected by the addition of fine grained sediment (braided runs; see Table 4.2).

4.8 Preparation of the stream table and sediment surface

The bed slope for an experiment was set by raising the flume with a hydraulic jack and inserting or removing small steel blocks at each corner. An approximately level surface was produced using a shovel and rake and then compacted using a large heavy duty PVC water filled roller. In order to achieve a flat sediment surface, a 3.6 m long steel beam was attached to the measuring bridge by two vertical steel girders. The bridge was then pushed successively over the surface to redistribute the sediment until the surface was level and parallel to the bridge rails. Cross-sections of the sediment surface were then taken using the point gauge and the magnitude of the lateral gradient errors

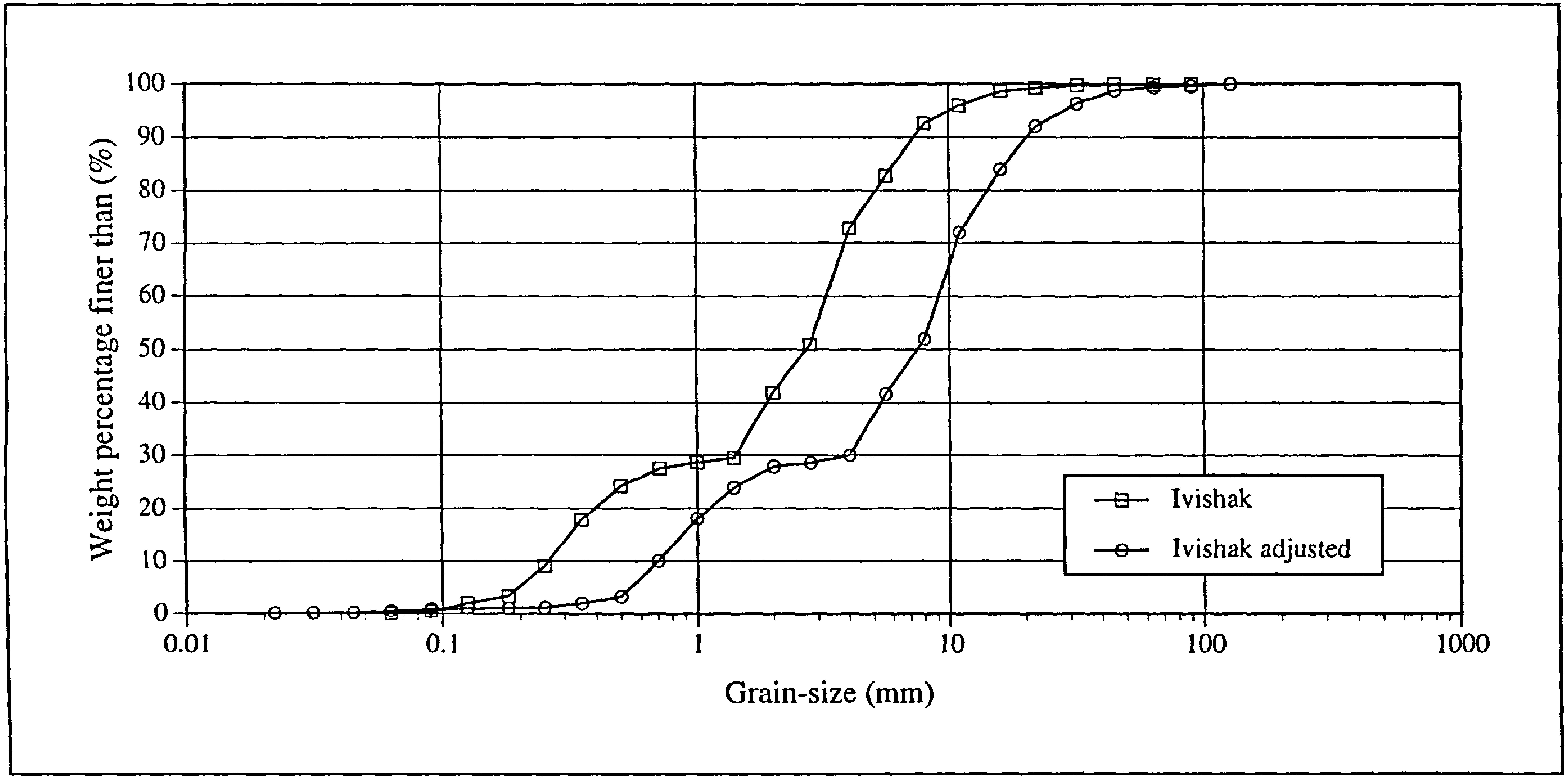

Figure 4.14. Comparison of Ivishak and translated grain-size distributions. The mean grain-size for the Ivishak Formation is 2.7 mm which is translated to 7.5 mm in order to allow later scaling from prototype to model. Data from Ashworth and Best (unpublished).

Table 4.1. Grain-size data for the flume experiments

Estimated Ivishak		Adjusted Ivishak		Adjusted Ivishak / 20		Flume	
Grain-size (mm)	Percentage Finer (%)	Grain-size (mm)	Percentage Finer (%)	Grain-size (mm)	Percentage Finer (%)	Grain-size (mm)	Percentage Finer (%)
90	100	128	100.0	6.4	100.0	7	100
64	99.91	90	99.6	4.5	99.6	5.4	99.7
45	99.88	64	99.4	3.2	99.4	4	99.5
32	99.72	45	98.8	2.2	98.8	3.2	99.4
22	99.31	32	96.3	1.6	96.3	2.2	97.6
16	98.69	22	92.1	1.1	92.1	1.6	95.7
11	95.92	16	84.0	0.8	84.0	1.1	92.4
8	92.66	11	72.0	0.56	72.0	0.8	82.3
5.6	82.69	8	52.0	0.4	52.0	0.56	72.0
4	72.77	5.6	41.6	0.28	41.6	0.4	63.3
2.8	50.99	4	30.0	0.2	30.0	0.28	55.1
2	41.91	2.8	28.6	0.14	28.6	0.2	49.0
1.4	29.43	2	27.9	0.1	27.9	0.14	44.6
1	28.67	1.4	23.9	0.07	23.9	0.1	38.9
0.71	27.52	1	18.1	0.05	18.1	0.07	34.0
0.5	24.17	0.7	10.0	0.035	10.0	0.05	28.2
0.35	17.88	0.5	3.3	0.025	3.3	0.035	21.9
0.25	9.12	0.35	2.0	0.018	2.0	0.025	17.1
0.18	3.39	0.25	1.2	0.0125	1.2	0.018	13.2
0.125	2.01	0.18	1.1	0.009	1.1	0.0125	10.0
0.09	0.44	0.125	1.0	0.0063	1.0	0.009	7.6
0.063	0.10	0.09	0.9	0.0045	0.9	0.0063	5.5
		0.063	0.6	0.0031	0.6	0.0045	2.2
		0.045	0.3	0.0022	0.3	0.0031	1.4
		0.031	0.2	0.00155	0.2	0.0022	0.5
		0.022	0.1	0.0011	0.1	0.00155	0.3
2.713	D_{50}	7.538	D_{50}	0.377	D_{50}	0.213	D_{50}
7.360	D_{90}	20.444	D_{90}	1.022	D_{90}	1.029	D_{90}

All data from Ashworth and Best (unpublished)

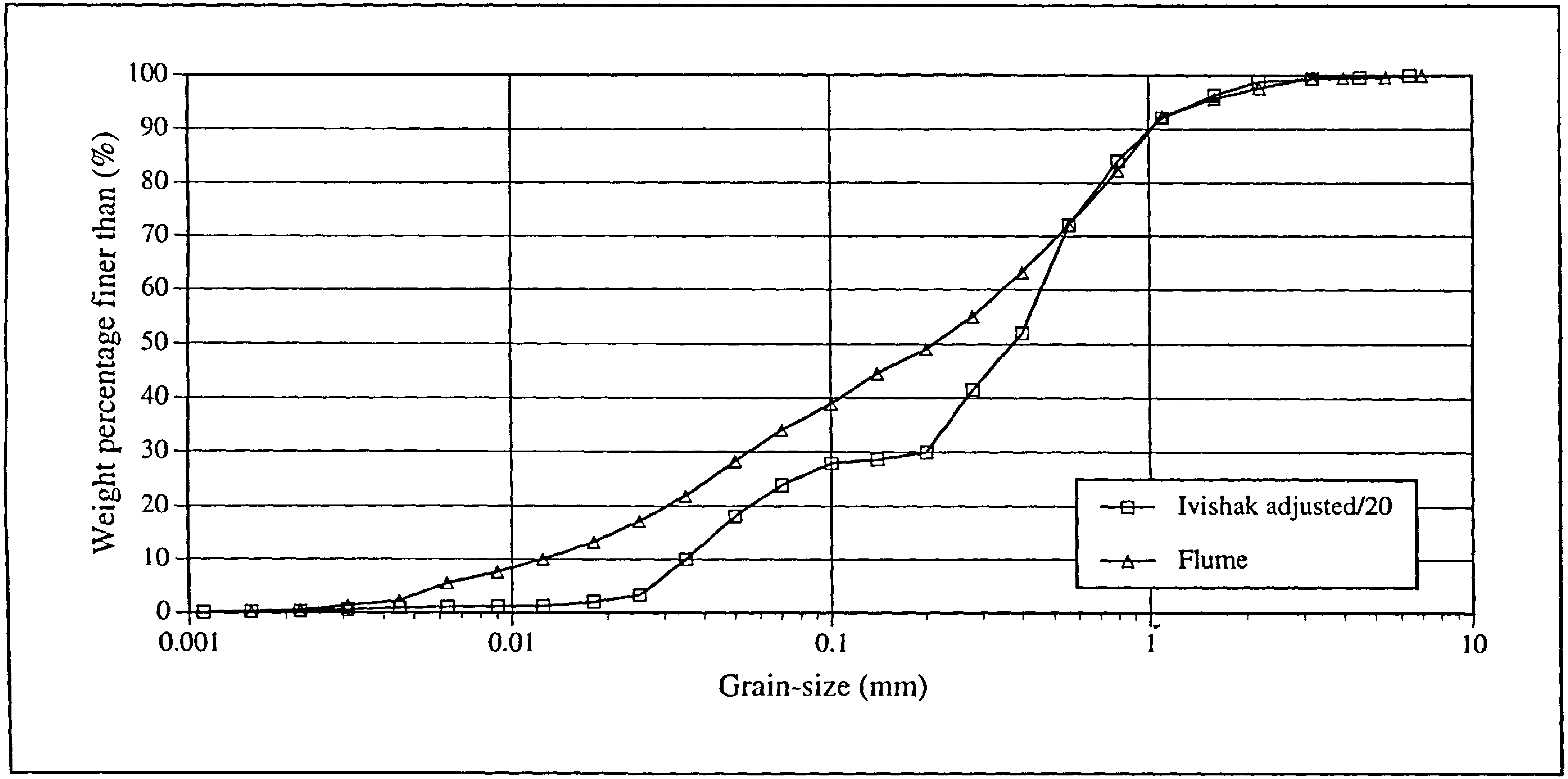

Figure 4.15. Comparison of 1:20 scaled adjusted Ivishak and flume grain-size distributions. The flume grain-size has a lower mean diameter and does not show the strong bimodality of the 1:20 adjusted Ivishak distribution.

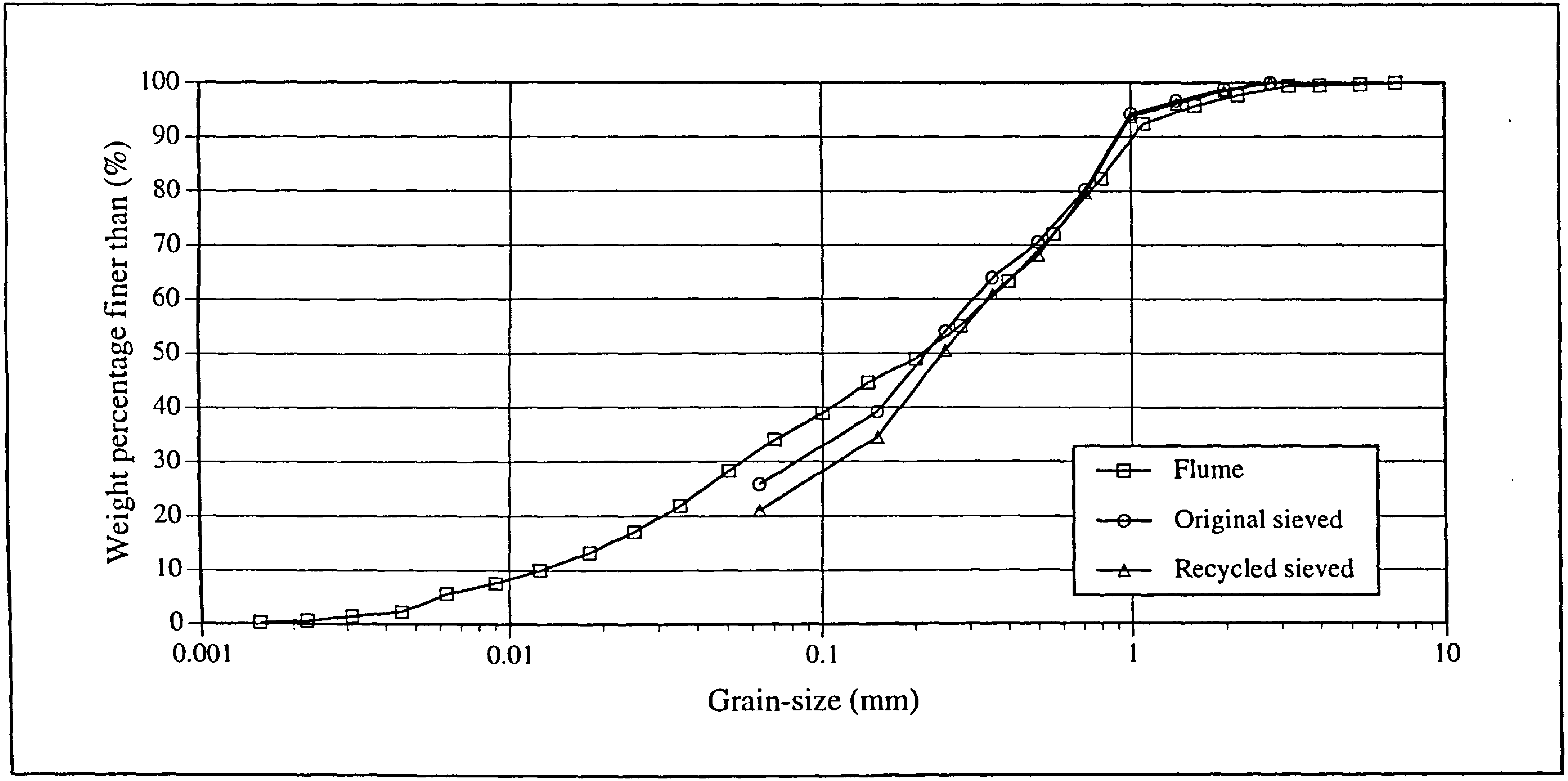

Figure 4.16. Comparison of sieved original and recycled sediment in relation to the calculated flume grain-size distribution. The recycled sieved sediment shows a lower proportion of the finer grain-sizes (<0.15 mm) relative to the original sieved material. The differences between the sieved and calculated distributions may reflect overloading of the sieves combined with variations in the commercial sediment mixes. Note: the sieved grain-size distributions are curtailed at 0.063 mm due to the limitations of sieve analysis at finer sizes.

Table 4.2. Estimation and correction of fine grained sediment depletion for experiments B1 and B2

Grain-size (mm)	Original sieved grain-size % Finer than	Recycled sieved grain-size % Finer than	Adjusted recycled grain-size % Finer Than
7.0	100	100	100
2.0	98.79	98.50	98.61
1.4	96.56	96.05	96.34
1.0	94.21	93.71	94.17
0.71	80.25	79.65	81.16
0.50	70.54	68.19	70.55
0.355	63.97	61.00	63.89
0.250	54.11	50.62	54.27
0.150	39.19	34.56	39.41
0.063	25.82	21.06	25.65
D_{50} (mm)	0.222	0.246	0.221
D_{90} (mm)	0.913	0.923	0.907

calculated. The main reason why the sediment surfaces were not absolutely level was because a spirit level was used to orientate the steel beam.

An initial straight channel was cut using a template attached to a vertical steel girder suspended from the bridge and moved over the surface as described above. Experiments M7 and M8 used a simple rectangular template 0.15 m wide and 20 mm deep. Runs M9-11 used a trapezoidal section 0.15 m wide at the top with 45° edges and a maximum depth of 25 mm which had a similar cross-sectional area to previous runs. For the braided model runs, a rectangular 0.40 m wide, 20 mm deep template was used. In all cases the inlet channel was adjusted vertically to be parallel to the base of the dredged channel. For the meandering planform experiments the inlet channel was narrowed to a width of 0.15 m and set at an angle of 30° to the longitudinal downstream axis of the flume, by the addition of two pieces of flexible sheet plastic fixed with silicone sealant (see Fig. 4.17). Use of an angled inlet channel accelerates meander development and has been widely used in previous studies (e.g., Schumm and Khan, 1972 (40°); Zimpfer, 1975 (40°) and Jin and Schumm, 1987 (30°)). At the start of each experiment, and after each break in an experiment, the flow rate was very gradually increased over a period of five minutes, in order to avoid widespread erosion. As sediment saturation increases the capillary forces begin to mimic cohesion (see Section 3.8.1) and consequently the sediment becomes more resistant to erosion. A slow rise in the discharge rate also allows air to be expelled slowly as the sediment becomes saturated.

4.9 Bed sectioning for quantifying alluvial architecture

After the completion of an experimental run, the flume sediment was left to dry for two to three weeks. A rough sediment face was excavated and then smoothed using a 0.7 m long by 0.2 m wide strip of aluminium, pushed into the sediment. The face was cleaned up by lightly pushing a small scraper along the face, parallel to the sedimentary layering. Faces were cut back successively at intervals between 25 mm and 250 mm and in both cross-stream and downstream orientations. Two spotlights spaced 2 m apart and 1 m from the sediment face were used for illumination and photographs taken using a camera with a 28 mm wide angle lens and 80 mm film (Fig. 4.18). Several frames were required for each face and then assembled into a montage.

4.10 Summary

The stream table has a number of unique features which allow simulation of alluvial sedimentation under equilibrium conditions or during basin-wide aggradation. Additionally, precise discharge control enables the modelling of flood hydrographs and

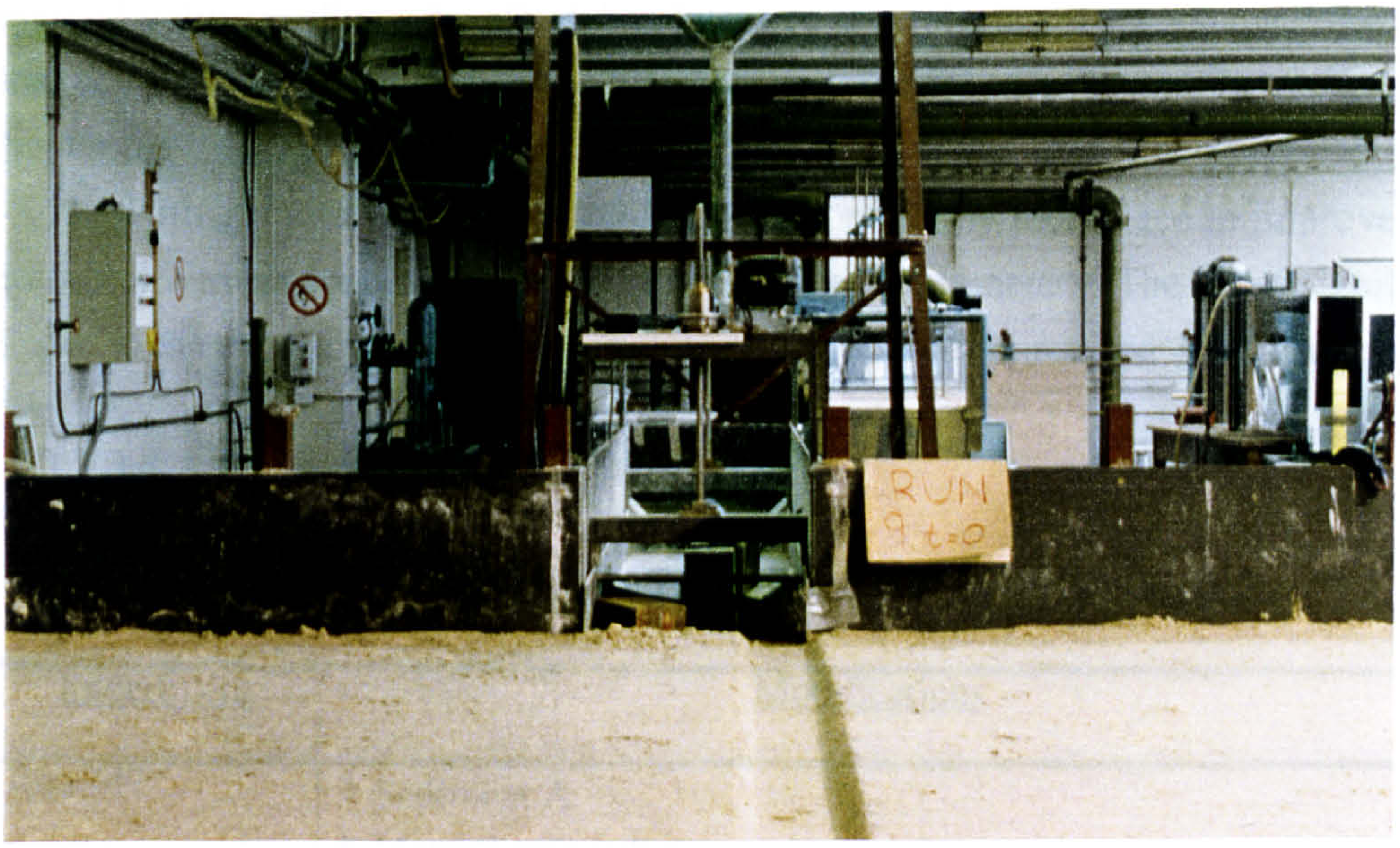

Figure 4.17. View of inlet channel with entrance bend at 30° angle. Two pieces of flexible plastic attached to wooden templates and sealed with silicone sealant form the entrance bend. The initial channel is 0.15 m wide.

Figure 4.18. Sectioning of the sediment in the stream table. The cut face shown is almost 2 m long and is in a downstream orientation (each white rule is 1 m long). Pieces of yellow and pink card are shown on top of the face where they are recorded by time-lapse video. Graduated marker pins are placed vertically in front of these cards and are recorded when the sections are photographed. The cards and the pins allows the video images and the flume cross-sections to be compared.

their impact on sedimentary preservation and the channel planform. Sectioning of the preserved sediment allows the alluvial architecture to be characterised and quantified. The flume can tilt in any direction and is therefore suitable for experiments on lateral tilting (Chapter 5).

During the experiments, modifications continually took place to improve both the control and measurement of flow and sediment parameters. The most significant changes to the experimental apparatus and procedure are summarised chronologically in Table 4.3.

Table 4.3. Evolutionary framework of experiments

Experiment	Modifications
Run M7	• Sediment A • Manual gate valve • No survey of flume
	• Initial flume survey • Electro-pneumatic valve installed with a variable resistance manual control
Run M8	
	• Flume re-surveyed and bridge rails adjusted • Electro-pneumatic valve removed due to abrasion • Manual gate valve used as replacement • Arc lights repositioned
Run M9	• Sediment B • New trapezoidal channel template
	• New pump installed • Tapered flange placed immediately before valve to reduce instantaneous pressure drops • Hardened valve stem and seat fitted to electric-pneumatic valve • Electro-pneumatic valve re-installed • Computer control of valve introduced • Calibration of computer controlled valve
Run M11	
	• Computer program for running hydrographs installed
Runs B1-2	• Marker pins for aggradation measurement • Layers of coloured sand used as time horizons • Exhausted fresh sediment • Recycled old sediment and adjusted grain-size to allow for depletion of finer grades

The experiments on both meandering and braided channel patterns use a grain-size distribution based on a scaled version of zones 2 and 3 of the Ivishak Formation, from the Prudhoe Bay oilfield. For the braided patterns, discharge and sediment feed rates for hydrographs are based on modern coarse grained upland braided rivers. Together, these parameters form the initial prototype for the models. Flow measurements from the experiments are compared with modern meandering and braided coarse grained rivers in Chapter 5.

Chapter 5. Experimental Study on the Effects of Lateral Tilting on Meandering and Braided Rivers

5.1 Synopsis

Two sets of physical scale modelling experiments were undertaken in order to test criteria for the recognition of lateral ground-tilting as previously identified in Leeder and Alexander (1987). This chapter documents a number of advances in the modelling of coarse grained meandering rivers and examines the impact of the imposition of a basin-wide lateral tilt on channel planform evolution. Additional flume experiments using braided rivers and the simulation of floodplain aggradation allow the preserved alluvial architecture to be analysed and quantified. A suite of key sedimentary niches in the braided river alluvium may be identified. Variations in the size, frequency of occurrence and spatial distribution of each niche class are examined and the influence of lateral tilting considered in terms of the timing, magnitude and incidence of tilt events.

5.2 Background to meandering river experiments

A series of meandering river experiments were undertaken to investigate the response of the channel planform to the effects of lateral ground-tilting. Three experiments, M8, M9 and M11 were run with imposed tilts of 0.43, 0.30 and 0.21% respectively with a single non-tilted experiment (M7) used as a control. All four experiments had an axial gradient of 1.0% and a constant discharge of approximately 0.5 l s^{-1} (see Table 5.1). The initial floodplain surfaces were not absolutely flat despite strenuous efforts. However, initial lateral surface gradients for most experiments were less than 0.1%, although parts of run M9 had lateral slopes up to 0.37% (Table 5.2). Flow was introduced at an angle of 30° to the axial direction in order to increase the rate of initial meander development (see Section 4.8).

5.3 Flow characteristics of the meandering river experiments

Mean values of the Froude and flow Reynolds numbers indicate that the average flow is fully rough, turbulent and subcritical (Table 5.3). The presence of trains of standing waves demonstrate that flow periodically crosses into the supercritical regime as

Table 5.1. Experimental conditions for the meandering river runs

Run	Downstream bed slope (%)	Discharge $(l\ s^{-1})$	Total run time (hr)	Imposed lateral tilt (%)	Timing of tilting (hrs after start)
M7	1.0	0.47	33.8	None	NA
M8	1.0	0.47	22	0.43	6
M9	1.0	0.47	15	0.30	6
M11	1.0	0.54	30	0.21	9

NA = Not applicable

Table 5.2. Initial lateral floodplain gradients for the meandering river experiments

Run	Downstream Location of Cross-Sections†					
	L.H.S (d/s) Lateral Slope (%)$^{\alpha}$			R.H.S (d/s) Lateral Slope (%)$^{\alpha}$		
	3.5 m	2.5 m	1.5 m	3.5 m	2.5 m	1.5 m
M8	+0.28	-0.05	-0.19	-0.03	+0.09	+0.03
M9	+0.36	+0.37	+0.32	-0.03	-0.02	-0.08
M11	+0.09	-0.02	+0.09	-0.06	-0.34	-0.09

† Note: Downstream exit of flume = 0 m and upstream end of flume = 5.5 m. $^{\alpha}$ L.H.S. and R.H.S = left hand side and right hand side of flume centreline, looking downstream (d/s). The applied lateral tilts were all towards the right hand side of the flume. Positive gradients are in the opposite and negative gradients are in the same direction to the imposed lateral tilt. All gradients calculated from ordinary least squares regression lines. No initial gradients were taken for run M7.

Table 5.3. Flow characteristics for the meandering channels

Parameter	Runs M7-M9				Run M11			
	Mean	Min	Max	N°	Mean	Min	Max	N°
Water temperature, T, (°C)	21.1	18.2	23.4	203	21.1	18.2	23.4	203
Dynamic viscosity, μ, $(\mu kg\ m^{-1}s^{-1})$	976	924	1048	203	976	924	1048	203
Mean flow velocity, V, $(m\ s^{-1})$ $^{\alpha}$	0.25	0.06	0.39	86	0.26	0.13	0.36	73
Channel bed slope, S_b, $^{\beta}$	0.008	0.006	0.010	50	0.008	0.005	0.010	11
Channel depth, d, (mm) $^{\gamma}$	14.8	4	28	14	14.4	5	22	18
Flow Reynolds N°, Re, $^{\delta}$	3725	216	11698	-	3906	641	8637	-
Grain Reynolds N°, Re*, $^{\delta\ \varepsilon}$	36.5	12.3	58.4	-	36.2	16.0	51.8	-
Froude number, Fr, $^{\delta}$	0.65	0.11	1.95	-	0.70	0.29	1.64	-
Weber number, We, $^{\delta}$	12.3	0.18	57.7	-	13.9	1.24	40.0	-

α calculated from surface velocities multiplied by 0.67. β Based on floodplain slopes / channel sinuosity. γ All values represent maximum channel depths. Depths for M11 represent the vertical difference between the top of the point-bar and the base of the channel, as measured from cross-sections. δ Minimum and maximum values are calculated from the corresponding minimum and maximum input parameters. ε Re* is calculated using the initial model bulk D_{90}.

is often the case in gravel-bedded meandering rivers (Lewin, 1976; Gustavson, 1978; Fig. 5.1). Additionally, mean Weber and grain Reynolds numbers fall within the range of critical values estimated in the literature (see Section 5.9 for further discussion). Limited flow data and grain-size distributions are available from field studies for detailed comparison with these experiments but the model flow conditions are in broad agreement with previously published data (Lewin, 1976; Gustavson, 1978; Carson, 1984, 1986), and consistent with the earlier arguments on scaling, the modelling runs are termed Froude scale models (FSM) (see Sections 3.2, 3.10).

5.4 Meander planform and depositional characteristics

The initial straight channel formed a series of alternate bars below the water surface which developed into point-bars by aggradation at the bar head and addition of successive lateral accretion increments (Fig. 5.2). In all cases a slough formed between the point-bar and the inner bank. Due to the limited length of the flume (5.5 m) meander wavelength and amplitude increased until a single bend occupied the entire length of the flume. However, since the channel outlet was unconstrained the sequence of bend development could be observed.

Four phases of meander development were identified from the untilted experiments (Figs. 5.3 and 5.4). Initially, the channel underwent rapid extension with increasing amplitude and sinuosity (Fig. 5.3a). Point-bar development was by accretion of migrating linguoid bars with the higher parts of the linguoid bars forming prominent scroll-bars and associated ridge and swale topography on the upper platform (Fig. 5.5). The fine grained silica flour, which simulates silt sized material, settled out on the bar platform and along the inner slough, gradually bringing the uppermost part of the point-bar up to the water-surface. As the amplitude and radius of curvature of the bend increased through time, linguoid bars began to stall at the apex of the bend with a corresponding shoaling of the thalweg upstream of the apex (Fig. 5.3b). With time a lobe formed a prominent constriction at the apex and accelerated erosion of the outer bank, leading to the formation of a secondary notch in the channel bank (Fig. 5.3c). This highly localised increase in bend curvature led to an upstream movement of the downstream limb, here referred to as channel roll-back. The increasing sinuosity and shoaling of the upstream meander limb eventually led to chute cutoff which could occur at any point across the point-bar, although the topographic low of the inner slough was a frequent location for avulsion (Figs. 5.3d, 5.4 and 5.6). The sudden increase in wavelength and corresponding decrease in sinuosity after chute cutoff led to a rapid extension of the bend and repetition of the bend development sequence.

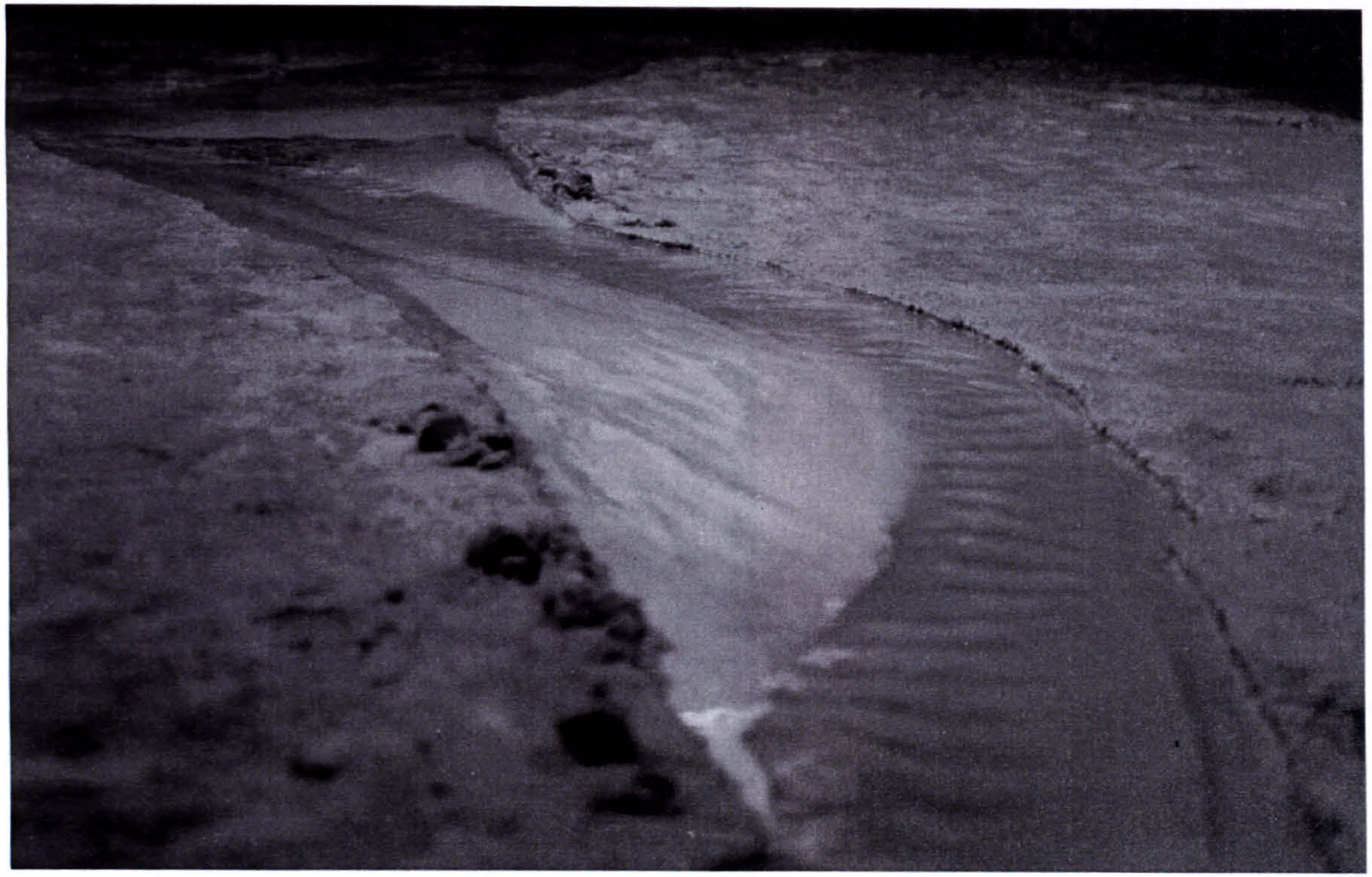

Figure 5.1. Photograph of a train of standing waves along the thalweg of a meander bend. Flow is away from the viewer. Channel width at upstream end is approximately 0.25 m.

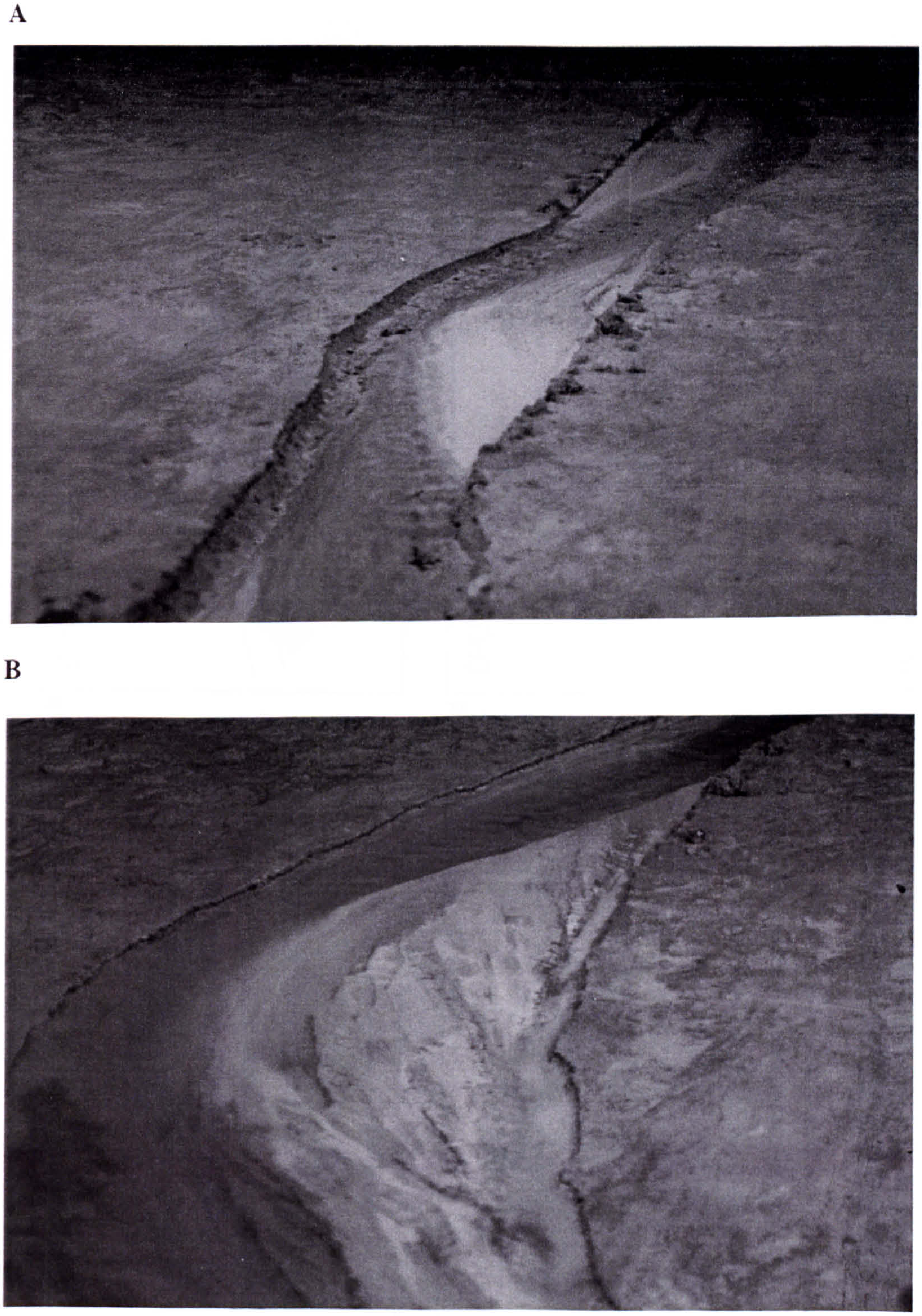

Figure 5.2. Photographs indicating the morphological contrast between alternate bars and point-bars. a) dry meandering channel showing alternate bars. These bars have very little surface expression and form below the water surface. Flow direction is away from the viewer. The initial channel, represented by the straight channel bank segments, is 0.15 m wide, and b) fully developed point-bar showing a number of scroll bars indicative of lateral accretion. The higher parts of the bar are up to or above the level of the local water surface. A small chute channel is present on the inner point-bar adjacent to the channel bank. Flow is towards the viewer. The channel width at the top of the photo is approximately 0.15 m.

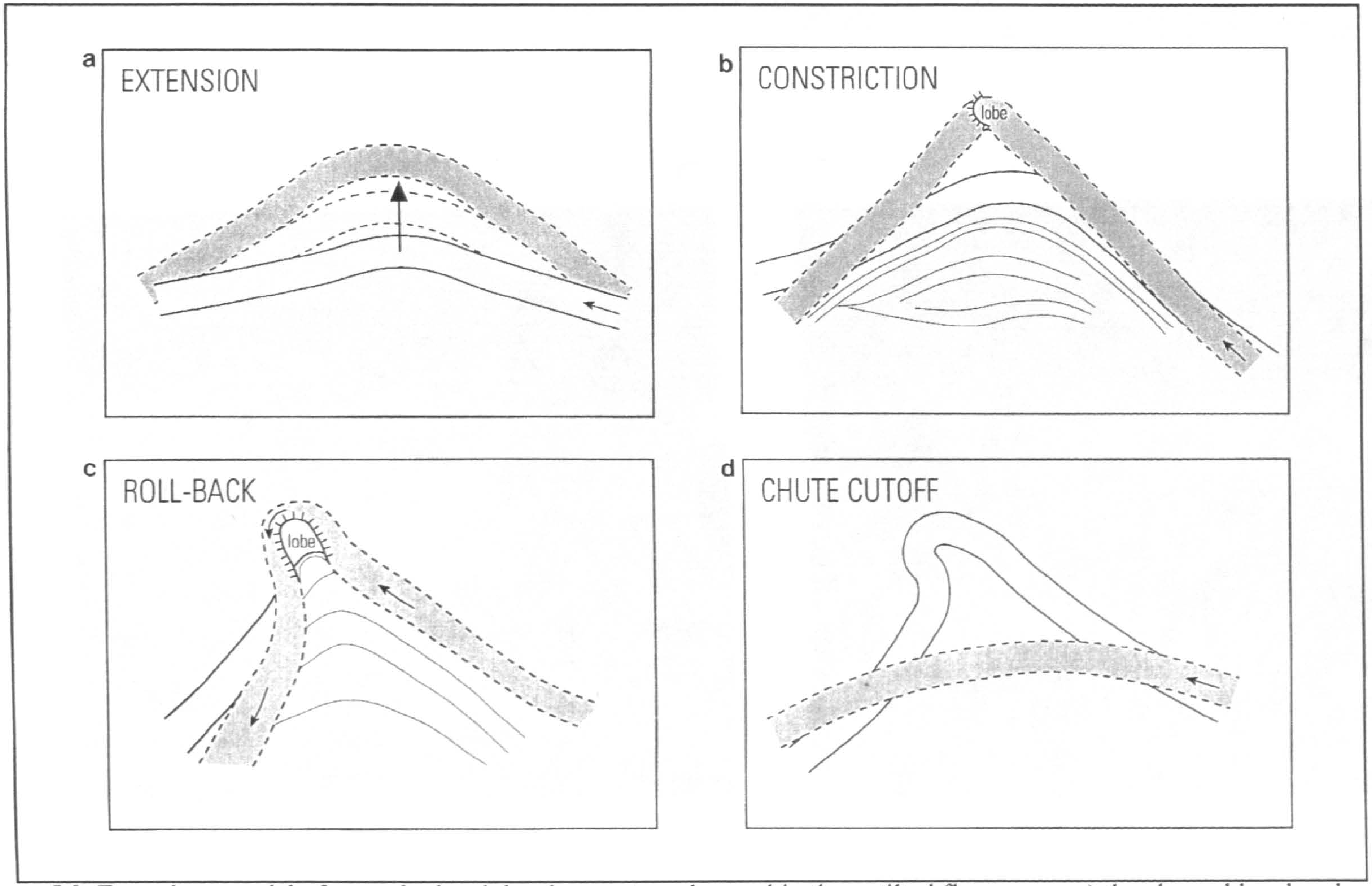

Figure 5.3. Four phase model of meander bend development as observed in the untilted flume runs. a) the channel bend undergoes rapid extension. b) stalling of a linguoid lobe produces constriction at the bend apex. c) Scour around the stalled lobe promotes localised outer bank erosion, bend asymmetry and roll-back of the downstream meander limb. d) Progressive shoaling of the bend entrance zone leads to chute cutoff across the point-bar and the channel returns to stage (a).

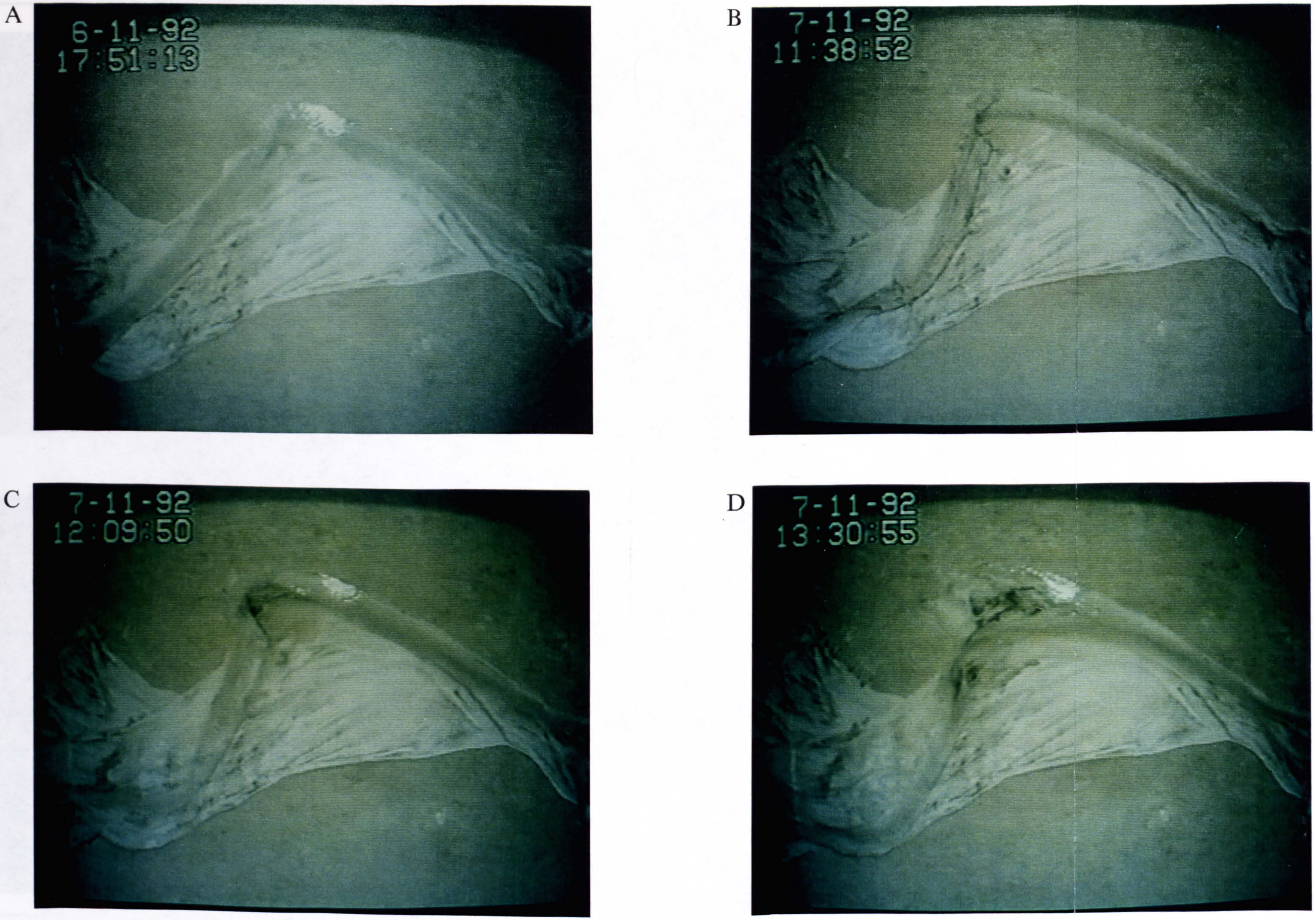

Figure 5.4. Video images of meander bend development in run M7. A) The initial stages of lobe formation at the bend apex, due to stalling of a linguoid bar. B) Dry channel illustrating the growth of the apex lobe and the abrupt avalanche face of the lobe. The bend entry zone has begun to shallow. C) Localised outer bank erosion and decreased radius of curvature around the stalled lobe. The downstream meander limb has just started to roll-back. D) Chute cutoff across the point bar. The field of view for each image is approximately 3.8 m by 2.5 m. Flow is from right to left.

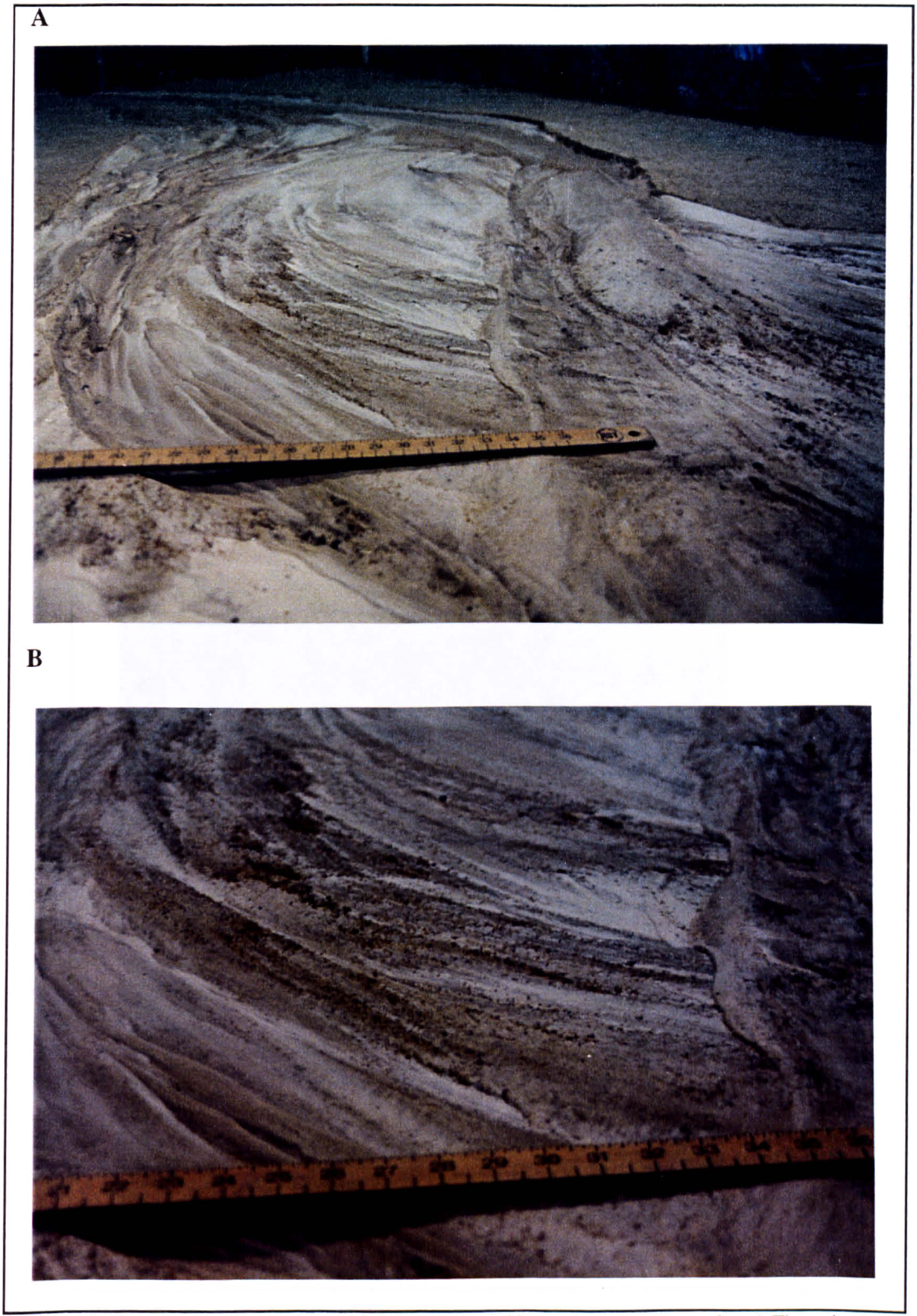

Figure 5.5. Photographs of scroll-bars and the associated ridge and swale topography. a) The point-bar in the centre of the photo is undergoing chute cutoff on the right hand side of the photo. Scroll bars are indicated by the curvilinear ridges. Note how the older scroll bars have a slightly reduced topography due to infilling of the swales by fine grained sediment (white silica flour). b) Enlargement of 'a' illustrating the alternation between coarse grained ridges and fine grained swales. Both views looking upstream. Measuring rule is in inches.

Figure 5.6. Photograph of chute cutoff and abandoned meander loop. Flow is towards the viewer. A large coarse grained sheet (X) has been pushed across the point-bar immediately prior to bend cutoff. These gravel sheets or lobes frequently form the upper layers of abandoned point-bars. The active channel in the centre of the photo is approximately 0.15 m across.

In cross-section the channels produce prominent lateral accretion surfaces with the steepest slopes at the bend apex and decreasing gradients towards the bend entrance and exit (see Fig. 5.7) as predicted by both field and theoretical studies (e.g. Willis, 1989, 1993). Scour surfaces infilled by successive layers of fine and coarse deposits are also prominent (Fig. 5.7).

Each of the four experiments showed a different rate of channel development (see Fig. 5.8) attributable to six factors:

1) The use of freshly mixed dry sediment in run M7 in contrast to the other experiments which re-used sediment from previous runs. The re-used sediment retained thin water films between the finest grains, thereby simulating cohesion,

2) The degree of initial sediment water retention (thin water films) in experiments M8, M9 and M11,

3) A gradual diminution of fine grained sediment through a run. The depletion of the fine grained tail of the grain-size distribution is most pronounced in the last experiment to use each sediment batch (M8, M11; see Section 4.7),

4) The possibility of slight differences between sediment batch A (M7, M8) and sediment batch B (M9, M11),

5) A slightly higher discharge in run M11 (0.54 to 0.47 l s^{-1}), and,

6) Intrinsic variability.

The key factor appears to be the degree of initial water saturation / retention. Sediment takes a long time to dry due to the capillary forces produced by the fine silica flour and therefore the second experiment with each sediment batch (M8, M11) had greater initial cohesion and lower bank erosion rates (see Fig. 5.8). However, these variations only affected the rate and not the mode of development.

5.5 Comparison of meander experiments with previous field and flume studies

There have been a large number of meandering experiments since the first study of water movement around a bend (Thomson, 1879). However, Schumm and Khan (1972) suggested that previous experimental work had only produced meandering thalwegs and noted that early workers such as Friedkin (1945) had lowered the discharge prior to photographing the runs, thereby exposing previously submerged bars. Schumm and Khan (1972) claimed to have produced true meanders for the first time, although these only developed in response to a decrease in the sand supply and the addition of a 3% concentration of kaolinite, mimicking the changes in sediment supply of many rivers during the Quaternary (e.g., the Murrumbidgee River, Australia; Schumm, 1968). The clay was initially deposited on the banks of the model channel leading to thalweg

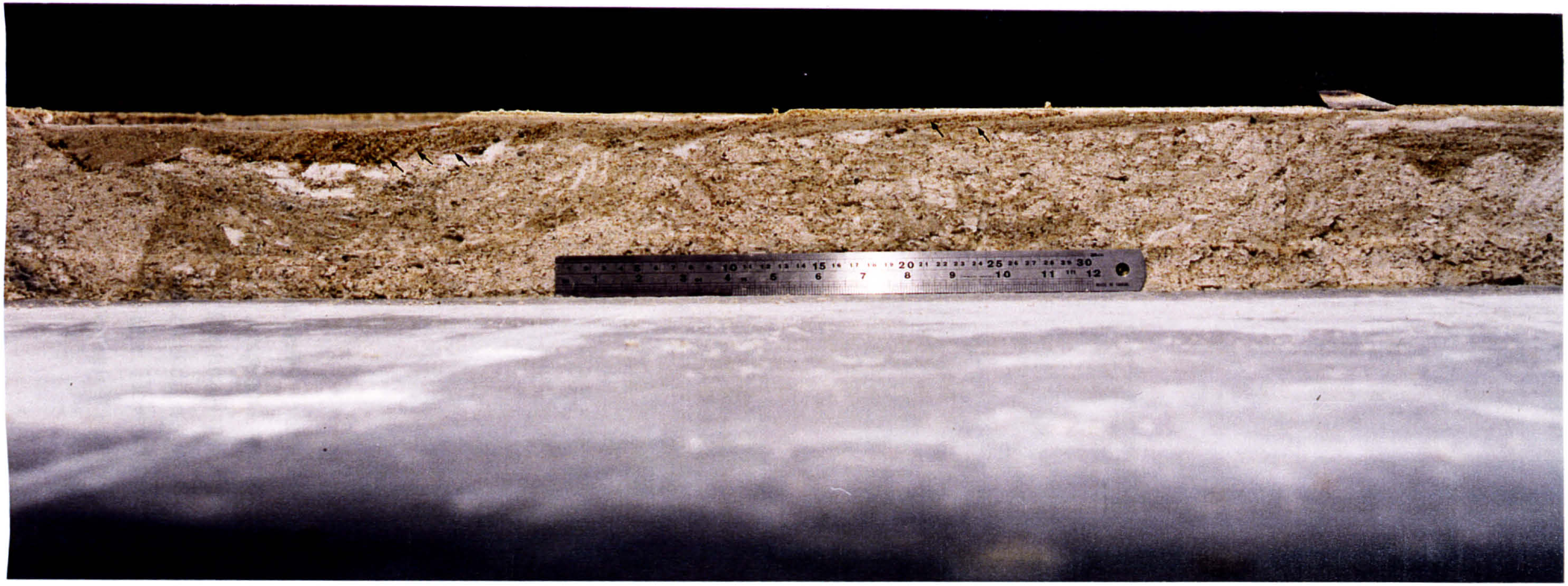

Figure 5.7. Cross-section of sedimentary fill, following migration of a meander bend. The meandering river deposits have a sharp erosive base which contrasts with the lighter coloured original sediment beneath. A prominent channel infill is present on the left hand side of the figure, with steeply dipping foresets suggesting that this was close to the bend apex. Low angle lateral accretion surfaces are also present to the right of the photo and indicate a shallower channel and deposition at the bend entrance or exit. Two prominent scours are present at the far right, infilled by alternate layers of coarse and fine grained sediment. The section is perpendicular to the main flow direction which was away from the viewer.

Figure 5.8 (overleaf). Video snapshots illustrating variations in the rate of channel development between experiments. All four snapshots were taken after 6 hours of run time and before lateral tilting was imposed. The time-lapse mode is indicated on two of the video images by the heading '48H' which indicates that 48 hours of time-lapsed images could be recorded onto a 3 hour video tape. Flow is from right to left in all images and the field of view for each image is approximately 3.8 m by 2.5 m.

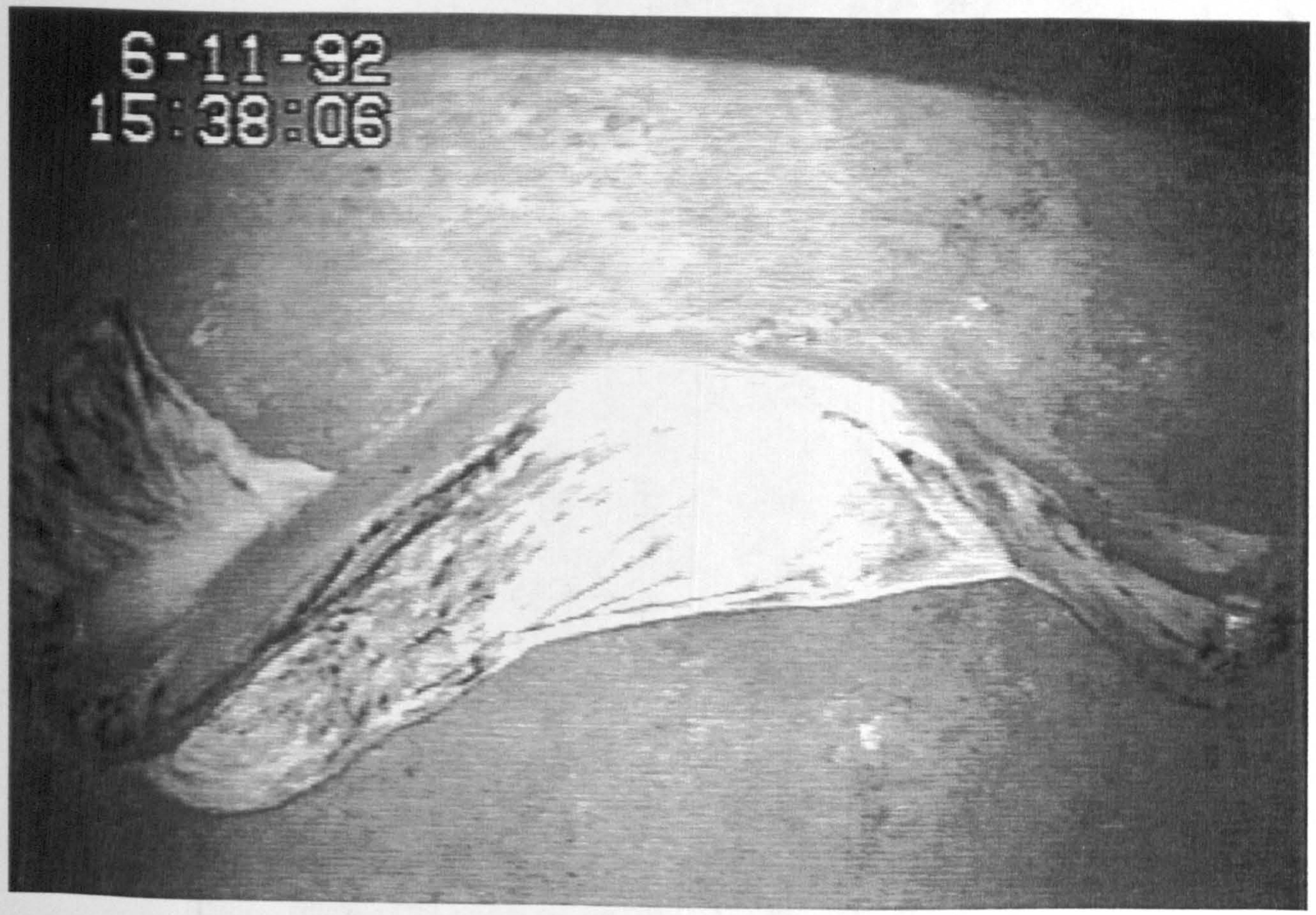

M7 t=6

M9 t=6

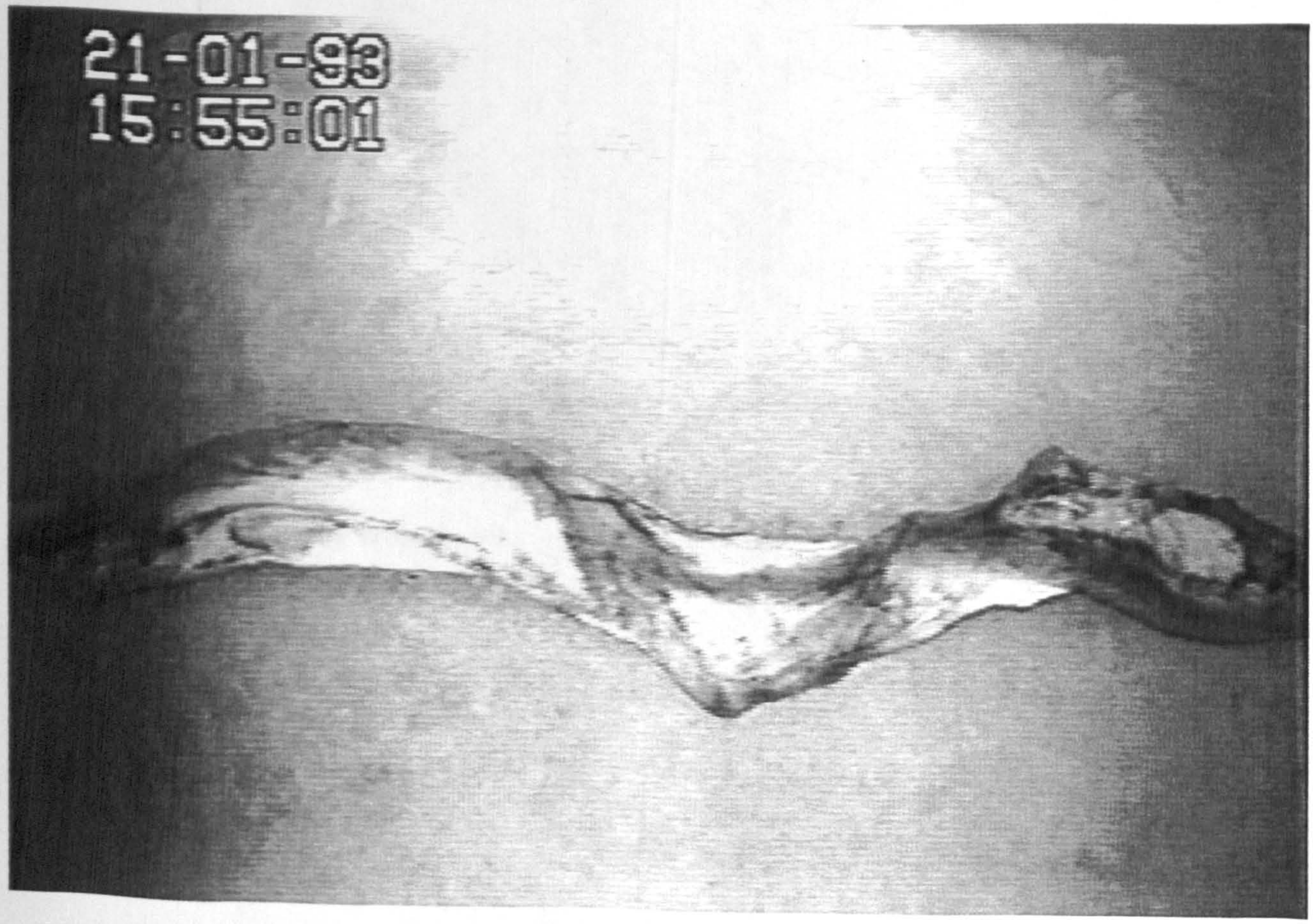

M8 t=6

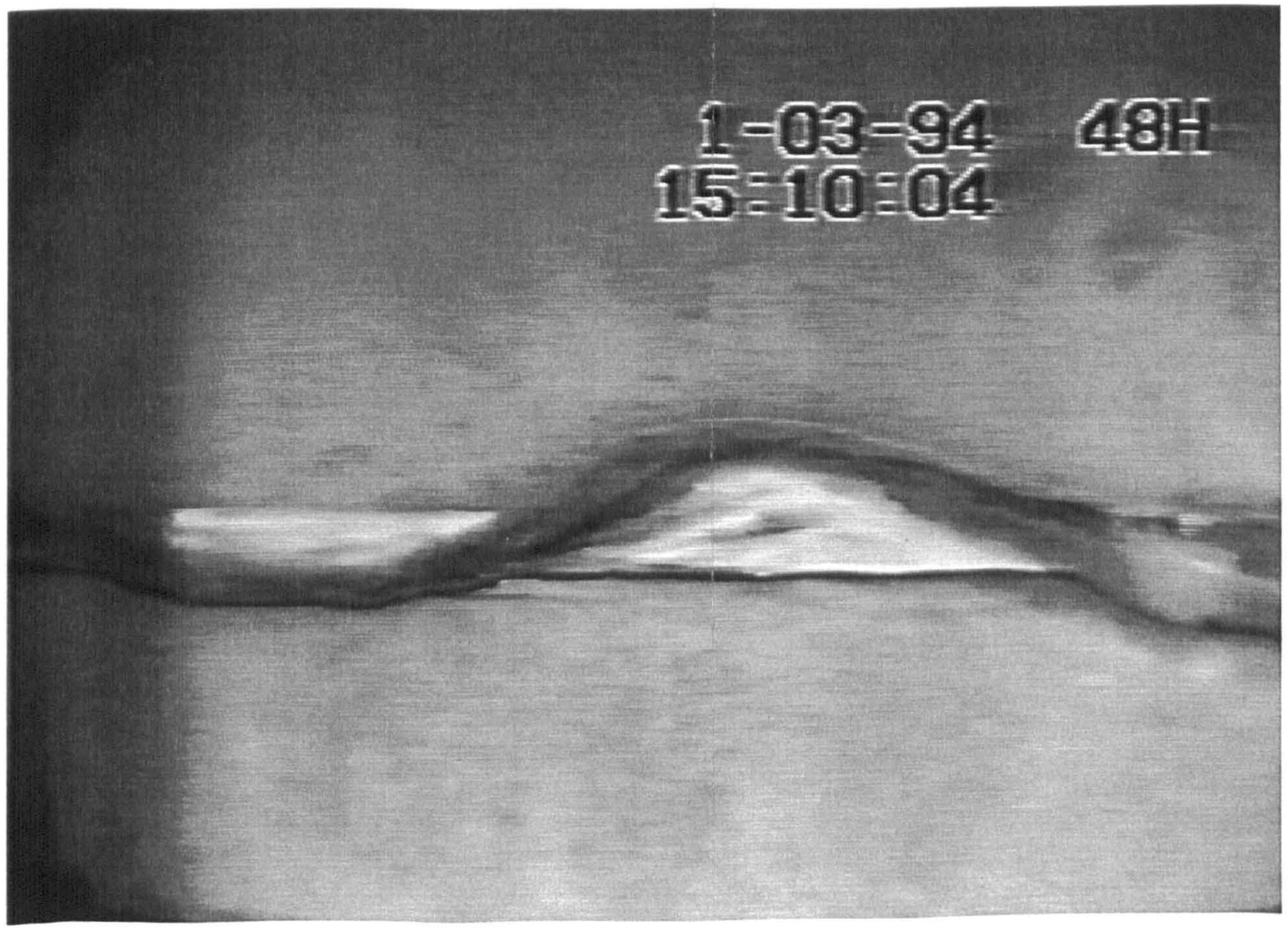

M11 t=6

scouring, channel deepening and the emergence of alternate bars to form point-bars. A mixed grain-size distribution consisting of an approximate 1:9 ratio of sand and kaolinite, in conjunction with suspended clay concentrations of 0.05-0.3%, enabled Ouchi (1983, 1985) to produce a meandering channel with recognisable point-bars without a change in sediment supply. Jin and Schumm (1987) took this approach a stage further by using a two-layer floodplain consisting of a lower non-cohesive sand layer overlain by an upper cohesive silt-clay layer (Fig. 5.9) and succeeded in producing constructional point bars with sigmoidal internal stratification. However, neither the studies of Ouchi (1983, 1985) or Jin and Schumm (1987) document point-bar characteristics in detail or display documentary evidence of lateral accretion surfaces and therefore these studies cannot be directly compared with the set of experiments described here. The present study builds on previous work by describing scroll-bar and ridge and swale development for the first time. Additionally, the use of a broad grain-size distribution produces fine sedimentary detail on the lateral accretion surfaces, which may not have been present in the study of Jin and Schumm (1987).

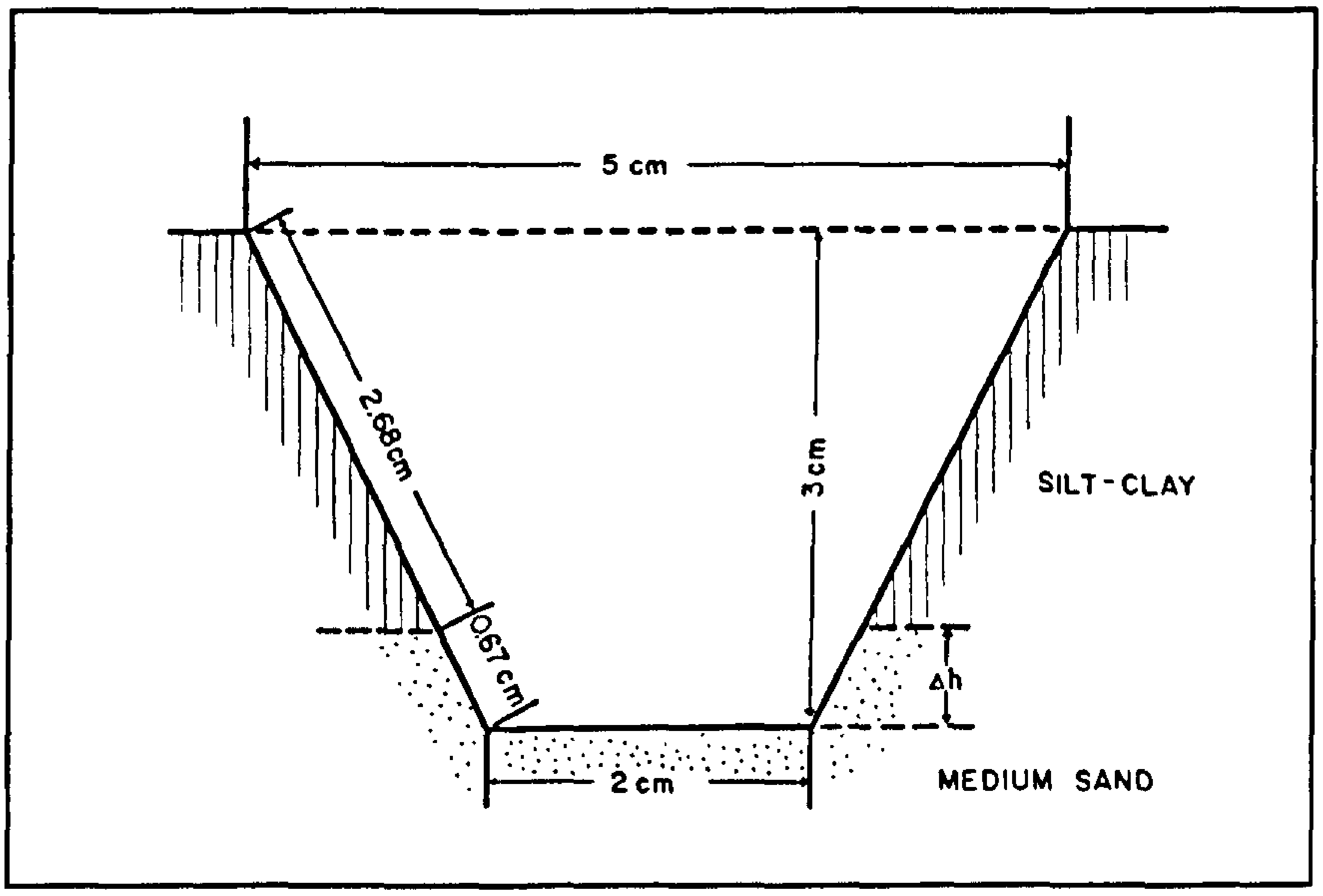

Figure 5.9. Cross-section of the two layer floodplain of Jin and Schumm (1987). From Schumm *et al.*, (1987).

Early work by Wolman and Brush (1961) described meandering in noncohesive sand channels at supercritical flow conditions, which they termed 'pseudomeanders'. These pseudomeanders evolve by the growth of point dunes which have a similar gross morphology to point-bars but are formed by transport across the stoss side of the dune and avalanching on the lee-side, producing low-angle accretion surfaces dipping upstream (Hickin, 1969, figure 2). Experiments with subcritical flows on pre-formed bends also produce point dune sedimentation and notches in the outer channel bank (Hickin, 1972).

Pseudomeanders are not thought to form in natural meandering rivers, although point-dunes at subcritical flows have been recognised in the underfit Hawkesbury River, Australia, which does not meander but is forced to change direction by relict meander loops (Hickin, 1969). A five-stage model of pseudomeandering development (Fig. 5.10) was proposed by Hickin (1969): 1) the development of surface undulations in a straight channel, 2) formation of regularly spaced mobile dunes, 3) growth of dunes and erosion between dune and banks, forming an inner slough and an outer channel, 4) a gradual increase in bend amplitude, and, 5) the formation of small channels on the point dune surface leading to braiding.

Field studies have compared gravel-bedded meandering rivers with flume studies of pseudomeandering (Lewin, 1976; Carson, 1986; Carson and Griffiths, 1987). However, this analogy is based on form rather than process and therefore appears to be of limited use. Similar patterns corresponding to stages 2, 3 and 4 of the developmental model of Hickin (1969) have been formed in non-cohesive sands at subcritical flows, although the shoals are less elongate than their supercritical counterparts (Ackers and Charlton, 1970). Unfortunately, there are no channel patterns comparable to stages 2 and 3 for previously documented mixed grain-size 'true' meander experiments or for this study, since flow was always introduced at an angle, leading to a gradual propagation of meander forms downstream.

New Zealand rivers on the Canterbury Plains have been compared with stages 4 and 5 of the pseudomeandering model (Carson, 1986; Carson and Griffiths, 1987). Points of similarity include over-widened point bars, premature bend deflection, chute cutoffs across the point-bar and notches in the outer channel bank. However, there are a number of points where the New Zealand rivers and the pseudomeandering model are dissimilar. At bankfull stage the flow is not competent to move sediment across the bar platform and therefore the bar must grow by lateral accretion. Secondly, there is not a tendency in these rivers for the channel to begin to braid after successive chute cutoffs across the point-bar as is the case in the pseudomeandering model. The bend development model outlined in this study (Fig. 5.3) also displays outer bank notches, chute cutoffs, overwidened bends and premature bend deflection. In addition, successive chute cutoffs can occur without a braided pattern forming. The mechanism controlling chute cutoffs also appears to be the same, since shoaling of the bend entry zone occurs in both the field and flume. Finally, Carson (1986) noted a tendency for upvalley channel migration. While this is a reach scale effect, evidence for upvalley migration has been noted in this study on the downstream meander limb and termed roll-back. A comparison of change in the Waireka (Fig. 5.11) with change in this flume study (Fig. 5.4) reveals a number of similarities, most notably for bend 4 of the Waireka which undergoes both roll-back and chute cutoff. The Waireka River can move fine grained gravel onto the point-bar platform

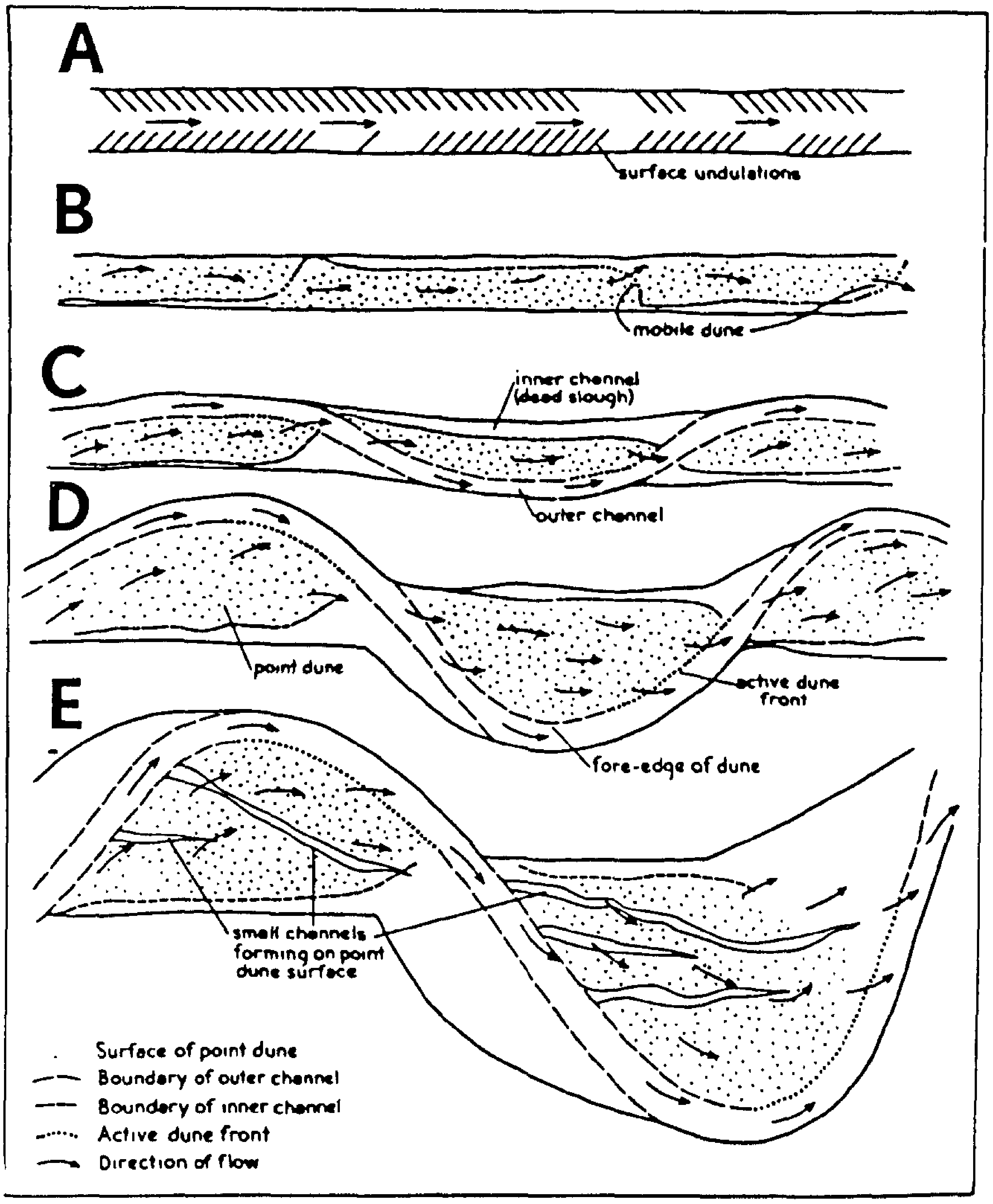

Figure 5.10. The five stage pseuodomeandering development model of Hickin (1969).

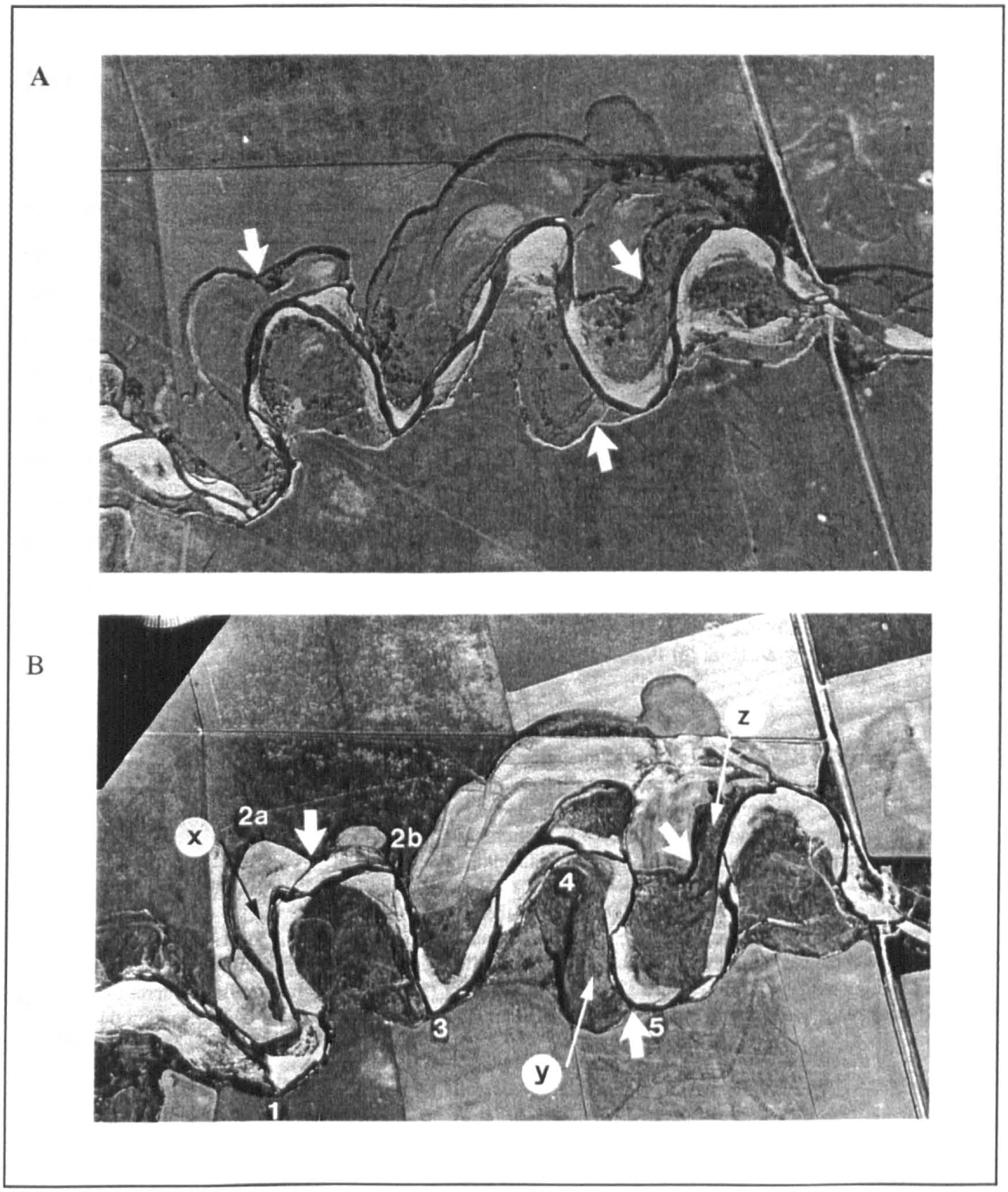

Figure 5.11. Temporal changes in a reach of the Waireka River, New Zealand. a) September 1940, and, b) October 1961. Flow is from left to right. Bold arrows are reference points. Letters refer to areas of significant upvalley migration, while numbers refer to individual bends. From Carson (1986).

at high flows allowing the surface to build up close to the bankfull level (Carson, 1986). However, there are a number of gravel bedded meandering rivers which have surficial coverings of silty sand or sand which build up to bankfull and provide the closest analogy to this flume study (e.g., Blacknell, 1982; Lewin, 1983b).

5.6 Planform response to imposed lateral tilting

Experiments M8, M9 and M11 were instantaneously tilted by 0.43, 0.30 and 0.21% respectively during the early part of each run (after 6-9 hours). Channel sinuosity, wavelength and the apex position of the first downstream bend were measured from video images at 1.5 hour intervals for each experiment. The temporal change in sinuosity for all four experiments is plotted in Figure 5.12 and reveals a gradual broad increase in sinuosity for each of the tilted runs. In contrast, run M7 has an undulating pattern of sinuosity change, reflecting periodic chute cut-offs which led to rapid reductions in sinuosity. With the exception of one anomaly, sinuosity reaches a maximum value of approximately 1.6. Meander wavelength values show a similar pattern to sinuosity with broad gradual increases for the tilted runs (Fig. 5.13). Run M7 shows a much higher degree of variability with gradual decreases reflecting roll-back or upstream movement of the downstream meander limb and the large drop reflecting a chute cutoff which temporarily increased the number of bends. Maximum wavelengths plateau at a length of 5 m which compares with a total flume length of 5.5 m. However, it is difficult to link changes in wavelength or sinuosity directly with tilting, as the rate of change is strongly dependent on the bend morphology and radius of curvature at any point in time (Hickin and Nanson, 1975; Hooke, 1987). In addition, due to differing initial rates of channel development (Section 5.4), bends were at markedly different stages of development prior to tilting, and may have continued to develop at different rates in the absence of imposed lateral tilting.

Since rates of change of morphometric variables are difficult to correlate with tilting, the position of the first bend apex was plotted in order to investigate the spatial response to imposed lateral tilting (Fig. 5.14). In all cases an increase in the negative gradient of the plotted line would reflect a channel that was adjusting to the resultant maximum gradient from the combination of cross-stream and downstream tilting. A number of trends can be identified from the plots of bend apex movement through time: i) an increase in the rate of channel movement towards the fault after tilting, ii) a short lag-time between tilting and increased rates of movement towards the fault (less than 3 hrs), and, iii) a possible relationship between tilt magnitude and the rate of increase in downdip movement (see Fig. 5.14). However, none of these relationships between tilting and bend migration are unambiguous, due to the complexity caused by bend development interacting with the impact of lateral tilting. For example, run M11 shows an increase in

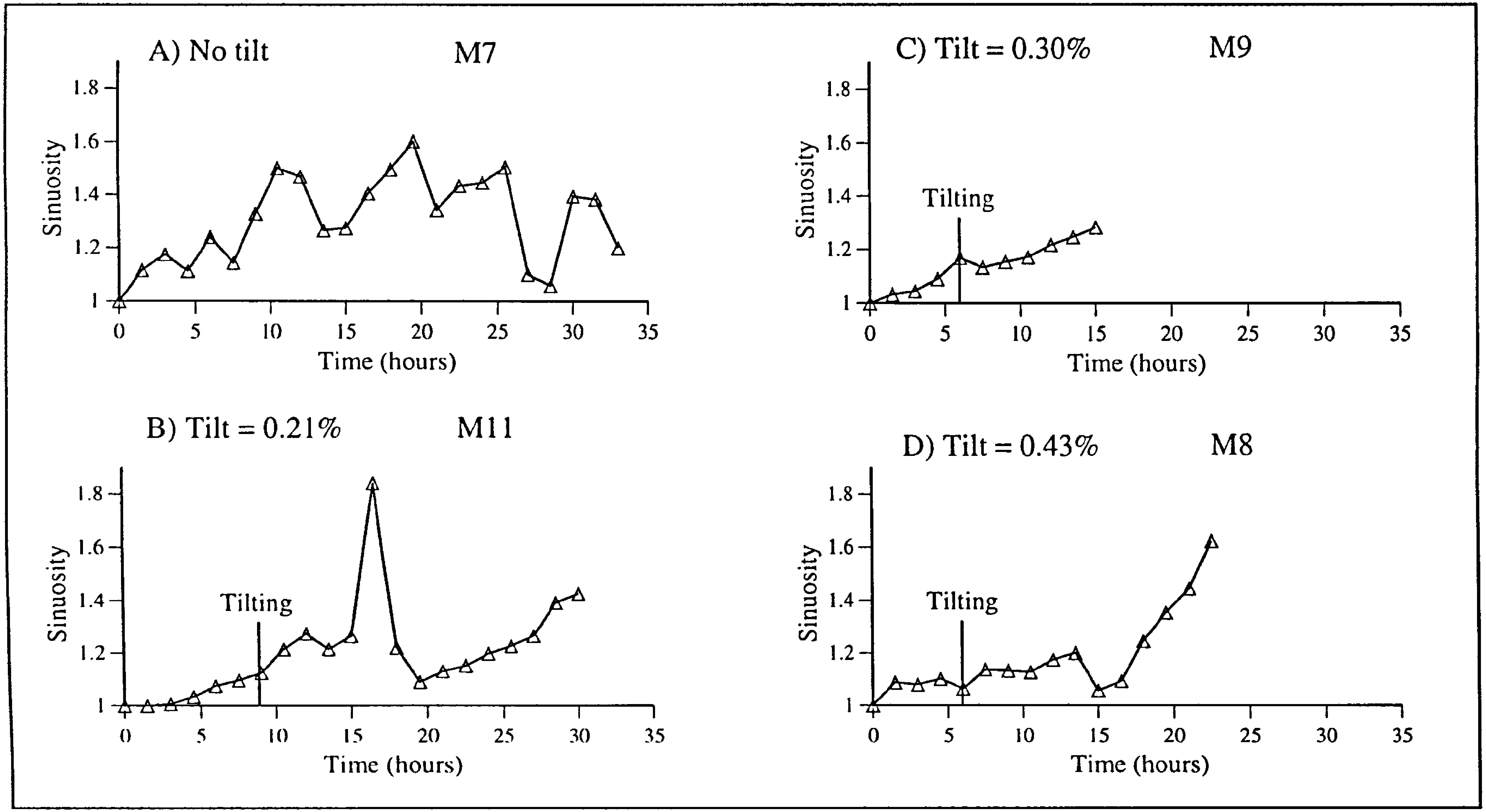

Figure 5.12. Temporal variation of sinuosity for each meandering experiment. The timing and magnitude of imposed lateral tilting is marked for each experiment. a) M7, b) M11, c) M9, d) M8.

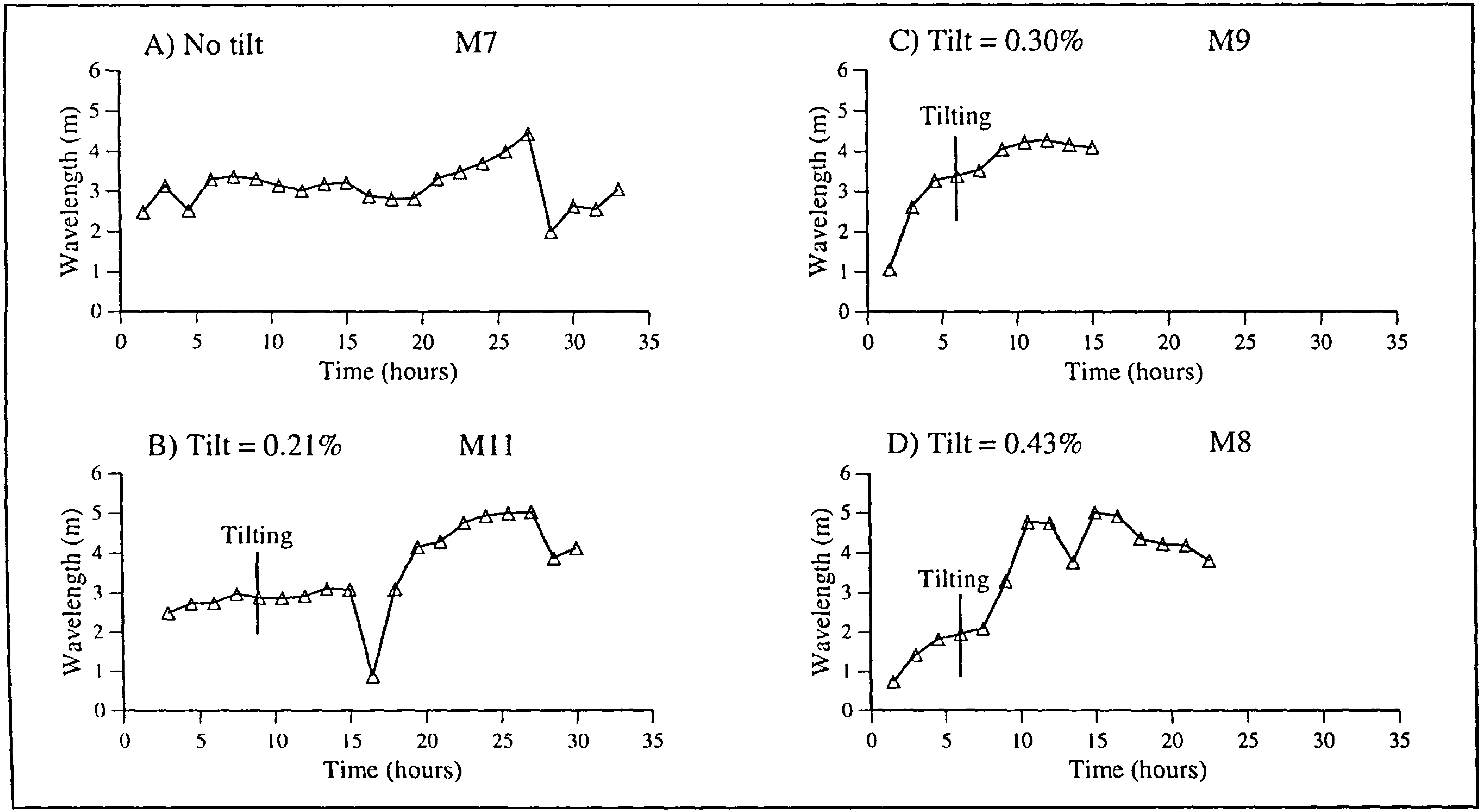

Figure 5.13. Temporal variation of wavelength for each meandering experiment. The timing and magnitude of imposed lateral tilting is marked for each experiment. a) M7, b) M11, c) M9, d) M8.

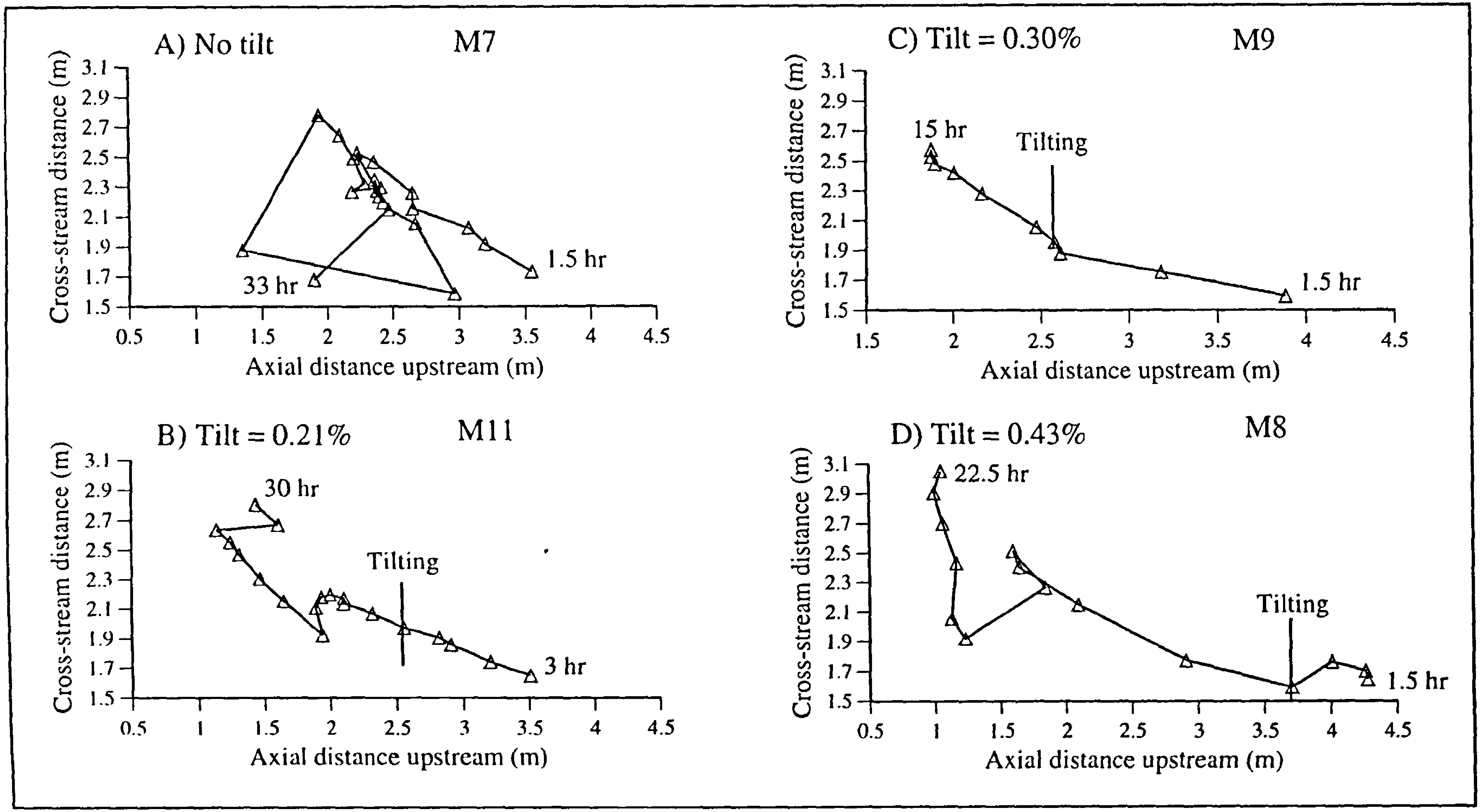

Figure 5.14. Temporal variation in the apex position of the first downstream bend. Measurements are at 1.5 hour intervals. The timing and magnitude of imposed lateral tilting is marked for each experiment. a) M7, b) M11, c) M9, d) M8.

the gradient which is less than that of the new resultant gradient, while M9 shows a much greater increase. In addition, the highest initial negative gradient is for the untilted run M7. While the nature and magnitude of the channel response to tilting may be difficult to quantify, there is a marked effect on channel dynamics since chute cutoff across the point-bar becomes rare after tilting.

The imposed tilts did restrict chute cutoff across the point-bar and therefore increased the mean sinuosity for these experiments. This reduction in bend cutoff appears to have important implications for the model of Leeder and Alexander (1987) which envisaged progressive abandonment of meander loops on the uptilt side of the river. However, these experiments were run at constant within bank discharge and the majority of permanent bend cutoffs probably occur during overbank floods. The apex of the main meander loop was always located on the downtilt side of the channel belt in these experiments, so the decrease in opportunity for cutoff is consistent with the Leeder and Alexander (1987) model.

5.7 Summary of meandering river experiments

These meandering river experiments are the first to document the formation of scroll-bars and ridge and swale topography. In addition, the mixed grain-size distribution has allowed the associated lateral accretion surfaces to be seen in unprecedented detail. A bend development model has been described in terms of four distinct phases; extension, constriction, roll-back and chute cutoff. This bend development model is similar to that described for some prototype gravel-bed meandering rivers and appears to be a better analogy both in terms of form and process than the equivalent stages 4 and 5 of Hickin's (1969) pseudomeandering model which has previously been used as a comparison. No unambiguous relationship between bend parameters and imposed lateral ground-tilting could be identified because the rate and morphology of bend development masks the precise impact of tilting. However, a number of trends can be identified: i) a marked decrease in the probability of chute cutoff occurring across convex downtilt bends, ii) an increase in the rate of channel movement towards the fault after tilting, iii) a short lag-time between tilting and increased rates of movement towards the fault (less than 3 hrs), and, iv) a possible relationship between tilt magnitude and the rate of increase in downdip movement. The present study has only examined planform changes to meanders, although the incorporation of flood hydrographs and increased floodplain cohesion into a model would allow basin-wide aggradation and quantification of the preserved alluvial architecture, as described for braided rivers in the following section.

5.8 Background to braided river experiments

Two experiments (termed B1 and B2 as in Chapter 4) were conducted to examine the influence of lateral tilting on the channel morphology of braided rivers and their preserved sedimentary deposits. The initial axial bed slope for both experiments was 2%, with a lateral tilt of 0.3% applied to experiment B1 at the mid-point of the run and three lateral tilt increments of 0.1% applied at equal time intervals to run B2 (Table 5.4). Both experiments were run at a uniform discharge of 1 l s^{-1} for the first 10 hours to develop a braided pattern over the full width of the stream table. A series of 31 and 17 scaled flood hydrographs (see Sections 4.3.2 and 4.6) were run in experiments B1 and B2 respectively, with an imposed aggradation rate of 2 mm hr^{-1} (Table 5.4). Since the general time scale for a model (λ_t) is equal to $(\lambda_L)^{0.5}$ (equation 3.56) aggradation should occur approximately 4.5 times quicker in the 1:20 scale model than in the prototype. Aggradation rates for the Ivishak Formation are unknown, however a model rate of 2 mm hr^{-1} (prototype of 0.44 mm hr^{-1}) is several orders of magnitude faster than observed long-term sedimentation rates (e.g., 0.3-2.0 mm yr^{-1}; Haynes, 1985). A second methodology for calculating the aggradation time-scale is to use the concept of magnitude-frequency analysis (Section 3.9). The continuous use of flood hydrographs which account for a high percentage of the work of a river system further compresses the time-scale for aggradation although the magnitude of the compression is difficult to quantify. Developing the magnitude-frequency argument further, single flood events can account for metres of sedimentation and may therefore be more important for localised erosion and sedimentary preservation than long-term sedimentation rates. The bed slope, aggradation rate, grain-size and flow hydrograph are in concordance with the experiments of Ashworth and Best (1994) which involved no lateral tilting.

Table 5.4. Experimental conditions for the braided river runs

Run	Downstream bed slope (%)	Aggrad^n rate (mm hr^{-1})	Start of aggrad^n (hr)	Start of hydro-graphs (hr)	N^o. of hydro-graphs	Total run time (hr)	Lateral tilt (%)	Timing of tilting (hrs)
B1	2.0	2.0	11.5	10	31	56.5	0.3	34
B2	2.0	2.0	11.5	10	17	35.5	3 x 0.1	13/20.5/28

5.9 Flow characteristics of the braided river experiments

Flow conditions in the model (Table 5.5) are in broad correspondence with observed figures for braided rivers (Young and Davies, 1990; Ashworth, 1995) and for comparable experiments (e.g. Ashworth *et al.*, 1994; this study - Table 3.1). Mean Froude numbers are below unity indicating subcritical flow whilst mean flow Reynolds numbers correspond to fully rough and turbulent flow, assuming the transitional/turbulent boundary is at a value of 2000 (e.g. Leeder, 1982; Richards, 1982 (see Section 3.4.2)). Grain Reynolds numbers fall below the critical value of 70 proposed by Yalin (1971) but above the minimum value recommended by other authors (Parker, 1979; Jaeggi, 1986; Ashworth *et al.*, 1994; see Section 3.4.3). Additionally, Weber numbers fall within or below the suggested range of critical values (10-120) but the magnitude of any surface-tension induced distortion is unknown (Peakall and Warburton, 1995; Section 3.6.1). Flow is locally supercritical as readily observed in the model by the occurrence of periodic trains of standing waves which have been widely observed in natural braided rivers (e.g., Williams and Rust, 1969; Boothroyd and Ashley, 1975; Ashworth *et al.*, 1994) and in flume models (Table 3.1). Transitional flow Reynolds numbers are also indicated by the presence of oblique diagonal standing waves and associated low relief rhomboidal bedforms (see Figs. 5.15 & 5.16) which have previously been identified experimentally in shallow transitional supercritical flows and observed on the top of braid bars in the field (Karcz and Kersey, 1980; see Section 3.6.2).

Table 5.5. Flow characteristics for the braided flume experiments

Parameter	Mean	Min $^{\delta}$	Max $^{\delta}$	N^{o}
Water temperature, T, (°C)	19.0	15.7	22.0	26
Dynamic viscosity, μ, (μkg m^{-1}s^{-1})	1028	955	1117	26
Mean flow velocity, V, (m s^{-1}) $^{\alpha}$	0.29	0.14	0.43	52
Channel bed slope, S_b, (%) $^{\beta}$	1.25	1.19	1.30	2
Channel depth, d, (mm) $^{\gamma}$	11.8	3	29	47
Flow Reynolds number, Re, $^{\gamma}$	3287	371	12969	-
Grain Reynolds number, Re$_*$, $^{\gamma\varepsilon}$	38.0	17.3	65.6	-
Froude number, Fr, $^{\gamma}$	0.84	0.26	2.49	-
Weber number, We, $^{\gamma}$	13.3	0.78	73.0	-

$^{\alpha}$ calculated from surface velocities multiplied by 0.67. $^{\beta}$ Based on thalweg bed surface slopes. $^{\gamma}$ Values from Ashworth and Best (unpublished) and represent maximum channel depths. $^{\delta}$ Minimum and maximum values are calculated from the corresponding minimum and maximum input parameters. $^{\varepsilon}$ Re$_*$ is calculated using the initial model bulk D_{90}.

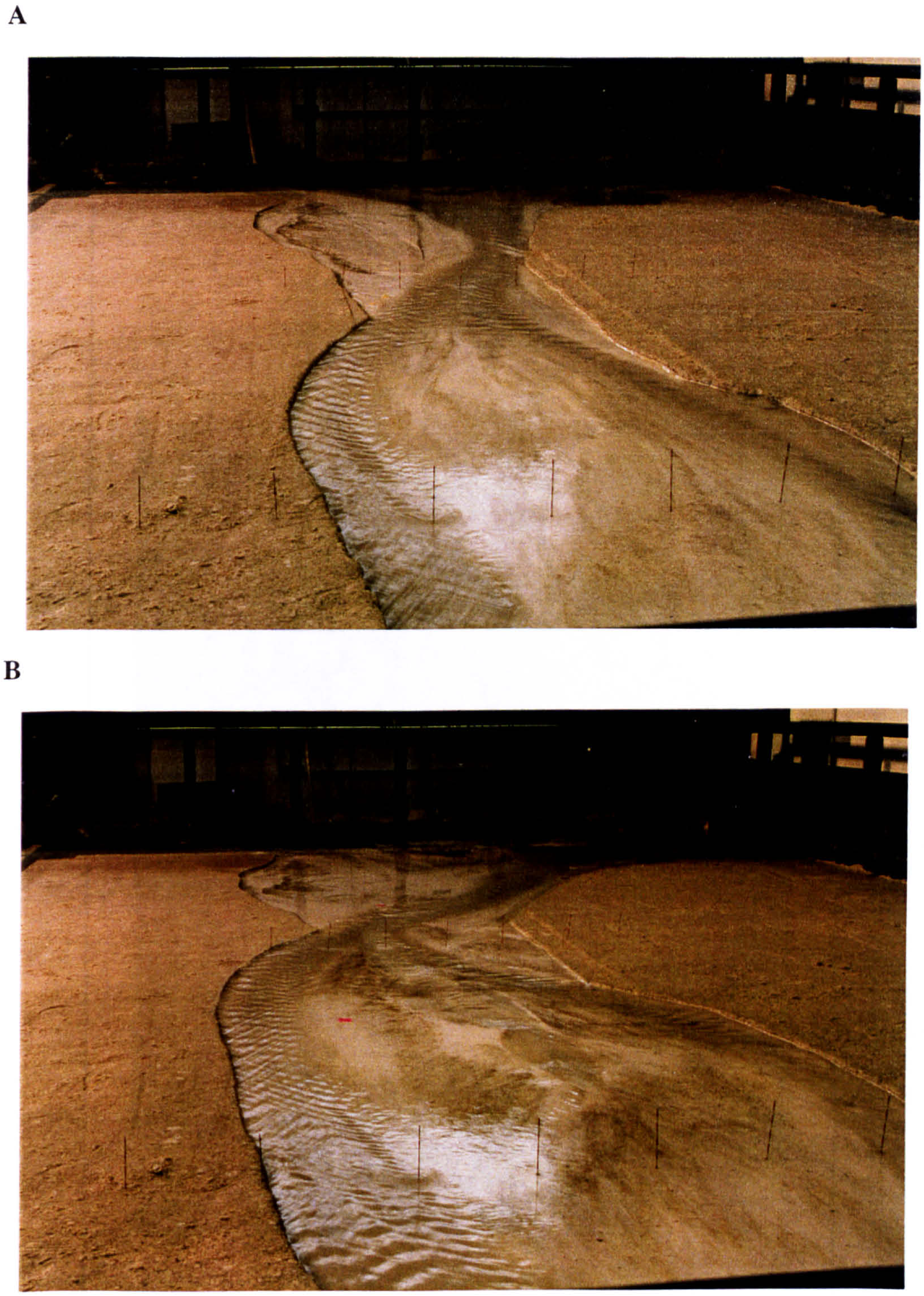

Figure 5.15. Photographs of oblique diagonal standing waves indicating transitional supercritical flow. (a) Prominent waves are present at bottom left of flow and towards the centre left of flow. Run time = 4 hrs 15 mins; (b) Channel width has increased (compare stationary marker pins) with a probable corresponding increase in channel depth at the bottom left of flow leading to a change to standing waves perpendicular to flow. Oblique diagonal standing waves are still present towards the centre left of flow. Run time = 5 hrs 40 mins. Both photographs from experiment B1, with flow towards the top of each photo. The flume width is 3.65 m and the flow rate = $1\ l\ s^{-1}$.

Figure 5.16. Photograph of rhomboidal bedforms indicating former transitional supercritical flow conditions. Rhomboidal bedforms a few centimetres long are present in the centre of the flow, on either side of the first set of marker pins. Experiment B1, flow rate = 1.35 l s^{-1}, run time = 22 hrs 50 mins. Flow direction is away from the camera.

Values of some of the flow parameters (e.g., Re, Re*, We) fall below or on the boundaries of those observed in field studies of braided rivers. Additionally, since the grain-size distribution for the experiments is based on the preserved rock record (Ivishak Formation, Section 4.7), there are no prototype hydraulic data to verify the experimental criteria. Some authors would therefore refer to this type of experiment as a generic model (Ashmore, 1991a,b; Leddy, 1993; Ashworth, 1995). However, as argued in Sections 3.2 and 3.10, the distinction between Froude scale modelling and generic modelling is not how closely they replicate reality, but in whether the degree of replication to reality can be estimated or not. In this example, those properties of the prototype that were known have been scaled (namely the grain-size curve) and a hydraulic comparison has been made with present day braided rivers. These factors distinguish this set of experiments from many previous generic models where no or few parameters were initially scaled and flow conditions were not compared with field examples. Therefore, these experiments on braided patterns are termed Froude scale models.

5.10 Sediment surface gradients

Despite careful attempts at floodplain levelling at the start of each experiment, the initial sediment surfaces for runs B1 and B2 were not absolutely level but showed low angle lateral gradients. Experiment B1 had low angle (<2%) lateral slopes which displayed no systematic pattern (Table 5.6). However, run B2 showed a slightly domed initial surface with gradients on the right hand side of the flume (looking downstream) of between 0.14% and 0.35% in the direction of the applied tilting (Table 5.6). These initial gradients for run B2 are of the same order of magnitude as the three tilting events applied through the run and therefore constitute a fourth tilt increment.

Rapid widening and shallowing of the initial dredged channel (0.40 m wide by 0.02 m deep) occurred during the first ten hours of each experiment while the flow rate was constant at 1 l s^{-1}. At a point 2 m downstream from the inlet channel, bed elevation reduced to half the initial depth after ten hours (Fig. 5.17a). Aggradation was higher further downstream, resulting in a slight decrease in the overall bed slope (Fig. 5.17b, c). The observed changes suggest that the initial channel dimensions do not have to be based on prototype dimensions since a channel will rapidly adjust to the imposed flow rate, sediment type and bed slope. Measured braided channel width:depth ratios from the comparable experiments of Ashworth *et al.* (1992) have a mean value of 34:1 (based on mean channel depth) which is in agreement with the range of 20-40 observed in some anabranches of braided river channels (Parker, 1976).

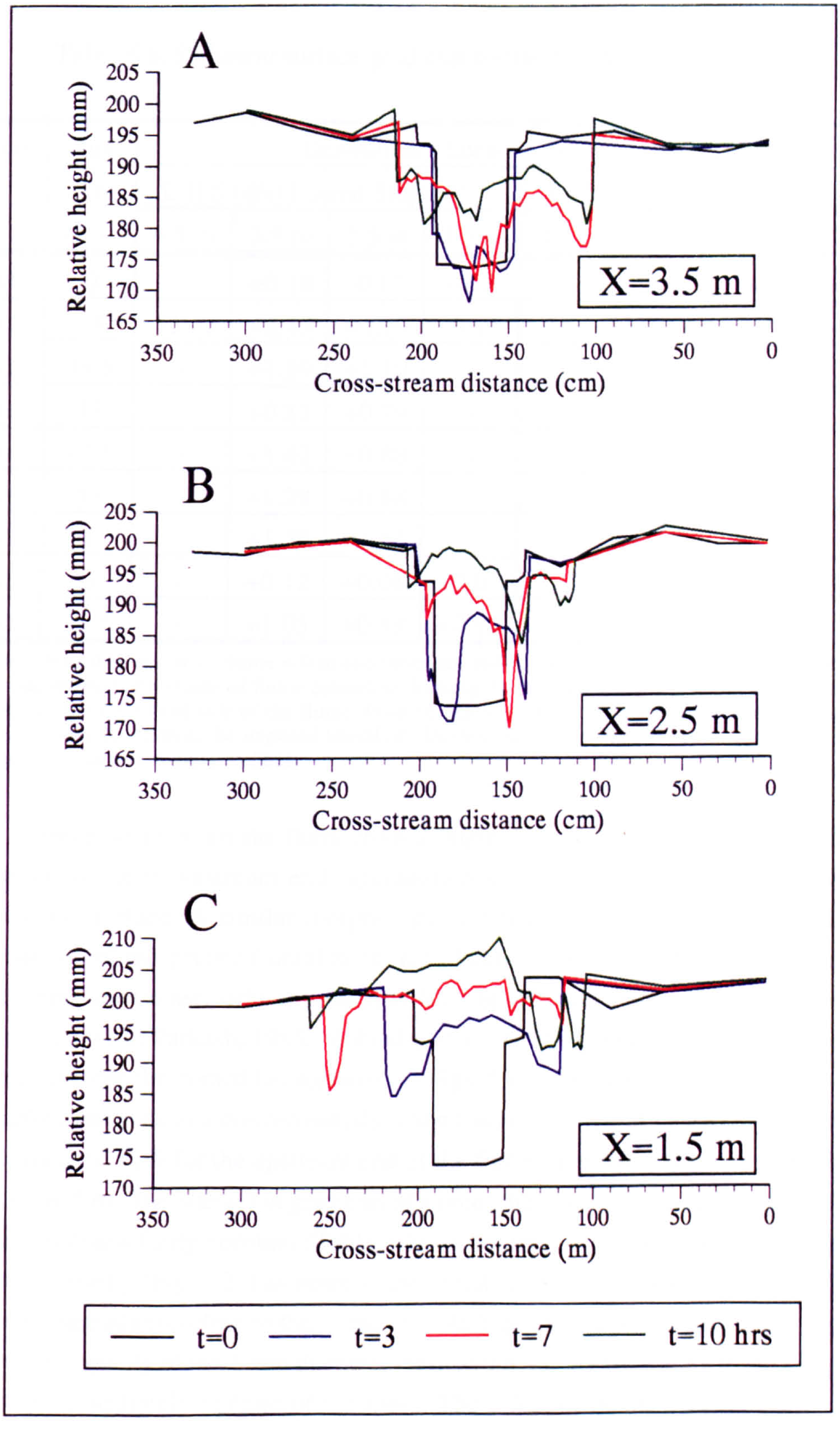

Figure 5.17. Cross-sections illustrating changes in initial channel development with distance upstream. All views are plotted with the upstream direction into the page. Cross-stream values are plotted with Y=0 at the right hand side of the flume, as looking upstream (see Fig. 5.22). Heights are relative to instrumentation on the flume bridge.

Table 5.6. Sediment surface gradients for the braided river experiments

Run	Run Time (hrs)	Downstream Location of Cross-Sections†							
		L.H.S (d/s) Lateral Slope (%)α				R.H.S (d/s) Lateral Slope (%)α			
		4.5 m	3.5 m	2.5 m	1.5 m	4.5 m	3.5 m	2.5 m	1.5 m
B1	0	-	+0.18	-0.17	+0.04	-	+0.15	-0.05	-0.18
B1	34	+2.42	+2.15	+0.99	-0.17	-2.03	-2.19	-1.24	-0.29
B1	38.5	-	+1.89	+1.19	-	-	-1.03	-0.73	-
B1	43	-	+0.83	+0.79	-	-	-1.31	-0.81	-
B1	47.5	-	+1.62	+0.88	-	-	-1.55	-0.66	-
B1	52	-	+1.29	+0.88	-	-	-1.25	-0.72	-
B1	56.5	-	+1.32	+1.41	-	-	-1.50	-0.93	-
B2	0	-	+0.12	+0.08	+0.07	-	-0.14	-0.27	-0.35
B2	35.5	-	+1.05	+0.89	+0.92	-	-1.30	-0.73	-0.40

† Note: Downstream exit of flume = 0 m and upstream end of flume = 5.5 m. α L.H.S and R.H.S = left hand side and right hand side of flume centreline, looking downstream (d/s). The applied lateral tilts were all towards the right hand side of the flume. Positive gradients are in the opposite and negative gradients are in the same direction as the imposed lateral tilt. Dashes indicate no data. All gradients calculated from ordinary least squares regression lines.

Since water enters the flume from a single fixed inlet channel, but can exit from any point at the downstream end, aggradation leads to the formation of a low-angle alluvial fan surface. A similar morphology is often seen in proglacial braided rivers downstream of the glacier frontal zone (e.g., Fahnestock, 1963; Bluck, 1987) or at the point where stream networks expand after leaving upland incised valleys (e.g., Weaver, 1984; Gohain and Parkash, 1985; Mohindra *et al.*, 1992). Cross-sections of the sediment surface illustrate the domed fan surface (see Figs. 5.18 and 5.19). Lateral gradients on the fan surface decrease in a downstream direction towards the toe of the fan (Fig. 5.20) from a maximum of >2% for the upstream end of the flume, to a minimum of 0.2-0.3% at the exit (Table 5.6). The lateral fan gradients at a point fluctuate through time but the average gradient remains fairly constant (Table 5.6). In contrast, average downstream gradients decline markedly (Fig. 5.21) as noted in the initial channel change (Fig. 5.17), reflecting increased aggradation close to the flume exit. At high discharges, bedload transport rates exceed the capacity of the 3 mm diameter mesh at the flume exit leading to the trapping of sediment immediately in front of the mesh. The effect of increased aggradation at the flume exit gradually propagates upstream, progressively reducing bed slopes through time.

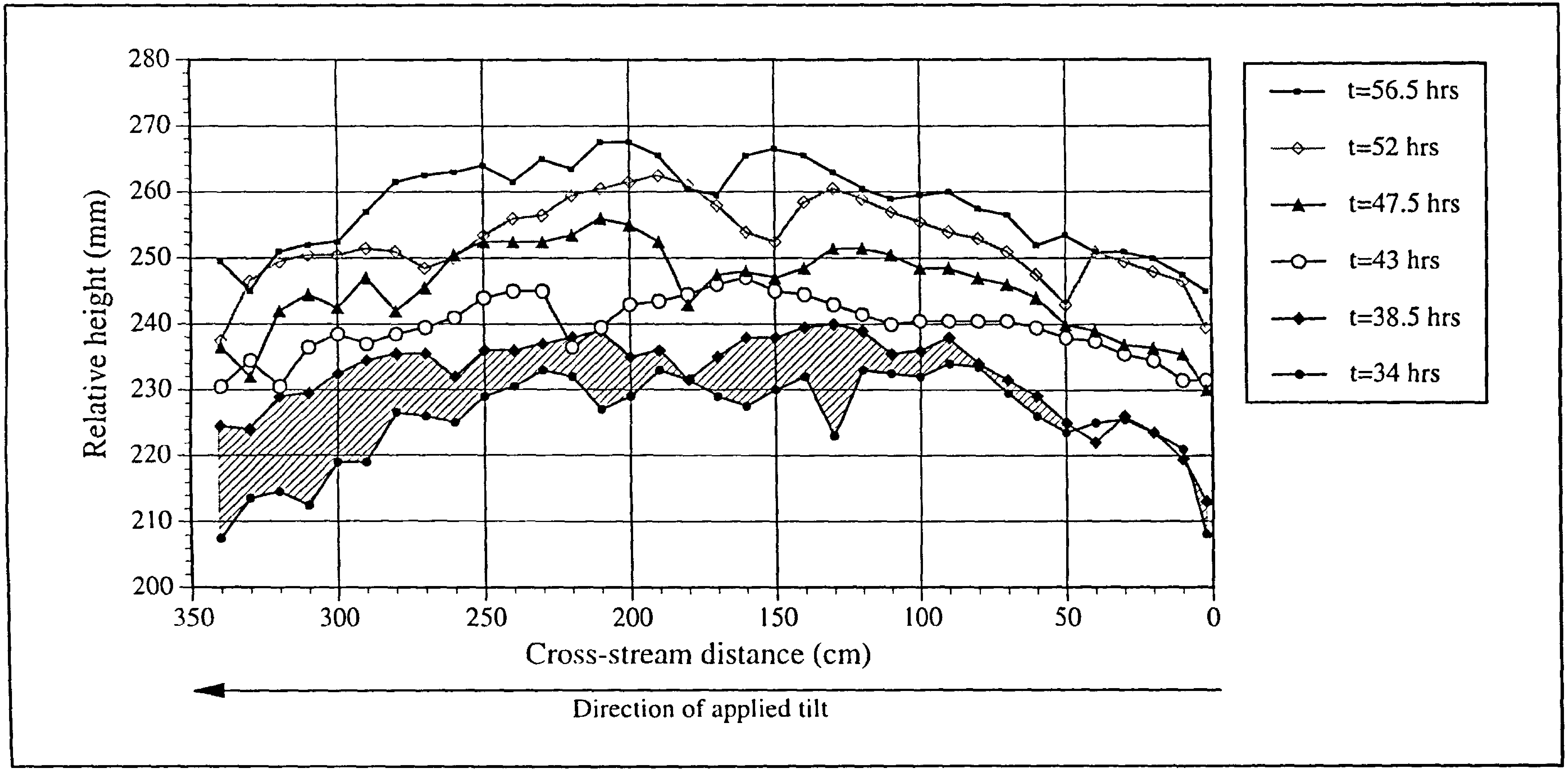

Figure 5.18. Temporal cross-sectional change of the flume surface after tilting. Cross-sections located at an axial distance of 3.5 m. The lowermost cross-section (t=34 hrs) is of the flume surface immediately after tilting and the shaded area represents the distribution of aggradation in the first 4.5 hours after tilting. Data from experiment B1.

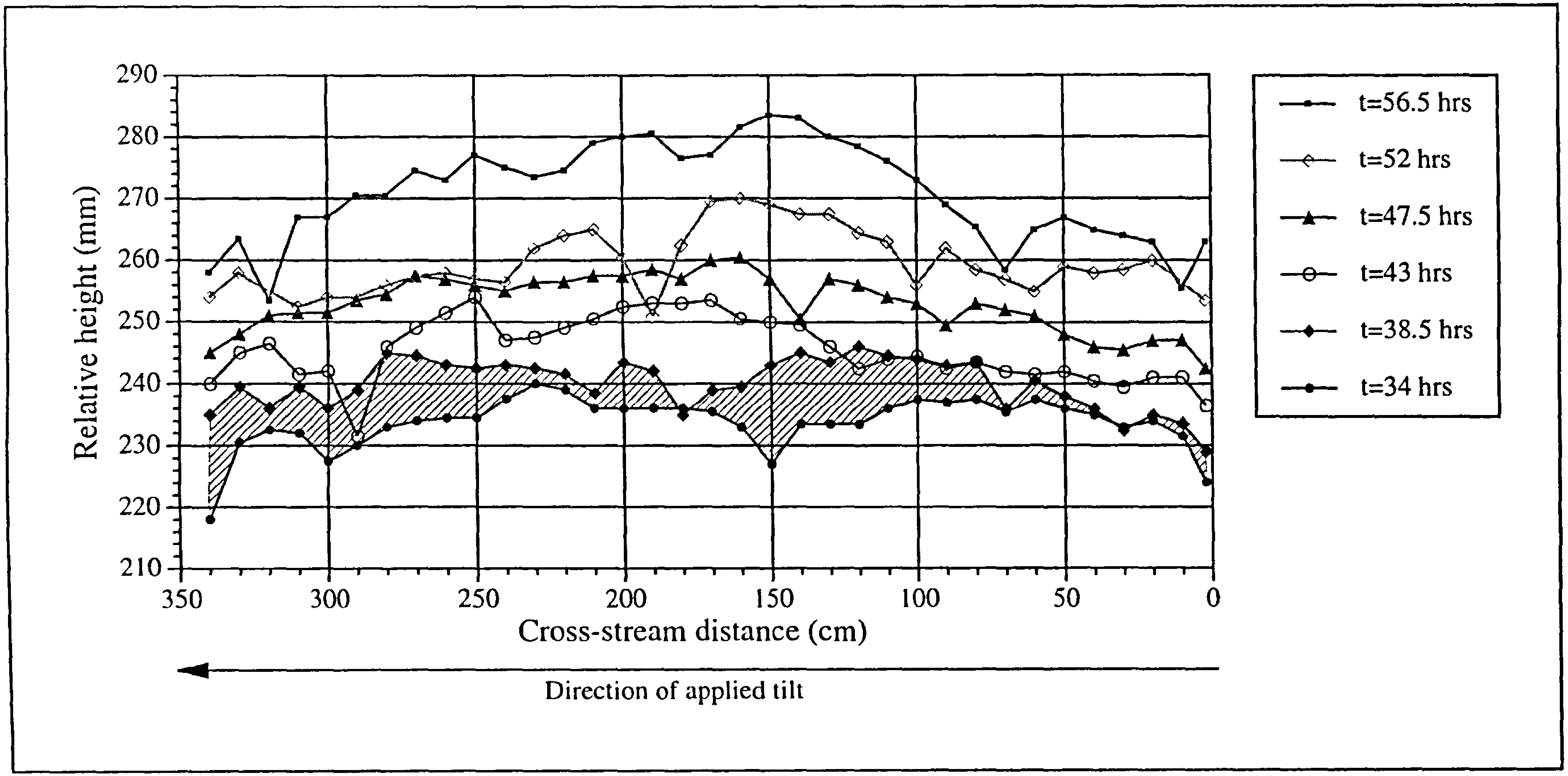

Figure 5.19. Temporal cross-sectional change of the flume surface after tilting. Cross-sections located at an axial distance of 2.5 m. The lowermost cross-section (t=34 hrs) is of the flume surface immediately after tilting and the shaded area represents the distribution of aggradation in the first 4.5 hours after tilting. Data from experiment B1.

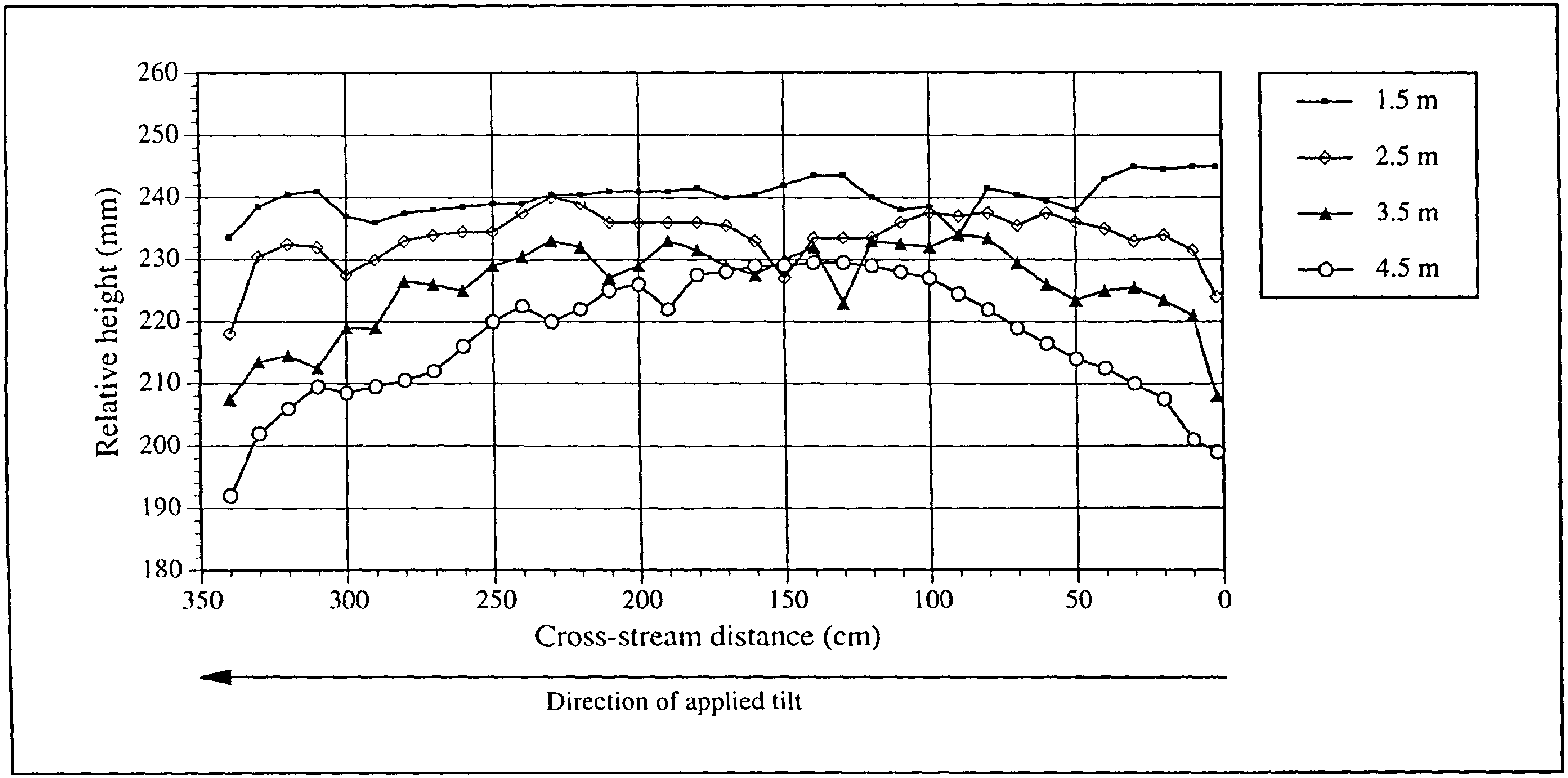

Figure 5.20. Variation in cross-section surface gradients with distance downstream, immediately after tilting (t=34 hrs). Note the continuous decrease in lateral gradients from X=4.5 m (upstream) to X=1.5 m (downstream). Values for the lateral gradients are compiled in Table 5.6. Data from experiment B1.

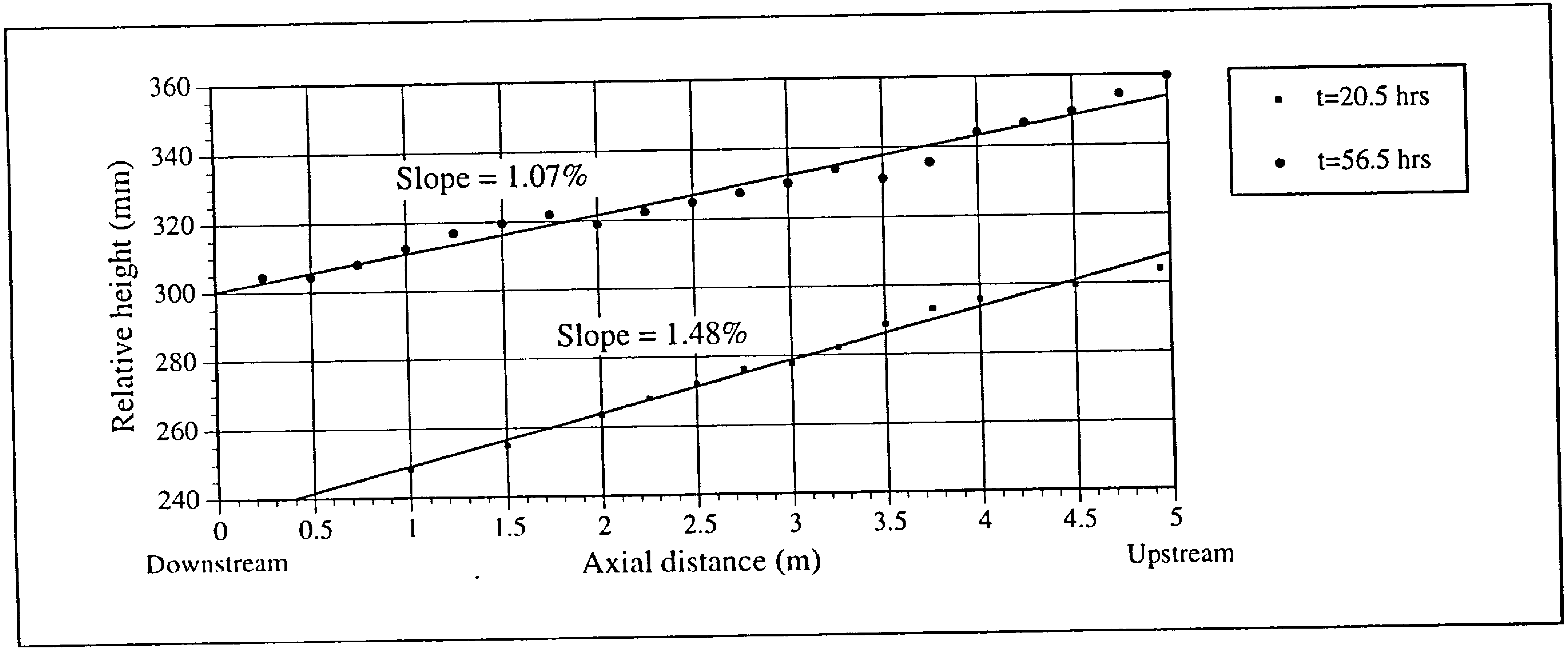

Figure 5.21. Temporal variation of average axial gradients, for the centre of the flume (Y=1.75 m). Each regression line is significant at a confidence level of 99.9% and the 95% confidence intervals for the two gradients do not overlap. Data from experiment B1.

Instantaneous Imposition of a 0.3% lateral slope at t=34 hours in experiment B1 led to nodal avulsion towards the locus of maximum subsidence. These changes in avulsion pattern can be identified in the spatial distribution of aggradation immediately after tilting. Aggradation was concentrated in and adjacent to the area of maximum subsidence for a period of at least 4.5 hours (34-38.5 hrs; see shaded sections, Figs. 5.18 and 5.19). However, because the surface is domed, the effects of tilting were relatively short lived (approximately 8% of total run time) and nodal avulsion and accompanying aggradation switched to the other side of the fan in the subsequent 4.5 hour period (38.5-43 hrs; Figs. 5.18 and 5.19).

5.11 Analysis of sediment faces

A total of 26 and 16 sediment faces were cut and photographed in experiments B1 and B2 respectively (see Section 4.9 for methodology). Of these faces, 12 cross-stream sections, 6 each for runs B1 and B2, were analysed and are shown in solid lines on Figure 5.22. All sections were greater than 2 m long and located towards the downthrown side of the flume (Fig. 5.22). For analysis, acetate overlays were placed over each photomontage and the geometries of all the fine and coarse grained depositional niches traced by hand. Niche lengths and thicknesses were measured and x,y,z spatial co-ordinates taken for the centroid of each niche (to within ±0.5 mm). In addition, the total depositional area of each section was recorded to allow calculation of the percentage area occurrence of each niche. Fine grained niches can be clearly differentiated from the ambient fill since the white silica flour contrasts well with the orange coloured sand. Equally, the coarse grained niches are much darker than the sand grades allowing unambiguous identification.

5.12 Niche classification

Niches were classified into four fine and four coarse grained categories using a classification scheme modified from the work of Ashworth *et al.*, (1992) and Ashworth and Best (1994). Fine grained niches were defined and interpreted as:

1) Splays - thin, horizontal deposits which often cap fining-up units. Dominantly deposited on bar tops and floodplain adjacent to the channels. Splays can be laterally extensive.

2) Abandoned channels - sharp-based lenses which frequently show asymptotic terminations ('wings') on each flank. These represent post-abandonment filling of both channels and scour holes.

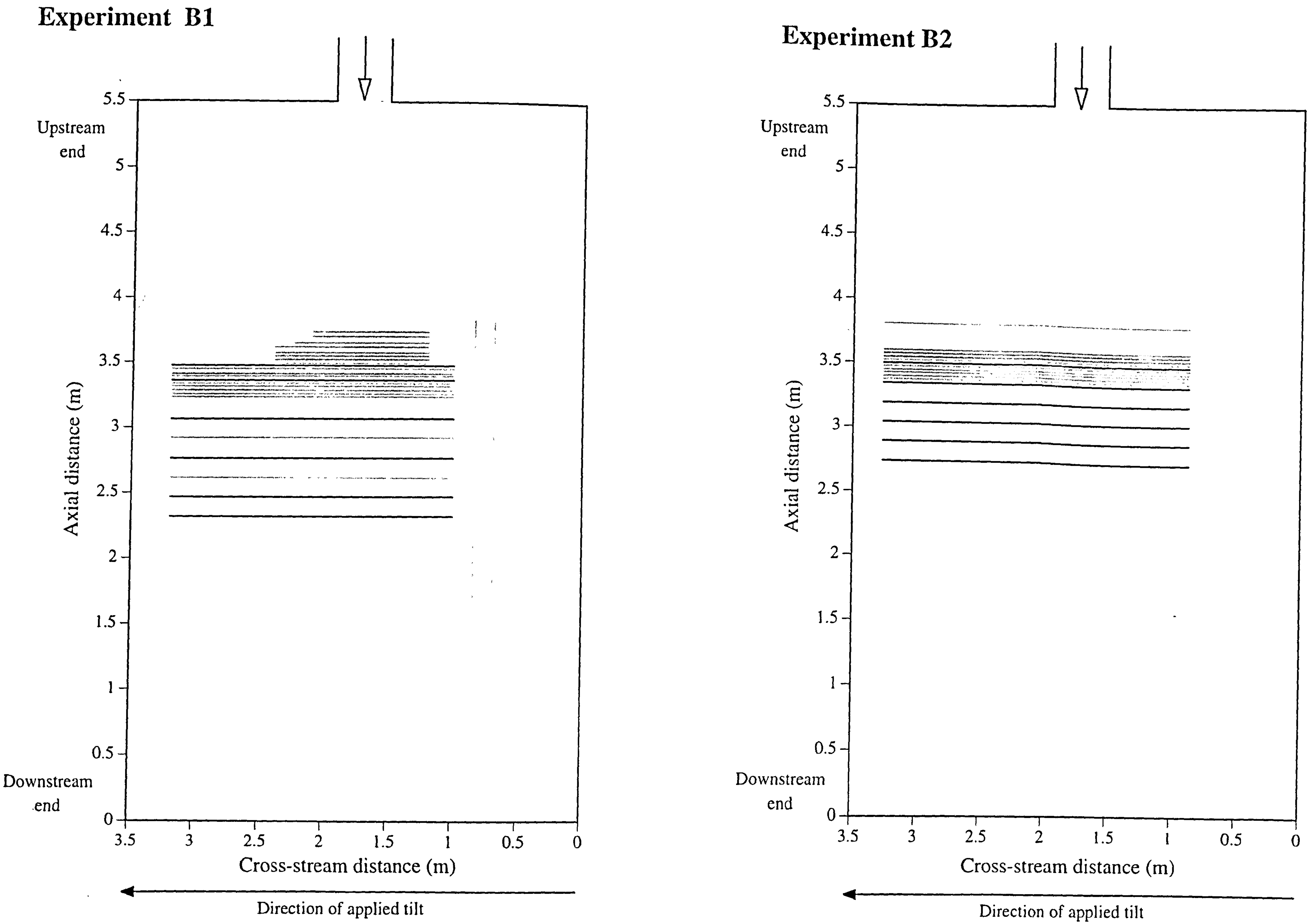

Experiment B1

Experiment B2

Figure 5.22. Location of sediment slices with respect to the flume, for runs B1 and B2. Water enters from the top centre (axial distance = 5.5 m) and exits at any point at the downstream end of the flume (axial distance = 0 m). Sections used for analysis are in black with additional sections shown as grey lines.

3) Barlees - inclined drapes representing lateral and lee-side deposition due to flow expansion and contraction. Sometimes found within coarse bar deposits.

4) Erosional remnants - small, irregular 'blocky' deposits, often with the long axis at a high-angle to the horizontal. Probably represent the erosional remnants of abandoned channels, small scour holes and backwater deposits.

Similarly, coarse grained niches were classified as:
1) Bar cores - large, tabular, horizontal deposits with amalgamation surfaces which also show indistinct lateral accretion surfaces and openwork textures.
2) Abandoned plugs - channel filling lenses which frequently fine upwards, recording channel filling and subsequent abandonment. These may also contain prominent lateral accretion surfaces and cross-bedding.
3) Bar margins - inclined packages which vary from short thin lags to large homogeneous deposits and depict lateral and downstream bar accretion.
4) Armour surfaces / pavements - thin laterally extensive lags, frequently associated with finer grained packages, and probably represent overbank and bar surface deposition of gravel sheets.

Two examples of the interpretation of sediment faces using this classification scheme are shown in Figure 5.23.

The background fill is composed dominantly of fine grained sand which could not be differentiated into individual niches (see Fig. 5.23). A weak horizontal stratification is present and combined with limited grading and sedimentary structures suggests periods of constant aggradation or sediment freezing, separated by rapid migration. Some internal sedimentary structures are present including cross-bedding and lamination but these are poorly preserved or difficult to identify because of limited grain-size differentiation. These sedimentary structures probably encompass a range of depositional units from washed-out individual bedforms to larger macroforms where flow reduction was insufficient for the finest sediment to be deposited. At flood peaks many macroforms were extensively reworked into large uniform sheets which then underwent progradation. Crudely stratified sheets have also been recognised in modern and ancient braided rivers (e.g., facies Gm of Miall, 1977; Steel and Thompson, 1983; Salter *et al.*, 1993) and may have formed through this process of high-stage reworking and vigorous grain transport during subsequent progradation.

C
M
P
S
R
S
S
S
B
S
S
M
B
S
S
AC
M
B
B
R
B
A
B
C
S
S
S
AC
S
S
P
C
M
R
P
S
S
S
S
S
C

Figure 5.23A. Sediment face showing braided alluvial architecture and subdivision into sedimentary niches. Face is orientated perpendicular to the mean flow direction. Symbols on overlay: fine grained niches; S = splay, B = barlee, R = erosional remnant, and AC = abandoned channel. Coarse grained niches; P = abandoned plug, M = bar margin, C = bar core, and, A = armour surface.

Figure 5.23A. Sediment face showing braided alluvial architecture and subdivision into sedimentary niches. Face is orientated perpendicular to the mean flow direction. Symbols on overlay: fine grained niches; S = splay, B = barlee, R = erosional remnant, and AC = abandoned channel. Coarse grained niches; P = abandoned plug, M = bar margin, C = bar core, and, A = armour surface.


B
S
S
S
S
AC
M
S
S
S
S
S
S
S
S
S
S
P
M
S
S
B
P
S
S
S
S
S
M
M
M
M
M
S
B
B
M
S
S
B
S
A
R
M
C
S
M

B

Figure 5.23B. Sediment face showing braided alluvial architecture and subdivision into sedimentary niches. Face is orientated perpendicular to the mean flow direction. Symbols on overlay: fine grained niches; S = splay, B = barlee, R = erosional remnant, and AC = abandoned channel. Coarse grained niches; P = abandoned plug, M = bar margin, C = bar core, and, A = armour surface.

B

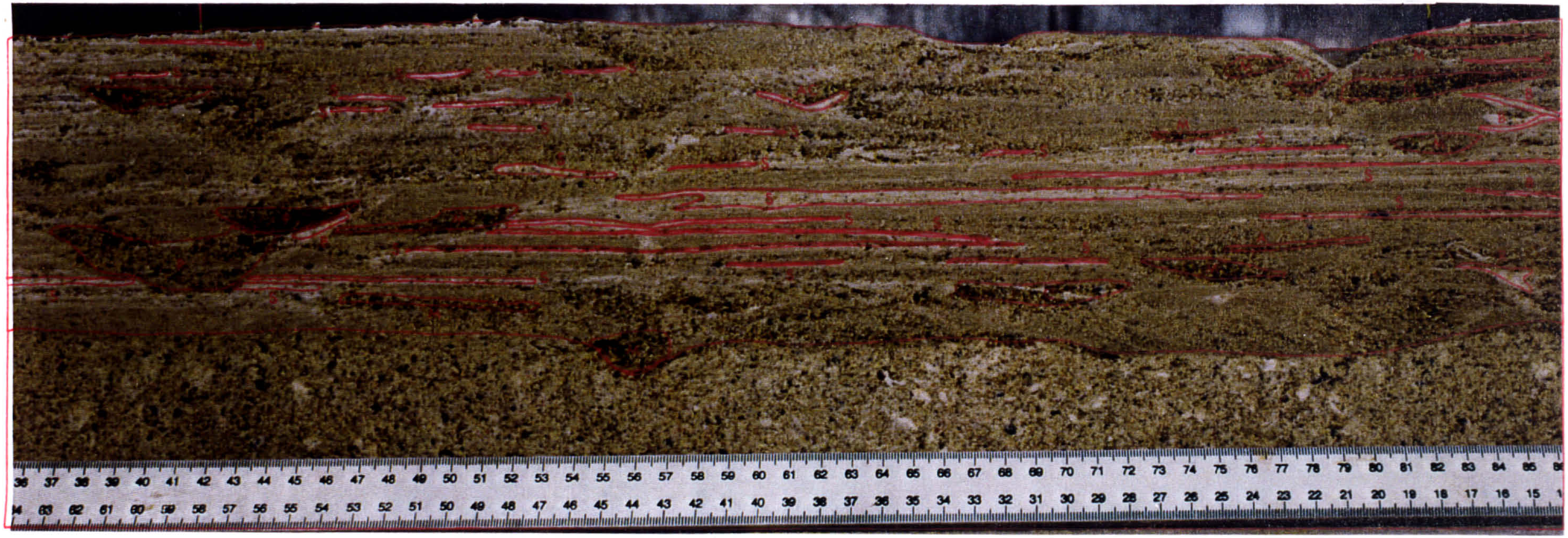

Figure 5.23B. Sediment face showing braided alluvial architecture and subdivision into sedimentary niches. Face is orientated perpendicular to the mean flow direction. Symbols on overlay: fine grained niches; S = splay, B = barlee, R = erosional remnant, and AC = abandoned channel. Coarse grained niches; P = abandoned plug, M = bar margin, C = bar core, and, A = armour surface.

5.13 General niche statistics

A total of 1126 and 880 sedimentary niches were measured for experiments B1 and B2 respectively. Comparative length and percentage occurrence statistics for the two runs are given in Tables 5.7-5.10. All statistics have been scaled up from the model by multiplying by the length scaling ratio of 20. Ashworth *et al.*, (1992) suggest that these lengths are representative of the 3rd and 4th order prototype (Ivishak) channels and that a further scaling factor of 53.2 must be used to scale up to 1st and 2nd order channels, based on a comparison of flume and Ivishak channel depths. Several points are immediately apparent. Firstly, splays are the most common fine grained niche accounting for over 70% of all braided river fine grained niches. Barlees and erosional remnants represent approximately 16% and 8% of all fine grained niches respectively, while abandoned channel fills are rare, accounting for just 3% (Table 5.7). However, only complete channel fills are measured and therefore the percentage occurrence will be underestimated. Splays have the highest mean length and the largest range of lengths in both experiments and although experiment B2 has marginally shorter lengths than run B1, the splays have a similar percentage occurrence in each.

These values can be compared with the similar experiments of Ashworth and Best (1994) which used the same grain-size distribution and initial run conditions. Their experiments had 41% splays, 4.7% abandoned channels and a combined class of barlees / erosional remnants with a percentage occurrence of 54.3%. The differences are due to a high incidence of unidentified niches in the experiments of Ashworth and Best (1994), which were classified as erosional remnants. Evidence that the majority of the undifferentiated fine grained niches were probably splays is provided by a comparison of downstream and cross-stream sections. Ashworth and Best (1994, p.13) noted that a higher proportion of splays were recognised in downstream sections (52.9%) compared to cross-stream sections (41.0%), with a corresponding drop in the frequency of occurrence of erosional remnants from 54.3% to 42.2%. If the assertion that the majority of the undifferentiated niches were splays is true, then their results are in broad agreement with Tables 5.7 and 5.8.

Although abandoned channels are rare, they are more abundant in terms of cross-sectional area than in number (Table 5.8). However, erosional remnants are less important in terms of length than in either percentage number or area. There are also differences between experiments B1 and B2 in terms of percentage area, most notably for splays.

Abandoned plugs have the longest lengths of any coarse grained niche (Table 5.9) and have a higher frequency of occurrence than the fine grained abandoned channels

Table 5.7. Summary statistics for cross-stream lengths of fine grained niches

Niche Type	Run	N	Mean (m)	Median (m)	St. Error of mean (m)	Min (m)	Max (m)	% N°. Occur.
Splays	B1	497	1.05	0.76	0.037	0.26	6.75	74.7
	B2	*360*	*0.65*	*0.52*	*0.026*	*0.13*	*4.20*	*70.3*
Aband. Channels	B1	23	0.72	0.68	0.050	0.41	1.39	3.5
	B2	*13*	*0.67*	*0.53*	*0.107*	*0.37*	*1.64*	*2.5*
Barlees	B1	104	0.76	0.63	0.039	0.29	2.24	15.6
	B2	*88*	*0.60*	*0.45*	*0.043*	*0.18*	*2.09*	*17.2*
Eros. Remnants	B1	41	0.49	0.44	0.039	0.21	1.40	6.2
	B2	*51*	*0.31*	*0.26*	*0.022*	*0.14*	*1.19*	*10.0*

Table 5.8. Summary statistics for percentage occurrence of fine grained niches

Niche Type	Run	% Number	% Length	% Area†
Splays	B1	74.7	81.8	73.7
	B2	*70.3*	*75.3*	*62.1*
Aband. Channels	B1	3.5	2.6	6.3
	B2	*2.5*	*2.8*	*10.8*
Barlees	B1	15.6	12.4	12.7
	B2	*17.2*	*16.8*	*17.4*
Eros. Remnants	B1	6.2	3.1	7.3
	B2	*10.0*	*5.1*	*9.6*

† Calculated using an ellipse of the form; area = π.a.b/4. Note: % number, % length and % area are percentages of the total number, length or area respectively of all fine grained niches.

Table 5.9. Summary statistics for cross-stream lengths of coarse grained niches

Niche Type	Run	N	Mean (m)	Median (m)	St. Error of mean (m)	Min (m)	Max (m)	% N°. Occur.
Bar Cores	B1	134	1.44	1.17	0.078	0.36	5.13	29.1
	B2	*114*	*1.36*	*1.12*	*0.094*	*0.32*	*7.44*	*31.0*
Aband. Plugs	B1	51	1.61	1.44	0.114	0.46	4.69	11.1
	B2	*49*	*2.00*	*1.37*	*0.026*	*0.52*	*9.53*	*13.3*
Bar Margins	B1	177	0.96	0.80	0.048	0.21	7.01	38.4
	B2	*103*	*0.88*	*0.68*	*0.050*	*0.19*	*2.66*	*28.0*
Armour Surfaces	B1	99	1.44	1.28	0.074	0.41	3.59	21.5
	B2	*102*	*1.17*	*1.00*	*0.058*	*0.39*	*3.32*	*27.7*

(Table 5.7). There are significant differences in percentage occurrence of the coarse grained niches between experiments B1 and B2, most notably for bar margins. However, the mean lengths for bar margins are very similar (Table 5.9). These are the first set of experiments to generate statistics for coarse grained niches in a cross-stream orientation and therefore cannot be compared with the work of Ashworth and Best (1994) as undertaken for the fine grained niches.

Fine grained abandoned channels show the same pattern as abandoned plugs since they are more important in terms of area than in frequency (Table 5.10). In contrast, bar margins and particularly armour surfaces are far less important in terms of area than in number.

Table 5.10. Summary statistics for percentage occurrence of coarse grained niches

Niche Type	Run	% Number	% Length	% Area†
Bar Cores	B1	29.1	32.9	44.3
	B2	*31.0*	*33.5*	*32.6*
Aband. Plugs	B1	11.1	14.0	18.5
	B2	*13.3*	*21.2*	*35.3*
Bar Margins	B1	38.4	28.8	28.6
	B2	*28.0*	*19.5*	*21.6*
Armour Surfaces	B1	21.5	24.3	8.6
	B2	*27.7*	*25.8*	*10.4*

† Calculated using an ellipse of the form; area = $\pi.a.b/4$. Note: % number, % length and % area are percentages of the total number, length or area respectively of all coarse grained niches.

Differences are apparent between runs B1 and B2 in terms of area. In particular, bar cores and abandoned plugs have a similar frequency of number but different areal extents, while bar margins and armour surfaces show the opposite relationship (Table 5.10).

These are the first set of alluvial architecture modelling results for both fine and coarse grained niches in a cross-stream orientation. Calculated fine grained niche statistics are in broad agreement with the similar experiments of Ashworth and Best (1994). However, there are some significant differences in summary statistics between experiments B1 and B2 and also with the experiments of Ashworth and Best (1994). One element that may be important is the inherent randomness within the system. Ashworth and Best (1994, p.20) compared alluvial architecture measurements from identical runs and found that the percentage frequency of occurrence for any fine grained niche varied by a maximum of 2 percentage points. They therefore concluded that the intrinsic variability of the experiments was low and that experiments were repeatable. However, since this is the first study of coarse grained niches in a cross-stream orientation, no estimate of the intrinsic variability of these niches can be made. In addition, since the same sediment was used for runs B1 and B2 the statistical differences may reflect the preferential removal of the finest sediment grades through time (see Section 4.7). In contrast, the experiments of Ashworth and Best (1994) used freshly mixed sediment for each run. Another possibility is that the statistical differences between experiments may reflect changes in the magnitude and timing of lateral tilting.

In order to examine the possible influence of lateral tilting, summary statistics have been generated for each tilt increment and the untilted initial section of run B1 (Tables 5.11 to 5.14). Details of the methodology for subdividing the alluvial architecture in the vertical (Z) direction are given in Section 5.15.2. The most notable feature of the summary statistics is the general increase in the ratio of fine to coarse grained niches (fg:cg) with time (increasing height in the sedimentary section). Experiment B1 shows an increase in the fg:cg ratio from 1.22 to 2.01, whilst run B2 increases from 1.06 for the lower layer, through 1.54 for the middle, to 2.08 for the upper layer. This change in alluvial architecture appears to be independent of tilting as both experiments show a similar pattern despite differing magnitudes and frequencies of tilting. Instead the figures may be interpreted in terms of an intrinsic factor such as fan growth. Whilst the fg:cg ratio increases with time, the frequency of occurrence of individual niches within either the fine or coarse grained subdivisions remains relatively constant. For some fine grained niches the variability within experiments is greater than the variability between experiments. However, for coarse grained niches, most notably bar margins and armour surfaces, the differences between experiments is much greater than that within runs (Tables 5.12 and 5.14). Trends are also present in the mean and maximum niche length statistics between sections and the statistical significance of these variations is considered in more detail in Section 5.15.3.

There are clear changes in niche geometries and frequency of occurrence between different tilt increments and between the two experimental runs. These can be summarised as:

i) variations in the frequency of occurrence, lengths and areas of individual niches between experiments, in terms of summary statistics for each run,

ii) an increase in the fg:cg ratio with time, within individual experiments, and,

iii) variations in individual niche geometries within an experiment. These differences may be greater than those between runs for some fine grained niches.

Table 5.11. Summary statistics for cross-stream lengths of fine grained niches with section position, run B1

Niche Type	Section Position	N	Mean (m)	Median (m)	St. Error of mean (m)	Min (m)	Max (m)	% N^{o}. Occur.
Splays	Upper	197	1.01	0.80	0.051	0.26	4.58	77.6
	Lower	300	1.07	0.74	0.051	0.26	6.75	73.0
	Combined	*497*	*1.05*	*0.76*	*0.037*	*0.26*	*6.75*	*74.7*
Aband. Channels	Upper	9	0.73	0.73	0.055	0.46	0.96	3.5
	Lower	14	0.71	0.68	0.075	0.41	1.39	3.4
	Combined	*23*	*0.72*	*0.68*	*0.050*	*0.41*	*1.39*	*3.5*
Barlees	Upper	35	0.84	0.68	0.079	0.29	2.24	13.8
	Lower	69	0.72	0.62	0.043	0.31	1.82	16.8
	Combined	*104*	*0.76*	*0.63*	*0.039*	*0.29*	*2.24*	*15.6*
Eros. Remnants	Upper	13	0.52	0.44	0.060	0.22	1.02	5.1
	Lower	28	0.47	0.43	0.050	0.21	1.40	6.8
	Combined	*41*	*0.49*	*0.44*	*0.039*	*0.21*	*1.40*	*6.2*
All Fine Grained	Upper	254	0.95	0.74	0.042	0.22	4.58	100
	Lower	411	0.96	0.68	0.039	0.21	6.75	100
	Combined	*665*	*0.95*	*0.70*	*0.029*	*0.21*	*6.75*	*100*

Table 5.12. Summary statistics for cross-stream lengths of coarse grained niches with section position, run B1

Niche Type	Section Position	N	Mean (m)	Median (m)	St. Error of mean (m)	Min (m)	Max (m)	% N^{o}. Occur.
Bar Cores	Upper	37	1.55	1.30	0.172	0.62	5.13	29.4
	Lower	97	1.40	1.11	0.086	0.36	4.38	29.0
	Combined	*134*	*1.44*	*1.17*	*0.078*	*0.36*	*5.13*	*29.1*
Aband. Plugs	Upper	14	1.90	1.40	0.296	0.78	4.69	11.1
	Lower	37	1.50	1.50	0.109	0.46	2.93	11.0
	Combined	*51*	*1.61*	*1.44*	*0.114*	*0.46*	*4.69*	*11.1*
Bar Margins	Upper	43	1.01	0.98	0.075	0.21	2.26	34.1
	Lower	134	0.94	0.74	0.059	0.34	7.01	40.0
	Combined	*177*	*0.96*	*0.80*	*0.048*	*0.21*	*7.01*	*38.4*
Armour Surfaces	Upper	32	1.62	1.29	0.141	0.62	3.59	25.4
	Lower	67	1.35	1.24	0.085	0.41	3.53	20.0
	Combined	*99*	*1.44*	*1.28*	*0.074*	*0.41*	*3.59*	*21.5*
All Coarse Grained	Upper	126	1.42	1.22	0.079	0.21	5.13	100
	Lower	335	1.22	1.03	0.042	0.34	7.01	100
	Combined	*461*	*1.27*	*1.09*	*0.038*	*0.21*	*7.01*	*100*

Table 5.13. Summary statistics for cross-stream lengths of fine grained niches with section position, run B2

Niche Type	Section Position	N	Mean (m)	Median (m)	St. Error of mean (m)	Min (m)	Max (m)	% No. Occur.
Splays	Upper	100	0.72	0.55	0.056	0.19	3.24	70.4
	Middle	133	0.59	0.50	0.033	0.19	2.33	78.7
	Lower	127	0.66	0.52	0.049	0.13	4.20	63.2
	Combined	*360*	*0.65*	*0.52*	*0.026*	*0.13*	*4.20*	*70.3*
Aband. Channels	Upper	3	0.55	0.48	0.126	0.37	0.79	2.1
	Middle	3	0.92	0.58	0.362	0.53	1.64	1.8
	Lower	7	0.62	0.42	0.124	0.37	1.24	3.5
	Combined	*13*	*0.67*	*0.53*	*0.107*	*0.37*	*1.64*	*2.5*
Barlees	Upper	27	0.72	0.60	0.085	0.21	1.98	19.0
	Middle	23	0.44	0.37	0.036	0.23	0.81	13.6
	Lower	38	0.61	0.44	0.072	0.18	2.09	18.9
	Combined	*88*	*0.60*	*0.45*	*0.043*	*0.18*	*2.09*	*17.2*
Eros. Remnants	Upper	12	0.31	0.28	0.028	0.14	0.47	8.5
	Middle	10	0.30	0.25	0.030	0.19	0.43	5.9
	Lower	29	0.32	0.26	0.037	0.16	1.19	14.4
	Combined	*51*	*0.31*	*0.26*	*0.022*	*0.14*	*1.19*	*10*
All Fine Grained Niches	Upper	142	0.68	0.51	0.044	0.14	3.24	100
	Middle	169	0.56	0.45	0.028	0.19	2.33	100
	Lower	201	0.60	0.45	0.035	0.13	4.20	100
	Combined	*512*	*0.61*	*0.47*	*0.021*	*0.13*	*4.20*	*100*

Table 5.14. Summary statistics for cross-stream lengths of coarse grained niches with section position, run B2

Niche Type	Section Position	N	Mean (m)	Median (m)	St. Error of mean (m)	Min (m)	Max (m)	% No. Occur.
Bar Cores	Upper	24	1.31	1.03	0.149	0.32	3.51	35.3
	Middle	33	1.09	0.98	0.064	0.52	1.77	30.0
	Lower	57	1.54	1.32	0.170	0.36	7.44	30.0
	Combined	*114*	*1.36*	*1.12*	*0.094*	*0.32*	*7.44*	*31.0*
Aband. Plugs	Upper	7	1.55	1.34	0.352	0.69	3.35	10.3
	Middle	17	1.67	1.37	0.254	0.52	4.11	15.5
	Lower	25	2.34	1.39	0.461	0.55	9.53	13.2
	Combined	*49*	*2.00*	*1.37*	*0.026*	*0.52*	*9.53*	*13.3*
Bar Margins	Upper	20	0.90	1.79	0.099	0.40	2.14	29.4
	Middle	29	0.71	0.58	0.091	0.19	2.66	26.4
	Lower	54	0.95	0.72	0.072	0.32	2.21	28.4
	Combined	*103*	*0.88*	*0.68*	*0.050*	*0.19*	*2.66*	*28.0*
Armour Surfaces	Upper	17	1.13	0.81	0.189	0.39	3.14	25.0
	Middle	31	1.12	1.06	0.089	0.39	1.96	28.2
	Lower	54	1.21	1.025	0.079	0.39	3.32	28.4
	Combined	*102*	*1.17*	*1.00*	*0.058*	*0.39*	*3.32*	*27.7*
All Coarse Grained Niches	Upper	68	1.17	0.93	0.086	0.32	3.51	100
	Middle	110	1.09	0.98	0.062	0.19	4.11	100
	Lower	190	1.38	1.08	0.090	0.32	9.53	100
	Combined	*368*	*1.26*	*1.01*	*0.053*	*0.19*	*9.53*	*100*

However, the influence of lateral tilting on the total occurrence statistics remains difficult to quantify without a knowledge of:

1) the change in niche percentage occurrence with variation in the grain-size distribution,
2) the intrinsic experimental variability for the coarse grained niches, and,
3) comparative statistics for vertical change in niche frequencies and lengths from untilted experiments.

Further geostatistics, in terms of probability density functions and the spatial distribution of niches are described in Sections 5.14 and 5.15 respectively.

5.14 Probability density functions (PDF's)

All alluvial architecture length distributions were measured from photographs of sediment faces. Any finite 2D sediment slice is composed of a mixture of complete, partial and unlimited lengths (see Fig. 5.24). Although corrections have been proposed for these boundary effects (Geehan and Underwood, 1993), they have not been incorporated into this study for two reasons. Firstly, unlimited lengths are not present as the faces are longer than the largest niches, and secondly this study adopts the approach of Ashworth and Best (1994) in not measuring partial lengths. However, since the length distributions represent 1D values taken from 2D slices of a 3D volume, they need to be corrected for a dimensionality bias in order to more precisely represent the true PDF's. Geehan and Underwood (1993) illustrate the importance of sample dimensionality using an example of 1D sampling of a 2D slice (Fig. 5.25) where a 1:1 ratio of short to long lengths is observed in the 1D samples instead of the true 2:1 ratio. There is a similar bias towards the longest lengths when sampling from a 2D slice of a 3D volume, as shown in Enclosure 1, where closely spaced 2D sections repeatedly cut several large splays, thereby overestimating the number of large splays. The nature and magnitude of the dimensionality bias depends on the shape and orientation distributions for each niche class and therefore in order to estimate the true PDF's from a 2D face the following information is required:

1) Length measurements accurately assigned to individual niche classes (assuming that each niche class has individual shape and orientation properties)
2) Identification of partial and unlimited lengths
3) The shape distributions (for instance in terms of ellipse eccentricity and lengths) for each niche type
4) The orientation distribution for each niche with respect to a reference axis (for instance the mean flow direction), and,
5) The orientation of the 2D face(s) with respect to the reference axis

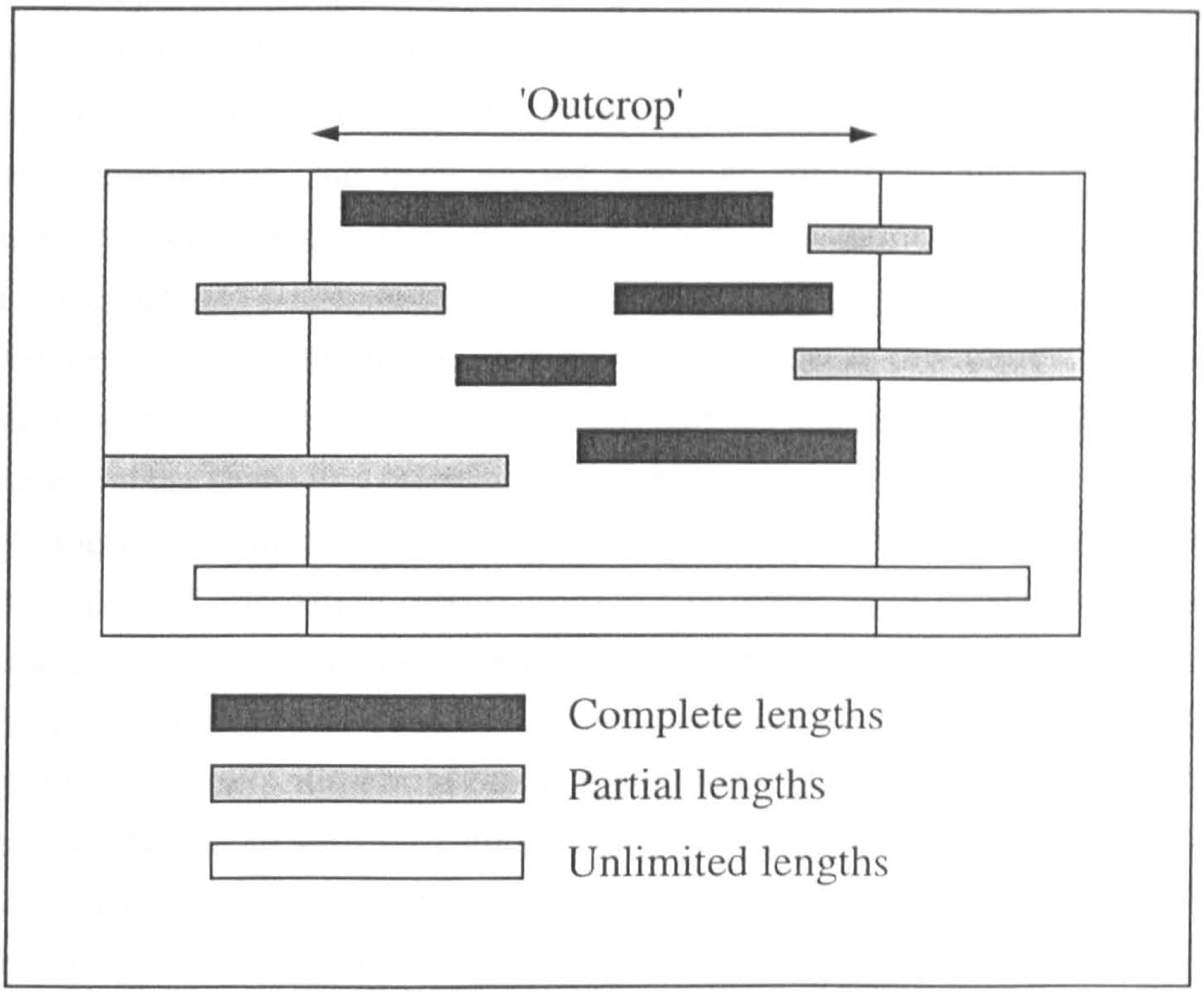

Figure 5.24. Definition of complete, partial and unlimited niche lengths from a 2D section. Vertical lines represent the limits of the exposed outcrop. Adapted from Geehan and Underwood (1993).

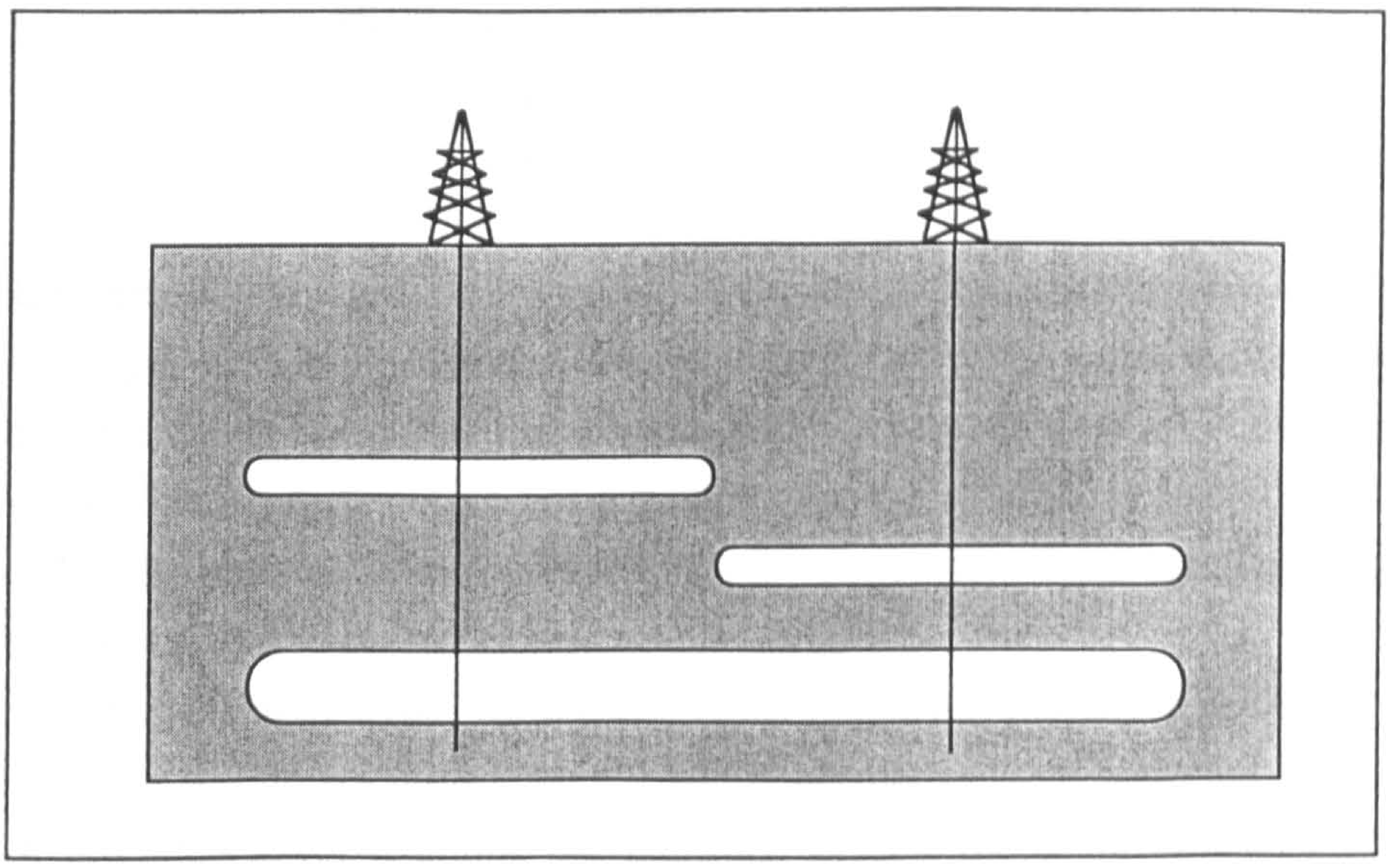

Figure 5.25. Illustration of 1D to 2D dimensionality correction from the subsurface. The shales have a true 2D distribution of 2 short to 1 long (2:1). However each well (1D sample) gives a 1:1 shale distribution, thereby biasing the resulting probability density function (PDF) towards the upper end of the length distribution. After Geehan and Underwood (1993).

Outcrop studies may be able to assign individual lengths to specific niches and identify partial and unlimited lengths but are rarely able to fulfil any of the other criteria. Consequently, work on solving the mathematical equations for these shape and orientation distributions has been limited, although solutions have been obtained for circular and elliptical discs assuming a fixed aspect ratio and orientation (King, 1988 as quoted in Geehan and Underwood, 1993). Additional criteria are met by this flume study since the mean flow direction is known and can be taken as the reference axis, and the orientation of the 2D slices with respect to this axis are also known. Information can also be gathered on the shape and orientation distributions of niches in planform using time-lapse photography during the experiment (Ashworth *et al.*, 1994). However, changes in surface shape and orientation distributions during subsequent preservation are poorly understood, although calculations of niche length/width ratios from cross-stream and downstream sections can be compared with planform data (Ashworth and Best, 1994). Sectioning the flume sediment at other orientations, or computer based interpolation between closely spaced sections could provide further information on changes in niche geometry during preservation. Consequently, further flume work coupled with more complex analytical solutions of niche geometries may provide the first true PDF's for individual niches in alluvial architecture.

For this present study, the simplifying assumption is made that the observed length class for each niche is isotropic, as incorporated in Geehan and Underwood's (1993) 2D to 3D stereology equation:

$$F_{3D}(L) = \frac{F_{2D}(L) \times 1/L}{\int_0^{\infty} (F_{2D}(L) \times 1/L)\, dL} \qquad \text{(Eq. 5.1)}$$

where L is length, and $F_{2D}(L)$ and $F_{3D}(L)$ are the frequency of occurrence of a particular length or length class in two dimensions and three dimensions, respectively. An example of the dimensionality correction for splay lengths from experiment B1 (Fig. 5.26) shows that the transformed distribution has a greatly increased number of small shales when compared to the untransformed distribution. This dimensionality correction is applied to all PDF's shown and discussed below.

Most of the niche types for the two experiments have strongly positively skewed PDF's, often with a lower cut-off below which no niches were recorded (Figs. 5.27 to 5.30). A few niches, for example bar margins, show a more uniform distribution for smaller lengths. Experiments B1 and B2 have very similar PDF's for coarse grained niches. However, there are differences between the finer grained distributions with

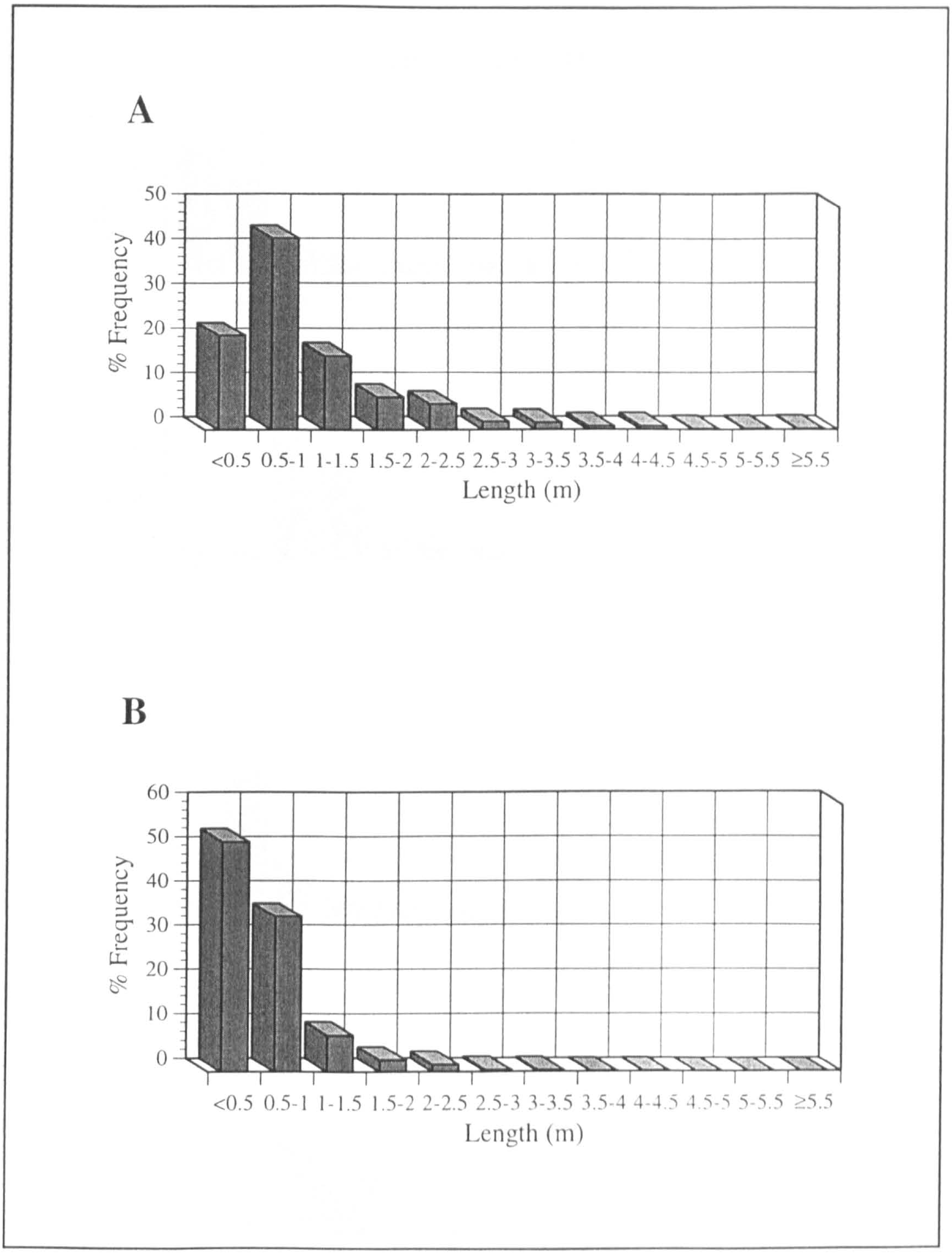

Figure 5.26. PDF 2D to 3D dimensionality correction using the stereology equation of Geehan and Underwood (1993). (a) PDF prior to transformation and (b) PDF after transformation. Splay lengths are taken from experiment B1.

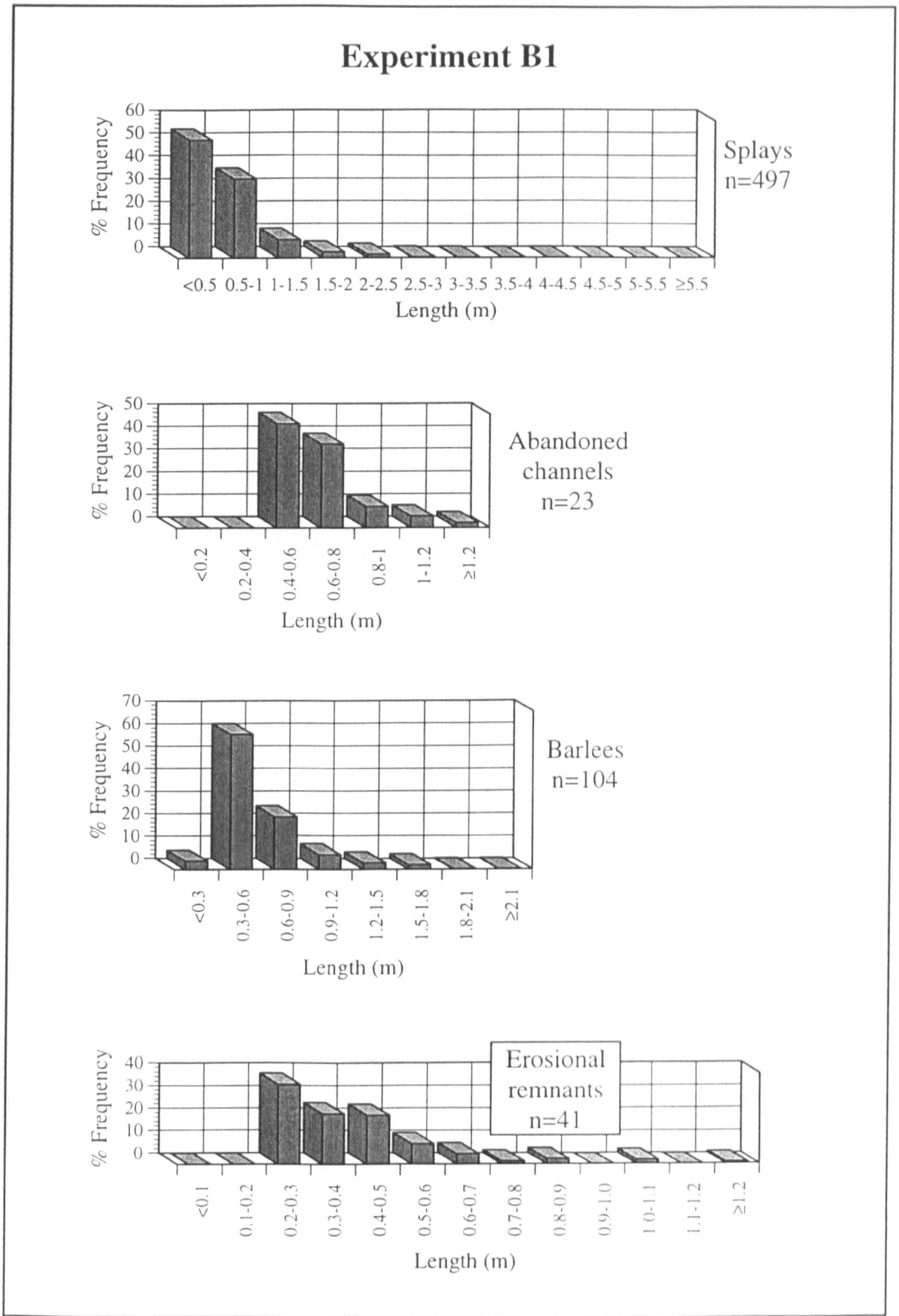

Experiment B1

Figure 5.27. PDF's for fine grained niches, experiment B1. PDF's have all been transformed using a 2D to 3D dimensionality correction. Note: frequency classes are not constant between different niches but are constant for individual niches between experiments.

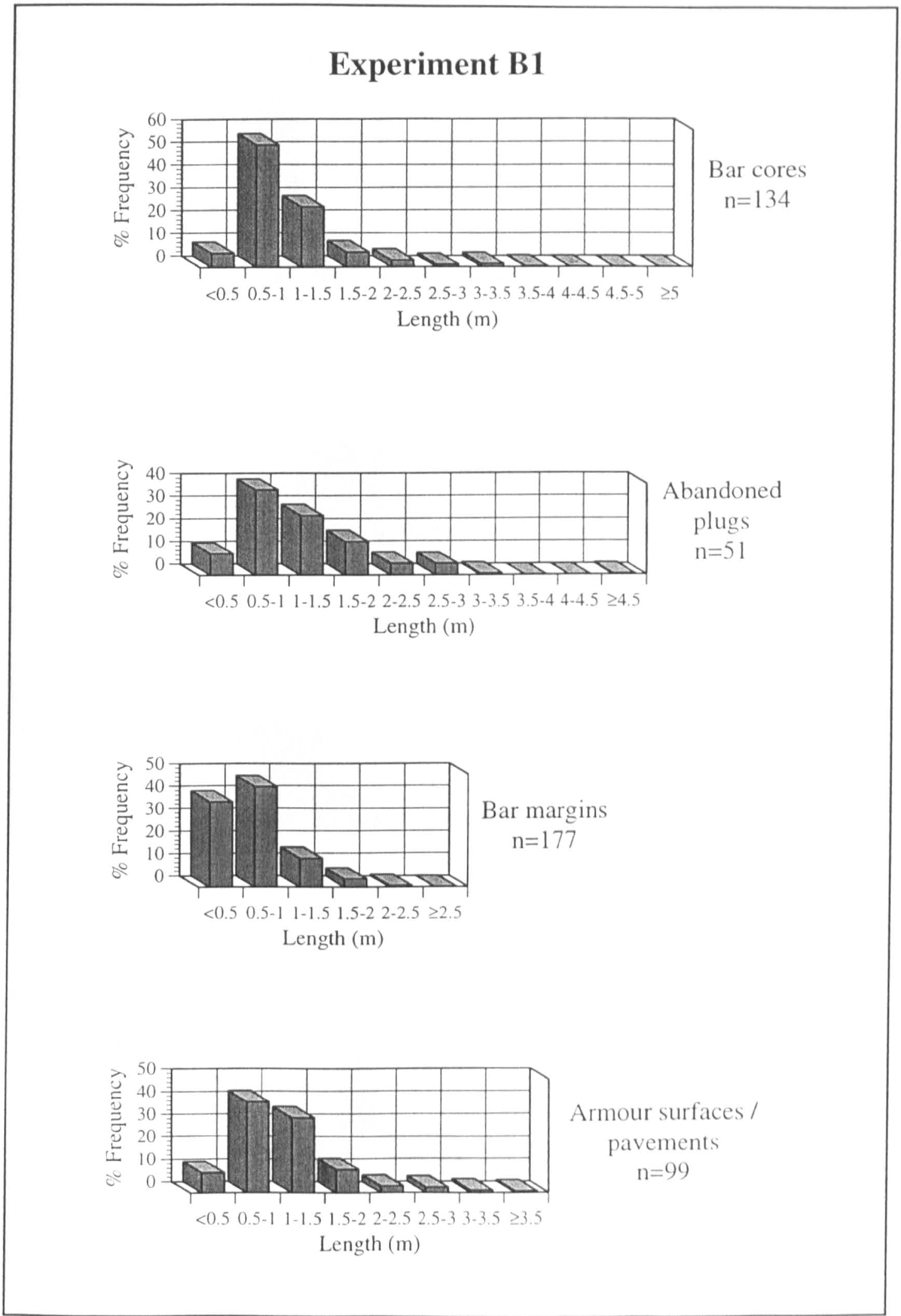

Figure 5.28. PDF's for coarse grained niches, experiment B1. PDF's have all been transformed using a 2D to 3D dimensionality correction. Note: frequency classes are not constant between different niches but are constant for individual niches between experiments.

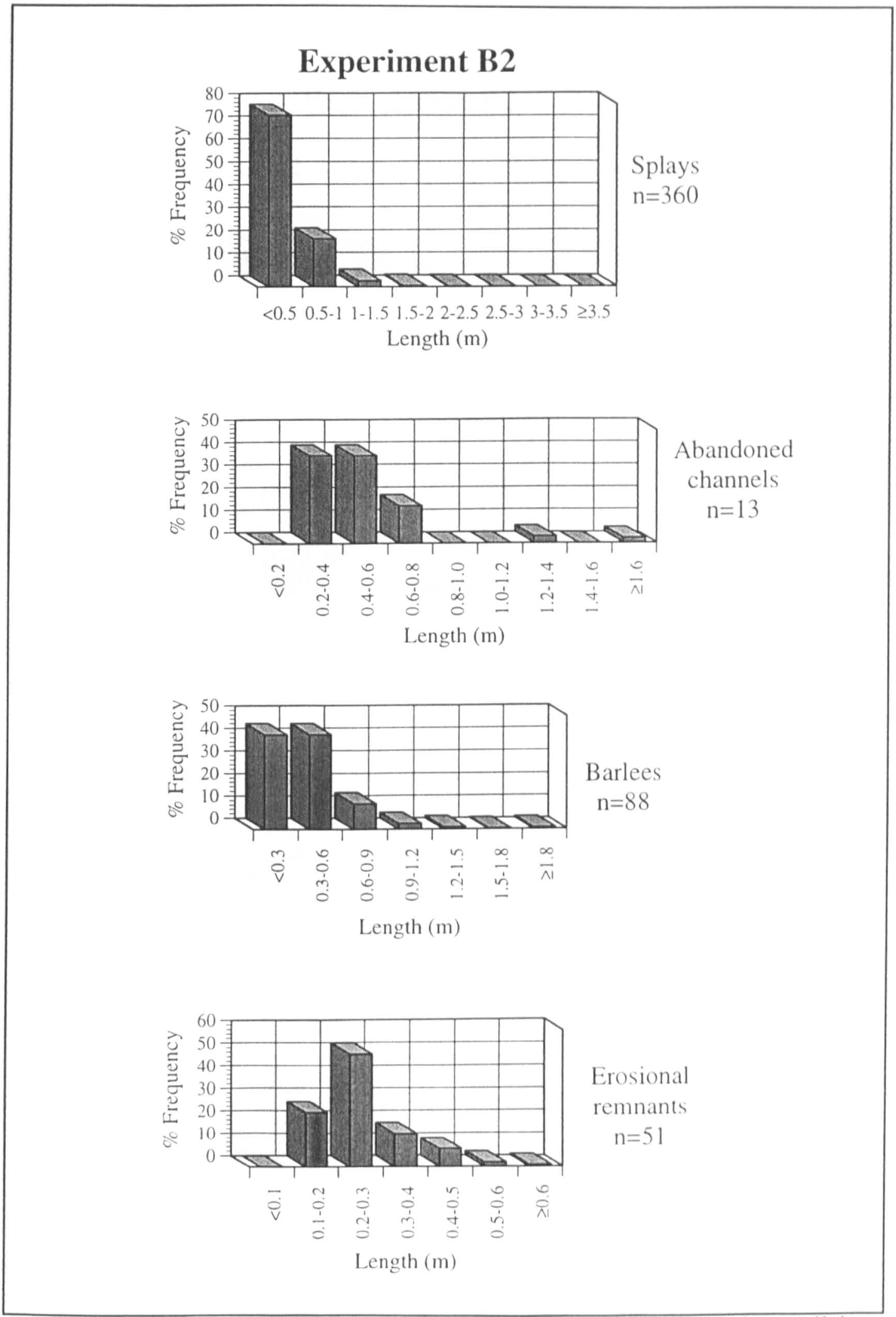

Figure 5.29. PDF's for fine grained niches, experiment B2. PDF's have all been transformed using a 2D to 3D dimensionality correction. Note: frequency classes are not constant between different niches but are constant for individual niches between experiments.

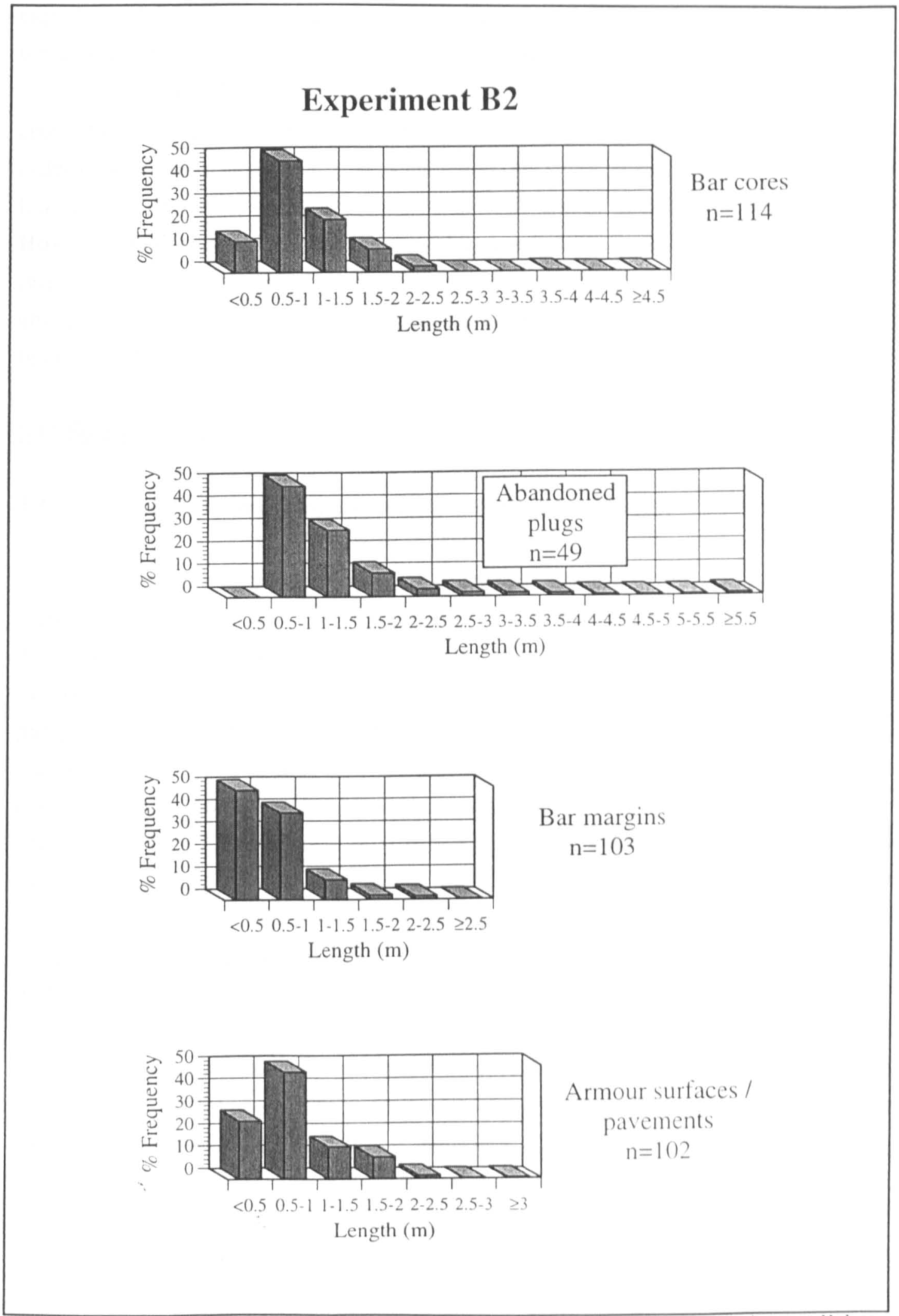

Figure 5.30. PDF's for coarse grained niches, experiment B2. PDF's have all been transformed using a 2D to 3D dimensionality correction. Note: frequency classes are not constant between different niches but are constant for individual niches between experiments.

experiment B2 having a much higher percentage of splays and barlees with lengths under 0.5 m and 0.3 m respectively than B1 (Figs. 5.27 and 5.29).

Individual PDF's have not been generated for pre- and post lateral tilting or for cross-stream proximity to the downtilted boundary, since this would require a database an order of magnitude larger than that collected in this study. Instead, mean and maximum lengths and areas are analysed in terms of their spatial distribution (Section 5.15). However, PDF's of niche lengths are widely used in stochastic reservoir simulations (e.g., Geehan *et al.*, 1986; Dranfield *et al.*, 1987; Begg *et al.*, 1989) and any spatial change in niche geometries due to lateral tilting must be quantified in terms of PDF's before the effects of lateral tilting can be incorporated into these stochastic models.

5.15 Spatial statistics

5.15.1 Criteria for the recognition of lateral tilting in the subsurface

Computer-based process models of half-graben alluvial architecture predict an increase in the number and interconnectedness of channels with increasing proximity to the down-tilted boundary (Fig. 1.2, Section 2.9). All of these models are based on avulsive down-dip channel movement. However, a combination of avulsive and progressive down-dip channel movement should also increase net to gross ratios of coarse to fine grained sediments close to the fault. Recent field studies of half-graben deposits demonstrate this spatial pattern of coarse grained sedimentation, but have not been able to distinguish between progressive and avulsive down-dip channel movement (Mack and Seager, 1990; Mack and James, 1993; Section 2.9). Three possible criteria have been previously identified from the study of Leeder and Alexander (1987) for recognition of progressive down-dip movement in the rock record (Section 2.9), only two of which are applicable for braided systems, namely:

1) an increase in the lateral extent of sandbodies (of single or multithread channel origin) relative to predicted values from general estimates of channel belt width (e.g., Collinson, 1978; Fielding and Crane, 1987; Bridge and Mackey, 1993b), and,

2) an increase in the width of channel belt sandbodies (of single or multithread channel origin) with increasing proximity to the basin-bounding or formerly active fault (see Fig. 2.16).

For both criteria, ancient gravel-bed rivers would show a contrast between coarse grained facies and sand or mud dominated overbank deposits. Subsurface data from experiments

B1 and B2 allow the progressive down-dip channel movement model of Leeder and Alexander (1987) to be tested for the first time. In addition, the two experiments allow a further test of the spatial distribution of coarse grained deposits predicted by half-graben process models.

5.15.2 Methodology

Spatial statistics for the alluvial architecture were generated by sub-dividing sedimentary niches on the basis of their centroid position. Each sediment face was divided into 11 (B1) or 10 (B2) equal segments in the cross-stream direction (Y-axis). To differentiate pre- and post tilted sediments in B1 and distinguish between tilt increments in B2, the sediment faces were also sub-divided in the vertical (Z-axis). The position of the vertical division is based on surface surveys immediately prior to tilting (B1) or on division of the sediment into three sections using the assumption of a constant basin-wide aggradation rate (B2). Both of these techniques produce irregular surfaces between vertical segments and therefore an average vertical (Z) value of the surface is taken for each cross-stream sub-division (see Fig. 5.31). A further complication is that sediment interfaces vary downstream (e.g., Fig. 5.20) and therefore Z values for each cross-stream increment were taken from an average of several sediment faces.

5.15.3 Experimental results

The percentage area occupied by coarse grained niches does not increase towards the downtilted margin in experiment B1, for either the lower untilted section or the upper tilted section (Fig. 5.32a). However, the lower and middle tilt increments of run B2 show a general increase in the area occupied by coarse grained niches, in the direction of tilting (Fig. 5.32b). Ordinary least squares (OLS) regression lines for the lower and middle sections of B2 have slopes of 0.271 and 0.249 which are significant at confidence levels of 84.7% and 96.6%, respectively (Table 5.15).

For experiment B1, the hypothesis of an increase in the lateral extent of sandbodies due to tilting can be tested by comparing the average coarse grained niche lengths for tilted and untilted sections. The upper tilted section of B1 has a mean coarse grained length of 1.42 m while the lower untilted section has a smaller mean length of 1.22 m (Table 5.12). In order to test for statistical significance between the two means, the shape of the distributions was first quantified. Both distributions are positively skewed and were tested for log-normality by transforming the length classes into natural logarithms and plotting against cumulative frequency on a probability scale (Fig. 5.33; R.B.G. Williams, 1984). The degree of log-normality is estimated by the closeness of fit

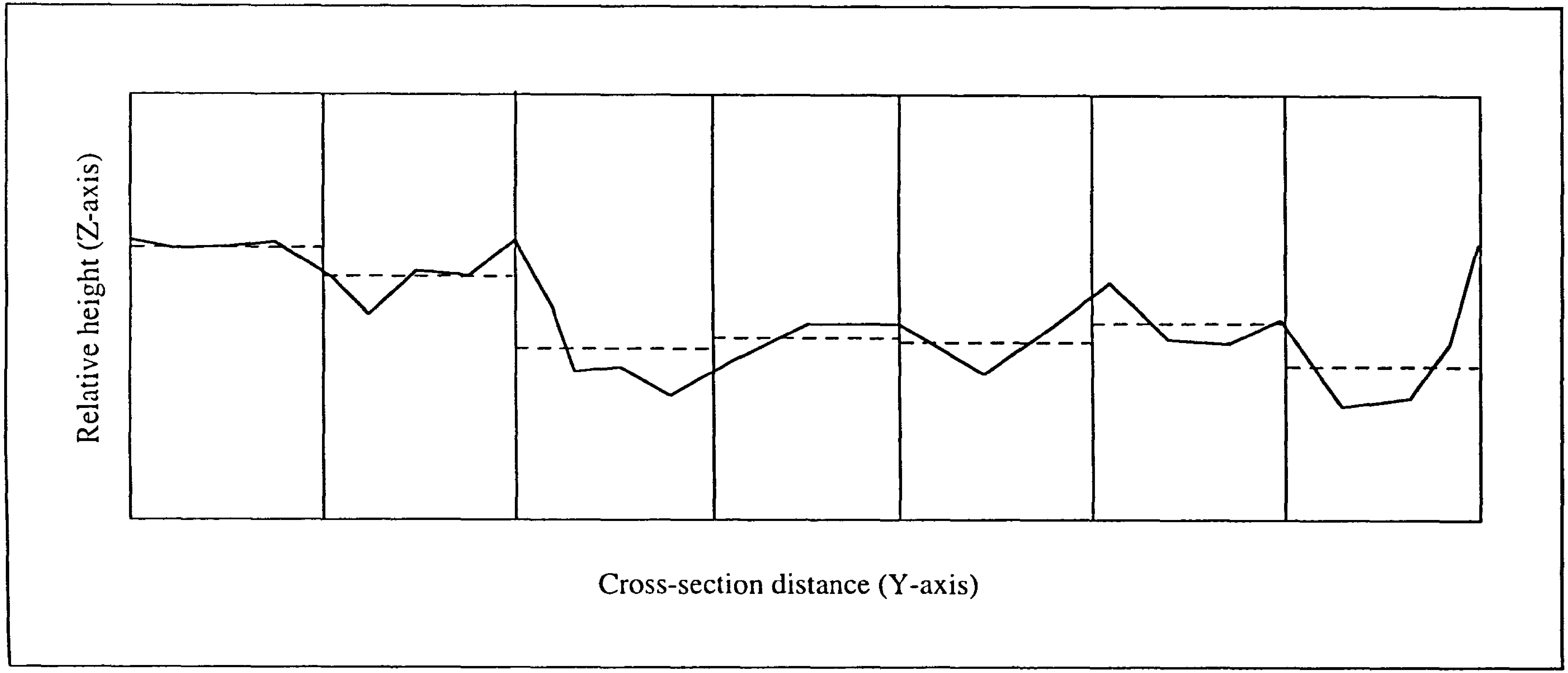

Figure 5.31. A hypothetical example of sediment face sub-division for the generation of spatial statistics. The face is first divided into equally spaced cross-stream segments. Vertical sub-divisions are based on plotting a known or inferred surface at the time of tilting on each face and then averaging the surface for each cross-stream increment.

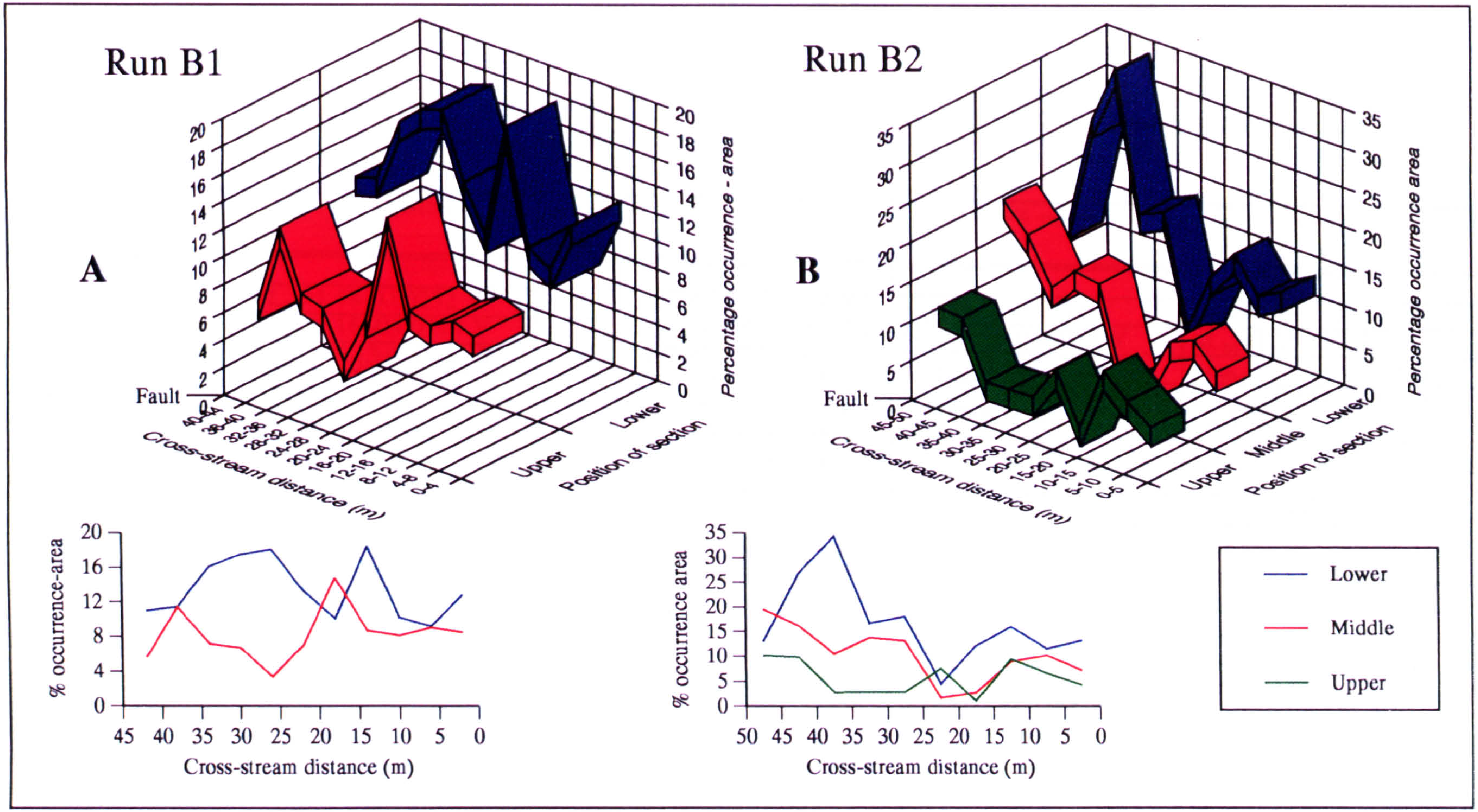

Figure 5.32. Spatial distribution of percentage area occupied by coarse grained niches, for experiment a) B1 and b) B2.

Table 5.15. Regression equations and confidence limits for spatial variation in mean and maximum niche lengths and percentage area occurrence

Parameters	Section position	Regression	Nº of points	SE $^{\alpha}$	p $^{\beta}$	r^2 $^{\gamma}$ (%)	95% min†	95% max†
Run B1								
nL_m on Y	Upper	nL_m=1.48-0.00252 Y	11	0.00453	0.592	3.3	nL_m=1.48-0.0114 Y	nL_m=1.48-0.00636 Y
nL_m on Y	Lower	nL_m=1.16+0.00310 Y	11	0.00356	0.407	7.8	nL_m=1.16-0.00388 Y	nL_m=1.16+0.0101 Y
nL_{max} on Y	Upper	nL_{max}=3.13+0.0136 Y	11	0.0265	0.621	2.8	nL_{max}=3.13-0.0384 Y	nL_{max}=3.13+0.0656 Y
nL_{max} on Y	Lower	nL_{max}=4.15-0.0251 Y	11	0.0302	0.427	7.1	nL_{max}=4.15-0.0843 Y	nL_{max}=4.15+0.0341 Y
nA on Y	Upper	nA=9.30-0.0523 Y	11	0.0735	0.491	5.4	nA=9.30-0.196 Y	nA=9.30-0.0919 Y
nA on Y	Lower	nA=12.3+0.0524 Y	11	0.0850	0.553	4.1	nA=12.3-0.114 Y	nA=12.3+0.219 Y
Run B2								
nL_m on Y	Upper	nL_m=1.27-0.00278 Y	10	0.00916	0.769	1.1	nL_m=1.27-0.0207 Y	nL_m=1.27+0.0152 Y
nL_m on Y	Middle	nL_m=0.835+0.00979 Y	10	0.00438	0.056	38.5	nL_m=0.835+0.00121 Y	nL_m=0.835+0.0184 Y
nL_m on Y	Lower	nL_m=0.981+0.0184 Y	10	0.00946	0.088	32.1	nL_m=0.981-0.000144 Y	nL_m=0.981+0.0369 Y
nL_{max} on Y	Upper	nL_{max}=2.35-0.00464 Y	10	0.0215	0.834	0.6	nL_{max}=2.35-0.0467 Y	nL_{max}=2.35-0.0374 Y
nL_{max} on Y	Middle	nL_{max}=0.887+0.0986 Y	10	0.0144	0.005	64.4	nL_{max}=0.887+0.0703 Y	nL_{max}=0.887+0.127 Y
nL_{max} on Y	Lower	nL_{max}=1.41+0.0986 Y	10	0.0498	0.083	32.9	nL_{max}=1.41+0.000962 Y	nL_{max}=1.41+0.196 Y
nA on Y	Upper	nA=4.41+0.0521 Y	10	0.0765	0.515	5.5	nA=4.41-0.0979 Y	nA=4.41+0.202 Y
nA on Y	Middle	nA=4.09+0.249 Y	10	0.0972	0.034	45.1	nA=4.09+0.0584 Y	nA=4.09+0.439 Y
nA on Y	Lower	nA=9.76+0.271 Y	10	0.171	0.153	23.8	nA=9.76-0.0648 Y	nA=9.76+0.607 Y

nL_m and nLmax = mean and maximum niche length, respectively. nA = niche percentage area occurrence. Y = cross-stream distance [α] SE= standard error of the mean gradient [β] p is the probability and p x 100 is the significance level (%). [γ] r^2= the coefficient of determination. [†] 95% confidence limits calculated using ±1.96 standard errors from the mean gradient.

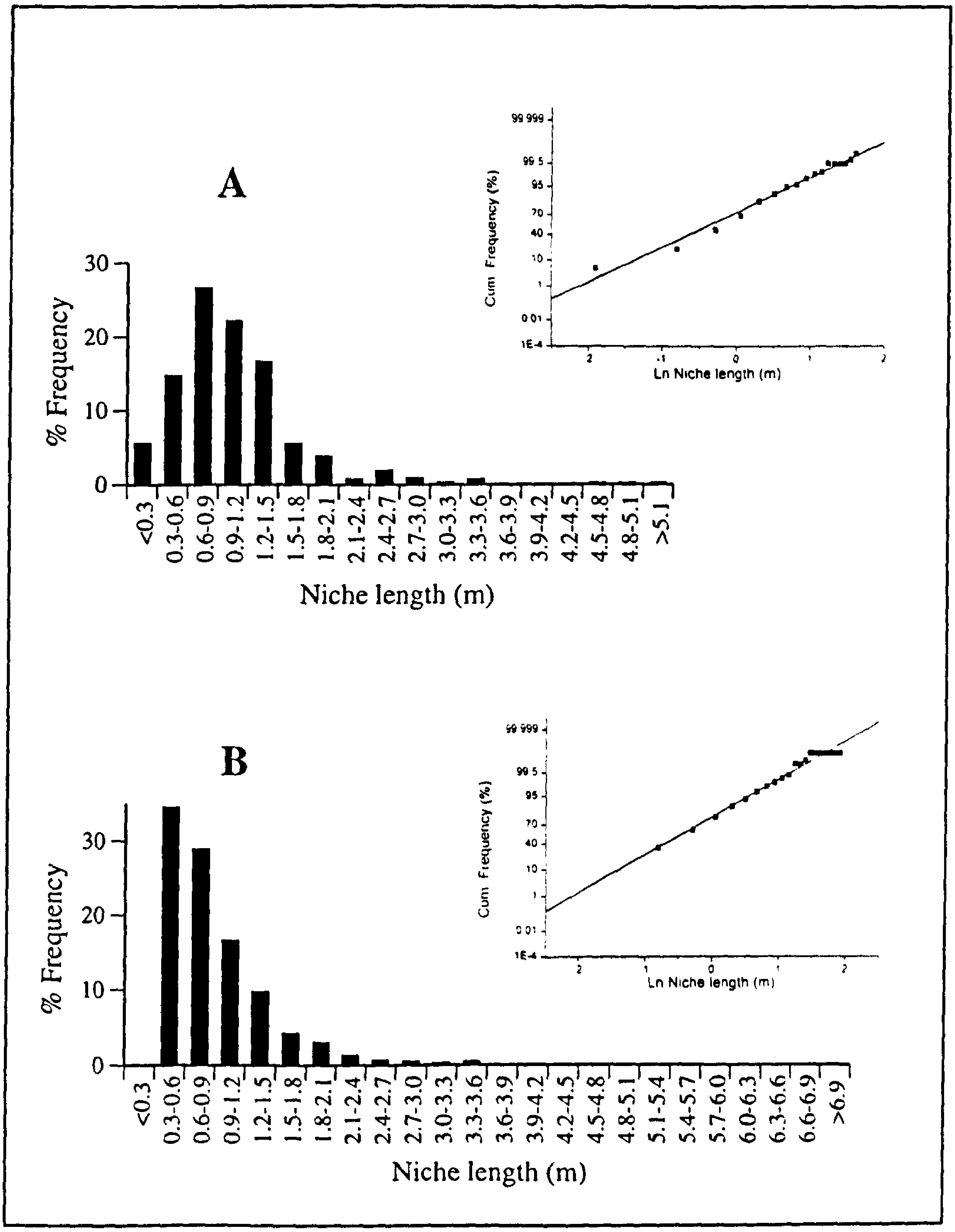

Figure 5.33. Estimation of log-normality for PDF's of; a) the upper, and, b) lower layers of experiment B1. The majority of each cumulative frequency distribution can be characterised by a straight line. The degree of log-normality is given by the strength of fit of a straight line for each log transformed cumulative frequency probability plot.

to a straight line. The lower section is strongly log-normal but the upper section has a distribution between normal and log-normal (Fig. 5.33). Consequently, the two means were compared for log transformed and untransformed distributions, using a two-tailed t-test. In both cases the difference between the means was significant with confidence levels of 98.0% (normal) and 99.1% (log-normal). The three tilt increments of experiment B2 allow the relationship between mean coarse grained niche lengths and the magnitude of tilting, to be analysed. The lower layer had a total tilt increment of 0.24-0.45% which varied downstream (see Section 5.10) and has a mean coarse grained niche length of 1.38 m, while the middle and upper layers were tilted by 0.1% and have mean lengths of 1.09 m and 1.17 m respectively (Table 5.14). All three distributions approximate to a log-normal distribution (Fig. 5.34) and therefore the PDF's were transformed using the natural logarithm. A comparison of means for the log transformed distributions, indicates that both the middle and upper layers, statistically differ from the lower layer (confidence levels of 98.4% and 79%, respectively) but exhibit a much weaker relationship with each other (confidence level of 59%), which suggests a direct correlation between coarse grained niche length and tilt magnitude.

The position of the vertical sediment sections affected by the largest tilt increments also differ between the two experiments, which further suggests that lateral tilting is the controlling factor and that the vertical changes in niche length are not due to an intrinsic factor such as fan progradation / aggradation leading to changes in depositional style. Together experiments B1 and B2 lend support to the hypothesis of increased sandbody or coarse grained niche length, with lateral tilting. However, there are a number of qualifiers to this conclusion, which include a limited knowledge of intrinsic experimental variability and the lack of comparative statistics from untilted runs (see Section 5.13).

The second hypothesis for the recognition of progressive down-dip channel movement is that the length (in a cross-stream orientation) of coarse grained niches increases towards the fault, reflecting increased tilting close to the fault. As the stream table base is rigid, applied lateral tilts were linearly distributed across the flume. However, the alluvial fan that forms during a run (Section 5.10) produces the same surface morphology as that produced by a growth fold on the basin margin, with increasing lateral slopes towards the downtilted boundary. Mean and maximum coarse grained niche lengths for experiment B1 do not show a statistical significant increase towards the downtilted boundary (Fig. 5.35; Table 5.15). In contrast, corresponding values for run B2 do show a weak correlation (r^2=32.1% to 64.4%) between increasing length and proximity to the downtilted boundary, for the lower and middle sections (Fig. 5.36). All the correlations are statistically significant at a confidence level of 90%, with the variation in the maximum coarse grained niche length of the middle section, significant at a confidence level of 99.5% (Table 5.15). These changes cannot be attributed to variations in the cross-stream frequency of occurrence of

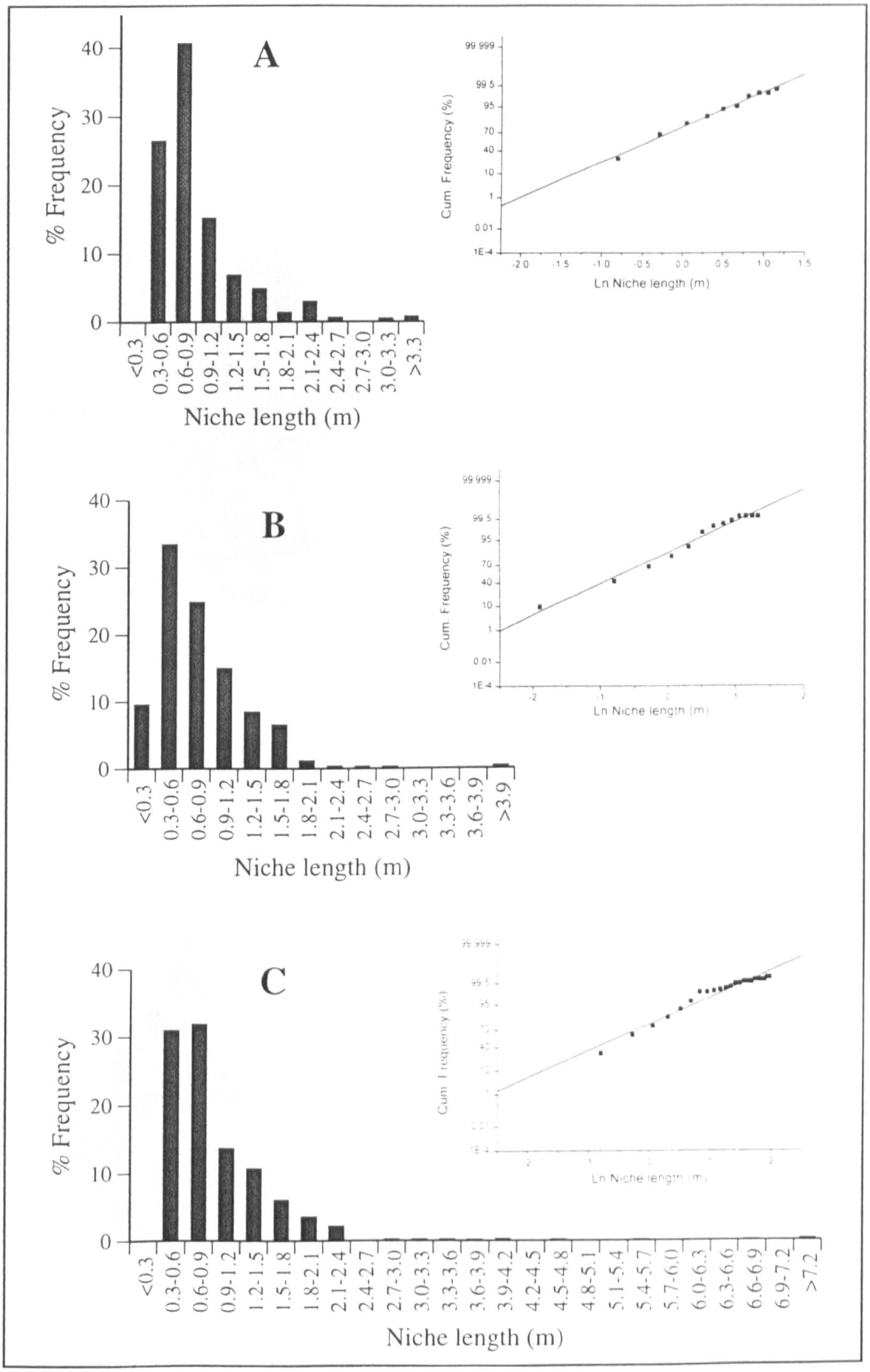

Figure 5.34. Estimation of log-normality for PDF's of, a) the upper, b) middle and c) lower layers of experiment B2. The majority of each cumulative frequency distribution can be characterised by a straight line. The degree of log-normality is given by the strength of fit of a straight line for each log transformed cumulative frequency probability plot.

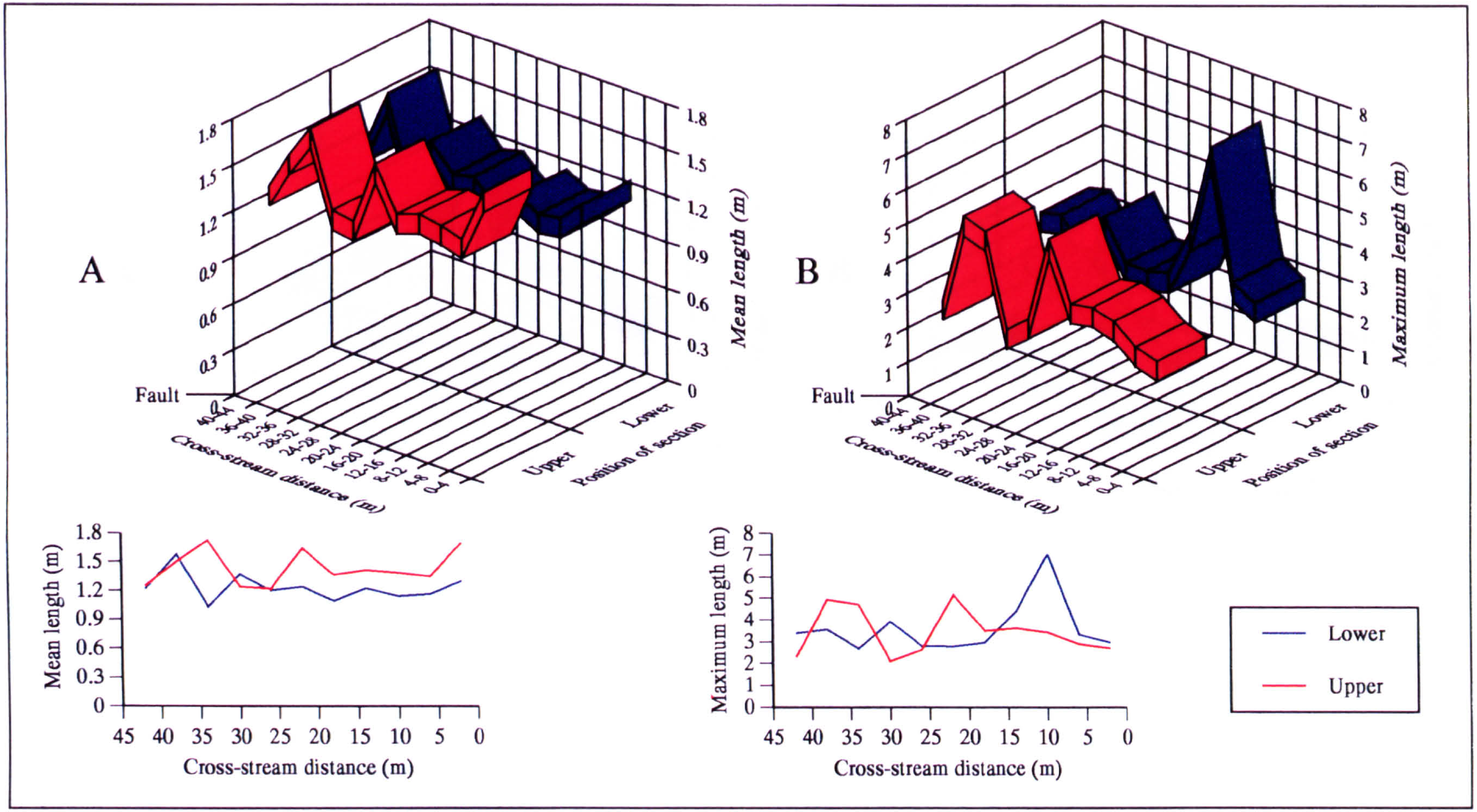

Figure 5.35. Spatial distribution of a) mean and b) maximum lengths for coarse grained niches in experiment B1.

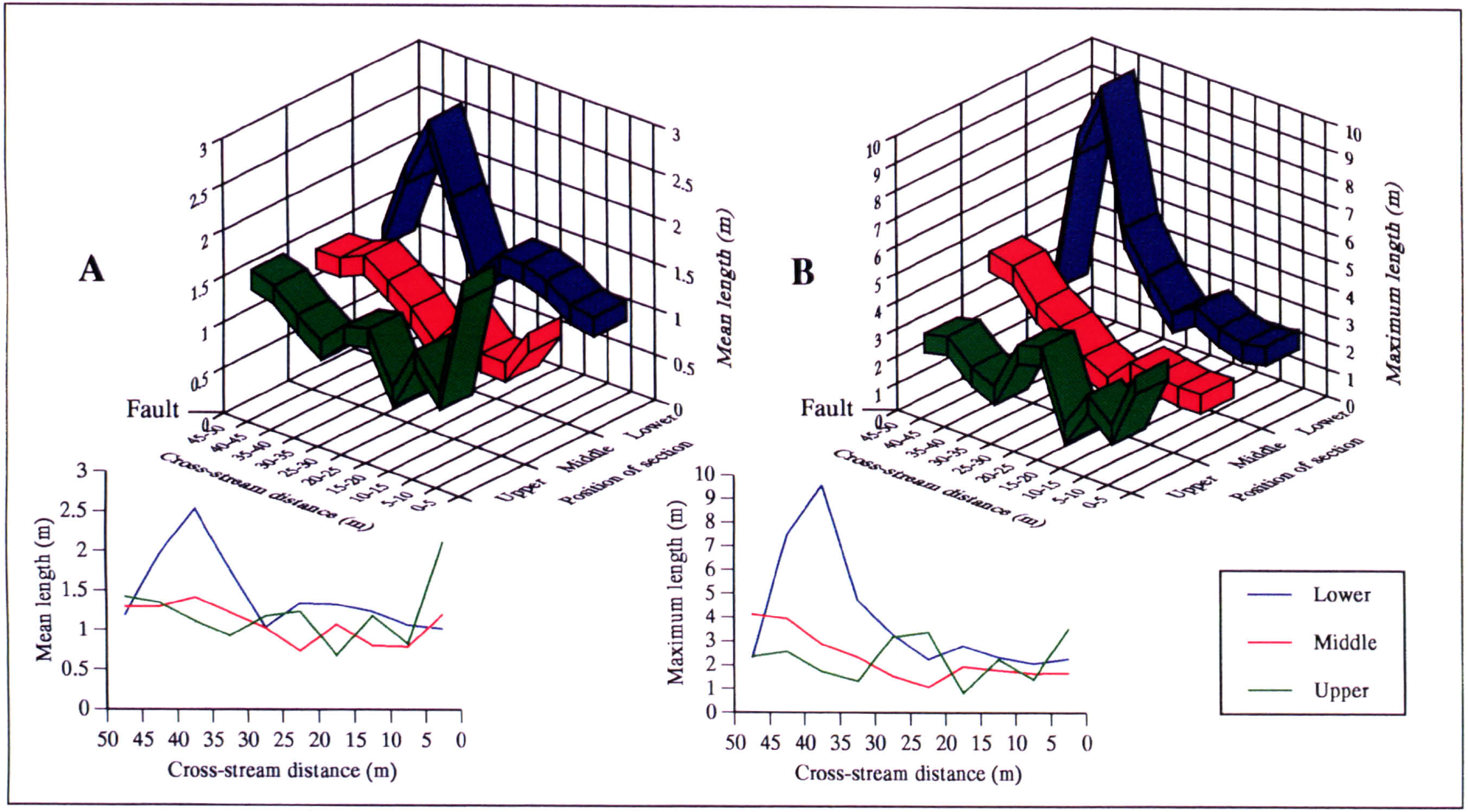

Figure 5.36. Spatial distribution of a) mean and b) maximum lengths for coarse grained niches in experiment B2.

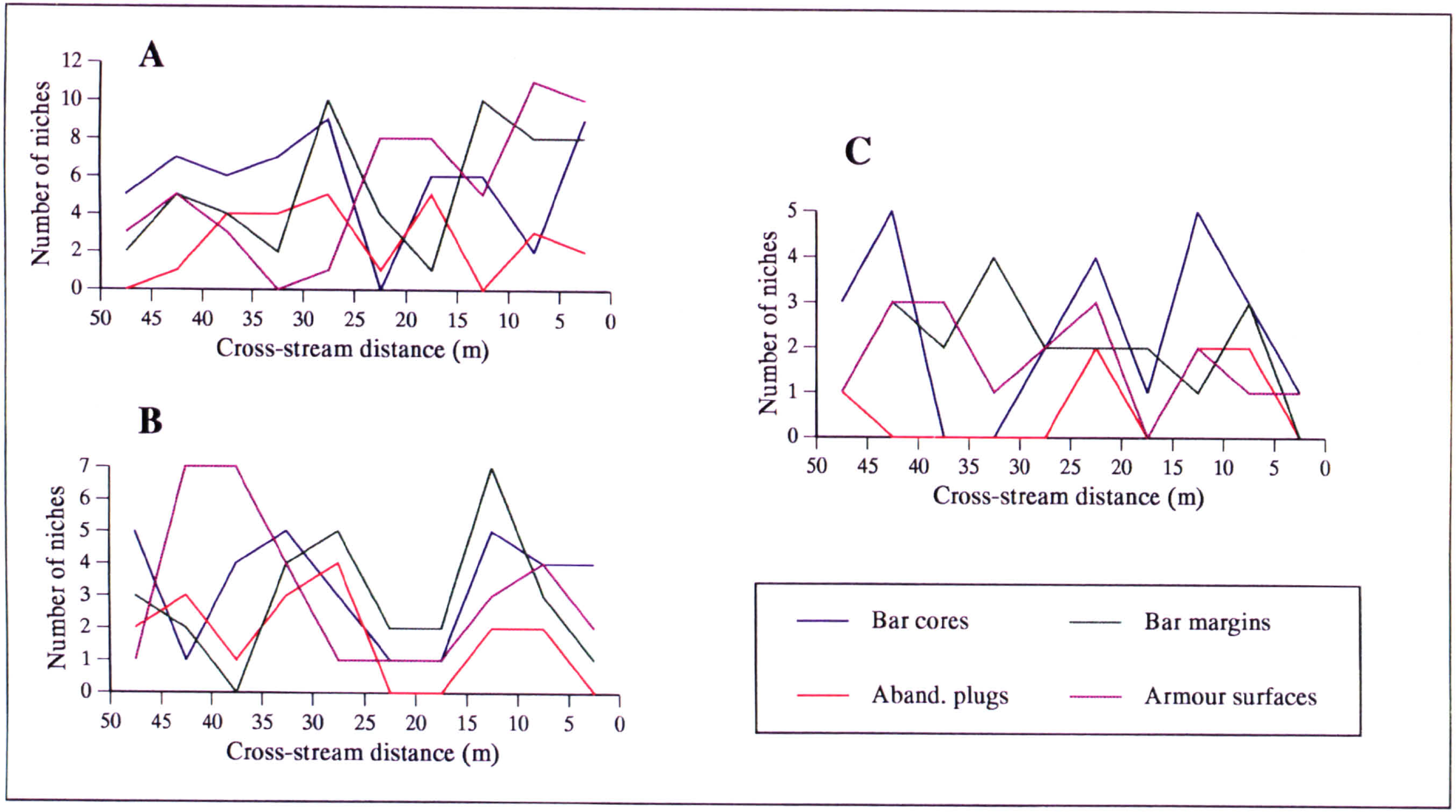

Figure 5.37. Spatial variation in the occurrence of coarse grained niches for individual tilted segments of experiment B2. a) lower segment, b) middle segment and c) upper segment.

different coarse grained niches, since these show no clear patterns with respect to the Y-axis (Fig. 5.37). Instead, the changes must be due to increasing lengths of the individual niches.

5.15.4 Limitations of spatial statistics

There are a number of limitations to these spatial statistics, namely:

1) There is an initial coarse grained depositional bias caused by rapid aggradation in the cut channel.

2) The use of the centroid as the sole criterion of niche position. Individual niches may encompass several cross-stream segments but the total length or area is assigned to the segment containing the centroid. This particularly affects the two ends of each section where maximum lengths are restricted to the length of the cross-stream segment. For example, the maximum length of coarse grained niches in run B2 (Fig. 5.36b) is >9 m and is located just 10 m from the boundary. The maximum possible length for the final segment is just 5 m and therefore the length distribution must decrease irrespective of the underlying pattern.

3) The exclusion of partial length statistics. This limitation affects the ends of each section and the upper boundary, resulting in a reduction of the percentage area occurrence values (Fig. 5.32). In addition, partial length exclusion reinforces the effects of using the centroid for niche position, by further limiting maximum and mean lengths / areas at each end of the section.

4) The use of a limited number of cross-stream segments, namely 11 for B1 and 10 for B2. Further segmentation would have required a larger sample size and would have increased the effects of using the centroid as the sole criterion of niche position.

The combined effect of these limitations therefore serves to restrict the strength and statistical significance of the correlations.

5.16 Discussion

The results from experiments B1 and B2 suggest there are differences between the two experiments, with B2 showing significant correlations between niche geometries and proximity to the downtilted boundary whilst B1 shows no significant relationship to fault position. All experimental parameters were kept constant between the two runs with the exception of four factors; 1) the total run time, 2) the total number of hydrographs, 3) the grain-size distribution which showed a progressive reduction of the finest grades, and 4) the timing and magnitude of the applied lateral tilting. Intrinsic variability between experiments can be ruled out as a possible cause of the observed differences, since the significance levels for the observed correlations in B2 are too high to be attributed to randomness. Equally, variation in the total run time, the number of hydrographs or the gradual diminution of fine grained sediment, appear incapable of providing a causative mechanism for the lateral variation of niche parameters. Therefore, it is concluded that the timing and magnitude of the applied tilting must account for the differences in the cross-stream distribution of niche geometries between experiments.

In the absence of an applied lateral tilt, fan gradients produce no observable cross-stream variation in niche parameters (lower section of B1). Therefore, the magnitude of the applied lateral slopes cannot be directly responsible for the observed differences between the two experiments, since they are an order of magnitude smaller than the alluvial fan gradients (Table 5.6). Instead, it appears that the timing and magnitude of the lateral tilting must be influencing a secondary controlling parameter. Alluvial fan morphology in the flume is controlled by a continuous process of nodal avulsion and localised aggradation and degradation. As a consequence, channels are usually evenly distributed and have only limited lateral movement. However, when an external lateral tilt is applied, the gradual aggradation and progradation (i.e., the dynamic equilibrium) of the fan is perturbed, reducing the capacity for symmetrical nodal avulsion. Most of the flow is directed towards the downtilted side of the fan, producing wider, deeper channels. With the reduction in nodal avulsion, channels can progressively migrate down the alluvial fan surface, producing a lateral variation in niche geometries.

Experiment B1 had a single imposed tilt of 0.3% at the mid-point of the run which caused large scale aggradation on the downtilt side of the fan (Section 5.10; Figs. 5.18 and 5.19). However, when averaged across the analysed sections (cross-stream position ≈1.2-3.2 m), the aggradation directly associated with tilting only accounted for approximately 15% of the total post-tilt aggradation (see Figs. 5.18 and 5.19). In contrast, run B2 had a greater total tilt, with three equally spaced tilt increments of 0.1% and an initial surface which had lateral gradients between 0.14-0.35% (Section 5.10). Unfortunately, detailed topographic cross-sections were not taken at regular intervals during run B2 and therefore the interaction between tilting and aggradation cannot be isolated in the same manner as experiment B1. However, if the tilt increment is large enough to perturb the dynamic equilibrium of the fan, then the resulting aggradation will be dominantly on the downtilted side. The three tilt increments along with the initial lateral gradient of run B2 were associated with approximately the same total aggradation as the single tilt increment of experiment B1. Therefore, it is proposed that the lateral variations associated with the single tilt increment of B1 are masked by the 85% of the sediment that is not directly affected by tilting. In contrast, the four tilt increments of B2 show strongly significant correlations for lateral variations in niche geometry. The lateral variations in run B2 do not reflect the magnitude of the imposed tilting but instead reflect the combination of the alluvial fan and applied slopes. The imposed tilt merely acts as a 'trigger' to perturb the alluvial fan system from a state of dynamic equilibrium.

In contrast, both experiments show a correlation between mean coarse grained niche length and tilt magnitude for individual vertical tilt increments. This relationship might be expected for run B2 due to increasing coarse grained niche lengths with proximity to the locus of maximum subsidence. However, the underlying process(es) that controlled the variation of coarse grained niche lengths in run B1 are difficult to quantify, since the importance of inherent or internal factors relative to lateral tilting effects cannot be estimated. Comparative statistics from a similar untilted experiment are required in order to assess the significance of these internal factors.

5.17 Comparison with field examples of lateral tilting

Both experiments had similar axial:downstream slope ratios to field examples of laterally tilted rivers, with B1 having a range of 20-164% (see Table 2.3). Estimation of tilt rates is more difficult since model time can be scaled in several different ways (Section 3.9). Nominally, the model time scale (λ_t) is equal to $(\lambda_L)^{0.5}$, while the gradient is not scaled, since it is dimensionless. On this basis, average tilt rates for B1 and B2 are 8.2 and 34.8 radians per 1000 years, which is several orders of magnitude greater than rates observed in the field (3×10^{-2}-5×10^{-7} radians / 1000 years; Table 2.3). However, these values can be questioned since processes such as basin-wide aggradation have already been shown to have rates in the flume experiments that are several orders of magnitude larger than long term rates from field studies (Section 5.8). Perturbation of an alluvial fan or river system also appears to be important in field studies, as shown by the Carson River, Nevada, where there is a strong relationship between faulting events and avulsive movement towards the fault (Chapter 7).

5.18 Summary of braided river experiments

Two braided river model experiments were run to investigate the effects of lateral tilting on channel migration and deposition. Aggradation was imposed on each experiment and since the inlet position was fixed a braided river system similar to a low-gradient alluvial fan developed. General descriptive statistics for different depositional niche geometries and their associated probability density functions were derived for the two experiments. There are a number of difficulties in producing true PDF's from outcrop or flume data. However, similar experiments, coupled with improved algebraic solutions, have the potential for producing true PDF's of individual niches for the first time.

Spatial statistics were generated by dividing the niches on the basis of their centroid positions into a series of cross-stream and vertical segments. A direct correlation between mean coarse grained niche length and the magnitude of tilting is present for different tilt increments in both experiments B1 and B2. However, comparative statistics are required from similar untilted experiments in order to fully validate that tilting is the controlling factor. The two experiments also showed differing results in terms of variations in niche statistics with cross-stream direction, with run B2 producing statistically significant correlations between niche geometries and proximity to the downtilted boundary, while B1 showed no significant correlations. These differences in spatial statistics between experiments may be explained in terms of the magnitude, timing and frequency of imposed lateral tilting events. Each tilt event perturbs the dynamic equilibrium of the alluvial fan, limiting nodal avulsion and allowing channels to progressively migrate down the fan surface. The four tilting events of experiment B2 produce strong lateral variations in niche geometries, while the spatial effects of the single tilt event in run B1 are masked by the ambient sedimentation after initial aggradation on the downthrown side.

Increases in coarse grained lengths with increasing proximity to a downtilted margin, and an increase in mean coarse grained niche length with tilting are two of three criteria identified from the study of Leeder and Alexander (1987) for the recognition of progressive down-dip channel movement in the rock record. In addition, they are the only parameters applicable to a braided river environment. Experiment B2 shows statistically significant correlations for both of these relationships and is therefore the first experimental or field based study to identify progressive down-dip channel movement. In addition, run B2 displays an increase in the percentage area occupied by coarse grained niches with proximity to the downtilted margin, which is in agreement with 2D process-based alluvial architecture models.

Chapter 6.
Meander Morphometry and Palaeohydrological Analysis

6.1 Synopsis

The study of meander morphometry has led to the definition of a series of empirically derived relationships between bend parameters which are the basis for the majority of palaeohydrological analyses of single thread channels. This chapter reviews the different approaches to measuring the meander planform and examines the definitions of each of the planform variables. Two new techniques for measuring and analysing morphometric data from meandering rivers are presented and discussed. Finally, the existing equations for the prediction of palaeodischarge are reviewed and more precise relationships defined using an enlarged database. These new equations, bend definitions and measurement techniques are used for palaeohydrological analysis of the Carson River in Chapter 7.

6.2 Approaches to meander planform analysis

The approaches to meander planform analysis can be sub-divided into four broad categories (Fig. 6.1); spatial series / spectral analysis, curve fitting, graphical methods and bend parameters (Hooke, 1984). There is a wide range in the degree of objectiveness between categories, from spectral analysis, which relies exclusively on the stream courses being digitised and then analysed numerically, through to the graphical methods which may be highly subjective.

6.2.1 Spatial series / spectral analysis

Spatial series and spectral analysis are two techniques for analysing a series dataset. For meandering rivers, the dataset is produced by digitising the centreline (Hooke, 1977a) or the thalweg (Ferguson, 1975) and can either be directional or curvature based (Fig. 6.2). An example of the application of spatial series analysis to meanders is the recognition of different bend types through a comparison of curvature with distance (Leighly, 1936). Spectral analysis is a powerful tool for examining series

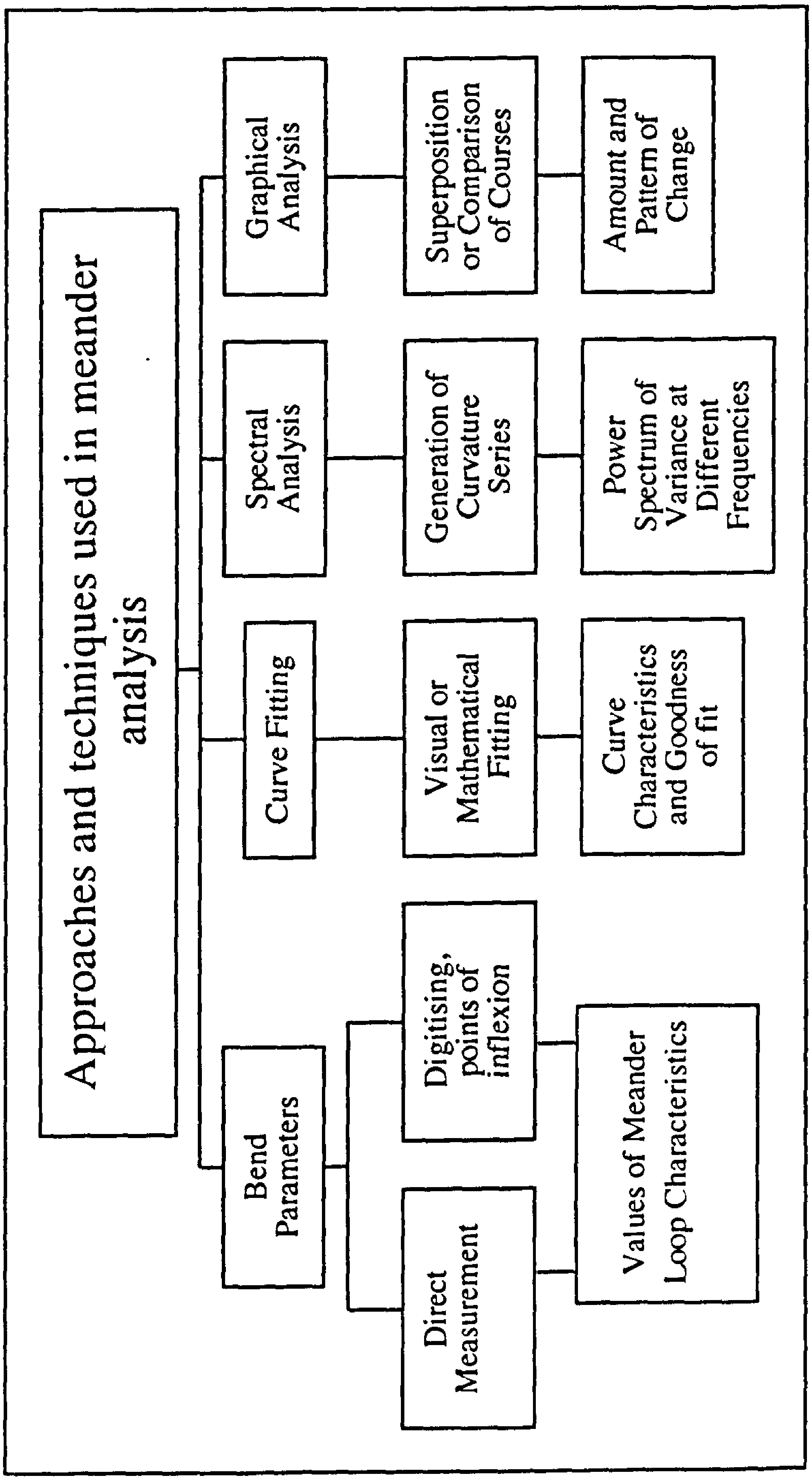

Figure 6.1. Approaches and techniques used in meander analysis. Adapted from Hooke, (1984).

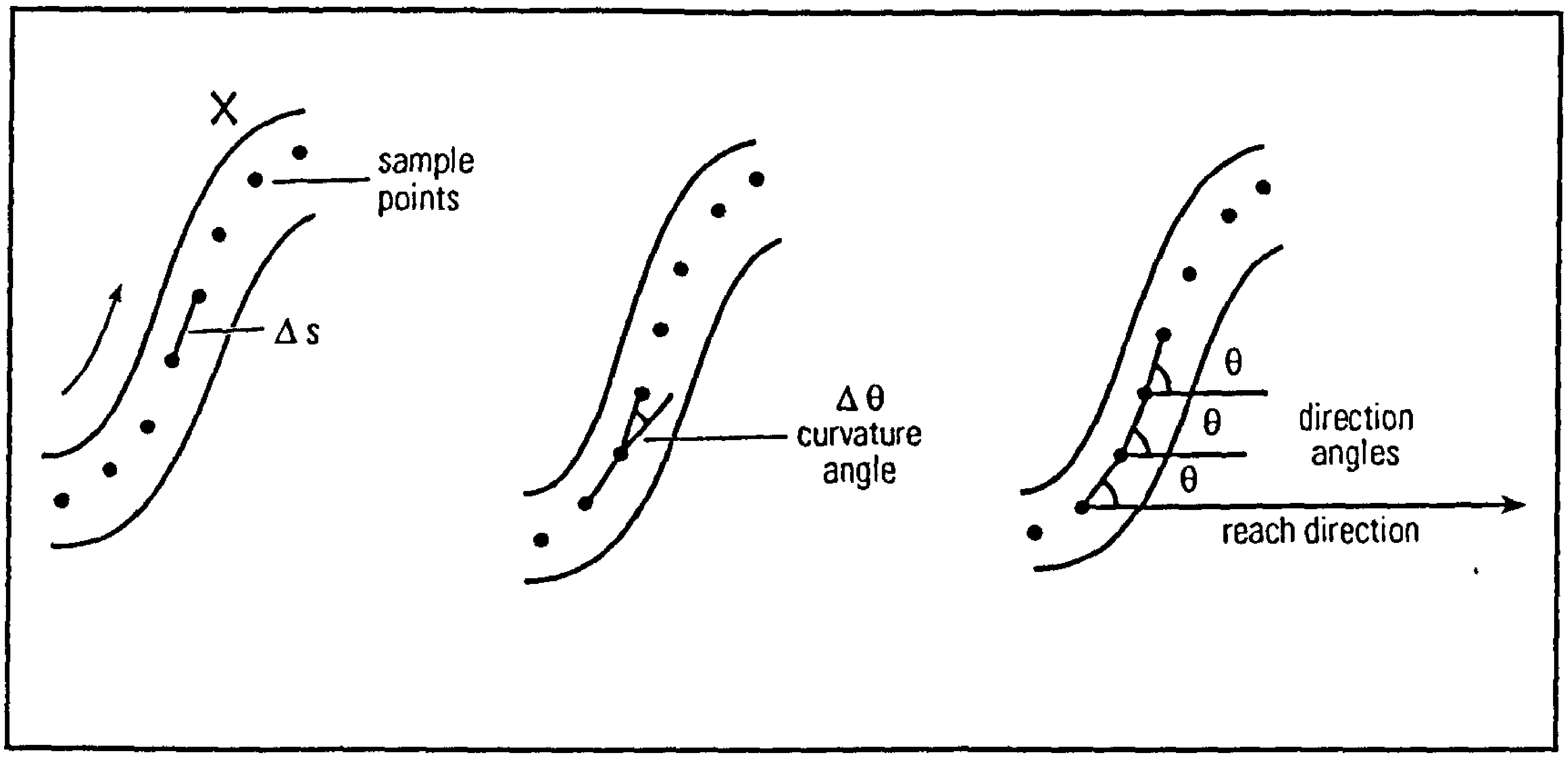

Figure 6.2. Sampling for series analysis: direction (θ) and curvature (Δθ) series. Δs represents the distance between sample points. From Richards, (1982).

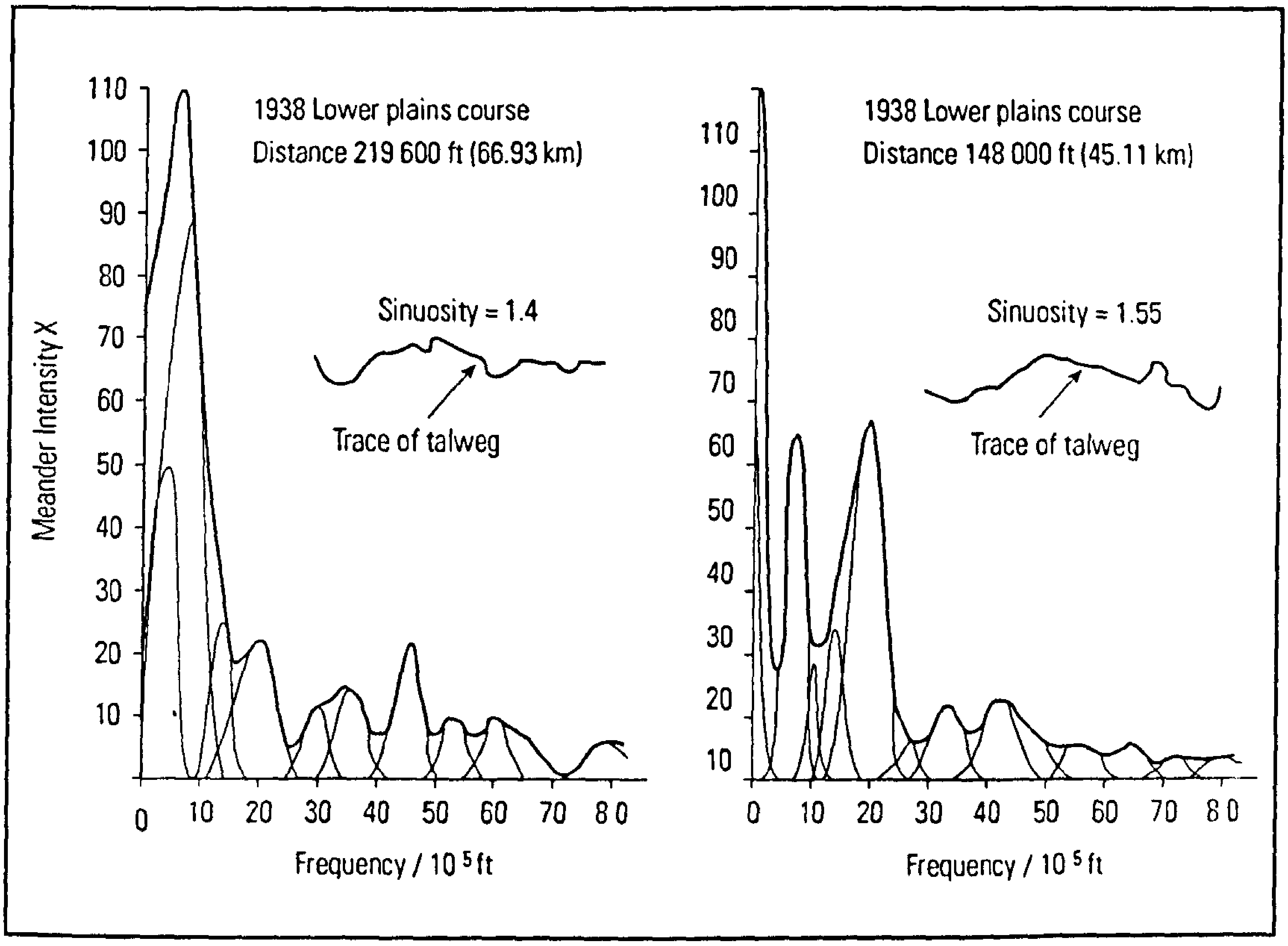

Figure 6.3. Meander spectra for reaches of the Angabunga River, with insets of the central reach segment. After Speight (1965a).

datasets since it separates the series into a spectral envelope consisting of a set of peaks (Fig. 6.3), with the area under the curve representing the variance. Spectral analysis provides an objective method for estimating characteristic values of bend parameters, and for indicating the overall regularity of the pattern. Both Hjulström (1949) and Schumm (1963) have suggested that a meandering river may have more than one characteristic wavelength, and spectral analysis has been used to identify these multiple wavelengths (Speight, 1965a, b; Ferguson, 1976). In addition, the direction variance from the power spectrum of a meandering river, shows a strong correlation with sinuosity (Fig. 6.4) and can be used as a surrogate for sinuosity in palaeohydrological studies, where only parts of a meander planform have been preserved (Ferguson, 1977).

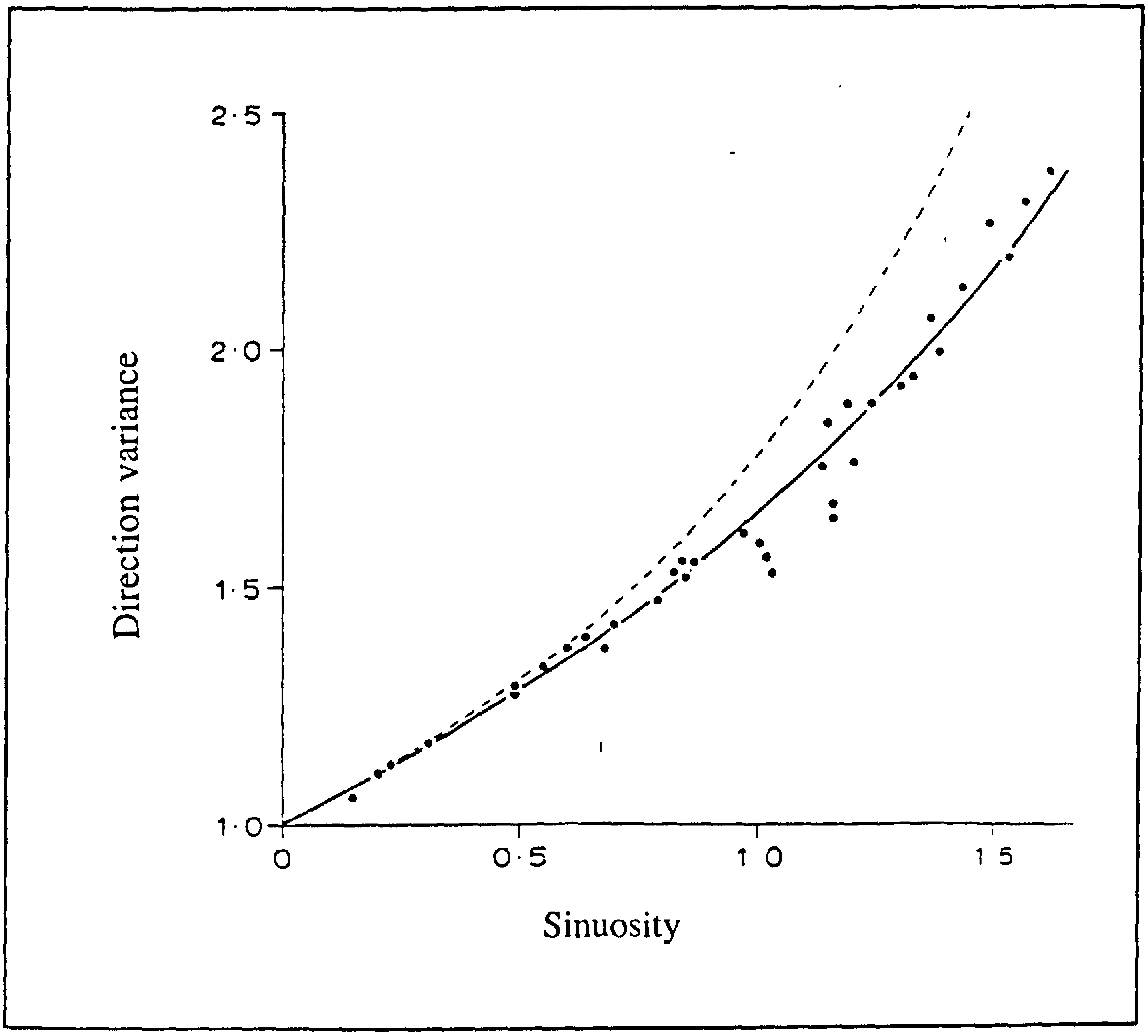

Figure 6.4. Plot of sinuosity against direction variance for meandering rivers, with expected relationships for sine-generated curves (broken line) and the normal direction distribution (solid line). Variance refers to directions in radians: to convert to degrees, multiply by 3.283. After Ferguson (1977).

Speight (1965a) identifies three factors which affect the resolution and reliability of the spectrum:

1) spacing of points in the series dataset
2) the total number of points in the series, and
3) the frequency step used to analyse the data.

A spatial sampling resolution of about one channel width has been found to be the most suitable spacing (Hooke, 1984). A higher sampling resolution leads to the generation of significant 'noise', which is characterised by large numbers of inflection points and small bends. The analysis is very sensitive to the chosen frequency step, since small changes may cause large differences to the predicted characteristic wavelength (Hooke, 1977b, 1984). However, the most significant problem in applying spectral analysis to meandering rivers is that most meandering reaches are not sufficiently regular for a suitably sized homogeneous dataset to be collected. For example, the entry of a tributary, or a sudden change in valley gradient, will affect bend parameters and therefore the spectral analysis.

6.2.2 Curve fitting

A range of mathematically derived curves have been fitted to meanders, including the sine curve (Bates, 1939; Leopold and Wolman, 1957), the sine-generated curve (Langbein and Leopold, 1966) and the Van Schelling and Fargue's spiral curves (Ferguson, 1975). Although Yalin (1992) argues that the sine-generated curve is the best approximation of a meandering thalweg, Leopold and Langbein (1966, p.63) state that "river meanders... deviate in a random way from the perfect symmetry of a sine-generated curve ..". Weihaupt (1989, p.46) goes further in stating that "they (*sine-generated curves*) do not provide a practical method for specifying quantitatively the shapes of individual natural meanders". Carson and Lapointe (1983) argued that asymmetry is a fundamental aspect of meandering and concluded that symmetrical curve fitting approaches were inappropriate.

Brice (1973, 1974) introduced a systematic method of curve fitting, in which arcs are fitted to a single centreline by superimposing a transparency with a series of arcs of differing radii of curvature. Arcs cannot overlap but can either join tangentially with other arcs or be joined by chords where the meander segment is essentially straight (Fig. 6.5). The two end points of an arc are joined by a chord (L_c) and the arc height (H) is measured perpendicular to the centre of L_c. The angle α is defined by the interception of the end points with the centre of radius and an arbitrary minimum value of 60° being set by Brice (1974). Asymmetric or compound loops are fitted with two or more arcs in this method of analysis.

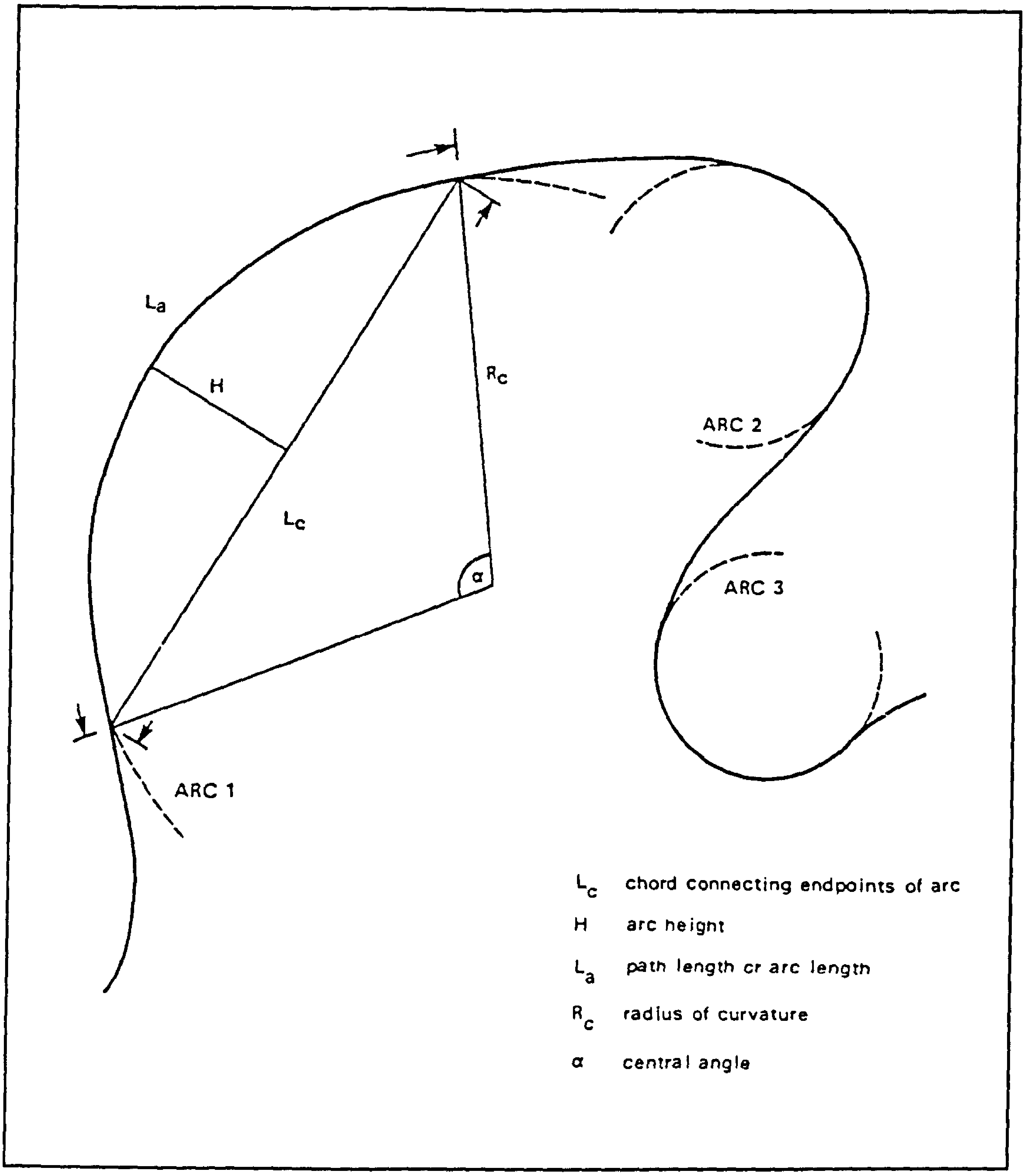

Figure 6.5. An example of circular arc fitting to meander bends, and the definition of arc features. From Williams (1984b).

However, there is debate on the ease of use and precision of Brices' (1973, 1974) curve fitting technique. Hooke (1984) suggests that the fitting of arcs is very difficult and as a consequence precision is very low. Williams (1984a) provided some statistical data on replicability by having two different analysts fit the loops and found that there was a 0-25% variation in radius of curvature, r_c, for a single arc and an average difference for r_c of 6%. It should be noted however that with such a small number of bends (10) and only two operators these results are unlikely to be statistically significant. While this method seems to work reasonably well it is time-consuming, and a more detailed study of likely errors is required to give an indication of the precision of estimate. The technique lends itself well to palaeohydrological studies since it measures radius of curvature with a high degree of precision and there is a strong correlation between r_c and discharge. Channel width shows a stronger correlation with discharge than radius of curvature in modern rivers (Williams, 1984a), but can rarely be measured with precision in the ancient.

Weihaupt (1989) introduced a more comprehensive curve fitting technique which uses circles, ellipses, parabolas and hyperbolas, defined by their conic intersection (Fig. 6.6). However, some bends can still not be matched precisely to any of these geometric forms and two or three forms must be used in conjunction (Fig. 6.7). Adjacent ellipsoids should ideally meet at the inflection points of each bend, in the same manner shown by Brice (1973, 1974). The main weaknesses of the template based, curve fitting approach, are the quantity of preparatory work to produce the templates (e.g. Weihaupt used over 1000 templates) and the time consuming nature of the subsequent data collection.

6.2.3 Graphical methods

This technique involves the plotting of the entire river course and quantification of the overall morphology (e.g. Lewin and Brindle, 1977). A graphical approach has the advantage of being a powerful, visual representation of a large dataset. In addition, river courses can be compared by overlaying them, which in the case of a time-series, allows rates of erosion to be quantified. The superposition of stream traces also allows bend development to be studied (Hooke and Harvey, 1983) or individual point vectors to be generated (Brice, 1973). However, these graphical approaches have a limited applicability in palaeohydrological analysis.

6.2.4 Bend parameters

There are two approaches to the measurement of bend parameters. The simplest and most popular method is to measure the parameters from a map. The alternative is to digitise the centreline of the stream course in order to create a series dataset and then

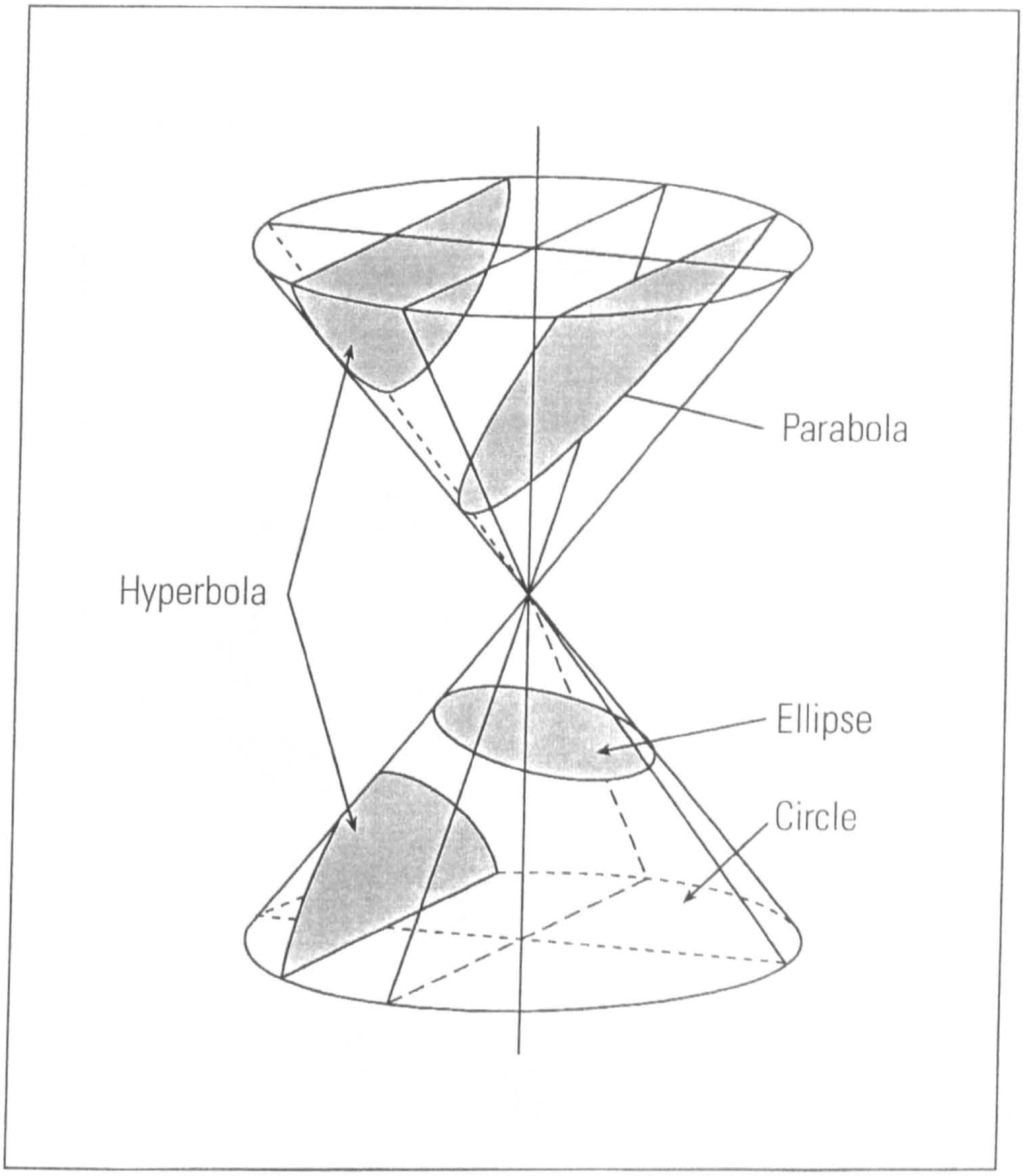

Figure 6.6. The generation of hyperbolas, parabolas, and ellipses using conic sections. After Ayre *et al.*, (1967).

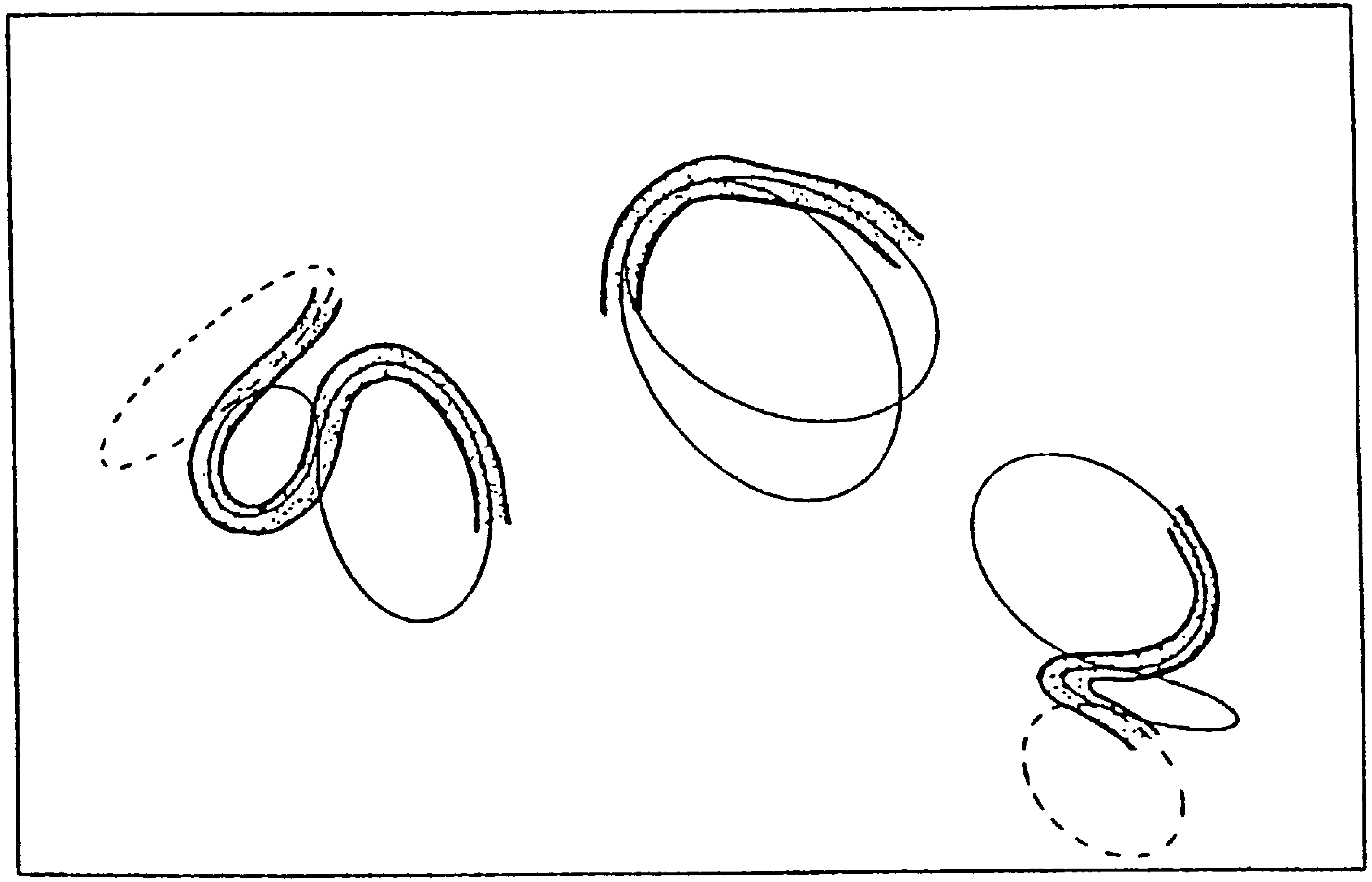

Figure 6.7. Examples of bend characterisation using conic sections. The asymmetric central bend requires two ellipses to adequately characterise the planform. From Weihaupt (1989).

analyse the data using a computer program. In both cases the most frequently measured attributes include: radius of curvature, channel width, arc length, bend wavelength and amplitude, and arc height (see Fig. 6.8). Hooke (1984) recognised four major problems with bend parameter estimation. First, if measurements are taken directly from maps then problems of subjectivity and replicability invariably arise. Second, the definitions of parameters are often not stated or vary widely. Thirdly, many authors measure a series of bends and quote statistical averages. There is often no standardisation of the averaging methodology, making comparisons between studies difficult. In addition, the underlying usefulness of these averages has been challenged (e.g. Cox and Jones, 1981). Finally, Hooke (1984) argues that single bend parameters should not be used to characterise the whole form of a river. While river morphology is best described using a multivariate approach, the majority of palaeohydrological equations only include a single bend parameter (see Section 6.5) which necessitates the analysis of the meander planform in terms of individual bend characteristics.

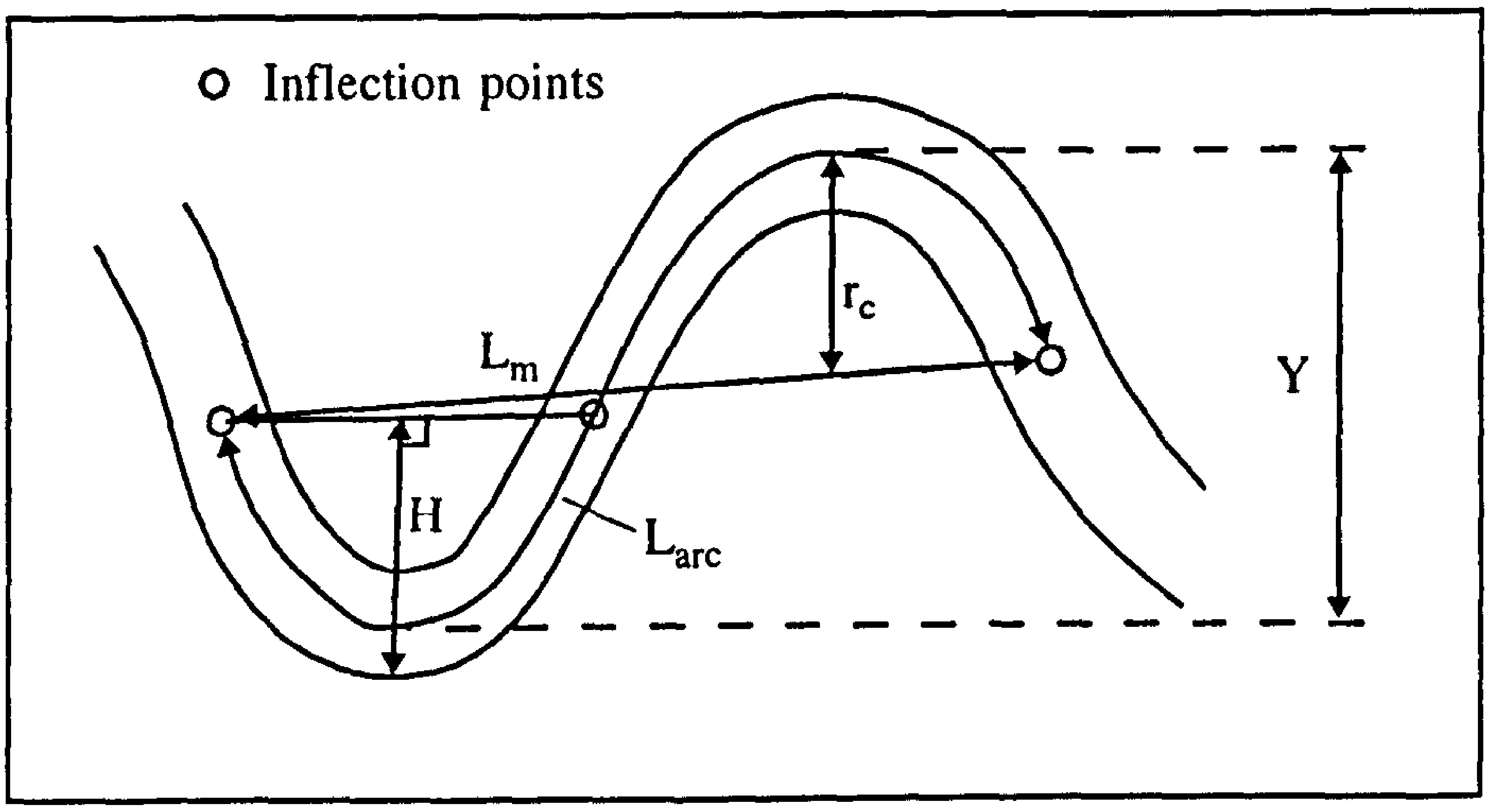

Figure 6.8. Variables describing meander bend geometry for symmetrical bends; L_m = meander wavelength, Y = bend amplitude, H = arc height, r_c = radius of curvature, and L_{arc} = arc wavelength. From Richards (1982).

6.3 Definition of meander parameters

Early work concerning the definition of meander parameters was associated with the concept of fitting symmetrical curves to meanders (Bates, 1939; Leopold *et al.*, 1964, Langbein and Leopold, 1966). The influence of this approach can still be seen in modern texts (Richards, 1982; Knighton, 1984; Morisawa, 1985; Weihaupt, 1989; Yalin, 1992) and has caused ambiguity when these parameters are applied to asymmetric meanders. As discussed above, two main problems arise in that, meander parameters are often imprecisely defined or undefined, and there is no agreement on the methodology for averaging parameters (Hooke, 1984).

6.3.1 Bend Apex

The bend apex can be defined as the tangent to the line that follows the centre of the bend. Several workers have used the bend apex to define other parameters, for instance the radius of curvature (Morisawa, 1985) and arc height (Yalin, 1992, Fig 5.2, p.163). However, the bend apex has proved to be very difficult to define computationally. Hooke (1977b, p.95) defined the apex as the point furthest away from the two points of inflexion, but deemed this unsatisfactory as a measure of meander breadth.

6.3.2 Arc height and meander amplitude

Early definitions of arc height appear to be mainly diagrammatic and based on a symmetrical curve. These definitions specify a perpendicular line from the centre of the arc length to the apex of the bend, which corresponds to the maximum perpendicular distance (e.g. Fig. 6.8; Richards, 1982). Therefore, this definition is ambiguous unless used exclusively for symmetrical bends. Milne (1979, p.223) defines arc height as "the maximum perpendicular distance from the line between bend inflections to the channel". This is essentially the same definition as that used by Brice (1964), although it was not explicitly stated in the latter work (see Fig. 6.9). The approach of Brice (1964) and Milne (1979) can cause ambiguity when using the arc height to examine the form of bends, especially in highly asymmetric meanders where the measured value does not reflect the dimensions of the bend (see Fig. 6.10). A new definition of arc height that slightly modifies the approach of Brice (1964), may be proposed and has been incorporated into a Meander Morphometry Analysis computer Program (M-MAP) (see Appendix B). *Arc height is defined as the maximum perpendicular distance from the line that characterises the half-wavelength.* Importantly, this definition allows arc height to intercept a point that is *not* part of the half-wavelength (see Fig. 6.10).

Several workers did not measure arc height (e.g. Langbein and Leopold, 1960) and instead used the related variable of meander amplitude. Five different definitions of meander amplitude are noted by Nagabhushanaiah (1967):

1) The amplitude of swing of a fully-developed meander from midstream to midstream,
2) The lateral perpendicular distance between tangents drawn to the outer-banks of the successive fully-developed meanders,

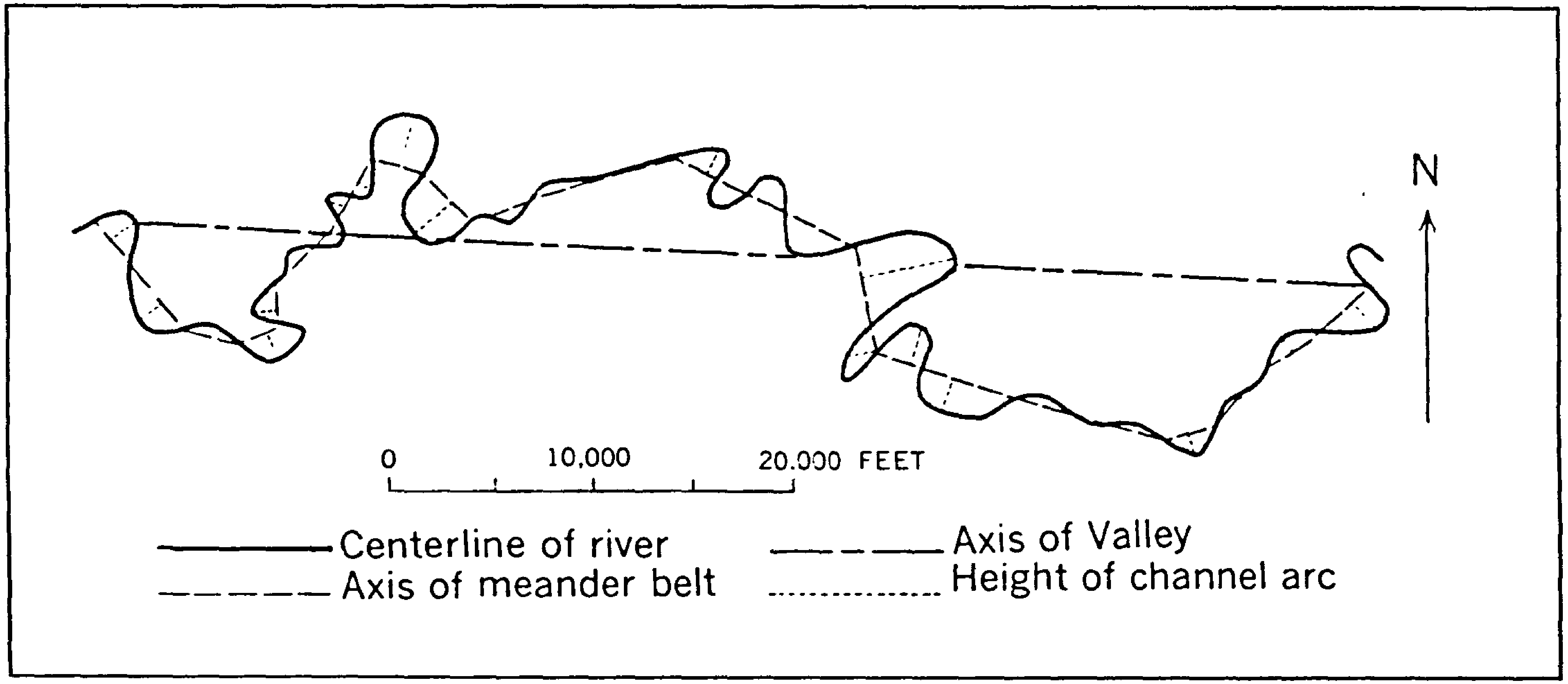

Figure 6.9. Delineation of a reach of the Buyuk Menderes River, Turkey, for measurement of wavelength, sinuosity and arc height. From Brice (1964).

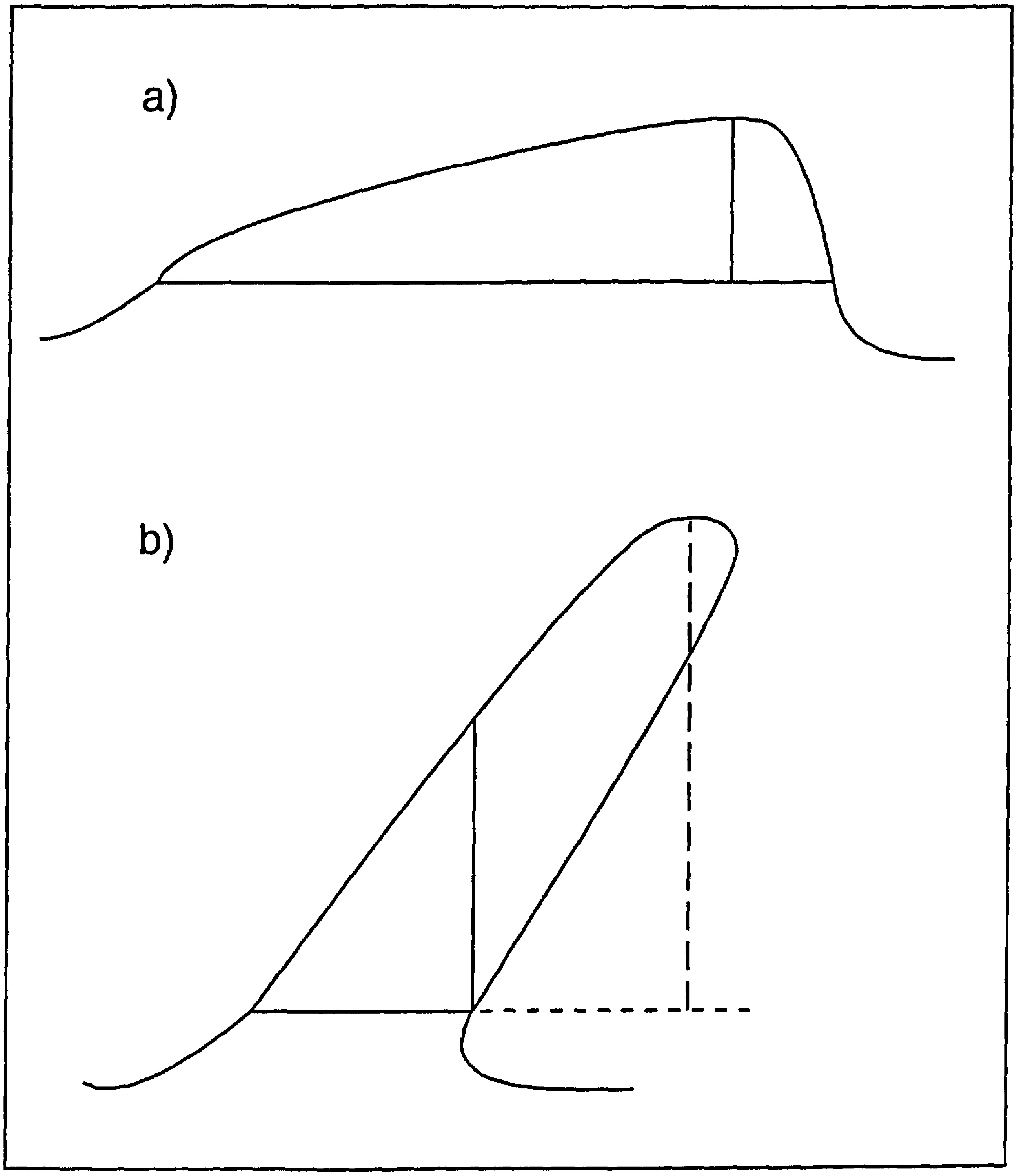

Figure 6.10. A new definition of arc height. The definition of Brice (1964) usually measures the maximum height of a bend, even for asymmetrical bends (a). However, for highly asymmetric bends (e.g. b) this parameter only measures some fraction of the height. A new definition (marked by dashed lines) always measures the maximum perpendicular distance to the line that characterises the half-wavelength.

3) The lateral perpendicular distance between tangents drawn to the extreme water marks of the successive fully developed meanders,
4) The lateral perpendicular distance between tangents drawn to the path of the centroid of the area of flow, or the lateral swing of the centroid of the flow between the successive fully developed meanders,
5) The distance between lines drawn tangential to the extreme limits of the thalweg of fully-developed successive meanders.

The latter definition was preferred by Nagabhushanaiah (1967), but is not appropriate for palaeohydrological studies because of the difficulty in recognising the extreme thalweg limit in a palaeochannel. The first two definitions are more suitable for applying to ancient rivers since the outer banks may be identifiable.

6.3.3 Radius of curvature

The earliest use of radius of curvature is that of Fergusson (1863) who considered a meandering river as a set of semi-circles. Despite the widespread use of radius of curvature, r_c, from the second half of the 19th century, there have been very few definitions of r_c in the literature. Hey (1984, p.31) defines r_c as, "the radius of the circle defining the curvature of an individual bend measured between adjacent inflexion points". Weihaupt (1989, p.28) defines r_c as "the radius of a circle which most nearly fits the curve of a given meander". While the definitions of Hey (1984) and Weihaupt (1989) are good general definitions they do not mathematically define how the parameter is measured. A similar, but more precise definition is given by Morisawa (1985, p.91) who states that "the radius of curvature is the radius of a circle drawn through the apex of the bend and the two crossover points". However, this definition can only be applied to meanders that can be considered as a sine wave, and is therefore very limited in its use. Milne (1979) used two different definitions for radius of curvature. For the local radius of curvature (see Fig. 6.11a) between three consecutive points, the following expression was given,

$$r_c = \frac{(L_c)^2}{8C_H} + \frac{C_H}{2} \qquad \text{(Eq. 6.1)}$$

where L_c is the chordlength for the bend and C_H is the perpendicular distance to the central point. For a whole bend, a second form of radius of curvature, which Milne (1979) termed the average bend radius (ABR), was defined as:

$$ABR=(r_c+r_2) \qquad \text{(Eq. 6.2)}$$

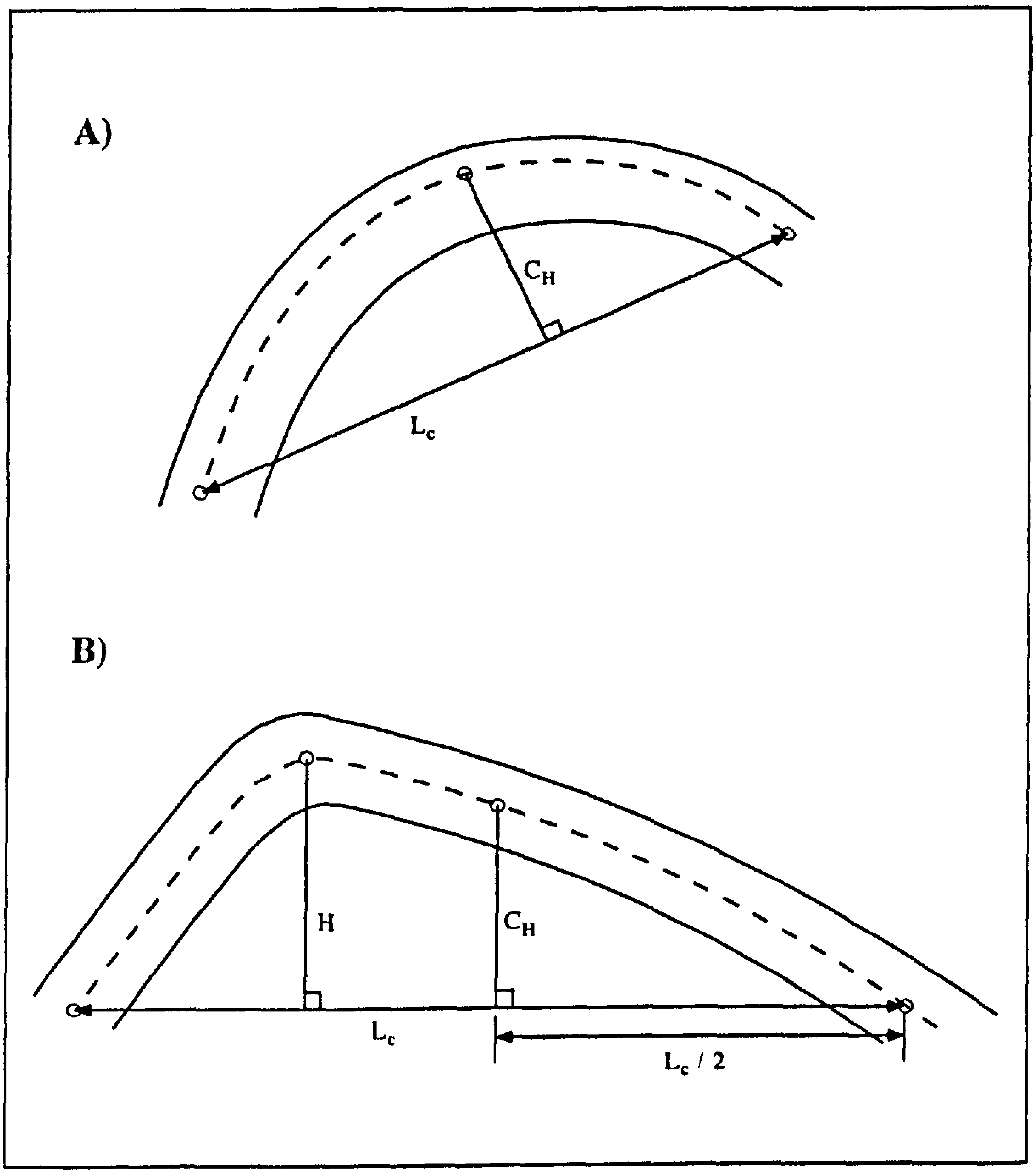

Figure 6.11. Illustration of bend parameters as defined by Milne (1979). A) Bend parameters based on three consecutive sections. C_H is the perpendicular height of the central section. L_c is the distance between upstream and downstream sections. B) Bend parameters for a continuously defined bend. C_H=perpendicular height from the centre of the chord length, L_c, and H is the arc height. See text for equations defining average bend radius (ABR) and radius of curvature. Adapted from Milne, (1979).

where

$$r_2 = \frac{L_c}{8H} + \frac{H}{2} \qquad \text{(Eq. 6.3)}$$

where H is the arc height, and C_H is the perpendicular height from the centre of the wavelength (Fig. 6.11b), and not to the chosen central point as defined for the local radius of curvature.

Hooke and Harvey (1983) computed the local radius of curvature, defined as $r_c=(L_c/\theta)$, where L_c is the length of chords between successive points and θ is curvature (measured in radians). The most complex definition of radius of curvature is provided by Richards (1982, 1991) and involves drawing the intersection of chord orthogonals and then connecting these to form a polygon (Fig. 6.12). The centre of the polygon is then taken as the mean centre of curvature which can be "used to initiate radii in order to find the mean radius" (Richards, 1991, p.89). The minimum curvature is the distance from the mean centre of curvature to the apex, although problems have been noted in adequately defining the apex (Section 6.3.1). The M-MAP computer program presented in Appendix B, defines the radius of curvature as the distance from the mean centre of curvature (as defined by Richards, (1991)) to the intersection of the arc height with the meander arc (defined previously).

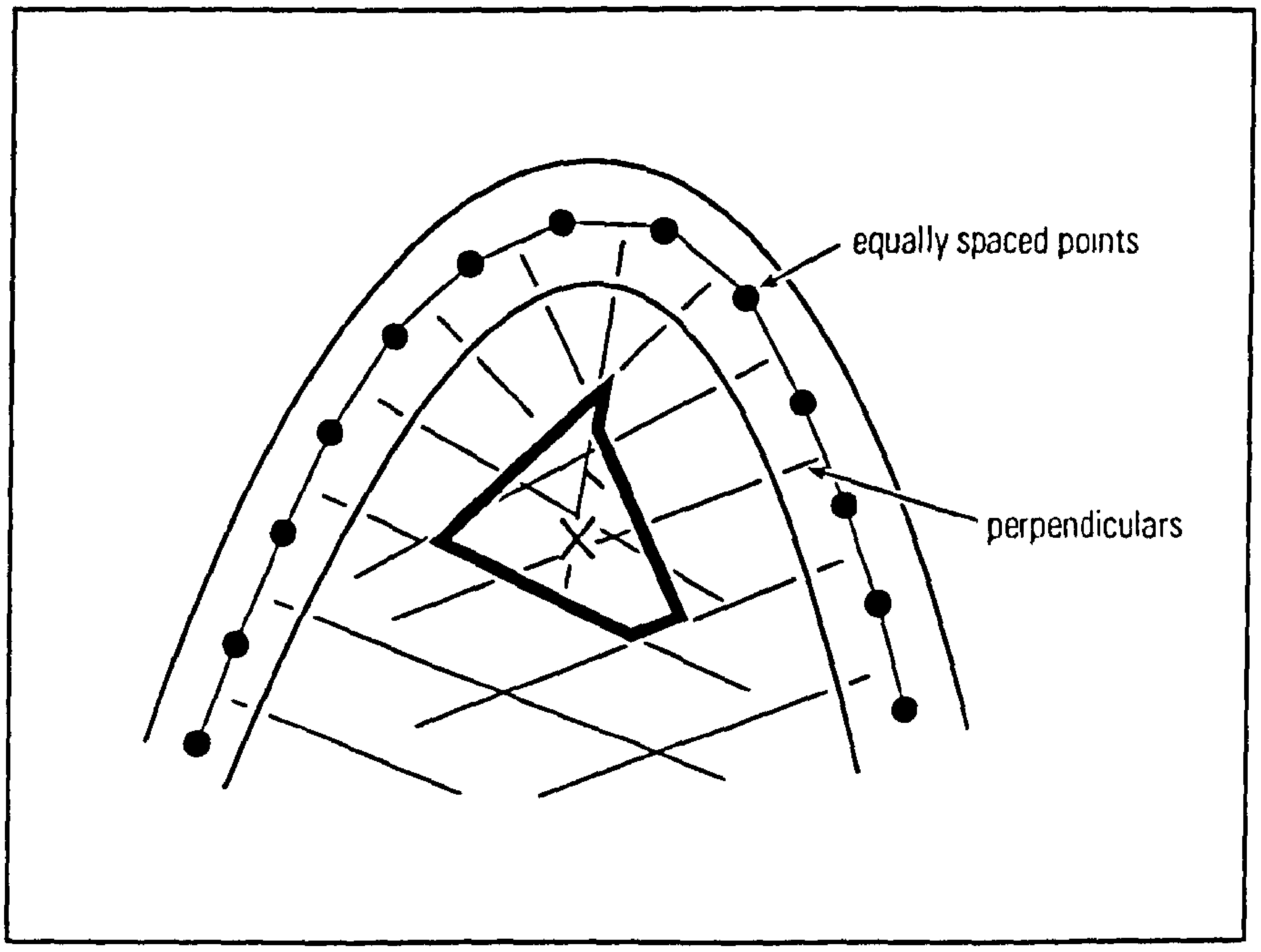

Figure 6.12. Definition of mean centre of curvature in a non-circular bend. X = mean centre of curvature and is defined by the centre of gravity of a polygon delineated by the intersection of perpendiculars. After Richards, (1982).

6.3.4 Channel width

Williams (1978) discusses the difficulties in defining channel width and notes that there are at least ten different definitions in the literature. Wahl (1984) breaks the majority of these down into just three groups, each measuring a specific reference height - i) within-channel bars, ii) active channel section and iii) main channel section (see Fig. 6.13). Within-channel bars are normally defined by the top of the point-bar, while the active channel (or active floodplain) is defined by "a break in the relatively steep bank slope of the active channel to a more gently sloping surface beyond the channel edge" (Osterkamp and Hedman, 1977). This second definition has been used in hydrology (Webber and Roberts, 1981; Osterkamp and Hedman, 1982; Omang *et al.*, 1983), but it is difficult to apply the equations generated by these studies to ancient sediments, since the break of slope marking the active channel may be imperfectly preserved and may be difficult to recognise in poor exposures. Most palaeohydrological expressions use the main-channel section definition, although a few studies have used the channel bars (Padgett and Ehrlich, 1976; Edwards *et al.*, 1983; Rotnicki, 1991). Koutaniemi and Ronkainen (1983) have previously suggested that determining the bankfull stage using the sole characteristics of the channel and floodplain morphology is too inaccurate for palaeohydrology, in which case the main alternative is the channel bar studies.

Values for mean channel width are commonly presented in the literature although frequently no sampling methodology is provided (Maizels and Aitken, 1991). Lapointe and Carson (1986) used data exclusively from crossover zones between bends as suggested by Lowham (1976), while Williams (1984a) took the average of 8 to 10 channel widths and avoided bend apices if they were considerably wider than elsewhere. Hickin and Nanson (1975) used an average of a set of equally spaced measurements centred on the erosional axis of each bend. Bridge and Diemer (1983) argue that if the point-bar height is being used as a measure of channel depth, then the apex of the bend should be used to measure channel width, since the point-bar should theoretically approach bankfull height at the bend apex. Care should also be taken to measure channel width and depth using the most recent point-bar, which may have to be located by drilling (Fig. 6.14).

6.3.5 Discussion

It is evident from the above discussion that there is a need for standardisation of definitions and sampling techniques for measuring meander planform. Two parameters (radius of curvature and arc height) have been redefined in order to measure asymmetric bends and to incorporate them into a computer program (Appendix B). In particular, a

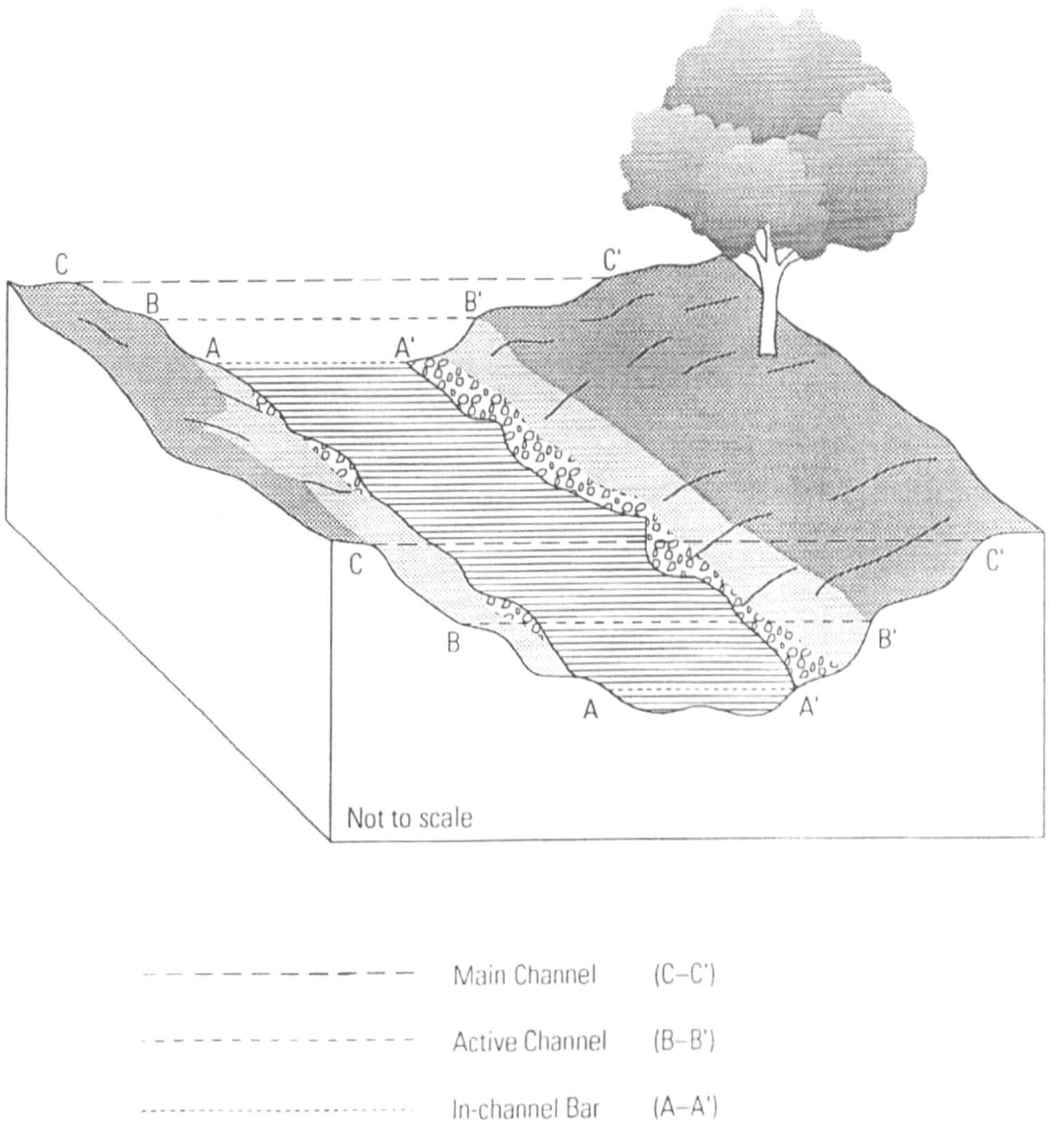

Figure 6.13. Commonly used reference levels for channel width. After Wahl, (1984).

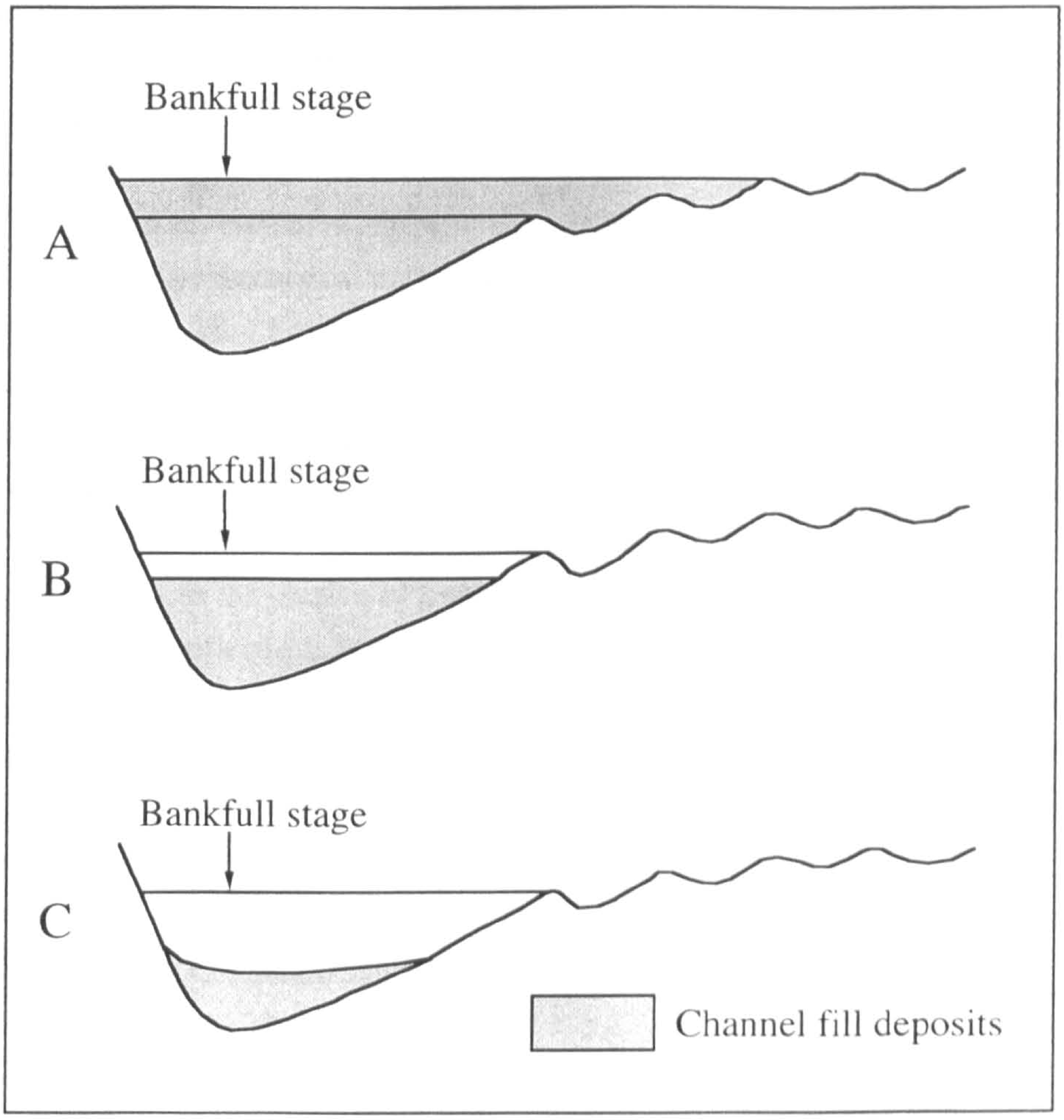

Figure 6.14. Location of the youngest point-bar ridge in relation to channel-fill deposits: (A) youngest point-bar ridge covered by channel-fill deposits and invisible on the present-day surface of the meander lobe; (B and C) youngest point-bar ridge located above the surface of channel-fill deposits. After Rotnicki, (1991).

new definition of arc height is presented which consistently measures the maximum 'width' of a bend and removes the ambiguity of previous definitions.

Bend parameter estimation using computer programs is recommended by Hooke (1984), but programs are not yet available from the literature. Accordingly, this study has developed a program for the Apple Macintosh computer that produces both directional and curvature data, plus the wavelength, arc length, sinuosity, total curvature, maximum point curvature, mean curvature, arc height and radius of curvature, for each bend, and is presented in Appendix B. It must also be established whether the increase in accuracy and precision provided by the time-consuming and tedious nature of digitising and the subsequent computer analysis is significant.

Several sources of error may be identified from digitising bend planforms. The sampling frequency of digitised points may produce an error since it affects the number of inflections that are produced. In addition, due to this spacing of points and the consequent loss of definition on the curve, there will invariably be a further error in predicting the inflection point. The theoretical maximum error is ±0.5 of the sampling distance, with an average of ±0.25. This error will show up more dramatically in arc lengths than in wavelengths. A third source of error, which is most pronounced on lower sinuosity systems are spurious high frequency inflections from digitising errors. These errors are due to inaccurate digitising which causes small oscillations around the smooth curve, but can be removed using a line-generalizing algorithm (e.g. Hickin, 1977), although there is some subjectivity in the choice of a tolerance limit. Alternatively, Hooke and Harvey (1983) ignored all inflections with a spacing of less than 3 channel widths, while Carson and Lapointe (1983) ignored inflections that had a direction angle of <30° to the local meander belt axis. Although no studies have quantified the magnitudes of these errors Hickin (1977) notes that his study gives markedly different results to the traditional meander 'laws' derived from map data.

6.4 Bend parameter estimation using image-analysis software

6.4.1 General outline of technique

A new technique is presented here that is more rapid and accurate to use than map or aerial photograph based measuring, particularly in the measurement of arcs. The palaeohydrological data presented in Chapter 7, was generated using this approach. Black and white aerial photographs are initially scanned and imported into NIH Image, a public domain image analysis program for the Apple Macintosh. The contrast and brightness of the image can then be adjusted to enhance photo-quality whilst a further aid to interpretation is provided by using a shadow filter on the image to highlight the topographic differences. The image can be rotated or the filter re-programmed to adjust the direction of the light. When working with abandoned channel belts which have undergone subsequent modification, this feature significantly aids identification of past channel courses.

Inflection points are chosen by eye and are therefore subjective. Small bends with an inflection spacing smaller than three channel widths are ignored, as suggested by Hooke and Harvey (1983). Values for arc length are produced using the freehand drawing tool while arc length, arc height and channel width are all measured using the straight line tool. The data from the image can be directly exported into a spreadsheet package for statistical analysis.

In palaeohydrological studies the definition of channel banks can be difficult making precise sampling techniques problematic. In the analysis here, widths have been measured at an irregular spacing, where channel definition permits, and bend apex regions were excluded in the calculation of average channel widths. Arc height was measured from the centre of the arc length. For symmetrical bends the arc height has been taken at 90° to the arc length and for highly asymmetric elongate bends the arc height is the distance to the bend apex. For bends in between these categories the angle is subjectively chosen at a point mid-way between 90° and the angle to the bend apex, in order to characterise the maximum height of the arc without producing erroneously large or small readings. This definition of arc height is partially subjective and can give misleading results for asymmetric bends that have a large radius of curvature. An improved definition of arc height was proposed in Section 6.3.2 and has been incorporated into the M-MAP computer program.

6.4.2 Limitations of the image analysis technique

The major limitation of the image analysis technique is its inability to measure total curvature or the radius of curvature. However, use of arc length divided by arc height generates an index indicating the relative tightness of a bend. Division of this index by channel width may give a comparable variable to r_c/w, as first used for stability analysis of meanders by Hickin and Nanson (1975). Additional limitations are imposed by the software and hardware and depend on the photo-area to be scanned and the scanning resolution.

6.5 Palaeohydrological equations

Once bend parameters have been obtained from fieldwork, maps, or aerial photographs, they can be used in palaeohydrology. Almost all of these relationships are derived from regressing empirically derived datasets. A large number of relationships exist for predicting one channel dimension or a meander geometry variable from another parameter, although there are relatively few relationships available for predicting palaeodischarge. This is largely due to discharge being used as the independent variable in regression analysis rather than the dependent (Williams, 1988). Williams (1984b, 1988) lists a total of nine equations for average daily discharge[1] in meandering rivers. In addition, there are a number of relationships for bankfull discharge and other miscellaneous discharges (see Table 6.1). These studies are all from temperate or semi-arid regions with the notable exception of Pickup and Warner (1984).

Carlston (1965) collated palaeohydrological data from 31 rivers, the majority of which are from the central United States. Williams (1984b) re-computed the dataset of Carlston (1965) with discharge as the dependent variable, and produced a relationship of the following form:

$$Q_m = 0.000017\ L_m^{2.15} \qquad \text{(Eq. 6.4)}$$

where Q_m and L_m are the average discharge and mean wavelength respectively. The standard error is 0.11 log unit, and the applicable range of wavelengths is 145 m to 15,500 m. Williams (1984b) also re-computed Schumm's (1972) data from the Great Plains of the United States and from Australia, to give:

$$Q_m = 0.029\ w_b^{1.28} d_{max}^{1.10} \qquad \text{(Eq. 6.5)}$$

where d_{max} is the maximum bankfull channel depth and w_b is the bankfull width. This equation has a standard error of 0.36 log units and an applicable range for w_b of 8-244 m and for d_{max} of 0.7 to 8 m. Williams (1984a) also generated two equations based on several Swedish rivers:

$$Q_m = 0.06 w_b^{1.66} \qquad \text{(Eq. 6.6)}$$

$$Q_m = 0.025\ r_c^{1.58} \qquad \text{(Eq. 6.7)}$$

However, all of these equations are based on very small datasets; 31, 36, 19, and 19 respectively. Two much larger analyses are given by Osterkamp and Hedman (1982) for average discharge;

---

[1] Calculated by averaging each daily flow, summing these and dividing by 365 to get annual average daily flow. These average daily rates are then summed and divided by the number of years of record.

Table 6.1. Palaeohydrologic equations for the prediction of discharge (modified from Williams (1984b) with additional data)

Equation	Author (s)	Number of data points	Standard error (%) †	Applicable Range
	Average daily discharge (Q_m)			
$Q_m = 0.027w_b^{1.71}$	Osterkamp and Hedman (1982)	252	79	$0.8 \leq w_b \leq 430$ m
$Q_m = 0.0074w_b^{1.54}S_b^{-0.26}$	Osterkamp and Hedman (1982)	252	73	$0.8 \leq w_b \leq 430$ m; $0.0000060 \leq S_b < 0.028$
$Q_m = 0.013w_b^{2.13}$	Pickup and Warner (1984)	No data	No data	$\sim 185 \leq w_b \leq 340$ m
$Q_m = 54.9d_b^{1.58}$	Pickup and Warner (1984)	No data	No data	No data
$Q_m = 0.21A_b^{1.17}$	Pickup and Warner (1984)	No data	No data	No data
$Q_m = 0.029w_b^{1.28}d_{max}^{1.10}$	Williams (1984b) Schumm (1972) revised	36	99	$8 \leq w_b \leq 244$ m; $0.7 \leq d_{max} \leq 8$ m
$Q_m = 0.000017L_m^{2.15}$ ‡	Williams (1984b) Data from Carlston (1965)	31	26	$145 \leq L_m \leq 15{,}545$ m
$Q_m = 0.06w_b^{1.66}$	Williams (1984a)	19	39	$1.8 \leq w_b \leq 67$ m
$Q_m = 0.025r_c^{1.58}$	Williams (1984a)	19	70	$8 \leq w_b \leq 169$ m
	Bankfull Discharge (Q_b)			
$Q_b = 0.0021r_c^{2.03}$ Δ	Alford and Holmes (1985)	31^{α}	43	No data
$Q_b = 0.000585S_b^{-2.01}$	Cheetham (1980)	13	114	$0.000066 \leq S_b \leq 0.0073$
$Q_b = (w / 2.99)^{1.81}$	Dury (1976, 1985)$^{\beta}$	52	58	No data
$Q_b = (L_m / 32.857)^{1.81}$	Dury (1976, 1985)$^{\beta}$	52	85	No data
$Q_b = 0.83\ A_b^{1.09}$	Dury (1976, 1985)$^{\beta}$	68	68	No data
$Q_b = (0.9208/n)\ A_bR^{0.167}*(RS_b)^{0.5}+2.362$ (Gaukler-Manning modified)	Rotnicki (1983)	1352	7-22	$0.00001 \leq S_b \leq 0.01$; $0.010 \leq n \leq 0.060$
$Q_b = 4.0A_b1.21S_b^{0.28}$	Williams (1978)	233	42	$0.7 \leq A_b \leq 8510$ m^2; $0.00041 \leq S_b \leq 0.081$
	Miscellaneous discharges			
$Q_{2.33} = 0.063Z_d^{1.59}$	Cheetham (1980) after Carlston (1963)	15	26	$1.9 \leq Z_d \leq 5.9$
$Q_v = 0.26A_g^{0.98}$	Clague (1975)	11	No data	$2 < A_g < 150$ km^2
$Q_{mm} = 0.43A_g^{1.06}$	Clague (1975)	11	No data	$2 < A_g < 150$ km^2
$Q_{2.33} = 2.66w_b^{0.90}d_{max}^{0.68}$	Schumm (1972)	36	53	$8 \leq w_b \leq 244$ m; $0.7 \leq d_{max} \leq 8$ m
$Q_{1.5} = 0.011L_m^{1.54}$	Williams (1984b), data from Carlston (1965)	28	41	$145 \leq L_m \leq 15{,}545$ m
Additionally, Osterkamp and Hedman (1982) produce data for Q_2, Q_5, Q_{10}, Q_{25}, Q_{50}, Q_{100}, as do other workers.				

† for the 95% probability level two standard errors should be used.

Δ imperial units. All other expressions are in metric units. $^{\alpha}$ Each value is an average of 5 bends.

$^{\beta}$ These equations were derived theoretically by Dury (1976). The number of data points and the SE% refer to a test of the equations against real data (Dury, 1985).

‡ Incorrectly quoted as $Q_m=0.000017L_{max}^{2.15}$ in Williams (1984b)

$$Q_m = 0.027 w_b^{1.71} \qquad \text{(Eq. 6.8)}$$

$$Q_m = 0.0074 w_b^{1.54} S_b^{-0.26} \qquad \text{(Eq. 6.9)}$$

and Williams (1978) for bankfull discharge:

$$Q_b = 4.0 A_b^{1.21} S_b^{0.28} \qquad \text{(Eq. 6.10)}$$

where S_b is the streambed slope and A_b is the channel cross-sectional area at bankfull. Equations 6.8 and 6.9 are based on 252 data points from the Missouri River Basin, and have an applicable range of 0.8-430 m for w_b and ≤ 0.0000060 S_b. It should however be noted, that this formula is based on a definition of bankfull that uses the active floodplain and not the main channel width (see Fig. 6.14). Equation 6.10, is based on a compilation of work covering much of the United States as well as parts of Canada, England and Wales (N^o=233).

To use equation 6.10, the slope and cross-sectional area at bankfull (A_b) are required. For most palaeohydrological studies, data on bankfull cross-sectional area (A_b) and slope are an unusual combination, although Williams (1983a) provides one example where both variables could be measured. In cross-sections of channels in the rock record, area may often be calculated but slope is normally difficult, if not impossible to measure, while in abandoned channel belts, accurate depth data across channels is difficult due to infilling of channels. However, several workers have obtained both measurements by using a large number of augured and vibracored samples and examining sedimentological changes down core (Rotnicki and Boròwka, 1985; Rotnicki, 1991). If equation 6.10 is applicable it should be used in preference to equations 6.8 and 6.9 since it has smaller error bars (Standard Error (SE) = 42%), an extremely high correlation coefficient of 0.98 and also covers a wider range of environments.

A large database of channel variables has been collated by Mackey (1993) based on an extensive survey of the literature (Jefferson, 1902; Bates, 1939; Inglis, 1940; Leopold and Maddock, 1953; Leopold and Wolman, 1957; Nixon, 1959; Leopold and Wolman, 1960; Schumm, 1960b; Carlston, 1965; Dury, 1965; Speight, 1965a; Leopold and Skibitzke, 1967; McKee *et al.*, 1967; Neill and Galay, 1967; Schumm, 1968; Coleman, 1969; Chitale, 1970; Collinson, 1970; Donaldson *et al.*, 1970; Rust, 1972; Leeder, 1973; Charlton *et al.*, 1978; Gustavson, 1978; Williams, 1978; Woodyer *et al.*, 1979; Blodgett and Stanley 1980; Rust, 1981; Johnson, 1982; Roberts *et al.*, 1983; Smith, 1983; Butler, 1984; Elliot and Pokrefke, 1984; Guccione, 1984; Haner, 1984; Harvey, 1984; King and Martini, 1984; Kopsick, 1984; Phelps, 1984; Williams, 1986;

Maizels, 1988; Neill and Yaremko, 1988). However, Mackey (1993) does not use this dataset to derive expressions for discharge, but instead uses discharge as the independent variable. A re-analysis of this data is presented here and provides a number of useful equations for predicting palaeodischarge (Table 6.2). Since the equations in Table 6.2 are derived from numerous data sources, there will be additional sources of error, caused by different authors using differing definitions for meander parameters. However, the majority of analysed studies use the main channel definition for channel width and depth (see Section 6.3.4). The equations listed in Table 6.2 also represent a wide range of river sizes and environments which has rarely been encompassed in previous studies.

Schumm (1960a, b; 1968) expressed the river-bed and banks in terms of weighted mean percent silt-clay (M), and demonstrated a strong relationship between M and channel shape. However, Schumm did not produce a direct expression relating these factors to discharge. Osterkamp (1977) initially incorporated these ideas into a small study of Kansas streams, and then Etheridge and Schumm (1978) produced two relationships incorporating M:

$$Q_m^{0.38} = \frac{wM^{0.39}}{37} \qquad \text{(Eq. 6.11)}$$

$$Q_m = \frac{w^{2.43}}{18F^{1.14}} \qquad \text{(Eq. 6.12)}$$

where $F = 255\ M^{-1.08}$. However, equations 6.11 and 6.12 were derived from the manipulation of earlier multiple regressions, which is not statistically valid and consequently no error bars can be calculated (see Williams (1983b, 1984c) for discussion on the misuse of regression). The expressions of Osterkamp and Hedman (1982) (Eqs., 6.8 and 6.9), can be further subdivided, depending on the bed and bank materials (Table 6.3). However, this is obviously at a loss of sample size.

Rotnicki (1983, 1991) notes that the errors for many of the regression equations are commonly greater than 100% at the 95% confidence limits, and has therefore suggested a different approach to the prediction of former discharges. Rotnicki (1991) also points out that when these equations are compared with modern rivers the errors commonly exceed 2*SE, due to the equations being used in different areas and river regimes to the original. In summary, Rotnicki (1991, p.437) suggests that "these limitations ... prevent these formulae from being universally applicable and make their standard errors too big even for the requirements of palaeodischarge retrodiction".

Instead of adopting empirical formulae, Rotnicki used a combined theoretical and physical approach. A series of variations of the Chézy equation were tested against the

Table 6.2. Equations for the calculation of palaeodischarge, from a re-analysis (this study) of the database of Mackey, (1993)

Parameters	Regression	R-Val	N° Points	SE log units	SE (%)$^{\Omega}$	95% min†	95% max†	Applicable Range
Q_m on M_b	$Q_m = 1.1E\text{-}4\ M_b^{1.99}$	0.965	35	0.218	54	$Q_{m(min)} = 4.1E\text{-}5\ M_b^{1.99}$	$Q_{m(max)} = 2.9E\text{-}4\ M_b^{1.99}$	$122 \leq M_b \geq 16764$
Q_m on w_m	$Q_m = 0.022\ w_m^{1.81}$	0.881	242	0.334	90	$Q_{m(min)} = 0.005\ w_m^{1.81}$	$Q_{m(max)} = 0.098\ w_m^{1.81}$	$2.80 \leq w_m \geq 883.90$
Q_m on d_m	$Q_m = 28.590\ d_m^{1.89}$	0.712	209	0.496	164	$Q_{m(min)} = 3.052\ d_m^{1.89}$	$Q_{m(max)} = 267.789\ d_m^{1.89}$	$0.13 \leq d_m \geq 15.50$
Q_m on w_b	$Q_m = 0.028\ w_b^{1.58}$	0.626	109	0.535	189	$Q_{m(min)} = 0.002\ w_b^{1.58}$	$Q_{m(max)} = 0.317\ w_b^{1.58}$	$1.50 \leq w_b \geq 1700$
Q_m on d_b	$Q_m = 2.265\ d_b^{1.80}$	0.366	105	0.645	284	$Q_{m(min)} = 0.123\ d_b^{1.80}$	$Q_{m(max)} = 41.653\ d_b^{1.80}$	$0.38 \leq d_b \geq 8.85$
Q_m on L_m	$Q_m = 2.5E\text{-}5\ L_m^{2.05}$	0.639	88	0.801	539	$Q_{m(min)} = 6.9E\text{-}7\ L_m^{2.05}$	$Q_{m(max)} = 9.6E\text{-}4\ L_m^{2.05}$	$105 \leq L_m \geq 15545$
Q_b on M_b	$Q_b = 0.096\ M_b^{1.34}$	0.761	69	0.424	126	$Q_{b(min)} = 0.014\ M_b^{1.34}$	$Q_{b(max)} = 0.653\ M_b^{1.34}$	$122 \leq M_b \geq 13716$
Q_b on w_m	$Q_b = 1.033\ w_m^{1.36}$	0.593	53	0.582	224	$Q_{b(min)} = 0.075\ w_m^{1.36}$	$Q_{b(max)} = 14.276\ w_m^{1.36}$	$5.80 \leq w_m \geq 883.90$
Q_b on w_b	$Q_b = 0.811\ w_b^{1.30}$	0.737	190	0.487	159	$Q_{b(min)} = 0.090\ w_b^{1.30}$	$Q_{b(max)} = 7.295\ w_b^{1.30}$	$3.40 \leq w_b \geq 9449$
Q_b on d_b	$Q_b = 32.359\ d_b^{1.97}$	0.520	188	0.659	300	$Q_{b(min)} = 1.667\ d_b^{1.97}$	$Q_{b(max)} = 641.156\ d_b^{1.97}$	$0.39 \leq d_b \geq 20.10$
Q_b on L_m	$Q_b = 0.007\ L_m^{1.51}$	0.743	158	0.441	134	$Q_{b(min)} = 8.9E\text{-}4\ L_m^{1.51}$	$Q_{b(max)} = 0.048\ L_m^{1.51}$	$145 \leq L_m \geq 24474$

All variables are in S.I. units. †95% confidence limits calculated using ±1.96 standard errors from the mean. $^{\Omega}$The standard error (SE) in % was computed with the equation $SE\% = 100(e^{SE(\wedge 2)} - 1)^{0.5}$, where e=2.71 and SE is in natural log units. SE was converted from base 10 units to base e units by multiplying the former by 2.303.

modern rivers in the Odra drainage basin, Poland, the most realistic of which was a variation of the Gauckler-Manning equation:

$$Q=\left(\frac{0.9208}{n}\right)AR^{0.167}*(RS_b)^{0.5}+2.362 \qquad \text{(Eq. 6.13)}$$

where A is the cross-sectional area, R is the hydraulic radius, and n is Manning's roughness coefficient 'n'.

Table 6.3. Palaeohydrologic equations for discharge, in relation to bed and bank materials

Category	SC_{bd} (%)	SC_{bk} (%)	D_{50} (mm)	Expression for Q_m	Number of data points	Standard error (%) †
High silt-clay bed	61-100		<2.0	$0.031w_b^{2.12}$	15	35
Med. silt-clay bed	31-60		<2.0	$0.033w_b^{1.76}$	17	56
Low silt-clay bed	11-30		<2.0	$0.031w_b^{1.73}$	30	83Ω
Sand bed, silt banks	1-10	70-100	<2.0	$0.027w_b^{1.69}$	33	57
Sand bed, sand banks	1-10	1-69	<2.0	$0.029w_b^{1.62}$	96	73Ω
Gravel bed			2-64	$0.023w_b^{1.81}$	42	54
Cobble bed			>64	$0.024w_b^{1.84}$	19	24

SC_{bd} = silt-clay content of bed material. SC_{bk} = silt-clay content of bank material. w_b is active channel width. (Adapted from Williams, (1988) and based on the work of Osterkamp and Hedman, (1982)). † for the 95% probability level two standard errors should be used.

Ω These percentage figures are from Osterkamp and Hedman (1982). If the original log unit errors from Williams (1988) are taken and substituted into the standard error equation of Williams (1984b) they fail to give the correct results. Williams (1984b, p.346) states that "The standard error (SE) in % was computed with the equation $SE = 100(e^{SE(\wedge 2)} - 1)^{0.5}$, where e = 2.71 and SE is in natural log units. SE was converted from base 10 units to base e units by multiplying the former by 2.303".

Four parameters are required for this equation to be used in palaeohydrological studies; a roughness coefficient Manning's n, hydraulic radius, slope and the cross-sectional area. The channel bed slope, S_b, or a surrogate such as water surface slope, can be obtained from high quality maps or by detailed surveying. The other variables can all be estimated by drilling a large number of boreholes through the meanders. Rotnicki and Borówka (1985) demonstrated that a variety of sedimentological criteria (mean diameter, inclusive graphic standard deviation, loss on ignition and the fraction of sand above a certain threshold grain-size) from these cores, could be used to accurately predict the base of the channel. However, they did note that in some rivers the active-channel deposits may not be significantly different from the channel-infill deposits, which limits the application of this technique. There may also be problems identifying the base of the channel adjacent to the outer bank, due to previous bank collapse. In addition, there is debate as to how accurately Manning's n can be estimated. Richards (1973) suggests that it cannot be measured accurately, while Rotnicki (1983) argues that using Cowan's (1956) procedure, the differences between estimated and calculated values were statistically insignificant.

6.6 Summary

Direct measurement of bend parameters, from maps or from computer programs, is the simplest method for generating data for palaeohydrologic analysis. However, there are very few definitions of planform parameters in the literature, and there is often considerable ambiguity in those that do exist. Two new definitions for arc height and for radius of curvature have been introduced in this chapter and these have been incorporated into a Meander Morphometry Analysis computer Program (M-MAP; Appendix B). The program can also provide data for series and spectral analysis. A second technique for channel morphometry analysis using modern image-analysis software has also been presented. Image-analysis provides increased speed and accuracy over traditional map measurement. However, it is still a largely subjective technique, particularly in the choice of inflexion points.

A large number of empirical and semi-empirical relationships exist for the prediction of palaeohydrology. There are only a limited number of expressions for the prediction of palaeodischarge due to discharge being widely used as the independent variable. Many of the available relationships are also restricted in terms of geographic area and sample size. Several new relationships for Q_m and Q_b have been proposed here, based on a large, spatially extensive database (Mackay, 1993). Most of these have larger error bars than alternative equations, which is to be expected since a wide range of environments is encompassed. However, the expressions are useful for cases where the palaeo-river regime is not well constrained, and should prove useful in studies where width, depth or wavelength can be estimated.

Chapter 7. The Impact of Half-Graben Neotectonics on Axial River Development: The Carson River, Nevada

7.1 Synopsis

The Carson River, in north-western Nevada, USA, has been proposed as an example of avulsive downdip channel movement towards an active basin bounding normal fault (Leeder, 1993). This chapter investigates the avulsive history of the palaeochannels of the Carson River using radiocarbon and luminescence dating, palaeohydrology and surveying at a range of scales. In addition, independent dating of the basin bounding fault allows the Holocene alluvial-tectonic interactions to be studied. Floodplain gradients were measured perpendicular to the range front and the spatial distribution of lateral gradients analysed. Avulsion periods, lag times between faulting and channel avulsion, and patterns of channel onlap and offlap have been generated, and could be used to constrain and improve half-graben process-models. The Holocene history of the Carson River is more complex than that envisaged by Leeder (1993), with interaction between tectonics, climate change and intrinsic channel processes.

7.2 Introduction

The Carson River Basin is located on the western margin of the Basin and Range Province of western North America adjacent to the Sierra Nevada massif. It is one of a large number of internally draining basins that are collectively known as the Great Basin which encompasses most of Nevada, and parts of Utah, California, Idaho, Oregon and Wyoming (Fig. 7.1). Orographic precipitation and spring snowmelt from the eastern Sierra Nevada feed the headwaters of the Carson which rise in California and flow north into Nevada. The two principal tributaries, the East and West Fork join to form the Carson River in Carson Valley, which is a broad alluvial basin up to 15 km wide and approximately 25 km long. After leaving Carson Valley, the Carson River enters Eagle Valley before turning NE through a narrow bed rock gorge. The Carson then flows NE along a tectonically controlled lineament for approximately 75 km before reaching the Carson Sink where the river repeatedly bifurcates and forms a series of lakes (Fig. 7.1).

The Carson Range of the Sierra Nevada forms the western edge of Carson Valley and has a relative relief of approximately 1280 m. The low density granitic composition

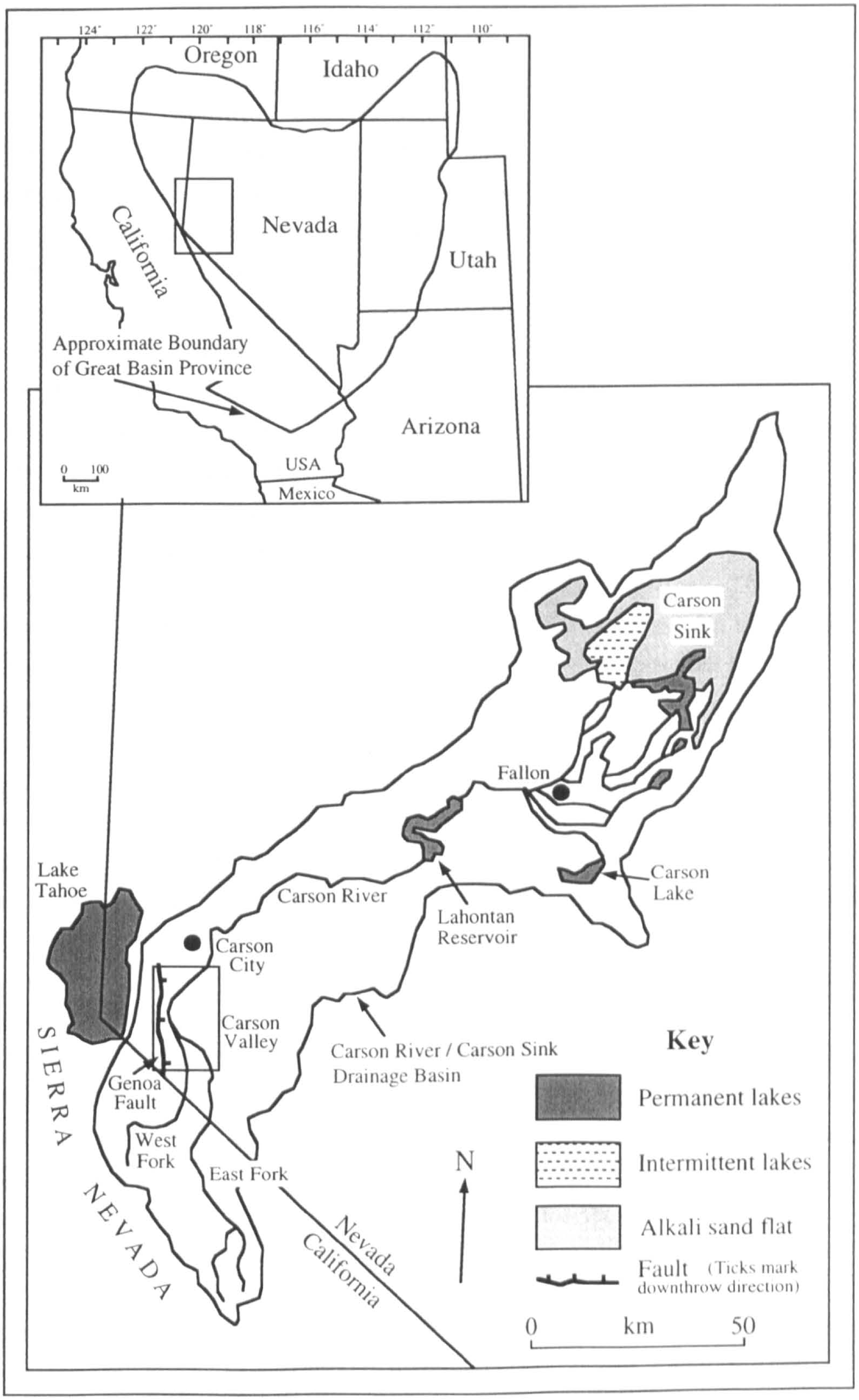

Figure 7.1. Location and main geographical features of the Carson River / Carson Sink drainage basin. The area enlarged in Figure 7.2 is shown by a rectangle.

of the Sierras has allowed them to rise through the crust as a large horst block. At least 7 km of vertical movement has occurred on the basin bounding Genoa fault which has been active during the Holocene (Pease, 1979a,b). Gravity surveys indicate that the Carson Valley is a half-graben structure with the westerly tilted Pine Nut Mountains on the eastern edge of the basin dipping towards the Carson Range (Fig. 7.2). The basin is filled by approximately 1500 m of sediment (Maurer, 1985) and is typical of block faulting or 'domino' style extensional tectonics. In addition to E-W regional extension, the tectonic history of the Carson Valley has been complicated by right-lateral strike slip movement on both the Genoa Fault and the Walker Lane Belt to the east, which are associated with the San Andreas fault system.

The Carson Valley has a drainage area of 2300 km^2 as measured to the south of the hydrological gauging station 7 km south-east of central Carson City (Fig. 7.2) and a total basin area of approximately 6800 km^2. A 'flashy' flow regime characterises the Carson River with a mean average discharge in the Carson Valley of 11 m^3 s^{-1} and peak discharges of up to 850 m^3 s^{-1} due to spring and summer snowmelt. The West Fork Carson River enters the Carson Valley through a dissected outwash fan that dates from the last two glacial advances (Armin *et al.*, 1983) and has a mean annual discharge which is only 30% of the flow of the East Fork. Westward tilting of the valley surface due to movement on the Genoa Fault has kept the West Fork pinned against the basin margin (Fig. 7.2). In the far south-eastern corner of the valley, the East Fork Carson River has built a large alluvial fan as flow expands from a narrow bedrock canyon. The present course of the East Fork River follows the path of maximum gradient but numerous partially occupied and abandoned channels testify to frequent avulsion on the fan (Fig. 7.2). Approximately 50% of the East Fork sediment load is deposited between entering the valley and reaching the town of Genoa which causes river avulsion by reducing channel capacity (Katzer and Bennett, 1983). The two tributaries join immediately south of the town of Genoa and flow on the western edge of the valley before turning NE and exiting the basin through a narrow canyon. A series of abandoned channel belts are well preserved on the eastern side of the valley several kilometres from the basin-bounding fault (see Fig. 7.3).

A preliminary analysis of channel deposits within the Carson Valley by Leeder (1993) concluded that three distinct channel belts are present which decrease in age towards the fault (see Fig. 7.4). Leeder (1993) suggested that these channel avulsions may have been directly controlled by fault movement. Previous workers have also recognised aspects of Leeder's (1993) hypothesis. Moore and Archbold (1969, p.18) noted that , "West tilting of Carson Valley has continued to very recent time and caused the Carson River to flow in its present anomalous course on the west side of the valley rather than in the middle". Pease (1979a, p.69) stated that, "detailed mapping ... strongly

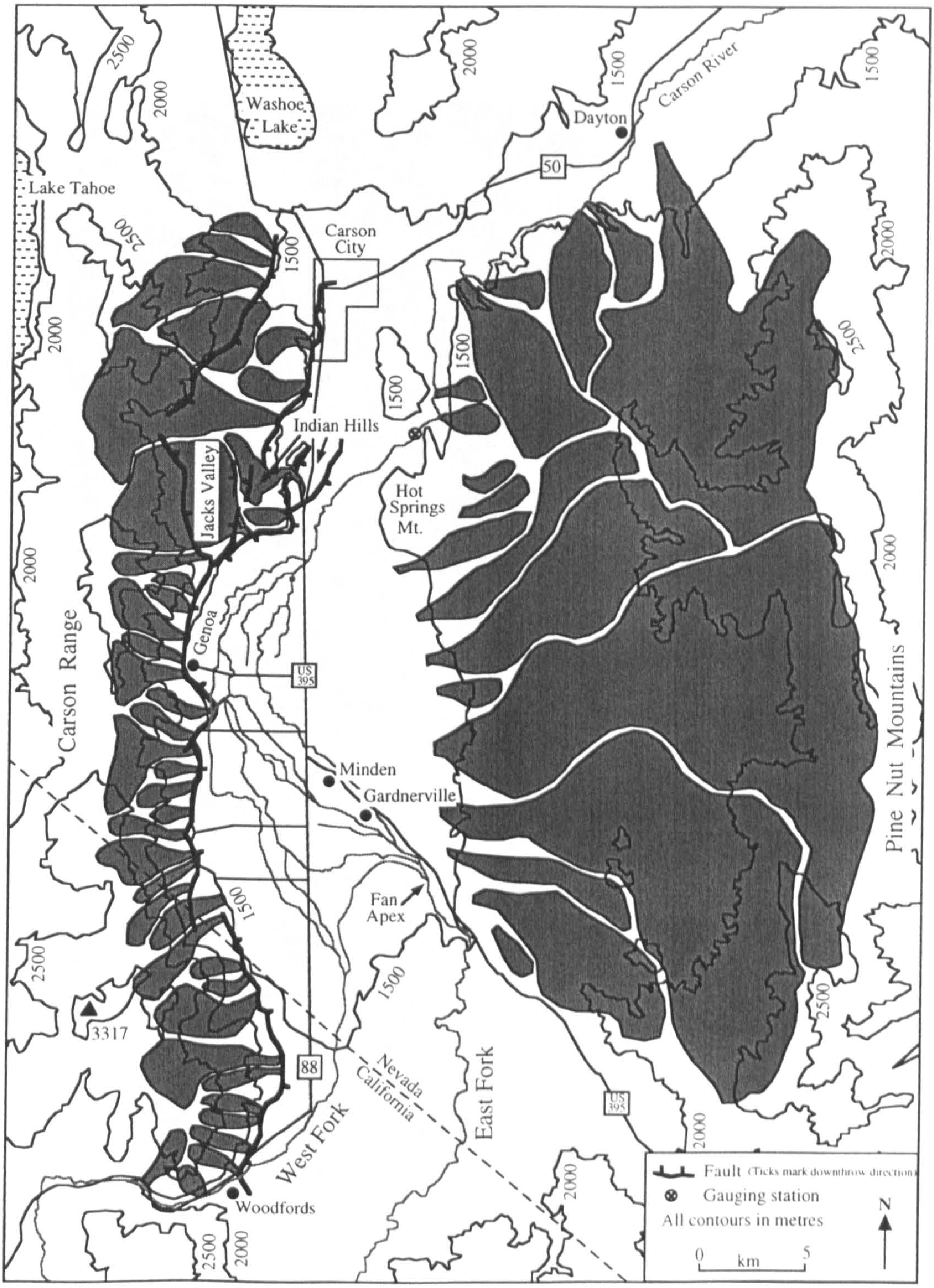

Figure 7.2. Map of the main geomorphological features of the Carson Valley. Drainage basins are marked in grey. Fault positions are based on Ramelli *et al.*, (1995) and Pease (1979b), and the axial channel system on USGS 1:100,000 scale maps.

Figure 7.3. Aerial view of the modern Carson River and palaeochannels, looking east towards the Pine Nut Mountains. Several large meander bends are preserved immediately west of the highway (US 395) and are shown by cusps cut into prominent field patterns marking the adjacent pediment surface.

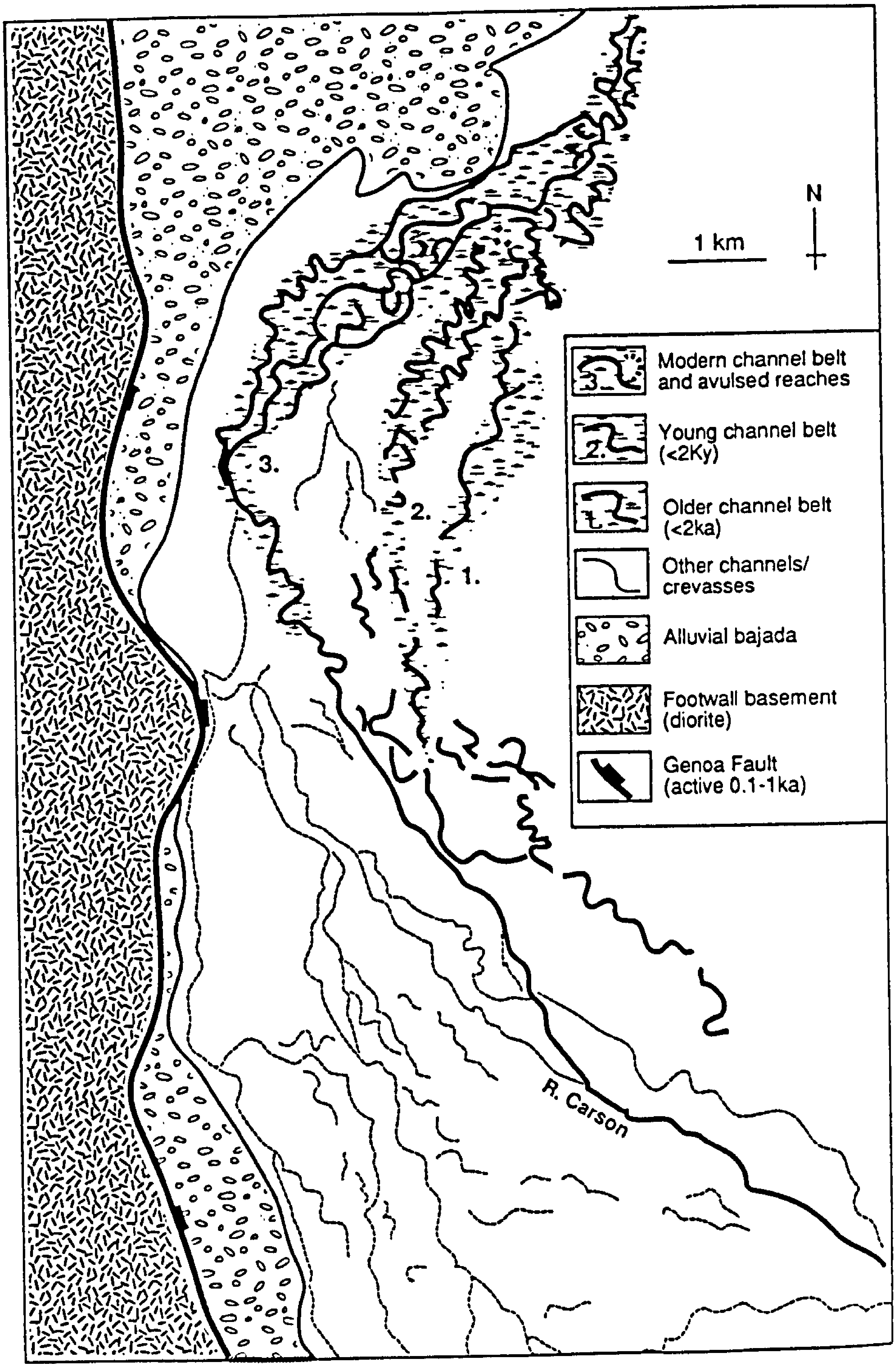

Figure 7.4. Schematic map of the Carson Valley, Nevada, with hypothesised avulsive channel movement towards the fault. Flow is from south to north. From Leeder (1993).

suggests that the Carson River has abandoned its youngest floodplain and cut a new channel west of the floodplain near Genoa" whilst Slemmons (1975, p.102) noted that "the Carson River flows quite close to the foot of the Carson Range, through an extensive marsh, indicating that depression of the valley floor has been so recent that debris washed from the high mountains has not been able to fill the marsh". This study examines these hypotheses by quantifying the Holocene history of channel movements in the Carson Valley.

7.3 Regional geologic setting

The initiation of high-angle block faulting and resultant extension in Nevada has been estimated at approximately 15-17 million years ago (Noble, 1972; Proffett, 1977; Stewart, 1980), forming a series of uplifted tilted half-grabens, grabens and horsts. However, the dating of initial block faulting is based on the volcanic transition between calc-alkaline and basaltic magmatism which have been interpreted as the products of a compressional and an extensional regime respectively (McKee, 1971). Evidence of tectonically controlled sedimentary deposits dates from 11-13 Ma (Robinson *et al.*, 1968) and the formation of the present distribution of basins in western Nevada has been estimated at 7.5 Ma (Gilbert and Reynolds, 1973).

The majority of the granitic Sierra Nevada terrane was emplaced from the early Jurassic to the late Cretaceous (Stewart, 1980) and was initially uplifted and eroded soon after emplacement, as part of the Cordilleran orogeny. A second phase of uplift is estimated to have started approximately 20 Ma ago and for the last 10 Ma the uplift rate of the Sierras has averaged 300 m per million years (Fiero, 1986). Westward tilting of the Sierra Nevada has been estimated to have started at approximately 5 million years ago with a tilting rate of 0.28° per million years (Unruh, 1991).

The dominant extension during most of the Late Cenozoic has been east-west but there has been interaction in north-west Nevada with NNW-SSE strike slip associated with the San Andreas fault system. The strike slip faulting is most evident in the Walker Lane Shear Zone (WLSZ) which extends for almost 600 km from Pyramid Lake into eastern California and is interpreted to be right lateral and to have a total displacement of 130 to 190 km (Stewart, 1980; Fig. 7.5). To the north-west of the WLSZ the ranges have only been affected by extension and show a strong preferred north-south orientation, while the ranges to the south-east of the WLSZ show a wide range of orientations depending on the interaction of normal and strike-slip faulting.

Earthquake epicentre maps (e.g., Slemmons *et al.*, 1964) and historical evidence of fault events indicate that there are two distinct zones of high seismicity in Nevada, with the rest of the state having a relatively low and even distribution of seismicity. One zone runs along the eastern foot of the Sierra Nevada mountains and south into the Mojave

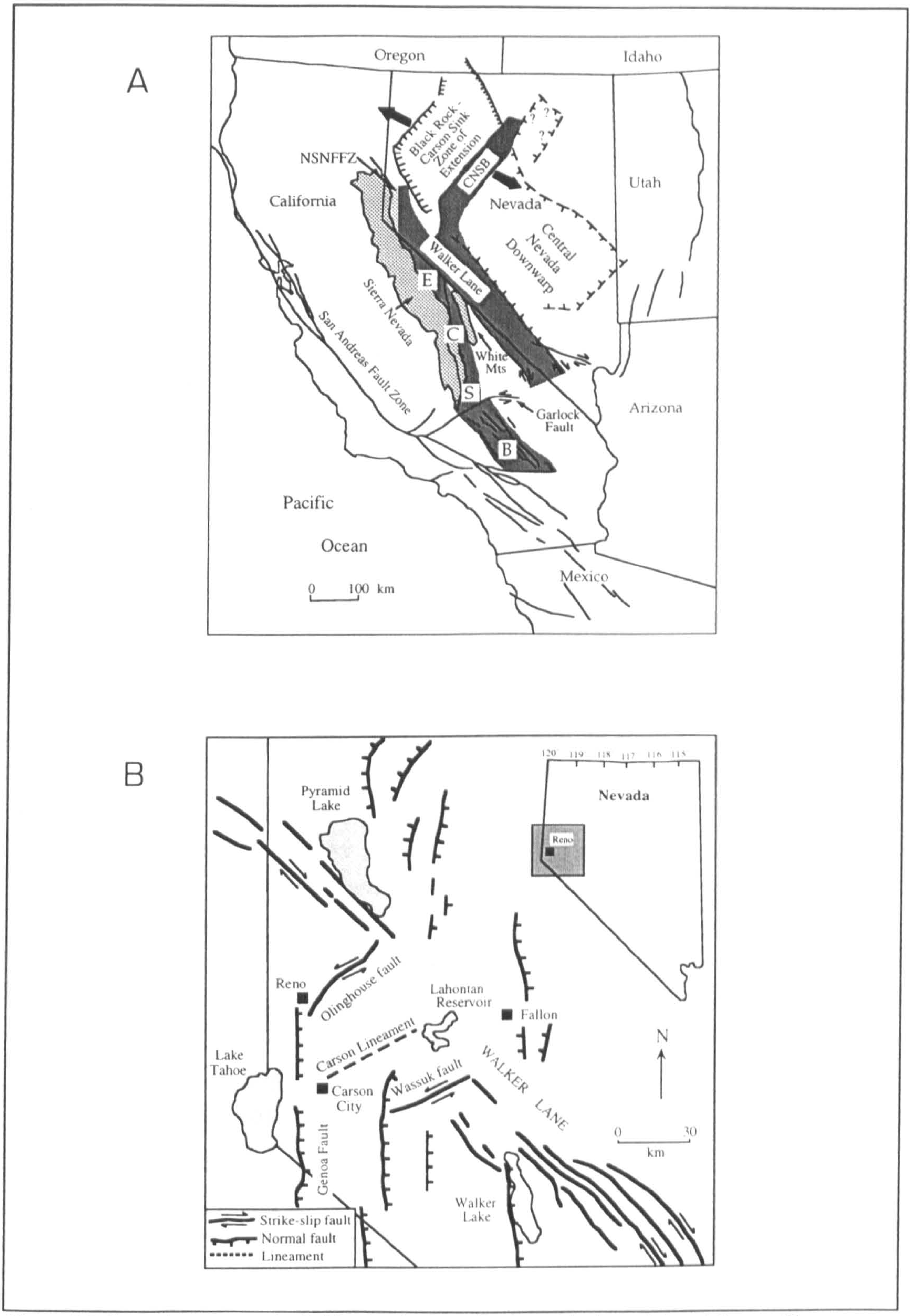

Figure 7.5. Tectonic structures in California, the Great Basin and in the vicinity of Carson City. A) Regional tectonic structures in the Great Basin and California. CNSB=Central Nevada Seismic Belt; ECSB=Eastern California Seismic Belt; NSNFFZ=Northern Sierra Nevada Frontal Fault Zone. Adapted from Wallace (1984). B) Tectonic features in the vicinity of Carson City, Nevada. Adapted from Link *et al.*, (1985) with additional data from John *et al.*, (1993). Ticks on faults mark the direction of downward displacement.

desert, and has been termed the Eastern California Seismic Belt (ECSB) (Wallace, 1984) (Fig. 7.5a). North of the Mojave, the zone has also been called the Sierra Nevada Frontal Fault Zone (Bell, 1984). The term Northern Sierra Nevada Frontal Fault Zone (NSNFFZ) is adopted here for the study section (see Fig. 7.5a). The ECSB consists of a series of left-stepping north-trending faults separated by heavily fractured cross-over zones and is intersected near its southern end by the left-lateral Garlock Fault which is a splay off the San Andreas fault system (Fig. 7.5a). A second band of enhanced seismicity, which has been marked by a series of large magnitude (>7 M) historical earthquakes (dePolo *et al.*, 1991) runs north and west from the White Mountains and has been called the Central Nevada Seismic Belt (CNSB). The ECSB has had less historical seismic activity than the CNSB, although the 1872 Owens Valley earthquake is the largest historical event in the Basin and Range with an estimated magnitude of 7.7-8+ (dePolo *et al.*, 1991). To the north of the White Mountains (Fig. 7.5a) both seismic zones are characterised by dip-slip motion with a small strike-slip component which increases to the south in the Eastern California Seismic Belt. Aseismic creep in the region may additionally account for 40% of the total slip. (King *et al.*, 1994).

The Carson Lineament and the Olinghouse and Wabuska fault zones trend ENE-WSW between the WLSZ and the NSNFFZ and have been interpreted as conjugate antithetic left-lateral shears of the Walker Lake Shear Zone (Bell and Slemmons, 1979; Livicarri, 1979; see Fig. 7.5b). An earthquake with an estimated magnitude of 6.7 (Sanders and Slemmons, 1979) is thought to have taken place in 1869 on the Olinghouse fault to the east of Reno. To the south of the Olinghouse fault is the Carson Lineament through which the Carson River passes, immediately east of the town of Dayton. No estimates of offset have been made for the Carson Lineament or the Olinghouse fault zone, but 4 km of movement has been estimated on the Wabuska fault zone (John *et al.*, 1993).

Limited volcanism has been associated with extension across the Basin and Range (Stewart, 1980; Shepard *et al.*, 1995) and was dominated by basaltic lava flows and cinder cones from small widely distributed vents. Within the last millenium a number of minor eruptive events have occurred in the Mono craters and Long Valley Caldera to the south of the Carson Valley (Wood, 1977; Miller, 1985; Sieh and Bursik, 1986).

7.4 Chronology and seismicity of the Northern Sierra Nevada Frontal Fault Zone (NSNFFZ)

The Northern Nevada Frontal Fault Zone (NSNFFZ) extends for approximately 100 km along the western margin of Nevada, through the towns of Reno and Carson City and into eastern California (Fig. 7.6). Ramelli *et al.*, (1995) divided the fault zone into five discrete segments based on geometric and/or structural discontinuities (Fig. 7.6). The

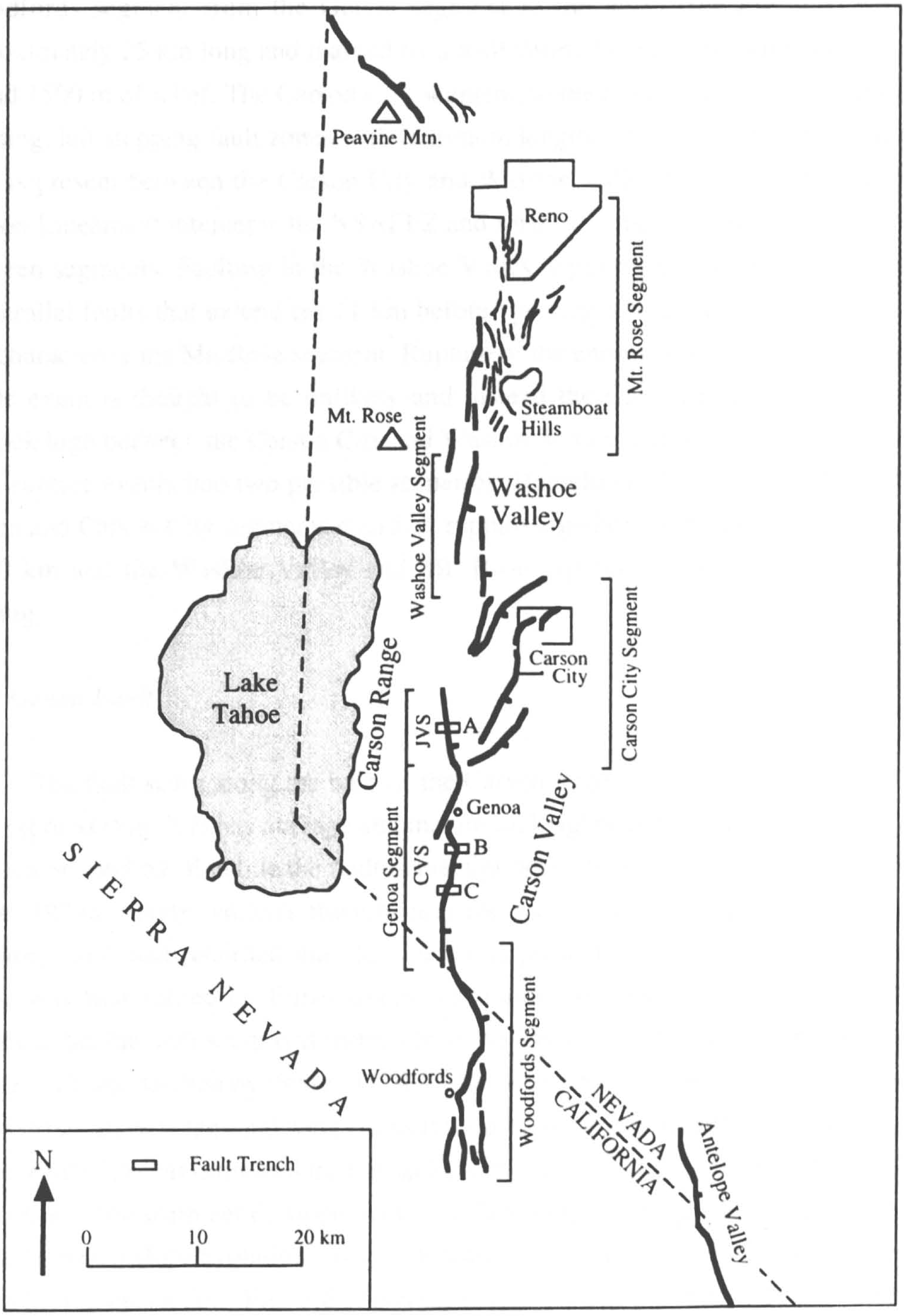

Figure 7.6. Generalized map of the Northern Sierra Nevada Frontal Fault Zone. The fault system has been subdivided into five discrete segments. CVS = Carson Valley Section; JVS = Jacks Valley Section. Trench sites, A = Jacks valley; B = Walleys; C = Sturgis. Adapted from Ramelli *et al.*, (1995).

Woodfords segment at the southern end of the NSNFFZ forms a prominent range front in the north which splays at the southern tip-zone. A 1.5 km left step separates the Woodfords segment from the Genoa segment to the north (see Fig. 7.6) which is approximately 25 km long and marked by a well defined range front with between 1200 m and 1500 m of relief. The Carson City segment, to the north, is composed of three NE trending, left stepping fault zones with minimum lengths of 7.5-14 km. A large bedrock high is present between the Carson City and Washoe Valley fault segments where the Carson Lineament intercepts the NSNFFZ and forms the most significant discontinuity between segments. Faulting in the Washoe Valley segment is distributed between two subparallel faults that extend for 11 km before splaying into a series of nested grabens that characterise the Mt. Rose segment. Rupture of the entire fault system (~100 km) in a single event is thought to be unlikely and instead the Carson Lineament influenced bedrock high between the Carson City and Washoe Valley segments is thought to divide large rupture events into two possible scenarios (Ramelli *et al.*, 1995). The Woodfords, Genoa and Carson City segments could all rupture together giving a total rupture length of 70 km and the Washoe Valley and Mt. Rose segments could produce 36 km of faulting.

7.4.1 Genoa Fault

The fault scarp along the base of the Carson range front in the Carson Valley is well exposed (Fig. 7.7) has average and maximum heights of 6.3 m and 13.4 m and dips between 36° and 60° E, while the fault plane dips between 58° and 61° E (Lawson, 1912; Pease, 1979a). Early workers thought that the scarp was very fresh (Russell, 1885; Lawson, 1912) and recorded that the scarp was present from at least 1854, when the valley was first settled by Euro-Americans. Later work by Slemmons (1975, 1977) predicted that the fault scarp was formed by up to five events. The geomorphology of the Genoa fault was studied by Pease (1979a) who noted that streams had not cut channels across offset alluvial fans and were characterised by sharp gradient changes due to knick-points. Pease (1979a) estimated the chronology of the fault at different localities by using the profile of the scarp debris slope, with each bevel representing a single faulting event. Using the debris slope evolution curve of Wallace (1977), Pease (1979a) estimated that in the Jacks Valley section (Fig. 7.6), faulting events occurred at 600 B.P. and 2500 B.P while in the Carson Valley section the fault was much younger with estimated movement at 100 B.P. and 300 B.P. A second soil-stratigraphic method was also used by Pease (1979a) and indicated two fault movements in the last 4,000 years which is in broad agreement with the scarp profile studies.

A detailed study of the NSNFFZ also subdivided the Genoa Fault at the same point as Pease (1979a) into two sections, based on different trend directions and a lower

Figure 7.7. Low sun-angle photograph of the Genoa fault scarp, immediately south of Jacks Valley. The double scarp to the right of the grain silos, has a total height of 13.4 m. An abandoned meander loop is present in the foreground. View is almost due west.

vertical offset across the range front (Fig. 7.6; Ramelli *et al.*, 1995). Radiocarbon dates from three trenches across the fault (Fig. 7.6) indicate that the range front forest burns down approximately every 100 years and that the preferred age ranges for fault events, taking into account sedimentation rates, are 550-650 B.P. for the most recent event (MRE) and 2000-2500 B.P. for the penultimate event (PE) (Ramelli *et al.*, 1995). Subsequent radiocarbon analyses have constrained these ages further with the MRE having a preferred age of 550-650 B.P. (two sigma calibrated age range of 480-920 B.P.), 2000-2300 B.P (1820-2719 B.P.) for the PE and >4000 B.P. (>2879 B.P.) for a third event (Ramelli, written communication, 1995). These ages agree well with the estimates of Pease (1979a) for the fault in the Jacks Valley section. Displacements for the MRE and PE vary between 3 m and 6 m (net dip slip), with a maximum throw for the MRE of 5-6 m at the Jacks Valley trench site which decreases southwards to 4-5 m at Walleys and 3 m at Sturgis (Fig. 7.6). Scarp profiles indicate that displacement drops off rapidly to the north of the Jacks Valley trench site.

Early seismic maps classified the Carson Valley as an area of relatively low seismic risk (Algermissen and Perkins, 1976; Applied Technology Council, 1978) but a re-analysis of the historical seismicity (Section 7.4.2), coupled with studies of the faulting (Pease, 1979a, b; Ramelli *et al.*, 1995), indicate that the Genoa Fault represents the zone of highest seismic risk in Nevada (VanWormer and Ryall, 1980). A lower limit on the magnitude of the last two movements of the Genoa Fault is given by the maximum background earthquake, which is the largest earthquake that is not associated with significant primary surface rupture, and has been estimated at M=6.5 for the Basin and Range province (dePolo, 1994). Ramelli *et al.*, (1995) estimate magnitudes of M=7.5 for the last two events, based on a comparison of displacements with those from the 1959 Hebgen Lake earthquake.

7.4.2 Historical seismicity of the Northern Sierra Nevada Frontal Fault Zone

Historical seismicity indicates that activity has been concentrated on the two ends of the NSNFFZ (VanWormer and Ryall, 1980; Somerville *et al.*, 1980). A series of earthquakes occurred in 1978 (M_L=5.0 for the main shock) near the centre of the Woodfords segment (Somerville *et al.*, 1980), and an area of frequent earthquake swarms, called Steamboat Hot Springs, is located close to the northern end (VanWormer and Ryall, 1980; Fig. 7.6). Fieldwork suggests that there is a right-lateral strike slip component on the Genoa Fault, estimated as up to 20% of the fault displacement (Slemmons, 1975). However, there are too few fault plane solutions on the main north trending portion of the Genoa Fault to confirm the fieldwork of Slemmons although there is evidence for right lateral strike slip movement on north west trending faults at either end of the fault zone (VanWormer and Ryall, 1980). Seismicity within the Carson Valley fluctuates (Somerville *et al.*, 1980) with one rapid increase linked to the 1992 Landers earthquake (M_w=7.3), 600 km to the SSE (Anderson *et al.*, 1994). The Double Spring Flat earthquake (11-9-1994, M=6.0, M_s=6.3) is the largest historical event to have occurred in the study area. Left-lateral normal slip occurred on a steeply east dipping NNE-trending structure (Ramelli, written communication, 1994) that forms part of the stepover zone between the Genoa fault and Antelope Valley to the SE. This NNE trending fault also forms the southern end of a line of north-striking, east dipping faults along the eastern side of Carson Valley (VanWormer and Ryall, 1980) which have a maximum calculated earthquake magnitude of 7.5 (Ryall and VanWormer, 1980). Additional evidence for fault activity is provided by several thermal springs that outcrop along mapped fault zones and by a region of high heat flow that underlies northern Carson Valley (Trexler *et al.*, 1983).

7.4.3 Chronology and slip-rates of fault segments along the Northern Sierra Nevada Frontal Fault Zone

Holocene and late Pleistocene slip-rates for the Genoa fault are in the range of 1-2 mm yr^{-1} based on trenching studies with preferred rates varying from 2.5 mm yr^{-1} at Jacks Valley to 1.4 mm yr^{-1} at the Sturgis trench site (Ramelli *et al.*, 1995). These slip rates are much higher than those estimated for the rest of the NSNFFZ of 0.5-1.0 mm yr^{-1} or less. A long term uplift rate for the Genoa fault over the last 3-5 Ma has been estimated at 0.3-0.7 mm yr^{-1}, from the separation of the valley floor with a sub-horizontal erosion surface preserved within the Carson Range. The entire NSNFFZ is thought to have ruptured within the latest Holocene and probably within the last 1000 years. However, there are less data on recurrence intervals although the Genoa fault has an estimated value of 2-4 ka for the Holocene and late Pleistocene, based on a flight of faulted glacial outwash terraces at Woodfords (Fig. 7.2; Ramelli *et al.*, 1995).

7.5 Structure and geomorphology of the Carson Valley

Gravity studies (Erwin and Berg, 1977; Plouff, 1984; Saltus, 1988a, b; Plouff, 1992) and magnetic anomaly maps (Hildenbrands and Kucks, 1988a, b) show that the Carson Valley has two separate sub-basins divided by a horst block composed of crystalline basement or igneous rock. The main basin is elongated N-S and reaches a maximum depth of approximately 1500 m at a point to the NW of Minden, adjacent to a large range front salient (see Fig. 7.8). A smaller sub-basin up to 750 m deep is located to the north of Fish Spring Flat on the eastern side of the valley. Between these basins is a horst block with a steeply dipping N-S trending western edge which has an estimated relief of 650 m (Maurer, 1985). The distribution of estimated depths is in broad

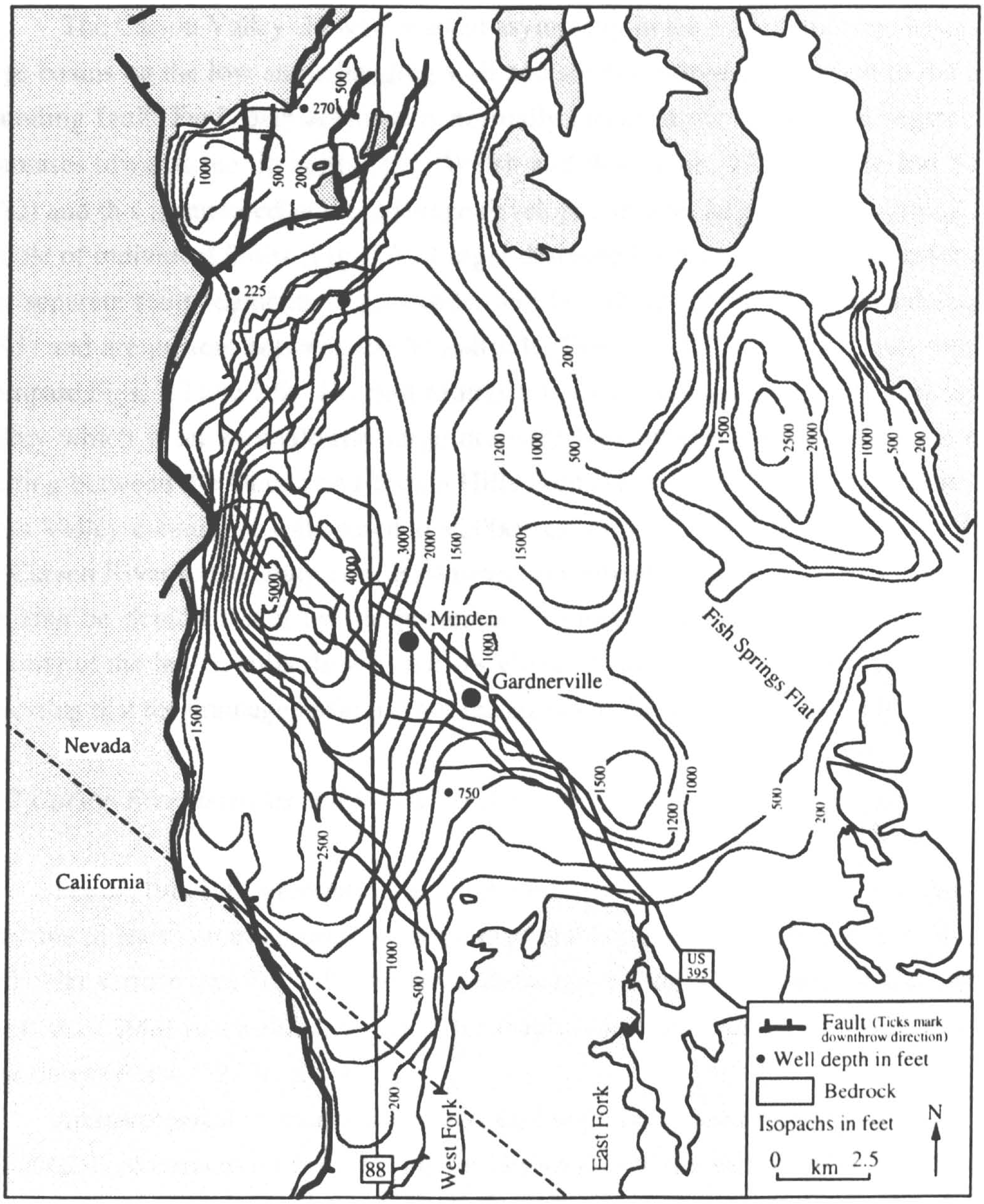

Figure 7.8. Calculated depth to basement for the Carson Valley. A central north-south trending bedrock ridge divides the sediments into two sub-basins. Adapted from Maurer (1985).

agreement with water wells which have penetrated over 300 m of sediment in the basin (Glancy and Katzer, 1975).

7.5.1 Tectonic controls on drainage basin development

The Carson Valley shows a marked asymmetry in the size of drainage basins with large basins on the low angle hanging wall and small catchments adjacent to the basin-bounding fault. Fault displacement is normally larger in the centre of a segment and decreases towards the tip zones (e.g., Walsh and Watterson, 1987; Cowie and Scholz, 1992) and this is mirrored in the drainage development with larger basins forming in the middle of individual faults (Fig. 7.2). Larger drainage basins also form in transfer zones that separate fault segments (e.g., Leeder and Gawthorpe, 1987; Leeder and Jackson, 1993) and are present between the Woodfords, Genoa and Carson City fault segments (compare Figs. 7.2 and 7.6). The best example of such a transfer zone in the area is Jacks Valley which is an anomalously large drainage basin that has formed oblique to the faulting between the Genoa and Indian Hills faults (Fig. 7.2). Large fan deposits from Jacks Valley containing soils dated at <2000 years (Pease, 1980; Fig. 7.9) have forced the Carson River to the south east. Basinward movement of the Indian Hills frontal fault can also be demonstrated by the preserved drainage basins. The basin draining the majority of the Indian Hills shows a narrow elongate section between two fault segments indicating that the drainage basin has not readjusted to the step-out of the fault (Fig. 7.2).

7.5.2 Carson River terraces and floodplain deposits

Pease (1980) differentiates the floodplain deposits of the Carson River into three units; the modern, areas around the two most notable palaeochannels and remnants of a third older surface (see Fig. 7.9). All three surfaces are dated on the basis of soil maturity as less than 2000 years old, although there maybe some uncertainty on the accuracy of these dates (Pease, 1979a, p.3-4).

Archaeological investigations associated with the widening of highway 395 have identified three terraces on two sites on the eastern side of the valley (NDOT, 1985). The northern site is located immediately above a prominent meander scar (see Fig. 7.9 and 7.10). Two terraces roughly coincident with the 4660 ft (1420 m) contour were identified on the basis of sedimentary characteristics revealed from trenching (NDOT, 1985). The upper terrace shows a widespread gravel lag deposit at a depth of 1.2 to 2.0 m. Overlying the centre of the gravel lag is an indurated laminated silt deposit which probably represents an abandoned meander loop. The silt layer also contains a powdery white substance that may be Mazama Ash (NDOT, 1985; see below). In contrast, the lower terrace consists entirely of a structureless sandy loam to a depth of at least 2 m. The

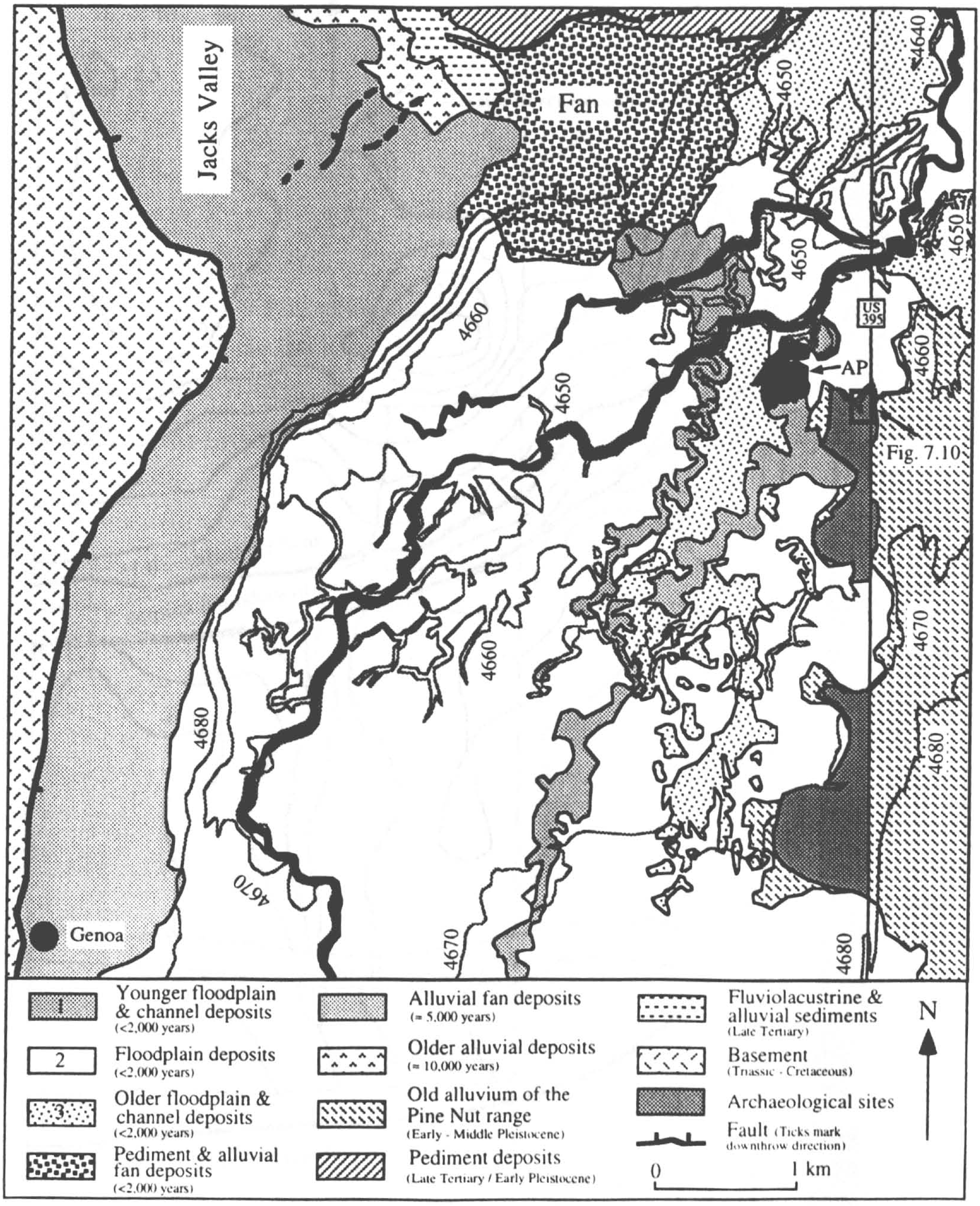

Figure 7.9. Geological map of the northern Carson Valley. The location of two archaeological sites is shown along with the position of Figure 7.10. AP = Ambrosetti Pond. For clarity, only contours between 4680 ft and 4640 ft are shown, see Figure 7.2 for general topography. Adapted from Pease (1980), with archaeological sites from NDOT (1985).

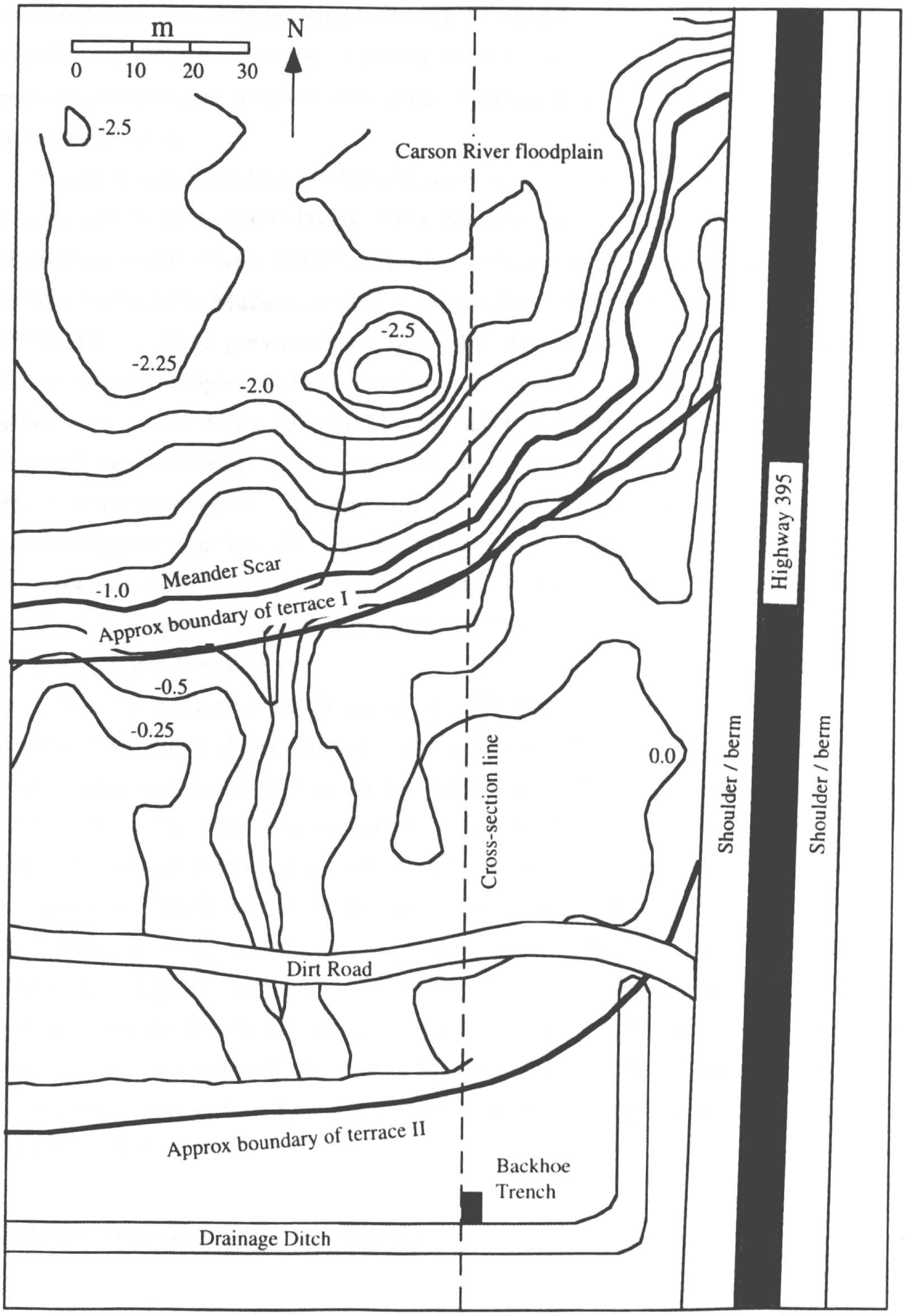

Figure 7.10. Location of the terrace boundaries, survey line and sedimentological trench for the northern archaeological site, Carson Valley. The approximate position of a schematic cross-section (Fig. 7.11) is shown. The highway has since been widened to a dual carriageway, obliterating part of the site. Adapted from NDOT (1985).

contact between the two terraces was never trenched but the proposed relationship is shown in the schematic cross-section (Fig. 7.11). Projectile points (e.g. arrow heads) recovered from the archaeological site can be used for dating and give a possible age range for occupation of the site of 5000 B.P. to 1300 B.P. Charcoal floated out from the centre of a hearth gave a radiocarbon date of 930 ±210 B.P. indicating some later human activity in the area.

Ash layers from Mount Mazama were deposited over much of Northern Nevada (Powers and Wilcox, 1964; Davis, 1978) and have dates of approximately 6800-7000 B.P (Bacon, 1983). Davis (1978) notes two widespread Mazama ash layers in northern Nevada, termed the Mazama and Tsoyawata beds of which only the Tsoyawata bed (~6900 B.P) has been previously recognised in the area around the Carson Valley. The white powdery samples from the archaeological investigation were never dated (H. Turner, *pers comm.*) but if they are Mazama ash the mid-Holocene history of the Carson River can be constrained. The river must have aggraded from at least 6900 B.P. to sometime before occupation to form terrace II. Within the same time period the river must have eroded part of terrace II and deposited terrace I. The archaeological deposits are in a layer approximately 0.4 m deep which suggests that the area was part of the floodplain during its occupation. At some point after abandonment of the site the river moved and formed its present floodplain.

A third terrace at an elevation of 4670 feet (1423 m) was identified on the southern archaeological site (NDOT, 1985), although the downvalley gradient suggests that the terrace may correlate with the two terraces identified in the north (Fig. 7.9). Pease (1980) mapped the three terraces and sediments to the east as a single unit of early to middle Pleistocene coarse sand and gravel deposits, so the extent of the terraces are unknown (Fig. 7.9). However, McKinney (1976) identified two paired terraces and one unpaired terrace on the Carson River in Eagle Valley to the north of Carson Valley. The terraces stand approximately 2 m, 5.5 m and 9 m above the height of the present day floodplain and the estimated age range is Late Quaternary to the present (McKinney, 1976). There is a 3 m height difference between terraces 1 and 2, and terrace 3 in the NDOT (1985) study, but it is not known how these correlate with the terraces of McKinney (1976).

7.6 Climatic history of north-west Nevada

The present day climate of Nevada is semi-arid and continental, and prone to extreme fluctuations due to the interaction of tropical and polar air masses. Orographically induced precipitation over the Sierra Nevada gives an annual snow fall in excess of 2.5 m and over 40 mm of rain (Houghton *et al.*, 1975). The Carson Valley lies in the

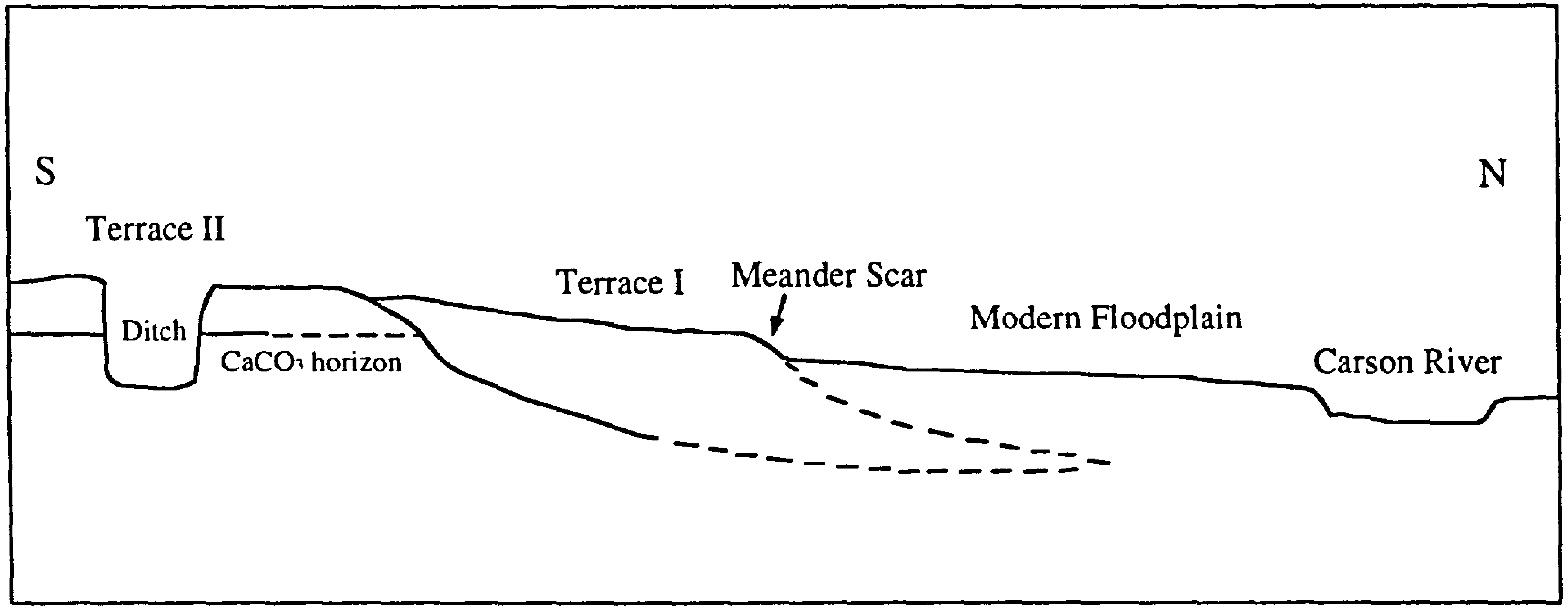

Figure 7.11. Schematic relationship of Carson River terraces as determined by trenching. The hypothetical position of the cross-section is shown in Figure 7.10. Adapted from NDOT (1985).

rainshadow of the Sierras and receives an average of 25 mm of precipitation per year and has a mean annual temperature of 9°C.

The age range of the last glaciation (the Late Wisconsinan, referred to locally as the Tioga (Burke and Birkeland, 1979)) in the Sierra Nevada is still strongly debated. In the review of Pinter *et al.*, (1994) the maximum and minimum constraints are quoted as >9.8 ka <26 ka while Dorn *et al.*, (1987) estimate an age of >13.2 ka, and Phillips *et al.*, (1990) suggest a range of 20-23 ka. There is some evidence of a minor readvance of glaciers within parts of the central Sierra between 11 and 9.7 ka (Mezger and Burbank, 1986; Dorn *et al.*, 1990).

The basins of north-west Nevada were the site of a large Pleistocene pluvial lake, named Lake Lahontan, which covered an area of 22,000 km^2 at its highstand (Benson and Mifflin, 1986). Fluctuations of Lake Lahontan and its sub-basins have acted as a barometer of climate in the Great Basin over the last 35 ka (Benson *et al.*, 1990, 1992; Benson, 1993, 1994). From about 9 ka lake levels have been at approximately their present levels and because of this apparent lake stability there is relatively little data on climatic change in the Great Basin during the Holocene. However, the Walker Lake basin has apparently desiccated twice within the last 5500 years, at >5300-4800 and 2700-2100 (Benson, *et al.*, 1991) but this may be due to the Walker River periodically flowing into the Carson River through Adrian Valley (King, 1978; Davis, 1982; Benson and Paillet, 1989). The elevation of Walker Lake in the last 2000 years and that of Mono Lake further south (Stine, 1990), do appear to act as a surrogate to climate (Benson *et al.*, 1991) showing an increase in lake level during the Little Ice Age and a decrease during the Medieval Warm Period. Lake level peaks have subsequently occurred in Walker Lake at an interval of approximately 250 years (1090, 760, 510 and 250 B.P.). Additionally, a 1000 year tree-ring dataset demonstrates that the 20th century has had anomalously high precipitation which has only been reached three times in the record (Graumlich, 1993). The tree-rings also show evidence of higher temperatures between ca. 1100 to 1375 A.D. and for colder temperatures from ca. 1450 to 1850 A.D. which correspond to the Medieval Warm Period and the Little Ice Age respectively.

7.7 Identification of palaeochannel belts

Analysis of black and white aerial photographs from 1938, 1953 and 1954 along with ground truthing and surveyed cross-sections (Section 7.12) has allowed six palaeochannel belts to be identified and mapped in the Carson Valley (Figs. 7.12-7.14). This expands upon the preliminary work of Leeder (1993) who recognised three channel belts (Fig. 7.4). The eastern channel belt is identified on the basis of a series of large meander bends which have been cut into a low angle pediment surface. Channel belts 2 and 3 are well preserved and are separated by a uniformly coloured surface which has a

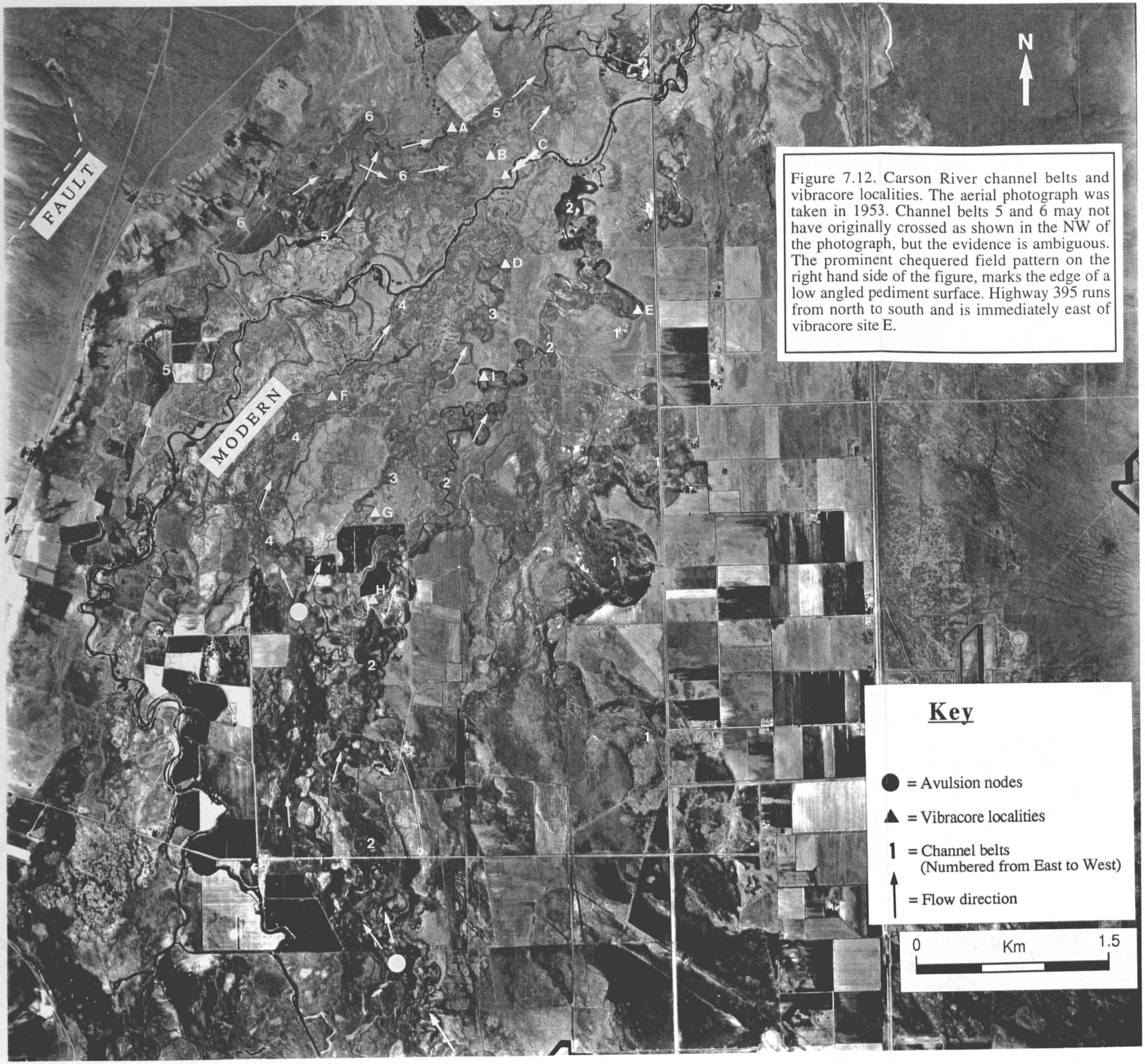

Figure 7.12. Carson River channel belts and vibracore localities. The aerial photograph was taken in 1953. Channel belts 5 and 6 may not have originally crossed as shown in the NW of the photograph, but the evidence is ambiguous. The prominent chequered field pattern on the right hand side of the figure, marks the edge of a low angled pediment surface. Highway 395 runs from north to south and is immediately east of vibracore site E.

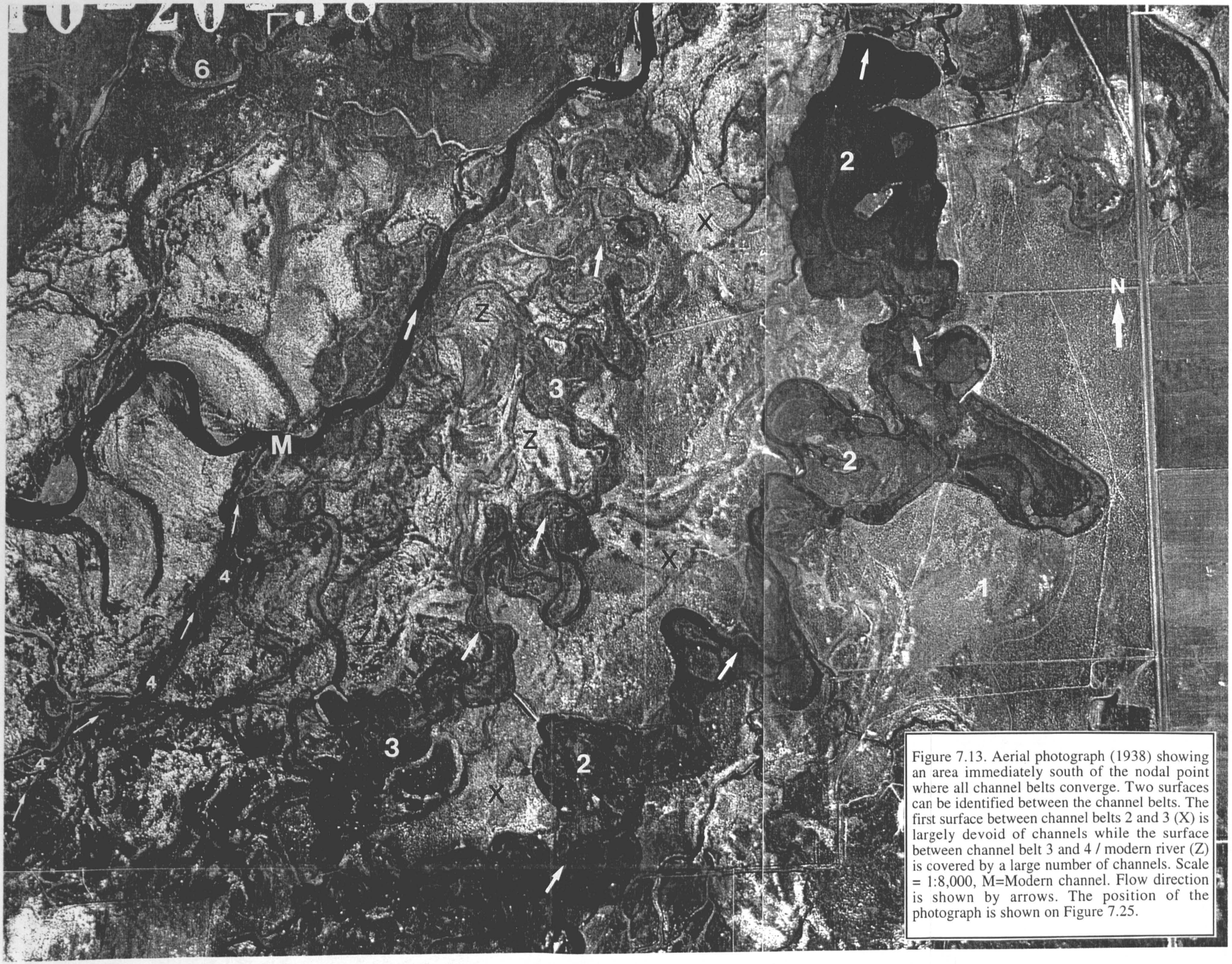

Figure 7.13. Aerial photograph (1938) showing an area immediately south of the nodal point where all channel belts converge. Two surfaces can be identified between the channel belts. The first surface between channel belts 2 and 3 (X) is largely devoid of channels while the surface between channel belt 3 and 4 / modern river (Z) is covered by a large number of channels. Scale = 1:8,000, M=Modern channel. Flow direction is shown by arrows. The position of the photograph is shown on Figure 7.25.

Figure 7.14. Aerial photograph (1938) showing subdued channel topography of channel belt 4. Two surfaces to the NE and SW of belt 4 (A, B) are picked out in white, have few channels on their surfaces and appear to have been cut into by channel belt 4. Scale = 1:8,000. Flow direction is shown by arrows and the circle indicates the position of an avulsion node. The position of the photograph is shown on Figure 7.25.

low density of relict channels (Figs. 7.12 & 7.13). In contrast, channel belt 4 has a far more subdued topography and is most clearly recognised on the 1938 photographs (Fig. 7.14). At the northern end of the valley, channel belt 4 is separated from channel belt 3 by an intensely reworked surface with abundant cross-cutting channels (Fig. 7.13), while to the south the two channel belts are divided by a prominent surface with very few relict channels (Fig. 7.14). Two further channel belts (5 and 6) are present to the west of the modern channel, with belt 5 cross-cutting belt 6 at present although this may be due to human interference. The eastern section of channel belt 6 shows a remarkably fresh series of sinuous meander loops which underwent limited migration prior to abandonment (Fig. 7.15).

Nodal avulsion points for channel belts 2, 3 and 4 have been identified on Figure 7.12 but the exact locations of nodal points for belts 5 and 6 are obscured by farmland. The avulsion nodes between, i) channel belt 1, ii) belts 2, 3 and 4, and, iii) belts 5, 6 and the modern, are all located at the apex of the alluvial fan formed by the East Carson River as it enters the southern end of the valley (see Fig. 7.2).

7.8 Sedimentological analysis of vibracores

A total of 19 vibracores were taken from 9 sites, covering all 6 palaeochannels and the modern river (Table 7.1 and Fig. 7.12). All of the sites were located either within the channels or on associated point-bars, so that all recovered datable materials represent past activity of the channel belt. In most cases, small pits were dug and filled with water prior to vibracoring, in order to aid liquefaction of the sediment. The 4 m long sections of 75 mm diameter aluminium tubing were then recovered using a large tripod and winch (Fig. 7.16). After slicing the core open with an electric saw (Fig. 7.17) each core was logged and sampled for radiocarbon and luminescence dating. Some downward movement of the core with respect to the core pipe occurred and is termed rodding (Table 7.1). This rodding either represents a loss of material at the end of coring when the vibracore has become stuck or a gradual loss of material through time which produces a condensed sedimentary sequence. The former case has been assumed for these cores and therefore the possible effects of condensation have been ignored when producing the sedimentological logs (Fig. 7.18)

The cores show very few sedimentological features (Fig 7.18) and are dominated by thick mud deposits and fine and medium sands with interstitial clay, representing abandoned channel fills. Some of the clay deposits have scattered fine and medium sand grains distributed through them. A number of prominent fining up sequences are present, most notably core 8 which has a gravel lag with an erosive base which gradually fines upwards over a height of approximately 1.5 m. Several other gravel lags with pebbles 20-30 mm in diameter mark the base of individual depositional units. Thin micaceous layers

Figure 7.15. Aerial view of channel belt 6 showing well preserved, highly sinuous bends. No abandoned bends can be identified on this channel belt, illustrating that the channel was only occupied for a limited period of time. The Modern Carson River is to the top of the photo.

Table 7.1. Vibracore locations and coring details

Core number	Channel belt	Vibracore site‡	Location	Core length (m)	Depth of surface pit (m)	Rodding † (m)	Loss of material at base of core pipe (m)	Total core depth Δ (m)
1	5	A	Centre of channel	1.93	0.00	0.34	0.14	1.93
2	3	G	Low on point bar, on bend axis	0.61	0.00	0.74	1.08	0.61
3	3	G	High on point bar, oblique to bend axis	0.92	0.00	1.32	0.63	1.12
4	4	F	Centre of channel in axis of bend	1.57	0.70	0.10	ND	2.27
5	3	D	Low on point bar on bend axis	1.51	0.40	0.24	0.05	1.91
6	3	D	High on point bar, oblique to bend axis	1.24	0.75	0.15	0.01	1.99
7	2	H	Centre of channel	1.56	0.25	0.39	ND	1.81
8	2	H	High on point bar	1.82	0.64	0.17	ND	2.46
9	Modern	C	Low on point bar	1.32	0.08	0.16	ND	1.40
10	Modern	C	High on point bar	1.01	0.10	0.69	0.17	1.11
11	6	B	Point bar on bend axis	0.76	0.10	0.95	0.06	0.86
12	6	B	On bend crossover	0.40	0.05	0.00	ND	0.45
13	1	E	High on concave bench	2.67	0.36	0.20	0.05	3.03
14	1	E	Low on concave bench	1.80	0.19	0.50	0.05	1.99
15	2	I	On plug infilling abandoned meander	1.28	0.35	0.15	0.10	1.63
16	2	I	On plug infilling abandoned meander	1.07	0.25	0.00	0.04	1.32
17	5	A	Centre of channel	1.83	0.14	0.30	ND	1.97
18	Modern	C	Downstream end of modern point bar	0.55	0.12	1.06	0.08	0.67
19	Modern	C	Downstream end of modern point bar	0.92	0.17	0.77	ND	1.09

‡ Vibracore localities are shown on Figure 7.12. ND = no data

† Rodding is the distance that the core gets pushed down the core pipe

Δ Total core depth is core length + depth of surface pit

Figure 7.16. Vibracoring on an abandoned meander loop of the Carson River. Reed beds occupy the centre of the channel, which is dammed further downstream. A prominent scarp can be seen in the background, where the river has cut into a low angled pediment surface. Vibracore site E.

Figure 7.17. Section through vibracore number 13, showing an overall fining-up sequence. The top of the core is at the top of the photograph. Total core length is 2.67 m and all cores were 75 mm wide.

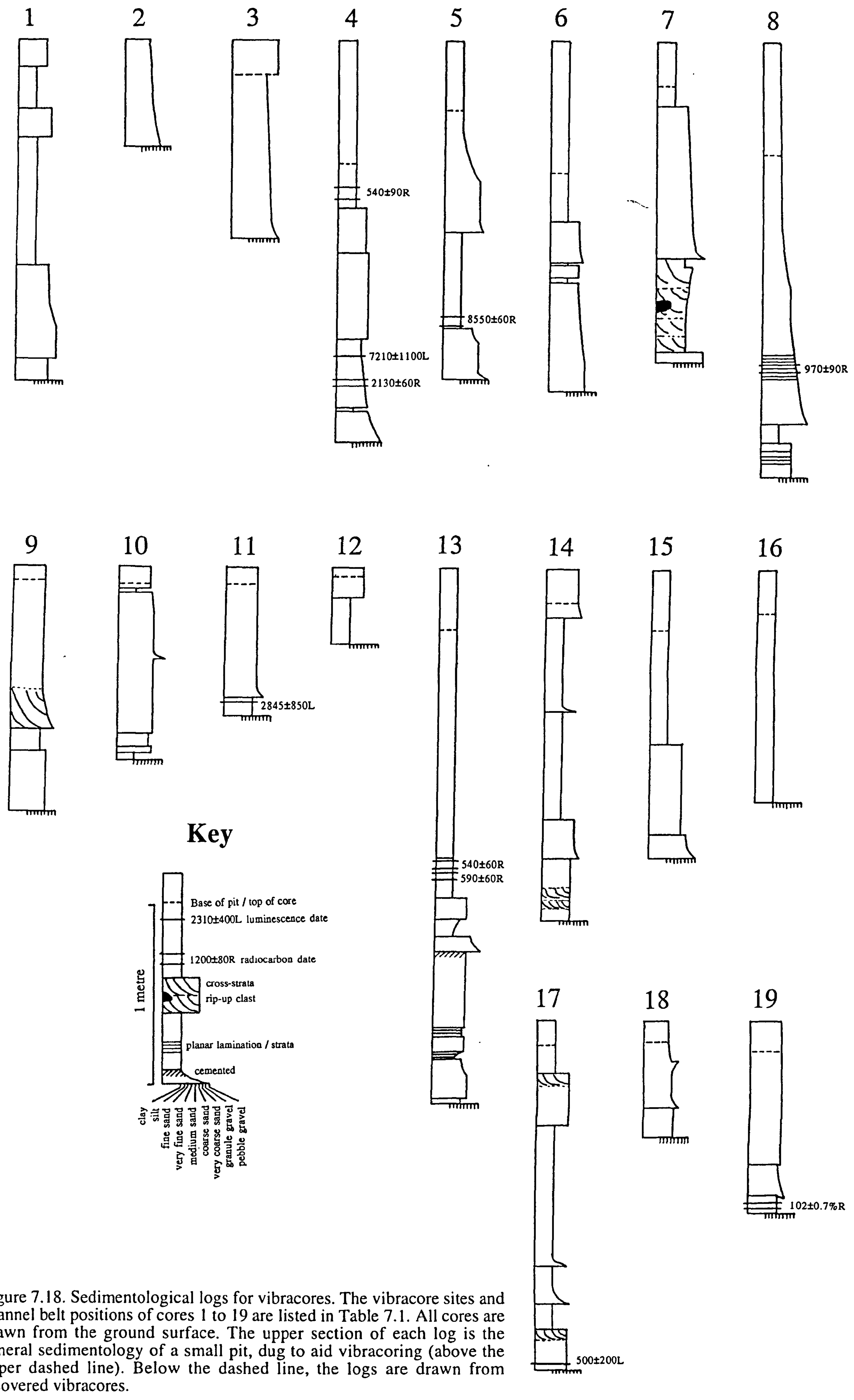

Figure 7.18. Sedimentological logs for vibracores. The vibracore sites and channel belt positions of cores 1 to 19 are listed in Table 7.1. All cores are drawn from the ground surface. The upper section of each log is the general sedimentology of a small pit, dug to aid vibracoring (above the upper dashed line). Below the dashed line, the logs are drawn from recovered vibracores.

pick out planar and cross-strata in a number of cores and indicate episodic deposition. The sediments are poor in organic materials with < 2 g of charcoal and wood recovered from all of the cores, of which the majority was concentrated in fine grained mud layers and micaceous laminae (see Table 7.2).

7.9 Radiocarbon dating

Charcoal and wood was hand-picked from vibracore sediment but the resulting samples were of insufficient weight (0.033-0.585 g pre-treatment) for traditional radiocarbon dating techniques. Six charcoal samples and one wood sample were therefore analysed by Accelerator Mass Spectrometry (AMS) at the Lawrence Livermore National Laboratory, California. A seventh charcoal sample taken from a river bank was dated using the conventional radiometric technique with an extended count time. The radiocarbon ages were calibrated to calendar ages using the Pretoria Calibration Procedure program (Talma and Vogel, 1993) which incorporates a 7,200 year dendrochronology record from sequoias, firs and south-central European oaks (Stuiver *et al.*, 1993; Vogel *et al.*, 1993). Törnqvist and Bierkins (1994) note that charcoal samples are more likely to contain contaminants than wood samples and consequently have a higher standard deviation of natural sample error, σ_n. However, they add that the calibration result is generally insensitive to σ_n and can be ignored if the age range of the sample is used.

Locations, descriptions and dates of the radiocarbon samples are collated in Table 7.2 and the spatial distribution is shown in Figure 7.19. All of the radiocarbon dates are internally consistent, with the charcoal samples ranging in age from 2130±60 B.P. to the modern while the wood sample has an age of 8550±60 B.P. There is a good agreement between the radiocarbon dates and the topography as observed from aerial photographs. Channel belt 4, which shows very indistinct features and subdued topography (Section 7.7), has an age of 2130±60 B.P. while the well preserved channel belts of 2 and 3 have ages < 1000 B.P. However, the wood sample in core 4 would appear to be anomalous as the topography of channel belt 3 is very similar to channel belt 2 which has a recorded age range of approximately 1000-500 B.P. The original age of the tree is included in the wood date, but even assuming that the tree was several thousand years old, the sample still appears to be anomalously old. A sample taken from a 20-30 mm thick layer of charcoal from the base of the river bank free face gave an age of 400±80 years B.P. The charcoal layer appears to represent a small log which was incorporated into the channel bank prior to incision and has now been re-exposed. As such, the sample may help constrain the age of channel incision for the Carson River.

In all cases, these dates represent maximum ages as there is a possibility that the materials may have been reworked from older deposits. However, charcoal is far less likely to have been reworked than wood because charcoal has a propensity to float and

Table 7.2. Radiocarbon and luminescence dates: sample localities, descriptions and ages

Channel belt $^{\alpha}$	Vibracore locality $^{\beta}$	Depth (m)	Sample description	Dating technique	Laboratory number	Measured age $^{\gamma}$	Calibrated range $^{\delta}$
2	E - 13	1.65-1.74	Charcoal in very dark organic rich mud layer	AMS	Beta-69958 CAMS-11189	540 ± 60	AD 1300-1460
2	E- 13	1.75-1.81	Charcoal in very dark organic rich mud layer	AMS	Beta-69961 CAMS-11192	590 ± 60	AD 1290-1440
2	H - 8	1.81-1.87	Charcoal in medium coarse sand in the centre of a fining up sequence	AMS	Beta-69957 CAMS-11188	970 ± 90	AD 890-1260
3	D - 5	1.55-1.65	Wood in mudstone layer, overlying fining up sequence	AMS	Beta-69963	8550 ± 60	Beyond the limit of dendrochronology
4	F - 4	0.83-0.90	Charcoal in clay with red/brown iron mottling	AMS	Beta-69960 CAMS-11191	540 ± 90	AD 1290-1510 and AD 1600-1620
4	F - 4	1.77	Fine to medium sand	IRSL	JP4-1	7210 ± 1100	
4	F - 4	1.91-1.95	Charcoal in fine to medium grained sand	AMS	Beta-69956 CAMS-11187	2130 ± 60	BC 370-0
5	A - 17	1.92	Fine-medium grained sand	IRSL	JP17-3	500 ± 200	
6	B - 11	0.78	Medium to coarse sand at base of sand unit	IRSL	JP11-3	2845 ± 850	
Modern	C - 19	1.03-1.08	Charcoal in fine sand	AMS	Beta-69959 CAMS-11190	102 ± 0.7%	Modern
Modern	River bank	2.00	2-3 cm charcoal layer just below soil horizon, at base of river bank free face	Radiocarbon (Extended count)	Beta-69962	400 ± 80	AD 1410-1660

α) Channel belts as shown on Figure 7.12. β) Vibracore localities are represented by a letter and are shown on Figure 7.12. Numbers refer to core numbers (see Fig. 7.18). γ) Radiocarbon ages are uncalibrated and are quoted to ± 1 sigma. IRSL dates are quoted with a total error.

δ) Dendrochronology calibrated result (2 sigma, 95% probability)

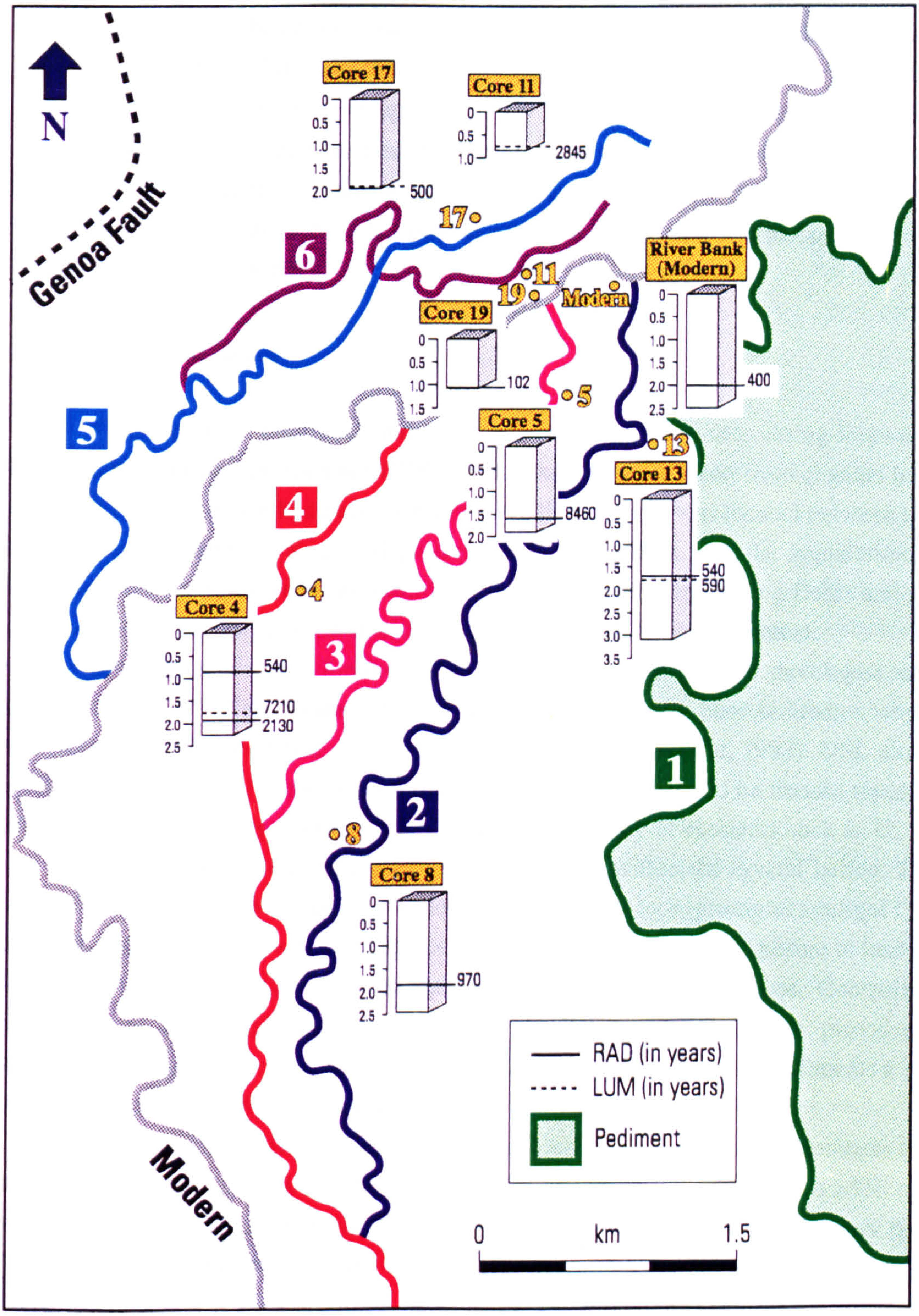

Figure 7.19. Spatial distribution of radiocarbon and optical luminescence dates for the Carson River channel belts.

therefore the travel distance prior to deposition is much greater. Additionally, the Carson Valley is an upland basin in close proximity to the drainage divide (Fig. 7.1) and therefore the total travel distance from the headwaters is comparatively short. The range front is also known to burn down approximately every 100 years (Ramelli *et al.*, 1995; Section 7.4.1) which suggests that most of the charcoal was input straight into the Carson Valley rather than from the headwaters. Finally, the date of 102±0.7% from the modern point bar would appear to be a reasonable estimate based on a comparison of aerial photographs from 1938-1980.

7.10 Luminescence dating

Three samples were analysed using a form of luminescence dating known as Infra-red stimulated luminescence (IRSL). Two samples were taken from channel belts where no organic carbon had been found, while a third sample was located between two radiocarbon dates to act as an independent calibration. IRSL and the application of luminescence dating to waterlain sediments are both rapidly developing fields and are therefore briefly reviewed below in order to place the dating results in context.

Optically stimulated luminescence (OSL) has recently been developed as a technique for dating late Quaternary and Holocene organically poor sediments where traditional radiocarbon dating is impossible (Berger, 1988; Wintle, 1993). OSL along with the associated technique of thermoluminescence (TL) is based on certain types of mineral grains absorbing energy from the radioactive decay of elements such as U, Th and ^{40}K, and producing electrons that are then trapped within the crystal lattice. The trapped electrons can be released by either heating (TL) or by exposure to sunlight (TL and OSL) and recombine within the lattice to produce luminescence. Exposure to heat or light evicts the electrons and zeros the measurable age of the crystal. Controlled application of heat or light and measurement of the resulting luminescence, provides a value for the elapsed time since the mineral was last zeroed. In the case of sediments a TL or OSL date represents the time elapsed since burial (removal from sunlight).

TL studies of waterlain sedimentation have shown that turbid water attenuates the shorter wavelengths of visible light (Jerlov, 1976) and therefore wavelengths >550 nm are used for TL dating of such materials (Berger, 1988). Fine grained silts and very fine sand (< 125 μm) from braided river deposits (Nanson and Young, 1987; Nanson *et al.*, 1988, 1992) have been successfully dated using TL, although many other studies of waterlain sediments have produced incorrect TL dates (see Fig. 17 of Berger, 1988). For TL dating, complete zeroing of the sediment requires exposure times in the order of hours to days (Fig. 7 of Berger, 1988) and therefore the main dating problem is over-estimation of age due to incomplete zeroing. Berger (1988) hypothesises that age overestimation will be even more pronounced in studies of large-grains (100-300 μm) as these will generally be carried in more turbid flows which cut down the incident light and increase the required exposure time. However, these grains may be incorporated in bedforms or macroscopic features such as braid and point-bars which may be exposed in periods of low flow.

In OSL a laser is used to stimulate a sample at wavelengths that are generally below 550 nm (Huntley *et al.*, 1985). Longer wavelengths of light (800-900 nm) are also used in Infra-red stimulated luminescence (IRSL) which is a form of OSL. In both of these techniques, the problem of age overestimation is much less severe as the methods sample electron trapping sites that are far more responsive to light (e.g., in a recent experiment 90% of the ISRL signal was lost in 10 seconds, while it took an hour to reduce the TL by 90% (M. Clarke, *pers comm.*)). The exposure time required to zero a sample is therefore much lower for OSL and IRSL than for TL. IRSL and OSL are also able to measure much younger sediments with greater precision than TL (Wintle *et al.*, 1994). Several recent studies have measured IRSL from waterlain sediments, both on an experimental basis (Rendell *et al.*, 1994) and from fluvial (Fuller *et al.*, 1994), glacio-fluvial (Duller *et al.*, 1992) and shallow marine and lacustrine environments (Balescu and Lamothe, 1994). However, the results of these studies have been mixed, with turbid conditions such as glacio-fluvial sedimentation producing unreliable dates whereas conditions with long exposure (shallow marine, experimental) produce dates in good agreement with known ages.

Due to the sensitivity of IRSL to light, a new sampling technique has been developed and used in this study to recover datable material from vibracores. After the core pipe had been sliced open, one half of the core-pipe was removed in a darkened room and the top millimetre of sediment scraped off the core in order to identify grain-size variations. Sediment was then sampled by pushing a short section of 25 mm diameter PVC pipe into segments of the core containing fine grained sand, and then placing a PVC slip-cap over one end. The core was then inverted, the gap filled with inert packing material and a second PVC slip-cap quickly added, thereby minimising exposure. Prior to laboratory processing the top 10 mm of material at either end of the pipe was removed. Potassium-rich feldspars in the 125-250 µm size range were analysed using the single aliquot infra-red stimulated luminescence (IRSL) method (Duller, 1991).

Locations and descriptions of each luminescence sample are given in Table 7.2 and details of the dose rate components are collated in Table 7.3. The equivalent dose rates (ED) for each aliquot, that is the laboratory dose required to simulate the observed luminescence, are listed in Table 7.4.

Table 7.3. Age, ED and attenuated dose rate components of each luminescence sample

Sample	Channel belt number	Internal β dose µGy a^{-1}	External α dose µGy a^{-1}	External β dose µGy a^{-1}	External γ dose µGy a^{-1}	Cosmic dose µGy a^{-1}	Total dose rate µGy a^{-1}	ED$^{\Delta}$ Gy	Age years
JP17-3	5	231±78	381±223	1903±276	1506±15	210±15	4231±364	2.10±0.83	500±200
JP11-3	6	309±104	145±84	1699±240	896±9	193±20	3242±276	9.22±2.64	2845±850
JP4-1	4	377±127	200±117	2070±296	1143±12	184±18	3974±343	28.66±3.67	7210±1110

µGy=microgray. $^{\Delta}$ ED = equivalent dose

Table 7.4. Single aliquot ED determinations for each luminescence sample

Aliquot number	JP4-1 (Channel belt 4) ED (Gy)	JP17-3 (Channel belt 5) ED (Gy)	JP11-3 (Channel belt 6) ED (Gy)
1	27.83	1.68	11.86
2	33.82	2.93	14.65
3	30.34	2.48	7.88
4	27.46	0.86	7.07
5	27.90	2.95	8.21
6	26.99	2.12	7.32
7	26.60	3.63	7.94
8	24.60	1.21	6.5
9	28.13	1.69	11.72
10	37.55	1.58	9.04
11	25.31	1.98	-
12	27.38	-	-
Mean, χ	28.66	2.10	9.22
Standard deviation, σ_{n-1}	3.67	0.83	2.64
S_N% †	12.8	39.4	28.7

† Percentage scatter about the mean $((\sigma_{n-1}/\chi)*100)$

Table 7.4 shows that the control sample JP4-1 in channel belt four is not internally consistent with the bracketing radiocarbon dates (Table 7.2; Fig. 7.19). As the radiocarbon dates are maximum ages, the much older IRSL date would appear to be incorrect. This could be due to either the sediment remaining unbleached (non-reset) or incompletely bleached (partially reset). Li (1994) in a study of colluvial and glacio-fluvial sedimentation, detected significant scatter of the equivalent dose (ED) values using the single-aliquot technique and concluded that this represented a mixture of well and poorly bleached grains caused by incomplete zeroing of the sediment. ED values for sample JP4-1 (Table 7.4) show a distinct clustering and therefore suggest that the sample was unbleached and represents the age of the eroded material. Two possible scenarios could explain this observation. Firstly, a high magnitude flood event could have carried the material in a very turbid flow and deposited the material so rapidly that the IRSL signal was unaffected. Secondly, if the flood was of a short temporal period, and / or if the event occurred on a moonless night, this would have again left the IRSL signal unchanged. Both of these hypotheses are possible as the Carson River has a flashy snowmelt driven regime and is situated in a mountain catchment where flood peaks will have short residency times. However, it is much harder to imagine a scenario where material is transported without mixing with sediment of different ages. This date, does however suggest a number of intriguing possibilities. Firstly, the date represents the age of the sediment prior to erosion and not deposition. Secondly, the dating technique in conjunction with radiocarbon dating could be used as a measure of sedimentation rate or of travel distance.

In contrast, the other two samples from channel belts 5 and 6 both show significant scatter of the ED values, suggesting that the samples represent a mixture of partially and well bleached grains and this is reflected in the larger errors bars of the dates. Channel belt 6 has a luminescence date of 2845±850 B.P. for a set of meander bends that are remarkably well preserved (Fig. 7.15). Radiocarbon dating of belt 4 gave an age of 2130±60 B.P. for a channel with a very subdued relief (see Section 7.9). The luminescence sample for channel belt 6 was taken immediately below the base of a small sandy unit (core 11, Fig. 7.18) and may therefore represent an older surface.

7.11 Palaeohydrology of the Carson River

Meander bend parameters for a section of the northern Carson Valley (Fig. 7.20) were measured from aerial photographs scanned into an image analysis package (Fig. 7.21 and Section 6.4). Statistics for sinuosity, channel width, arc height and wavelength are shown in Table 7.5 for channel belts 1, 2, 3 and 6. However, no statistics were generated for channel belt 4 as individual meander bends are insufficiently well preserved (see Figs. 7.12 and 7.14) and the majority of channel belt 5 is outside the studied area.

Channel widths measured from images were taken on cross-over zones between bends thereby avoiding changes in width around the apex of meander bends. Comparison of these widths with detailed surveys of the same meander loops (see Fig. 7.22 and Appendix C) indicated that significant under and over-estimations were present in the image analysis data. However, insufficient land surveys were taken to estimate the magnitude of these differences. A second measure of the internal consistency of the morphometric channel data is provided by the ratio of meander wavelength (L_m) to channel width (w) which is of the form $L_m = a w^b$ where the constant 'a' and the exponent 'b' are approximately 10-12 and 1-1.1 respectively (Leopold and Wolman, 1960; Zeller, 1967; Richards, 1982). Assuming a value of 1 for the exponent 'b', values for the constant 'a' have been calculated for each channel belt (Table 7.5). Channel belts 2 and 6 have values for 'a' which are in agreement with the accepted range, but belts 1 and 3 have anomalously high and low values respectively (Table 7.5). Since errors in measuring channel width from photographic images have already been noted, the anomalous L_m/w ratios for belts 1 and 3 are interpreted as under and over-estimation of the mean channel width respectively. Mean and bankfull palaeodischarges for each of the four channel belts were therefore calculated using the meander wavelength, using two new expressions derived in Section 6.5 along with the equations of Williams (1984b) and Dury (1985). The wavelength of channel belt 3 falls just outside the applicable range of three of the

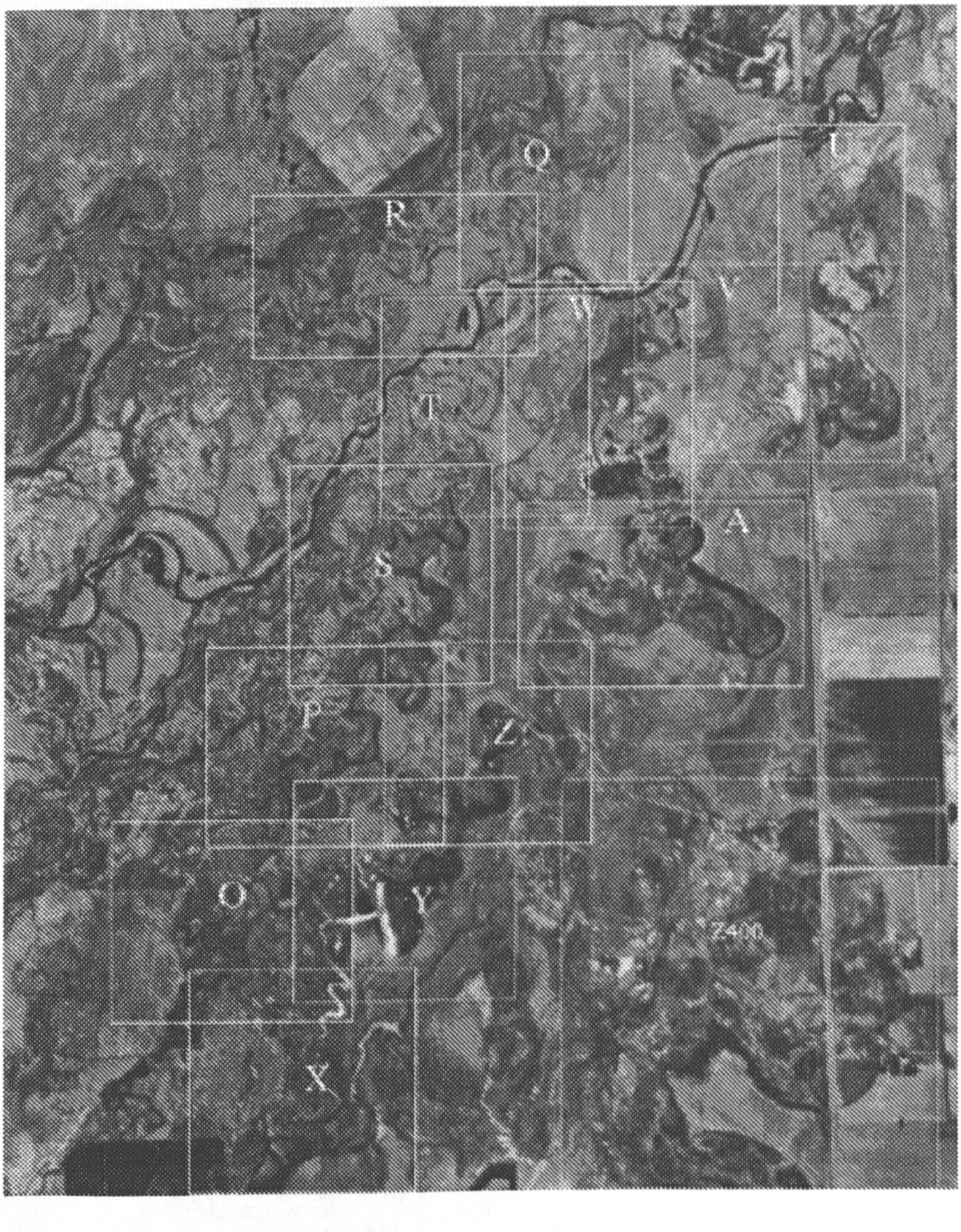

Figure 7.20. Areal extent of Carson Valley palaeohydrological analysis. Boxes represent individual scanned images. Image covers an area of 3.8 km by 2.9 km.

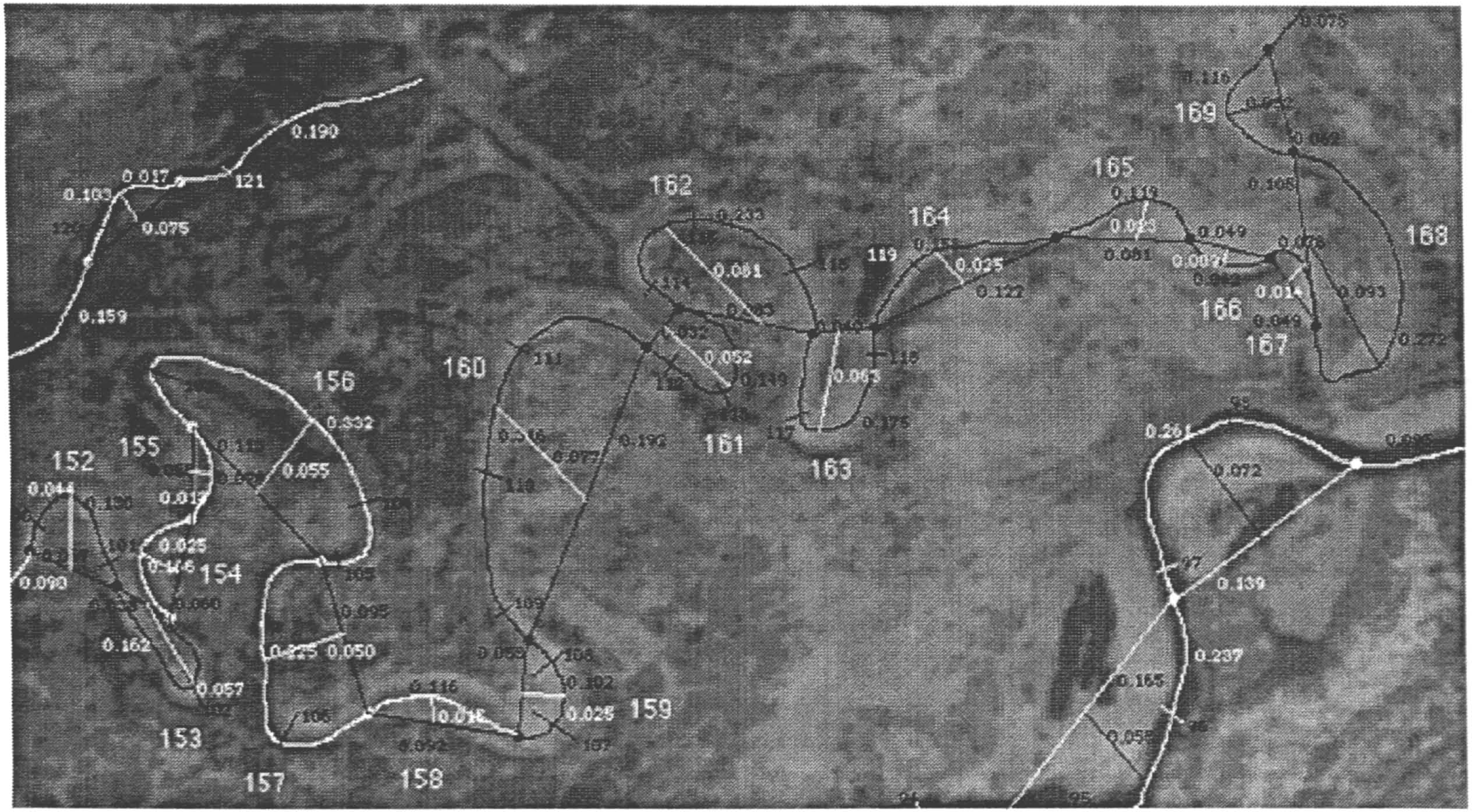

Figure 7.21. Example of palaeohydrological analysis using the NIH Image analysis package. Bend numbers, along with statistics for arc height, half-wavelength and arc distance are displayed on the image. Channel width measurements are numbered consecutively, but only those values on cross-over zones between bends were used for the statistics quoted in Table 7.5. The image covers an area of 0.9 km by 0.5 km.

Table 7.5. Palaeohydrological statistics for the Carson River channel belts

Channel Belt	Sinuosity ($\pm1\ \sigma$)	Channel width, w (m; $\pm1\ \sigma$)	Arc height, H (m; $\pm1\ \sigma$)	Meander wavelength, L_m (m; $\pm1\ \sigma$)	Constant 'a' in: $a=L_m/w^1$ #	Q_m (Williams, 1984b)† (m^3s^{-1})	Q_m (This study)‡ (m^3s^{-1})	Q_b (Dury, 1985)Δ (m^3s^{-1})	Q_b (This study)Ω (m^3s^{-1})
1	3.2±1.3	25.8±12.3	217.2±118.8	562.5±178.8	21.8	13.9	10.9	170.9	99.5
2	2.1±1.6	16.1±4.9	47.0±43.7	180.6±90.0	11.2	1.2	1.1	21.9	17.9
3	2.0±0.9	17.8±3.4	30.8±25.1	120.9±53.6	6.8	0.5	0.5	10.6	9.8
6	3.0±2.7	14.1±4.1	48.7±28.8	148.7±75.1	10.5	0.8	0.7	15.4	13.4

Sinuosity, width, arc height and wavelength are all mean values. σ = standard deviation. #Wavelength and width are both mean values

† $Q_m = 0.000017\ L_m^{2.15}$, Δ $Q_b = (L_m/32.857)^{1.81}$, from Table 6.1 ‡ $Q_m = 0.000025\ L_m^{2.05}$, Ω $Q_b = 0.007\ L_m^{1.51}$, from Table 6.2

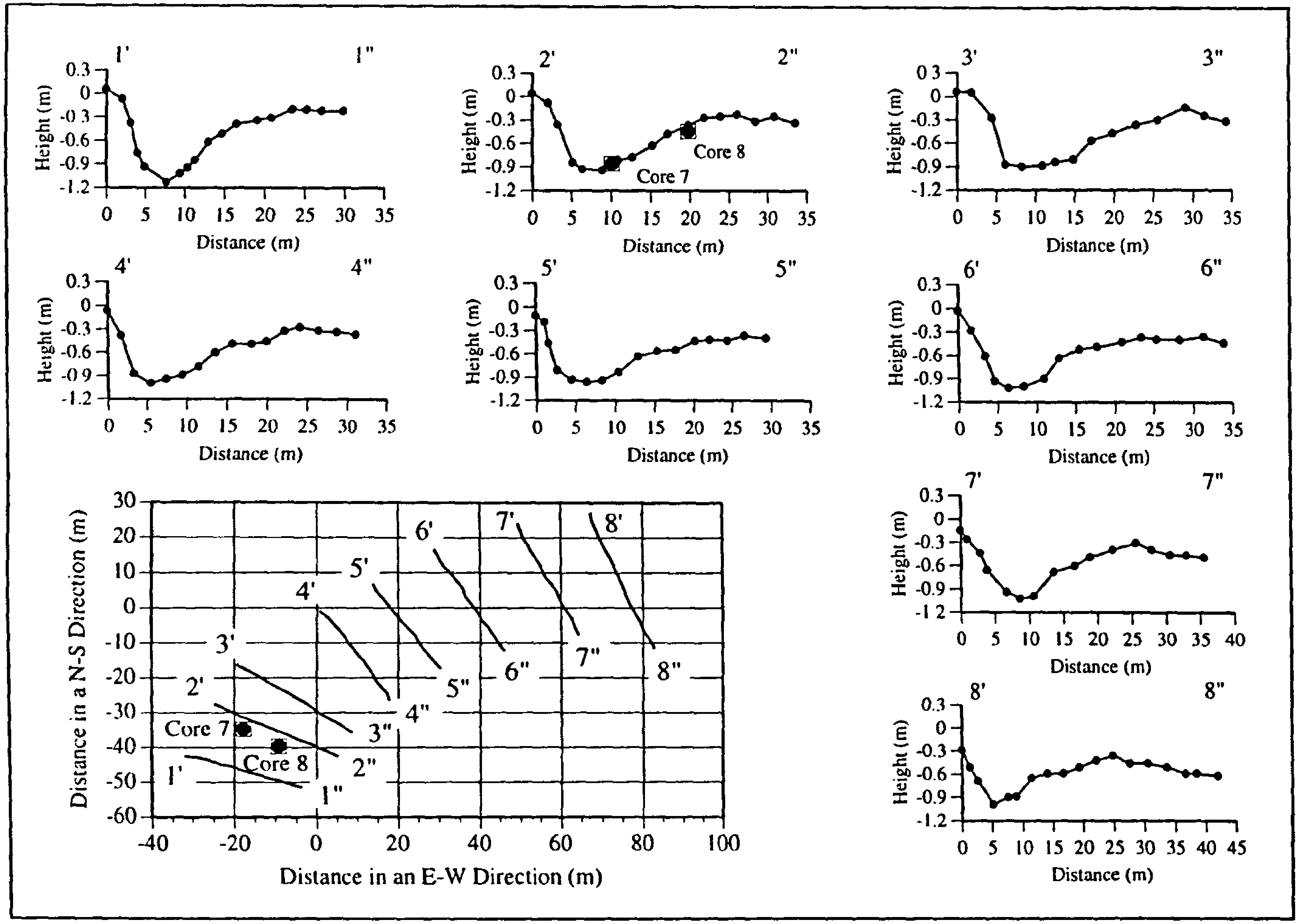

Figure 7.22. Channel cross-sections and core sites for vibracore site H, channel belt 2. See Figure 7.12 for vibracore localities.

discharge equations (see Tables 6.1 and 6.2), but the equations are used here in the absence of expressions covering a wider range.

The palaeohydrological history of the Great Basin is poorly understood (see Section 7.13) and no history of channel pattern change in the Holocene has been recorded. However, two different types of Holocene channel pattern change have been recognised in the temperate zone. In central Europe a cyclicity between braided, large meanders and small meanders has been recognised (Szumanski, 1983) with several periods characterised by large meander bends. Elsewhere, a change from a braided pattern to one dominated by large meanders has been identified at the end of the Holocene with a rapid diminution in the size of the meander bends with decreasing discharge (e.g., Knox, 1985; Starkel, 1991). The climate record of north-west Nevada (Section 7.6) suggests that total precipitation, and therefore river discharge, dropped rapidly after approximately 9,500 years ago with present lake levels being reached by approximately 9,000 years ago. While the climatic history between 9,000 and 2000 years ago is poorly constrained (Section 7.6), the absence of large lakes in these internally draining basins suggests that no large scale changes in discharge occurred and therefore that large changes in meander wavelength did not take place. This climate record strongly suggests that the large wavelength meanders (channel belt one) with estimated bankfull discharges of 100-170 $m^3 s^{-1}$ could not have been formed later than the early Holocene, although they could have been formed in an earlier interglacial. The other channel belts all have estimated discharges an order of magnitude lower than the large meander bends (Table 7.5) and are therefore considerably younger in age, as confirmed by the radiocarbon and luminescence dating (Sections 7.9 and 7.10). Two eastern terraces have been identified in the Carson Valley of which the upper terrace may contain Mazama ash (NDOT, 1985; Section 7.5.2), which would have an age of approximately 6900 B.P. If Mazama ash is present in the upper terrace, then the meander loops of channel belt 1 which have cut into the lower terrace would be much younger than the age inferred from the known climatic history of north-west Nevada. Large meander loops substantially younger than 6900 B.P. would lead to a reconsideration of Holocene climate change in the north-western Great Basin. Channel belt 1 is assumed to have an early Holocene age in this study, but the dating of the possible Mazama ash is required in order to remove the ambiguity.

7.12 Topographic surveys

A series of survey lines were taken across the Carson Valley in order to measure the longitudinal and lateral gradients of the Carson River and its palaeochannels. Four roads cross the valley in an east-west direction (see Fig. 7.2) and were surveyed using a continuous kinematic Global Positioning System (GPS). To the north of the roads, four

WNW-ESE cross-sections were taken using either a traditional level or an Electronic Distance Meter (EDM).

The GPS lines are approximately perpendicular to the range front and are either strongly oblique or perpendicular to the Carson River and its tributaries (Fig. 7.2). All of the lines show a low gradient dipping from east to west towards the fault and then a much steeper gradient marking the base of alluvial fans derived from the range front (Fig. 7.23). Low amplitude fluctuations in the survey profiles show the position of bridges crossing channels. These points have been removed for calculation of best-fit OLS regression lines for the points up to the base of the alluvial fans. Gradients for the GPS lines are in the range of 0.12-0.16% which is broadly in agreement with gradients calculated from topographic maps (Table 7.6). Repeat GPS surveys were undertaken for Waterloo Lane and Centerville Lane and vertical error magnitudes have been estimated by fitting 10th order polynomials to each set of points and calculating the differences between the resulting equations (Fig. 7.24). For the E-W section up to the base of the alluvial fan, vertical errors are in the range ± 0.05 m (Fig. 7.24).

The Genoa fault trace curves towards the NNE at the northern end of the Carson Valley (Fig. 7.2) and therefore the EDM generated survey lines to the north of the Genoa Lane were all taken approximately perpendicular to the fault in a WNW-ESE direction (Fig. 7.25). Surveys 1 and 2 are located close to the nodal junction where the palaeochannels meet and the Carson River exits to the NE (Fig. 7.25) and show surfaces that are dominantly horizontal (Fig. 7.26). However, the western end of survey 1 crosses an abandoned meander loop (Channel belt 6) and the scrolls and swales show a marked gradient dipping towards the fault (Fig. 7.27a). Point-bars are known to increase in height towards the apex of a bend (e.g. Bridge and Diemer, 1983; Willis, 1989) and therefore a rise in scroll-bar height might be expected if a survey was undertaken from the upstream / downstream end of an inner scroll towards the apex of an outer scroll. However, in this example the survey line is always slightly oblique to the scroll bar axes (Fig. 7.27b). The scroll bars may therefore have been initially level and subsequently tilted towards the fault during or after their abandonment. A prominent break of slope with approximately one metre of relief is present at the eastern end of survey line 2 (Fig. 7.26) and this corresponds to the transition between younger and older floodplain deposits as mapped by Pease (1980; see Fig. 7.9).

Two low gradient surfaces which dip towards the fault can be identified on survey 3 (Fig. 7.28). The upper surface has a very uniform gradient (Fig. 7.29a) with a magnitude of 0.053% and represents the older floodplain surface described by Pease (1980) (Fig. 7.9) between channel belts 2 and 3. In contrast, the lower gradient is difficult to estimate as the surface has far more topography (Fig. 7.29b) but is of a comparable magnitude to the upper gradient (0.072%). These topographic differences are clearly reflected in old air photographs where the surface between channel belts 2 and 3 is

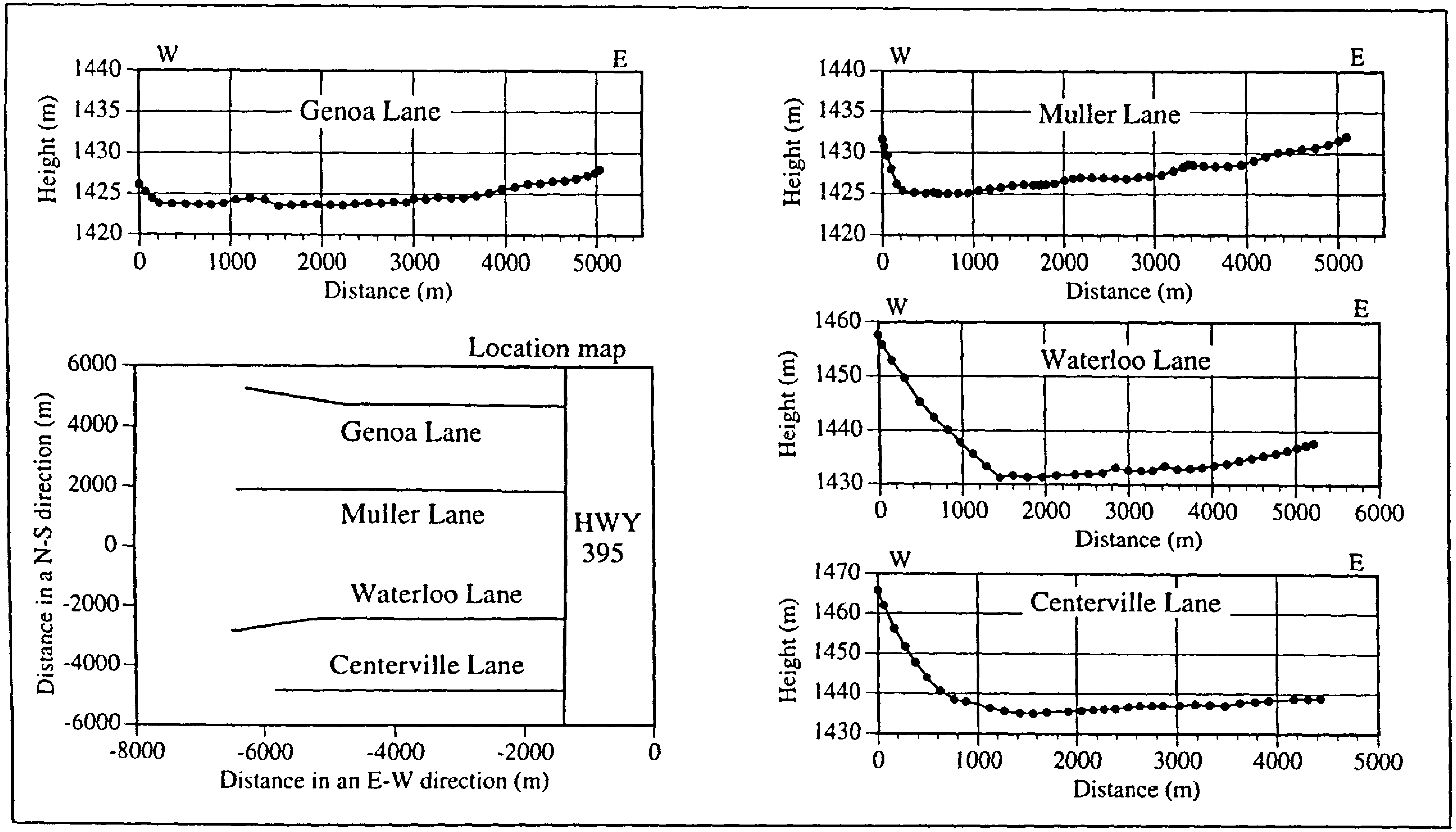

Figure 7.23. GPS sections across the Carson Valley. The relative position of the roads is shown in the bottom left hand corner. Actual positions of the roads are shown on Figure 7.2.

Table 7.6. Lateral and axial gradients for the Carson Valley

Survey Type	Survey Location	Gradient (%)	Standard Error of Gradient (%)	Regression Coefficient r^2 - (%)
Topographic map	**Axial Gradient**[†]	**0.1492**	**0.0058**	**99.1**
Theodolite +EDM	Surveys 1 and 2	Essentially horizontal	-	-
Theodolite + EDM	Survey 1 - western end[‡]	0.7421	0.0460	98.5
Kern level	Survey 3 - eastern section	0.0529	0.0066	56.8
Kern level	Survey 3 - western section	0.0717	0.0115	39.1
Theodolite + EDM	Survey 4 - eastern section	0.1042	0.0059	71.5
Theodolite + EDM	Survey 4 - western section	0.1153	0.0161	81.0
Continuous kinematic GPS	Genoa Lane	0.1205	0.0076	90.5
Topographic map	Genoa Lane	0.1304	0.0109	98.0
Continuous kinematic GPS	Muller Lane	0.1357	0.0048	95.0
Topographic map	Muller Lane	0.1498	0.0209	88.0
Continuous kinematic GPS	Waterloo Lane (a)	0.1578	0.0119	88.0
Continuous kinematic GPS	Waterloo Lane (b)	0.1551	0.0110	89.6
Topographic map	Waterloo Lane	0.1367	0.0424	77.6
Continuous kinematic GPS	Centerville Lane (a)	0.1316	0.0057	96.6
Continuous kinematic GPS	Centerville Lane (b)	0.1309	0.0056	96.0
Topographic map	Centerville Lane	0.1725	0.0172	98.1

[†] Axial gradient calculated along highway 395 from 4720 ft contour between Centerville and Waterloo Lanes (Minden Quadrangle 1:24,000 USGS topographic map) to the Cradelbaugh Bridge across the Carson River (Genoa Quadrangle 1:24,000 USGS topographic map)

[‡] Survey of scroll bar elevations across abandoned bend (see Fig. 7.27)

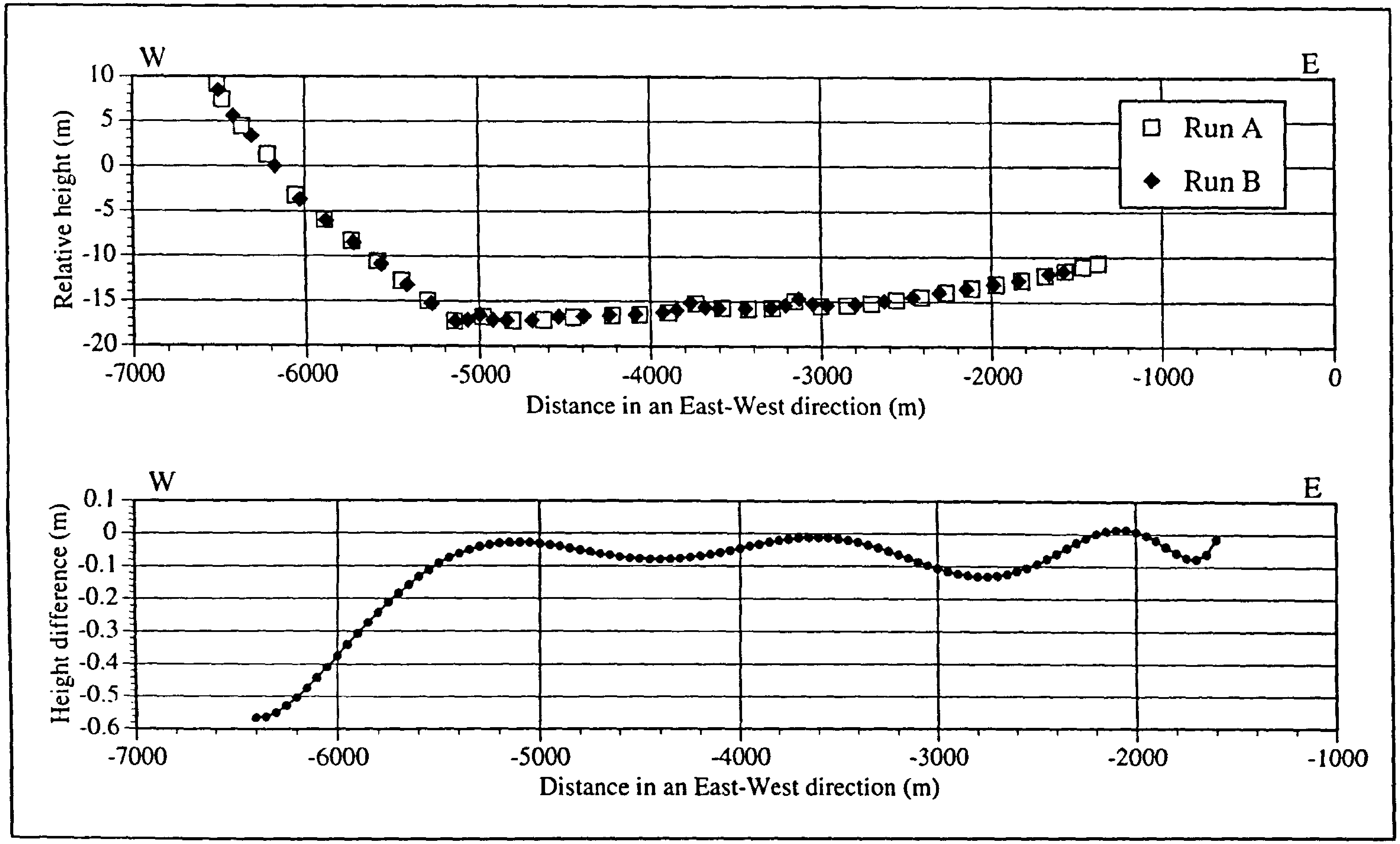

Figure 7.24. Determination of vertical errors for the GPS survey of Waterloo Lane. The upper figure is a plot of the actual data points, while the lower graph plots the differences between 10th order polynomials fitted to each dataset. Vertical errors are approximately ±0.05 m for the west dipping eastern surface.

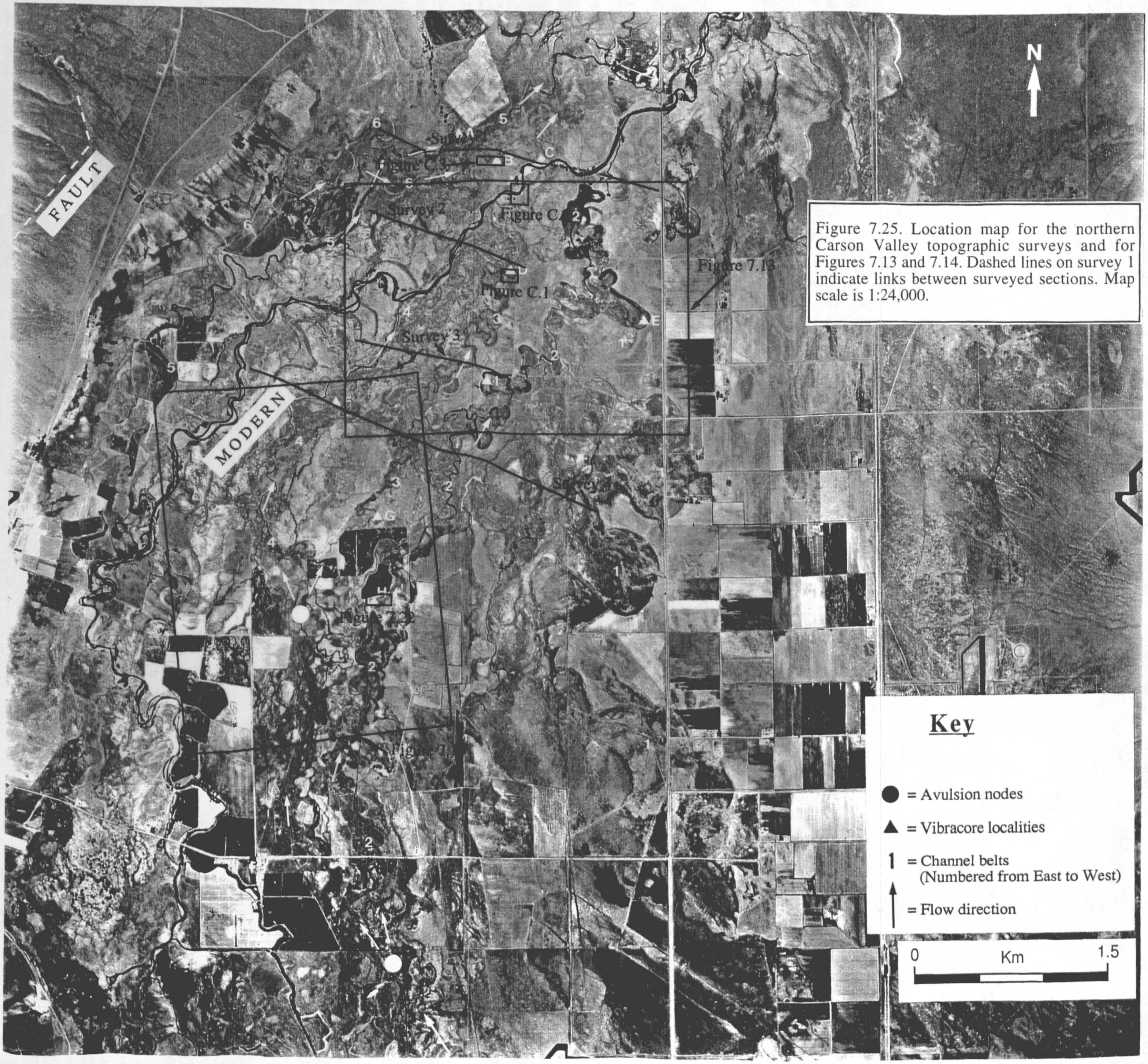

Figure 7.25. Location map for the northern Carson Valley topographic surveys and for Figures 7.13 and 7.14. Dashed lines on survey 1 indicate links between surveyed sections. Map scale is 1:24,000.

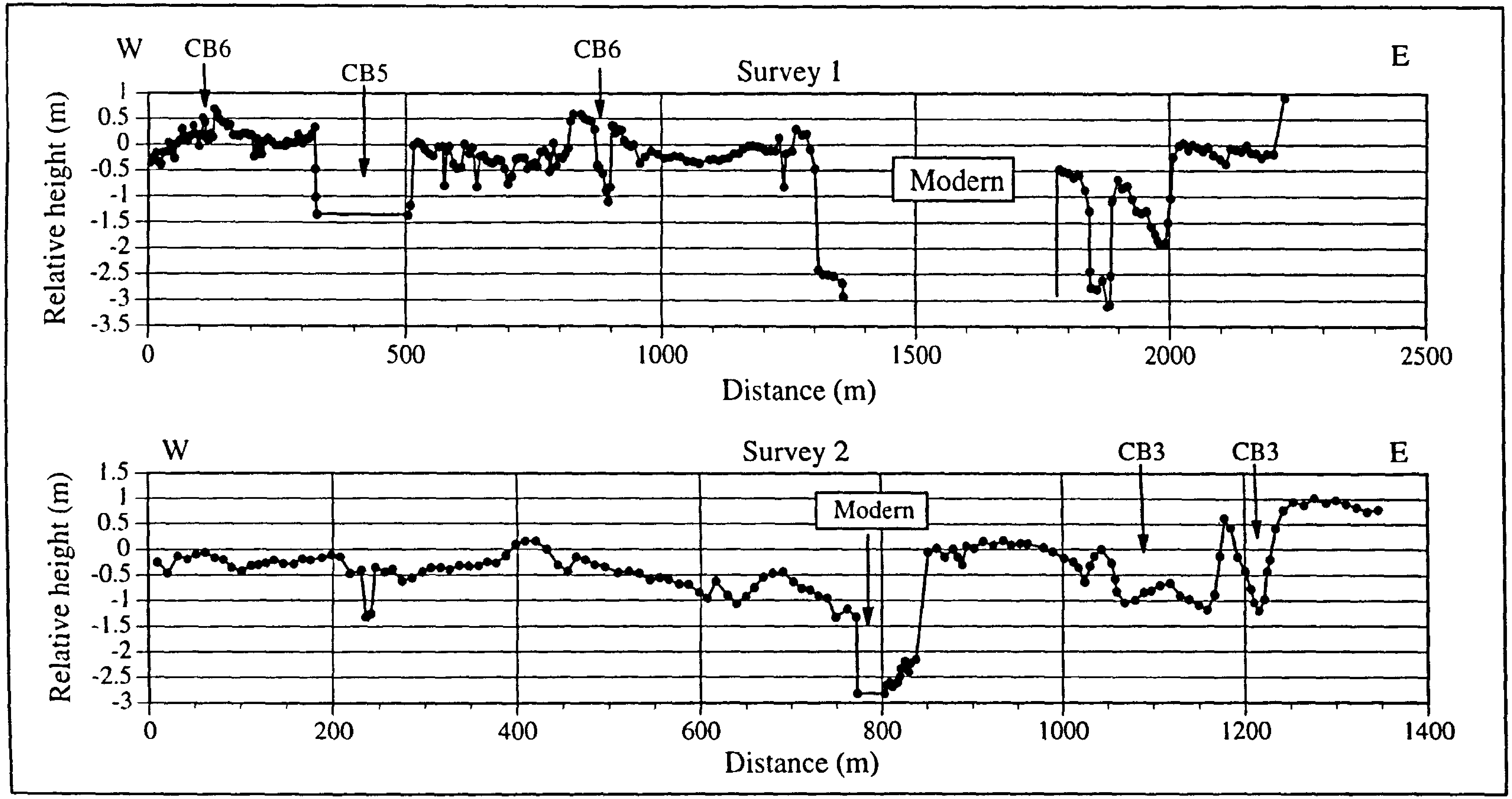

Figure 7.26. Surveys 1 and 2, northern Carson Valley. The western and central sections of survey line 1 are connected by water-levels taken across an abandoned channel (see Fig. 7.25). The central and western sections of survey 1 are not linked and therefore the relative heights of the two sections may be incorrect. The locations of surveys 1 and 2 are shown on Figure 7.25.

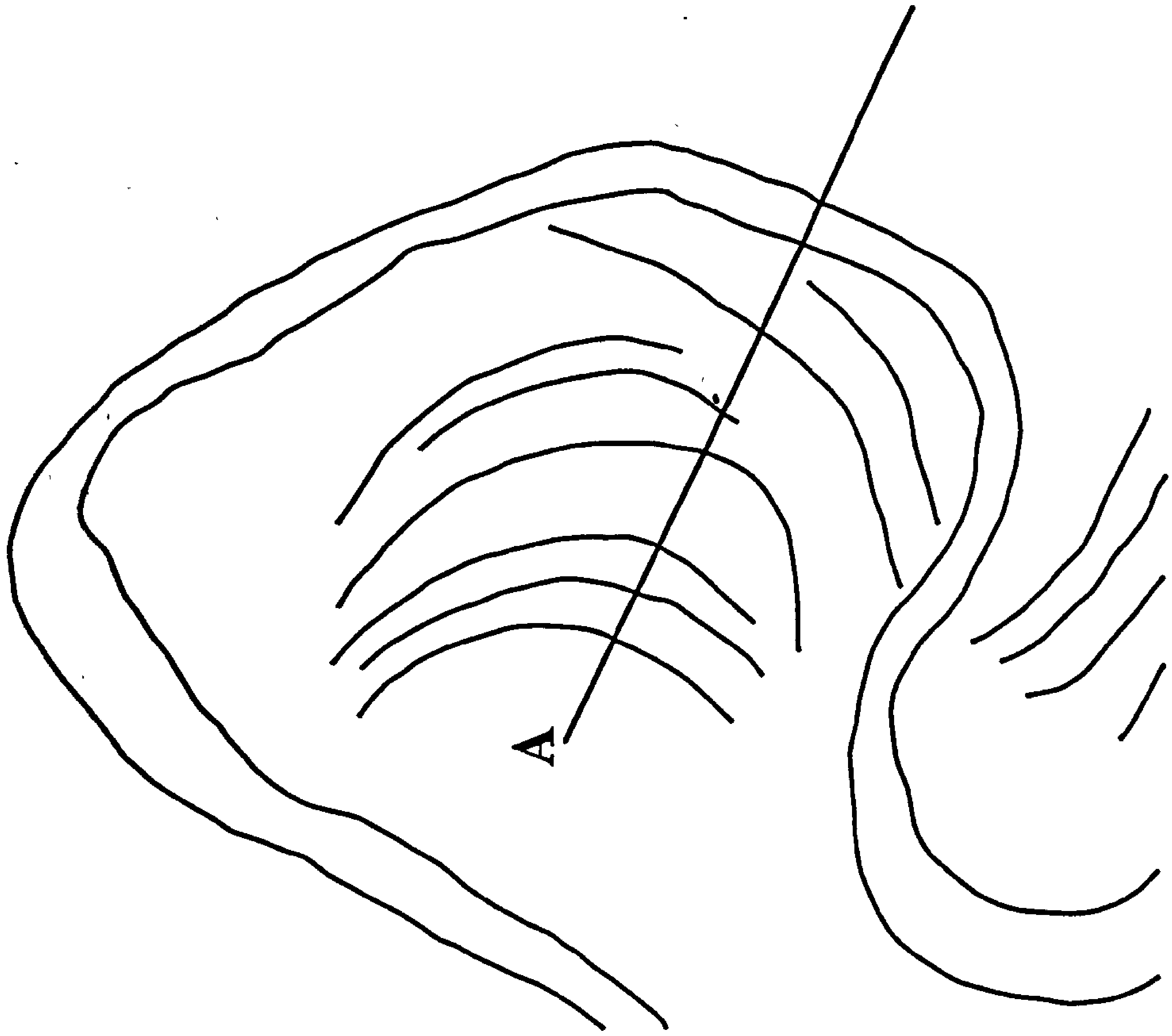
A

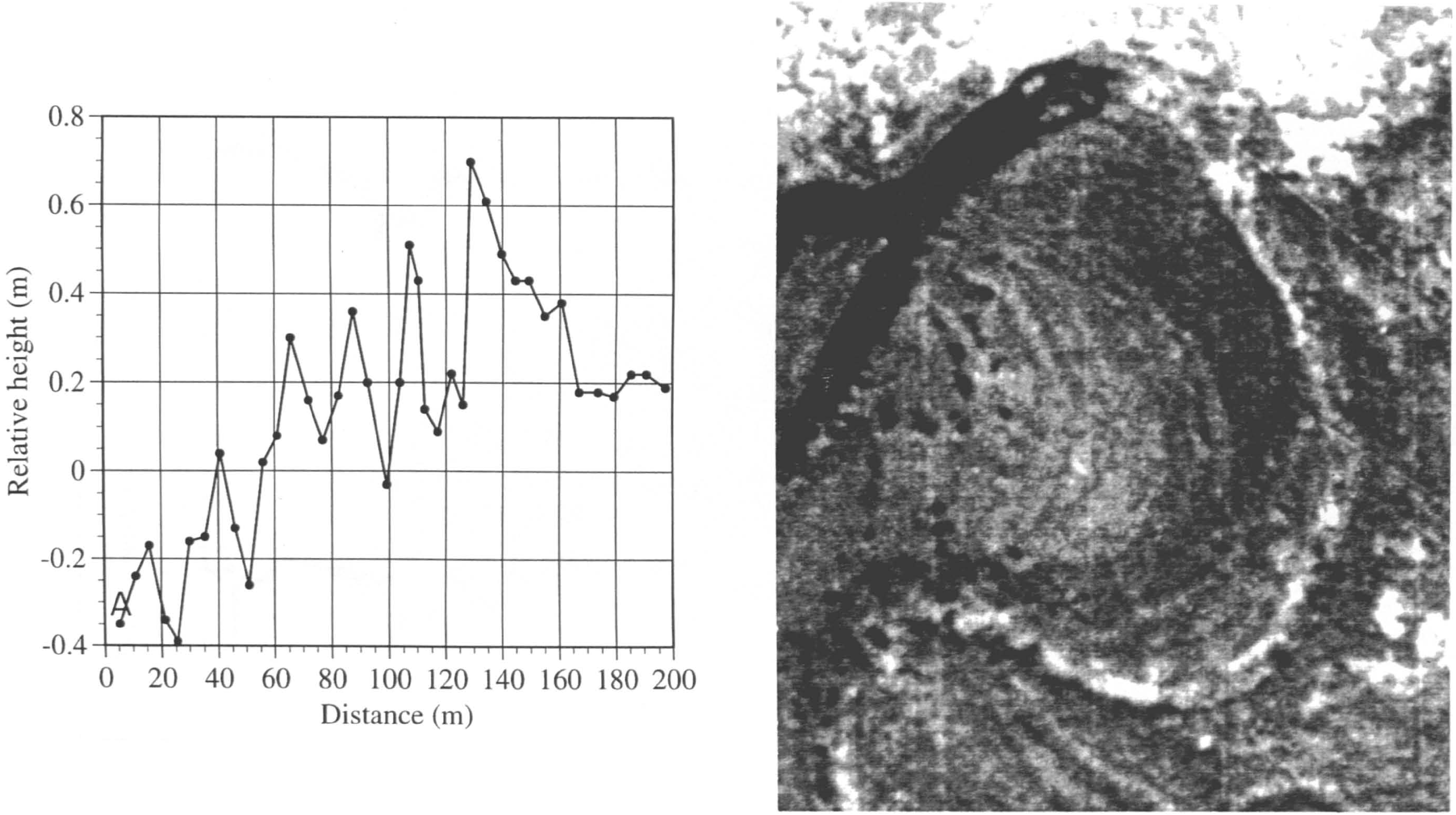

Figure 7.27. Scroll and swale topography at the western end of survey line 1. Both the survey and the position of the survey line on the aerial photograph are from west (left) to east (right). The lines identified from the photograph represent the position of swales. The abandoned channel is located between 115 m and 130 m on survey line. The location of survey line 1 is shown on Figure 7.25.

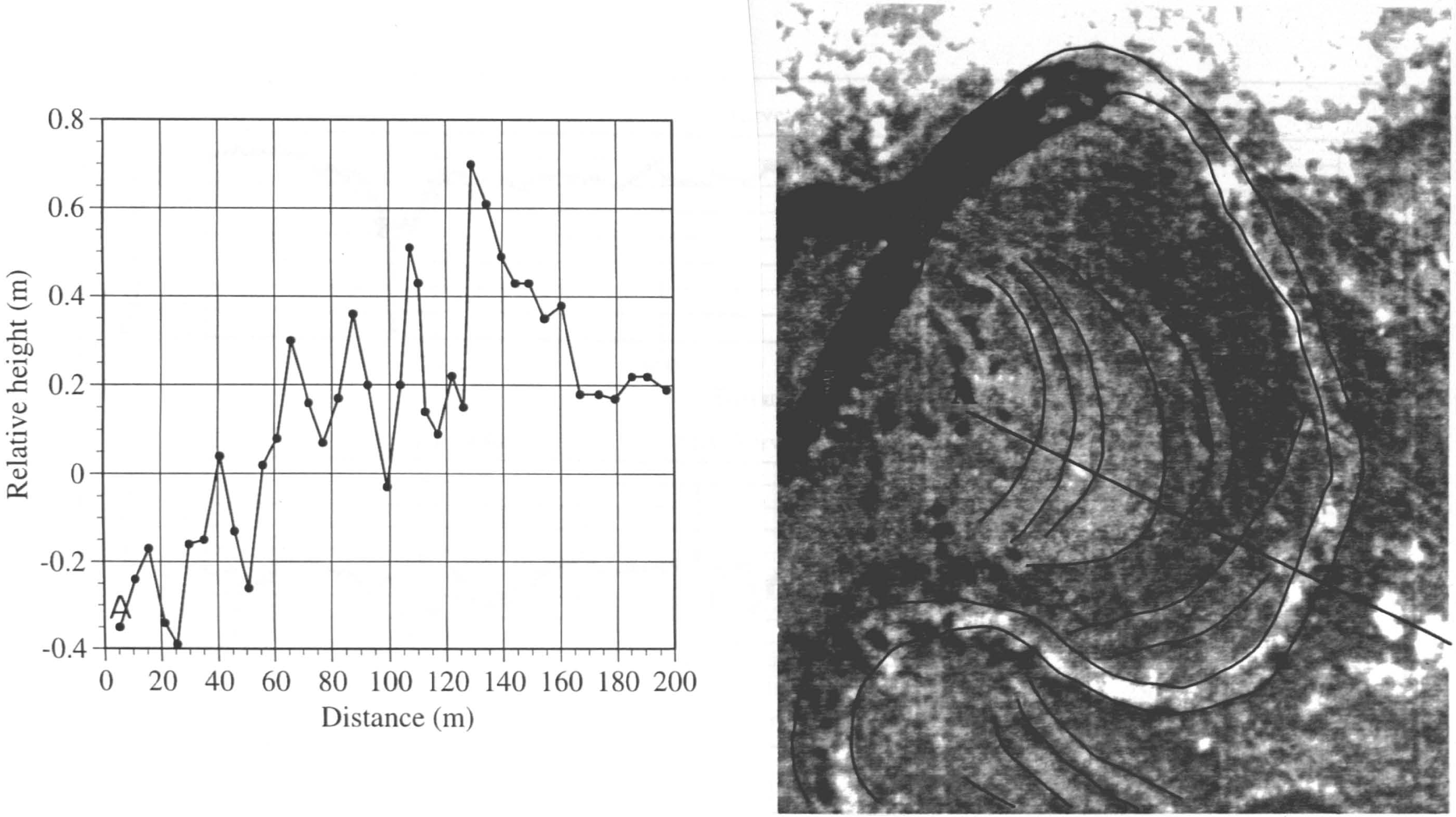

Figure 7.27. Scroll and swale topography at the western end of survey line 1. Both the survey and the position of the survey line on the aerial photograph are from west (left) to east (right). The lines identified from the photograph represent the position of swales. The abandoned channel is located between 115 m and 130 m on survey line. The location of survey line 1 is shown on Figure 7.25.

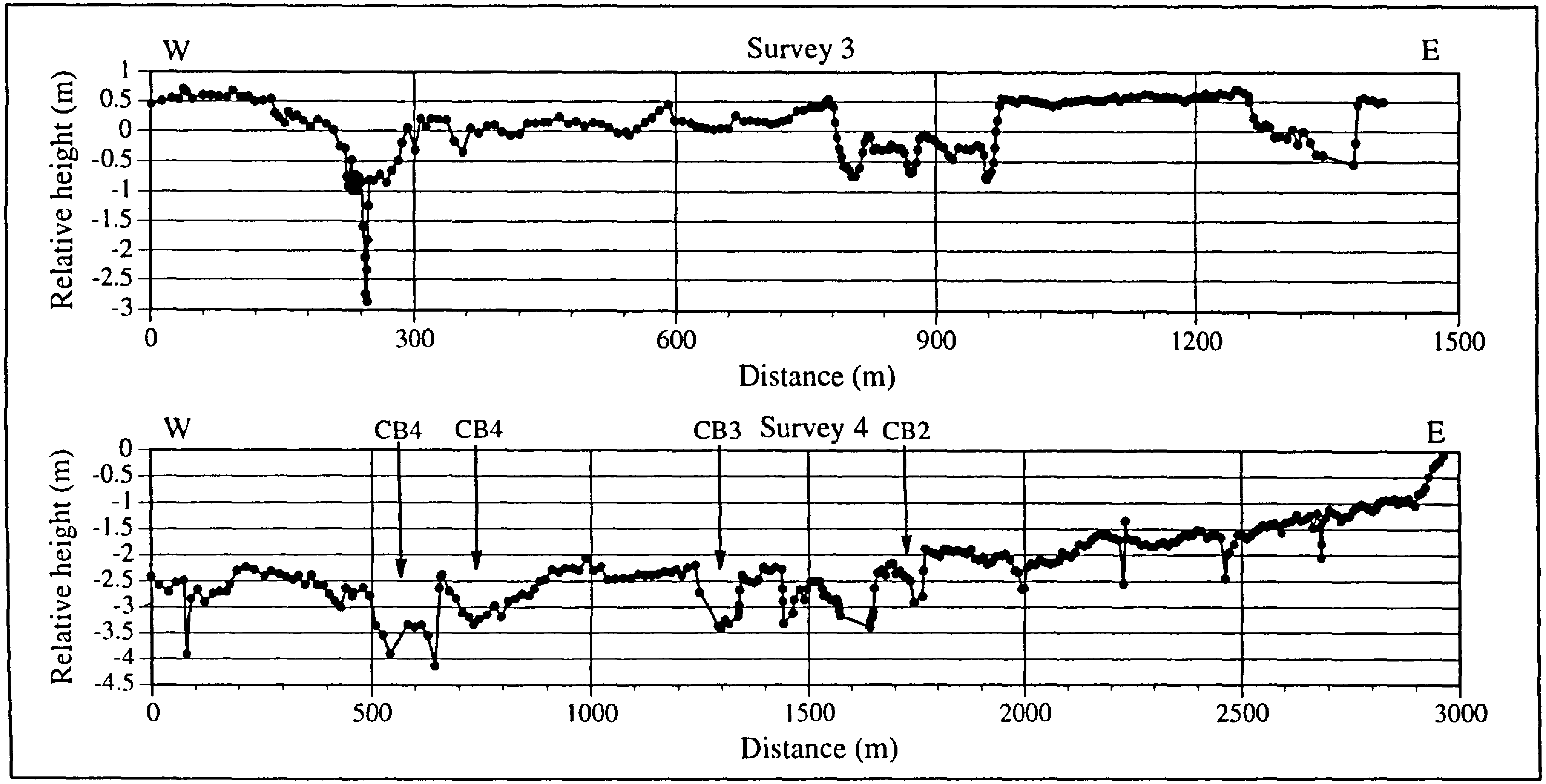

Figure 7.28. Surveys 3 and 4, northern Carson Valley. The survey locations are shown on Figure 7.25.

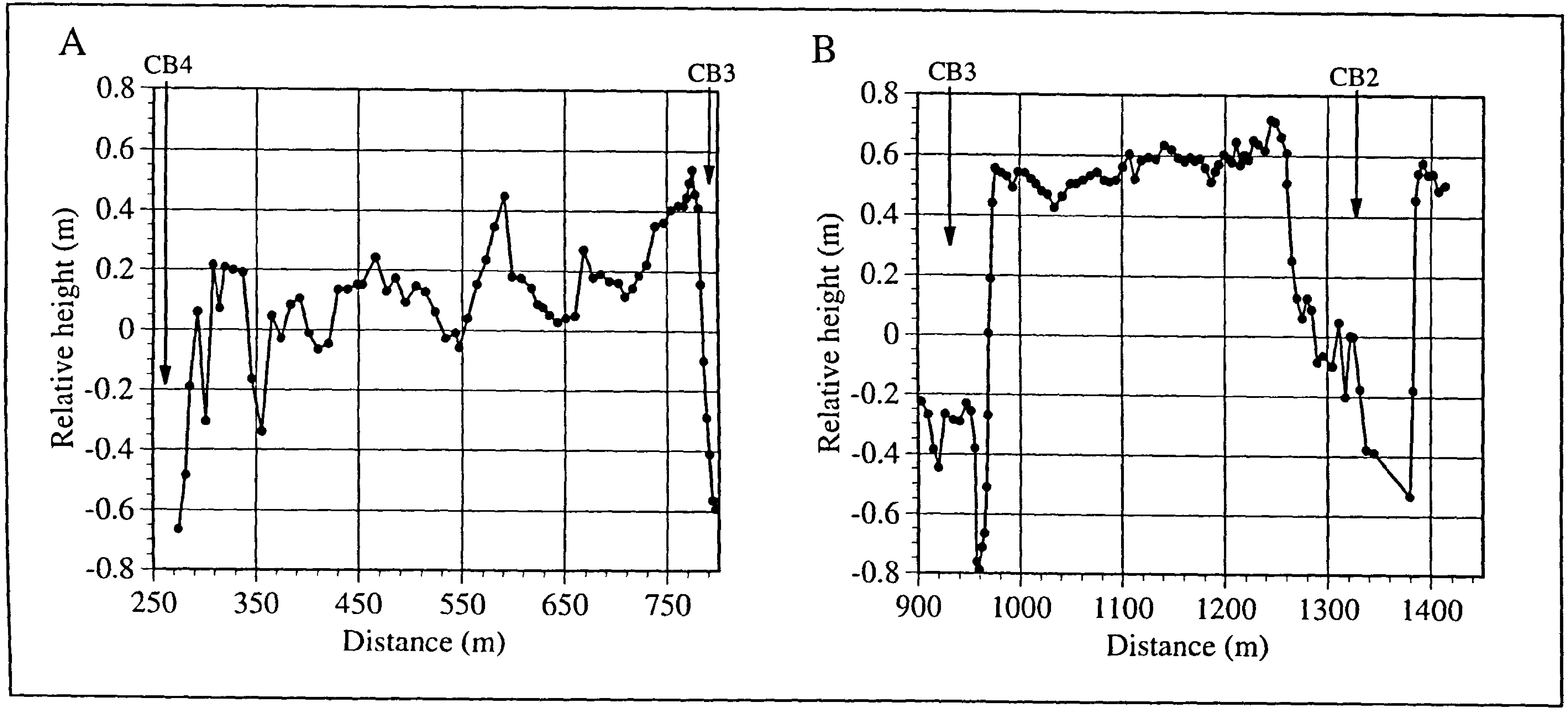

Figure 7.29. Tilted surfaces from survey line 3. A) Western tilted surface, gradient is 0.0717% B) Eastern tilted surface, gradient is 0.0529. The survey locations are shown on Figure 7.25.

uniform, while that between belt 3 and the modern river is covered in relict channels and bends (Fig. 7.13). Survey line 4, immediately to the south, also shows two low-angle westward dipping surfaces, one between channel belts 1 and 2 and the second between belts 3 and 4. The second of these (between 1220 m and 1020 m, Fig. 7.28) crosses a surface with a very similar appearance on air photographs to that between channel belts 2 and 3 to the north (see Fig. 7.14), although these two areas are mapped as different units on Pease's (1980) map (Fig. 7.9). Both surfaces have gradients in the range 0.10-0.11% which is higher than those to the north.

Lateral gradients for the Carson Valley are summarised in Table 7.6 along with the axial gradient as measured along the main N-S highway. Surveyed gradients have been listed from north to south within Table 7.6 and show a gradual increase from surveys 1 to 2 which were essentially horizontal, to Waterloo Lane in the south with a gradient of approximately 0.16%. The largest of these gradients are comparable with the axial gradient of approximately 0.15%. However, the ratios of lateral to axial gradients (35%-105%) for the Carson River are at the lower end of the observed range for other rivers that show evidence of channel adjustment to tectonic tilting (32%-1000%; see Table 2.3).

The presence of abundant channels on some of the surfaces, the example of the asymmetric scrolls and swales, and the fact that all recognised gradients dip towards the fault, suggests that tilting of the surfaces may have occurred, associated with basin bounding faulting and the gradual rotation of the half-graben block. Unfortunately, as only 1 or 2 westward dipping surfaces can be identified in the northern Carson Valley it is not possible to confirm that ground-tilting has occurred by identifying several surfaces with successively smaller gradients toward the fault. Repeated geodetic surveys of floodplains have previously shown tilting (Adams, 1980; Gomez and Marron, 1991) but previous surveys of asymmetric terrace flights have also been unable to identify this past progressive deformation (decreasing tilt towards the fault) (Alexander and Leeder, 1990; Cox, 1994).

7.13 Theoretical estimation of Holocene ground-tilting and comparison with survey data

Since the history and magnitude of Holocene faulting is well constrained for the Genoa fault (Section 7.4), then some estimates of Holocene ground-tilting can be made and compared with observed gradients. An estimated recurrence interval of 2-4 ka for Genoa fault events and a record of two events within the past 2500 years suggests that approximately 4 or 5 events have occurred within the Holocene. The average vertical offset for each event is between 3-4 m for the fault to the south of Jacks Valley, giving a combined throw for the Genoa fault of 12-20 m. However, in terms of ground-tilting only the slip and the associated tilting of the hangingwall is important. Recent geodetic measurements after the 1983 Borah Peak earthquake suggested that the ratio of footwall to hangingwall movement was 15:85 (Stein and Barrientos, 1985), although, aseismic creep may alter this ratio so that footwall movement accounts for a greater percentage of total offset. In the Carson Valley, the total sedimentation is estimated at 1000-1500 m (Fig. 7.8) and the total relief from valley floor is approximately 1600 m plus an unknown amount of topography that has now been eroded. A footwall / hangingwall ratio of 60:40 is therefore assumed which gives a vertical throw of the valley floor adjacent to the fault of approximately 4.8-8 m over the last 10,000 years. The total offset adjacent to the fault can also be calculated from the observed lateral gradients by assuming rigid block motion and the wavelength that tilting is occurring over (Table 7.7).

Table 7.7. Estimated vertical offsets at fault for westward dipping surfaces

Survey Location	Gradient (%)	Offset at fault length=10 km[Δ] (m)	Offset at fault length=35 km[†] (m)
Survey 3 - eastern section	0.0529	5.29	18.52
Survey 3 - western section	0.0717	7.17	25.10
Survey 4 - eastern section	0.1042	10.42	36.47
Survey 4 - western section	0.1153	11.53	40.36
Muller Lane - GPS	0.1357	13.57	47.50
Waterloo Lane - GPS (Av)	0.1560	15.60	54.6

[Δ] Length taken from Genoa fault to west edge of subsurface horst, see Figure 7.8
[†] Length taken from Genoa fault to fault on eastern edge of the Pine Nuts, see Figure 7.5b

If the entire block between the Genoa fault and the fault flanking the eastern side of the Pine Nut Mountains is assumed to have been tilted by the amount observed on the surveyed surfaces then approximately 18-50 m of vertical fault movement would have been required (Table 7.7). These offsets would suggest that surfaces would take 50,000 years to form. However, an analysis of the gravity data for the Carson valley (Fig. 7.8) shows that most of the sedimentation and accompanying ground-tilting has taken place in a zone just 10 km wide. Total vertical fault displacements of 5-16 m are then required if a tilt length of 10 km is assumed, which are in broad agreement with values estimated from the faulting history (4.8-8 m), particularly for those surfaces close to the nodal point in the north of the basin. While the evidence is far from conclusive, it does suggest that the northern Carson Valley may have had an almost flat surface after the last glaciation due either to reduced faulting, higher sediment loads or a combination of both. A flat surface may explain why large meander loops were eroding into the pediment surface on the eastern side of the valley during the early to mid-Holocene. The calculations also suggest that the surface between channel belts 2 and 3 and picked out by the eastern section of survey line 3, is older than the age suggested by Pease (1980) of <2000 years (Fig. 7.9). The scenario of 5-8 m of faulting during the Holocene, distributed across a length of 10 km, gives a lateral tilt rate of 5-8 x 10^{-5} radians ka^{-1}. Other examples of avulsive channel movement in response to lateral ground-tilting have much faster tilt rates (see Table 2.3), although the estimates are based on short time periods, in contrast to the long term average used in this study.

7.14 Discussion

The history of the Carson River palaeochannels as constrained by radiocarbon and luminescence dates, palaeohydrology and terrace ages, can be combined with the detailed history of the Genoa fault, in order to examine alluvial-tectonic interactions. Figure 7.30 summarises the fluvial and tectonic histories of the Carson Valley. The luminescence dates have large error bars which limit their use in identifying specific interactions between channels and faults. Additionally, the luminescence age for channel belt 6 appears to be anomalously old (Section 7.10) and therefore the luminescence dates are excluded from the majority of this discussion. While the total number of dates is limited, a number of points are immediately apparent from Figure 7.30. Firstly, the behaviour of the Carson River channel belts is more complicated than initially envisaged by Leeder (1993). The channels do not step successively towards the fault but have instead undergone a process of onlap and offlap from the fault. Secondly, onlap appears to occur immediately after faulting, while offlap takes place during periods of tectonic quiescence. Lag times between faulting and channel onlap towards the fault also appear to be very short. In fact, if the luminescence date for channel belt 5 is correct, avulsion may have occurred almost immediately after the last faulting event, with a subsequent period of offlap to the Carson River's present position. This study also shows that channels do not necessarily avulse to the lowest point of the floodplain as assumed in older half-graben models (Bridge and Leeder, 1979; Mackey and Bridge, 1992). Additionally, the avulsion period is approximately 500 years which is smaller than data from aggrading deltas (Törnqvist, 1994) and the value adopted by Bridge and Leeder (1979) in their half-graben alluvial architecture model.

There are, however, at least three possible interpretations of the alluvial-tectonic history of the Carson River.

1) The channel avulsions may have been caused by intrinsic fluvial factors such as channel switching on the alluvial fan at the southern end of the valley. Intrinsic channel switching has affected at least some of the channel belts, as the avulsion nodes between channel belts 1, 2-4 and belts 5 and 6 are situated on the apex of the alluvial fan (Section 7.7). Development of a large alluvial fan from Jacks Valley (Section 7.5.1) may have also aided avulsions of the western channel belts. The influence of intrinsic factors in the other

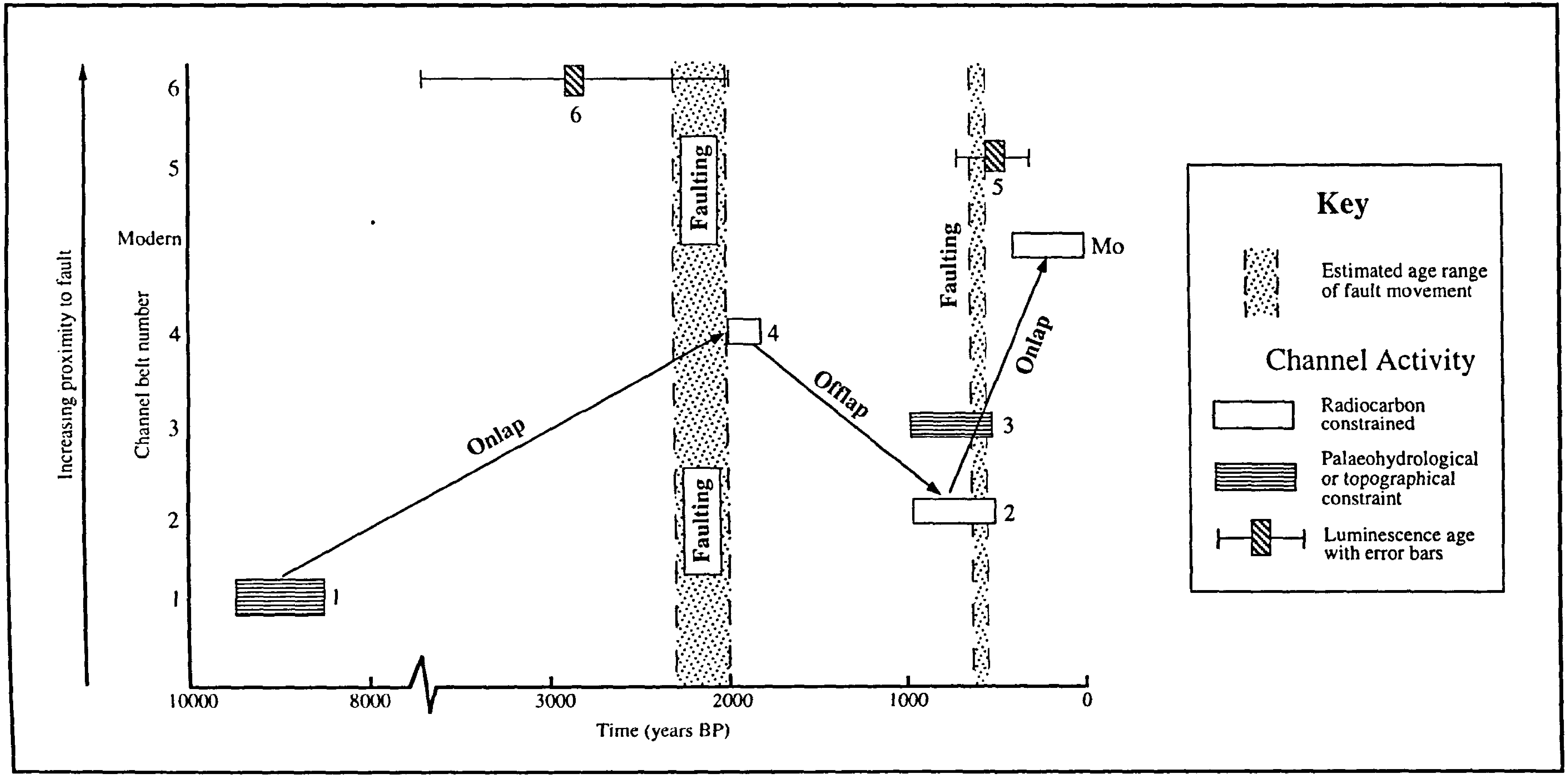

Figure 7.30. Spatial and temporal history of alluvial-tectonic interactions for the Carson Valley during the Holocene. Faulting events are based on Ramelli *et al.*, (1995) (see Section 7.4.1). Two or three other faulting events probably occurred in the early to mid-Holocene but are not shown on the diagram. Channel belt 3 had an anomalously old radiocarbon date but has similar palaeohydrological statistics and preserved topography to channel belt 2 and is therefore assumed to be approximately the same age. Channel belt numbers are adjacent to estimated periods of channel activity.

avulsions is unknown but the river regime is 'flashy' since it is dominated by snowmelt, with most of the western side of the valley flooded during large floods.

2) The history of channel movements may reflect regional periods of incision and aggradation related to regional climate change. Recent studies have demonstrated that the aggradation and degradation of river systems is very sensitive to climate change, on timescales as short as decadal (Graf *et al.*, 1991; Rumsby and Macklin, 1994) and several authors have correlated periods of Holocene river incision and aggradation across continents or world wide (Haynes, 1968; Brakenridge, 1980; Knox, 1983, 1984). Brakenridge (1980) compares Haynes' (1968) work in the western United States with data from Missouri and central Europe and identifies four periods of incision at 5,000-4,900 B.P.; 2,900-2,500 B.P; 1,600-1,500 B.P and 500-400 B.P. Additionally, Brakenridge (1980) correlates these periods of incision with the onset of little ice age climatic phases and therefore cooler, wetter conditions (see Fig. 7.31a). Knox (1983) identified four widespread alluvial discontinuities within the last 5,000 years across the United States although they vary from those of Brakenridge (1980) by as much as a few hundred years (see Fig. 7.31b). However, regional variations in channel response to climate change were noted in the United States (Fig. 7.31b) and were related to the influence of vegetation through the classification of six vegetation zones (Knox, 1983, 1984) (Fig. 7.1). In addition, Knox (1983) re-interprets Haynes (1968) study of the American South West in the light of more recent studies (Gile, 1975; American Quaternary Association, 1976; Hall, 1977) and notes that alluviation in the South West was out of phase with the rest of the United States during most of the Holocene (Fig. 7.31b).

Of the six U.S. vegetation zones identified by Knox (1983, 1984; see Fig. 7.32), the relationship between channel response and climate change is least well understood for the Great Basin and Northern West Sagebrush Steppe (GBNWSS) (Knox, 1983). Only one detailed fluvial history has been reconstructed in the Great Basin region and the surrounding vegetation zones have fluvial histories that are either poorly constrained or are out of phase with each other. Little is known about the Holocene channel history of the high elevation western woodlands which border the GBNWSS to the south, east and west but areas further east such as the western great plains are out of phase with the southwest desert shrubland which forms the southern border. A study of the Meadow Valley wash in south eastern Nevada indicated brief periods of incision at 3000, 1700, 1250, 900 and 250 years B.P. (Madsen, 1976), but these do not correlate strongly with either the SW desert shrubland or the eastern vegetation zones. Knox (1984) also modelled sediment yield fluctuations, which have been linked to channel response, for hypothetical changes of climate in the United States. However, yields for the area incorporating the Carson River drainage basin were undetermined and the south west

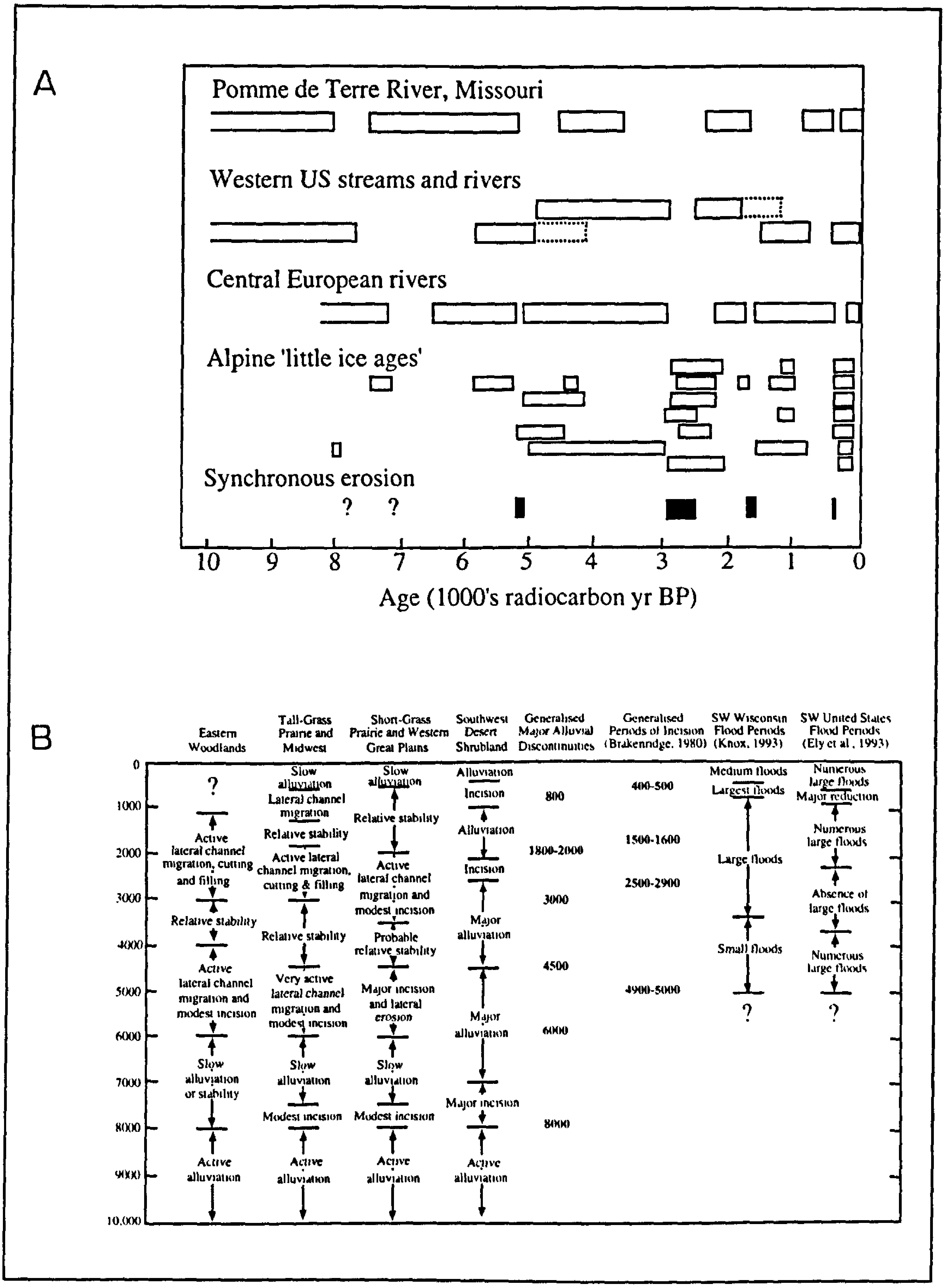

Figure 7.31. Holocene alluvial chronologies and glacial periods for the United States and the Northern Hemisphere. A) Comparison of Holocene alluvial and glacial periods. 'Little ice age' episodes represent in descending order: Alaska, Swedish Lapland, British Columbia and northern Washington; Norway; eastern and western Alps; Colorado Rocky Mountains, and Mexican volcanoes. Adapted from Brakenridge (1980). B) Comparison between Holocene regional alluvial chronologies of the contiguous United States of America, northern hemisphere incision intervals and US flood periods. The vegetation regions of the United States are shown in Figure 7.32. Based on Knox (1983) with additional data from Brakenridge (1980), Knox (1993) and Ely *et al.*, (1993).

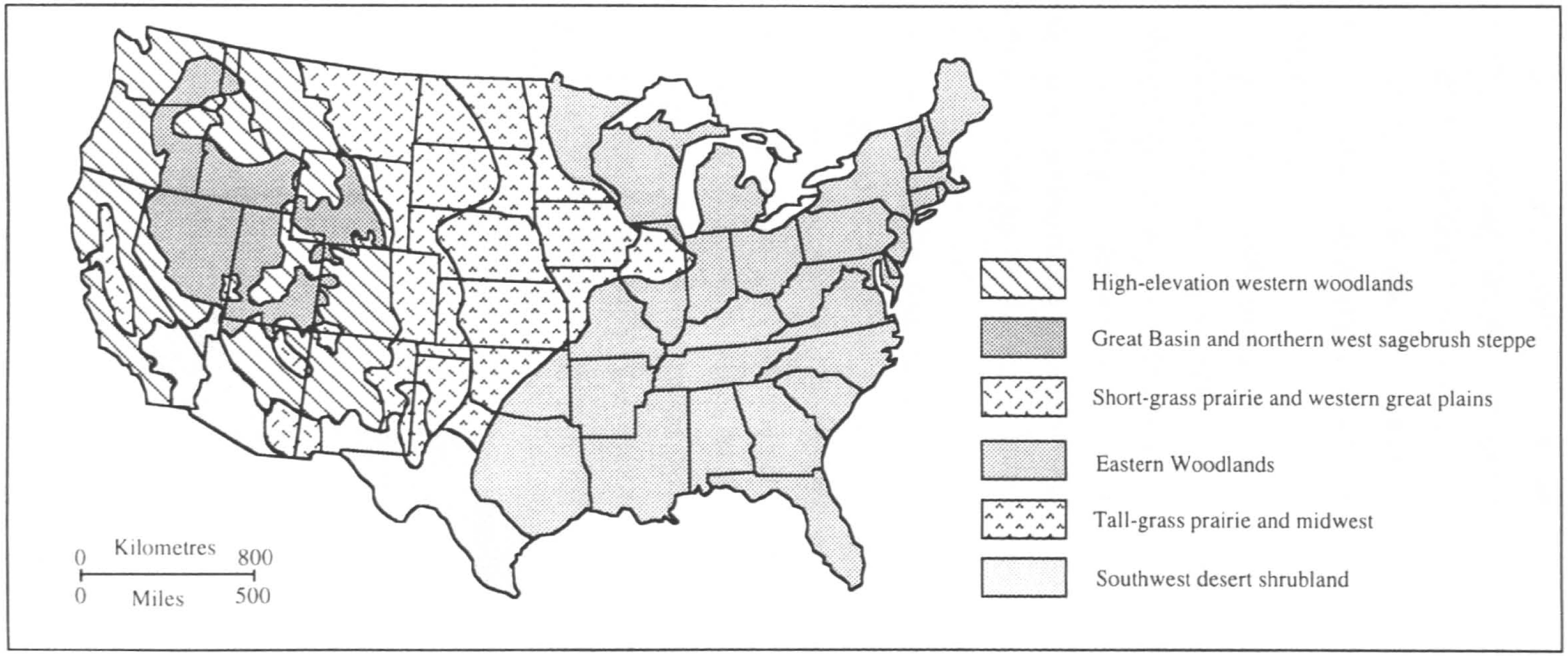

Figure 7.32. Natural vegetation regions of the United States. Adapted from Knox (1984).

shrubland province shows a patchwork of increased and decreased yields in cool/wet conditions.

In the absence of a good record of Holocene channel change for the Great Basin it is impossible to either dismiss or confirm the hypothesis that channel avulsions were related to regional climate change. However, the generalised major alluvial discontinuities of Knox (1984) at 1800-2000 B.P. and 800 B.P. do show a reasonable agreement with the avulsive history of the Carson. The last of Brakenridge's (1980) periods of incision at 400-500 years B.P. also seems to accurately match the observed time of channel incision in the modern Carson River.

3) The final possibility is that channel avulsion may have been triggered directly by tectonic movement (instantaneous avulsion) or by a rapid response to the increased lateral gradient. The trigger for the latter response may be either an intrinsic or extrinsic factor such as fan switching or climate change. Evidence for an instantaneous or rapid response to faulting and accompanying ground-tilting is provided by the strong temporal and spatial correlation between the last two fault events and subsequent avulsions. Additionally, calculations based on the recorded history of the Genoa Fault suggest that most of the present ground tilt could have formed during the Holocene and therefore that lateral gradients may have been increasing throughout the Holocene, thereby enhancing the possibility of avulsion. The presence of possible early Holocene meander bends eroding into terraces on the eastern side of the Carson Valley, also suggests that the valley has been strongly tilted towards the west during the Holocene.

In summary, there appears to be a strong correlation between channel avulsions and fault events with phases of onlap after faulting and offlap during periods of tectonic quiescence. The presence of instantaneous avulsion cannot be confirmed although the lag times between faulting and avulsion are short. However, a rapid response to increasing ground-tilting would appear to be important, although the actual trigger may be intrinsic or extrinsic.

7.15 Summary

Six palaeochannel belts have been identified, mapped and dated in the northern Carson Valley. The basin-bounding fault has also been independently dated allowing the detailed alluvial-tectonic interactions of a half-graben to be studied for the first time. Along with detailed surveying and palaeohydrological analysis the dating allows a Holocene history of the northern Carson Valley to be proposed.

At the start of the Holocene the valley probably had comparatively low lateral gradients dipping towards the main basin-bounding fault and large amplitude meander bends eroding into a low angle pediment surface on the eastern side of the valley. These large bends may mark a transition from late Pleistocene braided rivers. Two eastern terraces were still a site of floodplain sedimentation < 5000 years B.P. during human habitation. Subsequent incision led to the abandonment of the eastern terraces and the formation of the present floodplain. A detailed record of channel and fault movement during the last 2500 years indicates that channels have undergone onlap towards the fault after faulting and offlap during times of tectonic quiescence. Associated avulsion rates are high and lag times between faulting and avulsion are short. Rapid channel avulsions due to increasing ground-tilting would appear to be the most important factor in controlling channel movement, although the actual trigger may be intrinsic or extrinsic. Approximately 400 years ago the Carson River started incising into its present channel belt.

Ratios of lateral to axial gradients and long-term tilt rates for the Carson River are at the lower end of the range revealed by other studies of lateral ground-tilting, although the instantaneous lateral tilting rates are likely to be high. Finally, this study raises the intriguing possibility of using IRSL dating in conjunction with radiocarbon dating as a measure of sedimentation rate, or the travel time of a sediment pulse.

Chapter 8.
Conclusions and Opportunities for Further Work

8.1 Summary of conclusions

This chapter briefly summarises the main conclusions of this thesis and considers opportunities for further work.

8.1.1 Lateral ground-tilting

1) A criterion based on the rate of tilting is proposed in order to distinguish between channels that respond to tectonic tilting either by avulsion or gradual down-dip migration. A division between these two styles of channel response appears to exist at a tilt rate of approximately 7.5×10^{-4} to 7.5×10^{-3} radians ka^{-1}, although caution should be adopted when using these values since they are based on a relatively small number of poorly constrained examples. However, such a criterion would allow both avulsive and gradual migration to be incorporated into two and three-dimensional alluvial architecture models.

2) A new model of progressive downtilt migration has been presented that unifies the studies of Nanson (1980) and Leeder and Alexander (1987), which have previously been viewed as conflicting models. In addition, the initial channel response to tilting has been proposed, based on the example of the Long Valley Caldera, eastern California. Further supporting evidence for this conceptual model of gradual down-dip movement has been detailed from the Mississippi River, in the vicinity of the New Madrid Seismic Zone.

3) Lateral and vertical variations in the distribution of niche geometries have been identified from the preserved sedimentary fill of aggradational braided river experiments. A statistically significant correlation between mean coarse grained niche length and the magnitude of tilting has been observed for different tilt increments. Additionally, run B2 shows a significant correlation between increasing niche length and proximity to the downtilted boundary. This can be attributed to changes in the magnitude, timing and frequency of imposed lateral tilting events. These two relationships are criteria identified from the study of Leeder and Alexander (1987; see above) for the recognition of gradual down-dip channel movement from alluvial architecture. As such, this is the first

experimental or field based study to identify progressive down-dip channel movement in the subsurface. Run B2 also shows an increase in the percentage area occupied by coarse grained sediment with increasing proximity to the fault, as predicted for two-dimensional process-based alluvial architecture models.

4) No unambiguous relationship between bend parameters and imposed lateral ground-tilting can be identified in the meandering river experiments. This is because the rate and morphology of bend development masks the impact of tilting. However, a number of trends can be identified: i) a marked decrease in the probability of chute cutoff occurring across convex downtilt bends, ii) an increase in the rate of channel movement towards the fault after tilting, iii) a short lag-time between tilting and increased rates of movement towards the fault, and, iv) a possible relationship between tilt magnitude and the rate of increase in down-dip movement.

5) The Carson Valley has been proposed as a possible site of avulsive channel movement towards a basin bounding fault in an actively tilting basin (Leeder, 1993). The present study has dated the Carson River channel belts and in conjunction with independent dating of the basin-bounding fault provides a unique example of alluvial-tectonic interaction in a half-graben. Evidence for active lateral ground-tilting is provided (in the current study) by calculations based on the recorded history of the Genoa Fault which suggest that most of the present ground tilt could have formed during the Holocene. The presence of possible early Holocene meander bends eroding into terraces on the eastern side of the Carson Valley also suggests that the valley has been strongly tilted towards the west during the Holocene. The behaviour of the Carson River channel belts is considerably more complex than initially envisaged by Leeder (1993) since the channels do not step successively towards the fault but have instead undergone a process of onlap and offlap from the fault. Onlap appears to occur immediately after faulting, while offlap takes place during periods of tectonic quiescence. Lag times between faulting and channel onlap towards the fault also appear to be very short. This study also shows that channels do not always avulse to the lowest point of the floodplain as assumed in some half-graben models (e.g. Bridge and Leeder, 1979; Mackey and Bridge, 1992).

Despite the strong spatial and temporal correlation between faulting and channel movement, it is difficult to unambiguously determine cause and effect. In addition to the hypothesis of tectonically controlled channel movement, there are two other possible interpretations. Firstly, the channel movements may be affected by intrinsic channel avulsion and secondly, avulsion may be related to continent-wide periods of river incision and aggradation. While there is strong evidence for some intrinsic control of channel belts and several of the channel movements may correlate with regional periods of channel incision and aggradation, neither hypothesis appears to be as strong as tectonically controlled movement.

8.1.2 Froude scale models of meandering and braided rivers

1) This is one of the first studies to model aggrading braided rivers and builds on the initial work of Ashworth and Best (1992, 1994) and Ashworth *et al.*, (1994). A number of advances have been incorporated into this study, including: i) the use of computer-controlled flood hydrographs, ii) a reduction in the minimum spacing between sediment sections to approximately 25 mm, and, iii) a more elaborate niche classification scheme for fine and coarse grained deposition. These experiments are also the first to document coarse grained sedimentary niche geometries in the cross-stream direction.

2) The meandering river experiments in this study are the first to document the formation of scroll-bars and ridge and swale topography. In addition, a model of bend development has been described which exhibits many of the features common in meandering gravel-bed rivers and appears to be a better analogy than previous 'pseudomeandering' models.

8.1.3 Palaeohydrology

1) New definitions of arc height and radius of curvature have been proposed, both of which are suitable for the analysis of asymmetric meander bends. These parameters have been incorporated into a computer program (M-MAP) for the analysis of meander morphometry.

2) Several new relationships between discharge and meander bend parameters have been derived in this study from a re-analysis of a large database. The equations encompass studies from a large geographic area and will be useful for palaeohydrological studies where the channel regime is poorly constrained, but where channel width, depth or wavelength can be estimated.

8.1.4 Climate change

1) A history of channel development through the Holocene has been proposed for the Carson Valley and is the first study of its kind in the northern Great Basin. Large meander bends on the eastern side of the Carson Valley have been interpreted as early Holocene in age. However, approximately 7000 year old Mazama ash may be present in

the upper eastern terrace and if proven would lead to a significant reinterpretation of Holocene climate change in the north-west Great Basin.

8.1.5 Luminescence dating

1) A new technique for collecting sedimentary samples from vibracores for infra-red stimulated luminescence (IRSL) analysis has been detailed. Luminescence dating of several of these samples has indicated that there are problems in using this technique in fluvial environments, since the date of at least one sample was not reset or partially reset during transport. However, this result raises the intriguing possibility of using IRSL dating in conjunction with radiocarbon analysis as a measure of sedimentation rate or travel distance.

8.2 Opportunities for further work

A number of significant opportunities exist to apply or extend the ideas and results presented in this thesis, and a series of recommendations for further work are detailed below:

1) A major use of the Carson Valley dataset would be for testing the three-dimensional alluvial architecture model of Mackey and Bridge (1995) and other similar models (e.g. Meakin *et al.*, 1995). The code for the alluvial architecture model of Mackey and Bridge (1992) has already been successfully adapted by the author for simulation of half-graben sedimentation in the Rio Grande rift (Leeder *et al.*, *in press*). The Carson Valley study is presently unique since no comparable dataset is available to test the impact of lateral ground-tilting in these three-dimensional alluvial architecture models.

2) In order for lateral-tilt controlled spatial variations in niche geometries to be incorporated into stochastic reservoir simulation models, the geometric niche data need to be expressed in the form of probability density functions (PDF's). However, a much larger dataset is required in order to generate a spatially distributed set of PDF's for an individual experiment.

3) A similar modelling approach to that used in this study, could examine the effects of a large number of external controls on the preserved alluvial architecture of braided rivers (e.g. base-level change, magnitude and frequency of flooding, sediment supply rate and vegetation). Previous studies have detailed changes in the two-dimensional channel planform caused by uplift / subsidence and the associated changes in axial gradients.

However, these studies could all be extended into the third dimension using the methodology described herein.

4) Comparison of braided alluvial architecture between flume experiments and a field analogue / prototype is required to fully validate the model results. There is an absence of suitable field datasets, although, the retrogradational shoreline of parts of the Canterbury Plains (New Zealand) may offer a suitable field site for the collection of detailed sedimentological data on braided alluvial architecture.

5) Present PDF's are not a true reflection of actual sedimentological length distributions because they either do not use a dimensionality correction, or adopt a very simplistic approach. A more complex analysis is not adopted because geological outcrops cannot supply all of the relevant data. However, further aggradational flume experiments coupled with improved algebraic solutions have the potential for producing true PDF's of individual niches.

6) A spacing of 25 mm between two-dimensional sedimentary faces allows a large number of alluvial surfaces to be traced between consecutive sections (for example, see enclosure 1). At present, each of these faces is treated separately and adjusted for the dimensionality bias. However, if a series of faces were scanned into a three-dimensional computer package then it may be possible to interpolate directly between the surfaces and thereby image the entire dataset. Such a dataset would allow subsurface niche geometries and orientations to be studied in unprecedented detail. Comparison of planform niche geometries during an experiment with subsurface niches would allow the questions of preservation potential and morphological change during preservation to be addressed. A three-dimensional dataset would also allow reservoir modellers to directly estimate a range of properties from a physical model and use these as a grid-block or 'building block' for larger scale reservoir simulations. As such, this would be a form of semi-stochastic modelling.

7) Detailed sectioning of the preserved alluvial sediment in similar meandering river experiments would allow comparison with models of lateral-accretion geometry around meander bends (Willis, 1989; 1993). Further meandering experiments, undertaken in a longer flume, would also allow reach scale dynamics to be studied and could lead to an improved analogue for some coarse grained meandering rivers.

References

Ackers, P., (1964). Experiments on small streams in alluvium. *Journal of the Hydraulics Division, Proceedings of the American Society of Civil Engineers*, **90**, 1-37.

Ackers, P. and Charlton, F.G., (1970). The meandering of small streams in alluvium. Report 77, Hydraulics Research Station, Wallingford, U.K., 78pp.

Ackers, P., and White, W.R., (1973). Sediment transport: new approach and analysis, *Journal of the Hydraulics Division, Proceedings of the American Society of Civil Engineers*, **99**, 2041-2060.

Adams, J., (1980). Active tilting of the United States midcontinent: Geodetic and geomorphic evidence. *Geology*, **8**, 442-446.

Adams, K.D. and Locke, W.W., (1990). Obsidian hydration dating of naturally reworked fluvial sediments in the West Yellowstone region, Montana. *Quaternary Geology of the Western Madison Range, Madison Range, Tobacco Root Range, and Jefferson Valley, Rocky Mountains*. Friends of the Pleistocene Field Trip Guidebook, 89-111.

Adams, K.D., Locke, W.W. and Rossi, R., (1992). Obsidian-hydration dating of fluvially reworked sediments in the West Yellowstone region, Montana. *Quaternary Research*, **38**, 180-195.

Alexander, J. and Leeder, M.R., (1987). Active tectonic control on alluvial architecture. In: *Recent Developments in Fluvial Sedimentology*, Eds., Ethridge, F.G., Flores, R.M. and Harvey, M.D., Society of Economic Palaeontologists and Mineralogists Special Publication 39, 243-252.

Alexander, J. and Leeder, M.R., (1990). Geomorphology and surface tilting in an active extensional basin, SW Montana, USA. *Journal of the Geological Society of London*, **147**, 461-467.

Alexander, J., Bridge, J.S., Leeder, M.R., Collier, R.E.Ll. and Gawthorpe, R.L, (1994). Holocene meander-belt evolution in an active extensional basin, southwestern Montana. *Journal of Sedimentary Research*, **B64**, 542-559.

Alford, J.J. and Holmes, J.C., (1985). Meander scars as evidence of major climate change in southwest Louisiana. *Annals of the Association of American Geographers*, **75**, 395-403.

Algermissen, S.T. and D.M., Perkins., (1976). A probabilistic estimate of maximum acceleration in rock in the contiguous United States. *United States Geological Survey Open-File Report*, 76-416, 45pp.

Allen, J.R.L. and Williams, B.P.J., (1982). The architecture of an alluvial suite: rocks between the Townsend Tuff and Pickard Bay Tuff beds (Early Devonian), southwest Wales. *Philosophical Transactions of the Royal Society of London*, **B 297**, 51-89.

American Quaternary Association, (1976). Guidebook. San Pedro Valley Field Trip. October 11, 1976. American Quaternary Association, Fourth Biennial Meeting, Arizona State University, Tempe.

Anderson, J.G., Brune, J.N., Louie, J.N., Zeng, Y., Savage, M., Yu, G, Chen, Q. and dePolo, D., (1994). Seismicity in the western Great Basin apparently triggered by the Landers, California, Earthquake, 28 June 1992. *Bulletin of the Seismological Society of America*, **84**, 863-891.

Andrews, J.T. and Retherford, R.M., (1978). A reconnaissance survey of Late Quaternary sea level changes, Bella Bella / Bella Coola region, central British Columbia coast. *Canadian Journal of Earth Sciences*, **15**, 341-350.

Applied Technology Council, (1978). Tentative provisions for the development of seismic regulations for buildings. National Bureau of Standards, 514pp.

Armin, R.A., John, D.A. and Dohrenwend, J.C. (1983). Geologic Map of the Freel Peak 15-minute quadrangle, California and Nevada. United States Geological Survey Miscellaneous Investigations Map I-1424.

ASCE, (1942). *Hydraulic Models*. The American Society of Civil Engineers Manual of Practice, **25**, American Society of Civil Engineers, New York, 110pp.

ASCE, (1963). Report of the American Society of Civil Engineers' task force on friction factors in open channels. *Journal of the Hydraulics Division, Proceedings of the American Society of Civil Engineers*, **89**, 97-143.

Ashmore, P.E., (1982). Laboratory modelling of braided streams. *Unpublished M.Sc thesis*, University of Alberta, 201pp.

Ashmore, P.E., (1985). Process and form in gravel braided streams: laboratory modelling and field observations. *Unpublished Ph.D thesis*, University of Alberta, 414pp.

Ashmore, P.E., (1988). Bedload transport in braided gravel-bed stream models. *Earth Surface Processes and Landforms*, **13**, 677-695.

Ashmore, P.E., (1991a). Channel, morphology and bed load pulses in braided, gravel-bed streams. *Geografiska Annaler*, **68**, 361-371.

Ashmore, P.E., (1991b). How do gravel-bed rivers braid? *Canadian Journal of Earth Sciences*, **28**, 326-341.

Ashmore, P.E., (1993). Anabranch confluence kinetics and sedimentation processes in gravel-braided streams. In: *Braided Rivers*, Eds., Best, J.L. and Bristow, C.S., Geological Society Special Publication, **75**, 129-146.

Ashworth, P.J., (1995). Mid-channel bar growth and its relationship to local flow strength and direction. *Earth Surface Processes and Landforms*, **20**, (*in press*).

Ashworth, P.J. and Best, J.L., (1992). The scale modelling of braided rivers of the Ivishak Formation, Prudhoe Bay - BP discussion document, March 1992, 9pp.

Ashworth, P.J. and Best, J.L., (1994). The scale modelling of braided rivers of the Ivishak Formation, Prudhoe Bay II: Shale geometries and response to differential aggradation rates. Final BP project report, August 1994, 247pp.

Ashworth, P.J., Best, J.L. and Leddy, J.O., (1992). The scale modelling of braided rivers of the Ivishak Formation, Prudhoe Bay - Final BP project report phase 2, September 1992, 76pp.

Ashworth, P.J., Best, J.L., Leddy, J.O. and Geehan, G.W., (1994). The physical modelling of braided rivers and deposition of fine-grained sediment. In: *Process Models and Theoretical Geomorphology*, Ed., Kirkby, M.J., John Wiley and Sons, Chichester, 115-139.

Atkinson, C.D., McGowen, J.H., Bloch, S., Lundell, L.L. and Trumbly, P.N., (1991). Braidplain and deltaic reservoir, Prudhoe Bay Field, Alaska. In: *Sandstone Petroleum Reservoirs*, Eds., Barwis, J.H., McPherson, J.G. and Studlick, J.R.J., Springer-Verlag, New York, 7-29.

Ayre, H.G., Stephens, R. and Mock, G.D., (1967). *Analytic Geometry*. D. Van Nostrand, 332pp.

Bacon, C.R., (1983). Eruptive history of Mount Mazama and Crater Lake Caldera, Cascade Range USA. *Journal of Volcanology and Geothermal Research*, **18**, 57-115.

Bagnold, R.A., (1980). An empirical correlation of bedload transport rates in natural rivers. *Proceedings of the Royal Society of London*, **372A**, 453-473.

Bailey, R.A., Dalrymple, G.B. and Lanphere, M.A., (1976). Volcanism, structure, and geochronology of Long Valley Caldera, Mono County, California. *Journal of Geophysical Research*, **81**, 725-744.

Balescu, S. and Lamothe, M., (1994). Comparison of TL and IRSL age estimates of feldspar coarse grains from waterlain sediments. In: *Quaternary Geochronology*, supplement of *Quaternary Science Reviews*, **13**, 437-444.

Barr, D.I.H., (1983). A survey of procedures for dimensional analysis. *International Journal of Mechanical Engineering Education*, **11**, 147-159.

Bates, R.E., (1939). Geomorphic history of the Kickapoo region, Wisconsin. *Geological Society of America Bulletin*, **50**, 819-880.

Begg, S.H., Carter, R.R. and Dranfield, P., (1989). Assigning effective values to simulator gridblock parameters for heterogeneous reservoirs. *Society of Petroleum Engineers, Reservoir Engineering*, 455-463.

Bègin, Z.B., (1979). Aspects of degradation of alluvial streams in response to base-level lowering. *Unpublished Ph.D. dissertation*, Colorado State Univ., Fort Collins, Col., 239pp.

Behrensmeyer, A.K. and Tauxe, L., (1982). Isochronous fluvial systems in Miocene deposits of Northern Pakistan. *Sedimentology*, **29**, 331-352.

Bell, E.J., and Slemmons, D.B., (1979). Recent crustal movements in the central Sierra Nevada-Walker Lake region of California-Nevada-part II, the Pyramid Lake right-slip fault zone of the Walker Lane. *Tectonophysics*, **52**, 571-583.

Bell, J.W., (1984). Quaternary fault map of Nevada - Reno sheet. *Nevada Bureau of Mines and Geology* Map 79, scale 1:250,000.

Benson, L.V., (1993). Factors affecting ^{14}C ages of lacustrine carbonates: timing and duration of the last highstand lake in the Lahontan Basin. *Quaternary Research*, **39**, 163-174.

Benson, L.V., (1994). Carbonate deposition, Pyramid Lake Subbasin, Nevada: 1. Sequence of formation and elevational distribution of carbonate deposits (Tufas). *Palaeogeography, Palaeoclimatology, Palaeoecology*, **109**, 55-87.

Benson, L.V. and Mifflin, M.D., (1986). Reconnaissance bathymetry of basins occupied by Pleistocene Lake Lahontan, Nevada and California. *United States Geological Survey Water Resources Investigations Report*, 85-4262, 14pp.

Benson, L.V. and Paillet, F.L., (1989). The use of total lake-surface area as an indicator of climatic change: Examples from the Lahontan Basin. *Quaternary Research*, **32**, 262-275.

Benson, L.V., Currey, D.R., Dorn, R.I., Lajoie, K.R., Oviatt, C.G., Robinson, S.W., Smith, G.I. and Stine, S., (1990). Chronology of expansion and contraction of four Great Basin lake systems during the past 35,000 years. *Palaeogeography, Palaeoclimatology, Palaeoecology*, **78**, 241-286.

Benson, L.V., Currey, D.R., Lao, Y. and Hostetler, S., (1992). Lake-size variations in the Lahontan and Bonneville basins between 13,000 and 9000 ^{14}C yr B.P. *Palaeogeography, Palaeoclimatology, Palaeoecology*, **95**, 19-32.

Benson, L.V., Meyers, P.A. and Spencer, R.J., (1991). Change in the size of Walker lake during the past 5000 years. *Palaeogeography, Palaeoclimatology, Palaeoecology*, **81**, 189-214.

Berger, G.W., (1988). Dating Quaternary events by luminescence. In: *Dating Quaternary Sediments*, Ed., Easterbrook, D.J., Geological Society of America Special Publication, **227**, 13-50.

Blacknell, C., (1982). Morphology and surface sedimentary features of point bars in Welsh gravel-bed rivers. *Geological Magazine*, **119**, 181-192.

Blackwelder, E., (1931). Desert Plains. *Journal of Geology*, **39**, 133-140.

Blair, T.C. and Bilodeau, W.L., (1988). Development of tectonic cyclothems in rift, pull-apart, and foreland basins: sedimentary response to episodic tectonism. *Geology*, **16**, 517-520.

Blair, T.C. and McPherson, J.G., (1994). Historical adjustments by Walker River to lake-level fall over a tectonically tilted half-graben floor, Walker Lake Basin, Nevada. *Sedimentary Geology*, **92**, 7-16.

Blakey, R.C. and Gubitosa, R., (1984). Controls of sandstone body geometry and architecture in the Chinle Formation (Upper Triassic), Colorado Plateau. *Sedimentary Geology*, **38**, 51-86.

Blodgett, R.H. and Stanley, K.O., (1980). Stratification, bedforms, and discharge relations of the Platte braided river system, Nebraska. *Journal of Sedimentary Petrology*, **50**, 139-148.

Bluck, B.J., (1987). Bed forms and clast size changes in gravel-bed rivers. In: *River Channels: Environment and Process*, Ed., Richards, K.S., Blackwell, Oxford, 159-178.

Boguchwal, L.A. and Southard, J.B., (1990). Bed configurations in steady unidirectional water flows. Part 1. Scale model study using fine sands. *Journal of Sedimentary Petrology*, **60**, 649-657.

Boothroyd, J.C. and Ashley, G.M., (1975). Process, bar morphology and sedimentary structures on braided outwash fans, northeastern Gulf of Alaska. In: *Glaciofluvial and Glaciolacustrine Sedimentation*, Eds., Jopling, A.V. and McDonald, B.C., Society of Economic Paleontologists and Mineralogists, Special Publication, 23, 193-222.

Brakenridge, G.R., (1980). Widespread episodes of stream erosion during the Holocene and their climatic cause. *Nature*, **283**, 655-656.

Brice, J.C., (1964). Channel patterns and terraces of the Loup Rivers in Nebraska. *United States Geological Survey Professional Paper*, **422D**, 41pp.

Brice, J.C., (1973). Meandering pattern of the White River in Indiana: an analysis. In: *Fluvial Geomorphology*, Ed., Morisawa, M., Allen and Unwin, 178-200.

Brice, J.C., (1974). Evolution of meander loops. *Geological Society of America Bulletin*, **85**, 581-586.

Bridge, J.S., (1979). A FORTRAN program to simulate alluvial stratigraphy. *Computers and Geosciences*, **5**, 335-348.

Bridge, J.S. and Diemer, J.A., (1983). Quantitative interpretation of an evolving ancient river system. *Sedimentology*, **30**, 599-623.

Bridge, J.S. and Gordon, E.A., (1985). Quantitative interpretation of ancient river systems in the Oneonta Formation, Catskill Magnafacies. In: *The Catskill Delta*, Ed., Woodrow, D.L., Geological Society of America Special Paper 201, 163-181.

Bridge, J.S. and Leeder, M.R., (1979). A simulation model of alluvial stratigraphy. *Sedimentology*, **26**, 617-644.

Bridge, J.S. and Mackey, S.D., (1993a). A revised alluvial stratigraphy model. In: *Alluvial Sedimentation*, Eds., Marzo, M. and Puigdefábregas, C., International Association of Sedimentologists Special Publication 17, 319-336.

Bridge, J.S. and Mackey, S.D., (1993b). A theoretical study of fluvial sandstone body dimensions. In: *The Geological Modelling of Hydrocarbon Reservoirs*, Eds., Flint, S. and Bryant, I.D., Special Publication of the International Association of Sedimentologists 15, 213-236.

Brown, L.D. and Oliver, J.E., (1976). Vertical crustal movements from leveling data and their relation to geologic structure in the eastern United States. *Review of Geophysics and Space Physics*, **14**, 13-35.

Brush, L.M., Jr. and Wolman, M.G., (1960). Knickpoint behaviour in non-cohesive material: a laboratory study. *Geological Society of America Bulletin*, **71**, 59-74.

BS3680 (1987). Methods of measurement of liquid flow in open channels; Part 4 Weirs and flumes; Part 4A. Thin plate weirs. British Standards Institution, 27pp.

Buckingham, E., (1915). Model experiments and the forms of empirical equations. *Transactions of the American Society of Mechanical Engineers*, **37**, 263-292.

Burke, R.M. and Birkeland, P.W., (1979). Reevaluation of multiparameter relative dating techniques and their application to the glacial sequence along the eastern escarpment of the Sierra Nevada, California. *Quaternary Research*, **11**, 21-51.

Burnett, A.W. and Schumm, S.A., (1983). Active tectonics and river response in Louisiana and Mississippi. *Science*, **222**, 49-50.

Butler, P.R., (1984). Fluvial response to on-going tectonism and base-level changes, lower Amargosa River, southern Death Valley, California. *Sedimentary Geology*, **38**, 107-125.

Carey, R.P., (1969). Formation of floodplain lands. *Journal of the Hydraulics Division, Proceedings of the American Society of Civil Engineers*, **3**, 981-994.

Carlston, C.A., (1963). Drainage density and streamflow. *United States Geological Survey Professional Paper*, **422C**, 8pp.

Carlston, C.A., (1965). The relation of free meander geometry to stream discharge and its geomorphic implications. *American Journal of Science*, **263**, 864-885.

Carson, M.A., (1984). Observations on the meandering-braided transition, the Canterbury Plains, New Zealand: part one. *New Zealand Geographer*, **40**, 12-17.

Carson, M.A., (1986). Characteristics of high-energy "meandering" rivers: The Canterbury Plains, New Zealand. *Geological Society of America Bulletin*, **97**, 886-895.

Carson, M.A. and Griffiths, G.A., (1987). Bedload transport in gravel rivers. *New Zealand Journal of Hydrology*, **26**, 1-151.

Carson, M.A. and Lapointe, M.F., (1983). The inherent asymmetry of river meander planform. *Journal of Geology*, **91**, 41-55.

Castle, R.O., Estrem, J.E. and Savage, J.C., (1984). Uplift across the Long Valley Caldera, California. *Journal of Geophysical Research*, **89**, 11,507-11,516.

Chadwick, A.J. and Morfett, J.C., (1986). *Hydraulics in Civil Engineering*. Harper Collins, London, 492pp.

Charlton, F.G., Brown, P.M. and Benson, R.W., (1978). The hydraulic geometry of some gravel rivers in Britain. *Hydraulics Research Station, Wallingford*, U.K., Report IT 180.

Cheetham, G.H., (1980). Late Quaternary palaeohydrology: the Kennet Valley case-study. In: *The Shaping of Southern England*, Ed., Jones, D.K.C., Institute of British Geographers Special Publication, **11**, Academic Press, London and New York, 203-223.

Chitale, S.V., (1970). River channel patterns. *Journal of the Hydraulics Division, Proceedings of the American Society of Civil Engineers*, **96**, HY1, 201-221.

Chorley, R.J., (1967). Models in geomorphology. In: *Models in Geography*, Eds., Chorley, R.J. and Haggett, P., Methuen, London, 59-96.

Clague, J.J., (1975). Sedimentology and paleohydrology of Late Wisconsinan outwash, Rocky Mountain Trench, southeastern British Columbia. In: *Glaciofluvial and Glaciolacustrine Sedimentation*, Eds., Jopling, A.V. and McDonald, B.C., Society of Economic Paleontologists and Mineralogists Special Publication 23, 223-237.

Clarke, M.L., (1994). Infra-red stimulated luminescence ages from aeolian sand and alluvial fan deposits from the eastern Mojave desert, California. In: *Quaternary Geochronology*, supplement of *Quaternary Science Reviews*, **13**, 533-538.

Coleman, J.M., (1969). Brahmaputra River: channel processes and sedimentation. *Sedimentary Geology*, **3**, 129-239.

Collinson, J.D., (1970). Bedforms of the Tana River, Norway. *Geografiska Annaler*, **52A**, 31-55.

Collinson, J.D., (1978). Vertical sequences and sandbody shape in alluvial sequences. In: *Fluvial Sedimentology*, Ed., Miall, A.D., Canadian Society of Petroleum Geologists Memoir 5, 577-586.

Colton, R.B., Naeser, N.D. and Naeser, C.W., (1986). Drainage changes in eastern Montana and western North Dakota during late Cenozoic time. Abstract, Geological Society of America, Rocky Mountain Section Meeting, Flagstaff, 347pp.

Cotton, C.A., (1939). Lateral planation in New Zealand. *New Zealand Journal of Science and Technology*, **20**, 227B-232B.

Cowan, W.L., (1956). Estimating hydraulic roughness coefficients. *Agricultural Engineering*, **37**, 473-475.

Cowie, P.A. and Scholz, C.H., (1992). Growth of faults by accumulation of seismic slip. *Journal of Geophysical Research*, **97**, B7, 11,085-11,095.

Cox, N.J. and Jones, K., (1981). Exploratory data analysis. In: *Quantitative Geography*, Eds., Wrigley, N. and Bennett, R.J., Routledge and Kegan Paul, London, 135-143.

Cox, R.T., (1988a). Evidence for Quaternary ground tilting associated with the Reelfoot rift zone, northeast Arkansas. *Southeastern Geology*, **28**, 211-224.

Cox, R.T., (1988b). Evidence of late Cenozoic activity along the Bolivar-Mansfield Tectonic Zone, midcontinent, USA. *The Compass*, **65**, 207-213.

Cox, R.T., (1994). Analysis of drainage-basin symmetry as a rapid technique to identify areas of possible Quaternary tilt-block tectonics: an example from the Mississippi Embayment. *Geological Society of America Bulletin*, **106**, 571-581.

Crickmay, C.H., (1974). *The Work of The River*. Macmillan, London, 271pp.

Crickmay, C.H., (1975). The hypothesis of unequal activity. In: *Theories of Landform Development*, Eds., Melhorn, W.N. and Flemal, R.C., Publications in Geomorphology, SUNY, Binghamton, 102-109.

Crone, A.J. and Haller, K.M., (1991). Segmentation and the coseismic behaviour of Basin and Range normal faults: examples from east-central Idaho and southwestern Montana, U.S.A. *Journal of Structural Geology*, **13**, 151-164.

Dake, J.M.K., (1983). *Essentials of Engineering Hydraulics* (2nd Edition). Macmillan, London, 418pp.

Dart, C., Cohen, H.A., Akyüz, H.S. and Barka, A., (1995). Basinward migration of rift-border faults: implications for facies distributions and preservation potential. *Geology*, **23**, 69-72.

Davies,T.R.H., (1987). Problems of bed load transport in braided gravel-bed rivers. In: *Sediment Transport in Gravel-bed Rivers*, Eds., Thorne, C.R., Bathurst, J.C. and Hey, R.D., John Wiley and Sons, Chichester, 793-828.

Davies, T.R.H. and Lee, A.L., (1988). Physical hydraulic modelling of width reduction and bed level change in braided rivers. *New Zealand Journal of Hydrology*, **27**, 113-127.

Davis, J.O., (1978). Quaternary tephrochronology of the Lake Lahontan area, Nevada and California. *Nevada Archeological Survey Research Paper*, **7**, 137pp.

Davis, J.O., (1982). Bits and pieces: the last 35,000 years in the Lahontan area. In: *Man and Environment in the Great Basin*, Eds., Madsen, D.B. and O'Connell, J.F., Society for American Archaeology Papers, No 2, 53-75.

Davis, W.M., (1899). The geographic cycle. *Geographical Journal*, **14** (A), 481-504.

Demsey, K., (1987). Holocene faulting and tectonic geomorphology along the Wassuk range, west-central Nevada. *Unpublished M.S. thesis*, University of Arizona, Tucson.

dePolo, C.M., (1994). The maximum background earthquake for the Basin and Range province, western North America. *Bulletin of the Seismological Society of America*, **84**, 466-472.

dePolo, C.M., Clark, D.G., Slemmons, D.B. and Ramelli, A.R., (1991). Historical surface faulting in the Basin and Range Province, western north America: implications for fault segmentation. *Journal of Structural Geology*, **13**, 123-136.

Díaz-Molina, M., Arribas, J., Gómez, J.J. and Tortosa, A., (1995). Geological modelling of a reservoir analogue: Cenozoic meander belts, Loranca Basin, Spain. *Petroleum Geoscience*, **1**, 43-48.

Diffendal, R.F. and Corner, R.G., (1983). Asymmetrical distribution of Quaternary alluvial fills, Pumpkin Creek drainage basin, western Nebraska. *Geological Society of America Bulletin*, **94**, 720-729.

Dinga, C.F., (1969). A quantitative analysis of the effect of earth rotation on certain parameters of meandering alluvial channels. *Illinois Geographical Society Bulletin*, **12**, 1-28.

Dingman, S.L., (1984). *Fluvial Hydrology*. W.H. Freeman and Company, New York, 383pp.

Dohrenwend, J.C., (1982). Surficial geology, Walker Lake 1° by 2° quadrangle Nevada-California. *United States Geological Survey Miscellaneous Field Studies Map*, MF-1382C, scale 1:250,000.

Donaldson, A.C., Martin, R.H. and Kanes, W.H., (1970). Holocene Guadalupe delta of Texas Gulf Coast. In: *Deltaic Sedimentation - Modern and Ancient*, Eds., Morgan, J.P. and Shaver, R.H., Society of Economic Paleontologists and Mineralogists Special Publication 15, 107-137.

Dorn, R.I., Turin, B.D., Jull, A.J.T., Linick, T.W. and Donahue, D.J., (1987). Radiocarbon and cation-ratio ages for rock varnish on Tioga and Tahoe morainal boulders of Pine Creek, eastern Sierra Nevada, California, and their palaeoclimatic implications. *Quaternary Research*, **28**, 38-49.

Dorn, R.I., Jull, A.J.T., Donahue, D.J., Linick, T.W. and Toolin, L.J., (1990). Latest Pleistocene lake shorelines and glacial chronology in the western Basin and Range Province, USA: insights from AMS radiocarbon dating of rock varnish and palaeoclimatic implications. In: Paleoclimates: the record from lakes ocean and land, Eds., Meyers, P.A. and Benson, L.V., *Palaeogeography, Palaeoclimatology, Palaeoecology*, **78**, 315-332.

Dranfield, P., Begg, S.H. and Carter, R.R., (1987). Wytch Farm Oilfield: reservoir characterisation of the Triassic Sherwood Sandstone for input to reservoir simulation studies. In: *Petroleum Geology of North West Europe*, Eds., Brooks, J. and Glennie, K.W., Graham and Trotman, 149-160.

Duller, G.A.T., (1991). Equivalent dose determination using single aliquots. *Nuclear Tracks and Radiation Measurements*, **18**, 371-378.

Duller, G.A.T., Li, S.H., Musson, F.M. and Wintle, A.G., (1992). Use of infrared stimulated luminescence signal for scanning sediment cores. *Quaternary Science Reviews*, **11**, 115-119.

Dury, G.H., (1965). Theoretical implications of underfit streams. *United States Geological Survey Professional Paper*, **454-C**, 40pp.

Dury, G.H., (1976). Discharge prediction, present and former, from channel dimensions. *Journal of Hydrology*, **30**, 219-245.

Dury, G.H., (1985). Attainable standards of accuracy in the retrodiction of palaeodischarge from channel dimensions. *Earth Surface Processes and Landforms*, **10**, 205-213.

Edgar, D.E., (1973). Geomorphic and hydraulic properties of laboratory rivers, *Unpublished M.Sc thesis*, Colorado State Univ., Fort Collins, Col., 156pp.

Edwards, M.B., Eriksson, K.A. and Kier, R.S., (1983). Paleochannel geometry and flow patterns determined from exhumed Permian point bars in North-Central Texas. *Journal of Sedimentary Petrology*, **53**, 1261-1270.

Elliot, C.M. and Pokrefke, T.J., (1984). Channel stabilization in a straight river reach. In: *River Meandering*, Ed., Elliot, C.M., Proceedings Conference on Rivers '83, American Society of Civil Engineers, New York, 488-499.

Ely, L.L., Enzel, Y., Baker, V.R. and Cayan, D.R., (1993). A 5000-year record of extreme floods and climate change in the southwestern United States. *Science*, **262**, 410-412.

Erwin, J.W. and Berg, J.C., (1977). Bouguer gravity map of Nevada, Reno sheet. *Nevada Bureau of Mines and Geology*, Map 58. Scale 1:250,000.

Eth~~e~~ridge, F.G. and Schumm, S.A., (1978). Reconstructing palaeochannel morphological and flow characteristics: methodology, limitations and assessment. In: *Fluvial Sedimentology*, Ed., Miall, A.D., Memoir Canadian Society of Petroleum Geologists 5, 703-721.

Fahnestock, R.K., (1963). Morphology and hydrology of a glacial stream- White River, Mount Rainier Washington. *United States Geological Survey Professional Paper*, **422A**, 70pp.

Fairchild, H.L., (1932). Earth rotation and river erosion. *Science*, **76**, 423-427.

Fenton, J.D. and Abbott, J.E., (1977). Initial movement of grains on a stream bed: the effect of relative protrusion. *Proceedings of the Royal Society of London*, A, **325**, 523-527.

Ferguson, R.I., (1975). Meander irregularity and wavelength estimation. *Journal of Hydrology*, **26**, 315-333.

Ferguson, R.I., (1976). Disturbed periodic model for river meanders. *Earth Surface Processes and Landforms*, **1**, 337-347.

Ferguson, R.I., (1977). Meander sinuosity and direction variance. *Geological Society of America Bulletin*, **88**, 212-214.

Fergusson, J., (1863). On recent changes in the delta of the Ganges. *Journal of the Geological Society of London*, **19**, 321-354.

Fielding, C.R., (1987). Coal depositional models for deltaic and alluvial plain sequences. *Geology*, **15**, 661-664.

Fielding, C.R. and Crane, R.C., (1987). An application of statistical modelling to the prediction of hydrocarbon recovery factors in fluvial reservoir sequences. In: *Recent Developments in Fluvial Sedimentology*, Eds., Etheridge, F.G, Flores, R.M. and Harvey, M.D., Society of Economic Palaeontologists and Mineralogists Special Publication 39, 321-327.

Fiero, B., (1986). *Geology of the Great Basin.* University of Nevada Press, Reno, 197pp.

Franco, J.J., (1978). Guidelines for the design, adjustment and operation of models for the study of river sedimentation problems. Instruction Report H-78-1, *United States Waterways Experimental Station*, Vicksburg, Mississippi, 57pp.

Frazier, D.E., (1967). Recent deltaic deposits of the Mississippi River: their development and chronology. *Gulf Coast Association of Geological Societies, Transactions*, **17**, 287-311.

French, R.H., (1985). *Open-channel Hydraulics.* McGraw-Hill, New York, 739pp.

Friedkin, J.F., (1945). A laboratory study of the meandering of alluvial rivers. *United States Waterways Experimental Station*, Vicksburg, Mississippi, 40pp.

Fuller, I.C., Wintle, A.G. and Duller, G.A.T., (1994). Test of the partial bleach methodology as applied to the infra-red stimulated luminescence of an alluvial sediment from the Danube. In: *Quaternary Geochronology*, supplement of *Quaternary Science Reviews*, **13**, 539-543.

Fulton, R.J., (1969). Glacial lake history, southern Interior Plateau, British Columbia. *Geological Survey of Canada Paper*, **69-37**.

Gabrielsen, R.H., Steel, R.J. and Nottvedt, A., (1995). Subtle traps in extensional terranes: a model with reference to the North Sea. *Petroleum Geoscience*, **1**, 223-235.

Gardner, T.W., (1983). Experimental study of knickpoint and longitudinal profile evolution in cohesive, homogeneous material. *Geological Society of America Bulletin*, 94, 664-672.

Geehan, G.W., Lawton, T.F., Sakurai, S., Klob, H., Clifton, T.R., Inman, K.F. and Nitzberg, K.E., (1986). Geologic prediction of shale continuity, Prudhoe Bay Field. In: *Reservoir Characterisation*, Eds., Lake, L.W. and Carroll, H.B. Jr., Academic Press, Orlando, 63-82.

Geehan, G.W. and Underwood, J., (1993). The use of length distributions in geological modelling. In: *The Geological Modelling of Hydrocarbon Reservoirs and Outcrop Analogues*, Eds., Flint, S.S. and Bryant, I.D., Special Publication of the International Association of Sedimentologists 15, 205-212.

Gibbs, R.J., Mathews, M.D. and Link, D.A., (1971). The relationship between sphere size and settling velocity. *Journal of Sedimentary Petrology*, **41**, 7-18.

Gilbert, C.M. and Reynolds, M.W., (1973). Character and chronology of basin development, western margin of the Basin and Range province. *Geological Society of America Bulletin*, **84**, 2489-2509.

Gilbert, G.K., (1877). *Report on the Geology of the Henry Mountains.* United States Geographical and Geological Survey of the Rocky Mountains Region, United States Government Printing Office, Washington, D.C., 160pp.

Gile, I.H., (1975). Holocene soils and soil geomorphic relations in an arid region of southern New Mexico. *Quaternary Research*, **5**, 321-360.

Glancy, P.A. and Katzer, T.L., (1975). Water-resources appraisal of the Carson River basin, western Nevada. *Nevada division of water resources, reconnaissance report*, 59, 126pp.

Glen, P.K. and Osborn, G., (1986). Late Cenozoic river migration and diversion on the Alberta prairie. Abstract, American Quaternary Association, Ninth Biennial Meeting, Illinois, Program and Abstracts, 83.

Gohain, K. and Parkash, B., (1985). Morphology of the Kosi Megafan. In: *Morphology of Alluvial Fans - A Field Approach*, Eds., Church, M. and Rachocki, A., John Wiley and Sons, Chichester, 151-178.

Gomez, B. and Marron, D.C., (1991). Neotectonic effects on sinuosity and channel migration, Belle Fourche River, Western South Dakota. *Earth Surface Processes and Landforms*, **16**, 227-235.

Gordon, E.A. and Bridge, J.S., (1987). Evolution of Catskill (Upper Devonian) river systems: intra- and extrabasinal controls. *Journal of Sedimentary Petrology*, **57**, 234-249.

Gordon, I. and Heller, P.L., (1993). Evaluating major controls on basinal stratigraphy, Pine Valley, Nevada: implications for syntectonic deposition. *Geological Society of America Bulletin*, **105**, 47-55.

Graf, J.B., Webb, R.H. and Hereford, R., (1991). Relation of sediment load and flood-plain formation to climatic variability, Paria River drainage basin, Utah and Arizona. *Geological Society of America Bulletin*, **103**, 1404-1415.

Graumlich, L.J., (1993). A 1000-year record of temperature and precipitation in the Sierra Nevada. *Quaternary Research*, **39**, 249-255.

Gregory, D.I. and Schumm, S.A., (1987). The effect of active tectonics on alluvial river morphology. In: *River Channels: Environment and Process*, Ed., Richards, K.S., Blackwell, Oxford, 41-68.

Guccione, M.J., (1984). Causes of channel variations, Red River, Arkansas. In: *River Meandering*, Ed., Elliot, C.M., Proceedings Conference on Rivers '83, American Society of Civil Engineers, New York, 101-112.

Gustavson, T.C., (1978). Bed forms and stratification types of modern gravel meander lobes, Nueces River, Texas. *Sedimentology*, **25**, 401-426.

Hack, J.T., (1955). Geology of the Brandywine area and origin of the upland of southern Maryland. *United States Geological Survey Professional Paper*, **267A**, 43pp.

Hall, S.A., (1977). Late Quaternary sedimentation and paleoecologic history of Chaco Canyon, New Mexico. *Geological Society of America Bulletin*, **88**, 1593-1618.

Haner, B.E., (1984). Santa Ana River: an example of a sandy braided floodplain system showing sediment source area imprintation and selective sediment modification. *Sedimentary Geology*, **38**, 247-261.

Haq, B.U., Hardenbol, J. and Vail, P.R., (1987). Chronology of fluctuating sea-levels since the Triassic. *Science*, **235**, 1156-1166.

Hart, M.G., (1986). *Geomorphology: Pure and Applied.* Allen & Unwin, London, 228pp.

Harvey, M.D., (1984). A geomorphic evaluation of a grade-control structure in a meandering channel. In: *River Meandering*, Ed., Elliot, C.M., Proceedings Conference on Rivers '83, American Society of Civil Engineers, New York, 284-294.

Hassan, M.A., Church, M. and Ashworth, P.J., (1992). Virtual rate and mean distance of travel of individual clasts in gravel-bed channels. *Earth Surface Processes and Landforms*, **17**, 617-627.

Haynes, C.V., (1968). Geochronology of late-Quaternary alluvium. In: *Means of Correlation of Quaternary Successions*, Eds., Morrison, R.B. and Wright, H.E., University of Utah Press, Salt Lake City, 591-629.

Haynes, C.V., (1985). Mastodon-bearing springs and late Quaternary geochronology of the lower Pomme de Terre valley, Missouri. Geological Society of America Special Paper 204, 35pp.

Hays, J.D., Imbrie, J. and Shackleton, N.J., (1976). Variations in the Earth's orbit: pacemaker of the ice ages. *Science*, **194**, 2212-2232.

Heller, P.L., Angevine, C.L., Winslow, N.S. and Paola, C., (1988). Two-phase stratigraphic model of foreland-basin sequences. *Geology*, **16**, 501-504.

Henderson, F.M., (1966). *Open Channel Flow.* Macmillan, New York, 552pp.

Hey, R.D., (1984). Plan geometry of river meanders. In: *River Meandering*, Ed., Elliot, C.M., Proceedings Conference on Rivers '83, American Society of Civil Engineers, New York, 30-43.

Hickin, E.J., (1969). A newly identified process of point-bar formation in natural streams. *American Journal of Science*, **267**, 999-1010.

Hickin, E.J., (1972). Pseudomeanders and point dunes - a flume study. *American Journal of Science*, **272**, 762-799.

Hickin, E.J., (1977). The analysis of river planform responses to changes in discharge. In: *River Channel Changes*, Ed., Gregory, K.J., John Wiley and Sons, Chichester, 249-263.

Hickin, E.J., (1978). Concave-bank benches on the Squamish River, British Columbia, Canada. *Canadian Journal of Earth Sciences*, **16**, 200-203.

Hickin, E.J. and Nanson, G.C., (1975). The character of channel migration on the Beatton River, northeast British Columbia, Canada. *Geological Society of America Bulletin*, **86**, 487-494.

Hildenbrand, T.G. and Kucks, R.P., (1988a). Total intensity magnetic anomaly map of Nevada. *Nevada Bureau of Mines and Geology*, Map 93A, scale 1:750,000.

Hildenbrand, T.G. and Kucks, R.P., (1988b). Filtered magnetic anomaly maps of Nevada. *Nevada Bureau of Mines and Geology*, Map 93B, scale 1:1,000,000.

Hjulström, F., (1949). Climatic changes and river patterns. *Geografiska Annaler*, **31**, 83-89.

Hoey, T.B. and Sutherland, A.J., (1989). Self formed channels in a laboratory sand tray. Proceedings, 23rd Congress, International Association for Hydraulic Research, Ottawa, Canada, 41-48.

Hoey, T.B. and Sutherland, A.J., (1991). Channel morphology and bedload pulses in braided rivers: a laboratory study. *Earth Surface Processes and Landforms*, **16**, 447-462.

Hooke, J.M., (1977a). The distribution and nature of changes in river channel pattern. In: *River Channel Changes*, Ed., Gregory, K.J., John Wiley and Sons, Chichester, 265-280.

Hooke, J.M., (1977b). An analysis of changes in river channel patterns. *Unpublished Ph.D thesis*, University of Exeter.

Hooke, J.M., (1984). Changes in river meanders: a review of techniques and results of analyses. *Progress in Physical Geography*, **8**, 473-508.

Hooke, J.M., (1987). Changes in meander morphology. In: *International Geomorphology, 1986, Part I*, Ed., Gardiner, V., John Wiley and Sons, Chichester, 591-609.

Hooke, J.M. and Harvey, A.M., (1983). Meander changes in relation to bend morphology and secondary flows. In: *Modern and Ancient Fluvial Systems*, Eds., Collinson, J.D. and Lewin, J., International Association of Sedimentologists Special Publication 6, 121-132.

Houghton, J.G., Sakamoto, C.M. and Gifford, R.O., (1975). *Nevada's Weather and Climate*. Nevada Bureau of Mines and Geology, Special Publication 2, 78pp.

Huntley, D.J., Godfrey-Smith, D.I. and Thewalt, M.L.W., (1985). Optical dating of sediments. *Nature*, **313**, 105-107.

Imbrie, J., Hays, J.D., Martinson, D.G., McIntyre, A., Mix, A.C., Morley, J.J., Pisias, N.G., Prell, W.L. and Shackleton, N.J., (1984). The orbital theory of Pleistocene climate: support from a revised chronology of the marine $\delta^{18}O$ record. In: *Milankovitch and Climate: Part 1*, Eds., Berger, A., Imbrie, J., Hays, J., Kukla, G. and Saltzman, B., NATO ASI series, series C, Mathematical and Physical Sciences, v. 126, Reidel, Dordrecht, 510pp.

Inglis, C.C., (1940). Digest of answers to the Central Board of Irrigation questionnaire on meandering rivers with comments on factors controlling meandering and suggestions for future action. In: *Annual report (technical), 1939-1940, Central Board of Irrigation, India*, Ed., Edgecombe, A.R.B.

Jackson, J.A. and McKenzie, D., (1983). The geometrical evolution of normal fault systems. *Journal of Structural Geology*, **5**, 471-482.

Jackson, J.A. and White, N., (1989). Normal faulting in the upper continental crust: observations from regions of active extension. *Journal of Structural Geology*, **11**, 15-36.

Jackson, W.H., (1964). Changes in the floor of Hebgen Lake. *United States Geological Survey Professional Paper*, **435-H**, 51-54.

Jaeggi, M.N.R., (1986). Non distorted models for research on river morphology. Proceedings of the Symposium on Scale Effects in Modelling Sediment Transport Phenomena, August 1986, International Association of Hydrological Sciences, 70-84.

Jain, A.K., Raju, K.G.R. and Garde, R.J., (1978). Vortex formation at vertical pipe intakes. *Journal of the Hydraulics Division, Proceedings of the American Society of Civil Engineers*, **104**, 1429-1445.

Jefferson, M.S.W., (1902). Limiting width of meander belts. *National Geographic Magazine*, **13**, 373-384.

Jerlov, N.G., (1976). *Marine Optics* (second edition). Elsevier, New York, 231pp.

Jin, D. and Schumm, S.A., (1987). A new technique for modeling river morphology. In: *International Geomorphology, 1986 Part I*: Ed., Gardiner, V., John Wiley and Sons, Chichester, 681-690.

John, D.A., Stewart, J.H., Kilburn, J.E., Silberling, N.J. and Rowan, L.C., (1993). Geology and mineral resources of the Reno 1° by 2° quadrangle, Nevada and California. *United States Geological Survey Bulletin*, **2019**, 65pp.

Johnson, D., (1931). Planes of lateral corrosion. *Science*, **73**, 174-177.

Johnson, D.P., (1982). Sedimentary facies of an arid zone delta: Gascoyne Delta, western Australia. *Journal of Sedimentary Petrology*, **52**, 547-563.

Johnston, A.C., (1989). The seismicity of "stable continental interiors". In: *Earthquakes of North Atlantic Passive Margins; Neotectonics and Postglacial Rebound*, Eds., Gregersen, S. and Basham, P.W., Kluwer Academic Publishers, The Netherlands, 581-599.

Jorgensen, D.W., (1990). Adjustment of alluvial river morphology and process to localized active tectonics. *Unpublished Ph.D thesis*, Colorado State University at Fort Collins, 240pp.

Karcz, I. and Kersey, D., (1980). Experimental study of free-surface flow instability and bedforms in shallow flows. *Sedimentary Geology*, **27**, 263-300.

Katzer, T. and Bennett, J.P., (1983). Sediment transport model for the East Fork of the Carson River, Carson Valley, Nevada. 1983 Symposium on Urban Hydrology, Hydraulics and Sediment Control, University of Kentucky, July 25-28, 421-435.

Kesel, R.H., (1985). Alluvial fan systems in a wet tropical environment, Costa Rica. *National Geographic Research*, **1**, 450-469.

Kestin, J., Sokolov, M. and Wakeham, W.A., (1978). Viscosity of liquid water in the range -8°C to 150°C. *Journal of Physical and Chemical Reference Data*, **7**, 941-948.

Keulegan, G.H., (1938). Laws of turbulent flows in open channels. *Journal of Research, National Bureau of Standards*, **21**, 707-741.

King, G.C.P., Oppenheimer, D. and Amelung, F., (1994). Block versus continuum deformation in the Western United States. *Earth and Planetary Science Letters*, **128**, 55-64.

King, G.Q., (1978). The Late Quaternary history of Adrian Valley, Lyon County, Nevada. *Unpublished M.S. thesis*, Department of Geography, University of Utah.

King, W.A. and Martini, I.P., (1984). Morphology and recent sediments of the lower anastomosing reaches of the Attawapiskat River, James Bay, Ontario, Canada. *Sedimentary Geology*, **37**, 295-320.

Knighton, D., (1984). *Fluvial Forms and Processes*. Edward Arnold, London, 218pp.

Knox, J.C., (1983). Responses of river systems to Holocene Climates. In: *Late Quaternary Environments of the United States - Volume 2*, Eds., Porter, S.C. and Wright, H.E. Jr., University Minnesota Press, Minneapolis, 26-41.

Knox, J.C., (1984). Fluvial responses to small scale climate changes. In: *Developments and Applications of Geomorphology*, Eds., Costà, J.E. and Fleisher, P.J., Springer-Verlag, Berlin, 318-342.

Knox, J.C., (1985). Responses of flood to Holocene climatic change in the upper Mississippi valley. *Quaternary Research*, **23**, 287-300.

Knox, J.C., (1993). Large increases in flood magnitude in response to modest changes in climate. *Nature*, **361**, 430-432.

Kopsick, P.R., (1984). Dimensions of modern and relict meander loops of selected rivers in Kansas and Nebraska. In: *River Meandering*, Ed., Elliot, C.M., Proceedings Conference on Rivers '83, American Society of Civil Engineers, New York, 138-146.

Koutaniemi, L. and Ronkainen, R., (1983). Palaeocurrents from 5,000 and 1,600 – 1,500 BP in the main rivers of the Oulanka basin, North-Eastern Finland. *Quaternary Studies in Poland*, **4**, 145-148.

Krantz, W.B. and Goren, S.L., (1970). Finite-amplitude long waves on liquid films flowing down a plane. *Industrial and Engineering Chemistry: Fundamentals*, **9**, 107-113.

Krantz, W.B. and Goren, S.L., (1971). Stability of thin liquid film flowing down a plane. *Industrial and Engineering Chemistry: Fundamentals*, **10**, 91-101.

Kraus, M.J., and Middelton, L.T., (1987). Contrasting architecture of two alluvial suites in different structural settings. In: *Recent Developments in Fluvial Sedimentology*, Eds., Ethridge, F.G., Flores, R.M. and Harvey, M.D., Society of Economic Palaeontologists and Mineralogists Special Publication 39, 253-262.

Kuhnle, R.A. and Southard, J.B., (1988). Bed load transport fluctuations in a gravel bed laboratory channel. *Water Resources Research*, **24**, 247-260.

Langbein, W.B. and Leopold, L.B., (1966). River meanders - Theory of minimum variance. *United States Geological Survey Professional Paper*, **422-H**, 15pp.

Langhaar, H.L., (1980). *Dimensional Analysis and Theory of Hydraulic models.* Robert E. Krieger, Florida, 178pp.

Lapointe, M.F. and Carson, M.A., (1986). Migration patterns of an asymmetric meandering river: The Rouge River, Quebec. *Water Resources Research,* **22,** 731-743.

Lasca, N.P., (1967). Postglacial delevelling in Skeldal, Northeast Greenland. *Arctic,* **19,** 349-353.

Lawler, D.M., (1986). River bank erosion and the influence of frost: a statistical examination. *Transactions of the Institute of British Geographers, New Series,* **11,** 227-242.

Lawson, A.C., (1912). The recent fault scarp at Genoa, Nevada. *Seismological Society of America Bulletin,* 2, 193-200.

Lawton, T., (1985). Lithofacies and depositional environments of the Ivishak Formation, Prudhoe Bay Field, Vol. 1: a summary to accompany core description of nineteen wells. Internal report, SOHIO, 76pp.

Leary, P.C., Malin, P.E., Strelitz, R.A. and Henyey, T.L., (1981). Possible tilt phenomena observed as water level anomalies along the Los Angeles aqueduct. *Geophysical Research Letters,* **8,** 225-228.

Leddy, J.O., (1993). Physical scale modelling of braided rivers: avulsion and channel pattern change. *Unpublished M.Phil thesis,* University of Leeds, 130pp.

Leddy, J.O., Ashworth, P.J. and Best, J.L., (1993). Mechanisms of anabranch avulsion within gravel-bed braided rivers: observations from a scaled physical model. In: *Braided Rivers,* Eds., Best, J.L. and Bristow, C.S., Geological Society Special Publication, **75,** 119-127.

Leeder, M.R., (1973). Fluviatile fining-upwards cycles and the magnitude of palaeochannels. *Geological Magazine,* **110,** 265-276.

Leeder, M.R., (1982). *Sedimentology: Process and Product.* Unwin Hyman, London, 344pp.

Leeder, M.R., (1993). Tectonic controls upon drainage basin development, river channel migration and alluvial architecture: implications for hydrocarbon reservoir development and characterization. In: *Characterization of Fluvial and Aeolian Reservoirs*, Eds., North, C.P. and Prosser, D.J., Geological Society Special Publication 73, 7-22.

Leeder, M.R. and Alexander, J., (1987). The origin and tectonic significance of asymmetrical meander-belts. *Sedimentology*, **34**, 217-226.

Leeder, M.R. and Gawthorpe, R.L., (1987). Sedimentary models for extensional tilt block / half-graben basins. In: *Continental Extensional Tectonics*, Eds., Coward, M.P., Dewey, J.F. and Hancock, P.L., Geological Society of London Special Publication 28, 139-152.

Leeder, M.R. and Jackson, J.A., (1993). The interaction between normal faulting and drainage in active extensional basins, with examples from the western United States and central Greece. *Basin Research*, **5**, 79-102.

Leeder, M.R., Mack, G.H., Peakall, J. and Salyards, S.L., (*in press*). First quantitative field test of alluvial architectural models: southern Rio Grande rift, New Mexico, USA. *Geology*.

Leighly, J., (1936). Meandering arroyos of the dry southwest. *Geographical Review*, **26**, 270-282.

Leopold, L.B. and Langbein, W.B., (1966). River Meanders. *Scientific American*, **214**, N° 6, 60-70.

Leopold, L.B. and Maddock, T., (1953). The hydraulic geometry of stream channels and some physiographic implications. *United States Geological Survey Professional Paper*, **252**, 57pp.

Leopold, L.B. and Skibitzke, H.E., (1967). Observations on unmeasured rivers. *Geografiska Annaler*, **49**, 247-255.

Leopold, L.B. and Wolman, M.G., (1957). River channel patterns: Braided, meandering and straight. *United States Geological Survey Professional Paper*, **282-B**, 39-85.

Leopold, L.B. and Wolman, M.G., (1960). River Meanders. *Geological Society of America Bulletin*, **71**, 769-794.

Leopold, L.B., Wolman, M.G. and Miller, J.P., (1964). *Fluvial Processes in Geomorphology*, W.H. Freeman Co., San Francisco, 522pp.

Lewin, J., (1976). Initiation of bed forms and meanders in coarse-grained sediment. *Geological Society of America Bulletin*, **87**, 281-285.

Lewin, J., (1983a). Changes of channel patterns and floodplains. In: *Background to Palaeohydrology*, Ed., Gregory, K.J., Wiley and Sons, Chichester, 303-320.

Lewin, J., (1983b). Meander development and floodplain sedimentation: a case study from mid-Wales. *Geological Journal*, **13**, 25-36.

Lewin, J. and Brindle, B.J., (1977). Confined meanders. In: *River Channel Changes*, Ed., Gregory, K.J., John Wiley and Sons, Chichester, 213-233.

Li, S. H., (1994). Optical dating: insufficiently bleached sediments. In: Radiation Measurements, 23, 563-567.

Lighthill, M.J., (1978). *Waves in Fluids*. Cambridge University Press, 504pp.

Lin, S.P., (1970). Roles of surface tension and Reynolds stress on the finite amplitude stability of parallel flow. *Journal of Fluid Mechanics*, **40**, 307-314.

Lin, S.P., (1971). Profile and speed of finite-amplitude waves in a falling liquid layer. *Physics of Fluids*, **14**, 263-268.

Link, M.H., Roberts, M.T. and Newton, M.S., (1985). Walker Lake Basin, Nevada: an example of late Tertiary (?) to recent sedimentation in a basin adjacent to an active strike-slip fault. In: *Strike-Slip Deformation, Basin Formation and Sedimentation*, Eds., Biddle, K.T. and Christie-Blick, N., Society of Economic Paleontologists and Mineralogists Special Publication 37, 105-125.

Lisle, T.E., Ikeda, H. and Iseya, F., (1991). Formation of stationary alternate bars in a steep channel with mixed-size sediment: a flume experiment. *Earth Surface Processes and Landforms*, **16**, 463-469.

Livacarri, R.F., (1979). Late Cenozoic tectonic evolution of the western United States. *Geology*, **7**, 72-75.

Lowham, H.W., (1976). Techniques for estimating flow characteristics of Wyoming streams. *United States Geological Survey Water Resources Investigations*, 76-112, 83pp.

McKee, E.D., Crosby, E.J. and Berryhill, H.L., (1967). Flood deposits of Bijou Creek, Colorado, June 1965. *Journal of Sedimentary Petrology*, **37**, 829-851.

McKee, E.H., (1971). Tertiary igneous chronology of the Great Basin of Western United States - Implications for tectonic models. *Geological Society of America Bulletin*, **82**, 3497-3502.

McKinney, R.F., (1976). Environmental geology of southeast Carson City, Nevada. *Unpublished M.S. thesis*, University of Nevada, Reno, 130pp.

Mack, G.H. and James, W.C., (1993). Control of basin symmetry on fluvial lithofacies, Camp Rice and Palomas Formations (Plio-Pleistocene), southern Rio Grande rift, USA. In: *Alluvial Architecture*, Eds., Marzo, M. and Puigdefábregas, C., Special Publication of the International Association of Sedimentologists 17, 439-449.

Mack, G.H. and Seager, W.R., (1990). Tectonic control on facies distribution of the Camp Rice and Palomas Formations (Pliocene-Pleistocene) in the southern Rio Grande rift. *Geological Society of America Bulletin*, **102**, 45-53.

Mackey, S.D., (1993).Theoretical modelling of alluvial architecture. *Unpublished Ph.D thesis*, State University of New York at Binghamton, 421pp.

Mackey, S.D. and Bridge, J.S., (1992). A revised FORTRAN program to simulate alluvial stratigraphy. *Computers and Geosciences*, **18**, 119-181.

Mackey, S.D. and Bridge, J.S., (1995). Three-dimensional model of alluvial stratigraphy: theory and application. *Journal of Sedimentary Research*, **B65**, 7-31.

Mackin, J.H., (1937). Erosional history of the Big Horn Basin. *Geological Society of America Bulletin*, **48**, 813-894.

Madsen, D.B., (1976). Pluvial post pluvial vegetation changes in the southeastern Great Basin. In: *Holocene Environmental Change in the Great Basin*, Ed., Elston, R., Nevada Archaeological Survey Research Paper 6, 104-119.

Maizels, J., (1988). Sediment size and channel changes in braided and meandering gravel-bed streams, Upper Deeside, Scotland. In: *International Conference on River Regime*, Ed., White, W.R., Hydraulics Research Ltd., Wallingford, U.K., John Wiley and Sons, 215-230.

Maizels, J. and Aitken J., (1991). Palaeohydrological change during deglaciation in upland Britain: a case study from Northeast Scotland. In: *Temperate Palaeohydrology - Fluvial Processes in the Temperate Zone during the last 15000 years*, Eds: L.Starkel, Gregory K.J. and Thornes, J.B., John Wiley and Sons, Chichester, 105-145.

Marsden, N., (1981). Model simulation of effect of vegetation on braided rivers. *Unpublished Project Report*, Department of Agricultural Engineering, Lincoln College, Canterbury, New Zealand, 68pp.

Marzo, M., Nijman, W. and Puigdefábregas, C., (1988). Architecture of the Castissent fluvial sheet sandstones, Eocene, South Pyrenees, Spain. *Sedimentology*, **35**, 719-738.

Massey, B.S., (1983). *Mechanics of Fluids* (5th edition). Van Nostrand Reinhold, Wokingham, 582pp.

Mathews, W.H., (1978). Quaternary stratigraphy and Geomorphology of Charlie Lake (94A) map-area, British Columbia. *Geological Survey of Canada Paper*, **76-20**, 25pp.

Mathews, W.H., Fyles, J.G. and Nasmith, H.W., (1970). Postglacial crustal movements in southwestern British Columbia and adjacent Washington State. *Canadian Journal of Earth Sciences*, **7**, 690-702.

Maurer, D.K., (1985). Gravity survey and depth to bedrock in Carson Valley, Nevada-California. *United States Geological Survey, Water Resources Investigation Report* 84-4202, 20pp.

Maxwell, W.H.C. and Weggel, J.R., (1969). Surface tension in Froude models. *Journal of the Hydraulics Division, Proceedings of the American Society of Civil Engineers*, **95**, 677-701.

Maxwell, W.H.C. and Weggel, J.R., (1970). Surface tension in Froude models- errata. *Journal of the Hydraulics Division, Proceedings of the American Society of Civil Engineers*, **96**, 845.

Meade, B.K., (1975). Geodetic surveys for monitoring crustal movements in the United States. *Tectonophysics*, **29**, 103-112.

Meakin, P., Sun, T., Boger, F., Jossang, T. and Bliefnick, D., (1995). A three-dimensional meandering river model. Conference on quantification and modelling of spatial patterns in permeable rocks, Institute of Mathematics and its Applications, Scarborough, (Abstract).

Melvin, J., (1993). Evolving fluvial style in the Kekiktuk Formation (Mississippian), Endicott field area, Alaska: base level response to contemporaneous tectonism. *American Association of Petroleum Geologists Bulletin*, **77**, 1723-1744.

Mezger, L. and Burbank, D., (1986). The glacial history of the Cottonwood Lakes area, southeastern Sierra Nevada. *Geological Society of America*, Abstract Paper, **18**, 157.

Miall, A.D., (1977). A review of the braided-river depositional environment. *Earth Science Reviews*, **13**, 1-62.

Mike, K., (1975). Utilization of the analysis of ancient river beds for the detection of Holocene crustal movements. *Tectonophysics*, **29**, 359-368.

Miller, C.D., (1985). Holocene eruptions at the Inyo volcanic chain, California: implications for possible eruptions in Long Valley caldera. *Geology*, **13**, 14-17.

Milne, J.A., (1979). The morphological relationships of bends in confined stream channels in upland Britain. In: *Geographical Approaches to Fluvial Processes*, Ed., Pitty, A.F., Geo Abstracts, Norwich, 215-239.

Mohindra, R., Parkash, B. and Prasad, J., (1992). Historical geomorphology and pedology of the Gandak Megafan, Middle Gangetic Plains, India. *Earth Surface Processes and Landforms*, **17**, 643-662.

Moore, J.G. and Archbold, N.L., (1969). *Geology and Mineral Deposits of Lyon, Douglas and Ormsby Counties, Nevada*. Bulletin 75, Mackay School of Mines, University of Nevada, Reno, 45pp.

Morisawa, M., (1985). *Rivers*. Longman, New York, 222pp.

Mosley, M.P., (1976). An experimental study of channel confluences. *Journal of Geology*, **84**, 535-562.

Murphy, G., (1950). *Similitude in Engineering*. Ronald Press Company, New York, 302pp.

Myers, W.B. and Hamilton, W., (1964). Deformation associated with the Hebgen Lake earthquake of August 17, 1959. *United States Geological Survey Professional Paper*, **435I**, 55-98.

Nagabhushanaiah, H.S., (1967). Meandering of rivers. *Bulletin of the International Association for Scientific hydrology*, **12**, 28-43.

Nanson, G.C., (1980). A regional trend to meander migration. *Journal of Geology*, **88**, 100-108.

Nanson, G.C. and Page, K., (1983). Lateral accretion of fine-grained concave benches on meandering rivers. In: *Modern and Ancient Fluvial Systems*, Eds., Collinson, J.D. and Lewin, J., Special Publication of the International Association of Sedimentologists 6, 133-143.

Nanson, G.C. and Young, R.W., (1987). Comparison of thermoluminescence and radiocarbon age-determinations from late-Pleistocene alluvial deposits near Sydney, Australia. *Quaternary Research*, **27**, 263-269.

Nanson, G.C., Price, D.M. and Short, S.A., (1992). Wetting and drying of Australia over the past 300 ka. *Geology*, **20**, 791-794.

Nanson, G.C., Young, R.W. and Price, D.M., (1988). Stratigraphy, sedimentology and Late-Quaternary chronology of the channel country of Western Queensland. In: *Fluvial Geomorphology of Australia*, Ed., Warner, R.F., Academic Press, Sydney, Australia, 151-175.

Nash, D.B., (1984). Morphologic dating of fluvial terrace scarps and fault-scarps near West Yellowstone, Montana. *Geological Society of America Bulletin*, **95**, 1413-1424.

NDOT (Nevada Department of Transport), (1985). Archaeological Investigations of 26Do326 in Carson Valley, Nevada, NDOT-047-85T, 117pp.

Neill, C.R. and Galay, V.J., (1967). Systematic evaluation of river regime. *Journal of the Waterways Harbors Division, Proceedings of the American Society of Civil Engineers*, **93**, WW1, 25-53.

Neill, C.R. and Yaremko, E.K., (1988). regime aspects of flood control channelization. In: *International Conference on River Regime*, Ed., White, W.R., Hydraulics Research Ltd., Wallingford, U.K., John Wiley and Sons, 317-330.

Nikuradse, J., (1933). Strömungsgesetze in rauhen Rohren, VDI-Forschungsheft, 361. English translations: *NACA Technical Memo.* 1292 and *Petroleum Engineer* (1940) March, 164-166; May, 75, 78, 80, 82; June, 124, 127, 128, 130; July, 38, 40, 42; August, 83, 84 and 87.

Nixon, M., (1959). A study of the bankfull discharges of rivers in England and Wales. *Proceedings Institution of Civil Engineers*, **12,** 157-175.

Noble, D.C., (1972). Some observations on the volcano-tectonic evolution of the Great Basin, western United States. *Earth and Planetary Science Letters*, **17**, 142-150.

Novak, P. and Câbelka, J., (1981). *Models in Hydraulic Engineering*. Pitman, London. 459pp.

Nuttli, O.W., (1973). The Mississippi Valley earthquakes of 1811-1812; intensity, ground motion and magnitudes. *Bulletin of the Seismological Society of America*, **63**, 227-248.

Officer, L.B. and Drake, C.L., (1981). Epeirogenic plate movements. *Journal of Geology*, **90**, 139-153.

Ollier, C., (1981). *Tectonics and Landforms*. Longman, London, 324pp.

Omang, R.J., Parrett, C. and Hull, J.A., (1983). Mean annual runoff and peak flow estimates based on channel geometry of streams in southeastern Montana. *United States Geological Survey Water Resources Investigations*, 82-4092, 33pp.

Osborn, G. and du Toit, C., (1991). Lateral planation of rivers as a geomorphic agent. *Geomorphology*, **4**, 249-260.

Osterkamp, W.R., (1977). Effect of channel sediment on width-discharge relations, with emphasis on streams in Kansas. *Kansas Water Resources Board Bulletin*, **21**, 25pp.

Osterkamp, W.R. and Hedman, E.R., (1977). Variation of width and discharge for natural high gradient stream channels. *Water Resources Research*, **13**, 256-258.

Osterkamp, W.R. and Hedman, E.R., (1982). Perennial - streamflow characteristics related to channel geometry and sediment in Missouri River Basin. *United States Geological Survey Special Paper*, **1242**, 37pp.

Ouchi, S., (1983). Response of alluvial rivers to slow active tectonic movement. *Unpublished Ph.D dissertation*, Colorado State University., Fort Collins, 205pp.

Ouchi, S., (1985). Response of alluvial rivers to slow active tectonic movement. *Geological Society of America Bulletin*, **96**, 504-515.

Padgett, G.V. and Ehrlich, R., (1976). Palaeohydrologic analysis of a late Carboniferous fluvial system, southern Morocco. *Geological Society of America Bulletin*, **87**, 1101–1104.

Page, K. and Nanson, G.C., (1983). Concave-bank benches and associated floodplain formation. *Earth Surface Processes and Landforms*, **7**, 529-543.

Palmquist, R., (1983). Terrace chronologies in the Bighorn Basin, Wyoming. In: Geology of the Bighorn Basin, Ed., Boberg, W.W., Wyoming Geological Association 34th Annual Field Conference Guidebook, 217-231.

Parker, G., (1976). On the cause and characteristic scales of meandering and braiding in rivers. *Journal of Fluid Mechanics*, **76**, 457-480.

Parker, G., (1979). Hydraulic geometry of active gravel rivers. *Journal of the Hydraulics Division, Proceedings of the American Society of Civil Engineers*, **105**, 1185-1201.

Parker, G., Dhamothoran, S. and Stefan, H., (1982). Model experiments on mobile paved gravel-bed streams. *Water Resources Research*, **18**, 1395-1408.

Peakall, J. and Warburton, J., (1995). Comment: Surface tension in small hydraulic river models - the significance of the Weber number. *New Zealand Journal of Hydrology* (*in press*).

Pease, R.C., (1979a). Scarp degradation and fault history south of Carson City, Nevada. *Unpublished M.Sc thesis*, University of Nevada, Reno, 90pp.

Pease, R.C., (1979b). Genoa quadrangle earthquake hazards map (1:24,000). *Nevada Bureau of Mines and Geology*, map 1Ci.

Pease, R.C., (1980). Genoa quadrangle geologic map (1:24,000). *Nevada Bureau of Mines and Geology*, map 1Cg.

Phelps, D.M., (1984). River meander stability. In: *River Meandering*, Ed., Elliot, C.M., Proceedings Conference on Rivers '83, American Society of Civil Engineers, New York, 700-709.

Phillips, F.M., Zreda, M.G., Smith, S.S., Elmore, D., Kubik, P.W. and Sharma, P., (1990). Cosmogenic Chlorine-36 chronology for glacial deposits at Bloody canyon, eastern Sierra Nevada. *Science*, **248**, 1529-1532.

Pickup, G. and Warner, R.F., (1984). Geomorphology of tropical rivers II. Channel adjustment to sediment load and discharge in the Fly and Lower Purari, Papua New Guinea. *Catena Supplement*, **5**, 19-41.

Pinter, N., (1995). Faulting on the Volcanic Tableland, Owens Valley, California. *Journal of Geology*, **103**, 73-83.

Pinter, N., Keller, E.A. and West, R.B., (1994). Relative dating of terraces of the Owen River, Northern Owens Valley, California, and correlation with moraines of the Sierra Nevada. *Quaternary Research*, **42**, 266-276.

Plouff, D., (1984). Bouguer gravity map of Nevada, Walker Lake sheet. *Nevada Bureau of Mines and Geology*, Map 83, scale 1:250,000.

Plouff, D., (1992). Bouguer gravity anomaly and isostatic residual gravity maps of the Reno 1° by 2° quadrangle, Nevada and California. *United States Geological Survey Miscellaneous Field Studies Map*, MF-2154-E, scale 1:250,000.

Plumley, W.J., (1948). Black Hills terrace gravels: a study in sediment transport. *Journal of Geology*, **56**, 526-577.

Powers, H.A. and Wilcox, R.E., (1964). Volcanic ash from Mount Mazama (Crater Lake) and from Glacier Peak. *Science*, **144**, 1334-1336.

Prandtl, L., (1952). *Essentials of Fluid Dynamics: With Application to Hydraulics, Aeronautics, Meteorology and other Subjects*; authorized translation from the German by W.M. Deans. Blackie and Sons, London, 452pp.

Price, R.C. and Whetstone, K.N., (1977). Lateral stream migration as evidence for geologic structures in the eastern Gulf coastal plain. *Southeastern Geology*, **18**, 129-148.

Proffett, J.M. Jr., (1977). Cenozoic geology of the Yerington district, Nevada, and implications for the nature and origin of Basin and Range faulting. *Geological Society of America Bulletin*, **88**, 247-266.

Ramelli, A.R., dePolo, C.M. and Bell, J.W., (1995). Synthesis of data and exploratory trenching along the Northern Sierra Nevada Fault Zone. *United States Geological Survey, National Earthquake Hazards Reduction Program*, final project report (in press).

Reid, J.B. Jr., (1992). The Owens River as a tiltmeter for Long Valley Caldera, California. *Journal of Geology*, **100**, 353-363.

Rendell, H.M., Webster, S.E. and Sheffer, N.L., (1994). Underwater bleaching of signals from sediment grains: new experimental data. In: *Quaternary Geochronology*, supplement of *Quaternary Science Reviews*, **13**, 433-435.

Reynolds, O., (1887). On certain laws relating to the régime of rivers and estuaries, and on the possibility of experiments on a small scale. A Report of the British Association. In: Reynolds, O., *Papers on Mechanical and Physical Subjects, Volume II, 1881-1900*; Cambridge University Press, 1901, 326-335.

Reynolds, O., (1889). Report of the committee appointed to investigate the action of waves and currents on the beds and foreshores of estuaries by means of working models. British Association Report. In: Reynolds, O., *Papers on Mechanical and Physical Subjects, Volume II, 1881-1900*; Cambridge University Press, 1901, 380-409.

Reynolds, O., (1890). Second report of the committee appointed to investigate the action of waves and currents on the beds and foreshores of estuaries by means of working models. British Association Report. In: Reynolds, O., *Papers on Mechanical and Physical Subjects, Volume II, 1881-1900*; Cambridge University Press, 1901, 410-481.

Reynolds, O., (1891). Third report of the committee appointed to investigate the action of waves and currents on the beds and foreshores of estuaries by means of working models. British Association Report. In: Reynolds, O., *Papers on Mechanical and Physical Subjects, Volume II, 1881-1900*; Cambridge University Press, 1901, 482-518.

Richards, K.S., (1973). Hydraulic geometry and channel roughness - a non-linear system. *American Journal of Science*, **273**, 877-896.

Richards, K.S., (1982). *Rivers, Form and Process in Alluvial Channels.* Methuen & Co. Ltd, London, 361pp.

Richards, K.S., (1991). River channel form. In: *Geomorphological Techniques (2nd Edition)*, Ed., Goudie, A., with the assistance of Lewin, J., Burt, T., Richards, K.S., Whalley, B., Anderson, M. and Worsley, P., for the British Geomorphological Research Group, Unwin Hyman, London, 82-91.

Roberts, H.H., Wells, J.T. and Kahn, J.H., (1983). *AAPG Field Seminar Guide - Mississippi River.* American Association of Petroleum Geologists.

Robinson, P.T., McKee, E.H. and Moiola, R.J., (1968). Cenozoic volcanism and sedimentation, Silver Peak region, western Nevada and adjacent California. In: *Studies in Volcanology - A Memoir in Honour of Howel Williams*, Eds., Coats, R.R., Hay, R.L. and Anderson, C.A., Geological Society of America Memoir, 116, 577-611.

Rodda, J.C., (1969). The flood hydrograph. In: *Introduction to Physical Hydrology*, Ed., Chorley, R.J., Methuen & Co Ltd, London, 162-175.

Rossi, G., (1976). Carte géomorphologique d'Ambilobe. *Madagascar Révue de Géographie*, **28**, 155-171.

Rotnicki, K., (1983). Modelling past discharges of meandering rivers. In: *Background to Palaeohydrology*, Ed., Gregory, K.J., John Wiley and Sons, New York, 321-354.

Rotnicki, K., (1991). Retrodiction of palaeodischarges of meandering and sinuous alluvial rivers and its palaeohydrological implications. In: *Temperate Palaeohydrology, Fluvial Processes in the Temperate Zone during the last 15000 years*, Eds., Starkel, L., Gregory, K.J. and Thornes, J.B., John Wiley and Sons, Chichester, 431-471.

Rotnicki, K. and Borówka, R.K., (1985). Definition of subfossil meandering channels. *Earth Surface Processes and Landforms*, **10**, 215-225.

Rouse, H., (Ed.), (1950). *Engineering Hydraulics*. Proceedings of the fourth hydraulics conference, Iowa Institute of Hydraulics Research, June 1949, John Wiley and Sons, New York, 1039pp.

Rumsby, B.T. and Macklin, M.G., (1994). Channel and floodplain response to recent abrupt climate change: the Tyne basin, northern England. *Earth Surface Processes and Landforms*, **19**, 499-515.

Russ, D.P., (1982). Style and significance of surface deformation in the vicinity of New Madrid, Missouri. In: Investigations of the New Madrid, Missouri, earthquake region, Eds., McKeown, F.A. and Pakiser, L.C., *United States Geological Survey Professional Paper*, **1236H**, 95-114.

Russell, I.C., (1885). Geological history of Lake Lahontan, a Quaternary lake of northwestern Nevada. *United States Geological Survey, Monograph 11*, 288pp.

Rust, B.R., (1972). Structure and Process in a braided river. *Sedimentology*, **18**, 221-245.

Rust, B.R., (1981). Sedimentation in an arid-zone anastomosing fluvial system: Cooper's Creek, central Australia. *Journal of Sedimentary Petrology*, **51**, 745-755.

Ryall, A.S. and VanWormer, J.D., (1980). Estimation of maximum magnitude and recommended seismic zone changes in the western Great basin. *Bulletin of the Seismological Society of America*, **70**, 1573-1581.

Salter, T.M., Best, J.L. and Ashworth, P.J., (1993). Shale facies and geometries within gravelly braided alluvium, Unpublished BP Research report, 208pp.

Saltus, R.W., (1988a). Bouguer gravity anomaly map of Nevada. *Nevada Bureau of Mines and Geology*, Map 94A, scale 1:750,000.

Saltus, R.W., (1988b). Regional, residual and derivative gravity maps of *Nevada. Nevada Bureau of Mines and Geology*, Map 94B, scales 1:2,500,000 and 1:1,000,000.

Sanders, C.O. and Slemmons, D.B., (1979). Recent crustal movements in the Central Sierra Nevada-Walker lane region of California-Nevada - Part III, the Olinghouse fault Zone. *Tectonophysics*, **52**, 585-597.

Saucier, R.T., (1974). Quaternary geology of the lower Mississippi Valley. *Arkansas Archeological Survey, Research Series*, **6**, 26pp.

Saucier, R.T. and Smith, L.M., (1986). Geomorphic mapping and landscape classification of the Ouachita and Saline River Valleys, Arkansas. Nashville, Arkansas, Archeological Assessments Report 51, 13pp.

Savage, J.C., Cockerham, R.S., Estrem, J.E. and Moore, L.R., (1987). Deformation near the Long Valley Caldera, eastern California, 1982-1986. *Journal of Geophysical Research*, **92**, 2721-2746.

Schlee, J., (1957). Upland gravels of Southern Maryland. *Geological Society of America Bulletin*, **68**, 1371-1410.

Schlichting, H., (1968). *Boundary Layer Theory* (6th edition). McGraw-Hill, New York, 748pp.

Schoklitsch, A., (1962). *Handbuch des Wasserbaues*, 3rd edition. Springer-Verlag, Vienna.

Schumm, S.A., (1960a). The effect of sediment type on the shape and stratification of some modern fluvial deposits. *American Journal of Science*, **258**, 177-184.

Schumm, S.A., (1960b). The shape of alluvial channels in relation to sediment type. *United States Geological Survey Professional Paper*, **352-B**, 30pp.

Schumm, S.A., (1963). Sinuosity of alluvial rivers on the great plains. *Geological Society of America Bulletin*, **74**, 1089-1100.

Schumm, S.A., (1968). River adjustment to altered hydrologic regimen - Murrumbidgee River and paleochannels, Australia. *United States Geological Survey Professional Paper*, **598**, 65pp.

Schumm, S.A., (1972). Fluvial paleochannels. In: *Recognition of Ancient Sedimentary Environments*, Eds., Rigby, J.K. and Hamblin, W.K., Society Economic Paleontologists and Mineralogists Special Publication 16, 98-107.

Schumm, S.A., (1986). Alluvial river response to active tectonics. In: *Active Tectonics*, senior Ed., Wallace, R.E., National Academy Press, Washington, D.C., 80-94.

Schumm, S.A., (1993). River response to baselevel change: implications for sequence stratigraphy. *Journal of Geology*, **101**, 279-294.

Schumm, S.A. and Khan, H.R., (1972). Experimental study of channel patterns. *Geological Society of America Bulletin*, **83**, 1755-1770.

Schumm, S.A., Mosley, M.P. and Weaver, W.E., (1987). *Experimental Fluvial Geomorphology*. John Wiley and Sons, New York, 413pp.

Schumm, S.A., Watson, C.C. and Burnett, A.W., (1982). Phase 1: investigation of neotectonic activity within the Lower Mississippi Valley Division. United States Army Corps of Engineers, Vicksburg, Mississippi, Lower Mississippi Division, Potamology Program Report 2, 158pp.

Seager, W.R., Shafiquallah, M., Hawley, J.W. and Marvin, R., (1984). New K-Ar dates from basalts and the evolution of the southern Rio Grande rift. *Geological Society of America Bulletin*, **95**, 87-99.

Shepard, M.K., Arvidson, R.E., Caffee, M., Finkel, R. and Harris, L., (1995). Cosmogenic exposure ages of basalt flows: Lunar Crater volcanic field, Nevada. *Geology*, **23**, 21-24.

Shields, A., (1936). Anwendung der Aehnlichkeitsmechanik und der turbulenzforschung auf die geschiebebewegung (The application of dimensionless analysis and the investigation of turbulence and bedload movement). *Mitteilung der Preussischen versuchsanstalt fuer Wasserbau und Schiffbau*, Heft **26**, Berlin.

Shuster, M.W. and Steidtman, J.R., (1987). Fluvial-sandstone architecture and thrust-induced subsidence, northern Green River Basin, Wyoming. In: *Recent Developments in Fluvial Sedimentology*, Eds., Eth~~e~~ridge, F.G., Flores, R.M. and Harvey, M.D., Society of Economic Palaeontologists and Mineralogists Special Publication 39, 280-285.

Sieh, K.E. and Bursik, M., (1986). Most recent eruption of the Mono Craters, eastern central California. *Journal of Geophysics Research*, **91**, 12,539-12,571.

Singh, H., Parkash, B. and Gohain, K., (1993). Facies analysis of the Kosi megafan deposits. *Sedimentary Geology*, **85**, 87-113.

Slemmons, D.B., (1975). Cenozoic deformation along the Sierra Nevada province and Basin and Range province boundary. *California Geology Magazine*, **28**, No 5, 99-119.

Slemmons, D.B., (1977). State-of-the-art for assessing earthquake hazards in the United States, faults and earthquake magnitude. *United States Army Waterways Experimental Station, Soils and Pavement Laboratory*, Miscellaneous Paper 5-73-1, Report 6.

Slemmons, D.B., Gimlett, J.I., Jones, A.E., Greensfelder, R. and Koenig, J., (1964). Earthquake epicenter map of Nevada. *Nevada Bureau of Mines and Geology*, Map 29, scale 1,000,000.

Small, R.J., (1972). *The Study of Landforms*. Cambridge University Press, Cambridge, 486pp.

Smith, D.G., (1976). Effect of vegetation on lateral migration of anastomosed channels of a glacial meltwater river. *Geological Society of America Bulletin*, **87**, 857-860.

Smith, D.G., (1983). Anastomosed fluvial deposits: modern examples from Western Canada. In: *Modern and Ancient Fluvial Systems*, Eds., Collinson, J.D., and Lewin, J., International Association of Sedimentologists Special Publication 6, 405-420.

Somerville, M.R., Peppin, W.A. and VanWormer, J.D., (1980). An earthquake sequence in the Sierra Nevada-Great Basin Boundary Zone: Diamond Valley. *Bulletin of the Seismological Society of America*, **70**, 1547-1555.

Southard, J.B. and Boguchwal, L.A., (1990a). Bed configurations in steady unidirectional water flows. Part 2. Synthesis of flume data. *Journal of Sedimentary Petrology*, **60**, 658-679.

Southard, J.B. and Boguchwal, L.A., (1990b). Bed configurations in steady unidirectional water flows. Part 3. Effects of temperature and gravity. *Journal of Sedimentary Petrology*, **60**, 680-686.

Southard, J.B., Smith, N.D. and Kuhnle, R.A., (1984). Chutes and lobes: newly identified elements in braiding in shallow gravelly streams. In: *Sedimentology of Gravels and Conglomerates*, Eds., Koster, E.H. and Steel, R.J., Canadian Society of Petroleum Geology Memoir, **10**, 51-59.

Speight, J.G., (1965a). Meander spectra of the Angabunga River. *Journal of Hydrology*, **3**, 1-15.

Speight, J.G., (1965b). Flow and channel characteristics of the Angabunga River, Papua. *Journal of Hydrology*, **3**, 16-36.

Starkel, L., (1991). Long-distance correlation of fluvial events in the temperate zone. In: *Temperate Palaeohydrology: Fluvial Processes in the Temperate Zone During the last 15,000 Years*, Eds., Starkel, L., Gregory, K.J. and Thornes, J.B., John Wiley and Sons, Chichester, 473-495.

Starkel, L., Gregory, K.J. and Thornes, J.B., (1991) (Eds). *Temperate Palaeohydrology: Fluvial Processes in the Temperate Zone During the Last 15,000 years.* John Wiley & Sons, Chichester, 548pp.

Steel, R.J. and Thompson, D.B., (1983). Structures and textures in Triassic braided stream conglomerates ('Bunter' Pebble Beds) in the Sherwood Sandstone Group, North Staffordshire, England. *Sedimentology*, **30**, 341-367.

Stein, R.S. and Barrientos, S.E., (1985). Planar high-angle faulting in the Basin and Range: geodetic analysis of the 1983 Borah Peak, Idaho, earthquake. *Journal of Geophysical Research*, **90**, 11,355-11,366.

Stewart, J.H., (1980). *Geology of Nevada. Nevada Bureau of Mines and Geology Special Publication* 4, 136pp.

Stine, S., (1990). Late Holocene fluctuations of Mono Lake, eastern California. In: Paleoclimates: the record from lakes, ocean and land, Eds., Meyers, P.A. and Benson, L.V., *Palaeogeography, Palaeoclimatology, Palaeoecology*, **78**, 333-381.

Stuart, J.T., (1965). Hydrodynamic stability. *Applied Mechanics Reviews*, **18**, 523-531.

Stuiver, M., Long, A., Kra, R.S. and Devine, J.M., (1993). Calibration. *Radiocarbon*, **35 (1)**, 244pp.

Summerfield, M.A., (1991). *Global Geomorphology: An Introduction to the Study of Landforms*. Longman, Harlow, 537pp.

Szumanski, A., (1983). Palaeochannels of large meanders in the river valleys of the Polish Lowland. *Quaternary Studies in Poland*, **4**, 207-216.

Talma, A.S. and Vogel, J.C., (1993). A simplified approach to calibrating ^{14}C dates. *Radiocarbon*, **35 (2)**, 317-322.

Tani, I., (1969). Boundary layer transition. *Annual Review of Fluid Mechanics*, **1**, 169-196.

Ten Brink, N., (1974). Glacio-isostasy: new data from West Greenland and geophysical implications. *Geological Survey of America Bulletin*, **85**, 219-228.

Thomson, J., (1879). Flow round river bends. *Proceedings of the Institute of Mechanical Engineers*, 456-460.

Thornbury, W.C., (1969). *Principles of Geomorphology*, 2nd Edition. Wiley and Sons, New York, 594pp.

Tiffany, J.B. and Nelson, G.A., (1939). Studies of meandering of model streams. *Transactions of the American Geophysical Union* (Part IV), 644-649.

Törnqvist, T.E., (1994). Middle and late Holocene avulsion history of the River Rhine (Rhine-Meuse delta, Netherlands). *Geology*, **22**, 711-714.

Törnqvist, T.E. and Bierkens, M.F.P., (1994). How smooth should curves be for calibrating radiocarbon ages? *Radiocarbon*, **36 (1)**, 11-26.

Travis, C.J. and Nunn, J.A., (1994). Stratigraphic architecture of extensional basins: insights from a numerical model of sedimentation in evolving half grabens. *Journal of Geophysical Research*, **B99**, 15,653-15, 666.

Ulrich, F.P., (1941). The Imperial Valley earthquakes of 1940. *Bulletin of the Seismological Society of America*, **31**, 13-32.

Trexler, D.T., Flynn, T., Koenig, B.A. and Ghusn, G., (1983). Map of the Geothermal Resources of Nevada. *United States Department of Energy*, scale 1:500,000.

Unruh, J.R., (1991). The uplift of the Sierra Nevada and implications for late Cenozoic epeirogeny in the western Cordillera. *Geological Society of America Bulletin*, **103**, 1395-1404.

Vail, P.R., Mitchum, R.M. Jr. and Thompson, S., (1977). Seismic stratigraphy and global changes of sea level, Part 4: global cycles of relative changes of sea level. In: *Seismic Stratigraphy - Applications to Hydrocarbon Exploration*, Ed., Payton, C.E., American Association of Petroleum Geologists Memoir 26, 83-97.

VanWormer, J.D. and Ryall, A., (1980). Sierra Nevada-Great Basin boundary zone-earthquake hazard related to structure, active tectonic processes, and anomalous patterns of earthquake occurrence. *Seismological Society of America Bulletin*, **70**, 1557-1572.

Vargaftik, N.B., Volkov, B.N. and Voljak, L.D., (1983). International tables of the surface tension of water. *Journal of Physical and Chemical Reference Data*, **12**, 817-820.

Veldkamp, A., (1992). A 3-D model of Quaternary terrace development, simulations of terrace stratigraphy and valley asymmetry: a case study for the Allier terraces (Limagne, France). *Earth Surface Processes and Landforms*, **17**, 487-500.

Vernon-Harcourt, L.F., (1889). The principles of training rivers through tidal estuaries, as illustrated by investigations into the methods of improving the navigation channels of the estuary of the Seine. *Proceedings of the Royal Society*, **45**, 504.

Vogel, J.C., Fuls, A. and Visser, E., (1993). Pretoria calibration curve for short-lived samples, 1930-3350 BC. *Radiocarbon*, **35 (1)**, 73-85.

Wadia, D.N., (1975). *Geology of India*. Tata McGraw-Hill, New Delhi, 508pp.

Wahl, K.L., (1984). Evolution of the use of channel cross-section properties for estimating streamflow characteristics. *United States Geological Survey Water Supply Paper*, 2262, 53-66.

Wallace, R.E., (1977). Profiles and ages of young fault scarps, north-central Nevada. *Geological Society of America Bulletin*, **88**, 1267-1281.

Wallace, R.E., (1984). Patterns and timing of Late Quaternary faulting in the Great Basin Province and relation to some regional tectonic features. *Journal of Geophysical Research*, **89**, B7, 5763-5769.

Walsh, J.J. and Watterson, J., (1987). Distributions of cumulative displacement and seismic slip on a single normal fault surface. *Journal of Structural Geology*, **9**, 1039-1046.

Warburton, J. and Davies, T.R.H., (1994a). Variability of bedload transport and channel morphology in a braided river hydraulic model. *Earth Surface Processes and Landforms*, **19**, 403-421.

Warburton, J. and Davies, T.R.H., (1994b). Variability of bedload transport and channel morphology in a braided river hydraulic model - correction. *Earth Surface Processes and Landforms*, **19**, Issue 8, ii.

Weaver, W.E., (1984). Experimental study of alluvial fans. *Unpublished Ph.D dissertation, Colorado State University.*, Fort Collins, 423pp.

Webber, E.E. and Roberts, J.W., (1981). Floodflow characteristics related to channel geometry in Ohio. *United States Geological Survey Open-file Report*, 81-1105, 28pp.

Weihaupt, J.G., (1989). *Disparities in the Forms of River Meanders and Oxbow Lakes (A Case Study).* Water Resources Publications, Littleton, 186pp.

Wells, N.A. and Dorr, J.A., (1987a). Shifting of the Kosi River, northern India. *Geology*, **15**, 204-207.

Wells, N.A. and Dorr, J.A., (1987b). A reconnaissance of sedimentation on the Kosi alluvial fan of India. In: *Recent Developments in Fluvial Sedimentology*, Eds., Ethridge, F.G., Flores, R.M. and Harvey, M.D., Society of Economic Paleontologists and Mineralogists Special Publication, 39, 51-61.

Wescott, W.A., (1993). Geomorphic thresholds and complex response of fluvial systems - some implications for sequence stratigraphy. *American Association of Petroleum Geology Bulletin*, **77**, 208-218.

Williams, G.P., (1978). Bank-full discharge of rivers. *Water Resources Research*, **14**, 1141-1154.

Williams, G.P., (1983a). Paleohydrological methods and some examples from Swedish fluvial environments, I - cobble and boulder deposits. *Geografiska Annaler*, **65A**, 227-243.

Williams, G.P., (1983b). Improper use of regression equations in earth sciences. *Geology*, **11**, 195-197.

Williams, G.P., (1984a). Paleohydrological methods and some examples from Swedish fluvial environments II - river meanders. *Geografiska Annaler*, **66A**, 89-102.

Williams, G.P., (1984b). Paleohydrologic equations for rivers. In: *Developments and Applications of Geomorphology*, Eds., Costa, J.E. and Fleischer, P.J., Springer-Verlag, Berlin and New York, 343-367.

Williams, G.P., (1984c). Comments and Reply on "improper use of regression equations in earth sciences". *Geology*, **12**, 125-126.

Williams, G.P., (1986). River meanders and channel size. *Journal of Hydrology*, **88**, 147-164.

Williams, G.P., (1988). Paleofluvial estimates from dimensions of former channels and meanders. In: *Flood Geomorphology*, Eds., Baker, V.R., Kochel, R.C. and Patton, P.C., John Wiley and Sons, New York, 321-334.

Williams, M.A.J., Dunkerley, D.L., Deckker, P.De., Kershaw, A.P. and Stokes, T., (1993). *Quaternary Environments*, Edward Arnold, London, 329pp.

Williams, P.F. and Rust, B.R., (1969). The sedimentology of a braided river. *Journal of Sedimentary Petrology*, **39**, 649-679.

Williams, R.B.G., (1984). *Introduction to Statistics: for Geographers and Earth Scientists*. Macmillan, London, 349pp.

Williams, V.S., (1982). Tectonic tilting of mountain front alluvial fans near the Sapta Kosi gorge, eastern Nepal. In: *Himalaya Landforms and Processes*, Eds., Verma, V.K. and Saklani, P.S., Today and Tomorrow Printers, New Delhi, 115-132.

Willis, B.J., (1989). Palaeochannel reconstructions from point bar deposits: a three-dimensional perspective. *Sedimentology*, **36**, 757-766.

Willis, B.J., (1993). Interpretation of bedding geometry within ancient point-bar deposits. In: *Alluvial Sedimentation*, Eds., Marzo, M. and Puigdefabregas, C., Special Publication of the International Association of Sedimentologists 17, Blackwell, 101-114.

Wintle, A.G., (1993). Luminescence dating of aeolian sands: an overview. In: *The Dynamics and Environmental Context of Aeolian Sedimentary Systems*, Ed., Pye, K., Geological Society Special Publication, **72**, 49-58.

Wintle, A.G., Lancaster, N. and Edwards, S.R., (1994). Infrared stimulated luminescence (IRSL) dating of late-Holocene aeolian sands in the Mojave desert, California, USA. *The Holocene*, **4**, 74-78.

Wolman, M.G. and Brush, L.M. Jr., (1961). Factors controlling the size and shape of stream channels in coarse noncohesive sand. *United States Geological Survey Professional Paper*, **282G**, 183-210.

Wolman, M.G. and Miller, J.P., (1960). Magnitude and frequency of forces in geomorphic processes. *Journal of Geology*, **68**, 54-74.

Wood, S.H., (1977). Distribution and radiocarbon dating of late Holocene tephra, Mono and Inyo Craters, eastern California. *Geological Scociety of America Bulletin*, **88**, 89-95.

Woodyer, K.D., (1975). Concave-bank benches on the Barwon River, New South Wales. *Australian Geography*, **13**, 3-15.

Woodyer, K.D., Taylor, G. and Crook, A.W., (1979). Depositional processes along a very low-gradient, suspended-load stream: the Barwon River, New South Wales. *Sedimentary Geology*, **22**, 97-120.

Woolfe, K.J., (1992). Complex sand sheets from non-avulsive meandering streams. Fifth meeting of the Australia and New Zealand geomorphology Research Group, Abstract Volume, 7.

Woolfe, K.J., Arnot, M.J., Barrett, P.J. and Francis, J.E., (1991). Contrasting fluvial styles in the Weller Coal Measures at Allan Hills. Sixth International Symposium on Antarctic Earth Sciences, Tokyo, Abstract volume, 668-673.

Yalin, M.S., (1963). An expression for bed-load transportation. *Journal of the Hydraulics Division, Proceedings of the American Society of Civil Engineers*, **89**, 221-250.

Yalin, M.S. (1971). *Theory of Hydraulic Models*. Macmillan, London, 266pp.

Yalin, M.S., (1992). *River Mechanics*, Pergamon, Oxford, 220pp.

Youd, T.L. and Wieczorek, G.F., (1982). Liquefaction and secondary ground failure. In: The Imperial Valley, California, Earthquake of October 15, 1979, *United States Geological Survey Professional Paper,* **1254**, 223-246.

Young, W.J. and Davies, T.R.H., (1990). Prediction of bedload transport rates in braided rivers: a hydraulic model study. *New Zealand Journal of Hydrology,* **29**, 75-92.

Young, W.J. and Davies, T.R.H., (1991). Bedload transport processes in a braided gravel-bed river model. *Earth Surface Processes and Landforms,* **16**, 499-511.

Zeller, J., (1967). *Meandering channels in Switzerland.* International Association Scientific Hydrologists, Publication No. 75, 174-186.

Zhang, P., Slemmons, D.B. and Mao, F., (1991). Geometric pattern, rupture termination and fault segmentation of the Dixie Valley-Pleasant Valley active normal fault system, Nevada, U.S.A. *Journal of Structural Geology,* **13**, 165-176.

Zimmerman, R.C., Goodlett, J.C. and Comer, G.H., (1967). The influence of vegetation on channel form of small streams. *Publication of the International Association of Scientific Hydrology,* **75**, 255-275.

Zimpfer, G.L., (1975). Development of laboratory river channels. *Unpublished M.Sc thesis,* Colorado State Univ., Fort Collins, Col., 111pp.

Zoback, M.L., (1992a). First- and second-order patterns of stress in the lithosphere: the world stress map project. *Journal of Geophysical Research,* **97**, **B8**, 11,703-12,014.

Zoback, M.L., (1992b). Stress field constraints on intraplate seismicity in eastern North America. *Journal of Geophysical Research,* **B97**, 11,761-11,782.

Zoback, M.L. and Zoback, M.D., (1989). Tectonic stress field of the continental United States. In: *Geophysical Framework of the Continental United States,* Eds., Pakiser, L.C. and Mooney, W.D., Geological Society of America Memoir 172, 523-539.

Zwamborn, J.A., (1967). Solution of river problems with movable bed hydraulic models, Symposium paper S.24, Council for Scientific and Industrial Research, Pretoria, South Africa, 40pp.

Appendix A. Example of a gamma function fit to a scaled prototype hydrograph

This program is written in Microsoft QuickBASIC for the Macintosh.

```
REM Example of gamma function fitting to a scaled prototype hydrograph.
OPTION BASE 1
DEFINT a-z
DIM Qs! (12): DIM Qa! (12)
FOR c=1 TO 12
  READ Qa! (c)
NEXT c
REM Data from a scaled prototype hydrograph
DATA  0.534,1.915,3.689,4.440,2.430,1.915,1.471,1.096,0.785,0.534,0.534,0.5
E1!=10000!: F1!=10000!
m!=.1

REM Values for t are adjusted so that they calculate values at the original points
FOR a = 1 TO 200
t1!=20/m!
Qo!=3.94/((20)^m!*EXP(-m!))
  FOR b=1 TO 12
  t=5
  Qs! (b)=(Qo!*(t)^m!*EXP(-t/t1!))+.5
  IF t>=25 THEN
    t=t+10
  ELSE
    t=t+5
  END IF
  NEXT b
  REM read through the array and compare with original hydrograph
  E!=0!: F!=0!
  FOR d=1 TO 12
    z!=(Qa! (d)-Qs! (d))^2
```

```
      y!=ABS(Qa! (d)-Qs! (d))
      E!=E!+z!
      F!=F!+y!
   NEXT d
IF E!<E1! THEN
   E1!=E!: Em!=m!: Et1!=t1!: EQo!=Qo!
END IF
IF F!<F1! THEN
   F1!=F!: Fm!=m!: Ft1!=t1!: FQo!=Qo!
END IF
m!=m!+.1
PRINT "a" a
PRINT "E1!" E1! "Em!" Em! "Et1!" Et1! "EQo!" EQo!
PRINT "F1!" F1! "Fm!" Fm! "Ft1!" Ft1! "FQo!" FQo!
NEXT a
INPUT "press return to continue", dummy$
END
```

Appendix B. Explanation of the Meander Morphometry Analysis Program (M-MAP)

B.1 Introduction

The M-MAP program is written in Microsoft QuickBASIC for the Apple Macintosh, and is provided on disk in the enclosed folder. The program analyses a digitised set of (x,y) points that represent either the meander thalweg or the meander centreline. The following data are then generated; direction angles, change of direction angle with distance, curvature angles, inflection points, and then for each bend; total curvature, maximum point curvature, mean curvature, wavelength, arc length, sinuosity, arc height and the radius of curvature. Radius of curvature and arc height are only calculated for bends with an inflection spacing of 4 or more chord lengths. The other parameters are calculated for all bends.

Two columns of values are read from any file that has comma separators. All DOS based ASCII (text) files are in this format but Macintosh files must be saved in comma separated values (CSV) format. The program can accept files with or without headers as long as the header is on the first line. The example datasets used here were digitised using the NIH Image package. The export file format for Image is Microsoft Excel, and the files must therefore be pulled into Excel and re-saved in the CSV format, before M-MAP can read them.

The digitised trace can be plotted to the screen and either the direction or curvature angles added, along with the inflection angles, the arc height and the radius of curvature. Pressing 'command-shift 3' generates a snapshot to file, with the files automatically named sequentially, starting from 'Picture 1'. Importing these images into MacPaint or any drawing package that will accept MacPaint files (almost all do) will permit printing from within the application.

The individual datasets (e.g. Mean curvature) can be exported by checking them in the Data menu and then selecting Export from the File menu. Each dataset is saved into a separate file in comma separated form and can be imported into most application programs as either ASCII or CSV data.

B.2 Program structure and logic

The M-MAP program has a very simple structure (Fig. B.1), and is essentially composed of blocks of code, organised in a linear fashion, with relatively few control

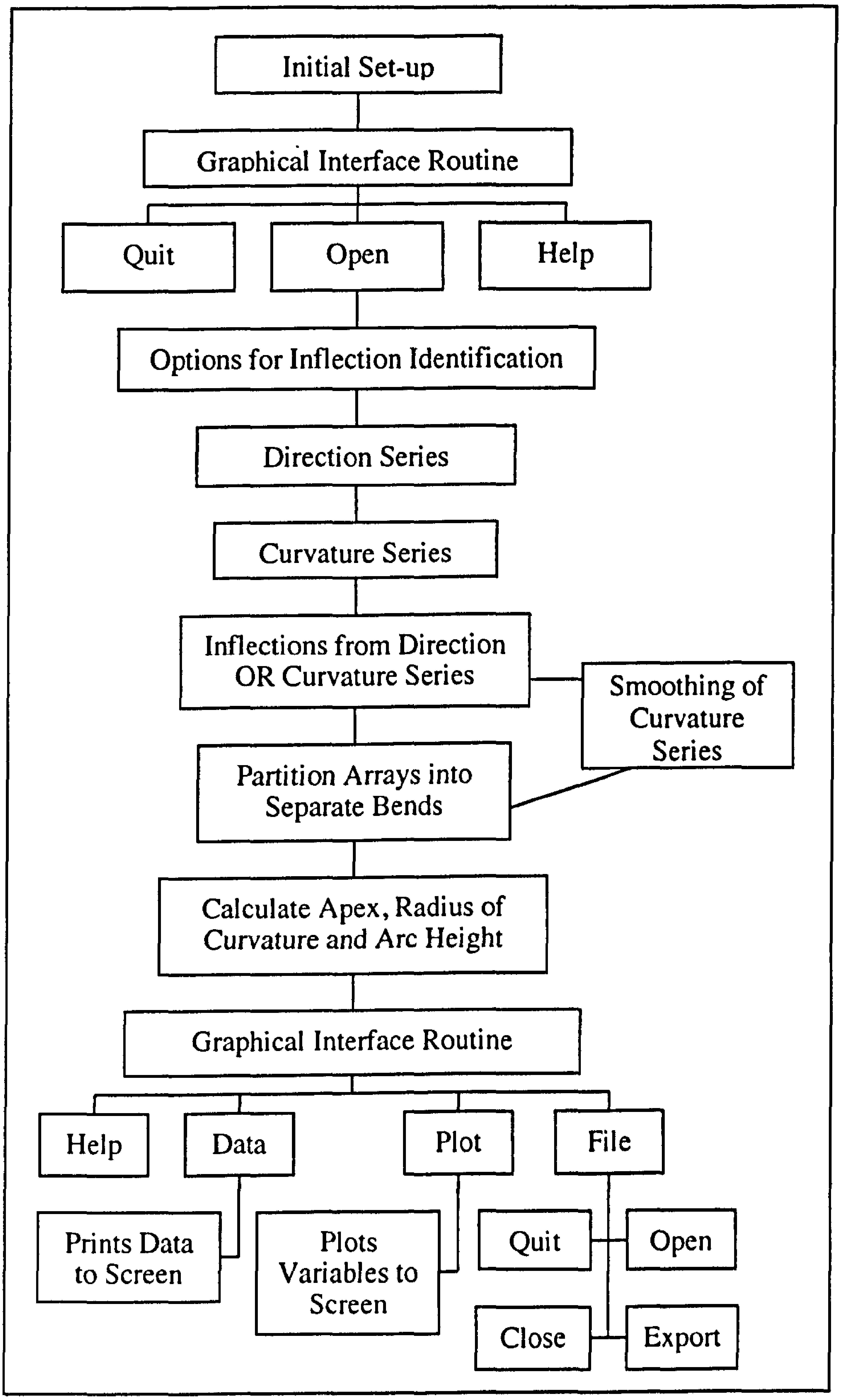

Figure B.1. Flow chart for Meander Morphometry Analysis Program (M-MAP) loops between blocks. The 'Graphical Interface Routine' shows the options available at any point and allows the user to operate the program almost entirely from pull-down menus, or quick-keys. Three options are available at first, 'Help', 'Open' and 'Quit'. The 'Help' menu outlines the following; range of data that the program calculates, how to import and export files, and how to plot and export graphical data. The 'Quit' option is self-explanatory and the 'Open' option brings up the standard Macintosh dialogue box. Once a file is opened the user gets a series of 'Options for Inflection Identification' which requires yes/no (y/n) input. This is the only part of the program that is not menu driven. The options given are to use either the direction series or the curvature series. If the direction series is chosen, an option is given to use a horizontal line or a regression line through the data. Alternatively, if the curvature series is chosen a smoothing option is offered. For the direction angles, the regression line may be different from the valley direction or regional slope, and, if the user wishes to adopt one of these, it is fairly easy to modify the source code by inputting different values for gradient and the y-axis intercept.

The direction and curvature series are then calculated and the inflection points identified. If chosen, the smoothing technique works by identifying inflection points that are adjacent to one another, i.e. are only one chord length apart (see Fig. B.2). These small wavelength inflections are normally due to digitising errors. When two adjacent points have inflections, the program loops from the inflection routine back to the curvature series and calculates the gradients for a new chord between the points either side of the inflections (see Fig. B.2). New angles are calculated for these lines and the program returns to the inflection routine. There are a number of advantages of this simple smoothing technique over more complex routines. Most significantly, there is no dramatic change in bend geometry (and the majority of points remain the same), which can occur with many smoothing techniques. In addition, no points are removed from the analysis, as may happen if a filtering routine is passed across the data. A smaller number of points will generally lead to a loss of accuracy in the radius of curvature routine.

After the inflection points are chosen, total curvature, maximum point curvature, mean curvature, wavelength, arc length, and sinuosity are calculated for each bend. The arrays containing information on 'geometric properties' are then partitioned into separate bends and are used to calculate the arc height and radius of curvature. All bends under four chord lengths in size are ignored since radius of curvature can not be accurately calculated for these.

Arc height is redefined as the perpendicular distance from the line that characterises the chord between consecutive inflection points, and the apex of the bend (see Fig. 6.10). The apex of a bend is defined within the program as the intersection of the arc height line with the meander arc. To calculate radius of curvature, a polygon is

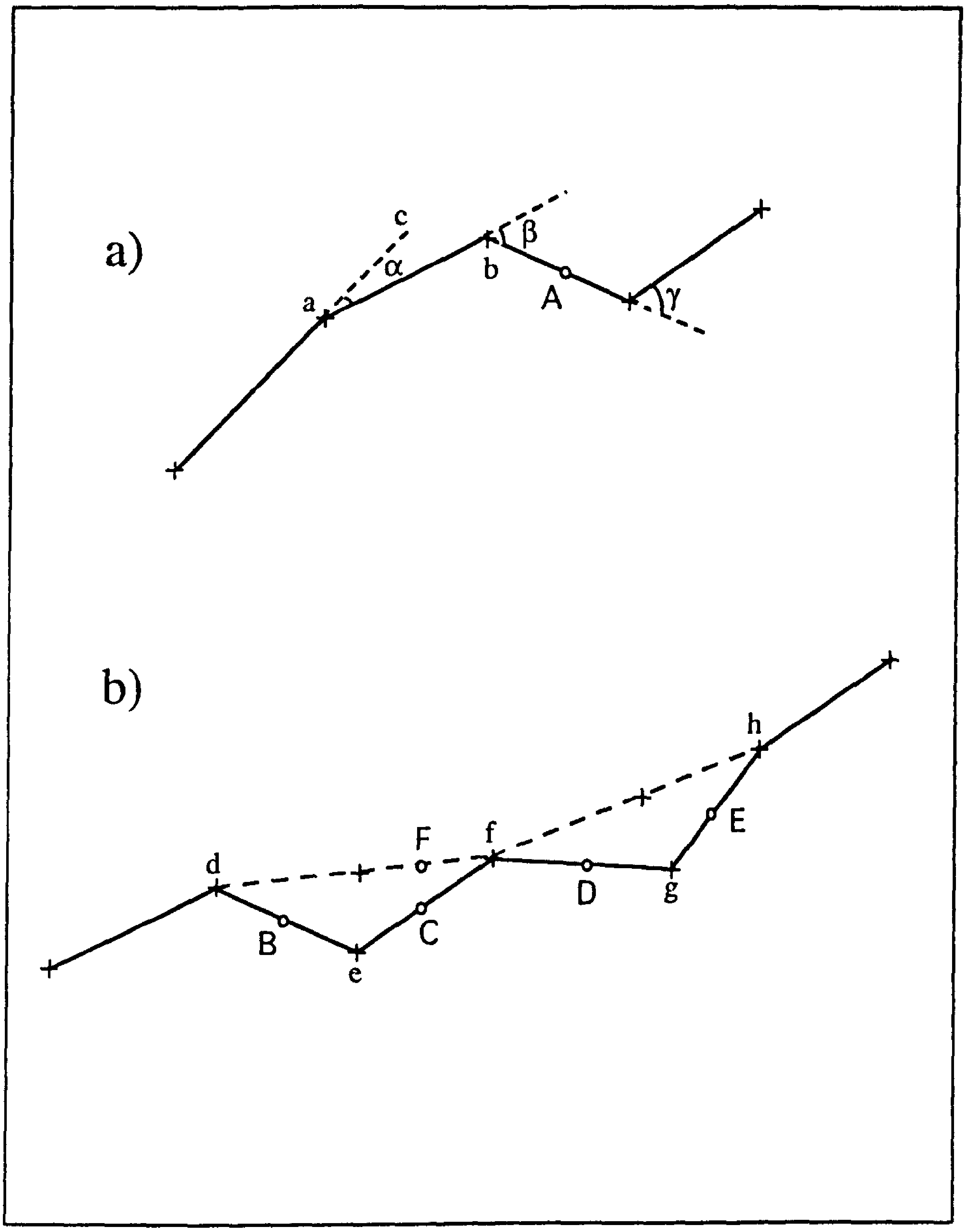

Figure B.2. Explanation of inflection prediction and the smoothing routine, for the M-MAP program.
a) A digitised meander trace, with individual (x,y) points (marked by crosses) and their associated chords. Points were digitised from left to right. The previous chord is projected to the next chord, so that curvature angles (α, β, γ) can be calculated. If the projected line (ac) is higher than the associated chord line (ab) then the angle is given a negative sign. Otherwise, the angle is taken as positive (e.g. γ). Inflections are taken at the mid-point, between curvature angles of different sign (A).
b) Small fluctuations due to digitising can cause successive points to have inflections (B, C, D, E). The smoothing technique works by drawing a new chord (df), between the (x,y) points either side of the inflections, and then re-analysing the trace for inflections. For the line df the inflections are entirely removed. If inflection points D and E are also smoothed, the new line (fh) produces an inflection point at F.

formed by the intersection of the orthogonals to the chords between points. The polygon is broken into triangles around any point that lies within the polygon (Fig. B.3a). The centre and area of each triangle can then be found (Fig. B.3b) and resolving these areas around the arbitrary point, gives the centre of the polygon, which corresponds to the mean centre of bend curvature. Radius of curvature is the distance from the mean centre of bend curvature to the apex (Fig. 6.13). The program then exits to the 'Graphical Interface Routine' again. Numeric data and graphics can be printed to screen and subsequently exported.

B.3 Notes for M-MAP Version 1.0

This is a copy of the 'Read Me' file supplied on disk with the M-MAP program (folder at back).

Double click on the 'M-MAP1.0 Apl' icon to launch the program. A series of menus come up, above a blank window. The on-line help can be used at any stage and can be accessed through the Special menu. To open a file simply go to the File menu and choose Open which produces the standard Macintosh dialog box. Several test files are provided, but other files can be imported very easily. See the help menu and the documentation for further details. The source code is also provided in Microsoft word format. The file 'shortlib' can not be opened separately but is used by the program. The program will run on Power-Macs, although 'modern memory manager' needs to be turned off, and the extensions may need to be temporarily disabled by holding down the shift key while starting the computer.

B.3.1 Known bugs / errors

Most of the test examples work well, however there are a number of known problems. One or two of the lines that connect the radius of curvature plots to the meander trace, are occasionally plotted incorrectly. This may also happen with the curvature and directional series plots. These are plotting errors and do not affect the results. Inflection identification using the radius of curvature routine appears to work very well. Theoretically, taking the difference in angles between adjacent directional angles, should produce exactly the same results as using the curvature routine. The magnitudes are correct if b! (the regression gradient) is set the same (Note: this option is offered), although a few of the signs (+ve and -ve) and therefore the directions do occasionally vary. The direction routine is presented by way of example, but generally the curvature routine ought to be used. The most serious error appears to be generated by the smoothing routine. Rarely, M-MAP fails to pick up an inflection after smoothing. An

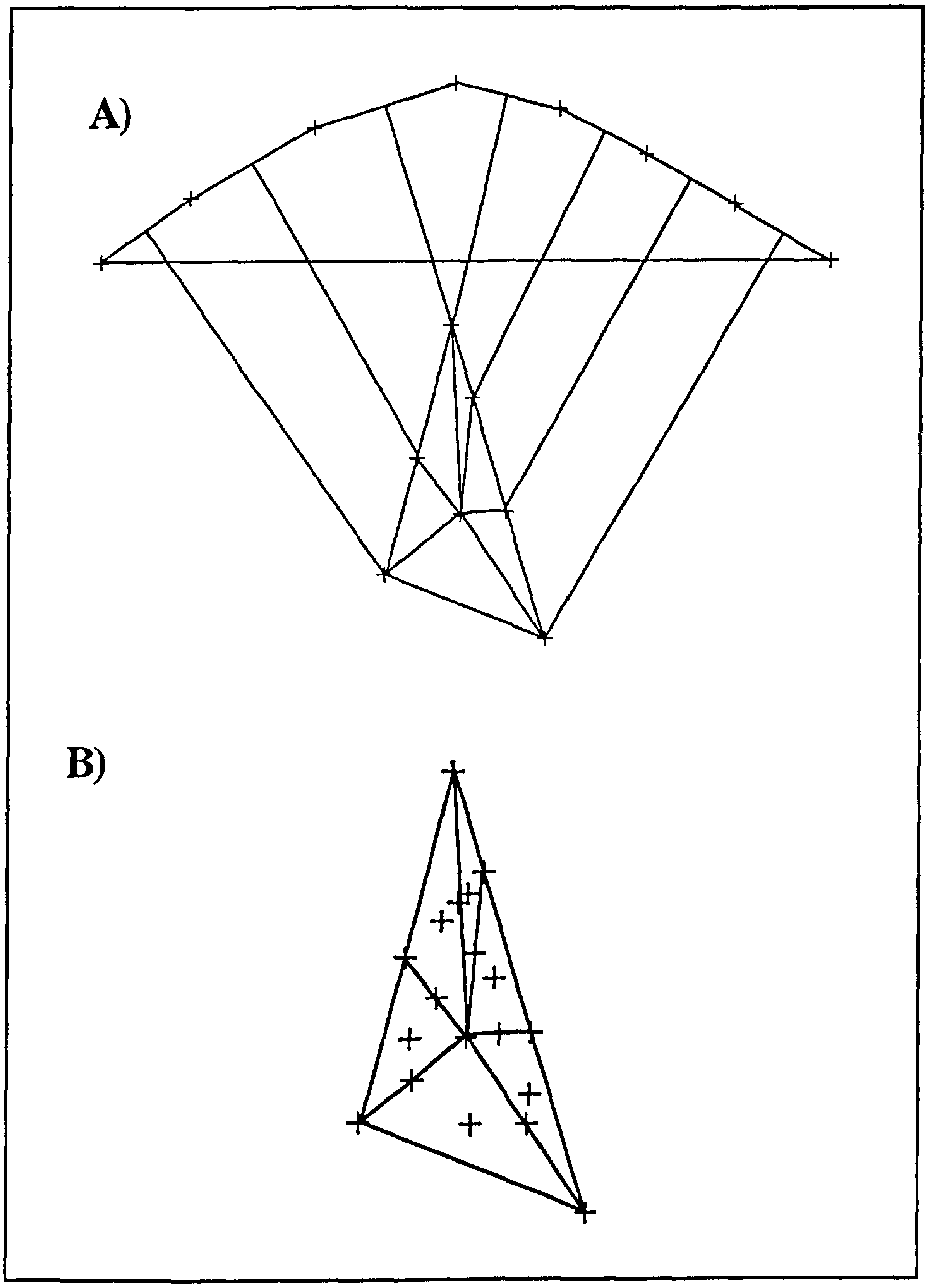

Figure B.3. Solving for the centre of a polygon. A) The intersection of the orthogonals from a digitised meander arc form a polygon, which in this case is a triangle. A point is picked that lies within the polygon, by taking three points (e.g. first and last, and a central point) and finding the centre of the resulting triangle. The polygon is then broken down into a series of triangles, by linking every point of the polygon to the point that lies within the triangle. B) The centre of each triangle, and the area of each triangle are calculated, and the areas are considered as weights, hanging from the centre of each triangle. These weights are then resolved relative to any point, to give the centre of the polygon. Note: In this simplified case where the polygon is a triangle, the centre of the polygon, exactly matches the centre of the triangle.

example of this is file 'Test Z' where one of the central bends can clearly be seen to inflect (Note: the radius of curvature routine plots almost equally on either side of the meander trace).

B.3.2 Program limitations

The program is currently configured to accept a maximum file size of 200 (x,y) points. This can be changed by altering the relevant line of code and recompiling. Microsoft QuickBASIC for the Macintosh has serious memory limitations, and therefore the program cannot accept large data files. This is not an inherent problem in the code, and porting the program to another language would solve the problem. Another possible adaptation would be to write and retrieve data from disk. Due to memory limitations, all numbers are in single-precision format. With small numbers this can lead to loss of precision and 'division by zero' errors. Numeric input, should be scaled up into the range of hundreds or thousands, and the output should be scaled back down. Some of the test examples give memory errors (Type 7 errors) if the smoothing option is not chosen.

Appendix C. Additional ground surveys of Carson River channel belt meander bends

This appendix contains additional cross-sections of meander bends from the Carson River channel belts. Each survey represents a single vibracore site.

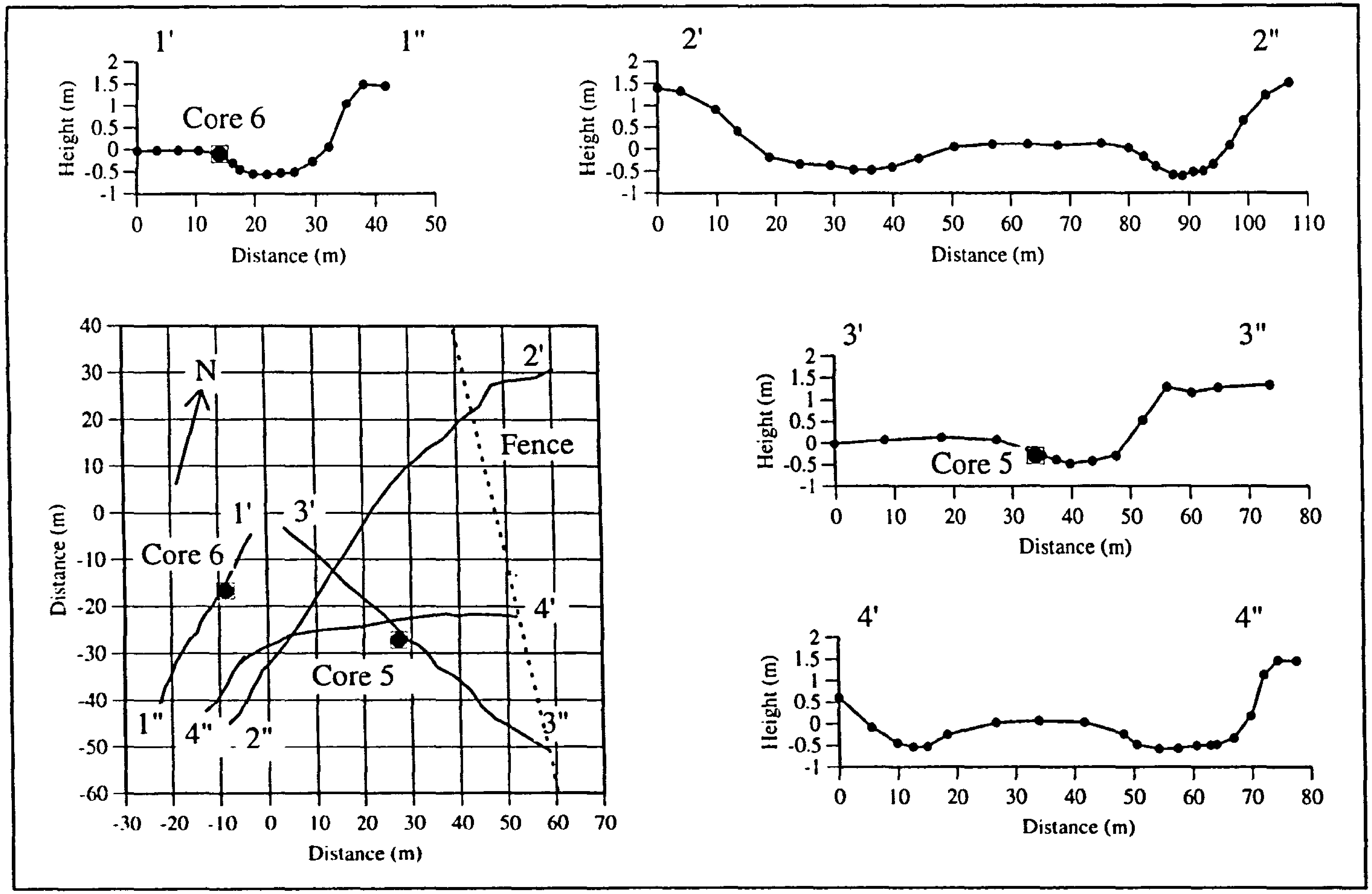

Figure C.1. Channel cross-sections and core sites for vibracore site D, channel belt 3. See Figure 7.12 for vibracore localities.

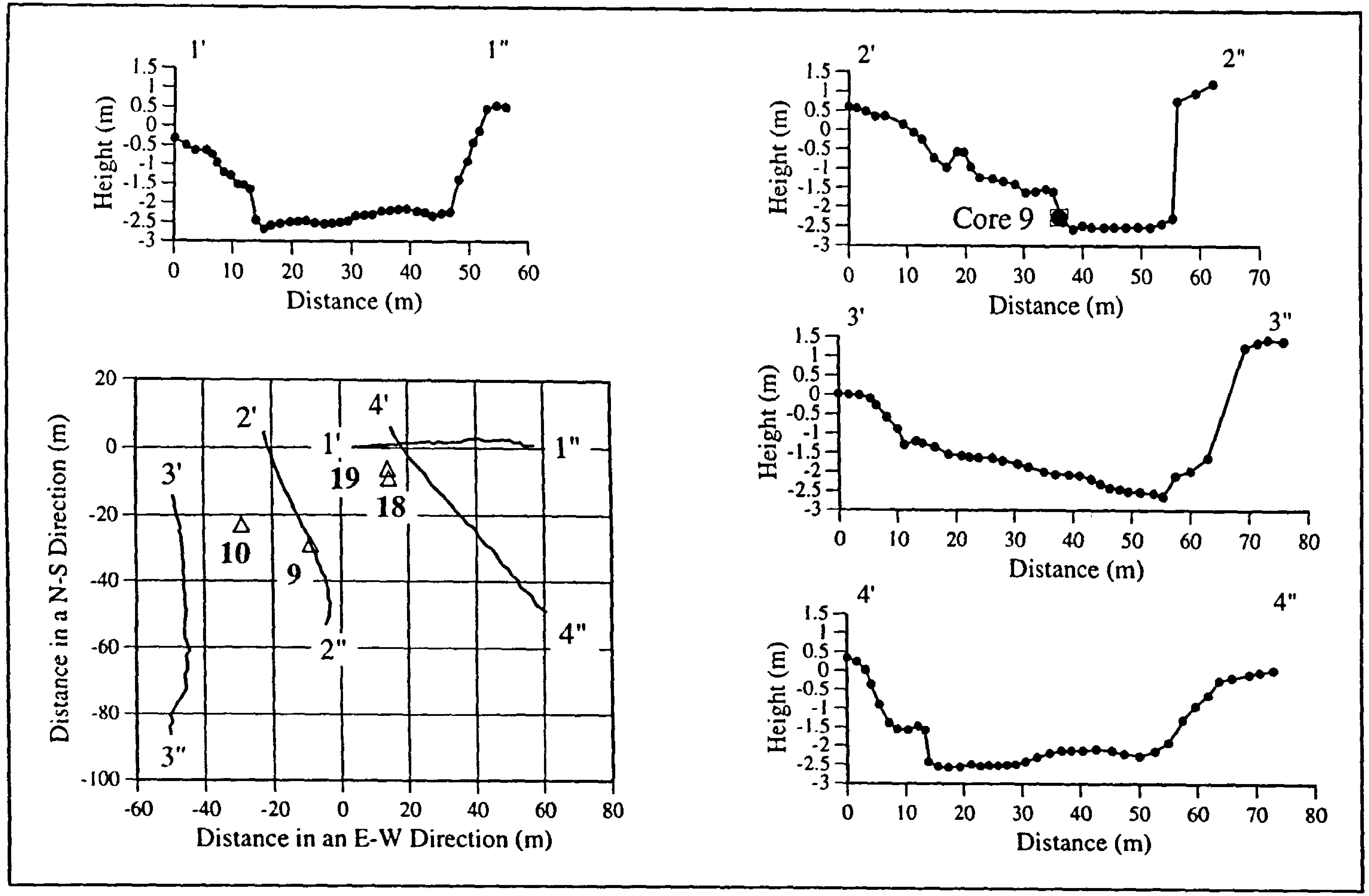

Figure C.2. Channel cross-sections and core sites for vibracore site C, modern point-bar. See Figure 7.12 for vibracore localities.

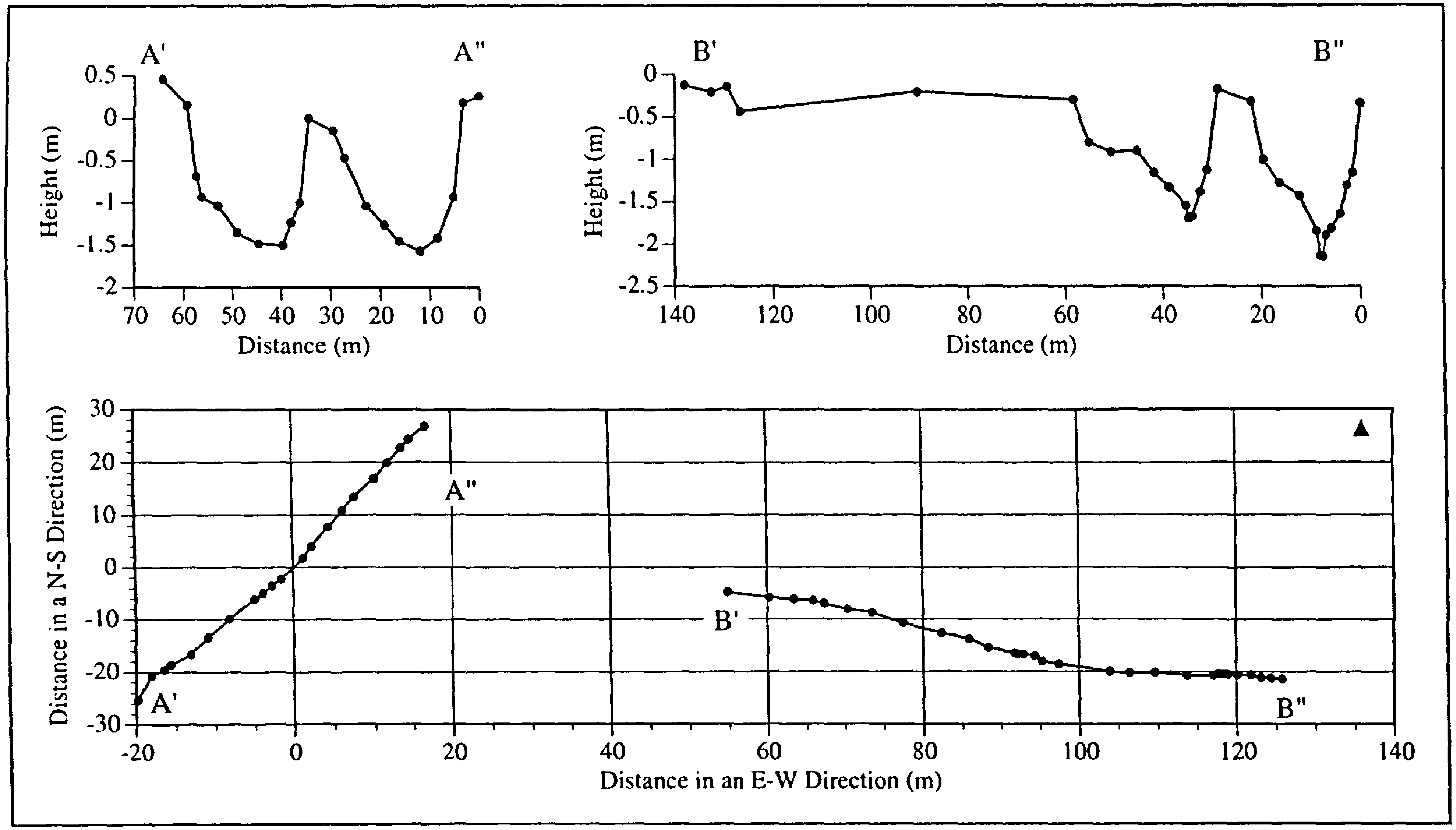

Figure C.3. Channel cross-sections for channel belt 5, Vibracore site B. See Figure 7.12 for vibracore localities.

A

B

C

D

E

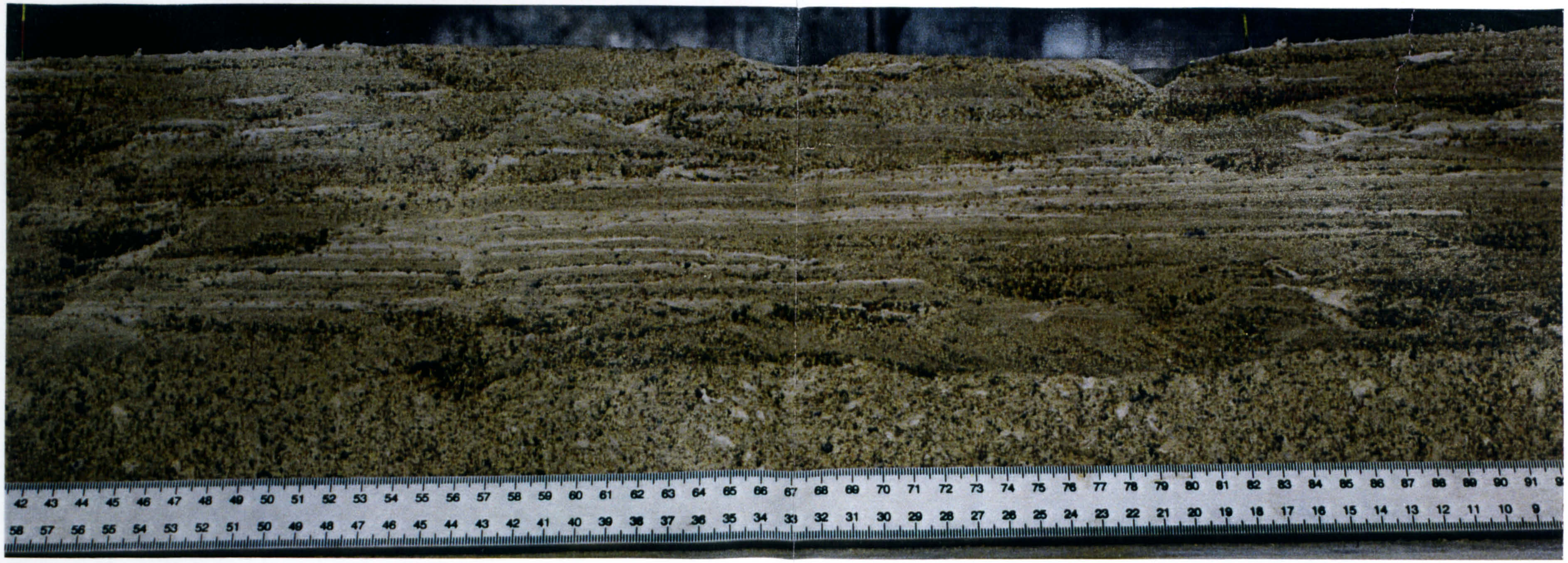

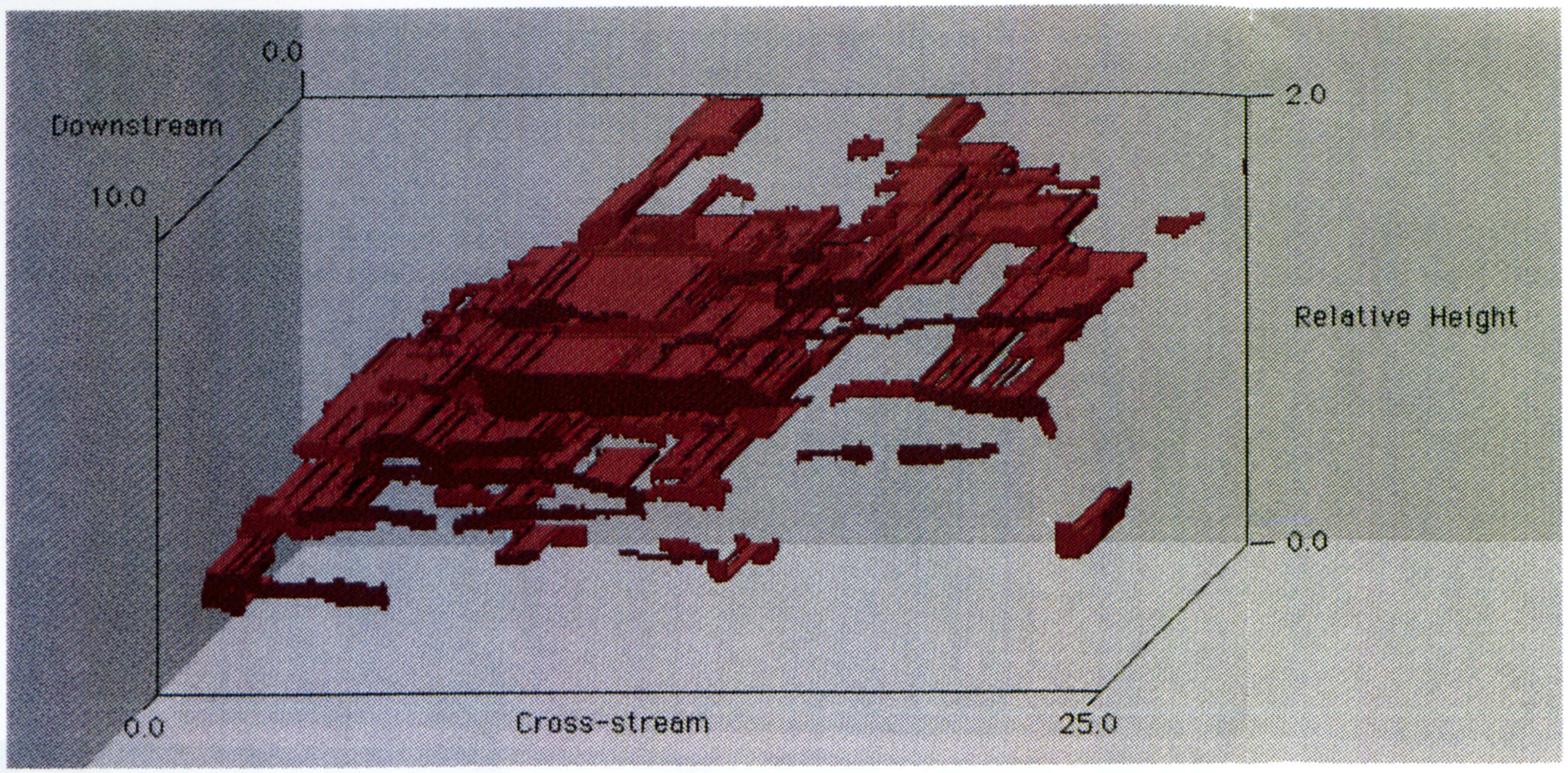

Enclosure 1. Illustration of 2D to 3D dimensionality correction. Sediment faces A-E are spaced at 2.5 cm intervals downstream from section A. At this small sampling interval some units can be clearly traced between sections, most notably the longer splays. In order to produce a 3D block model (diagram at lower left), the fine grained (white) units were digitised and a simple linear interpolation used to link sections. The 3D block diagram shows that a large number of the longer fine grained units are linked between sections and are therefore over represented in the resulting probability density function (PDF), while many of the smaller units are linked by very few or no sections. The block diagram represents the same dimensions as the sections, although the axes numbers do not represent specific units.